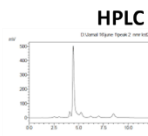UNIVERSITÀ
DI PAVIA

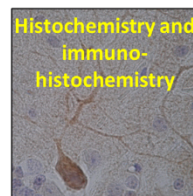*Dipartimento di Biologia e Biotecnologie*

*"L. Spallanzani"*

Nootropic and antioxidant metabolites of *Hericium erinaceus* enhanced healthy aging in a preclinical model and improved mood disorders in patients



*Hericium erinaceus*

HPLC

Ethanol extraction and quantification of nootropic and bioactive metabolites

**Behavioral tests**

**Gut microbiome composition analysis**

**Histochemistry and immuno-histochemistry**

**Self administered questionnaires**

*Daniela Ratto*

*Dottorato di Ricerca in*
*Genetica, Biologia Molecolare e Cellulare*
*Ciclo XXXIV – A.A. 2018-2021*

# UNIVERSITÀ DI PAVIA

## *Dipartimento di Biologia e Biotecnologie*
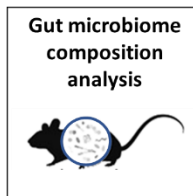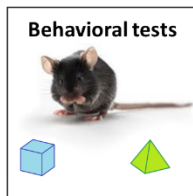
## *"L. Spallanzani"*

Nootropic and antioxidants metabolites of *Hericium erinaceus* enhanced healthy aging in a preclinical model and improved mood disorders in patients



*Hericium erinaceus*

HPLC

Ethanol extraction and quantification of nootropic and bioactive metabolites

**Behavioral tests**

**Gut microbiome composition analysis**

**Histochemistry and immuno-histochemistry**
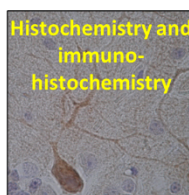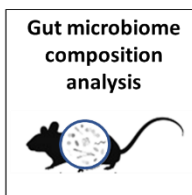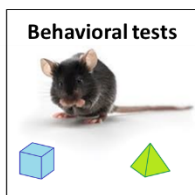
**Self administered questionnaires**

**Daniela Ratto**

Dottorato di Ricerca in

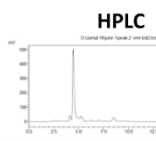Genetica, Biologia Molecolare e Cellulare

Ciclo XXXIV – A.A. 2018-2021

Summary

# 1. Abstract

Aging and frailty are two increasing problems associated with locomotor and cognitive decline, implicated in poor quality of life and adverse health consequences. One main issue surrounding frailty is whether phenotypic frailty is associated with cognitive decline during physiological aging. By monitoring mice through spontaneous behavioral tests, we tuned a non-invasive methodology for accessing frailty in mice through which we demonstrated that locomotor and recognition memory decline was linear and developed with different timing during physiological aging: locomotor performances decreased steeper than cognitive ones.
According to the gut-microbiota-brain axis, we also demonstrated that physiological aging impacted the overall microbiota composition. Indeed, gut bacteria are able to influence central nervous system activity and function, influencing cognitive and behavioral performances.

*Hericium erinaceus* is a medicinal mushroom with excellent health-promoting properties, particularly improving the recognition memory in mice. However, the standardization of dietary supplements, medicinal mushrooms and herbs is a very pressing and actual problem. In this work, through the HPLC-UV-ESI/MS technique, we found the exact amount of bioactive and nootropic metabolites (erinacine A, hericenones C and D, and L-ergothioneine) in two different *H. erinaceus* samples (He1 sporophore and mycelium, and He2 primordium), obtaining standardized extracts. In particular, He1 standardized extracts were enriched in erinacine A, hericenones C and D molecules, with a discrete L-ergothioneine concentration, whereas He2 standardized extract was L-ergothioneine-enriched, without nootropic molecules.

Next, firstly, we investigated the effect of two months of He1 oral supplementation in reverting frailty. To achieve this aim, we supplemented frail aged mice for two months with a He1 concentration (1mg/die) used to mimic human supplementation. We demonstrated that two months of He1 oral supplementation significantly improved locomotor activity, novelty-seeking behavior, and cognitive performances in frail mice, reporting their performances similar to non frail mice. To investigate the cellular and molecular mechanisms underlying the beneficial He1 effects, we investigated the cerebellar cytoarchitecture and oxidative stress, inflammation, BBB functionality, cell proliferation, and neurogenesis, using specific markers in the central nervous system. We demonstrated

that He1 mice displayed more preserved cytoarchitecture and BBB functionality, lower oxidative stress and inflammation levels, and a higher neurogenesis rate than untreated control mice. Moreover, we also found a higher SIRT1 expression in He1 treated mice, suggesting that *H. erinaceus* could have a senomorphic effect, restoring the phenotype of senescent cells. Furthermore, we investigated the He1 effect on microbiota composition, exploring its possible role as a prebiotic. We found that He1 oral supplementation did not change the overall microbiota composition but significantly altered the relative abundance of critical bacterial species. In agreement with the microbiota-gut-brain axis, these results allow us to speculate that *H. erinaceus* could be a prebiotic able to decrease gut pathobionts and increase gut psychobiotics, improving brain function.

In another set of experiments, we investigated the effect of He2 primordium standardized extract in frailty prevention, treating for eight months, from adulthood to senescence, random mice. Remarkably, He2 contains a high amount of L+-ergothioneine, the longevity vitamin. Herein, we demonstrated the preventive effect of the ergothioneine-enriched He2 extract in the preclinical model on novelty-seeking behavior, locomotor, and cognitive decline during physiological aging. This effect was twinned by a significant decrease in oxidative stress levels and increased p53 expression in CNS, suggesting that He2 seems able to eliminate degraded senescent cells, which over time would cause damage to brain tissue.

Given the *H. erinaceus* ability to enhance CNS adult neurogenesis and improve novelty-seeking behavior, we investigated its potential in reducing mood and sleep disorders in obese and overweight human individuals who underwent a low-calorie diet. Several works demonstrated a correlation between obesity and an increased risk of mood disorders onset and *vice versa*. We demonstrated that two months of oral supplementation with a dietary supplement based on *H. erinaceus*, the "*Micotherapy Hericium*" (provided by A.V.D. Reform s.r.l.), significantly reduced symptoms related to sleep disorders, anxiety, and depression, and notably, these beneficial effects remained also after two months of washout. In this case, for investigating the underlying mechanism, we investigated the serum proBDNF/BDNF ratio since BDNF dysregulations have been found both in obese subjects and patients with mood disorders; and proBDNF and BDNF play two opposite roles in CNS. We found that proBDNF/BDNF ratio significantly increased after two months of oral supplementation for the increase in proBDNF levels, and the increase was

maintained after two months of *H. erinaceus* washout for decreased serum BDNF levels.

Altogether, these results demonstrated the potential of *H. erinaceus* metabolites in (i) reverting and avoiding physical frailty, (ii) preventing and treating aging-related cognitive decline and neurodegenerative diseases, (iii) reducing sleep disorders, anxiety, and depression; acting on several different pathways, involving gut microbiota, oxidative stress, inflammation, and neurotrophic factors.

**Frail aged mice**

**Healthy aged mice**

*Hericium erinaceus* standardized extracts oral supplemenation
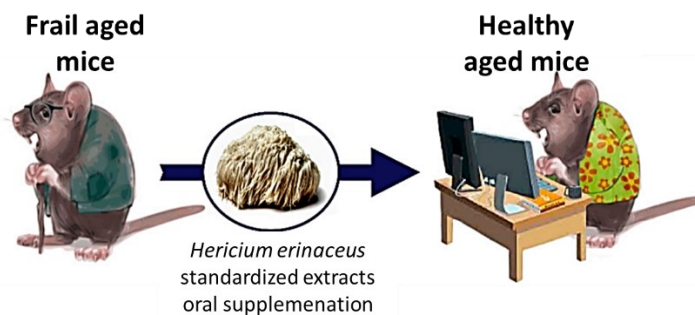
➢ Decrease in novelty exploration, locomotor and cognitive performances
➢ Neurogenesis decrease
➢ Oxidative stress increment
➢ Inflammaging
➢ Modification in microbiota composition leading to dysbiosis

➢ Improvement of novelty-seeking behavior, locomotor and cognitive performances
➢ Increased neurogenesis
➢ Reduction of oxidative stress and inflammation
➢ Improvement of BBB functions
➢ Microbiome changes

**Patients with mood and sleep disorder**

**Reduction of mood and sleep disorder symphoms**

*Hericium erinaceus* oral supplemenation

## 2. Abbreviations

Adhesion Molecules (AMs)

Alzheimer's Disease (AD)

Amplicon Sequence Variant (ASV)

ANalysis Of VAriance (ANOVA)

Autonomic Nervous System (ANS)

Binge Eating Scale (BES)

Blood-Brain Barrier (BBB)

Body Mass Index (BMI)

Brain-Derived Neurotrophic Factor (BDNF)

Carbohydrates (CHO)

Central Nervous System (CNS)

Cornu Ammonis area 3 (CA3)

CycloOXygenase 2 (COX2)

Danger-Associated Molecular PatternS (DAMPS)

Dentate Gyrus (DG)

DeoxyriboNucleic Acid (DNA)

Diagnostic and Statistical Manual of Mental Disorders 5 (DMS-5)

Discrimination Index (DI)

Distilled water ($H_2 0d$)

Doublecortin (DCX)

Enteric Nervous System (ENS)

Enzyme-Linked Immunosorbent Assay (ELISA)

Ergothioneine (EGT)

Faith Phylogenetic Metrics (PD)

Frailty Index (FI)

Glial cell-Derived Neurotrophic Factor (GDNF)

Glial Fibrillary Acidic Protein (GFAP)

Golgi cells (GCs)

Granular Layer (IGL)

Hematoxylin and Eosin (H&E)

*Hericium erinaceus* strain 1 mycelium and sporophore extract (He1)

*Hericium erinaceus* strain 2 primordium extract (He2)

High Performance Liquid Chromatography (HOLC)

Histone DeAcetylation (HDAc)

Hypothalamic-Pituitary-Adrenal axis (HPA)

Hypoxia-Inducible Factor 1-alpha (HIF1α)

Inflammatory Bowel Diseases (IBD)

Interleukin 6 (IL-6)

Irritable Bowel Syndrome (IBS)

Long Term Potentiation (LTP)

Mass spectrum (MS)

Molecular Layer (ML)

Multiple-Reaction-Monitoring (MRM)

Nerve Growth Factor (NGF)

Nitric Oxide Synthases 2 (NOS2)

Non-Metric Multidimensional Scaling (NMDS)

Novel Object Recognition (NOR)

Nuclear Factor (NF) κB

Object Location (OL)

Optical Density (OD)

Phosphate-buffered saline (PBS)

PostSynaptic Density (PSD)

pro–Brain-Derived Neurotrophic Factor (proBDNF)

Proliferating Cell Nuclear Antigen (PCNA)

Purkinje Cell (PC)

Purkinje Layer (PL)

Reactive Nitrogen Species (RNS)

Senescence-Associated Secretory Phenotype (SASP)

Short-Chain Fatty Acids (SCFAs)

Sirtuin 1 (SIRT1)

Stenberg Item Recognition Paradigm (SIRP)

Subgranular zone (SGZ)

SuperOxide Dismutase (SOD1)

Transmission Electron Microscope (TEM)

Tumour Necrosis Factor (TNF)

Ultra Violet (UV)

Vascular-Endothelial Growth Factor (VEGF)

Zonula Occludens-1 (ZO-1)

Zung Anxiety Scale (ZAS)

Zung Depression Scale (ZDS)

# 3. Introduction

## 3.1 Hericium erinaceus

Edible mushrooms are acceptable functional foods, having special health benefits for humans and are being used for several hundred years for their excellent source of nutrients (Wang et al. 2014).

*Hericium erinaceus* is an edible and medicinal mushroom that seems to stand out as a unique health-promoting species. *H. erinaceus* belongs to the Phylum *Basidiomycota*, Class *Agaricomycetes*, Order *Russulales*, and Family *Hericiaceae* (Khan et al., 2013). The first taxonomist, Bulliard, who described this species in 1797, found a solid resemblance to the hedgehog (in Latin erinaceus) and chose the appellation "erinaceus" for this *Hericium*. Indeed, thanks to its particular morphological aspect and the wide geographical distribution, many common names have been attributed to this fungus: the German name is IgelStachelbart; some familiar names in the UK are Bearded Hedgehog or Hedgehog Mushroom; in Japan is known as Yamabushitake (Yamabushi means mountain priest); in China, the most common name is Houtou, which means monkey head. In other parts of the world, it is also called pompom mushrooms, bear's head, white beard, etc. Nowadays, the most popular common name is Lion's mane mushroom. So, available in America, Europe, Asia, and generally in North temperate latitudes (Figure 1 A; Jiang et al., 2013), *H. erinaceus* is characterized by a conspicuous pileate, fleshy, hydnoid, and globose sporophore (Figure 1 B and C), consisting of numerous single, typically long, dangling, fleshy spines, which are at first white, becoming yellowish, and then brownish with age (Wang et al. 2014). The *H. erinaceus* fruit body is a large, irregularly bulbous, compact mass of 5-40 cm in diameter. The basidia (spore-producing organs) are about 20-40 x 5-7 µm, four-spored, and have a basal clamp. The spores are white in mass, finely roughened or warty, and about 5-7 x 4-5 µm.

It was demonstrated that *H. erinaceus* presents many beneficial effects on the health of animals and humans. The health effects are related to its bioactive compounds, such as polysaccharides, steroids, alkaloids, β-glucans, erinacines, and hericenones. The *H. erinaceus* beneficial activities are numerous, including antimicrobial, immunomodulatory, anticancer, antioxidant, anti-aging, anti-hyperglycemic, anti-hypertensive, and neuroprotective ones (Wang et al. 2014; Friedman, 2015; He et al., 2017).

*Figure 1: A: The geographic distribution of H. erinaceus worldwide (www.gbif.org). B and C: Hericium erinaceus fruiting body in nature (B: from Wang et al., 2014).*

### 3.1.1 Composition of *H. erinaceus*

Rodrigues and collaborators, in 2015, first described five mushroom species' composition and nutritive values (*Pleurotus citrinopileatus var cornucopiae, P. eryngii, P. salmoneo stramineus, Pholiota nameko,* and *H. erinaceus*). On average, dry mushrooms contained 16.22−26.6 % of proteins, 52.7−64.9 % of sugars, and 2.3−3.5 % of fats. These five mushrooms also contained a high concentration of phenolic compounds and more unsaturated (both mono- and poly-) fatty acids than saturated ones, being a good source of linoleic acid (>30 g/100 g fat). Furthermore, they were good sources of magnesium, phosphorus, and potassium. The mushrooms also contained high copper, iron, and zinc levels (Rodrigues et al., 2015).

Further works focused the attention only on *H. erinaceus* composition. In particular, the *H. erinaceus* fruiting body dried powder contains about 21% of proteins, 61% of total carbohydrates, 5% of fats, and 7% of ash, whereas the *H. erinaceus* mycelium contains 43% of protein, 43% of total carbohydrate, 6% of fat, and 4 % of ash (Cohen et al., 2014). The sugars contained in *H. erinaceus* comprise arabitol, glucose, mannitol, myo-inositol, and trehalose (Jiang et al., 2014). *H. erinaceus* fruiting body and mycelium contain about 14 and 31 mg/g dry weight of free aminoacids, respectively. The *H. erinaceus* fruiting body provides 374 kcal/100g, whereas *H. erinaceus* mycelium provides 398 kcal/100g (Cohen et al., 2014). These dietary nutritional values suggest that mushrooms are a potential nutritional source of different macro- and micro-nutrients.

*H. erinaceus* fruiting body and mycelium also contain many bioactive components: *H. erinaceus* can biosynthesize at least 70 different secondary metabolites, including polysaccharides, erinacines, hericerins, hericenones, resorcinols, steroids, mono- and di-terpenes, and volatile aroma compounds (Friedman, 2015).  Both in *H. erinaceus* fruiting body and mycelium γ-aminobutyric acid (GABA) and ergothioneine were found (Cohen et al., 2014). The *H. erinaceus* fruiting body also contains few enzymes, such as amylase (Du et al., 2013), laccase (Wang and Ng, 2004), and fibrinolytic metalloprotease (Wang et al., 2014). Amylase is an enzyme that catalyzes the hydrolysis of starch into sugars (Janeček et al., 2014), laccase is an enzyme able to inhibit HIV-1 reverse transcriptase activity (Wang et al., 2014), and fibrinolytic metalloprotease can degrade fibrin clot and activated plasminogen (Wang et al., 2014).

A review by Friedman (2015) lists all metabolites found in *H. erinaceus*, subdividing *H. erinaceus* compounds arbitrarily into five classes: erinacines, aromatic compounds, steroids, alkaloids, and lactones (Figure 2), and a review by Khan *et al.* (2013) explains the different effects of the different metabolites (Table 1).

In the past, most of the studies were focused only on polysaccharides, such as β-glucans, as the main active compounds of *H. erinaceus* (Yang et al., 2018). However, more recent works have discovered other components, such as sterols, hericenones, erinacines, erinacerines, isohericenones, alkaloids, glycosides, ergosterols, and ergosterol peroxide, that play a fundamental role in the *H. erinaceus* beneficial activities. For example, hericenones (extracted from *H. erinaceus* fruiting body) and erinacines (isolated from *H. erinaceus* mycelia) are the more active *H. erinaceus* components in neuroprotective function (Kawagishi and Zhuang, 2008). *H. erinaceus* compounds confer *H. erinaceus* health-

promoting properties, such as antibiotic (Kim et al., 2012; Liu et al., 2016), anti-cancer (Li et al., 2014; Li et al., 2015), anti-diabetic (Wu et al., 2015), anti-oxidant (Wu and Xu, 2015; Wang et al., 2018; Lu et al., 2014), anti-fatigue (Liu et al., 2015), anti-hypertensive, anti-hyperlipidemic (Choi et al., 2013), anti-senescence (Noh et al., 2015; Diling et al., 2017), cardioprotective, hepatoprotective (Zhang et al., 2012), nephroprotective (Friedman, 2005), neuroprotective (Zhang et al., 2016; Phan et al., 2015), antidepressive, and antianxiety (Nagano et al., 2010) activities (Table 1; Figure 3).

Furthermore, *H. erinaceus* can regulate cytokines and mitogen-activated protein kinases expressions and transcription factors at the molecular level: *H. erinaceus* performs therapeutic activities at cell, tissue, organ, and organism levels (Jiang et al., 2014). Consequently, *H. erinaceus* is an excellent candidate to prepare novel mushroom-based pharmaceuticals/medicines and functional foods.

| Compounds | Beneficial bio-activities |
| --- | --- |
| β-Glucans (polysaccharides) (e.g. β-1,3-branched-beta-1,6-glucan with laminarin-like triple helix conformation) | Anti-cancerous, immuno-modulatory, neuro-protective and anti-oxidant |
| HEP1 [a hetero-polysaccharide, with (1›6)-linked α-ᴅ-galactopyranosyl backbone)] | Anti-cancerous and immuno-modulatory |
| HEPF3 (a hetero-polysaccharide, with a branched penta-saccharide repeating unit) Endo-polysaccharides | Anti-cancerous and immuno-modulatory Hepato-protective and anti-oxidant |
| Other polysaccharides: 6-methyl-2,5-dihydroxymethyl-γ-pyranone; 2-hydroxymethyl-5-α-hydroxy-ethyl-γ-pyranone; 4-chloro-3,5-dimethoxybenzoic-O-arabitol ester; 4-chloro-3,5-dimethoxybenzoic methyl ester and 4-chloro-3,5-dimethoxybenzoic acid | Wide spectrum health beneficial effects, including anti-cancerous and immuno-modulatory activities |
| Lipid compounds: palmitic and stearic acid mixture; behenic acid and tetracosanic acid mixture; 5-α-ergostan-3-one; 5-α-stigmasten-22-en-3-one and 5-α-stigmastan-3-one | Wide spectrum health beneficial effects |
| Hericenone B (phenolic compound) | Anti-platelet aggregation (protection of myocardial infarction, stroke, etc.) |

*Table 1: H. erinaceus bioactive components and their beneficial effects on human health. From Khan et al., 2015.*
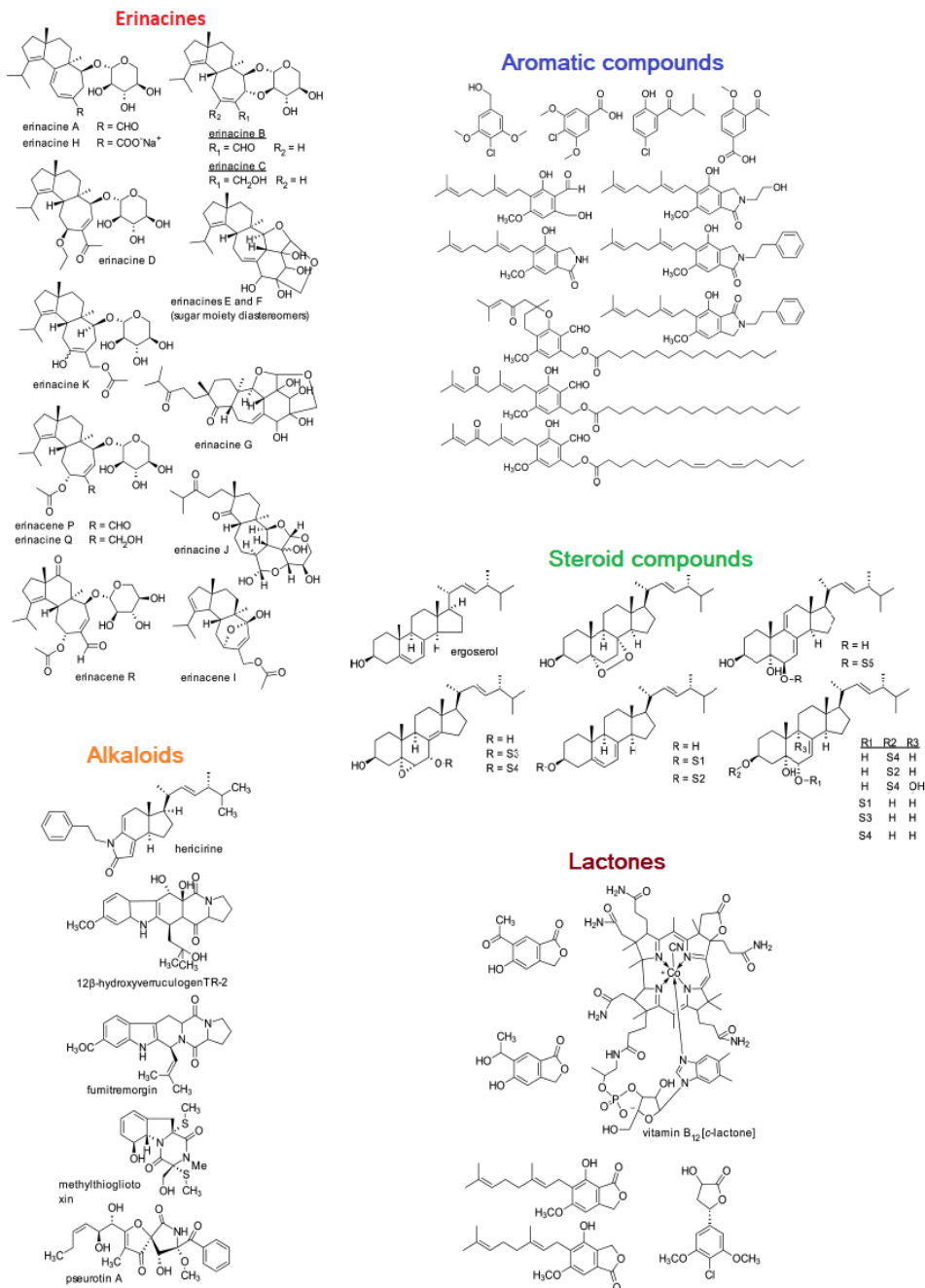
*Figure 2: Structure of principal compounds isolated from H. erinaceus fruiting body and mycelia (adapted from Friedman, 2015).*

# *Hericium erinaceus* effects



Immunostimulator        Antisenescence

Anti-inflammatory        Neuroprotective

Antidiabetic                     Antifatigue

Gastrointestinalprotective        Antibiotic

Antihyperlipidemic

Antihypertensive

Antioxidant

Nephroprotective        Hepatoprotective

Anticarcinogenic        Cardioprotective
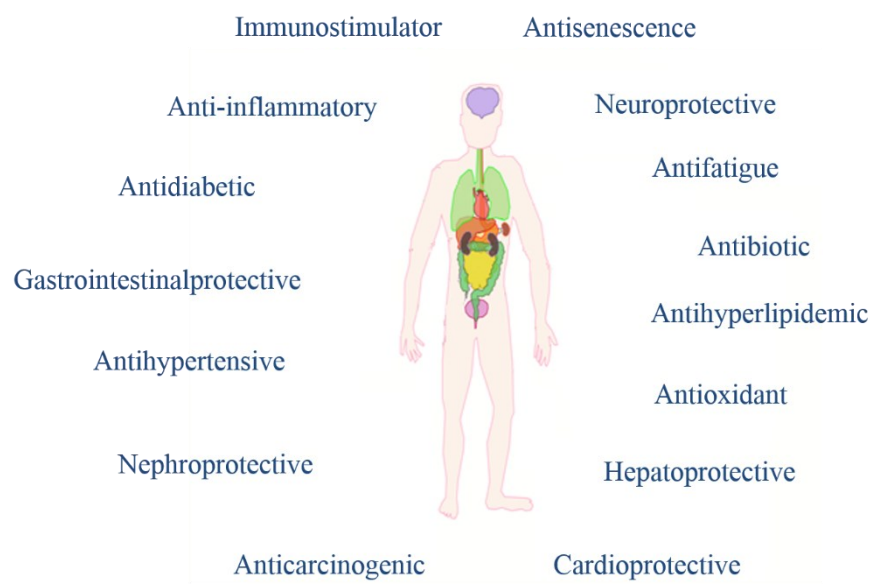
*Figure 3: Effects of H. erinaceus.*

## 3.1.2 Bioactive metabolites

The most known bioactive metabolites of medicinal mushrooms are beta-glucans for their hypocholesterolemic, hypoglycemic, and immunomodulatory effects. In addition to beta-glucans, other bioactive metabolites have been found in *H. erinaceus*, such as erinacines, hericenones, and ergothioneine.

Ergothioneine has been named the "vitamin of longevity" for its outstanding antioxidant activity in several tissues. Regarding the central nervous system (CNS), erinacines and hericenones present in *H. erinaceus* display neuroprotective and nootropic effects. These secondary metabolites can induce neurotrophins, i.e., nerve growth factor (NGF) and brain-derived neurotrophic factor (BDNF), synthesis and release in CNS (Kawagishi and Zuang, 2008). NGF is a highly conserved protein with a high molecular weight. It plays a crucial role in survival and proliferation and is involved in repairing, regenerating, protecting neurons, supporting

synapse formation, and enhancing memory function (Obara and Nakahata, 2002; Kawagishi and Zuang, 2008). It is assumed that functional deficiency of NGF is related to dementia-like diseases and progressive neurodegeneration of the brain, commonly diagnosed in the aging population over 65 years old. Nowadays, dementia and dementia-like diseases are significant causes of decreased quality of life in humans during aging. However, NGF cannot cross the blood-brain barrier (BBB), and its effect by direct injection into the brain is an invasive treatment for patients. On the other hand, erinacines and hericenones are natural compounds with a low molecular weight capable of passing the BBB.

### 3.1.2.1 Erinacines

Erinacines are diterpenoids known as bioactive compounds of *H. erinaceus* mycelium*.* Up to now, 15 erinacines have been recognized and isolated (from A to K and from P to S) (Figure 4).
Several erinacines display both *in vitro* and *in vivo* different health-promoting properties, such as anticancer capability, neuroprotective activity, reduction of inflammatory levels, protection against cerebral ischemia damages, increasing the growth factors in CNS, reducing beta-amyloid plaques deposition, and reducing neuropathic pain (Table 2; Kawagishi et al., 1994; Shimbo et al., 2005; Lee et al., 2014; Li et al., 2018; Bailly and Gao, 2020).

Erinacine A is the main representative of the erinacines groups, with higher effects on CNS compared to other erinacines (Li et al., 2018). Indeed, several works demonstrated the potential of erinacine A in preventing and alleviating neurodegenerative disease. A retracted (for conflict of interest) article published by Kuo et al. (2016) demonstrated the neuroprotective activity of erinacine A in decreasing the 1-Methyl-4-phenylpyridinium-induced neural injury in mice, suggesting the potential role of erinacine A in treating Parkinson's Disease. Tsai-Teng and collaborators in 2016 showed that erinacine A-enriched *Hericium erinaceus* mycelium reduced the beta-amyloid plaques deposition, the inflammation and promoted hippocampal neurogenesis in APPswe/PS1dE9 transgenic mice, a model of Alzheimer disease. Moreover, erinacine A-enriched *Hericium erinaceus* mycelium could reduce chronic stress, and restore the physiological levels of neurotransmitters deregulated during mood disorders, suggesting a potential role of this bioactive metabolite also for treating depression (Chiu et al., 2018; Li et al., 2018). Furthermore, Li and colleagues (2021) recently published a paper demonstrating that *Hericium erinaceus*

mycelium containing erinacine A could reduce anxiety and improve sleep disorders in a preclinical model.
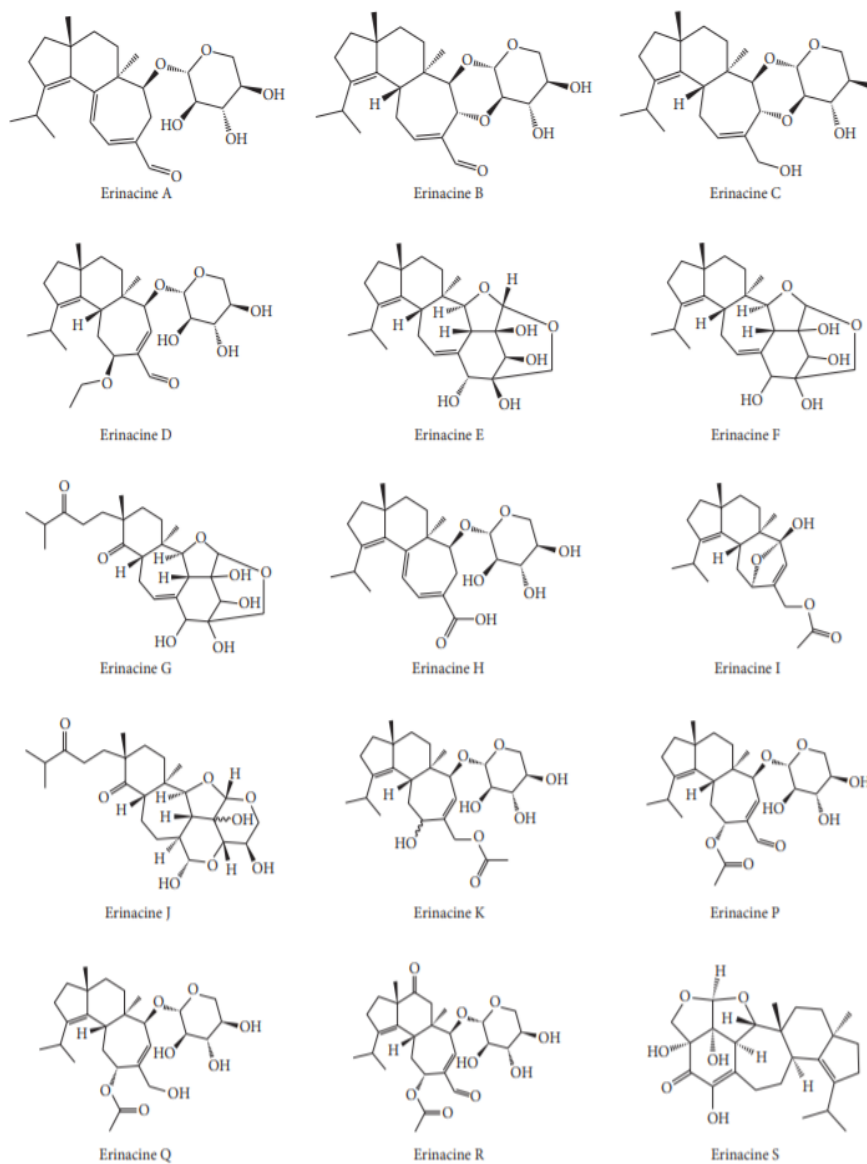


Figure 4: Chemical structures of the known 15 erinacines. From Li et al., 2018.

| Erinacines | Tests | Concentration | Biological activities |
|---|---|---|---|
| Erinacine A | *In vitro* | 1 mM | Induced $250.1 \pm 36.2$ pg/ml NGF synthesis |
| | *In vivo* | 30 mg/kg body weight/day | (1) Reduced amyloid burden by $38.1 \pm 19.7\%$<br>(2) Increased IDE levels by $141.1 \pm 63.7\%$ |
| | *In vivo* | 1 mg/kg body weight/day | Inhibited DLD-1 tumor growth by 66% |
| | *In vivo* | 30 mg/kg body weight/day | (1) Reduced both the size and number of amyloid plaques<br>(2) Increased IDE levels by 303.5%<br>(3) Recovered from impairments in burrowing, nesting, and Morris water maze tasks |
| Erinacine B | *In vitro* | 1 mM | Induced $129.7 \pm 6.5$ pg/ml NGF synthesis |
| Erinacine C | *In vitro* | 1 mM | Induced $299.1 \pm 59.6$ pg/ml NGF synthesis |
| Erinacine D | *In vitro* | 1.67 mM | Induced $141.5 \pm 18.2$ pg/ml NGF synthesis |
| Erinacine E | *In vitro* | 5 mM | Induced $105.0 \pm 5.2$ pg/ml NGF synthesis |
| | *In vitro* | $IC_{50}$ | Binding inhibitor for $\kappa$-opioid receptor at 0.8 $\mu$M |
| Erinacine F | *In vitro* | 5 mM | Induced $175.0 \pm 5.2$ pg/ml NGF synthesis |
| Erinacine H | *In vitro* | 70.8 mM | Induced $31.5 \pm 1.7$ pg/ml NGF synthesis |
| Erinacine S | *In vivo* | 30 mg/kg body weight/day | (1) Reduced amyloid burden by $40.2 \pm 15.2\%$<br>(2) Increased IDE levels by $130.5 \pm 68.9\%$ |
| | *In vivo* | 30 mg/kg body weight/day | (1) Reduced the size of amyloid plaques<br>(2) Increased IDE levels by 269.8%<br>(3) Recovered from impairments in burrowing, nesting, and Morris water maze tasks |

*Table 2: Biological activities of different kinds of erinacines in the nervous system. From Li et al., 2018.*

Table 3 summarizes the most known biological effects *in vivo* of erinacine A or erinacine A-enriched *H. erinaceus* mycelium in CNS (Li et al., 2018): (i) increase of NGF concentrations and restore neurotransmitters levels (Kuo et al., 2016; Chiu et al., 2018); (ii) reduction of $Ca^{2+}$-induced neurotoxicity (Liu et al., 2017); (iii) reduction of brain injury and inflammation in transient stroke, (iv) reduction of beta-amyloid burden, promoting neurogenesis and improving behavior (Tsai-Teng et al., 2016), (v) decrease of depressive-like behavior, regulating BDNF pathway and reducing inflammation (Chiu et al., 2018).

Furthermore, a recent study also demonstrated the potential of erinacine A-enriched *Hericium erinaceus* mycelium in promoting longevity in different preclinical models, such as *Drosophila melanogaster* and senescence-accelerated P8 (SAMP8) mice. The erinacine A lifespan-prolonging activity was suggested to be attributed to the ability to reduce oxidative stress and related damages (Li et al., 2019)

| Material studied (dose used) | *In vivo* models | Effects |
|---|---|---|
| Erinacine A | Normal Wistar rats | Enhanced NGF and catecholamine secretion in the LC and hippocampus after intragastric dosing erinacine A at 8 mg/kg body weight |
| Erinacine A-enriched mycelia and erinacine A | Ischemic stroke in Sprague-Dawley rats | (1) Mycelia at 50 and 300 mg/kg body weight reduced infarcted volume in cortex and subcortex of transient stroke rats (2) Erinacine A at 1, 5, and 10 mg/kg body weight reduced levels of proinflammatory cytokines such as iNOS, IL-1$\beta$, IL-6, and TNF-$\alpha$ in the serum of transient stroke rats |
| Erinacine A-enriched mycelia | APPswe/PS1dE9 transgenic mice | (1) Mycelia at 300 mg/kg body weight reduced amyloid plaque burden in the area including the cerebral cortex and hippocampus (2) Increased NGF/proNGF ratio and promoted hippocampal neurogenesis (3) Restored nesting behavior |
| Erinacine A Erinacine S | APPswe/PS1dE9 transgenic mice | (1) Both compounds at 30 mg/kg body weight reduced amyloid plaque burden in the cerebral cortex (2) Increased the level of IDE in the cortex by $130.5 \pm 68.9\%$ and $141.1 \pm 63.7\%$, respectively |
| Erinacine A-enriched mycelia | MPTP-induced neurotoxicity in C57BL/6 mice | (1) Treatment at 10.76 and 21.52 mg/day elevated dopamine, NGF, and GSH levels (2) Reduced motor dysfunction (3) Reduced dopaminergic neurons apoptosis in the striatum and substantia nigra |
| Mycelia ethanolic extract | C57BL/6 mice | (1) Treatment at 2000 mg/kg body weight blocked the rise in $[Ca^{2+}]$ induced by ATP (2) Increased the latency in tail-flick and paw-lifting times exposed to a thermal stimulus |
| Erinacine A-enriched mycelium | Restraint stress induced depression in ICR mice | (1) Treatment at 200 and 400 mg/kg body weight increased dopamine and serotonin levels (2) Increased BDNF, Tr$\kappa$B, and PI3K expressions in the hippocampus (3) Reduced IL-6 and TNF-$\alpha$ levels (4) Reduced the immobility time in the tail suspension test and forced swimming test, as well as decreased the number of entries and the time spent in the open arm |

*Table 3: The biological effects of erinacine A or erinacine A-enriched H. erinaceus mycelium in CNS. From Li et al., 2018.*

### 3.1.2.2 Hericenones

Hericenones are benzyl alcohol derivates with simple fatty acids that could be isolated from *H. erinaceus* basidium. To date, eleven hericenones (A-J; Figure 5) are known, and they display different biological activities (Deshmukh et al., 2021). The peculiar health-promoting effects of single hericenones depend on the chain length and double bonds in fatty acids. Hericenones A and B are well-known for their anti-platelet aggregation activity and potential application in treating vascular disease, stroke, and thrombosis (Mori et al., 2010). These hericenones could also exert cytotoxic activity against cancer cells (Kawagishi et al., 2010), like Hericenone L (Ma et al., 2012).

Hericenones from C to H exert neuroprotective and neuro-regenerative effects, suggesting a potential implication for the management of dementia, depression, and Alzheimer and Parkinson diseases (Kawagishi

et al., 1991; Kawagishi et al., 1992; Phan et al., 2014; Saitsu et al., 2019; Kobayashi et al., 2021). In particular, hericenones C-H display their biological activity similar to erinacine A, inducing NGF synthesis and release. Hericenone F also has anti-inflammatory activity (Lee et al., 2016).

Furthermore, in 2015, Inanaga reported that Amyloban3399, a product made with standardized extract of *H. erinaceus* containing hericenones and amyloban, improves sleep, mood, attentiveness, and the level of mental alertness, in addition to recovery from schizophrenia.
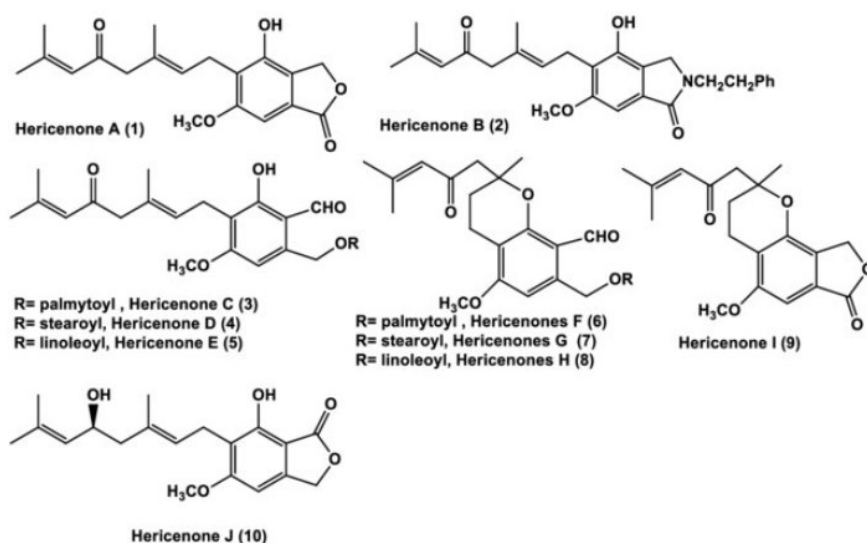


*Figure 5: Chemical structures of the known hericenones.*
*From Deshmukh et al., 2021.*

### 3.1.2.3 Ergothioneine

The ergothioneine (EGT) is a histidine-derived amino acid containing a sulfur atom of the imidazole ring (Figure 6; Stampfli et al., 2020). EGT was first isolated from ergot, from which it takes its name. Despite EGT is synthetized exclusively by mushrooms (non-yeast fungi, including *Hericium erinaceus*), cyanobacteria, and mycobacteria, it is ubiquitously present at micromolar-millimolar levels in most cells and tissues of plants and animals (Ey et al., 2007; Cheah and Halliwell, 2012). Whereas plants can accumulate EGT from the soil, where are present EGT-producer microorganisms, animals and mammals take and absorb EGT through the diet (Cheah and Halliwell, 2012).
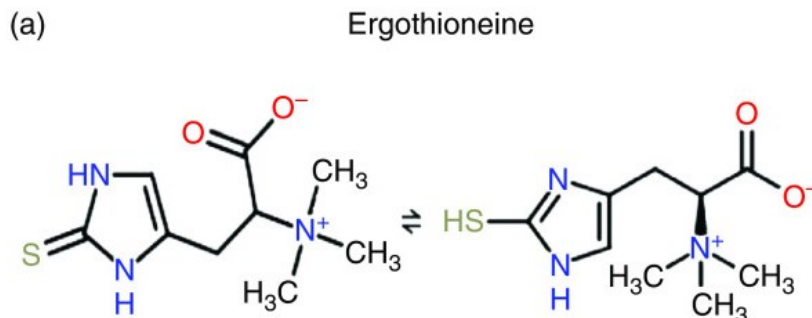
*Figure 6: Structure of EGT (2-mercaptohistidine trimethylbetaine; C9H15N3O2S) and its tautomers. The thione form (left) predominates at physiological pH (from Borodina et al., 2020).*

In animals, EGT then is taken up from the cells *via* an organic cation transporter (OCTN1), known in humans also as solute carrier family 22 member 4 (SLC22A4) (Borodina et al., 2020). The EGT uptake is saturable and temperature-, pH-, and sodium-dependent (Nakamura et al., 2007; Cheah and Halliwell, 2012) and EGT is favorably accumulated in cells and tissues predisposed to higher levels of oxidative stress.

Several works demonstrated the EGT antioxidant and cytoprotective activities: EGT is able to neutralize free radicals and hypochlorous acid, to inhibit the production of oxidants from metal ions, to regulate several antioxidant enzymes activities, and to mitigate telomere shortening (Misiti et al., 2001; Borodina et al., 2020; Samuel et al., 2020), suggesting a potential role of EGT for healthy aging. Indeed, decreased EGT levels have been observed in several pathologies; hence, EGT integration has been suggested as a potential treatment for several disorders, such as neurodegenerative, metabolic, and cardiovascular diseases (Cheah et al., 2016; Cheah and Halliwell, 2021).

Several works demonstrated the neuroprotective activity of EGT. Indeed, dietary EGT was shown to cross the blood-brain barrier (BBB) *via* OCTN1 (Wu et al., 2000; Koh et al., 2021) and accumulate in the brain and in the cerebrospinal fluid (Halliwell et al., 2018; Tang et al., 2018; Ishimoto and Kato, 2022).

A first paper in 2004 demonstrated that EGT *in vitro* might attenuate in a dose-dependent manner cell death caused by beta-amyloid, eliminating free radicals derived from the neurotoxic peptide (Jang et al., 2004). In 2010, Song and collaborators showed the potential of EGT both *in vitro*

and *in vivo* in protecting neurons against cisplatin-induced damages by inhibiting oxidative stress and reducing lipid peroxidation. In 2012, Yang et al. demonstrated that EGT has a protective activity against neuronal injury induced by beta-amyloid peptides in mice, also mitigating the cognitive decline. In 2014, Song and colleagues confirmed the potential of EGT in attenuating oxidative stress and protecting mice against learning and memory impairment in mice treated with D-galactose.

Altogether these findings suggest EGT as a potential new therapeutic strategy for preventing or treating inflammatory and neurodegenerative diseases.

## 3.2 Aging

Aging is a natural process that affects and produces changes in all living organisms (Kirkwood, 2005). Aging is characterized by a deterioration in physiological processes, leading to a higher probability of developing several disorders, i.e., cancer, metabolic, cardiovascular, and neurodegenerative diseases (Lopez-Otin et al., 2013). Notably, the decrease in physiological functions has different rates from individual to individual, making aging a heterogeneous process. Indeed, one of the primary goals of actual society is "healthy aging".

Over the years, numerous theories, which can be gathered into two main ones, have been proposed to explain the bases of aging: the theory of programmed aging and the theory of aging due to accumulation of errors within the cell. To date, the main leading cause of aging is usually considered the time-dependent increase of cellular damages (Lopez-Otin et al., 2013). Among others, in mammalians, the cause of aging has often been attributed to DNA damage accumulation, injuries induced by free radicals, inflammation increase, apoptosis resistance, genomic instability, telomere shortening, epigenetic alterations, deregulated nutrient-sensing, mitochondrial dysfunction, stem cell exhaustion, altered intercellular communication, and dysregulated neuronal $Ca^{2+}$ homeostasis (Lopez-Otin et al., 2013; Hernandez-Segura et al., 2018; Wen et al., 2021). To date, scientists agree that aging is a multifactorial mechanism that includes multiple interdependent and interactive processes (da Costa et al., 2016).

During aging, also in the CNS, there is an accumulation of senescent cells, and this is related to cognitive decline, often due to changes and disruption in synaptic transmission. Senescent cells cannot divide, and develop a specific phenotype, known as senescence-associated secretory phenotype (SASP), that leads to a pro-inflammatory environment (Sikora et al., 2018; Sikora et al., 2021; Figure 7).
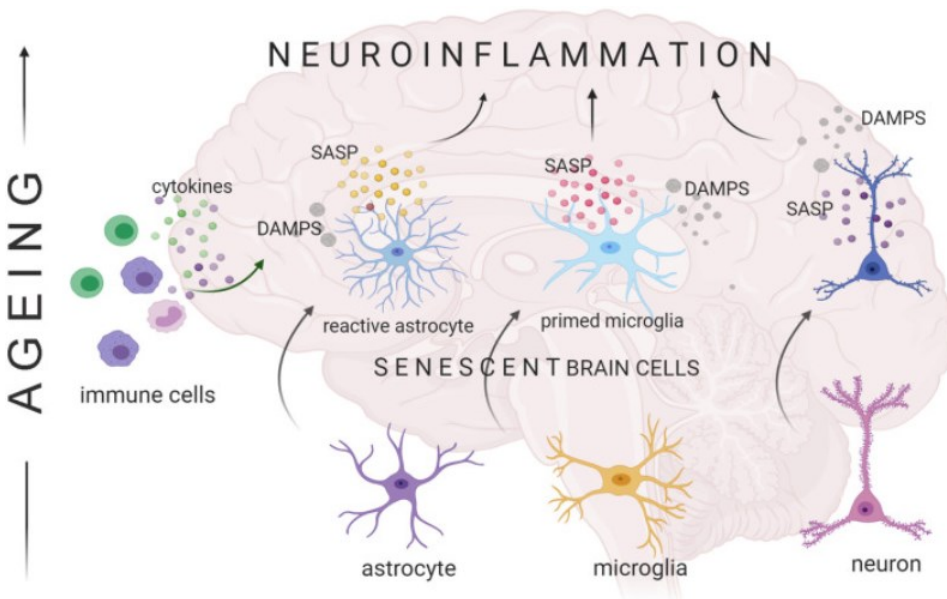
*Figure 7: Brain senescent cells characterized by senescence-associated secretory phenotype (SASP) contribute to the inflammaging in CNS. Neuroinflammaging is also supported by pro-inflammatory cytokines and danger-associated molecular patterns (DAMPS), molecules released from damaged or dying cells to send a danger signal. From Sikora et al., 2021.*

Senescent cells exhibit also altered morphology with the accumulation of lipid droplets, DNA methylation, and chromatin remodeling, leading to a changed gene expression. In particular, the aging-related cognitive decline is principally associated with modifications in gene expression and in the activity of neurons in the hippocampus and prefrontal cortex (Sikora et al., 2021). In the brain cortex, both in aged animals and in animal models of accelerated aging (SAMP10 mice), the regression of dendritic arbors associated with a reduction in dendritic spine density has been demonstrated (Turner and Deupree, 1991; Shimada et al., 2006). On the contrary, the hippocampus seems to be more stable against the aging process (Adams et al., 2010; Newton et al., 2008; Dickstein et al., 2013), despite the decrease of spine density in the dentate gyrus (DG) and Cornu Ammonis area 3 (CA3) and the post synaptic density reduction with regression of apical dendrites in CA1 during aging (Figure 8; De Groot and Bierman, 1987; Markham et al., 2005; Sikora et al., 2021).

Notably, also cerebellum changes occur during aging, showing modifications in cerebellar volume and Purkinje cells soma atrophy and regression of dendric arbors (Rogers et al., 1984; Chen and Hillman, 1999; Bernard and Seidler, 2014).

The impairment in neuronal structure and plasticity that characterizes aging is one of the principal causes of the development of cognitive decline.

The aging-related modifications in CNS were also widely demonstrated in electrophysiological experiments, which demonstrated impairment in Long Term Potential (LTP) induction, a slow after hyperpolarization, and decreased size in the postsynaptic density (PSD) in the aged brain (Sikora et al., 2021).
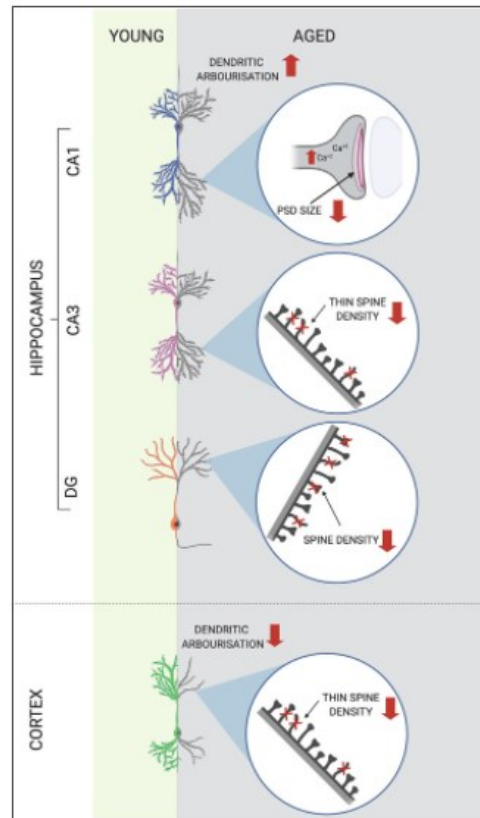


*Figure 8: Changes in dendrites during aging in the different hippocampal areas (up) and the cortex (down). From Sikora et al., 2021.*

## 3.2.1 Oxidative stress in the central nervous system during aging

Free radicals, such as reactive oxygen species (ROS) and reactive nitrogen species (RNS), are produced by various processes, and the antioxidants have the task of removing them. When antioxidants activity does not counterbalance the destructive effects of free radicals, oxidative

stress occurs. Aging is related to increasing free radicals and chronic oxidative state, affecting and disrupting all tissues and organs and contributing to the onset of aging-related pathologies or syndromes (Kudryavtseva et al., 2016; Liguori et al., 2018). Indeed, one of the most accredited theories of aging is that of free radicals (Kudryavtseva et al., 2016). The oxidative stress theory of aging hypothesizes that the physiological deterioration is caused by an accumulation of damaged macromolecules (DNA, RNA, proteins, and lipids) derived from oxidative stress within cells (Lin and Beal, 2003). In particular, recent studies demonstrated an association between oxidative stress and neuronal damage during aging, suggesting that oxidative stress plays a crucial role in the etiopathogenesis and progression of neurodegenerative diseases (Wang et al., 2014).

Notably, first of all, in CNS, the free radicals' generation has an essential role in neuronal synaptic plasticity through a process called "redox signaling". However, the CNS has characteristics that make it particularly susceptible to oxidative stress: elevated unsaturated lipid amount, high metabolism level, high-level oxygen consumption, endogenous neurotransmitter metabolism that generates hydrogen peroxide, calcium oscillations, and lower levels of antioxidant defenses (Lehtinen and Bonni, 2006; Cobley et al., 2018). Furthermore, a consequence of chronological aging is increased redox-active transition metal ions in the brain (Chen et al., 2012). These features make the CNS very vulnerable to oxidative stress (Lehtinen and Bonni, 2006; Figure 9). So, during aging, in the CNS, there is depletion in antioxidants functions, disruption of calcium balance, and mitochondrial impairment that altogether lead to oxidative stress. Indeed, ROS accumulate in the CNS during aging and the damages induced by free radicals negatively affect normal brain functions. Some researchers suggested that oxidative stress contributes to the formation of neuronal plaque and abnormal interactions between proteins with the consequence of protein aggregations. Many studies demonstrated the ability of antioxidant molecules to reduce the onset of age-related neurodegenerative diseases (Andersen, 2004; Salim, 2016; Chen et al., 2020). Furthermore, oxidative stress is also related to mood disorders: brain autopsies of depressed patients were characterized by higher free radicals' levels (Salim, 2016). Indeed, new drugs against oxidative stress are being developing for treating neuropsychiatric disorders (Visentin et al., 2020).
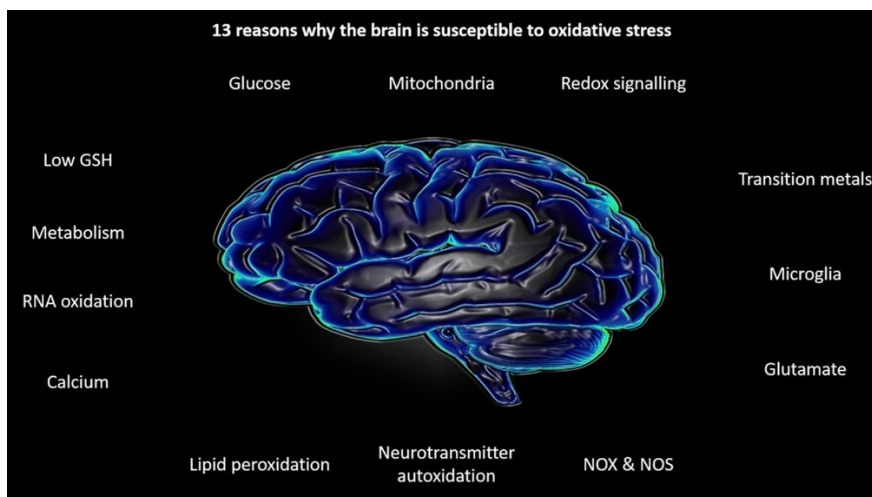
*Figure 9: 13 reasons why the brain is susceptible to oxidative stress. From Cobley et al., 2018.*

Different types of neurons display different susceptibility to free radicals-induced damages; for example, hippocampus and cerebellar granule cells are very vulnerable. The oxidative stress in these areas significantly affects cells proliferation, remodeling capacity, neuronal plasticity, and synaptic transmission, explaining the cognitive impairment induced by oxidative stress during aging (Salim, 2016).

Furthermore, free radicals are involved in triggering chronic inflammation (von Bernhardi et al., 2015). As reported in Figure 10, the aging-related homeostasis loss leads to several metabolic changes, leading to oxidative stress. These aging-related impairments determine responses both in the CNS and the immune system. In the CNS, in addition to neuroinflammation, impaired neuronal signaling, metabolic changes, and impaired glial cell signaling occur. In particular, the astrocytes and the microglia functions are strictly regulated by factors of the CNS microenvironment. With environmental stress or aging, astrocytes became reactive/activated astrocytes, and microglia became primed microglia (Wolf et al., 2017; Palmer and Ousman, 2018). These reactive or primed phenotypes are characterized by an exaggerated and uncontrolled inflammatory response to immune stimuli. Thus, reactive astrocytes and primed microglia do not enhance immune response correctly but exaggerate the inflammatory response, leading to neuroinflammaging (Norden et al., 2015; Ben Haim et al., 2015). In addition, the dysfunctions in glial and neuronal signaling, also lead to CNS

functional decline and a higher risk of developing neurodegenerative diseases.
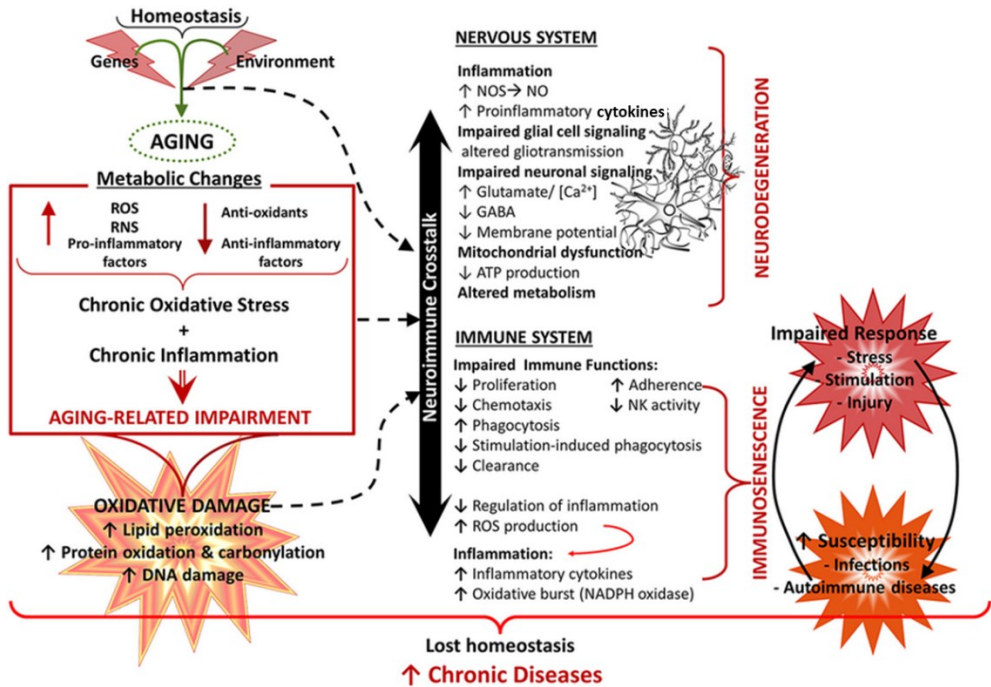


*Figure 10: Aging is associated with oxidative stress and inflammation increase. Both the CNS and the immune system are particularly vulnerable to oxidative damage, such as the increase in lipid peroxidation, protein oxidation and carbonylation, and DNA damage. In the CNS, oxidative damage leads to increased inflammation, impaired glial and neuronal signaling, increased mitochondrial dysfunctions, and altered metabolism. These disruptions affect the normal function of the brain, leading to neurodegeneration. From von Bernhardi et al., 2015.*

## 3.2.2 Inflammaging

Oxidative stress is involved in the formation of chronic inflammation. This can determine impairment of the immune system (Sadighi Akha, 2018), which can lead to a chronic asymptomatic systemic low-grade inflammatory state that can lead to several age-related chronic diseases. Indeed, more and more evidence indicates that an increase in systemic inflammation is strongly correlated with aging (Chung et al., 2008; Rea et

al., 2018), during which the sustained levels of pro-inflammatory mediators and aberrant migration of pro-inflammatory factors in various tissues are demonstrated. So, the term inflammaging refers to a chronic, asymptomatic, systemic, and low-grade inflammation that occurs in the absence of infection in old age. This chronic inflamed state has harmful effects on health and contributes to biological aging and the development of age-related diseases.

One of the principal factors involved in the immune response during age-related inflammation is the activation of the nuclear factor (NF) κB. Several studies have shown an increase in the expression of pro-inflammatory genes in response to the age-related NF-κB activity such as (i) Tumour Necrosis Factor (TNF) α and β; (ii) pro-inflammatory interleukins and chemokines (including IL-1β, IL-6, and IL-8); and (iii) adhesion molecules (AMs). All these molecules in physiological conditions are usually present at low concentrations, whereas during aging they undergo an up-regulation, probably due to an increase in oxidative stress (Chung et al., 2006; Ferrucci and Fabbri, 2018; Chung et al., 2019). In particular, a continuous dysregulation of IL-6 synthesis leads to a state of chronic inflammation and autoimmunity (Hirano, 2021).

Despite what is known, the precise causes behind inflammaging remain unknown and since aging is a complex process, inflammaging is probably the result of several factors, including (i) an increase in the number of senescent cells that release pro-inflammatory molecules; (ii) the release of altered molecules by damaged cells, resulting in the activation and development of inflammation; (iii) alteration of the gut microbiota; (iv) chronic stress condition (Franceschi and Campisi, 2014; Franceschi et al., 2018).

Several evidence also denote a significant role in aging and age-related diseases of a particular group of microRNAs, called inflamma-miRs, capable of modulating specific pathways of signaling (including NF-κB, SIRT, and TGF-β) involved in inflammation and senescence (Quinn and O'Neill, 2011; Dhahbi, 2014).

To resume, in the elderly, inflammation regulation mechanisms are altered, leading to a higher risk of developing age-related infections and chronic diseases, such as neurodegenerative and cardiovascular diseases and dementia. This impairment is partly due to the increase in circulating pro-inflammatory cytokines even in the absence of infections, suggesting the presence of a chronic and latent age-related inflammation. This basal inflammatory state induces tissue damage, which in turn leads

to greater inflammation, creating a vicious circle that predisposes to age-related diseases (Baylis et al., 2013; Ferrucci and Fabbri, 2018). Notably, the anti-inflammatory treatment is proving to be excellent for the treatment of various chronic diseases (Tabas and Glass, 2013; Hussain et al., 2020)

### 3.2.2 Apoptosis in the central nervous system during aging

Apoptosis already occurs in the central nervous system (CNS) during embryogenesis, supporting the correct neuronal network organization. Nevertheless, the regulation of apoptosis in the CNS is fundamental for controlling the longevity of neurons. Apoptosis in the CNS plays a dual role (i) determining the loss of irreplaceable neurons and as a side effect neurodegeneration and leading to neurodegenerative diseases (Radi et al., 2014) and (ii) eliminating damaged cells that could evolve in cancer cells or could produce misfolded or damaged proteins (Higami and Shimokawa, 2000; Ziv and Melamed, 2010).

Independently of whether and to what extent neurogenesis occurs, clearance of senescent cells in preclinical models is *per se* enough for inducing functional improvements in models of neurodegenerative diseases (Zhang et al., 2019).

### 3.2.3 Senotherapeutics and new approaches for reverting or preventing aging

The first study related to the reversion or prevention of aging dates to 1939, demonstrating that a reduced caloric intake increased the lifespan of rodents (McCay et al., 1975). Later, many other investigations showed how, alongside the increase in lifespan, caloric restriction seems to delay aging and the onset of age-related diseases, by eliminating selectively senescent cells (Robbins et al., 2021).

Most recently, a new class of drugs, known as senotherapeutics, has received interest for their capability to delay or prevent senescence. Recent searches on preclinical models demonstrated that senotherapeutics reduce disorders in different tissues and organs. Among senotherapeutics, senolytics can selectively kill senescent cells, whereas senomorphics can restore the phenotype in aged cells (Monganelli et al., 2020; Robbins et al., 2021). In particular, senomorphics can prevent or

revert aging without changing the total number of senescent or pre-senescent cells, whereas senolytics induce programmed death (i.e., apoptosis and autophagia) in senescent cells affecting their total number (Figure 11).
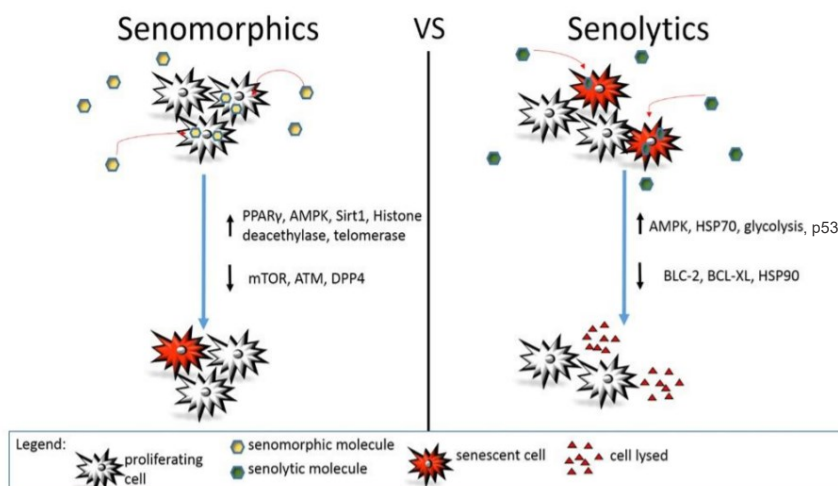


*Figure 11: Action mechanism of senotherapeutics: senomorphics on the left and senolytics on the right. From Monganelli et al., 2020.*

Senomorphics are effictive against aging regulating pathways involved in reducing inflammation and oxidative stress and increasing DNA repair and correct mitochondrial functions (Monganelli et al., 2020). In particular, senomorphics are known as a Sirtuin pathway activator (i.e., SIRT1; Mitchell et al., 2014), improving energy metabolism, stress response, DNA repair, and general health (Giblin and Lombard, 2016).

On the other hand, senolytics can induce death in senescent cells, modulating AMPK, p53, BCL-2, and BCL-XL pathways (Monganelli et al., 2020). Specifically, p53 is known as the guardian of the genome because it is essential in aging and cancer prevention. P53 has a pivotal role in (i) the activation of DNA repair mechanisms, (ii) the regulation of the progression of the cell cycle, impeding the growth of damaged cells and inducing their apoptosis, and (iii) the management of telomeres shortning (Fujita, 2019; Brady and Attardi, 2010).

Recent works demonstrated the ability of senolytics to improve cognitive function in aging and in different models of dementia (Figure 12; Sikora et al., 2021).
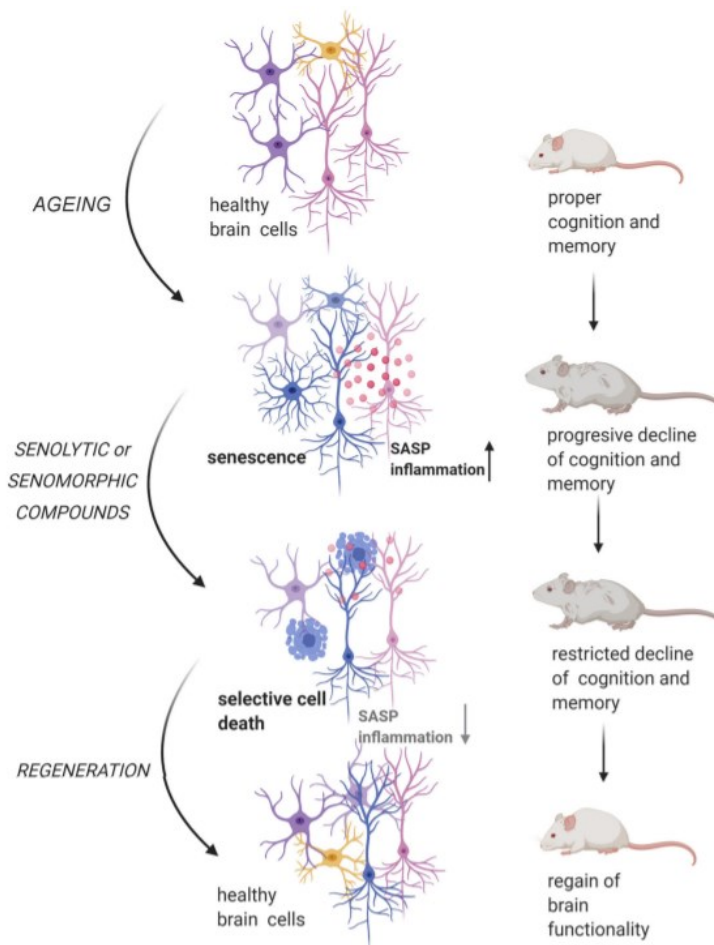
*Figure 12: During physiological aging, brain cells undergo senescence displaying the SASP, increasing the neuroinflammation levels and leading to a progressive decline of cognition and memory. The treatment with senolytic or senomorphic compounds determines the death or the restoration of functions in senescent cells, leading to a regain of brain functionality.*
*From Sikora et al., 2021.*

## 3.3 Frailty

The progressive deterioration of physiological functions during aging often leads to people's hospitalization, hence the need to develop a universal term that describes the clinical symptoms of aging, led to the formulation of the concept of "frailty". Among the elderly, frailty is often defined as "a clinical state characterized by an increased vulnerability of the organism

to stressors, exposing individuals to negative health-related outcomes" (Robertson et al., 2013; Cesari et al., 2017), in the absence of recognized pathologies. Frailty is a multisystem dysregulation leading to decreased physiological reserve (Fried et al., 2001; Bandeen-Roche et al., 2006). Thus, frailty is related to aging, but it does not reflect chronologic age, showing the heterogeneity of the aging course between different subjects (Piggott and Tuddenham, 2020). To date, an international standard method for detecting frailty is not available. However, usually, frailty can be diagnosed in the presence of at least three of the following indicators: slow walking and movement speed, involuntary weight loss, weakness, fatigue, and decreased physical activity (Fried et al., 2001). Furthermore, frailty is often identified by assessing the frailty index (FI), considering the number of accumulated deficits in the individual, including disability, physical and cognitive decline, and previous pathologies. Thus, the frailty index reflects the amount of deficits present in a given subject (Mitnitski et al., 2001; Rockwood and Mitnitski, 2007; Rockwood et al., 2017; Palliyaguru et al., 2019). A review of Dent and colleagues (2016) listing and discussing the main frailty measurements used in preclinical and clinical researches confirmed that the two most common methods for frailty measurement are Fried's phenotype and accumulated deficits models, such as Rockwood and Mitnitski's Frailty Index.

Currently, it has not yet been clarified what the main cause of frailty is, and aging itself cannot fully justify the onset of this syndrome, given that not all elderly people are frail. However, it is known that, from a clinical point of view, this syndrome simultaneously involves several organs, i.e., musculoskeletal, nervous, and immune systems. Indeed, to date, the concept of frailty is still in evolution, and there is no universal definition of this condition. Recently, the relationship between physical weakness and cognitive deterioration has been well documented in the literature. During the last years, the term "cognitive frailty" was coined for indicating a "heterogeneous clinical manifestation characterized by the simultaneous presence of both physical frailty and cognitive impairment". Two main aspects must be detected to define this condition: the presence of physical frailty and cognitive impairment and exclusion of dementia or neurodegenerative diseases (Aubertin-Leheudre et al., 2015; Kelaiditi et al., 2013).
The relationship between physical frailty and cognitive decline could be explained by the direct crosstalk between muscle and brain functions, also known as brain muscle loop theory, in which the CNS has a crucial role in preserving muscle functionality, and muscle integrity is essential in maintaining neuronal physiology. Indeed, muscle secretes myokines contribute to regulating brain functions, and neurotransmitters significantly influence muscle activity (Lauretani et al., 2017; Pedersen, 2019; Figure 13).
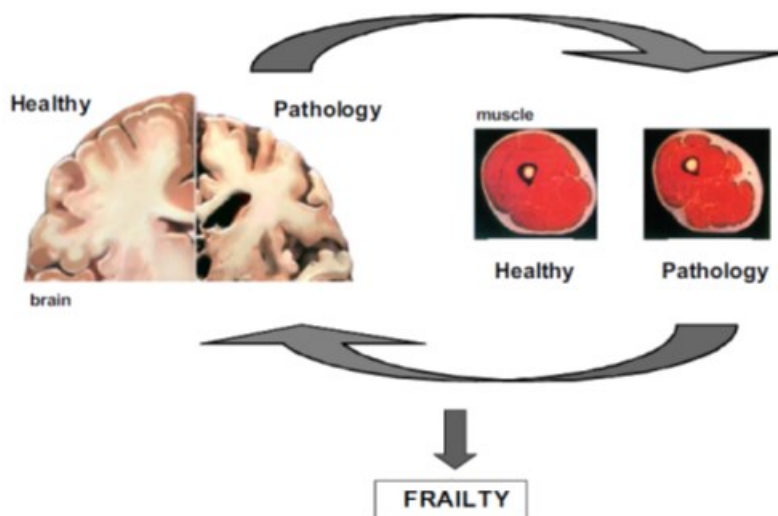
*Figure 13: Muscle-brain crosstalk. Modified by Lauretani et al., 2017.*

Finally, recent studies reported the existence of a correlation between cognitive frailty and the onset of health decline, with a consequent increase in hospitalization and mortality and worsening of the quality of life, which also negatively affects cognitive abilities leading to neurodegenerative diseases and the progression of dementia (Ruan et al., 2015; Ruan et al., 2017).

## 3.4 Recognition memory

The idea that memory is not a single mental faculty has a long and exciting history, but it became a subject of biological investigation only in the mid-twentieth century (Squire, 2004). To date, there is a consensus about the multicomponent nature of memory, which is supported by different brain systems. One of the most important distinctions is between short- and long-term memory. Long-term memory can be separated into declarative (explicit) memory and few non-declarative (implicit) forms of memory, which include habits, skills, priming, perceptual learning, nonassociative learning, and conditioning (Figure 14).
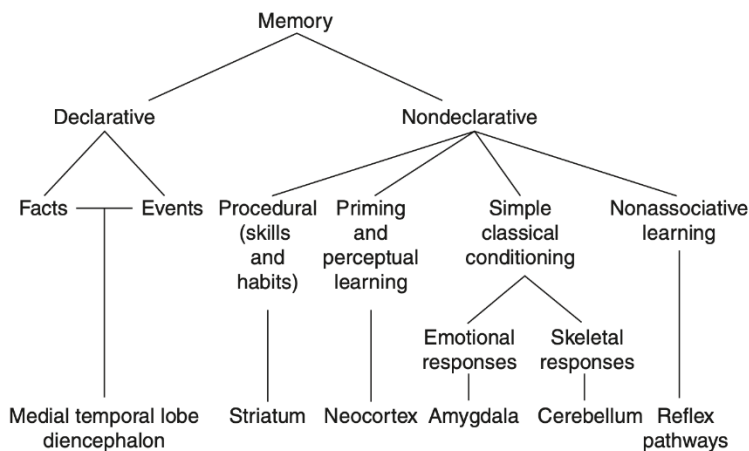
*Figure 14: Configuration of long-term memory in mammals: long-term memory could be divided into declarative and non-declarative memories. The figure shows the brain structures necessary for each type of memory. From Squire and Dede, 2015.*

Nondeclarative memory is fundamentally supported by the amygdala, striatum, cerebellum, and neocortex, whereas declarative memory principally depends on the hippocampus and parahippocampal cortices (Squire and Dede, 2015). Declarative memory, which provides a way to represent the outside environment, comprises two main components: semantic memory and episodic memory. Episodic memory refers to consciously recalling individual episodes or experiences (Squire and Dede, 2015). Conceptually, episodic memory involves a series of steps, including encoding, consolidation, and retrieval. The encoding describes the information processing, the consolidation involves storing this information in a form that will be mentally accessible in the future, and the recovery refers to remembering such information (Matthews, 2015).

Among episodic memory, recognition memory refers to the capability to discriminate a stimulus or an environment as familiar or novel. Recognizing objects, people, or environments previously encountered is a vital cognitive function in animals. Indeed, the recognition memory is considered one of the essential features of human and mammalian personalities (Bird, 2017).

Researchers have long been interested in the mechanisms underlying recognition memory, developing two principal models: the single-process and dual-processes models. For both models, recognition memory is composed of two components: knowledge or knowing (the ability to

discriminate something familiar from something new) and remember or remembering (the ability to remember the spatial and temporal context of events and stimuli previously encountered). The single-process model considers recognition memory as a unitary process directly linked to other explicit memory forms and dependent on the same system (Brown and Aggleton, 2001). On the contrary, the dual-process model proposes that recognition memory is supported by two functionally distinct processes mediated by different structures of the medial temporal lobe: the hippocampus (which supports the associations collected and the relationships between stimuli) and the parahippocampal regions (which support the recognition of single objects) (Eichenbaum et al., 1994; Tulving, 1985).

So, for the single-process model, recognition memory is a process based on familiarity, in which "knowing" reflects a weaker memory and "remembering" is associated with a more intense memory:  these two processes differ only quantitatively. Conversely, for the dual-process model, recognition memory processes are qualitatively distinct (Ameen-Ali et al., 2015). In particular, Brown and Aggleton (2001) hypothesized that the hippocampus belongs to an extended circuit specifically required for episodic memory, while the perirhinal cortex is part of a circuit involved in the judgments of familiarity of a stimulus encountered and of what is recent.

Studies conducted in our laboratory supported the dual-process model of recognition memory, suggesting that "knowledge" and "remembering" are placed in two different brain areas, i.e., hippocampus and parahippocampus, confirming and reinforcing this paradigm about memory in neuroscience and neurobiology (Rossi et al., 2018). In particular, we demonstrated in adult mice that *H. erinaceus* sporophore and mycelium extracts exert their nootropic effect only on the knowledge component (assessed using specific spontaneous behavioral tests: NOR and emergence tasks), whereas they did not modulate the remembering component (assessed using specific spontaneous behavioral tests: OL and Ymaze tasks) (Figure 15).
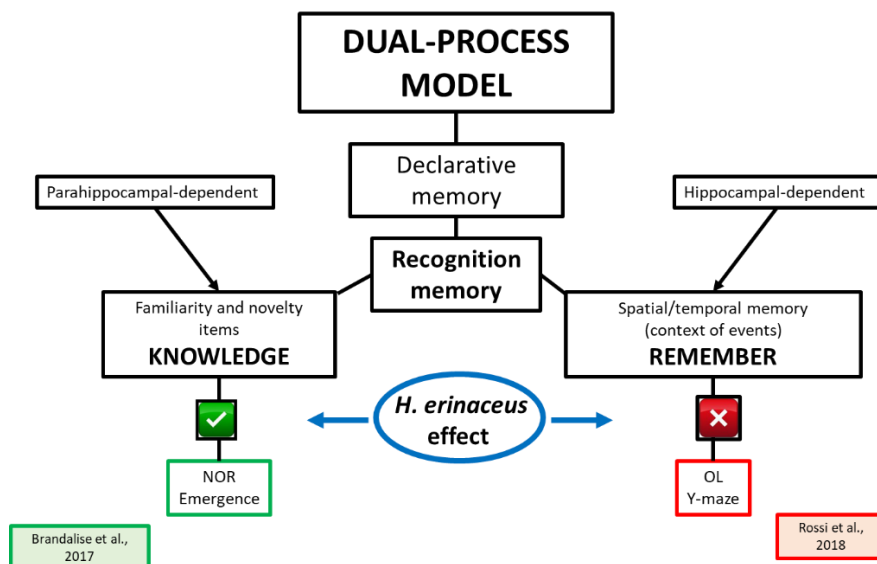
*Figure 15: Effects of H. erinaceus on the two components of recognition memory.*

Notably, the recognition memory is one of the memories most affected by aging; indeed, elderly people display an impairment in free recall and item recognition tasks compared to younger adults (Graves et al., 2017; Fraundorf et al., 2019). A recent meta-analysis, in particular, suggests that knowledge and remember components are affected in a different way during aging, and the effect of aging is most important on the knowledge component (Rhodes et al., 2019), confirming once again the dual-process model.

## 3.5 Novelty-seeking behavior

Novelty-seeking behavior is the propensity to explore new and unfamiliar stimuli and environments. It can be evaluated in humans using questionnaires and in mice using spontaneous behavioral tests.

Novelty-seeking behavior is principally dependent on dopamine circuits (Costa et al., 2014). Discovering novel objects and environments decreases insecurity, and it is essential for improving choice behavior and creative performances in all mammalian species (Cloninger, 1987; Cohen et al., 2007; Gocłowska et al., 2019).

The contrary of novelty-seeking behavior is neophobia, which is the hesitation to explore new stimuli, such as objects and environments. A

decrease in novelty-seeking behavior is a risk factor for the development of mood disorders, such as depression and anxiety (Stedenfeld et al., 2011). Notably, novelty-seeking behavior decreases during aging (Faraji et al., 2019; Stanojlovic et al., 2019).

## 3.6 Sleep and mood disorders

Sleep is fundamental for mood and physical health, influencing the quality of life. Indeed, sleep disorders (such as difficulty falling asleep, insomnia, poor sleep quality, continuous awakenings, etc.) are risk factors for the development of different diseases, from metabolic (i.e., obesity and type 2 diabetes) to cardiovascular. Often people with inadequate sleep report daytime fatigue with cognitive difficulty and decrease in memory and learning abilities (Xie et al., 2017; Zhao et al., 2020). These impairments could lead to unhealthy mental states, leading to mood disorders and over the long term to neurocognitive alterations, leading to dementia. Notably indeed, sleep disorders are frequent in patients affected by cognitive impairment (Shenker and Singh, 2017). Furthermore, sleep disorders can predict the probability of developing depression, anxiety, and dementia and aggravate already present symptoms (Chance Nicholson and Pfeiffer, 2021).

Anxiety is a standard and adaptative emotion with a protection meaning towards danger in an evolutionary perspective, and already the Greek and Latin authors discussed about this sensation. In the last two centuries, there have been talking about anxiety disorders for situations in which anxiety is a distressing pathological feeling and not normal adaptative anxiety (Crocq et al., 2015). The latest Diagnostic and Statistical Manual of Mental Disorders (DMS-5) defined anxiety disorder as "Excessive anxiety and worry (apprehensive expectation), occurring more days than not for at least six months, about many events or activities (such as work or school performance)".
Anxiety disorders are an extreme apprehension accompanied by irritability and nervousness. Anxiety disorders display several specific and non-specific symptoms, such as restlessness, fatigue, impaired attention, concentration, and information processing, irritability, excessive anxiety and worry, and sleeping difficulty. Excessive anxiety and worry about several issues, experiences, or events determine difficulty carrying out everyday activities on multiple levels, impacting health and predisposing to neophobia (Nechita et al., 2018; Glasofer, 2021). Furthermore, anxiety

disorders are a predictor factor for the development of depression (Nechita et al., 2018).

Depression is "the persistent feelings of sadness and hopelessness and loss of interest in activities they once enjoyed" for at least two weeks. Like anxiety, depression displays several symptoms, and to diagnose this mood disorder, the patient must have at least five symptoms between (i) diminished interest in everyday activities, (ii) depressed mood, (iii) modification in appetite, (iv) reduction of physical activity, (v) fatigue, (vi) feelings of worthlessness or inappropriate guilt, (vii) impaired concentration or attention, and (viii) thoughts of death or suicidal ideation or attempt. The DMS5 subdivided depression into two different diagnoses: (i) with mixed features and the presence of manic symptoms, and (ii) with anxious distress (Truschel, 2020), suggesting the critical link between these two mood disorders, beyond that with sleep disorders.

The main regions and circuits of the brain mainly involved in mood disorders belong to the limbic system, among which (i) amygdala, fundamental in cognitive and emotional processing of fear and anxiety (Tovote et al., 2015); (ii) pre-frontal cortex, necessary for the regulation of appropriate behavior in response to fear and stress (Hare and Duman, 2020; Tovote et al., 2015); (iii) hippocampus, essential for cognitive process and regulation of feelings (Bartsch and Wulff, 2015).

Among the hypothesis about the pathogenesis of mood disorders, one proposes that the alteration of concentration of growth factors in CNS (such as neurotrophin-3, NGF, and BDNF) plays a crucial role in the onset and maintenance of depression, as demonstrated by (i) the antidepressant effect obtained through the neurotrophins infusion in the brain, (ii) the increase in neurotrophin brain levels during antidepressant treatment, and (iii) the increased neurogenesis as a consequence of antidepressant drugs treatment (Altar, 1999; Malberg et al., 2000; Levy et al., 2018; Lino de Olivera et al., 2020). Neurotrophins are essential in regulating the response to different stimuli reorganizing the structure, function, and connections between neurons, impacting their survival and proliferation. The neurotrophin most described as related to mood disorders is BDNF. BDNF stimulates the growth, differentiation, and survival of neurons and synapses in the CNS and regulates neuroplasticity. Furthermore, the correct pro-BDNF/BDNF ratio is crucial during the control and stimulation of hippocampal neurogenesis (Leal et al., 2017). Notably, dysregulation in pro-BDNF/BDNF ratio is observed both in depression and in obesity. Hence, both obese and depressed

subjects display an impairment in adult hippocampal neurogenesis (Duman and Monteggia, 2006; von Bohlen Und Halbach et al., 2018).

So, in modern society, mood disorders are more and more common, and finding an efficacy therapy without side effects for their treatment is a crucial challenge. In addition to western medicine, which often determines the side effects onset, more and more papers have suggested the impact of nutrition and supplements intake on mood and sleep quality. Indeed, using diet and supplements management to improve mood and sleep disorders is effective (Liu et al., 2015; Zhao et al., 2020).

## 3.7 Adult neurogenesis in the hippocampus

It has been known for several years that the hippocampus is one of the areas in which adult neurogenesis occurs. This event attracted considerable attention because it appears to be involved in cognitive functions, memory, and behavior control. Adult neurogenesis has so far been extensively described and characterized in animal models such as rodents, but it is also supposed to occur in humans whose study on the actual functional role is limited to the analysis of post-mortem samples. For this reason, despite it is still not completely clear how this phenomenon can participate in normal brain functions, it is known that its dysregulation can lead to the onset of diseases in humans (Toda et al., 2019; Fares et al., 2019).

In mammals, the proliferation of new neurons in the hippocampus occurs in the subgranular zone (SGZ) of the dentate gyrus (DG). SGZ possesses a particular microenvironment, called "neurogenic niche", that allows neuronal proliferation. The neurogenic niche consists of precursor cells, immature neurons, glial, endothelial cells, immune system cells, microglia, macrophages, and extracellular matrix proteins (Andreotti et al., 2019; Mercier et al., 2002). In particular, the proliferative neural stem cell can generate granular excitatory granule neurons in the DG of the hippocampus, and to date, there is no specific evidence that other neuronal types are generated under physiological conditions, although some researchers have reported the generation of different kinds of neurons (Liu et al., 2003; Rietze et al., 2000).

The adult neurogenesis process takes about seven weeks to be completed and can be divided into four phases: (i) a precursor cell phase which has the task of keeping the progenitor cell pool active, (ii) an early

survival phase which determines the exit of the cells from the cell cycle, (iii) a postmitotic maturation phase in which they develop cytoplasmic extensions and establish connections, and (iv) a late survival phase in which the cells establish themselves in their final location.

About 70-85 % of newborn neurons die within the first two weeks of life in physiological conditions. Instead, the surviving neurons became granule cells of DG that receive synapses from the entorhinal cortex and extend their axons to the CA3 area (Snyder et al., 2009; Kempermann et al., 2015).

Notably, neurotrophic factors, i.e., BDNF and NGF, can promote and regulate the neural stem proliferation through the TrkB pathway and intersecting with the serotonin system (Mattson et al., 2004; Gardier et al., 2009; Taliaz et al., 2010; Zhang et al., 2013; Foltran and Diaz, 2016; Corvaglia et al., 2019). Notably, neurotrophins also play critical roles in the survival and differentiation of neurons during adult neurogenesis (Frielingsdorf et al., 2007; Vilar and Mira, 2016).

The adult neurogenesis in the hippocampus seems to be regulated both positively and negatively by several environmental stimuli, psychological state, and lifestyle of the individual. An environment rich in stimuli (such as open spaces and new objects) increases the adult neurogenesis rate, whereas stress and aging reduce adult neurogenesis frequency (Urban and Guillemot, 2014; Toda et al., 2019). Indeed, during aging, a physiological decline in adult neurogenesis occurs and it is partially explainable to the significant differences in gene expression in the hippocampus of young and aged individuals (Singhal et al., 2020).

## 3.8 Gut microbiota

The human gut is inhabited by a huge number of mutualistic/commensal bacterial, fungal, archaeal, viral, and protozoal communities, which together form the microbiota (Guarner and Malagelada, 2003; Jandhyala et al., 2015; Rinninella et al., 2019). Notably, in the human body, the number of microorganisms is almost ten times (up to 100 trillion) higher than eukaryotic cells (Bäckhed et al., 2005; Ursell et al., 2012).

The colonization of the gut begins during pregnancy until it is more stable at three years old (Figure 16), despite undergoing numerous changes until the end of adolescence, becoming more steady in adulthood (Lynch and Pedersen, 2016).
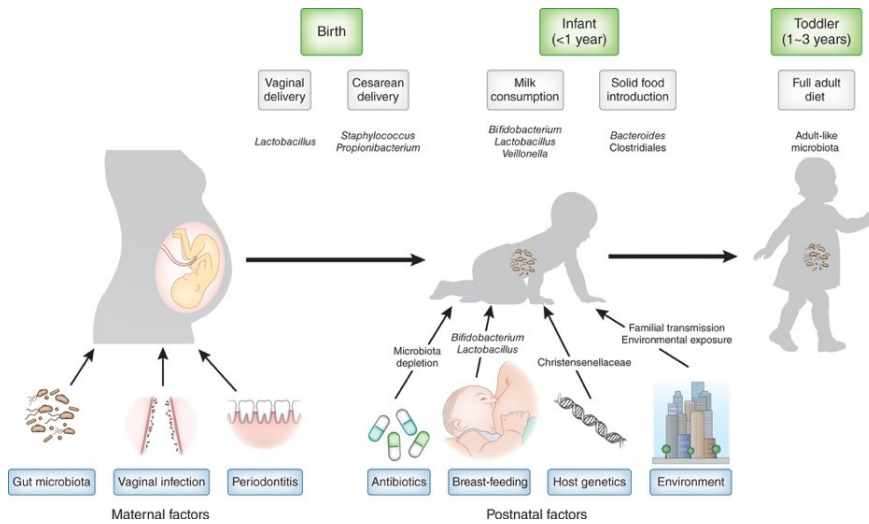
*Figure 16: The figure shows all the modifications that can affect the development of the intestinal microbiota in early life until it is stabilized at three years old. From Tamburini et al., 2016.*

Several factors, such as host diet, lifestyle, environmental exposure, genotype, and physio-pathological states influence, both positively or negatively, gut microbiota composition, which changes dynamically throughout the host's life (Turnbaugh et al., 2007). Several recent works underline that correct diet, probiotics, prebiotics, and synbiotics supplementation positively influence microbiota composition, inducing the growth of healthy bacteria. Moreover, antibiotics, the type of birth, feeding types, environmental factors, genetic conditions, geographic location, and age can influence the gut microbiota composition, and not always positively. As regards the kind of birth, it has been demonstrated that children born naturally seem to resemble gut microbiota of the mother's vagina, where the main phylum is *Bifidobacteria*, while microbiota of children born through cesarean section is like the mother's skin microbiota (Perez-Munoz et al., 2017; Lloyd-Price et al., 2016). Modifications or alterations during the colonization in infancy can heighten the risk of metabolic diseases onsets in adulthood, like obesity, diabetes, and hypertensive pathologies. Upon aging, modifications or alterations of gut microbiome composition occur, and the individual becomes more susceptible to developing neurodegenerative diseases like Alzheimer's disease and dementia.

Nowadays, thanks to high-through sequencing technologies, it is possible to determine the taxonomy of the gut microbiota, which is composed of different bacteria species taxonomically classified by species, genus, family, order, class, and phyla (Rinninella et al., 2019). In this way, differences in distribution at the species and genus level and beyond can be evaluated. Additionally, the new omics sciences, such as metagenomic, metabolomic, metaproteomic, and metatranscriptomic techniques, can provide information about microbial activity (Heints-Buschart and Wilmes, 2018).

The bacterial composition of the gut microbiota shows a wide inter-individual variation due to environmental and genetic factors (Bibbò et al., 2016). Consequently, an optimal microbiota composition may never be defined. Furthermore, even though general gut microbial composition remains constant in the same individual, gut microbiota exhibits temporal and spatial differences in microorganisms distribution (Bäckhed et al., 2005). However, the correct microbiota composition is an essential factor for host health: several studies demonstrated that microbiota dysbiosis is related to different pathologies, from intestinal disorders to metabolic and neurodegenerative diseases (Clemente et al., 2012; Quigley, 2013). So, intervening in gut microbiota composition is fundamental to preventing and treating different diseases.

Despite the variability, a functional core microbiome composed of abundant bacterial taxa seems common to various individuals regardless of gender, geographic location, and age (Kim and Jazwinski, 2018). So, healthy human and rodents gut microbiota, which dynamically interacts with to host, contains two predominant phyla, *Bacteroidetes* and *Firmicutes*, followed by the *Actinobacteria, Proteobacteria,* and *Verrucomicrobia* phyla (Shortt et al., 2018; Rinninella et al., 2018). In particular, the *Firmicutes/Bacteroidetes* ratio is critical: a ratio imbalance is related to different diseases, such as obesity and cardiovascular diseases (Ley et al., 2006), and also to aging (Mariat et al., 2009).

Regarding genera level, the predominant genera are *Bacteroides, Bifidobacterium, Eubacterium, Clostridium, Peptococcus, Peptostreptococcus,* and *Ruminococcus.* On the contrary, the aerobes (facultative anaerobes) genera, such as *Escherichia, Enterobacter, Enterococcus, Klebsiella, Lactobacillus, Proteus*, etc., are among the subdominant genera. Furthermore, microbiota also includes viruses, especially phages, such as *Eukarya*, and again *Fungi, Blastocystis, Amoebozoa,* and *Archaea* (Bibbò et al., 2016).

The human organism and microbiota are in a mutualistic symbiosis to give a superorganism (Figure 17). Indeed, humans are the result of the integration of their genome with the genome of all the microorganisms throughout evolutionary history. So, the human-microbiome is considered a superorganism, a further step of evolution (Salvucci, 2019).
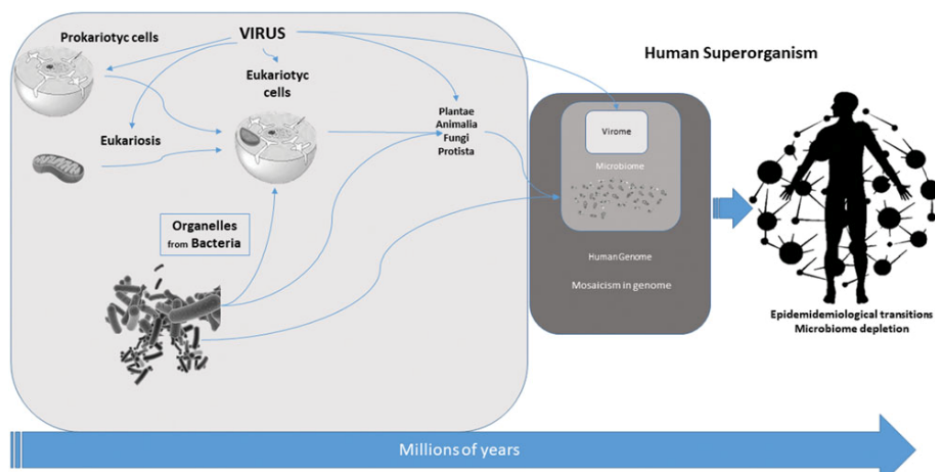


*Figure 17: The figure shows the human superorganism due to the interactions between the human genome and microorganisms. From Salvucci, 2019.*

The main functions of healthy gut microbiota are (i) metabolic (expressing several enzymes not produced by the host), (ii) trophic by maintaining the structural integrity of gut mucosal barrier, (iii) protective against pathogens, and (iv) immunological by regulating cytokines production and Th1-Th2 balance (Guarner and Malagelada, 2003; Jandhyala et al., 2015; Rinninella et al., 2019; Gomaa, 2020). Furthermore, commensal bacteria sustain the structural integrity of the intestinal mucosal barrier by maintaining the expression of tight junction proteins, such as claudin-1, Zonula Occludens-1 (ZO-1), and occludin (Morrison and Preston, 2016). Gut microbiota also has a barrier function, defined as protecting the intestine from damaging substances and controlling the intake of different substances across the mucosa. Additionally, the gut microbiota is implicated in xenobiotic and drug metabolisms. Finally, another fundamental gut microbiota function is the synthesis of vitamin K and several components of vitamin B (Jandhyala et al., 2015) (Table 4).

| Main functions of healthy gut microbiota |
|---|
| **Metabolic** |
| Fermentation of non-digestive dietary residue;<br>Salvage of energy;<br>Production of SCFAs, folic acid, arginine, glutamine, vitamin B components, and vitamin K;<br>Absorption of ions;<br>Participation in drug metabolism. |
| **Protective** |
| Prevention of colonization by pathogens. |
| **Trophic** |
| Control of epithelial cell proliferation, differentiation, and renewal;<br>Development and homeostasis of immune system. |
| **Immunological effects** |
| Stimulation of IgA production;<br>Promotion of  anti-inflammatory cytokines release;<br>Down-regulation of  pro-inflammatory cytokines release;<br>Induction of regulatory T (Treg) cells. |

*Table 4: Main Function of healthy gut microbiota*

Gut bacteria can also biotransform diet-introduced polyphenols allowing their portal vein absorption and, therefore, their metabolic effects. *Bacteroides, Roseburia, Bifidobacterium, Fecalibacterium,* and *Enterobacteria* can ferment digestion-escaped carbohydrates and indigestible oligosaccharides, producing short-chain fatty acids (SCFAs; i.e., acetate, propionate, and butyrate), which are energy sources for the host (Macfarlane and Macfarlane, 2003) and help to prevent the accumulation of toxic metabolic by-products (Jandhyala et al., 2015). SCFAs are fundamental for gut health, leading to eubiosis, stimulating epithelial barrier function, regulating immune response, and protecting against cancer (La Rosa et a., 2018; Zhang et al., 2018). Furthermore, SCFAs can modulate the immune system and inflammation process and elicit epigenetic mechanisms (Kogut et al., 2020). In particular, recent studies confirm that the decrease of the SCFAs increases the inflammation in CNS. Indeed, therapies focusing on SCFAs are being developed for treating CNS diseases (Silva et al., 2020). Moreover, it has

been demonstrated on animal models that butyrate can pass through the blood-brain-barrier (BBB) and exerts significant neuroprotective effects. Butyrate leads to the inhibition of histone deacetylation (HDAc), an enzyme involved in epigenetic mechanisms associated with inflammatory responses. The HDAc inhibition also brings to the inhibition of the nuclear factor kappa-$\beta$ (NF-$\kappa$B) present in macrophages or microglia, localized in the lamina propria of the gut and in the CNS, resulting in reduced pro-inflammatory responses (Levy et al., 2017).

Recently, more and more interest is focused on the gut microbiota: dysbiosis has been associated with several human diseases, such as inflammatory bowel diseases (IBD), irritable bowel syndrome (IBS), obesity, diabetes, allergic disorders, and neurodegenerative diseases (Jandhyala et al., 2015; Konjevod et al., 2021; Goyal et al., 2021; Li et al., 2022).

### 3.8.1 Microbiota and aging

The hallmarks of aging lead to the decrease of functions of tissues and to inflammation, in particular in the gastrointestinal system, increasing the predisposition to gut-associated diseases by causing alterations in the gut microbiota composition in elderly people (Napgal et al., 2018).

In literature, many scientists confirm that gut microbiota significantly changes during aging (Kim and Jazwinski, 2018). Overall, the aging-associated microbiota is characterized by (i) a decline in microbial diversity, (ii) a decrease of the two main phyla (*Firmicutes* and *Bacteroidetes*), and (iii) an increase in the subdominant species belonging to other phyla, as well as a rearrangement in their co-occurrence network. Furthermore, there is an imbalance between the two principal bacterial phyla: *Firmicutes* and *Bacteroidetes*. Specifically, it has been described during aging a decrease in the *Firmicutes* phylum, corresponding to a reduction in SCFAs levels, and in contrast, an increase in *Bacteroidetes* phylum. Furthermore, analysis of aged gut microbiota composition showed an increase of opportunistic pathogens and potential pathobionts (Figure 18), including the pro-inflammatory *Desulfovibrio spp*., *Clostridium perfringens, C. difficile*, and *Proteobacteria spp*., and a decline of the health-promoting SCFAs-producers and anti-inflammatory bacteria, such as *Bifidobacteria spp., Ruminococcus obeum, Roseburia intestinalis, Faecalibacterium prausnitzii, Akkermansia spp*., and *Lactobacillus spp*. (Mariat et al., 2009; Salazar et al., 2014; Salazar et al., 2017; Van der

Lurgt et al., 2018; Napgal et al., 2018; Mangiola et al., 2018; Bana and Cabreiro, 2019; Goma et al., 2020). Consequently, the gut microbiota of aged individuals leads to an increase in pro-inflammatory levels.
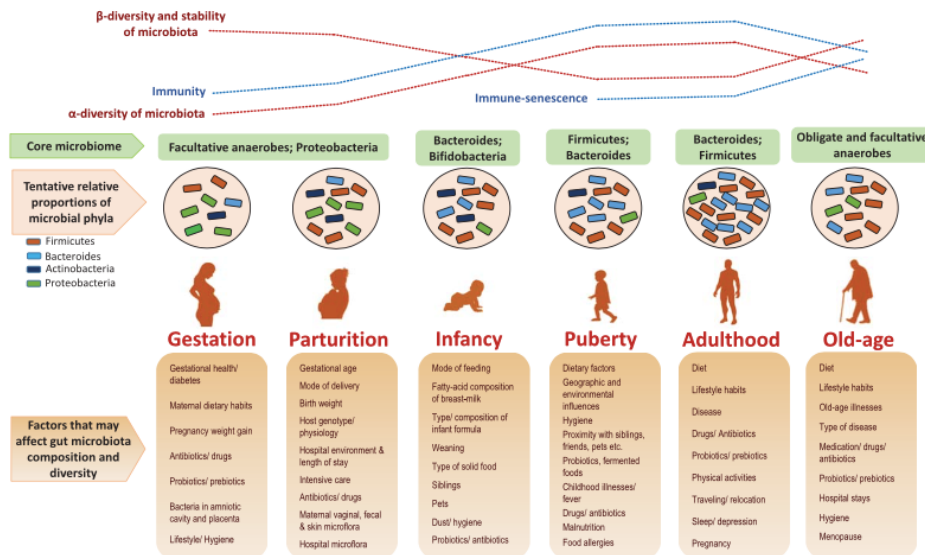


*Figure 18: Age-related changes in the human gut microbial ecosystem and factors affecting bacterial composition. From Nagpal et al., 2018.*

However, these changes can also lead to longevity and extreme longevity (Wu et al., 2019). Centenarians and super-centenarians represent the best model of "successful" aging, showing a lower index of illness, a reduction of comorbidity, and an extension of lifespan. The study of centenarians' gut microbiota needs to understand how bacteria can adapt in an extremely long lifespan, influenced by age-related environmental factors (lifestyle, diet, age-related diseases, etc.) and endogenous changes. The principal changes in the gut microbiota of centenarians are similar to ones found in aged people: (i) the decrease of relative abundance of the core microbiota, (ii) the enrichment of subdominant taxa, (iii) the accommodation of allochthonous bacteria, and (iv) the "Longevity adaptation" seems to involve enrichment in health-associated gut bacteria (Biagi et al., 2016). In centenarians, in particular, the core gut microbiota, composed of dominant symbiotic bacterial taxa *Ruminococcaceae, Lachnospiraceaeae,* and *Bacteroidaceae* loses diversity during aging. This phenomenon is counterbalanced by increased longevity-adapted and possibly health-promoting species like *Akkermansia, Bifidobacterium,* and *Christensenellaceaea.* Moreover, several butyrate producers, such as *Rominococcus obeum, Roseburia intestinalis,* and *Fecalibacterium prausnitzii* have been found in a lower concentration in centenarians' gut microbiota, while *Anaerotruncus*

*colihominis* and *Eubacterium limosum* increased. Additionally, in the gut microbiota of centenarians and supercentenarians have been found micro-organisms typical of other niches, such as *Mogibacteriaceae* and *Synergistaceaea* (Biagi et al., 2016). Therefore, scientists can confirm that, even if the most important core components are lost in centenarians' gut microbiota, they acquire in parallel a wealth of new microbial components. Indeed, higher diversity and enrichment of *Prevotella, Treponema, Bacteroidetes,* and *Clostridiales* bacteria occur. A recent study performed on Italian and Chinese people confirmed that the centenarians' gut microbiota is enriched with *Akkermansia* and *Christensenellaceaee*, considered a marker of longevity (Santoro et al., 2018).

### 3.8.2 Microbiota and frailty

Some authors, i.e., Jackson et al. (2016) and Ticinesi et al. (2018, 2019), defined frailty as a problem associated with gut microbiota dysbiosis by promoting chronic inflammation and anabolic resistance. Comparing the gut microbiota of adult and elderly frail people, many differences in the relative abundance and diversity have been noted that may be connected with frailty. *Clostridiales,* in particular *Ruminococcaceae* and *Fecalibacterium prausnitzii* are negatively correlated with frailty, whereas *Eubacterium dolichum* and *Eggerthella lenta* are positively correlated (Jackson et al., 2016). Like aging, frailty is associated with an overall decrease in microbial diversity, with the increase in *Bacteroides* relative abundance and the decrease in *Firmicutes* that leads to a decrease in SCFAs production (Morgan et al., 2013). Concordantly, the presence of SCFAs producers, such as *Lachnospiraceaea*, *Roseburia, Fecalibacterium prausnitzii,* is considered a suitable parameter for preventing frailty. These bacteria are able to metabolize SCFAs, which induce inhibition of the inflammation processes, considered one of the leading causes of frailty (Jackson et al., 2016). Indeed, inflammation increases gut permeability and the overexpression of several bacteria, including the pathobionts, such as *Porphyromonadaceae*, *Odoribacter, Butyricimonas, Clostridium,* and *Oxalobacter*. Furthermore, a recent study on elderly patients evidenced that the increased relative abundance of *Enterobacteriaceae*, *Fusobacteriaceae,* and *Porphyromonadaceae* is negatively correlated with patients' cognitive performances, while the overexpression of *Lactobacillus* is positively correlated with cognitive performances in elderly patients (Ticinesi et al., 2018). Moreover, phenotypic frailty was also associated with the decreased relative

abundance of other anti-inflammatory and overexpression of other species, including *Eubacterium, Eggerthella, Ruminococcus,* and *Coprobacillus* (Ticinesi et al., 2019).

Furthermore, notably, higher frailty index scores were significantly related to a reduction in alpha diversity, a decrease of anti-inflammatory and butyrate producers bacteria, and an increase of pro-inflammatory and LPS producers microorganisms such as *Enterobacteriaceae* (van Tongeren et al., 2005; Jackson et al., 2016; Haran et al., 2018; Piggott and Tuddenham, 2020).

Thus, it is possible to confirm a correlation between gut microbiota and frailty. Currently, it is still unclear if a modification in the gut microbiota causes the manifestation of frailty or *vice versa*. However, probiotics and prebiotics are used in animal models to modulate the gut microbiota and avoid frailty. Indeed, the first action of the probiotics and prebiotics is to inhibit the inflammation process and promote longevity in mice (Santoro et al., 2017).

## 3.9 The microbiota-gut-brain axis

Already in 460 – 370 BC, Hippocrates of Kos wrote "All disease begins in the gut", but only at the end of 1800, Elie Metchnikoff was the first who supposed a theory about the connection between gut and brain, known as the *gut-brain axis* according to the beneficial bacteria contained in the gut can positively influence health and delay cognitive decline (Scott et al., 2017; Cryan et al., 2019). In the beginning, this idea was not accepted by the scientific community, but today it is proved that the absence or imbalance of the gut microbiota leads to alteration in behavior and cognitive functions, such as memory and learning. It also leads to the manifestation of pathologies associated with the CNS like anxiety, depression, and neurodegenerative diseases.
Even if today the processes leading to the communication between the gut microbiota and the brain are not yet totally clear, it is known that this axis is made of a network that includes gut microbiota and its metabolic products, enteric nervous system (ENS), neuroendocrine system, CNS, hypothalamic-pituitary-adrenal axis (HPA), sympathetic and parasympathetic branches of the autonomic nervous system (ANS) (Mayer et al., 2015; Wang and Wang, 2016).
Notably, the gut microbiota-brain communication is bidirectional: the gut can influence the brain activity and metabolism, and the brain can lead to

modifications in the functions of the gut microbiota (Suganya and Koo, 2020; Figure 19). In both cases, these modifications can lead to positive or negative results (Forsythe et al., 2012).
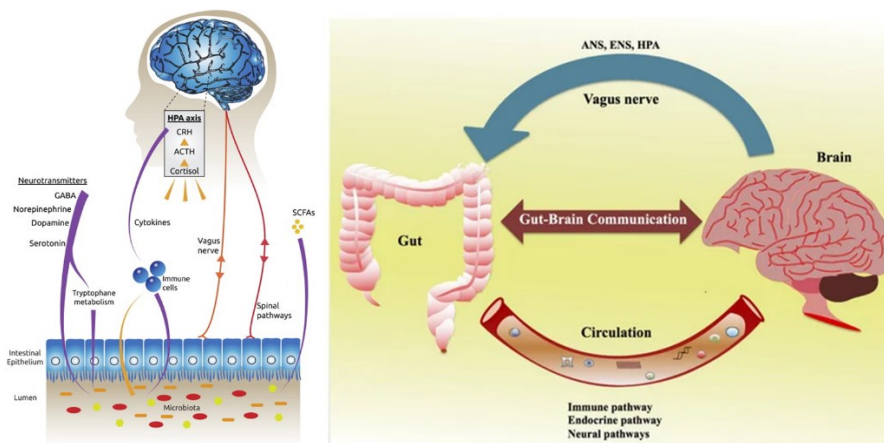


*Figure 19: Gut-brain axis and the bidirectional communication thanks to the use of circulating molecules (involved in immune, neural, and endocrine pathways and metabolites produced after the digestion), vagal nerve, spinal pathway, autonomic nervous system (ANS), enteric nervous system (ENS), and hypothalamic–pituitary–adrenal (HPA. From Suganya and Koo, 2020; Dinan and Cryan, 2017.*

One of the ways of communication between gut and brain is signaling molecules using. Gut bacteria can send to the brain molecules involved in immune responses or in neuroendocrine signaling pathways, like catecholamines, GABA, serotonin, cytokines, and others. The same metabolites can be released into the gut lumen by neurons, immune cells, and enterochromaffin cells (Mayer *et al.,* 2015).

Gut bacteria are also able to metabolize neurotransmitters for obtaining other neurotransmitters (for example, *Lactobacillus* and *Bifidobacterium* can metabolize glutamate to produce GABA), influencing the expression of the subunits of neurotransmitter receptors in brain regions connected with stressful responses (Foster and McVey-Neufeld, 2013).

On the other hand, it was demonstrated that variations in neurotransmitter CNS concentrations influence the proliferative activity of several gut bacteria, including pathobionts.

Another way of communication involved the parasympathetic and sympathetic branches of the ANS, the vagal nerve, spinal pathways, and the neurons that belong to the ENS. ANS and ENS can regulate intestinal

functions, such as regional motility, secretion of acids, production of bicarbonates, microbiota activity, and mucosal immune responses.

Furthermore, the microorganisms' metabolites, such as SCFAs, branched-chain amino acids, and peptidoglycans, can influence the functions of neurons in the gut mucosa,  stimulating fibers, like the vagal nerve, that sends informations to the brain. Consequently, brain activity or behavior can also be influenced by the same molecules (Mayer *et al.*, 2015; Cryan et al., 2019). Moreover, the gut microbiota and the brain can also communicate through the immune system and tryptophan metabolism. So, for all these communications, the host and his cognitive functions can be influenced by the activity of bacteria and *vice versa.*

Several recent papers demonstrated that the treatment with prebiotics or probiotics could alter neuroplasticity and behavior, influencing the microbiota composition (Vázquez et al., 2015; Allen et al., 2016; Burokas et al., 2017; Yang et al., 2018; Gronier et al., 2018; Osadchiy et al.,  2019; Cryan et al., 2019). In addition to probiotics and prebiotics that improve the microbiota-gut-brain axis, many other factors impact the bidirectional communications, such as diet, drugs, genetics, epigenetics, environmental factors, and exercise (Sandhu et al., 2017; Dalton et al., 2019; Cryan et al., 2019). On the other side, several host functions are affected by microbiota-gut-brain axis activity, including food intake, cognitive behavior, stress, social interaction, and fear (Cryan et al., 2019; Figure 20).

Nowadays, the microbiota-gut-brain axis receives more and more interest given its implication in several pathologies, from epilepsy to autism to mood disorders (anxiety, stress, depression) to inflammatory (IBS) to metabolic (obesity) to neurodegenerative diseases (Quigley, 2017; Liang et al., 2018; Martin et al., 2018; Cryan et al., 2019; Saurman et al., 2020; Figure 21). Indeed, targeting the gut-brain axis, for example, through the supplementation with psychobiotics (which confer mental health benefits by impacting microbiota composition), is one innovative intervention for delaying the onset of and treating different diseases (Sarkar et al., 2016; Cryan et al., 2019; Bermúdez-Humarán et al., 2019; Barrio et al., 2021).
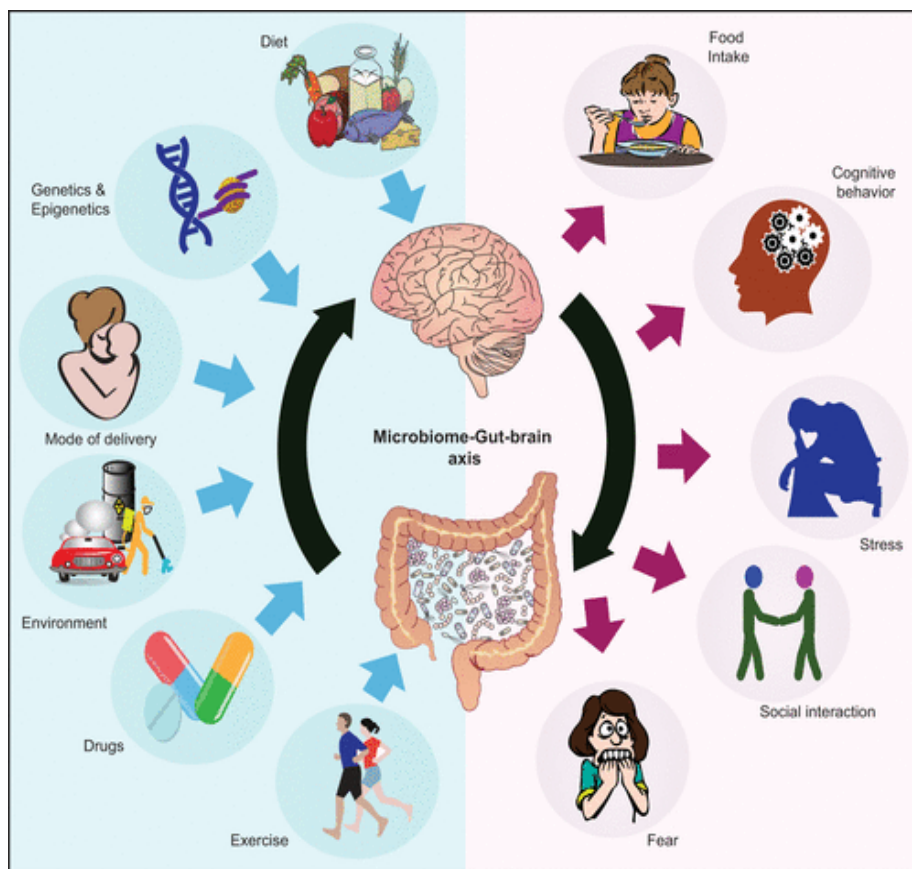
*Figure 20: Factors that affect microbiota-gut-brain axis: diet, genetics and epigenetics, congenital heredity and associated epigenetics, environment, medications, exercise, and mode of delivery at birth, as well as the various behaviors known to be affected by microbiota-gut-brain axis perturbation, including cognitive and social behaviors, stress, fear, and food intake. From Cryan et al., 2019.*
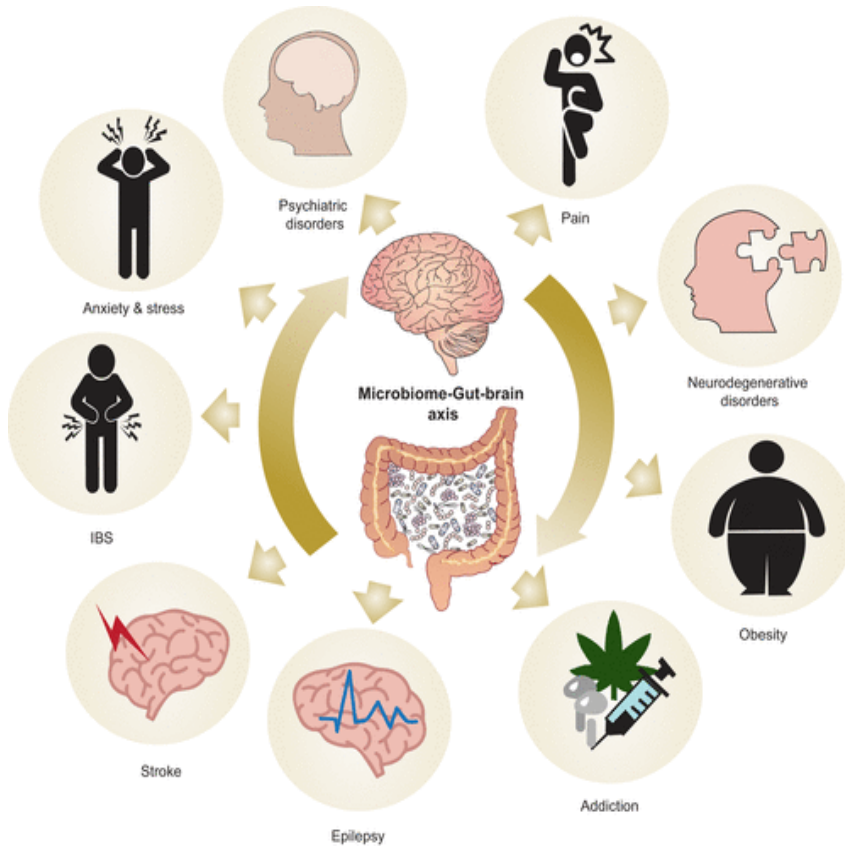
*Figure 21: Diseases related to a dysregulation in the microbiome-gut-brain axis.
From Cryan et al., 2019.*

# 4. Aims of the research

At the end of the early 2000s, about 8% of the world population was 65 years old, and it is estimated that by 2050, 1.5 billion people aged over 65 years old will live in the world, about 16% of the entire population. The constant increase in the average age and life expectancy has led to a higher incidence of neurodegenerative diseases associated with aging. Therefore, it has necessitated studying mechanisms that improve patients' quality of life to age healthily. Indeed, aging is a natural process that affects all living organisms, and the deterioration in physiological functions characterizes it, but notably, the decrease in physiological functions has different rates from individual to individual, making aging a heterogeneous process. However, the social isolation resulting from COVID-19 pandemic social distancing measures has significantly accelerated cognitive decline, depression, and sarcopenia in aged and frail people (Kirwan et al., 2020). Hence, further investigations are mandatory to develop strategies to prevent and reverse frailty, cognitive impairment, and disability in the elderly (Harai et al., 2018), as well as mood disorders in the population.

This Ph.D. project aimed, firstly, (i) to investigate the effect of physiological aging on locomotor and cognitive decline and microbiome composition changes in rodents, next (ii) to study the effects of standardized extracts of *Hericium erinaceus* in mice on frailty reversion and prevention, focusing on novelty-seeking behavior, recognition memory, locomotor performances, and microbiota composition, and, finally, (iii) to explore the effect of *Hericium erinaceus* dietary supplementation on mood and sleep disorders in overweight and obese humans.

Regarding the studies conducted on the preclinical model, in this Ph.D. work, the animal model and behavioral tests were chosen to reach a translational approach and to translate the acquired knowledge from "bench to bedside." Furthermore, we used an interdisciplinary and integrated approach based on physiology and cellular biology techniques.

So, the first purpose of this Ph.D. research was to generate a frailty index (FI) to monitor in a simplified and non-invasive method both locomotor and cognitive aging-related decline in mice. Hence, to assess whether phenotypic frailty was associated with cognitive impairment (evaluated as recognition memory), C57BL/6 wild-type mice were examined during physiological aging *in vivo* in a longitudinal study. In particular, to investigate locomotor and recognition memory performances during

physiological aging, we carried out spontaneous behavioral tests at several experimental times, from adulthood to senescence, evaluating both locomotor and cognitive FIs at each experimental time. Furthermore, we also evaluated the effect of physiological aging on gut microbiota composition since intestinal dysbiosis is known to increase during aging, with enrichment in pro-inflammatory bacteria at the expense of beneficial microorganisms.

Next, in a first set of animals, we selected the frailer aged mice (at 21.5 months) that were supplemented with a blend of sporophore and mycelium *H. erinaceus* extracts (He1) containing 150 µg/g of erinacine A, 500 µg/g of hericenone C, about 20 µg/g of hericenone D, and 460 µg/g of L-(+)-ergothioneine (EGT). In a second set of mice, we started to treat random mice from the adulthood phase, maintaining the oral supplementation until the senescence phase, with an *H. erinaceus* primordium extract (He2) containing 1.30 mg/g of EGT and no nootropic molecules. Notably, we obtained the exact amount of nootropic and bioactive metabolites in *H. erinaceus* using HPLC-UV-ESI/MS technique. In particular, thanks to the first set of animals, we investigated the potential of *H. erinaceus* in reverting frailty, and thanks to the second set of mice, we investigated the potential of *H. erinaceus* in preventing frailty.

The molecular mechanisms of *H. erinaceus* effects were investigated in the central nervous system (CNS) of aged treated and untreated mice using histochemistry and immunohistochemistry with specific markers of inflammation, gliosis, oxidative stress, senescence, blood-brain barrier (BBB) functionality, cell proliferation, and neurogenesis. Furthermore, given the importance of the microbiota-gut-brain axis, we investigated the effect of *H. erinaceus* supplementation on microbiota composition, exploring its possible role as a prebiotic.

Regarding the study in humans, we studied the effect of a commercial dietary supplement based on *H. erinaceus*, the "*Micotherapy Hericium*" provided by A.V.D. Reform s.r.l. (Noceto, Parma, Italy), on mood and sleep disorders, using self-assessment questionnaires, in overweight and obese humans who underwent a low-calorie diet regimen. In this case, to investigate the mechanism based on *H. erinaceus* effect, we examined the concentrations of serum pro-BDNF and BDNF as potential clinical biomarkers.

# 5. Material and methods

## 5.1 Hericium erinaceus collection and extraction procedures

The strains 1 and 2 of *H. erinaceus* were isolated from two *H. erinaceus* collected in Siena province (Tuscany, Italy) from a live specimen of *Quercus ilex*. The basidiomas of *H. erinaceus* were aseptically cut in small portions (about one mm$^3$) and were placed into Petri dishes with 2% malt extract agar as a culture medium (MEA, Biokar Diagnostics). Chloramphenicol at 50 ppm was added in this first step. Incubation was performed at 24°C in complete darkness. The strains were maintained in the Italian Culture Collection of Pavia University (MicUNIPV).

Lyophilized mycelium and sporophores of *H. erinaceus* strain 1 (He1) and primordium of strain 2 (He2) were extracted in 70% ethanol, following the procedure described. One gram of dry substrate was blended with 10 mL of 70% ethanol and left in the thermostat in agitation overnight at 50°C. Before withdrawing, the material was stirred for one hour and was centrifuged at 4000 rpm for 3 minutes (Gerbec et al., 2015). The supernatant was stored at −20 °C until it was analyzed through HPLC-UV-ESI/MS method.

## 5.2 Quantification of bioactive metabolites through HPLC-UV-ESI/MS

HPLC-UV-ESI/MS analyses were carried out on a Thermo Scientific LCQ FLEET system, equipped with a PAD-UV detector working at 254 nm (Thermo Scientific®, San Jose, CA, USA). The chromatographic separation was performed using an Ascentis Express F5 HPLC column (150 × 3.0 mm, 2.7 µm particle size, Sigma Aldrich, Milan, Italy) maintained at 40 °C, with a flow rate of 0.3 ml/min and an injection volume of 20 µL. The following gradient method was utilized with water containing 0.1% formic acid (solvent A) and acetonitrile (solvent B): 0–9 min (30–50% B), 9–27 min (50–60% B), 27–54 min (60–100% B), 54–69 min (100–30% B), and 69-75 min (30% B). All solvents were purchased from Sigma

Aldrich, Milan, Italy. The HPLC system was interfaced to the ion trap mass spectrometer with an Electro Spray Ionization (ESI) ion source. The compounds were analyzed under positive (ESI+) ion conditions. The ion spray and capillary voltage were set at 5kV and 10V, respectively, in positive ion mode. The capillary temperature was 400 °C. The acquisition was performed both in Full Scan mode (mass range 200–2000 Da) and MS/MS Dependent Scan mode. The data station utilized the Xcalibur MS Software Version 2.1 (Thermo Scientific®, San Jose, CA, USA).

Standards of erinacine A and hericenones C and D were provided by Professor Kawagishi (Shizuoka University, Japan). Stock solutions (1 mg/mL) of erinacine A and hericenones C and D were prepared in 70% ethanol to mimic the procedure with which we obtained *H. erinaceus* extracts. Standard solutions with the final concentration range of 1–25 µg/mL for erinacine A and 20–100 µg/mL for hericenones C and D were prepared. Linear least-squares regression analysis for the calibration curves showed correlation coefficients of 0.9968, 0.9945, and 0.9951, respectively, for erinacine A, hericenones C, and hericenones, demonstrating an excellent linear relationship in the different ranges tested. In particular, each concentration was analyzed in triplicate.

Given the absence of a formerly published standardized extraction protocol for the ergothioneine (EGT), we conformed with the extraction procedure already reported for erinacine and hericenones. L-(+)-Ergothioneine (EGT; E7521-5MG, Sigma Aldrich, Milan, Italy) was used as standard. The EGT calibration curve was constructed using standard mixture solutions at five concentrations (10, 70, 150, 350 µg/mL; each concentration was analyzed in triplicate) and linear least-square regression analysis demonstrating, also in this case, an excellent linear relationship in the different ranges tested.

## 5.3 Study designs in preclinical model

All the animals used in this work were wild-type pathogen-free male mice (strain C57BL-6J), purchased by the Charles River company (Calco, Italy). The mice were acclimated to their environmental conditions for almost one month before starting experiments conducted in the Animal Care Facility at the University of Pavia. The mice were housed in single plastic cages at 21 ± 2 °C, with humidity at 50 ± 10%, with an automatically controlled light/dark cycle: the dark period lasted from 07:00 to 19:00, and

the light period was from 19:00 to 07:00. Water and food (standard chow) were furnished *ad libitum*. All experimental protocols and animal handling were carried out in strict conformity with European Council Directive 2010/63/EU and with the Ethics Committee of Pavia University (Ministry of Health, License number 774/2016-PR).

## 5.3.1 Study of the effects of *H. erinaceus* mycelium and sporophore standardized extracts (He1) treatment during aging in reverting frailty

These experiments were conducted on 15 male wild-type mice. *In vivo* experiments, used to evaluate frailty in mice, were performed at six different experimental times: 11, 14, 17, 20, 21.5, and 23.5 months, as reported in Figure 22.
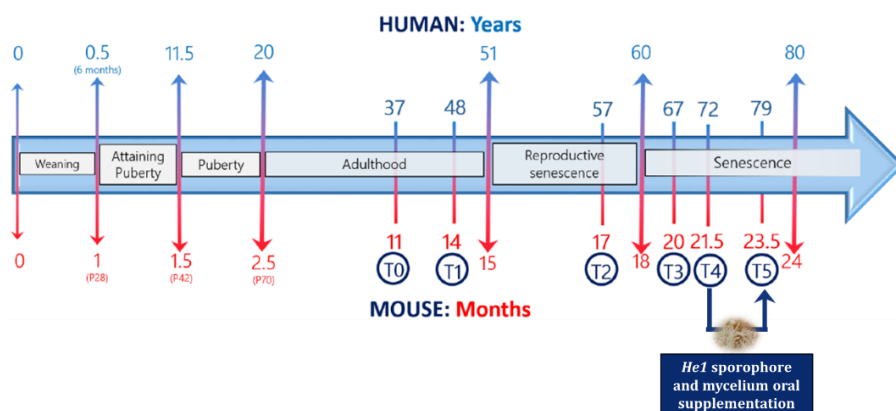


*Figure 22. Proportional age between humans and mice during their life span and the experimental times for experiments concerning He1. Modified from Dutta and Sengupta, 2016 and Ratto et al., 2019.*

The seven frailer mice (He1 group), starting from 21.5 months old (T4), received for two months a drink made by a mixture of mycelium and sporophore ethanol extracts (He1) solubilized in water, in such a way that every mouse received 1 mg of supplement per day. This amount was chosen to mimic the oral supplementation in humans (about one g/day). Daily consumption of water and supplements was monitored for each mouse every week.

At each experimental time, mice were weighed, and no statistically significant changes were recorded during aging or between the He1 and control groups.

## 5.3.2 Study of the effects of *H. erinaceus* primordium standardized extract (He2) treatment on the prevention of aging and frailty

These experiments were conducted on 15 other male wild-type mice. In this experimental set, *in vivo* experiments were performed at four different experimental times: 11 and 14 (T0 and T1, including in adulthood), and 20 and 23 (T2 and T3, including in the senescence) months old. For studying the potential of *H. erinaceus* in preventing frailty onset, starting from 15 months, nine random mice (He2 group) were supplemented with a drink of *H. erinaceus* primordium ethanol extract (He2) solubilized in water at the final dose of 1 mg/die, whereas the remaining six mice did not receive any supplement (C group). As before, we selected this dose for simulating the oral supplementation used in humans.

Figure 23 shows the experimental design:
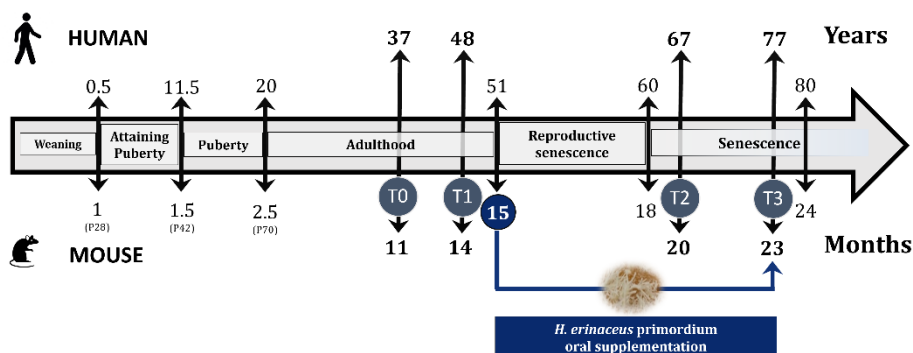


*Figure 23. Proportional age between humans and mice during their life span and the experimental times for experiments concerning He2. Modified from Dutta and Sengupta, 2016 and Ratto et al., 2019.*

Also in this case, at each experimental time, mice were weighed, and no statistically significant changes were recorded during aging or between the He2 and C groups.

## 5.4 Behavioral tests

Spontaneous behavioral tests were performed without any external reward or punishment to evaluate the mice's recognition memory and novelty-seeking behavior. The activity of mice was investigated and quantified through the "SMART Video Tracking System" program with a sampling time of 40 ms/point (Biological Instruments, Besozzo, Varese,

Italy) and a charge-coupled device (CCD) Sony color (PAL). At all different experimental times, all mice were subjected to five spontaneous behavioral tests: Open arena, Emergence, Novel Object Recognition (NOR), Object Location (OL), and Y Maze. Different locomotor or cognitive parameters were selected and investigated for each of them, as followed reported. For each test, as the mice alternated, the arena was carefully sanitized with 70% ethanol to eliminate the previous mouse's traces.

## 5.4.1 Open arena test

The open field or open arena test is widely used to investigate anxiety-related and exploratory behavior in rodents, but principally locomotor activity. In our conditions, during the test, mice were left free to explore an empty arena of 63 x 42 cm for 15 minutes and their movements were tracked by SMART Video Tracking System.

In this test, we evaluated the following parameters of interest: (i) total distance traveled in the 15 minutes (cm), (ii) resting time, so time when mice stay still (s), mean speed (cm/s), and (iv) max speed (cm/s).

## 5.4.2 Emergence test

The emergence test allows studying the "knowledge" component of recognition memory and the "novelty-seeking behavior".

In this test (Figure 24), the mouse is placed in a familiar environment (a same cage as the one it usually lives in, 33 cm long, 15 cm wide, and13 cm high) with a hole (5 cm long and 4 cm wide) through which it can go out into a larger arena with a laminated floor but without walls (90cm long and 60 cm wide), which represents a new safe environment. This test, lasting 8 minutes, allows the mouse to freely choose between a new environment or a family one.

In this test, the parameters of interest were the (i) latency of the first exit (the time that elapses before the first exit from the cage with all four limbs), (ii) the number of exits (the number of times a mouse completely emerged from the cage), and (iii) the time of exploration of the new environment (the amount of time a mouse spent exploring the new environment outside the familiar cage).

Emergence test

Test phase 8 min
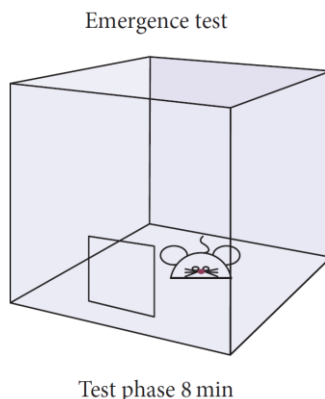
*Figure 24: Experimental set-up and procedure for emergence test.*
*From Brandalise et al., 2017.*

### 5.4.3 Novel Object Recognition test

The Novel Object Recognition (NOR) test evaluates exploratory behavior towards novelty and recognition memory (knowledge component) in rodents. The test, which lasts three days, is characterized by three main phases: habituation (or open arena), familiarization, and testing. During the first phase of habituation, which is carried out in the first two days, the mice were placed one at a time inside a white arena with no objects inside. Each mouse was left free to explore the empty arena for 15 minutes to familiarize themselves with the environment in which the test would later take place. Following this, the mice were removed from the arena and repositioned in their respective cages.

On the third day, during the familiarization phase, the mice were positioned, always one at a time, within the same arena in which two identical objects were placed. The animals were left free to explore the two objects for 5 minutes, after which they were transferred back to their cages for 10 minutes (retention phase). During this time-lapse, the arena and the objects were cleaned with 70% ethanol, and one of the two objects was replaced with another object with a different shape, size, and color. Next, during the test phase, the mice were returned to the same arena and were left free to explore the familiar object and the new object for 5 minutes, after which they were returned to their respective cages (Figure 25).
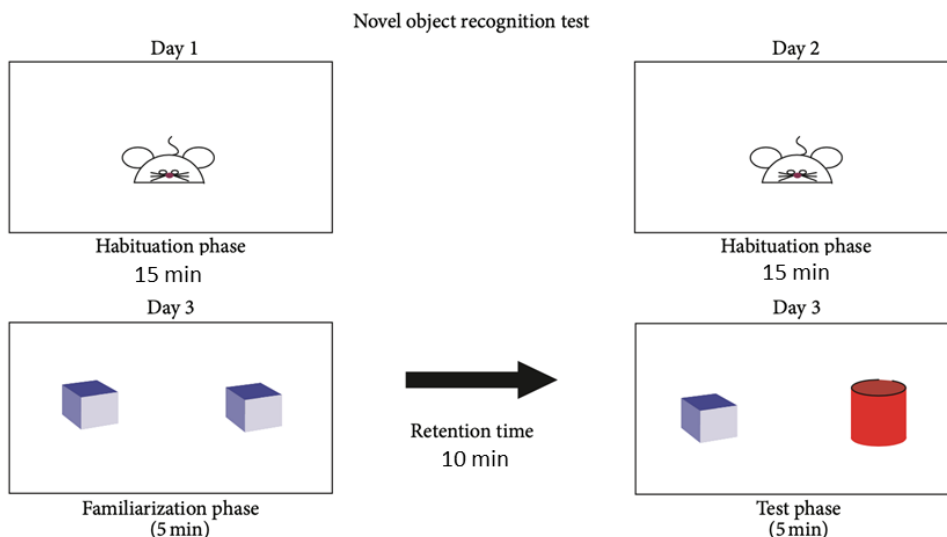
*Figure 25: Experimental set-up and procedure for NOR task.*
*From Brandalise et al., 2017.*

In this test, we evaluated two cognitive parameters: (i) the number of approaches and (ii) the total duration of the approaches for both the familiar object and the new object. The approaches were defined as when the distance between the mice's snout and the object is equal to or less than 2 cm.

To assess the mice capability to discriminate between the familiar and the novel object, we calculated the mean novelty discrimination index (DI) using the formula:

$$DI = (n - f) / (n + f)$$

where $n$ is the number or duration of approaches to the new object and $f$ is the number or time of approaches to the familiar one. The DI value can range from -1 to 1, where -1 indicates complete preference towards the familiar object, 0 no preference, and 1 complete preference for the new object.

## 5.4.4 Object Location test

The Object Location (OL) is a spontaneous behavioral test that allows to investigate the "remember" component of the recognition memory in rodents (Rossi et al., 2018). This test consists of the same phases as the NOR task: two days of habituation (15 minutes per day) and the

familiarization, retention, and test phase on the third day. The test procedure is identical to the NOR up to the test phase. After 5 minutes of the familiarization phase, the mouse was removed from the arena and placed inside its cage for 10 minutes. During this period, the arena and objects were cleaned with 70% ethanol, and one of the two was moved to a different location in the arena. In the subsequent test phase, the animals were repositioned in the same arena and were left free to explore the familiar object and the repositioned object for 5 minutes (Figure 26).

In the OL test, we investigated the exact parameters of the NOR test: (i) the number of approaches and (ii) the duration of the approaches for both the familiar object and the repositioned one.

To assess the discrimination between the familiar object and the repositioned one, the discrimination index (DI) was calculated in the same way as it was done for the NOR task.
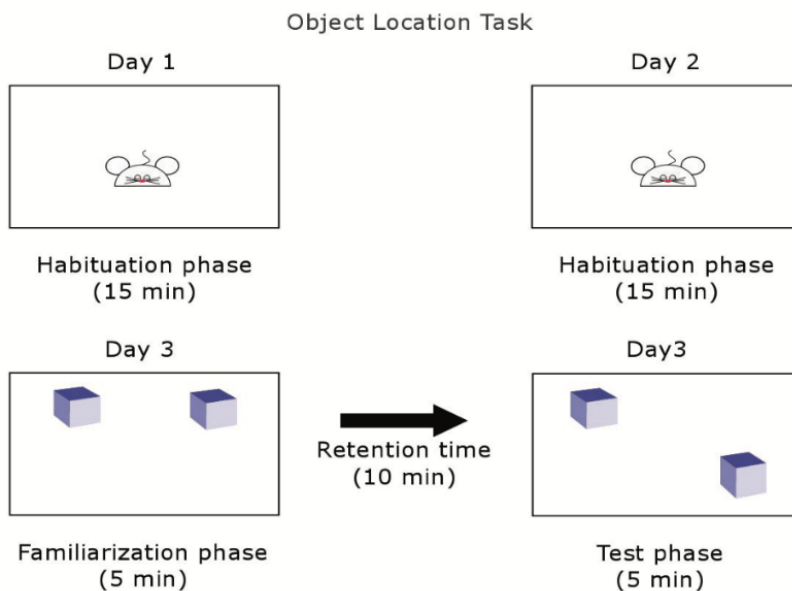


*Figure 26: Experimental set-up and procedure for NOR task.*
*From Rossi et al., 2018).*

## 5.4.5 Y maze

The Y maze test is usually used to study the "remember" component of the recognition memory and spatial working memory. This test is carried out in a Y-shaped labyrinth consisting of three symmetrical solid gray plastic arms (40 cm long, 12 cm high, 8 cm wide) positioned at an angle of 120 ° to each other. Each session began with placing the mouse in the center of the maze. The mouse is left free to explore the three arms for 8 minutes (Figure 27). In this test, an "arm entry" was defined as all 4 of the animal's limbs entering an arm of the maze. A "triad" or "triplet" was defined as a set of 3 arm entries in which each consecutive entry was into a different arm of the maze. If the arms of the Y maze are designated A, B, and C, an entry will proceed as ABC, ACB, BAC, BCA, CAB, or CBA. On the contrary, a failure was defined as repeated entry into the same arm (AAA, ABA, ACA, AAB, AAC, BBB, BAB, BCB, BBC, CCC, CBC, CAC, CCB, or CCA). The number of arm entries and the number of triads were measured.
In particular, the percentage of triplet alternation was considered as cognitive parameters, calculated by using the following formula:

$$\frac{\text{Number of triplets}}{\text{Number of total entries - 2}} \times 100$$



The Ymaze test

Test phase 8 min
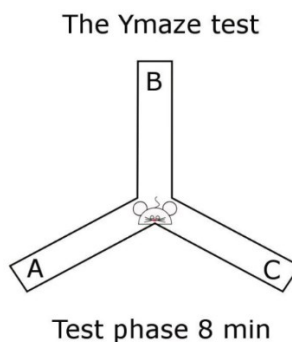
*Figure 27: Experimental set-up and procedure for Y maze task.*
*From Rossi et al., 2018).*

## 5.5 The Frailty Index development

We used a variant of Parks's procedure to measure the frailty index (FI) during aging (Parks et al., 2012). Park's FI procedure is as follows. Mean reference values for each parameter used to construct the FI are obtained at T0. For each mouse and at different experimental times, the values of these parameters are compared with the mean reference values. The values that are 1 standard deviation (SD) above or below the mean reference value are given a FI value of 0.25; the values that are different of 2 SD are scored as 0.5; the values that are different of 3 SD are 0.75; the values that are more than 3 SD above the mean reference receive the maximal frailty value of 1. Parameters that are different from the mean reference values by less than 1 SD receive a score of 0. These values are averaged to obtain an FI for each animal so that a mouse with no deficits has a FI score of 0 and an animal with all possible maximal deficiencies has a FI score of 1 (Parks et al., 2012).

Whereas Parks's method for creating the FI used a graded scale, we developed a method to derive more accurate values during aging. The mean reference value and the SD for each studied parameter were calculated at T0 (11 months). The values obtained from each mouse at different experimental times were compared to the mean value at T0 using the following formula:

$$FI=(Value-Mean\ at\ T0)/(SD\ at\ T0)^*\pm0.25$$

This procedure was used for creating both Locomotor FI and Cognitive FIs.

## 5.6 Tissue Sampling: Hippocampal and Cerebellar Samples Preparation

All mice were decapitated at 23.5 (for the study concerning He1) or 23 (for the study concerning He2) months after anesthetization with isofluorane (Aldrich, Milwaukee, WI, USA). The cerebral hemispheres and cerebellum were immediately excised, washed in 0.9% NaCl, and fixed by immersion for 48 hours at room temperature in Carnoy's solution (6 absolute ethanol/3 chloroform/1 acetic acid; for the study concerning He1) or for 7 hours in 4% paraformaldehyde in 0.1 M phosphate buffer (pH 7.4; for the study concerning He2). The tissues were then dehydrated through a graded series of ethanol and finally embedded in Paraplast X-TRA (Sigma

Aldrich, Milan, Italy). Eight-μm thick sections, collected on silane-coated slides, were cut in the sagittal and transversal plane.

At the time of use, the sections included in Paraplast X-tra were then deparaffinized for 20 minutes in xylene (Carlo Erba, Cornaredo, Italy), subsequently rehydrated by using a descending alcoholic scale protocol that includes five steps of 5 minutes each, as follows: xylene 50%/absolute ethanol 50%, absolute ethanol, ethanol 95%, ethanol 80%, and finally ethanol 70%. Next, the sections were rinsed in phosphate-buffered saline (PBS). Then the sections were used both for brightfield and fluorescence immunohistochemistry evaluations.

## 5.7 Hematoxylin/eosin staining

The deparaffinized and rehydrated sections were immersed in hematoxylin for 10 minutes and then washed with running water for about 2 minutes. Next, the sections were washed twice in distilled water ($H_2Od$) and immersed in eosin for 2 minutes. After two washes in $H_2Od$, the slices were dehydrated following an ascending alcoholic scale protocol consisting of five steps: 80% ethanol (fast), 95% ethanol, absolute ethanol, xylene 50%/absolute ethanol 50%, and xylene (3 minutes each). Finally, the slides were mounted with Eukitt (Kindler gmbH) for the bright-field microscope analysis.

## 5.8 Nissl staining

To determine the neuronal morphologies of the section, the Nissl histological staining was performed. This reaction allows highlighting the ribosomes contained in the endoplasmic reticulum, cytoplasm, and nucleus. For the procedure, the sections included in Paraplast X-tra (Sigma) were spun in xylene, rehydrated, and washed two times in $H_2Od$ for 3 minutes. Next, the sections were incubated in an incubator at 58°C with a solution of Toluidine blue for 20 minutes. Subsequently, the sections underwent two washes in $H_2Od$ (the first of a few seconds and the second of 3 minutes) and then were dehydrated with the previously described ascending alcoholic scale. Finally, the slides were mounted with Eukitt (Kindler gmbH) for the bright-field microscope analysis.

## 5.9 Immunohistochemistry

Immunohistochemistry was performed using specific commercial antibodies to localize and eventually quantify the presence and distribution of different specific markers. We performed immunohistochemical reactions simultaneously on slides from different experimental groups to avoid potential staining differences due to small procedural changes.

### 5.9.1 Brightfield Microscopy Assessment

After deparaffination, rehydration, and rinse in phosphate-buffered saline (PBS), the hippocampal and cerebellar slides were incubated at room temperature for 7 minutes in a blocking buffer for the suppression of the endogenous peroxidases (3% $H_2O_2$ in 10% methanol in PBS). Then the slices were washed in PBS and incubated for 20 minutes in fetal serum to block non-specific antigen-binding sites. Next, the sections were incubated for 2 hours in agitation in a humid and dark chamber. Subsequently, after two washes in PBS, the slides were incubated with biotinylated secondary antibodies (Vector Laboratories, Burlingame, CA, USA) for 30 minutes, washed two times in PBS, and incubated with horseradish peroxidase-conjugated avidin-biotin complex (Vector Laboratories, Burlingame, CA, USA) for 30 minutes at room temperature. Then, 0.05% 3,3-diaminobenzidine tetrahydrochloride (DAB; Sigma Aldrich, Milan, Italy) with 0.01% $H_2O_2$ in Tris–HCl buffer (0.05 M, pH 8) was used as chromogen followed by nuclear counterstaining with Hematoxylin. Then, sections were dehydrated in ascending scale of ethanol, cleared in xylene, and finally mounted with Eukitt (Kindler, Freiburg, Germany).

The primary antibody was omitted in some sections incubated with PBS only for control staining. No immunoreactivity was observed in this condition. The slides were observed with an Olympus BX51 microscope (model BX51TF), and the images were acquired with an Olympus Camedia c-2000 Z digital camera and stored on a PC running Olympus software.

Immunopositivity quantification was performed by calculating (i) the percentage of immune-positive nervous cells and (ii) the optical density (OD) by using ImageJ program.

Table 5 shows the primary and secondary antibodies used in brightfield microscopy:

| | Antigen | Species | Manufactures | Dilution |
|---|---|---|---|---|
| **Primary antibodies** | Interleukin-6 (IL6) | Goat | Santa Cruz Biotechnology (Santa Cruz, CA, USA), Goat polyclonal IgG, Cat# sc-1265, RRID: AB_2127470 | 1:100 |
| | Glial Fibrillary acidic protein (GFAP) | Goat | Santa Cruz Biotechnology (Santa Cruz, CA, USA), Goat polyclonal IgG, Cat# sc-6170, RRID: AB_641021 | 1:100 |
| | Hipoxia inducible factors-1α (HIF 1α) | Mouse | Santa Cruz Biotechnology (Santa Cruz, CA, USA), Mouse monoclonal IgG, Cat# sc-53546, RRID: AB_629639 | 1:100 |
| | Vascular-Endothelial Growth Factor (VEGF) | Rabbit | Santa Cruz Biotechnology (Santa Cruz, CA, USA), Rabbit polyclonal IgG, Cat# sc-507, RRID: AB_2212666 | 1:100 |
| | Superoxide Dismutase-1 (SOD1) | Rabbit | Santa Cruz Biotechnology (Santa Cruz, CA, USA), Rabbit polyclonal IgG, Cat# sc-11407, RRID: AB_2193779 | 1:100 |
| | Nitric Oxide Synthases-2 (NOS2) | Rabbit | Santa Cruz Biotechnology (Santa Cruz, CA, USA), Rabbit polyclonal IgG, Cat# sc-650, RRID: AB_631831 | 1:100 |
| | Cyclooxygenase-2 (COX2) | Goat | Santa Cruz Biotechnology (Santa Cruz, CA, USA), Goat polyclonal IgG, Cat# sc-1747, RRID: AB_2084976 | 1:100 |
| | *Zonula Occludens 1 (ZO-1)* | Goat | Santa Cruz Biotechnology (Santa Cruz, CA, USA), Goat polyclonal IgG, Cat# sc-1265, RRID: AB_2127470 | 1:100 |
| | *Occludin* | Mouse | Santa Cruz Biotechnology (Santa Cruz, CA, USA), Mouse monoclonal IgG, Cat# sc-133256, RRID: AB_2156317 | 1:100 |
| | *Glucose Transporter 1 (Glut1)* | Human | Purified antibody raised against amino acids218-260 of Glut1 of human origin. | 1:100 |
| | p53 | Mouse | Sigma-Aldrich (St. Louis, MO, USA), Mouse monoclonal IgG2a, Cat# OP33-100UG, RRID:AB_564977 | 1:100 |

| | | | | |
|---|---|---|---|---|
| **Secondary antibodies** | Biotinylated horse anti-mouse IgG | Gamma-immunoglobulin | Vector Laboratories (Burlingame, CA, USA), Horse, Cat# PK-6102, RRID:AB_2336821 | 1:200 |
| | Biotinylated goat anti-rabbit IgG | Gamma-immunoglobulin | Vector Laboratories (Burlingame, CA, USA), Goat, lot# PK-6101, RRID:AB_2336820 | 1:200 |
| | Biotinylated rabbit anti-goat IgG | Gamma-immunoglobulin | Vector Laboratories (Burlingame, CA, USA), Rabbit, Cat# PK-6105, RRID:AB_2336824 | 1:200 |

*Table 5: Primary and secondary antibodies used for immunocytochemical reactions.*

## 5.9.2 Fluorescence Microscopy Assessment

After the deparaffination, rehydration, and rinse in PBS, the sections were incubated for 7 minutes at room temperature with a blocking solution (100 mg BSA, 10 µl Tween 20, 3.3 ml glycine 0.3 M in 7ml PBS) to block non-specific binding sites. Then, the slices were left overnight in a humid and dark chamber in incubation with the primary antibody reported in Table 6. The next day, the sections were washed twice in PBS and then incubated for 1 hour with the secondary antibody (Table 6). After washing in PBS, nuclei were counterstained with 0.1 µg/ml Hoechst 33258 for 5 minutes. Further, the slices were rinsed in PBS and then mounted with Mowiol (Calbiochem, Inalco, Italy or Calbiochem, San Diego, CA, USA).

The sections were observed by fluorescence microscopy with an Olympus BX51 microscope equipped with a 100 W mercury lamp. The following equipment was used: 330 to 385 nm excitation filter (excf), 400 nm dichroic mirror (dm), and 420 nm barrier filter (bf), for Hoechst 33258; 450 to 480 nm excf, 500 nm dm, and 515 nm bd for Alexa 488; and 540 nm excf, 580 nm dm and 620 nm bf for Alexa 594. Images were recorded with an Olympus MagnaFire camera system and processed with the Olympus Cell F software.

As in bright-field microscopy, immunofluorescence quantification was performed by (i) calculating the percentage of immune-positive nervous cells and (ii) the optical density using ImageJ program.

| | Antigen | Species | Manufactures | Dilution |
|---|---|---|---|---|
| **Primary antibodies** | SIRT1 | Rabbit | Polyclonal antibody (Abcam (Cambridge, MA, USA) | 1:100 |
| | PCNA (PC10) | Mouse | monoclonal antibody (Abcam, Cambridge, MA, USA) | 1:600 |
| | Double cortin (DCX) | Goat | Polyclonal antibody (Santa Cruz Biotechnology, Santa Cruz, CA, USA) | 1:100 |
| **Secondary antibodies** | Alexa Fluor 488-conjugated anti-mouse | Goat | Molecular Probes, Space, Milano, Italy | 1:100 |
| | Alexa Fluor 594-conjugated anti-goat | Donkey | Molecular Probes, Space, Milano, Italy | 1:100 |

*Table 6: Primary and secondary antibodies and respective dilution used in immunofluorescence experiments.*

### 5.9.3 Quantitative analysis

After assembly, the slides were dried and then analyzed under an Olympus BX51 microscope. At 4x and 10x magnifications, a first panoramic observation was made to define the state of integrity of the slice and the encephalic area of interest. Larger magnifications, 20x, 40x, and 100x, were used to evaluate cytoarchitecture and cell population.
For all markers, it was helpful to measure the density of pixel here referred to as optical density (OD) of the immunopositive areas after immunohistochemical reactions. After the acquisition, in the bright field immunoreactions, the color was inverted to have the positive areas lighter than the background or the non-expressed neurons. The background and

the hematoxylin staining were always subtracted with a plugin of the ImageJ (ImageJ 1.46p, NIH, Bethesda, MA, USA) program.

The OD measurements, used for evaluating the immunocytochemical intensity, were evaluated in 3 randomized images/section (making at least ten measurements/image) per 5 slides/animal from each experimental group and were carried out using the polygonal selections tool of the ImageJ program (Figure 28) to best capture the marker expression.
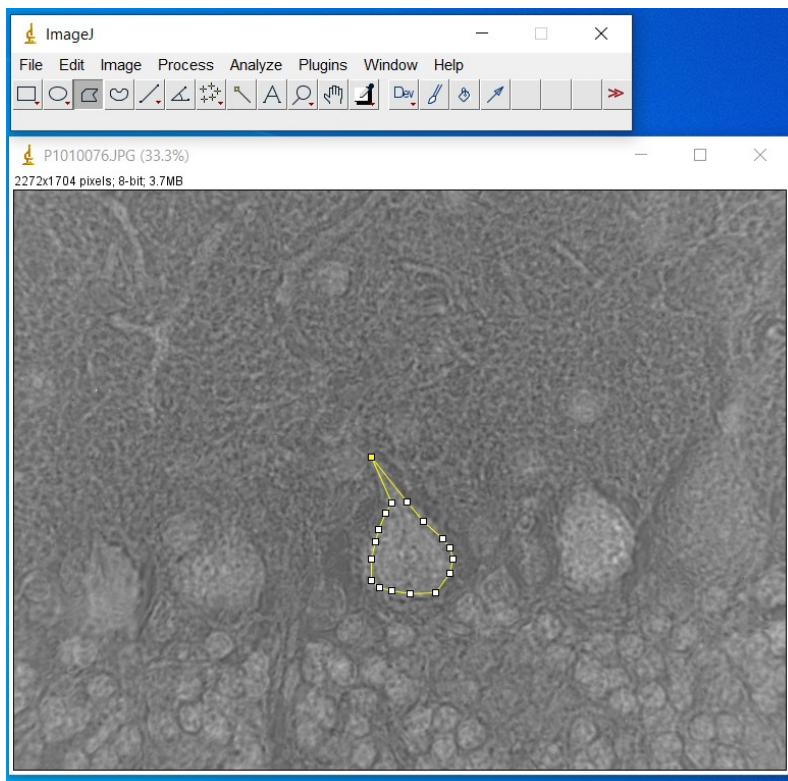


*Figure 28: ImageJ toolbar with "Polygonal selections" and an example of a captured area for calculating the OD.*

## 5.10 Microbiota analysis

### 5.10.1 Bacterial DNA extraction and 16s rRNA sequencing

Total microbiota genomic DNA in the mice stools was extracted using a QIAamp DNA stool mini kit (Qiagen, Dusseldorf, Germany) according to the manufacturer's instruction. DNA quantification was performed using Qubit FluorometerTM (Invitrogen, Molecular Probes, USA). Libraries for 16S rDNA amplicons sequencing of the V3 and V4 regions were obtained by using PCR primers containing a barcode (V3 Forward: 5′-CCTACGGGNGGCWGCAG-3′; V4 Reverse: 5′-GACTACHVGGGTATCTAATCC-3′). Furthermore, for preparing the amplicons for the sequencing by MiSeq Illumina, we used the specific forward (V3 F: 5'-TCGTCGGCAGCGTCAGATGTGTATAAGAGACAG-3') and reverse (V4 R: 5'-GTCTCGTGGGCTCGGAGATGTGTATAAGAGACAG-3') adapters. Finally, we performed the PCR analysis using Bio-Rad MJ Mini Personal Thermal Cycle, and PCR amplicons were sequenced by MiSeq Illumina, relying on the *BMR Genomics SRL di Padova*.

### 5.10.2 Illumina data processing and microbiota characterization

The raw paired-end FASTQ reads were imported into the Quantitative Insights Into Microbial Ecology 2 program (QIIME2, ver. 2020.2.01) (Bolyen et al., 2019) and demultiplexed using the native plugin. The Divisive Amplicon Denoising Algorithm 2 (DADA2) (Callahan et al., 2016) was used to quality filter, denoise, and mergepair the data, and remove chimeric sequences.
The resulting Amplicon Sequence Variants (ASVs) with less than a 50x coverage were discarded from further analyses. The classification of the obtained ASVs was run using the feature-classifier plugin (Bokulich et al. 2018), implemented in QIIME2 against the SILVA SSU non-redundant database (138 release) (Quast et al., 2013), adopting a consensus confidence threshold of 0.7.

### 5.10.3 Microbiota Data analysis

The analysis of the bacterial diversity, and the corresponding figures, was done using the phyloseq R package (Mcmurdie and Holmes, 2013).

Microbiota diversity was described within (alpha) and between (beta) sample diversities. The Shannon index and Phylogenetic Distance (PD) alpha diversity metrics were calculated to estimate the variation of bacterial diversity at the different time points. Values were compared using the pairwise Krustall-Wallis test.

Beta diversity was estimated with quantitative distance metrics using the *diversity* function in the phyloseq R package. We estimated the Bray-Curtis dissimilarity indexes by sampling 10,000 reads per sample.

Canonical Analysis of Principal Coordinates (CAP) was computed using the cap-scale function from the vegan R Package (Anderson & Willis, 2003; Oksanen et al., 2015). Variance partitioning and significance on bacterial communities for experimental factors: time groups and Cognitive Frailty Index (FI), were determined by running a permutation-based ANOVA test using 999 permutations on the Bray Curtis distance metric. PerMANOVA Pairwise contrast was performed by the *adonis* function in the phyloseq package. Non-Metric Multidimensional Scaling (NMDS) explored microbial communities' structure, an ordination approach.

The DESeq2 R package (Love et al., 2014) was used to identify the bacteria with the most significant changes in ASV differential abundance considering the Cognitive FI. Improvements to the stability and dispersion of the counts (variance) were required before it was possible to calculate the differential abundances for the different species present in the samples being compared. To this end, we used the estimated SizeFactors function in DESeq2 to transform the stabilization of the variance. The differential abundances were measured with the log2foldchange value, and the different conditions were compared using the Wald test with the Benjamini–Hochberg correction (Q parameter = 0.1, FDR < 10%). The differential-abundance measurements were statistically significant if the adjusted p-value was < 0.05.

## 5.11 Study design in Humans

The experimental plan for the clinical study developed as follows: recruitment time (T0), after two months of *H. erinaceus* supplementation (T1), and after two months wash-out (T2). Seventy-seven volunteers (62 females and 15 males; mean age 53.2 ± 0.7 years old) with a body mass index (BMI) ≥ 25 Kg/ were enrolled from the Department of Preventive Medicine, Luigi Devoto Clinic of Work, Obesity Centre, at the IRCCS Foundation Policlinico Hospital (Milan, Italy).

The patients were invited to participate in the study through an individual interview during which the study was presented. Subjects with the

following characteristics were excluded from the study: antidepressant or anti-anxiety treatment, mushroom allergies, pregnancy, language barrier, and organ transplantation. Furthermore, we included only patients with one or more sleep and mood disorders, evaluated by Zung's Depression Self-Assessment Scale, Zung's Anxiety Self-Assessment Scale, Symptom Checklist-90 (SCL-90), and the binge eating scale (BES).

Each participant signed an informed consent form and provided detailed information about their general health, dietary intake, and lifestyle when starting the study. This study was performed according to the Declaration of Helsinki for Research on Human Subjects and was approved by the local ethics committee (study registration number: 1370).

From T0, all participants were undergoing a low-calorie diet of 1400 kcal for women and 1700 kcal for men (CHO 52%, Lipids 30%, and protein 18%) and were randomly assigned to the control group (n = 37) or the *H. erinaceus* group (n = 40). In the *H. erinaceus* group, we recorded three dropouts at T1 and five drop-outs at T2, while in the control group, we had no dropouts. Figure 29 displays the experimental design.

Patients belonging to the *H. erinaceus* group received three capsules/die for two months of an *H. erinaceus* dietary supplement (*Micotherapy Hericium*) provided by A.V.D. Reform s.r.l. (Noceto, Parma, Italy). This supplement is composed both of mycelium and sporophore of the mushroom. In particular, extraction conditions from both fruiting body and mycelium were the following: biomass/solvent ratio was 1/15 and the extraction time was three hours. Solvents for distinct extractions were water and pure ethanol, respectively. The remaining liquid phase was dried under vacuum at 70°C and -0.9 bar and further milled by UPZ mill (Hosokawa Alpine Aktiengesellschaft, Augsburg, Germany). Final particles were mostly smaller than 100 $\mu$m.

The polysaccharide content was determined by $\beta$-Glucan Assay Kit (Megazyme, Ireland) and expressed as total ($\alpha$ plus $\beta$) glucan content: 50 mg of polysaccharides were present in each capsule so that each subject assumed 150 mg/die.

**T0**
Recruitment of 77 Patients

| 37 randomized to low calorie diet | 40 randomized to low calorie diet + *H. erinaceus* |
|---|---|
| BMI ($\geq 25$ kg/m$^2$) | BMI ($\geq 25$ kg/m$^2$) |
| Zung's Depression<br>Zung's Anxiety<br>Binge Eating | Zung's Depression<br>Zung's Anxiety<br>Binge Eating |
| | SCL-90 |
| | BDNF and pro-BDNF measures |

**Low Calorie Diet** — 2 months — **Low Calorie Diet + *H. erinaceus* supplementation**

**T1**

| 37 patients on low calorie diet | 37 patient son low calorie diet + *H. erinaceus* supplementation |
|---|---|
| BMI | BMI |
| Zung's Depression<br>Zung's Anxiety<br>Binge Eating | Zung's Depression<br>Zung's Anxiety<br>Binge Eating |
| | SCL-90 |
| | BDNF and pro-BDNF measures |

**Low Calorie Diet** — 2 months — **STOP H. erinaceus supplementation / Low Calorie Diet**

**T2**

| 37 patients on low calorie diet | 35 patients on low calorie diet |
|---|---|
| BMI | BMI |
| Zung's Depression<br>Zung's Anxiety<br>Binge Eating | Zung's Depression<br>Zung's Anxiety<br>Binge Eating |
| | SCL-90 |
| | BDNF and pro-BDNF measures |

*Figure 29: experimental design of the study.*
*From Vigna et al., 2019.*

The composition (Table 7) and nutritional values (Table 8) of *Micotherapy Hericium* supplement are reported in the following tables:

| Component | mg/capsule | mg/die |
|---|---|---|
| *H. erinaceus* mycelium | 400 | 1200 |
| *H. erinaceus* sporophore extract | 100 | 300 |
| Total polysaccharides amount | 50 | 150 |

*Table 7: Composition of the supplement Micotherapy Hericium: 80 % of mycelium and 20 % of sporophore extract. From Vigna et al., 2019.*

| | Sporophore extract | Mycelium |
|---|---|---|
| Kcal/g | 2.23 | 1.98 |
| Proteins % | 8.25 | 10.22 |
| Fats % | 0.17 | 1.02 |
| Fibers % | 5.92 | 39.2 |
| Polysaccharides/total glucans % | >45 | >37 |
| Sodium % | 0.0146 | 0.0031 |

*Table 8: Nutritional values of the components (sporophore extract and mycelium powder) of supplement Micotherapy Hericium. From Vigna et al., 2019).*

## 5.11.1 Self-Evaluation Scales

The effect of hypocaloric diet on mood disorders, i.e., depression, anxiety, and binge eating disorders, was investigated by using the Zung Self-Rating Depression Scale (ZDS) Zhang et al., 2019), Zung Self-Rating Anxiety Scale (ZAS) (Palagini et al., 2019), and Binge eating scale (BES). In the *H. erinaceus* group, the effects on mood disorders were also investigated using an Italian version of the SCL-90 (Prunas et al., 2012), since the SCL-90 test is considered a psychometrically more advanced tool than Zung's tests. The SCL-90 differs from other psychiatric questionnaires as it measures both externalizing (such as impulsivity, hostility, and aggressiveness) and internalizing (such as depression, anxiety, sleep, and somatizations) symptoms. Indeed, in clinical practice, the SCL-90 is considered a more articulated psychometric test. We recruited only patients with one or more mood disorders evaluated by these tests.

For each test, we determined the range values to define the entity of the disorder, such as "low", "moderate", and "high" (Table 9).

| Zung's Depression Scale (1974) | |
|---|---|
| 20-31 | Very low |
| 32-43 | Low |
| 44-55 | Moderate |
| 56-67 | High |
| 68-80 | Very High |
| Zung's Anxiety Scale (1971) | |
| 20-40 | Low |
| 41-60 | Moderate |
| 61-80 | High |
| Sympton Checklist – 90 (SCL - 90) scale | |
| <1 | Low |
| ≥1 | Score of interests about items considered (depression, anxiety, sleep disorders) |
| Binge eating scale (BES; 1982) | |
| <9 | Low risk of food disorder |
| 10-16 | Emotional eating |
| >17 | High risk of food disorder |

*Table 9: the range values to define the entity of the disorder: very low, low, moderate, high, and very high. From Vigna et al., 2019.*

## 5.11.1.1 Zung Self-rating Depression Scale

Zung's Self-Rating Depression Scale (ZDS) is a rapid self-administered test used to quantify the depressed status of a patient. This test is considered the prototype of the self-assessment scales and allows to obtain a fast and quantitative evaluation of psychological (10 items), affective (2 items), and somatic (8 items) symptoms of depression in humans. The patient must evaluate the frequency of the symptom described in the item on a scale from 1 to 4, in which 1 is "a little of the time", 2 is "some of the time", 3 is "good part of the time", and 4 is "most the time" (Figure 30). Then, the different scores obtained for the 20 items were added to find a total final score. We considered patients very low depressed with a score between 20-31, low depressed for 32-43, moderate depressed for 44-55, high depressed for 56-67, and very high depressed with 68-80. Indeed, we considered a patient positive for depression with a score equal to or greater than 44 (Table 9).

77

| Place check mark (✓) in correct column. | A little of the time | Some of the time | Good part of the time | Most of the time |
|---|---|---|---|---|
| 1. I feel down-hearted and blue. | | | | |
| 2. Morning is when I feel the best. | | | | |
| 3. I have crying spells or feel like it. | | | | |
| 4. I have trouble sleeping at night. | | | | |
| 5. I eat as much as I used to. | | | | |
| 6. I still enjoy sex. | | | | |
| 7. I notice that I am losing weight. | | | | |
| 8. I have trouble with constipation. | | | | |
| 9. My heart beats faster than usual. | | | | |
| 10. I get tired for no reason. | | | | |
| 11. My mind is as clear as it used to be. | | | | |
| 12. I find it easy to do the things I used to. | | | | |
| 13. I am restless and can't keep still. | | | | |
| 14. I feel hopeful about the future. | | | | |
| 15. I am more irritable than usual. | | | | |
| 16. I find it easy to make decisions. | | | | |
| 17. I feel that I am useful and needed. | | | | |
| 18. My life is pretty full. | | | | |
| 19. I feel that others would be better off if I were dead. | | | | |
| 20. I still enjoy the things I used to do. | | | | |

*Figure 30: Zung Self-Rating Depression Scale (from http://www.mentalhealthministries.net/resources/flyers/zung_scale/zung_scale.pdf).*

## 5.11.1.2 Zung Self-Rating Anxiety Scale

Similarly, the Zung's Self-Rating Anxiety Scale (ZAS) is a rapid self-administered test used to quantify the anxiety status of patients. The evaluation is precise as described for Zung's depression scale: the patient must evaluate the frequency of the symptom described in each item on a scale from 1 to 4, in which 1 is "a little of the time", 2 is "some of the time", 3 is "good part of the time", and 4 is "most the time" (Figure 31). For 5 items (numbers 5, 9, 13, 17, and 19), the score value was opposite to the

other 15 items addressing anxiety symptoms. In this way, the risk that the patient mechanically provided the same score to all items was reduced. Next, the different scores obtained for the 20 items were added to find a total final score. We considered a patient with a low degree of anxiety with a final score between 20-40, moderate for 41-60, and high for 61-80. Indeed, we considered a patient positive for anxiety with a score equal to or greater than 41 (Table 9).

| Place check mark (✓) in correct column. | A little of the time | Some of the time | Good part of the time | Most of the time |
|---|---|---|---|---|
| 1 I feel more nervous and anxious than usual. | | | | |
| 2 I feel afraid for no reason at all. | | | | |
| 3 I get upset easily or feel panicky. | | | | |
| 4 I feel like I'm falling apart and going to pieces. | | | | |
| 5 I feel that everything is all right and nothing bad will happen. | | | | |
| 6 My arms and legs shake and tremble. | | | | |
| 7 I am bothered by headaches neck and back pain. | | | | |
| 8 I feel weak and get tired easily. | | | | |
| 9 I feel calm and can sit still easily. | | | | |
| 10 I can feel my heart beating fast. | | | | |
| 11 I am bothered by dizzy spells. | | | | |
| 12 I have fainting spells or feel like it. | | | | |
| 13 I can breathe in and out easily. | | | | |
| 14 I get feelings of numbness and tingling in my fingers & toes. | | | | |
| 15 I am bothered by stomach aches or indigestion. | | | | |
| 16 I have to empty my bladder often. | | | | |
| 17 My hands are usually dry and warm. | | | | |
| 18 My face gets hot and blushes. | | | | |
| 19 I fall asleep easily and get a good night's rest. | | | | |
| 20 I have nightmares. | | | | |

*Figure 31: Zung g Self-Rating Anxiety Scale (from https://www.mnsu.edu/comdis/isad16/papers/therapy16/sugarmanzunganxiety.pdf)*

## 5.11.1.3 BES

The BES includes 16 groups of statements (findable on https://www.dors.it/public/ar28/Binge%20Eating%20Scale.pdf), and the patient chooses the statement that is closest to describing their emotional feelings. A value from 0 to 3 is assigned to each statement. The total score is obtained by summing all of the values. A score lower than 10 indicates an optimal score, a range between 10 and 16 indicates the beginning of binge eating. A score > 17 indicates a high risk for a food disorder. We considered a patient positive for binge eating with a score equal to or greater than 10 for the BES (Table 9).

### 5.11.1.4 SCL-90-R

The SCL-90-R is a short self-report psychometric questionnaire composed of 90 items. For each item, the patient provides an evaluation from 0 ("not at all") to 4 ("very much"), as reported on https://www.aslvco.it/wp-content/uploads/2021/04/ALL04.2-S.C.L.90-TEST-PSICOLOGICI-AUTOVALUTAZIONE.pdf. The different items assess ten different states of the mind, including some related to "depression" (13 items), "anxiety" (10 items), and "sleep disorders" (3 items). For each dimension, we calculated the mean score value. We considered a patient positive for a mood disorder when the score was equal to or greater than 1 (Table 9).

### 5.11.2 Determination of pro-BDNF and BDNF Serum Levels by Direct Enzyme-Linked immunosorbent Assay (ELISA)

Blood samples were collected after an overnight fast, and the serum was immediately isolated and stored at −20°C. To avoid seasonal variations and correlation with the amount of ambient sunlight, we collected serum between June and December (Molendijk et al., 2012). By using two different competitive ELISA immunoenzymatic colorimetric kits (one for pro-BDNF (SK00752-09) and one for BDNF (SK00752-01) provided by Aviscera-Bioscience, Santa Clara, CA, USA), serum pro-BDNF and BDNF levels were measured in patients of the *H. erinaceus* intervention group (n = 10). The specifications of the kits are reported in Table 10:

| Kit | Detection range | Sensitivity | Intraassay precision |
|---|---|---|---|
| SK00752-09 (directed against pro-BDNF) | 0.78–25 ng/ml | 0.25 ng/ml | 4–6% |
| SK00752-01 (directed against BDNF) | 23–1500 pg/ml | 5–8 pg/ml | 4–6% |

*Table 10: Specifications of the two different competitive ELISA immunoenzymatic colorimetric kits: SK00752-09 for pro-BDNF evaluation and SK00752-01 for BDNF quantification.*

The protocols were performed according to the manufacturer's instructions. Blank, standard dilutions, positive control, and samples were assayed at least in duplicate. Briefly, after bringing all reagents and samples to room temperature, we added 100 $\mu$L per well of dilution buffer to blank wells and 100 $\mu$L of standard dilutions, positive control, or samples per well, covered with the plate sealer, and incubated for 2 hours on microplate shaker at room temperature. Then, we washed four times with 1x Wash Buffer (300 $\mu$L), and after complete removal of Wash Buffer, we added 100 $\mu$L of Detection Antibody working solution to each well and incubated for 2 hours on microplate shaker at room temperature. After washing, we added 100 $\mu$L of Streptavidin-HRP Conjugate working solution to each well and incubated for 60 minutes on a microplate shaker at room temperature, protecting from the light. We washed again, and then we added 100 $\mu$L of Substrate Solution to each well, and we incubated on a microplate shaker at room temperature, protecting from light. Finally, we added 100 $\mu$L of Stop Solution. The color in the wells changed from blue to yellow. Next, we determined the optical density of each well using an automated microplate reader (ELx808, BioTek,Winooski, VT, USA) set to 450 nm within 5 min.

## 5.12 Statistical analysis

All data were reported as mean ± SEM (standard error of the mean).
We performed Bartlett and Shapiro Wilk Tests to establish and confirm the homogeneity and normality of parameters.
In preclinical studies, to verify statistically significant differences in behavioral tests, we used one-way analysis of variance (ANOVA) for repeated measures followed by Bonferroni *post hoc* test to study the physiological aging in mice and two-way ANOVA followed by Bonferroni *post hoc* test for studying the effect of *H. erinaceus* supplementations.
To verify statistically significant differences in immunohistochemistry was used Unpaired Student's t-test.
To compare the groups in the clinical study, we performed the one-way ANOVA for repeated measures, two-way ANOVA, and Student's t-test.

The differences were considered statistically significant for $p < 0.05$ (*), $p < 0.01$ (**), $p < 0.001$ (***), and $p < 0.0001$ (****). Statistical analyses were performed with GraphPad Prism 7.0 software (GraphPad Software Inc., La Jolla, CA, USA) and R package.

# 6. Results

## 6.1 Identification and quantification of bioactive metabolites in He1 and He2

To identify and quantify the bioactive metabolites of interest in *H. erinaceus* samples, we analyzed the mycelium and sporophore extracts of *H. erinaceus* strain 1 (He1) and primordium extract of *H. erinaceus* strain 2 (He2) using the HPLC-UV-ESI/MS technique. In particular, we investigated the presence and the abundance of three nootropic metabolites (Erinacine A, Hericenone C, and Hericenone D) and L-+-Ergothioneine (EGT).

### 6.1.1 Quantification of nootropic and bioactive metabolites in He1

Erinacine A, hericenones C and D, and ergothioneine (EGT) in He1 were identified and quantified by comparing both retention times and ESI/MS spectra with the standards provided by Professor Kawagishi (University of Shizuoka, Japan) or purchased from Sigma Aldrich, Milan, Italy. Table 11 shows the molecular structure of bioactive metabolites, the molecular weight, the specific ions in the ESI/MS spectrum, and the content in 1 g of dried He1 mushroom, identified and quantified by comparing the retention time and molecular ion or mass spectra in HPLC/ESI-MS methods.

For Erinacine A, the calibration curve was constructed using five concentrations (1, 5, 10, 15, and 25 µg/ml) of standard. The linear least-square regression analysis for the calibration curve showed a good correlation coefficient ($R^2$ = 0.9968; Figure 32 A). By comparison the He1 mycelium extract spectrum with the calibration curve and Erinacine A spectrum (Figure 32 A and B), we quantified the Erinacine A (with a retention time of 10.57 minutes) content in He1 mycelium: 150 µg/g of dried He1 mycelium (as reported in Table 11).

To quantify Hericenone C and D concentration in the He1 sporophore extract, we used UV detection that allows the quantification by comparing the peak areas in the UV trace with those of the standards (Figure 33 A). The calibration curves for the two Hericenones were constructed by using

four concentrations (20, 50, 75, 100 µg/ml) of the respective standards. The linear least-square regression analysis for the calibration curves showed a good correlation coefficient both for Hericenone C ($R^2$ = 0.9945) and D ($R^2$ = 0.9951). By comparison the UV traces of He1 sporophore with Hericenone C and D standard ones (retention time of 42.57 and 44.34 minutes, respectively) and with the calibration curve (Figure 33 A and B), we quantified the Hericenones C and D content in He1 sporophore:  500 µg/g and less than 20 µg/g, respectively (Table 11).

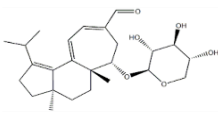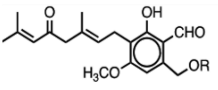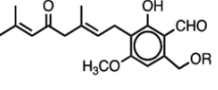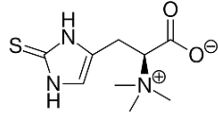| | Chemical structure | Molecular weight (g/mol) | Characteristic Ions | Content (µg/g) |
|---|---|---|---|---|
| **Erinacine A** |  | 432.56 | 455 [M+Na]+ 452 [2M+K+H]+ 668 [3M+K+H]+ 949 [2M+HCOOH+K]+ | 150 (mycelium) |
| **Hericenone C** |  R = Palmitoyl | 570.81 | 571 [M+H]+ 593 [M+Na]+ | 500 (sporophore) |
| **Hericenone D** |  R = Stearoyl | 598.87 | 599 [M+H]+ 593 [M+Na]+ | About 20 (sporophore) |
| **Ergothioneine** |  | 229.3 | 230 [M+H]+ 252 [M+Na]+ 268 [M+K]+ | 580 (mycelium) 340 (sporophore) |

*Table 11: Erinacine A, Hericenones C and D, and EGT chemical structure, molecular weight (g/mol), characteristic ions, and content (µg) in 1 g of dried He1 mycelium and sporophore. Modified from Ratto et al., 2019 and Roda et al., 2021.*
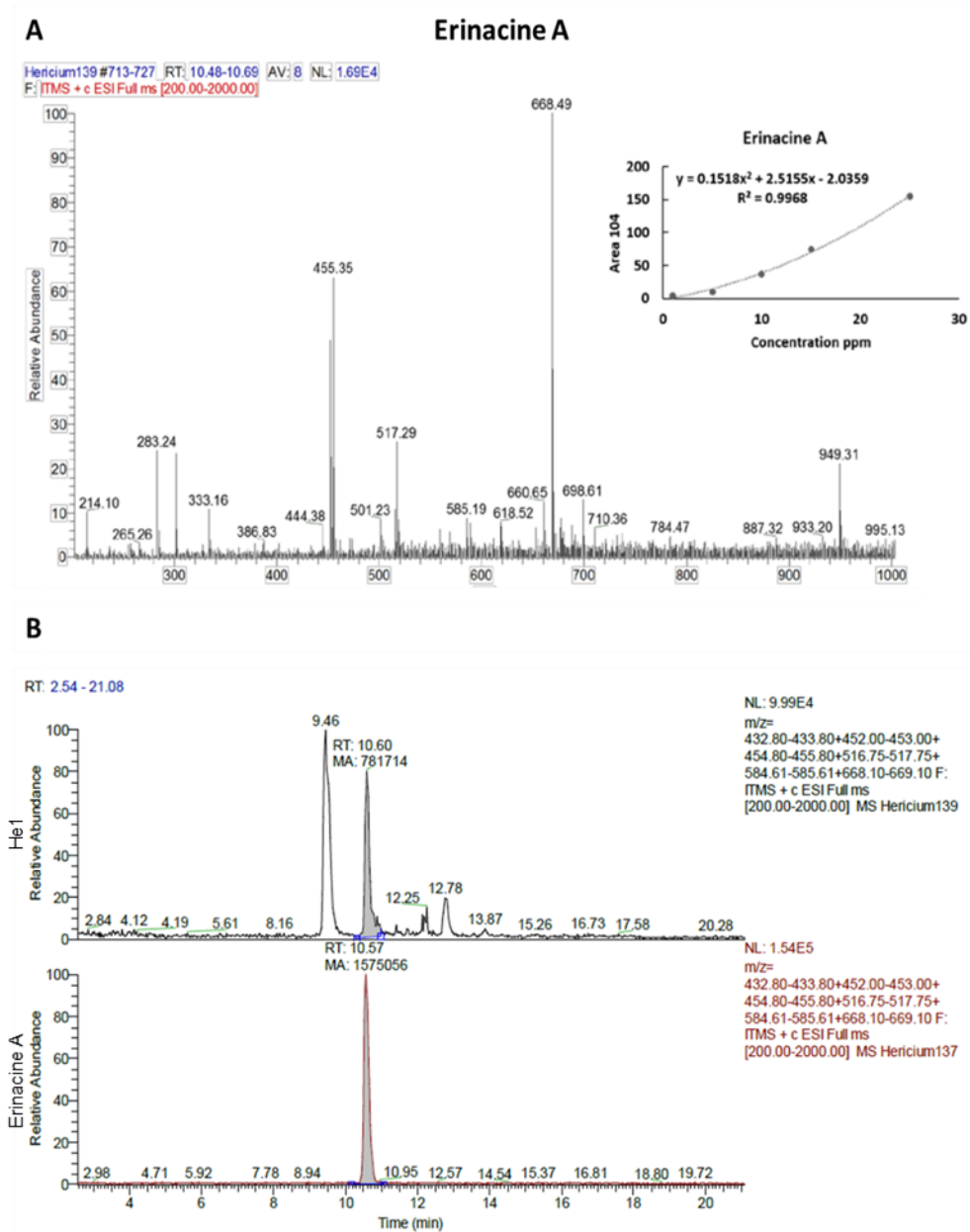
*Figure 32: Quantification of Erinacine A in He1 mycelium. A: ESI/MS spectrum of Erinacine A. The top right panel shows the calibration curve and linear regression curve for Erinacine A. B: the Mass Spectrum traces of He1 mycelium and Erinacine A standard (Retention time = 10.57 minutes). From Ratto et al., 2019.*
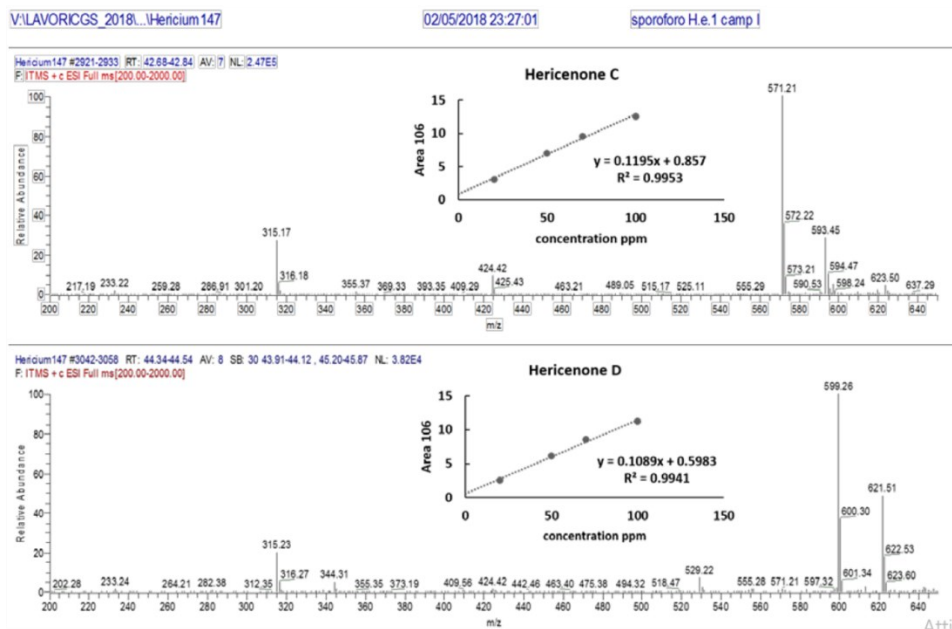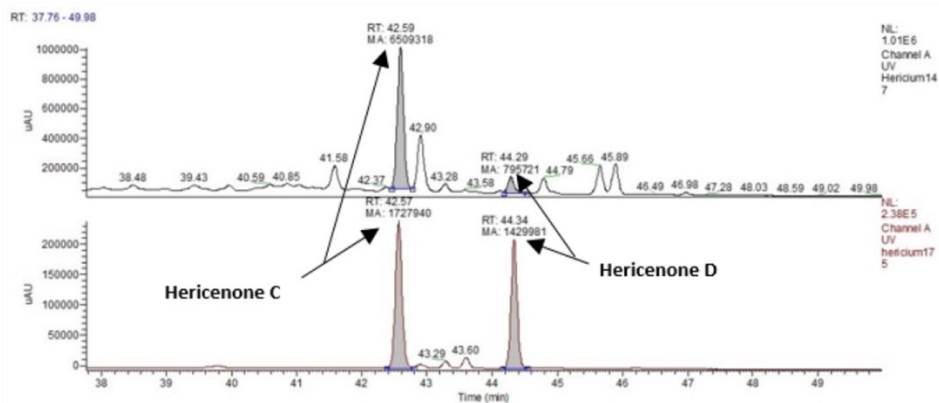
*Figure 33: Quantification of Hericenones C and D in He1 sporophore. A: ESI/MS spectrum of Hericenones C (top) and D (below). The top right panel shows the respective calibration curves and linear regression analysis. B: Ultra Violet traces of He1 sporophore (top) and Hericenone C (Retention time= 42.57 min) and D (Retention time = 44.34 min) standards (down). The peak area corresponding to Hericenone C or D is pointed. From Ratto et al., 2019.*

We also evaluated the ergothioneine (EGT) content in He1 extracts. The calibration curve for EGT was constructed by using five concentrations (10, 70, 150, 350 µg/ml). The linear least-square regression analysis for the calibration curve showed a good correlation coefficient ($R^2$ = 0.9925; Figure 34 A). Next, the EGT was identified by comparing retention time and the ESI/MS-MS spectrum with the authentic standard. ESI-MS/MS spectrum of EGT (Figure 34 B) obtained by fragmentation of ion m/z 230 showed two fragment ions m/z 186 and m/z 127. To obtain better sensitivity, EGT was then quantified by multiple-reaction-monitoring (MRM) transition m/z 230 > 127. Figure 34 C displays the traces regarding the standard molecule of ET at 70 ppm. On the top, the figure shows the UV trace and, on the bottom, it represents the mass spectrum (MS) trace (MS/MS Selected Reaction Monitoring m/z 230 > m/z 186 traces). Figure 34 D displays the mass spectrometry (MS) chromatographic traces of He1 lyophilized mycelium. Notably, both ESI-MS/MS spectrum of the standard molecule of EGT at 70 ppm (retention time at 3.16 min; Figure 34 C) and the He1 mycelium (retention time at 3.09 min; Figure 34 D) and sporophore (retention time = 3.00 min; Figure 34 E) spectrum showed the peak of EGT. Finally, by comparing with the calibration curve, we found that the EGT content in He1 lyophilized mycelium was 580 µg/g and in sporophore was 340 µg/g (Table 11).
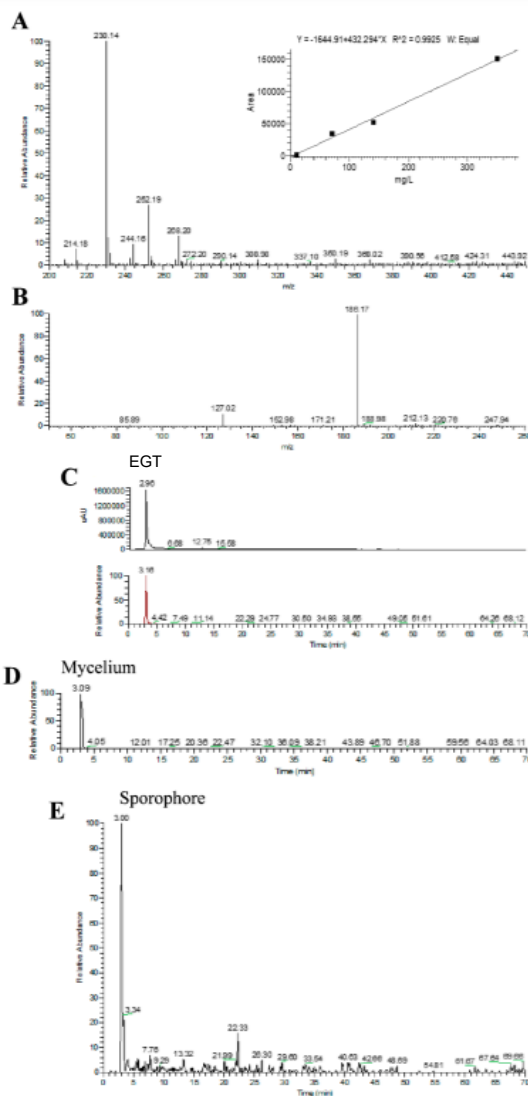
Figure 34. Quantification of EGT in He1. A: the ESI/MS spectrum of EGT. The upper right part shows the calibration curve and linear regression analysis for the EGT standard. B: the ESI-MS/MS spectrum of EGT obtained by fragmentation of ion m/z 230 shows two fragment ions m/z 186 and m/z 127. C: the standard molecule of L-(+)-EGT at 70 ppm: UV trace (top) and mass spectrum (MS)/MS Selected Reaction Monitoring m/z 230 > m/z 186 trace (bottom) (retention time = 3.09 minutes). D: MS/MS Selected Reaction Monitoring m/z 230 > m/z 186 trace of He1 mycelium. E: the MS/MS Selected Reaction Monitoring m/z 230 > m/z 186 trace of He1 sporophore. From Roda et al., 2021.

## 6.1.2 Quantification of bioactive metabolites in He 2

The He2 primordium extract spectrum did not display Erinacine A, Hericenone C, and D peaks.

To identify and quantify the EGT content in He2 primordium extract, we used the same previously described procedure for He1: HPLC-UV-ESI/MS. The used calibration curve for this evaluation was the same previously described. Using HPLC-UV-ESI/MS and comparing with the EGT calibration curve (Figure 35), we found that the EGT content in He2 lyophilized primordium was 1.30 mg/g, a higher concentration compared with that found in mycelium and sporophore.

In particular, Figure 35 A shows the UV (Ultra Violet) trace of He2 primordium, panel B shows ESI full MS (mass spectrum) trace of He2 primordium, and panel C displays the standard molecule of L-(+)-EGT in MS/MS Selected Reaction Monitoring m/z 230 &gt; m/z 186 trace.
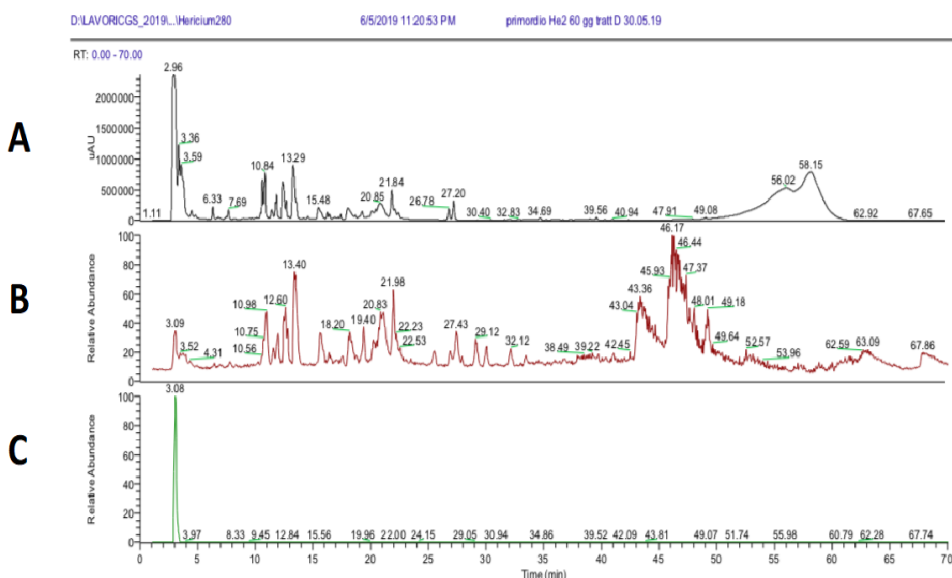


*Figure 35: Quantification of EGT in He2. A: UV trace of He2 primordium. B: ESI full MS trace of He2. C: Standard molecule of L-(+)-EGT: MS/MS Selected Reaction Monitoring m/z 230 > m/z 186 trace (retention time: 3.08 minutes).*

## 6.2 The effect of aging on locomotor performances, cognitive functions, and microbiota composition

The effects of physiological aging on wild-type mice were recorded in two different experimental sets (previously named experiments concerning He1 and experiments concerning He2), both performed on 15 animals, using different spontaneous behavioral tests, specifically for evaluating locomotor capabilities, recognition memory performances, and novelty-seeking behavior. In particular, we investigated the two different components of the recognition memory using (i) emergence and NOR tests for accessing the "knowledge" component and (ii) Y maze and OL tasks for evaluating the "remember" component.

Table 12 resumes all selected locomotor and cognitive parameters evaluated in the different tests:

| Spontaneous behavioral test | Selected locomotor Parameters |
|---|---|
| Open arena | Resting Time (s) Total Distance (cm) Max Speed (cm/s) Mean Speed (cm/s) |

| Spontaneous behavioral test | Selected cognitive Parameters |
|---|---|
| Emergence | Exit Number (n) Latency of First Exit (s) Time of Exploration (s) |
| NOR | Number of Approaches: DI Time of Approaches: DI |
| Y maze | Alternation triplet % |
| OL | Number of Approaches: DI Time of Approaches: DI |

*Table 12: Selected parameters to evaluate locomotor and cognitive performances in mice during physiological aging.*

## 6.2.1 Physical activity decline

The gait speed and the physical activity level are indicators of phenotypic frailty in humans (Fried et al., 2011). To accomplish a translational approach, we selected similar locomotor parameters in mice. So, total distance (Figure 36 A), resting time (Figure 36 B), mean (Figure 36 C), and maximum speed (Figure 36 D) were recorded in two different experimental sets in an open arena for 15 minutes, where mice were freely exploring the open-field in the absence of objects.

For the first set of animals (belonging to He1 experiments), all selected parameters worsened during aging from 11 (T0) to 23.5 months (T5), but with different trends. Whereas total distance and resting time decreased earlier, from 11 to 14 (T1), stabilizing at 20 (T3) months, mean speed started to worsen at 17 months (T2), and maximum speed worsened later, in the senescence phases (21.5 and 23.5 months, T4 and T5, respectively).
For all studied parameters, we obtained the Locomotor FIs and then, averaging these, a combined Locomotor FI, which increased linearly during physiological aging ($R^2$ = 0.8912; Figure 36 E), indicating that locomotor performances decline linearly from adulthood to senescence age. In particular, linear least-square regression analysis showed that locomotor activity declined in a statistically significant manner by about 35% every three months.

Similar to previously reported data, also for the second set of animals (belonging to He2 experiments), all selected parameters worsened during aging from 11 (T0) to 23 months (T3), but with different trends (Figure 37). The resting time (Figure 37 B) and max speed (Figure 37 D) decreased earlier, from 11 to 14 (T1) months, the mean speed (Figure 37 C) and total distance (Figure 37 A) started to worsen in a period between 14 and 20 months (T2) (Figure 37).
Also in this case, for all studied parameters, we obtained the Locomotor FIs and then a combined Locomotor FI, which increased linearly during physiological aging ($R^2$ = 0.9838; Figure 37 E), indicating that locomotor performances decline linearly from adulthood to senescence. In particular, linear least-square regression analysis showed that locomotor activity declined in a statistically significant manner by about 42% every three months, indicating that the locomotor decline in the second set of mice was analogous but slightly steeper than in the first set of animals.
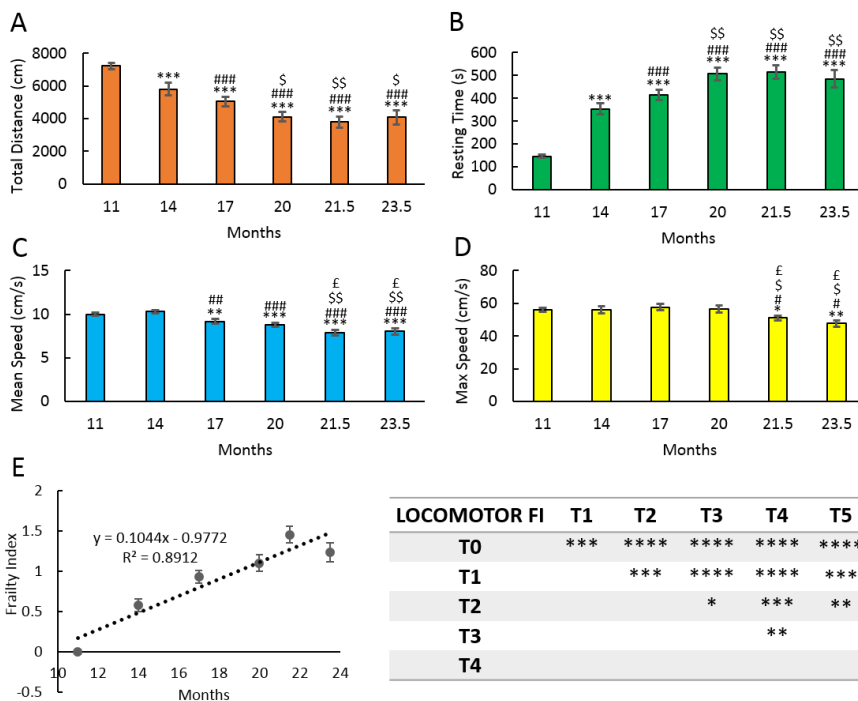
*Figure 36: Locomotor decline during aging (in mice belonging to He1 experiments). A: Total distance; B: Resting time; C: Mean speed; D: Maximum speed; E: Locomotor FI and linear least-square regression during aging. The table represents the statistical analysis regarding the Locomotor FI. Statistical results were performed by the One-Way ANOVA for repeated measures: * vs. T0, # vs. T1, $ vs. T2, and £ vs. T3. For all symbols reported p < 0.05 (*), p < 0.01 (**), p < 0.001 (***), p < 0.0001 (****).*
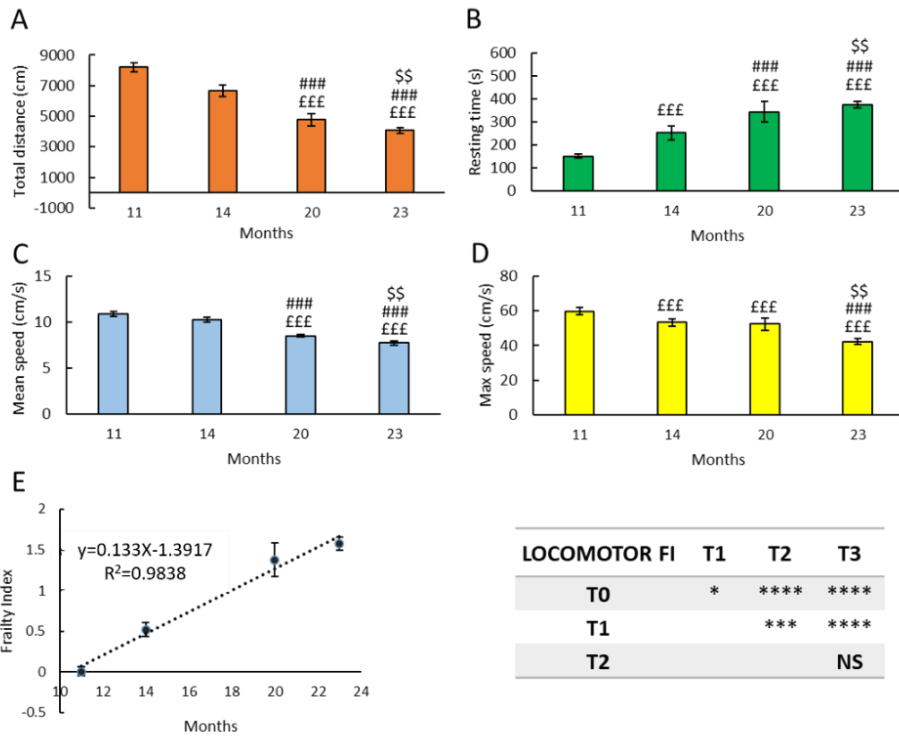
Figure 37: Locomotor decline during aging (in mice belonging to He2 experiments). A: Total distance; B: Resting time; C: Mean speed; D: Maximum speed; E: Locomotor FI and linear least-square regression during aging. The table represents the statistical analysis regarding the Locomotor FI. Statistical results were performed by the One-Way ANOVA for repeated measures: £ vs. T0, # vs. T1, $ vs. T2. For all symbols reported p < 0.05 (*), p < 0.01 (**), p < 0.001 (***).

## 6.2.2 Cognitive decline

We monitored cognitive performances during aging in the same wild-type mice (2 sets of 15 mice) in parallel to locomotor parameters.

### 6.2.2.1 Knowledge component of recognition memory

To achieve a translational approach during physiological aging, we selected in mice spontaneous behavioral tests resembling those described for humans, the emergence and the NOR tasks. The emergence task allows to study the novelty recognition memory for a new environment and to assess anti-neophobia behavior, whereas the NOR task assesses the novelty recognition memory for new objects. In particular, as reported in Table 12, in the emergence test, we investigated the latency to the first exit (Figure 38 and 39 A), the exits number (Figure 38 and 39 B), and the exploring time (Figure 38 and 39 C). In the NOR task, we studied the discrimination index (DI) of the time of approaches (Figure 38 and 39 D) and of the number of approaches (Figure 38 and 39 E).

In the first set of animals, regarding the emergence test, all the selected parameters worsened from 11 (T0) to 14 months (T1), but whereas the number of exits and the exploring time remained relatively stable in later times, the latency to the first exit worsened again during senescence. Regarding the NOR test, DIs both for the time and the number of approaches decreased from 17 months (T2) and even more during senescence (Figure 38).

For all these parameters, we obtained the Cognitive FI and then a combined Cognitive FI, which increased linearly during physiological aging ($R^2$ = 0.8077; Figure 38 F). Linear least-squares regression analysis on Cognitive FI experimental points demonstrated that, from 11 months, every three months, novelty recognition memory decreases in a statistically significant manner by about 26%.
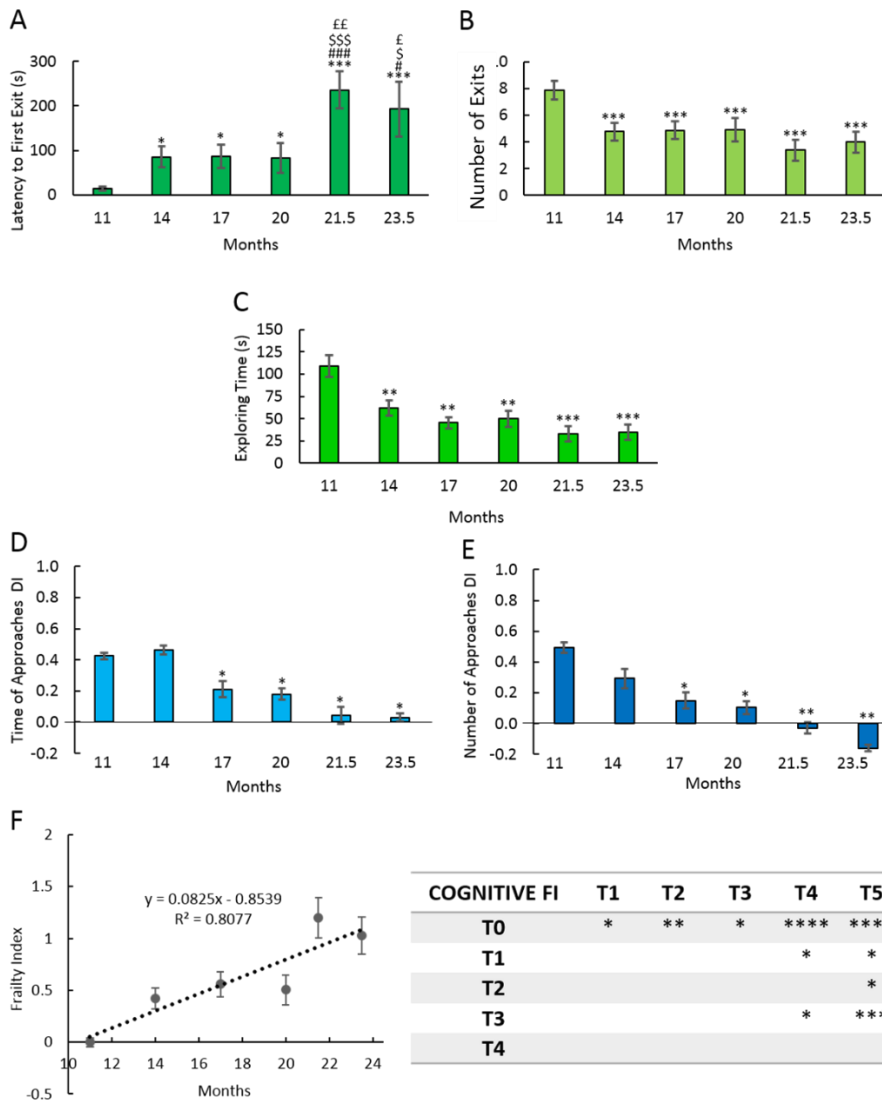
*Figure 38: Cognitive decline of knowledge component of recognition memory during aging (in mice belonging to He1 experiments). Panel A, B, C show cognitive parameters measured during the emergence test. A: latency to the first exit; B: number of exits; C: exploring time. Panel D and E report cognitive parameters evaluated during the NOR task. D: DI of the time of approaches; E: DI of the number of approaches. F: Cognitive FI and linear least-square regression during aging. Statistical results were performed by the One-Way ANOVA for repeated measures: \* vs. T0, # vs. T1, $ vs. T2, and £ vs. T3. For all symbols reported p < 0.05 (\*), p < 0.01 (\*\*), p < 0.001 (\*\*\*).*

In the second set of animals, regarding the emergence test, the exits number and the exploring time significantly worsened from 11 (T0) to 14 (T1) months, whereas the latency to the first exit significantly increased only at 20 months (T2). All parameters worsened again during the senescence.

Regarding the NOR test, DIs both for the time and the number of approaches significantly decreased from 20 months (T2) and even more during senescence (Figure 39).

For all these parameters, we obtained the Cognitive FI and then a combined Cognitive FI regarding the knowledge component of recognition memory, which increased linearly during physiological aging ($R^2 = 0.9912$; Figure 39 F). Linear least-squares regression analysis on Cognitive FI experimental points demonstrated that, from 11 months, novelty recognition memory decreases in a statistically significant manner by about 26% every three months, as reported in the other set of animals.
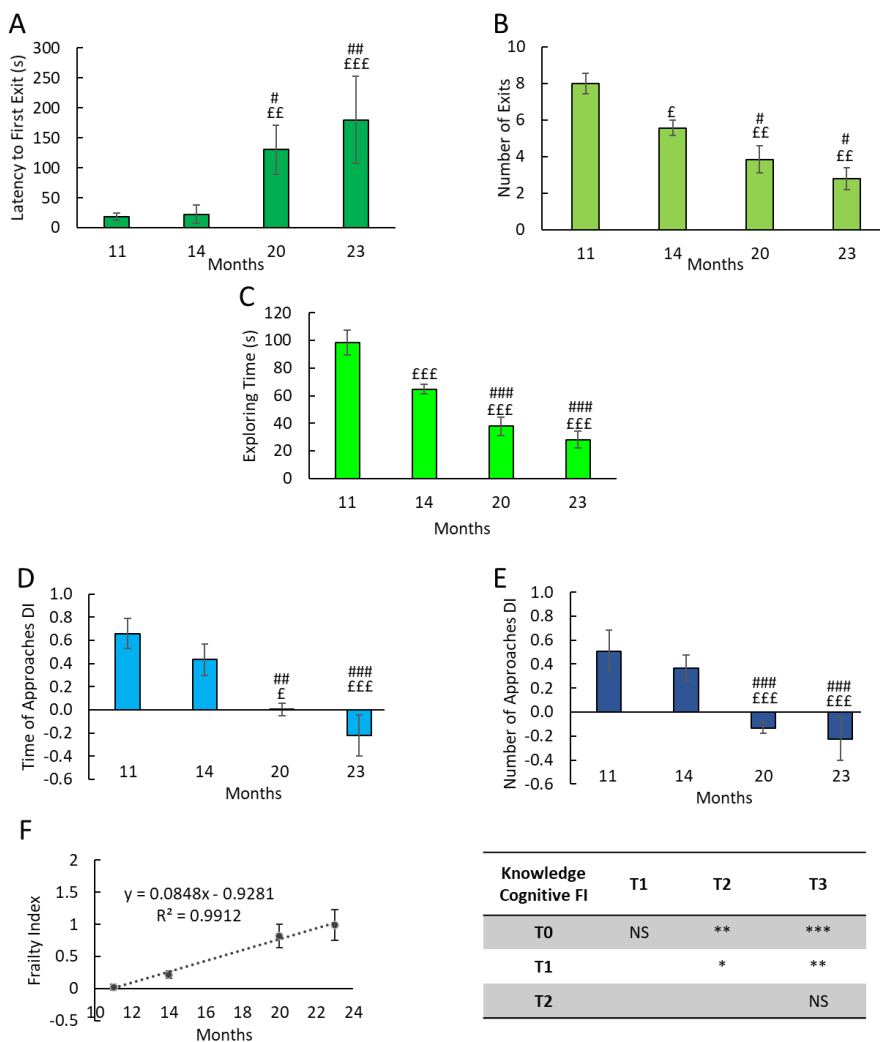
Figure 39: Cognitive decline of knowledge component of recognition memory during aging (in mice belonging to He2 experiments). Panel A, B, C show cognitive parameters measured during the emergence test. A: latency to first exit; B: number of exits; C: exploring time. Panel D and E report cognitive parameters evaluated during the NOR task. D: DI of the time of approaches; E: DI of the number of approaches. F: Cognitive FI and linear least-square regression during aging. Statistical results were performed by the One-Way ANOVA for repeated measures: £ vs. T0, # vs. T1, $ vs. T2. T3. For all symbols reported p < 0.05 (*), p < 0.01 (**), p < 0.001 (***) .

### 6.2.2.1 Remember component of recognition memory

To achieve a translational approach during physiological aging, we selected in mice spontaneous behavioral tests resembling those described for humans, Y maze and OL tests. In particular, we evaluated the alternation triplet percentage in the Y maze (Figure 40 A) and the discrimination index (DI) of the time of approaches (Figure 40 B) and of the number of approaches (Figure 40 C) in the OL task (Table 12).

The remember component of recognition memory was evaluated only in the second set of animals. During physiological aging, the cognitive parameter evaluated during the Y maze task, such as the alternation triplets' percentage, decreased appreciably between 14 and 20 months (T2), whereas the two cognitive parameters recorded during the OL test, such as the number and the time of approaches DIs, significantly worsened between 20 and 23 months (T3) in wild-type mice.
Next, we calculated the cognitive FI for each parameter and averaging the various FIs, we obtained the cognitive FIs for the remember component of recognition declarative memory (Figure 40 D). Notably, remember cognitive FI significantly increased during aging in control animals in straight way, as demonstrated by linear least-square regression analysis ($R^2 = 0.9814$).
Remarkably, from 11 months, remember component of recognition memory decreases in a statistically significant manner by about 2 % every three months, suggesting that this kind of memory is not affected by aging or has already deteriorated before 11 months.
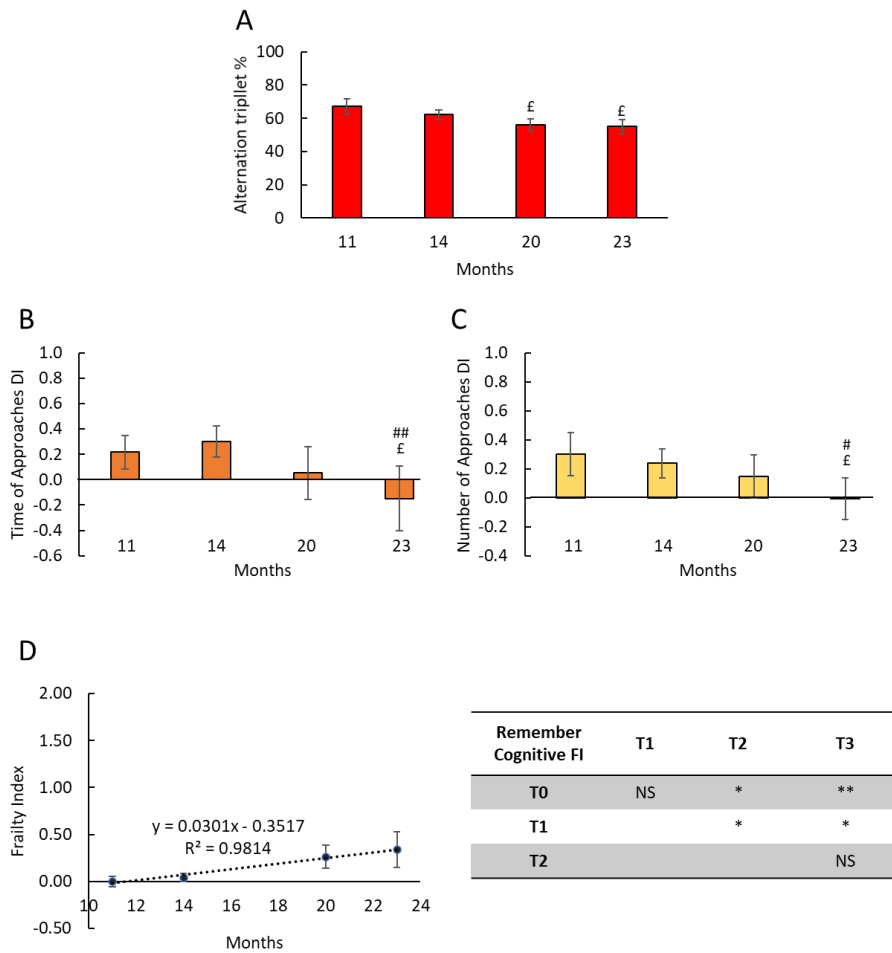
Figure 40: Cognitive decline of the remember component of recognition memory during aging (in mice belonging to He2 experiments). A: triplet alternation percentage in the Y maze test. Panel B and C show cognitive parameters evaluated during the OL task. B: DI of the time of approaches; C: DI of the number of approaches. F: Cognitive FI and linear least-square regression during aging. Statistical results were performed by the One-Way ANOVA performed statistical results for repeated measures: £ vs. T0, # vs. T1, $ vs. T2. T3. For all symbols reported $p < 0.05$ (*), $p < 0.01$ (**).

## 6.2.3 Gut microbiome composition

### 6.2.3.1 Sequencing data results

The microbiota of 15 mice (belonging to the experimental group concerning He1) at different experimental times was examined by sequencing the bacterial 16S rRNA gene to study the effect of physiological aging on the intestinal microbial communities. After the quality control analysis, the sequences of entire libraries resulted in 1,748,748 million sequence reads, ranging from 564 to 43,360 reads, with a median of 25801 for samples. No reads were reported in negative controls. A total of 1458 Amplicon Sequence Variant (ASV) was identified. Figure 41 shows the exact number of reads obtained per mouse at each time.
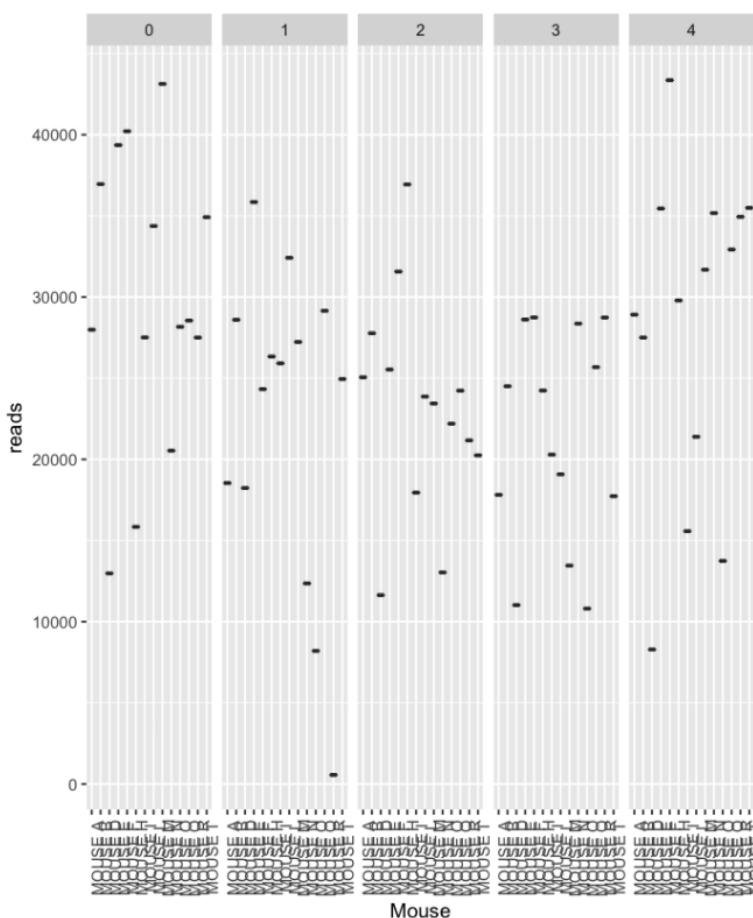


*Figure 41. The number of reads obtained in each mouse at each time.*

## 6.2.3.2 Aging affects overall gut microbiome composition

Stool profiling revealed significant microbiota composition differences between mice of different ages. In particular, the alpha diversity (microbial diversity within the sample) analysis based on Faith phylogenetic metrics (PD) and Shannon index exhibited conflicting results ( Figure 42).

In the case in which the Shannon is considered as the alpha-diversity index, an increase in the diversity was noted. Specifically, there was a significant variation (Wilcoxon Rank-Sum Test p-value < 0.05) between T1 and T2 of minor intensity and a greater significant variation between time T2 and til T4 and T5. The variations recorded between T0 and T1 and between T3, T4, and T5 were not significant considering the Shannon index (Figure 42 A). On the other hand, regarding the Faith index, the estimated bacterial diversity decreased during aging, but no variation was significant except that between T0, T1, T2 vs. T3, T4, and T5 (Wilcoxon Rank-Sum Test p-value < 0.05; (Figure 42 B).
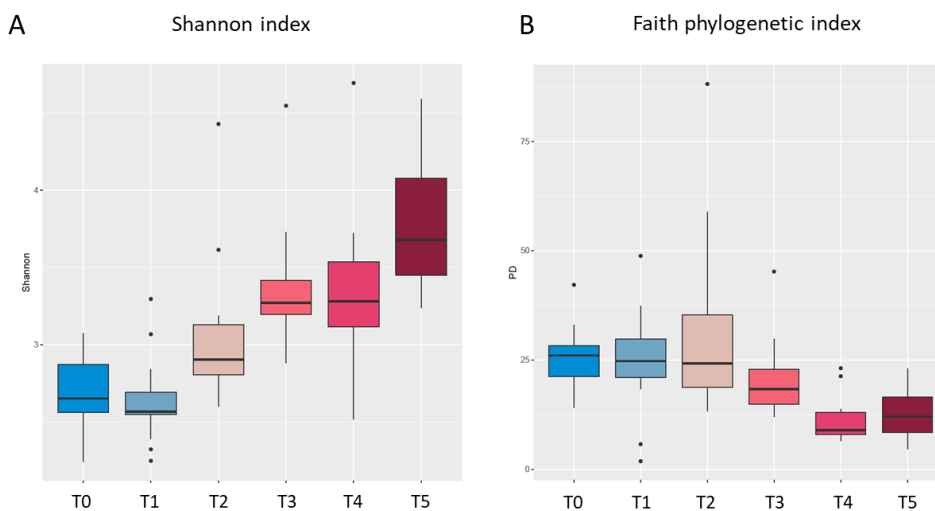


*Figure 42: Alpha diversity distribution box plot.*
*A: Shannon diversity index. B: Faith phylogenetic index (PD).*

To get a complete picture of the variation over time of the measured diversity, we estimated the magnitude of change between successive time points considering the distance in terms of estimated diversity (beta-diversity). Figure 43 shows the Non-Metric Multidimensional Scaling (NMDS) based on the Bray-Curtis distance matrix (with stress value = 0.12), demonstrating that the mice' microbiomes were more similar to each other at different times than to themselves in a subsequent time. In

particular, we found the formation of 5 consequential clusters in reference to each time. The effect of time between the different times was not strong but added up over time, creating a large gap between T0 and T5 groups.
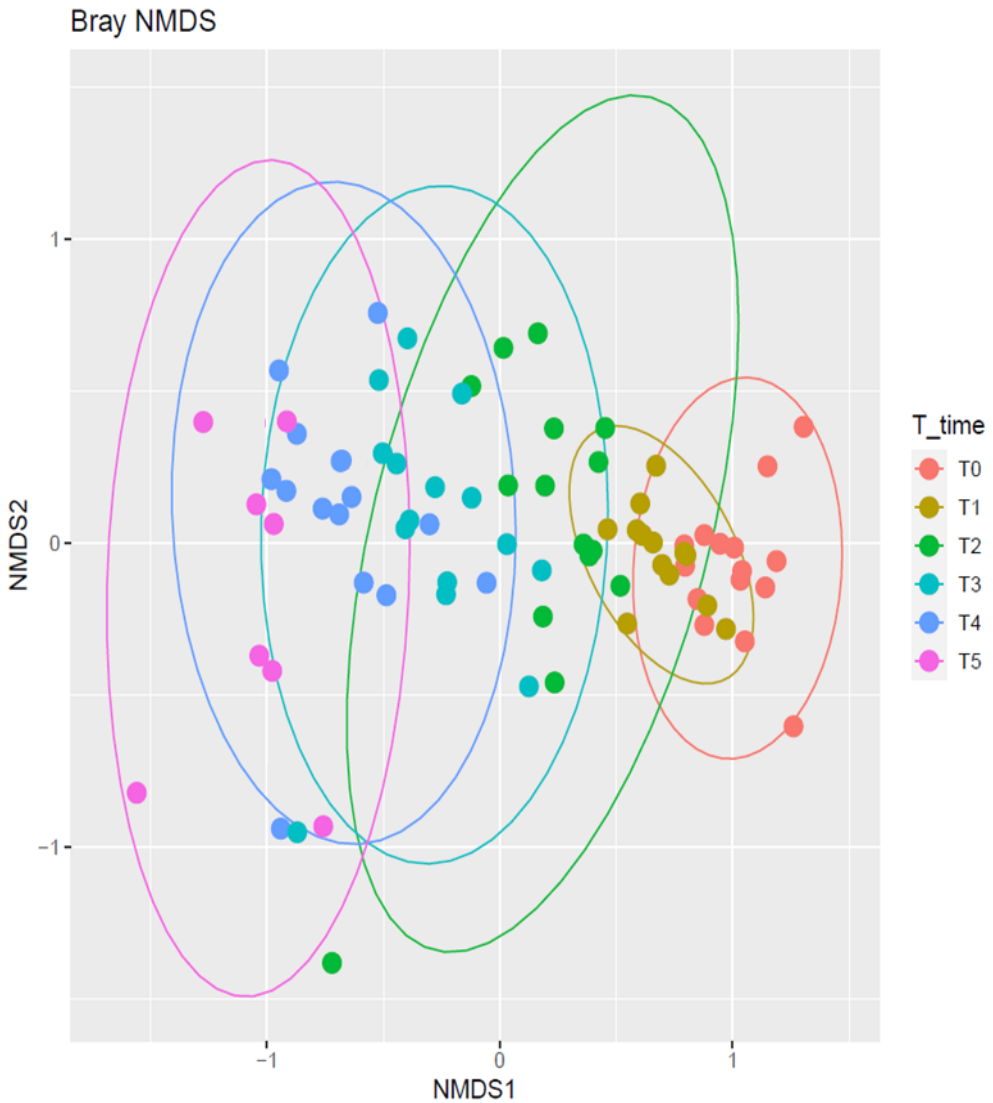


*Figure 43: Non-metric multidimensional scaling (NMDS) of different time points. Colors in the bidimensional NMDS plot are used according to the different sample origin as shown in the legend: T0 in pink, T1 in olive, T2 in green, T3 in light blue, T4 in blue, and T5 in purple. The ordinate analysis was based on the Bray-Curtis distance matrix.*

### 6.2.3.3 Microbiota Composition and Distribution

The 76% of the ASV calculated was assigned at least at the phylum level. In particular, for the 1458 ASV, we found: 13 Phyla, 20 Class, 54 Order, 76 Family, and 145 Genera.

The most represented phyla in all samples (Figure 44) was *Bacteroidota* followed by *Firmicutes,* whose ratio did not change during aging. The most significant evidences in phyla level were (i) the disappearance of *Verrucomicrobiota*, which passed from 11.05% at 11 months (T0) to undetectable in the senescence (T4 and T5), and (ii) the high decrease of *Deferribacterota,* which passed from 4.96% at T0 to 0.38% at T5.

Other important significant variations were recorded at family (Figure 45) and genera (Figure 46) levels. The most represented families were the *Tannerellaceae* and *Lacnospiraceae* (Figure 45), whose relative abundance remained relatively stable during physiological aging. Notably, during aging, the *Akkermansiaceae* (phylum *Verrucomicrobiota,* genus *Akkermansia*) gradually disappeared from T0 (11.05%) to T5 (Figure 47 A). Concomitantly, the *Muribaculaceae* appeared with a relative abundance of 6.77% at T3 that further increased to 12.69% at T4 and 15.31% at T5 (Figure 47 B). The *Rikenellaceae,* totally represented by *Alistipes* genus, increased from 0.01-0.36% at T0-T1-T2 to 1.59 at T3, 9.60% at T4, and 12.18% at T5 (Figure 47 C and D).

Regarding the genera, the most represented genera were *Parabacteroides* and *Lachnospiraceae_NK4A136_group* (Figure 47 E), both these did not significantly fluctuate during aging. The genus with greater variations was, besides the genera *Akkermasia* and *Alistipes*, *Clostridia_vandinBB60*. A substantial increase of *Clostridia_vandinBB60* was observed, which grew from 0.05-0.25% at T0 and T1, to 8.03% at T2, and 10.07% at T3, and then remained stable (10.02% at T4, and 9.92% at T5; Figure 47 F).
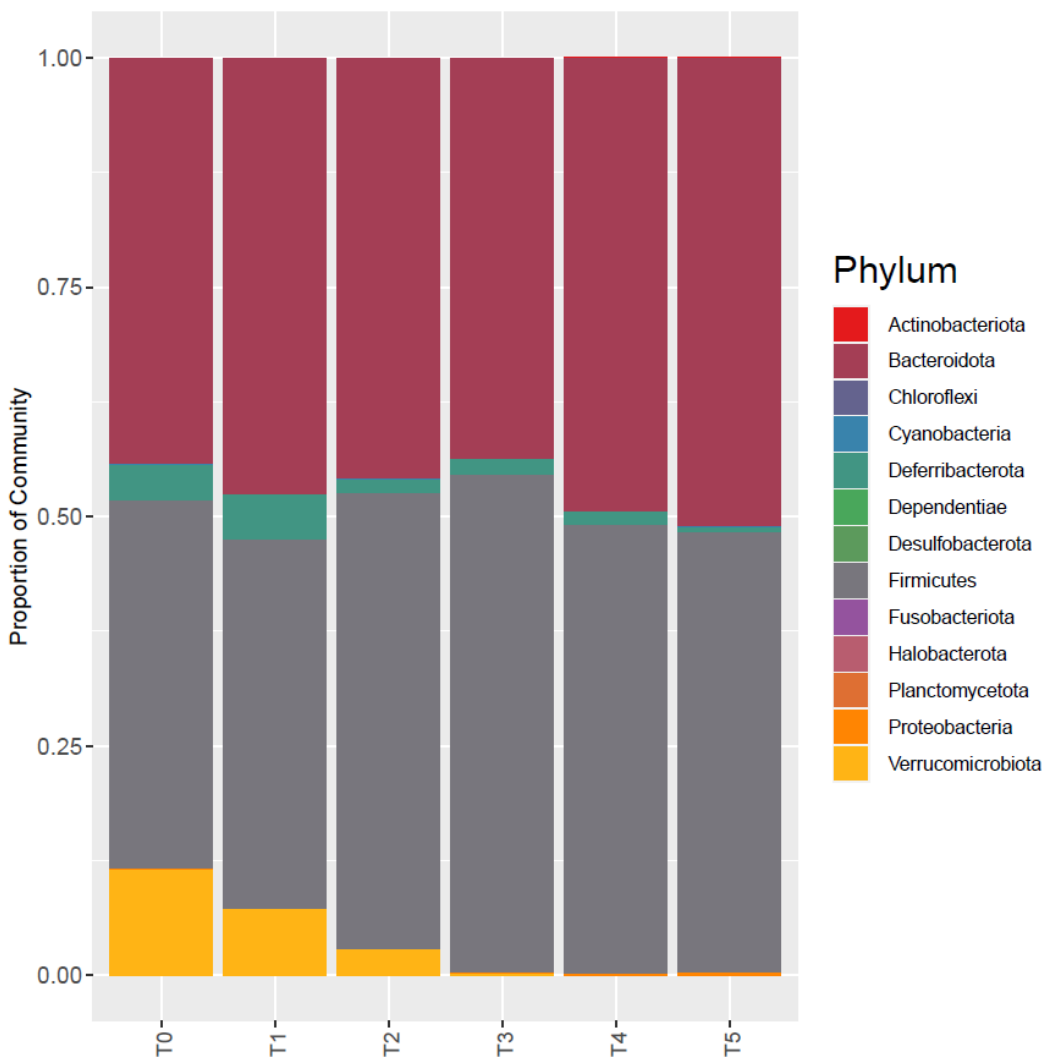
*Figure 44: Bar chart regarding the distribution of the most abundant AVS assigned to a specific Phylum.*
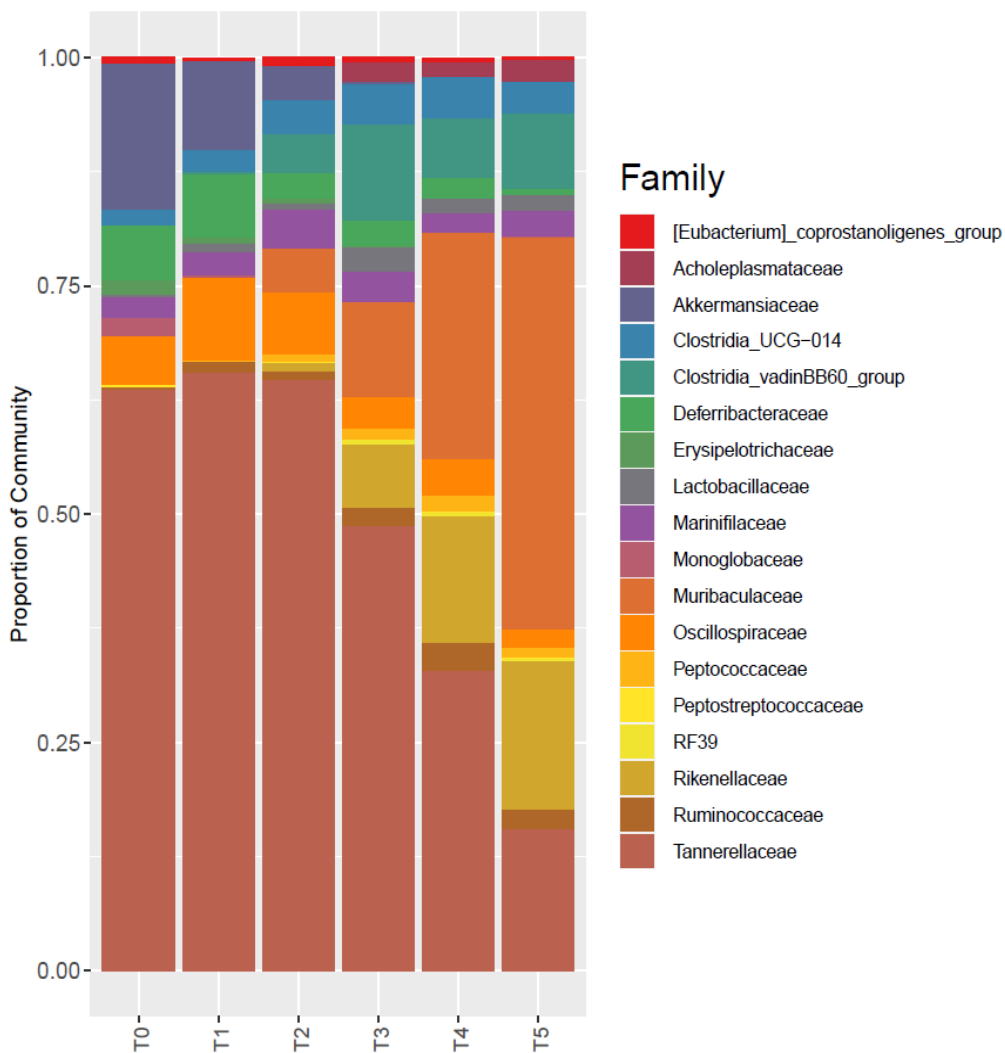
*Figure 45: Bar chart regarding the distribution of the most abundant AVS assigned to a specific family.*
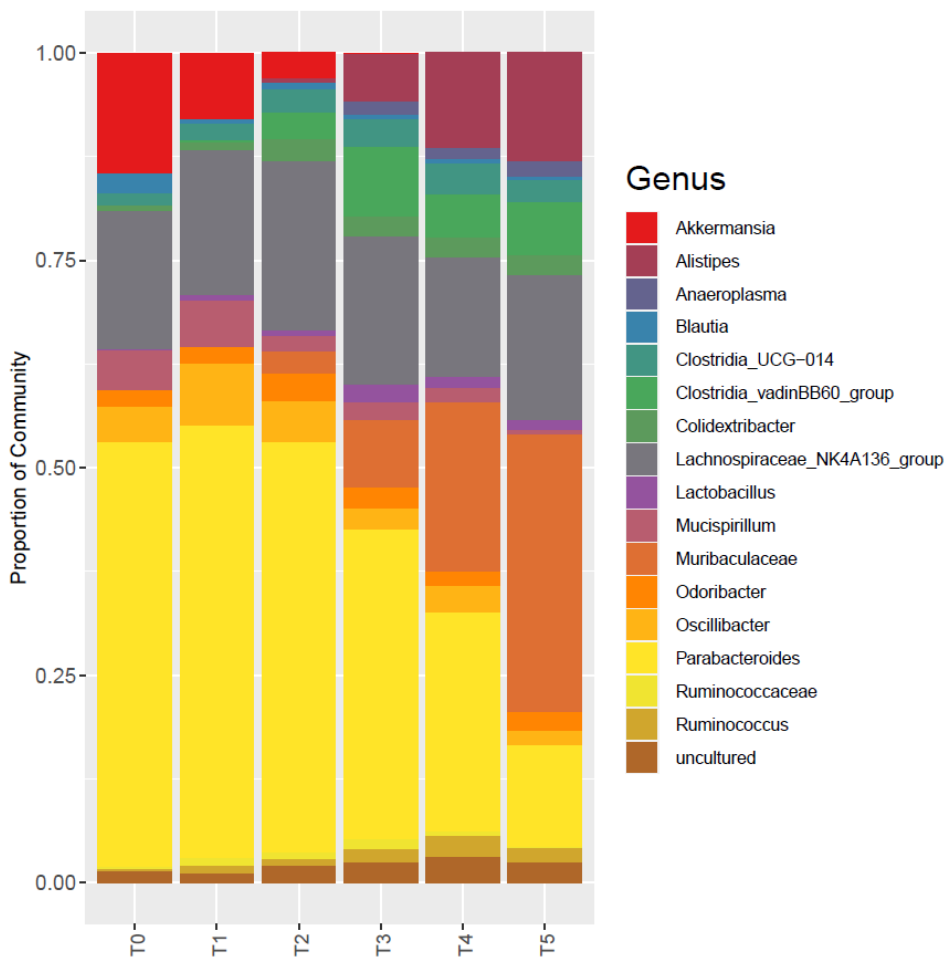
*Figure 46: Bar chart regarding the distribution of the most abundant AVS assigned to a specific genus.*

**Relative abundances**
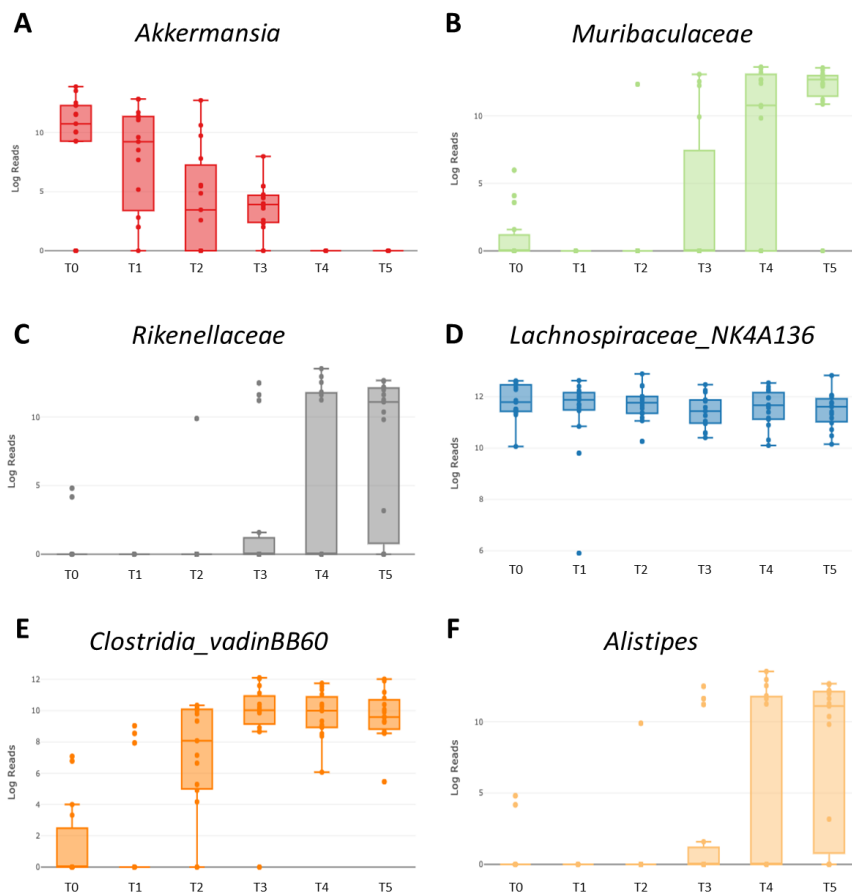


*Figure 47: Box plots representing the relative abundance of (A) Akkermansia, (B) Muribaculaceae, (C) Rikenellaceae, (D) Lachnospiraceae_NKA136_group, (E) Clostridia_vadinBB60_group, (F) Alistipes.*

## 6.3 The effect of He1 on wild type mice in reverting frailty

In the first set of animals, we investigated the effect of two-months *H. erinaceus* strain 1 sporophore and mycelium standardized extracts (He1) oral supplementation in aged mice on (i) locomotor performances, (ii) cognitive functions, (iii) cerebellar histology and morphology, (iv) oxidative stress pathway in CNS, (v) inflammation in CNS, (vi) neurogenesis in CNS, (vii) BBB functions, and (viii) gut microbiota composition. To achieve these aims, the seven mice with the highest locomotor and cognitive FIs at T4 received He1 (i.e., the blend of *H. erinaceus* strain 1 mycelium and sporophore ethanol standardized extracts) for two months during senescence, from 21.5 (T4) to 23.5 (T5) months. In order to get a translational approach, we treated mice with oral supplementation (1 mg/die) to mimic the supplementation used in humans (about one g/die).

### 6.3.1 Effects on locomotor and cognitive performances

Firstly, we investigated the effects of He1 oral supplementation on locomotor and cognitive performances (regarding the knowledge component of recognition memory) in aged wild-type mice.

At T4, the overall locomotor FI of the seven frailer mice (pre-He1 treated animals) was 44% higher than that measured in untreated mice (2.36 ± 0.07 vs. 1.63 ± 0.21, Figure 48 A). As previously reported, the locomotor activity of control mice significantly decreased from 21.5 to 23.5 months (Locomotor FI: 1.63 ± 0.21 vs. 1.79 ± 0.17, respectively) on the contrary of *H. erinaceus* group (He1), in which Locomotor FI significantly decreased from 2.36 ± 0.07 at T4 to 2.12 ± 0.09 at T5, indicating a locomotor improvement. Notably, whereas the He1 mice at T4 were significantly frailer than control animals, the treatment brought mice back to comparable levels, with no significant differences in the locomotor frailty index at T5 between the two experimental groups (Figure 48 A).

At T4, the knowledge cognitive FI of the seven frail animals (pre-He1 mice) was 128% bigger than FI of control mice (1.71 ± 0.21 vs. 0.75 ± 0.21; respectively; Figure 48 B). As previously reported, control mice showed a non-significant trend in increasing the recognition memory FI score: cognitive FI increased from 0.75 ± 0.21 at T4 to 1.03 ± 0.18 at T5. He1 oral supplementation significantly improved recognition memory, causing a Cognitive FI statistically significant reduction (from 1.71 ± 0.21 at T4 to 0.72 ± 0.22 at T5, Figure 48 B). Notably, whereas the He1 mice at T4 were significantly cognitively frailer than control animals, the treatment brought

mice back to comparable levels, with no significant differences in the cognitive FI at T5 between the two experimental groups (Figure 48 B).

Altogether, these results demonstrated that two months of He1 oral supplementation reverted aging-related frailty in mice.
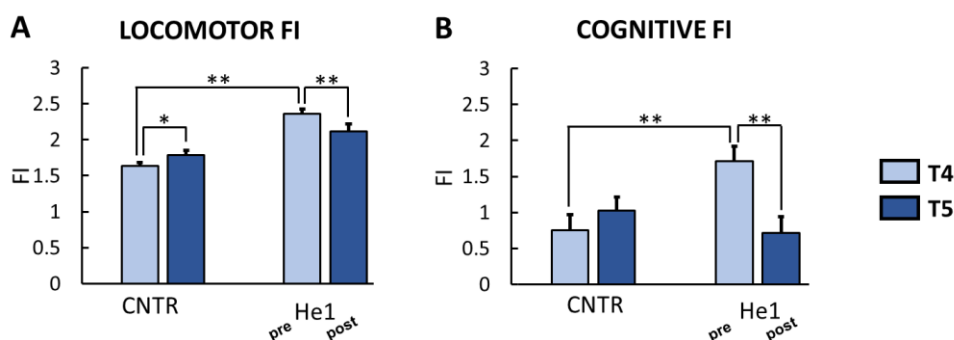


*Figure 48: The effect of He1 treatment in aged mice. A: Locomotor FI, and B: Cognitive FI measured at T4 (light blue)and T5 (dark blue) in control and H. erinaceus treated mice (He1). Statistical results were performed Two-Way ANOVA for repeated measures: p < 0.05 (*); p < 0.01 (**). Modified by Ratto et al., 2019 and Roda et al., 2021.*

## 6.3.2 Effects on cerebellar cytoarchitecture, inflammation, and oxidative stress

To evaluate the mechanisms underlying the effect of He1 treatment in mice, we performed histochemical and immunohistochemical reactions on sagittal slides of (i) the cerebellar vermis and (ii) hippocampus from untreated control animals and He1 treated mice at T5 (23.5 months). In particular, regarding cerebellar specimens, we performed the reactions on the neocerebellar lobules VI-VIII because they are especially affected by aging and correlated with cognitive and locomotor performances (Paul et al., 2009).

### 6.3.2.1 Cerebellar morphological characteristics, cytoarchitecture alterations, and fibrillar collagen networks evaluation during aging

The general characteristics and cytoarchitecture of the cerebellum of control and He1 treated mice were evaluated using Hematoxylin and

Eosin (H&E) and Nissl staining. Both H&E and Nissl results (Figure 49 and 50) showed a preserved cerebellar cytoarchitecture in both groups, displaying the three typical distinct layers in the cerebellar cortex: molecular (ML), Purkinje (PL), and granular (IGL) layers. The ML was made by a few small cells together with numerous fibers. The large pyriform Purkinje cells appeared regularly placed in a single line next to the outer margin of the IGL. The IGL showed closely packed small rounded cells with deeply stained nuclei.

Aging-related changes were found in control mice, in which (i) the volume of the cerebellum was diminished ($43.73 \pm 0.44$ mm$^3$), (ii) about 44% of the Purkinje cells appeared smaller, and (iii) the ML thickness was reduced ($47.81 \pm 2.23$ µm). Notably, the He1 supplementation considerably prevented these age-related changes: He1 animals exhibited a bigger cerebellar volume ($45.35 \pm 0.39$ mm$^3$), only 24% of the Purkinje cells were shrunken, and the ML thickness was greater ($62.02 \pm 0.98$ µm) (Figure 49 and 50).
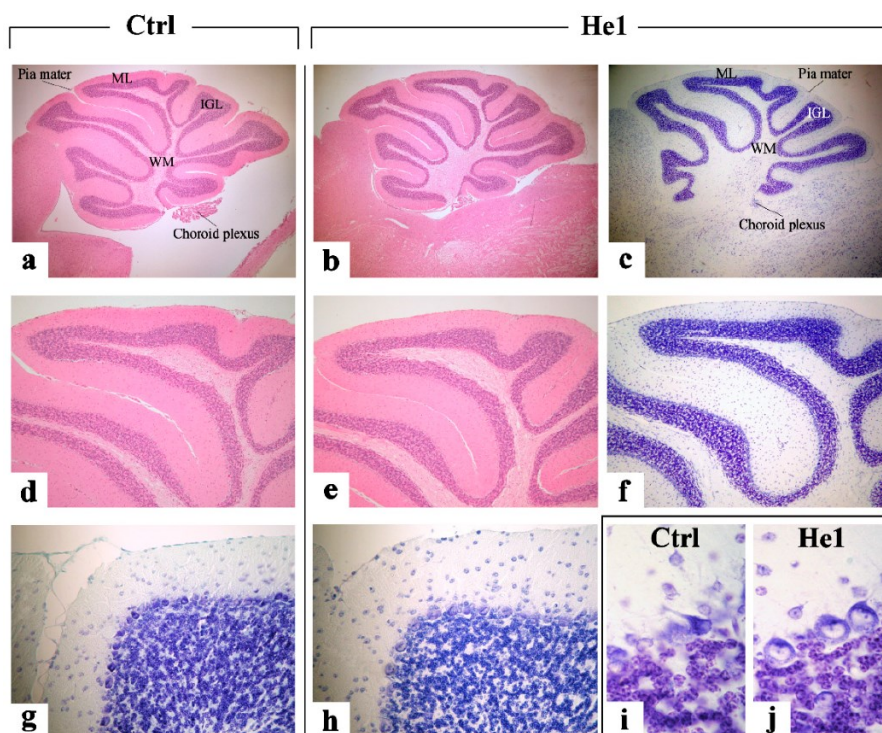


*Figure 49. Representative H&E and Nissl-stained cerebellar specimens, in untreated (a,d,g,i) and He1-treated mice (b,c,e,f,h,j). Light microscopy magnification: 20x (a–c); 40x (d–h); 100x (i,j). From Roda et al., 2021.*
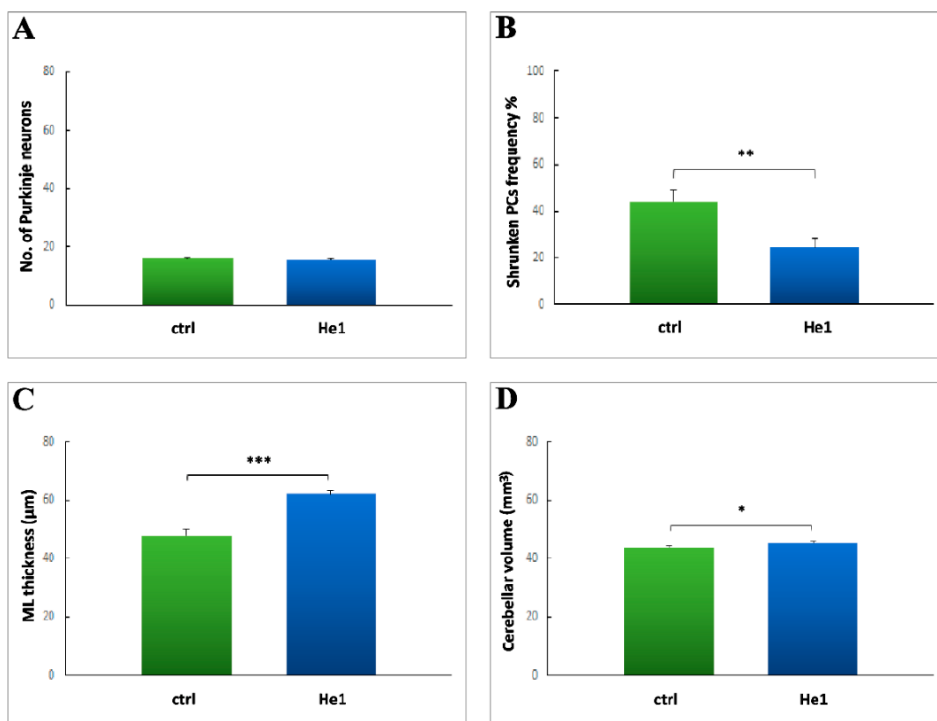
*Figure 50: Panel A–D display histograms showing (A) the number of Purkinje cells (PCs), (B) the shrunken PCs frequency percentage, (C) the ML thickness and (D) the cerebellar volume. Statistical results were performed by the Unpaired Student's t-test: significant values were reported for p < 0.05 (\*); p < 0.01 (\*\*); p < 0.001 (\*\*\*). From Roda et al., 2021.*

For evaluating the collagen networks, we performed the Picrosirius Red staining. In aged mice, the collagen fibers, both in control and He1 groups, were identified in the meninges (Figure 51). Both control and He1 mice also showed Picrosirius Red staining positive basal laminae of the cerebellar capillaries (Figure 51). Furthermore, some clusters of positive cells were also detected in the upper external part of the ML in control untreated mice only (Figure 51 c), whereas the ML of He1 treated mice was not positive for Picrosirius Red staining.

Interestingly, the collagen fibers OD was significantly higher in control mice compared to He1 treated mice both in ML layer (84.71 ± 1.82 vs. 74.22 ± 2.15, respectively) (Figure 51 H) and meninges (85.91 ± 1.79 vs. 74.39 ± 2.89, respectively) (Figure 51 I).
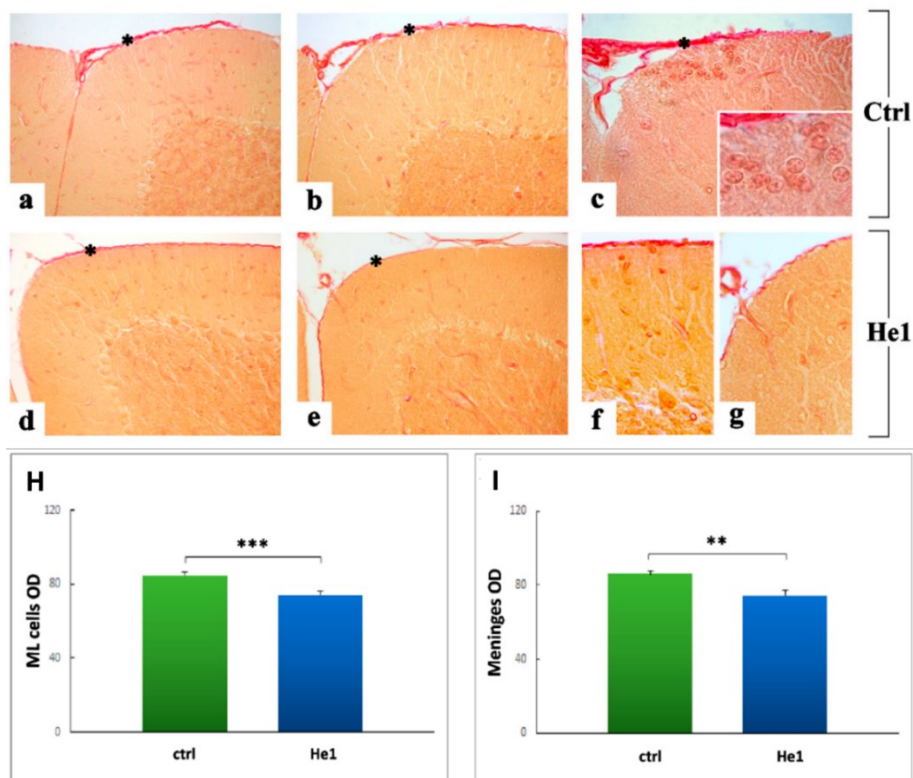
*Figure 51: Picrosirius Red staining in light microscopy on cerebellar slices, in control (a–c) and He1-treated mice (d–g). Magnification: 40x in panels a–e; 100x: insert in c. Asterisks in a–e marked the meningeal fibers. Panels H and I show histograms indicating the quantitative analysis of Picrosirius Red staining positive (H) ML cells OD and (I) meningeal fibers OD. Statistical results were performed by the Unpaired Student's t-test, significant values were reported for: $p < 0.01$ (\*\*), and $p < 0.001$ (\*\*\*). From Roda et al., 2021.*

## 6.3.2.2 Inflammation (IL-6), gliosis (GFAP), and hypoxia (HIF-alpha and VEGF) evaluation

Given the importance of aging-dependent neuroinflammation in cerebellum functions (Simen et al., 2011), we investigated the expression of interleukin 6 (IL-6), a pro-inflammatory cytokine.

IL-6 was expressed both in untreated mice and He1 animals, and its immunopositivity was mainly detected in cells close to the Purkinje cells soma (Figure 52). Furthermore, numerous IL-6-positive fibers running in the ML that reached the pial surface were detected only in control mice

(Figure 52). These fibers presented a higher OD in the upper part of the ML layer. The IL-6 immunopositive cells and fibers probably represented the main constituents of the Bergmann glia (BG, i.e., the radial glia that remains even after the development of the cerebellum, that is involved in the regulation of synaptic plasticity), with specialized astrocyte cell bodies around the Purkinje cells and the radial fibers extending over the full depth of the ML (Figure 52).

The analysis of IL-6 expression demonstrated a significant increase in the frequency percentage ($69.24 \pm 2.60$ vs. $50.92 \pm 3.23$) (Figure 52 J) and in the OD (Figure 52 K) ($105.56 \pm 0.72$ vs. $100.02 \pm 0.31$) of BG cells in control mice compared to He1 mice.



*Figure 52. IL-6 DAB-immunostaining reaction in control (a–d,i) and He1 mice (e–h). Light microscopy magnification: 40× (a,b,e,f); 100× (c,d,g,h,i). Panels J and K: Histograms showing the immunopositive BG cells frequency (A) and OD (B). Statistical results were performed by the Unpaired Student's t-test: significant values were reported for p < 0.05 (\*); p < 0.001. From Roda et al., 2021.*

Since gliosis is frequently related to a pro-inflammatory environment and CNS damages (Burda et al., 2014), we investigated the expression of Glial Fibrillary Acid Protein (GFAP) as specific marker of the Bergmann glia (BG). The untreated control animals showed GFAP-positive glial fibers that sometimes appeared thickened and twisted, with an irregular course in the ML (Figure 53 a–d). On the contrary, He1 mice displayed an almost complete absence of GFAP-positive glial fibers. Furthermore, control animals also showed many GFAP-immunopositive IGL astrocytes, whereas in He1 treated mice, GFAP-immunopositive IGL astrocytes were rare (Figure 53 a-h). These data were confirmed by quantitative analysis:

- the GFAP-immunopositive BG cells density was significantly higher in control animals compared to He1 mice (539.95 ± 46.57 vs. 87.61 ± 22.75, respectively) (Figure 53 I);
- The GFAP-immunopositive BG area/ML area ratio was significantly higher in control animals compared to He1 mice (34.49 ± 5.68 vs. 6.53 ± 1.53) (Figure 53 L);
- The GFAP-immunopositive IGL astrocytes density was significantly higher in control animals compared to He1 mice (1557.39 ± 80.76 vs. 1033.43 vs. 110.54) (Figure 53 M);
- The GFAP immunopositive astrocytes OD was significantly higher in control animals compared with He1 mice (122.28 ± 0.68 vs. 112.12 ± 1.90) (Figure 53 N).
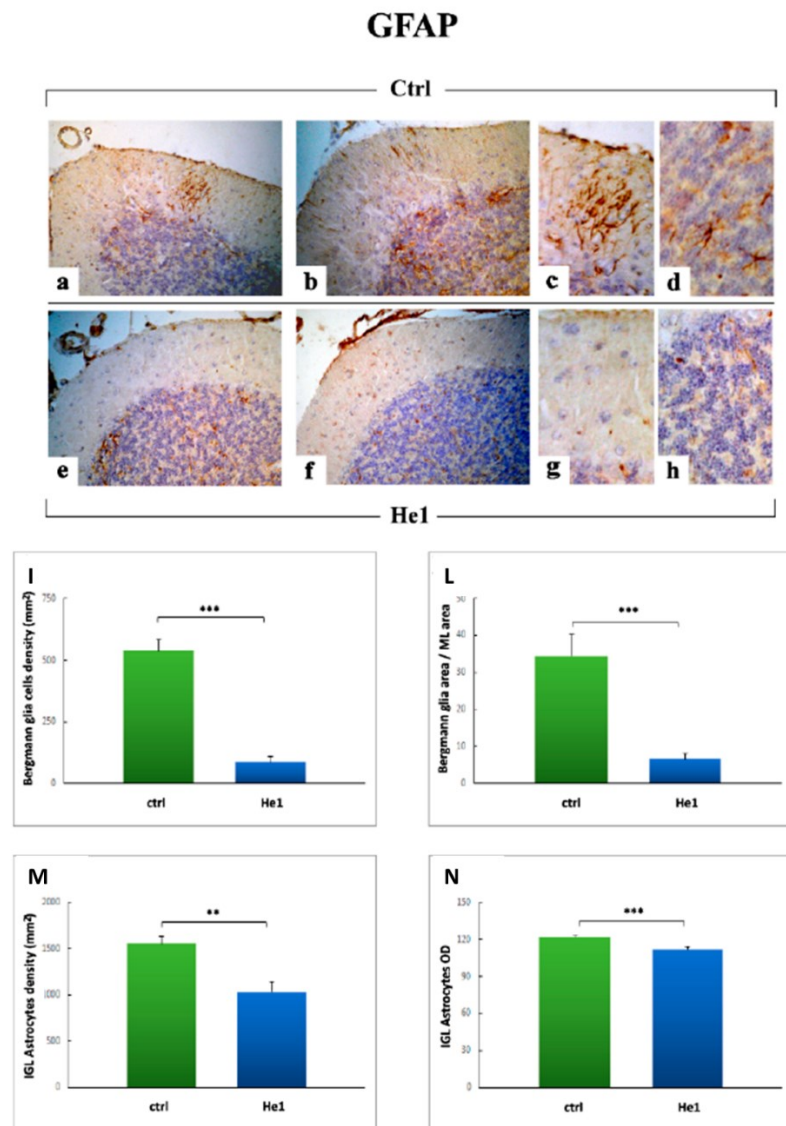
*Figure 53. GFAP DAB-immunostaining reaction in control (a–d) and He1-treated mice (e–h). Light microscopy magnification: 40x (a,b,e,f); 100x (c,d,g,h). Panels I-N show the histograms representing quantitative analyses of (I) BG immunopositive cell density, (L) ratio between GFAP-immunopositive area in the ML and whole ML area,(M) IGL immunopositive astrocytes density and (N) IGL immunopositive astrocytes OD, respectively. Statistical results were performed by the Unpaired Student's t-test: significant values were reported for: p < 0.01 (\*\*), and p < 0.001 (\*\*\*). From Roda et al., 2021.*

Next, we investigated the expression of Hypoxia-inducible factor 1-alpha (HIF1α), for investigating the decrease of oxygen availability in the cellular environment during aging. The HIF1α was expressed in vascular endothelial cells in the whole width of the cerebellar cortex, both in control and He1 mice (Figure 54). The HIF1α-positive vessels were mainly localized in the width of ML and characterized by the presence of several intricate ramifications (Figure 54). In particular, we detected a significant increase of both blood vessels area (5.60 ± 0.59 vs. 1.65 ± 0.15) and OD (178.21 ± 3.57 vs. 161.66 ± 3.16) in control animals compared to He1 mice (Figure 54 I and L).

**HIF1α**
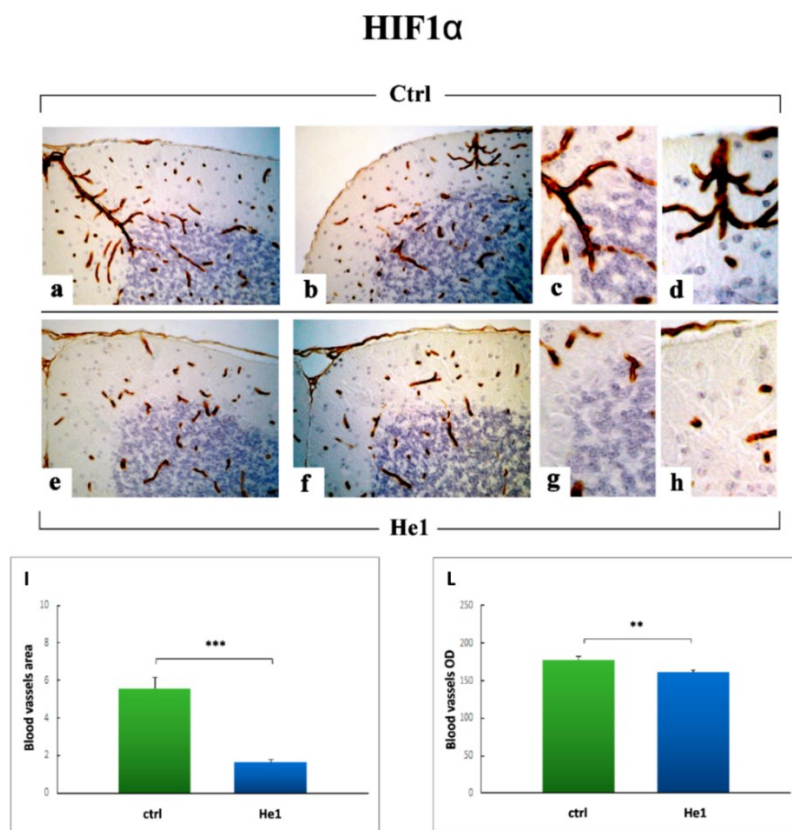


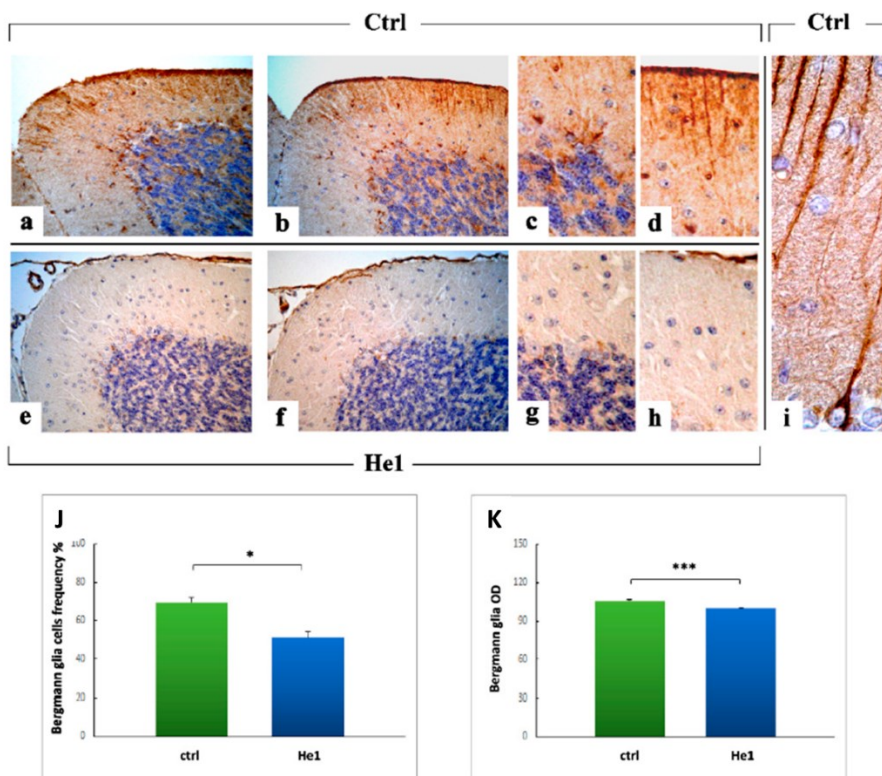*Figure 54. HIF1α DAB-immunostaining in control (a–d) and He1 mice (e–h). Light microscopy magnification: 40× (a,b,e,f); 100× (c,d,g,h). Panels I and L show histograms indicating HIF1α-immunopositive blood vessels area (I) and OD (L). Statistical results were performed by the Unpaired Student's t-test: significant values were reported for: p < 0.01 (\*\*), and p < 0.001 (\*\*\*). From Roda et al., 2021.*

Subsequently, we investigated the expression of the Vascular-Endothelial Growth Factor (VEGF), whose expression is related to vasculogenesis and angiogenesis and is essential for endothelium function. VEGF expression was detected in PCs and mossy fiber rosettes, both in control and He1 animals (Figure 55). The quantitative analysis demonstrated a significant decrease in VEGF expression in control mice than He1 animals:

- VEGF-immunopositive PC cells frequency (44.10 ± 1.22 vs. 62.80 ± 1.76, respectively) (Figure 55 G);
- VEGF-immunoreactivity OD in PC cells soma (117.93 ± 0.77 vs. 130.94 ± 1.82, respectively) (Figure 55 H);
- VEGF-immunoreactivity OD in mossy fiber rosettes (117.62 ± 1.82 vs. 128.74 ± 0.96, respectively) (Figure 55 I).

## 6.3.2.3 Oxidative Stress Pathway: SOD1, NOS2, and COX2 evaluations

Oxidative stress is one of the significant factors involved in neurodegeneration associated with aging (Finkel and Holbrook, 2000; Chen et al., 2012). So, we performed immunohistochemistry for detecting the expression and localization of specific markers of oxidative stress pathway: Superoxide Dismutase (SOD1), Nitric oxide synthase inducible (NOS2), and Cyclooxygenase 2 (COX2).

SOD1 immunohistochemistry showed a general expression of this marker both in control and in He1 mice (Figure 56 a-h). In particular, the most SOD1-expressed cells were in the ML. The quantitative analysis demonstrated that He1 oral supplementation determined a significant decrease in the SOD1 immunopositive ML cells frequency (63.52 ± 1.26 in control vs. 54.44 ± 1.86 in He1 mice), but not in the OD (123.15 ± 0.43 in control vs. 122.99 ± 0.68 in He1 mice) (Figure 56 I and L).

NOS2 immunohistochemistry showed the expression of this marker in PC cells (Figure 57 a-c and e-g) and large mossy fiber rosettes (Figure 57 d and h) both in control and in He1 mice. Quantitative analysis showed that the He1 oral supplementation significant decreased NOS2 expression in mice during aging:

- immunopositive PC cells frequency: 31.31 ± 0.99 in controls vs. 22.01 ±1.07 in He1 animals (57 Figure I);
- mossy fibers rosettes OD: 76.52 ± 0.28 in controls vs.59.81 ± 0.91 in He1 animals (57 Figure L);

- PC cells OD: 64.98 ± 0.62 in controls vs. 57.66 ± 0.59 in He1 animals (57 Figure M).
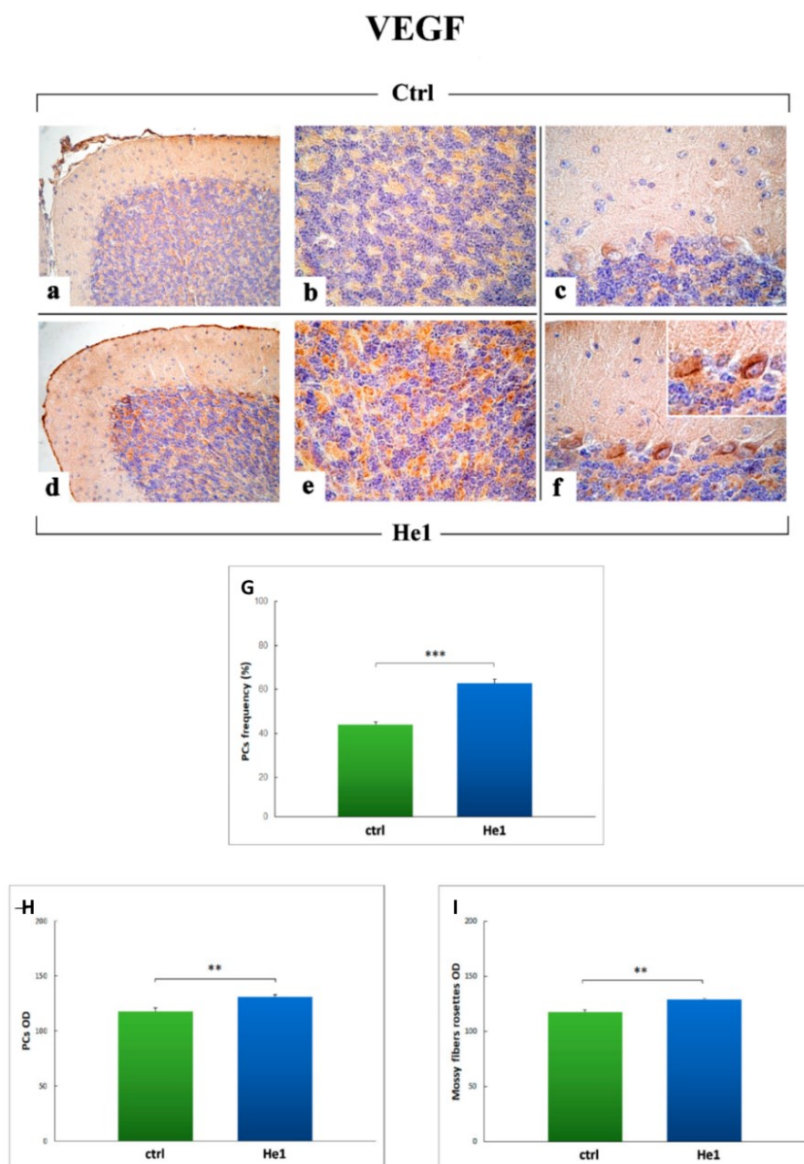
**VEGF**



*Figure 55. VEGF DAB-immunostaining in control (a–c) and He1-treated mice (d–f). Light microscopy magnification: 40x (a–f); 100x (insert in f). Panels G, H, and I show histograms presenting the quantitative measurement of VEGF-immunoreactive cell frequency (G) and OD (H) for PC neurons and mossy fibers rosettes OD (I). Statistical results were performed by the Unpaired Student's t-test: significant values were reported for: p < 0.01 (\*\*), and p < 0.001 (\*\*\*). From Roda et al., 2021.*

# SOD1
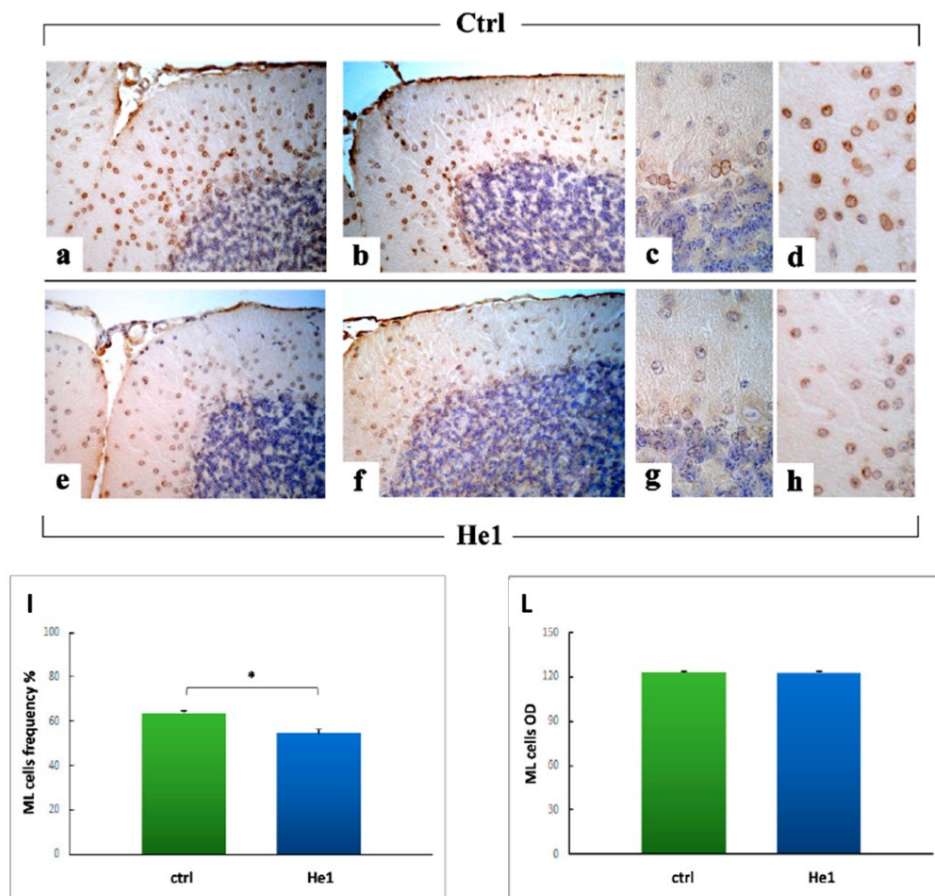


*Figure 56. SOD1 DAB-immunostaining in control (a–d) and He1 treated mice (e–h). Light microscopy magnification: 40x (a,b,e,f); 100x (c,d,g,h). Panels I and L show the histograms representing the quantitative measurement of SOD1-immunoreactive cell frequency (I) and OD (L) in the ML cells. Statistical results were performed by the Unpaired Student's t-test: significant values were reported for: p < 0.05 (*). From Roda et al., 2021.*
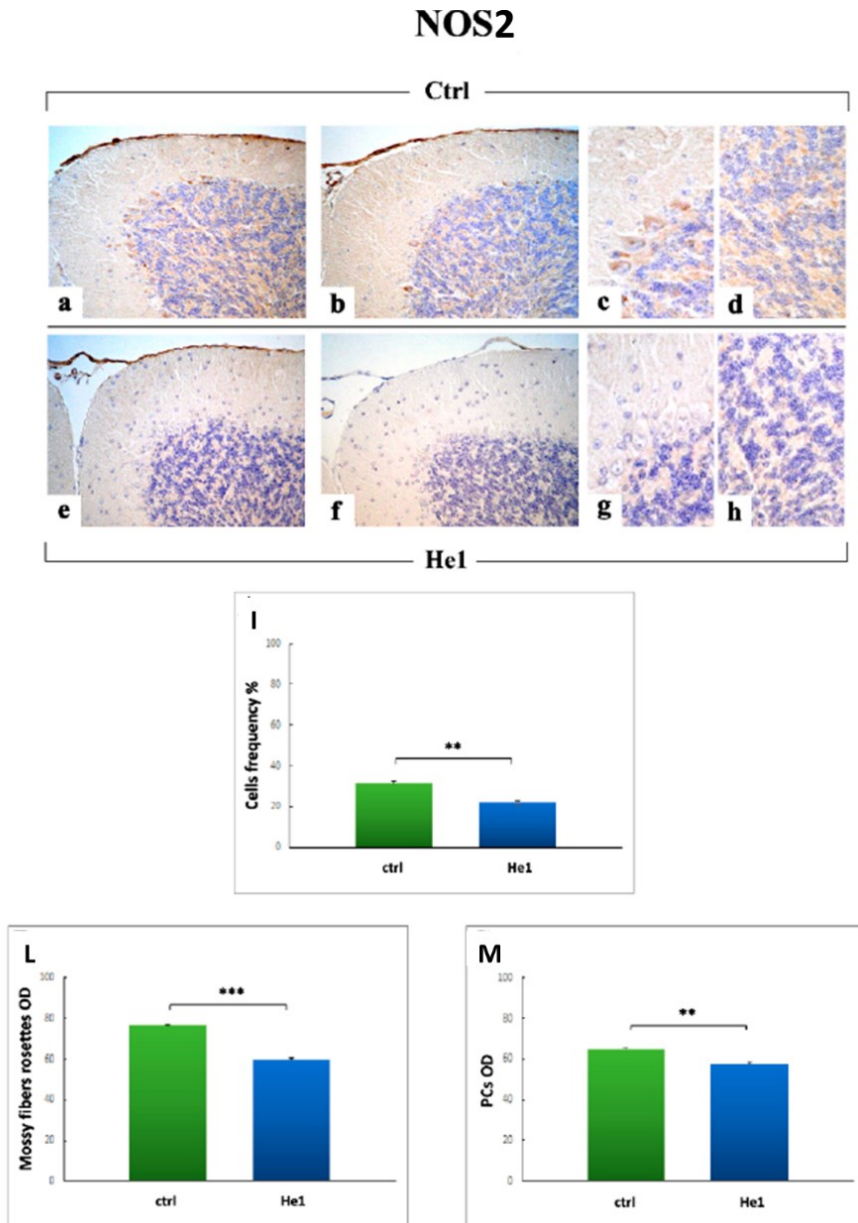
Figure 57. NOS2 DAB-immunostaining in control (a–d) and He1-treated mice (e–h). Objective magnification: 40x (a,b,e,f); 100x (c,d,g,h). Panels I, L, and M show histograms representing the quantitative measurement of NOS2 immunopositive PC cells frequency (I), and OD evaluation for both mossy fibers rosettes (L) as well as PC cells (M). Statistical results were performed by the Unpaired Student's t-test: significant values were reported for p < 0.01 (**) and p < 0.001 (***). From Roda et al., 2021.

COX2 immunohistochemistry showed the expression of this marker in PC cells soma and dendrites (Figure 58 a-h) both in control and in He1 mice, whereas in IGL, COX2 was expressed only in control mice. Quantitative analysis showed that the He1 oral supplementation significant decreased COX2 expression in mice during aging:

- immunopositive PC cells frequency: $79.67 \pm 1.71$ in controls vs. $62.32 \pm 1.67$ in He1 animals (Figure 58 I);
- PC cells OD: $121.93 \pm 0.49$ in controls vs. $108.65 \pm 0.30$ in He1 animals (Figure 58 L).
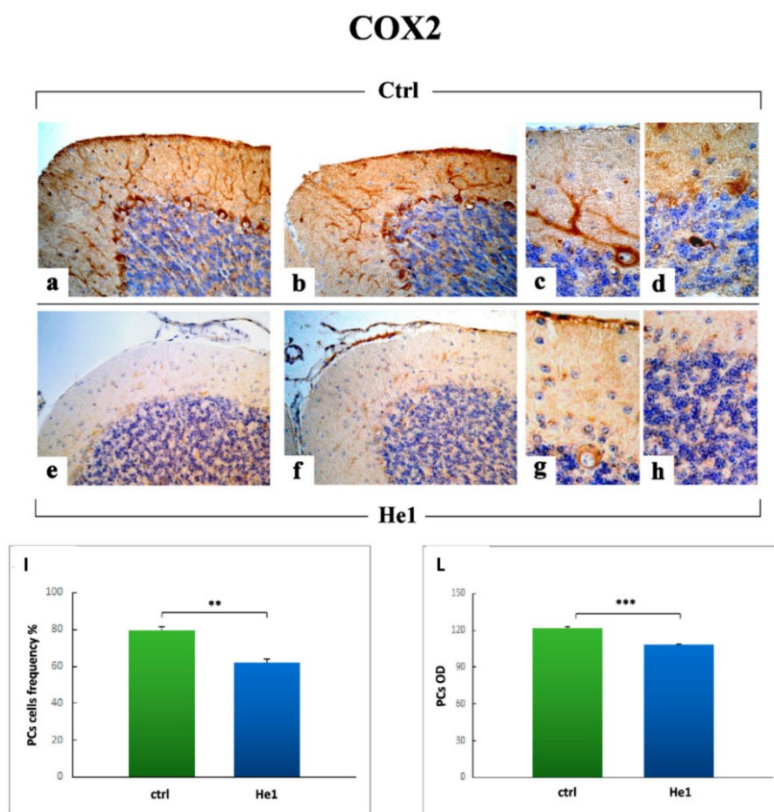


Figure 58. COX2 DAB-immunostaining in control (a–d) and He1-treated mice (e–h). Objective magnification: 40x (a,b,e,f); 100x (c,d,g,h). Panels I and L display histograms showing the quantitative measurement of COX2 immunopositive PC cells frequency (I) and OD (L). Statistical results were performed by the Unpaired Student's t-test: significant values were reported for: $p < 0.01$ (**) and $p < 0.001$ (***). From Roda et al., 2021.

### 6.3.3 He1 had a potential senomorphic activity: SIRT1 evaluation

Next, we investigated the expression of SIRT1, a protein with a critical role in aging and lifespan, fundamentally in influencing the functions of neurons. Some recent papers defined as senomorphic the molecules able to activate SIRT1.

In our samples, SIRT1 was prevalently localized in PL and ML cells, with a significantly higher expression in He1 treated mice compared to controls (Figure 59 a–f), as confirmed by quantitative analysis of:

- immunopositive PC cells frequency (72.32 ± 2.46 in He1 mice vs. 48.00 ± 1.44 in control mice) (Figure 59 G);
- immunopositive ML cells frequency (59.00 ± 3.81 in He1 mice vs 19.00 ± 1.08 in control mice) (Figure 59 H);
- immunopositive PC cells OD (39.01 ± 1.33 in He1 mice vs. 22.6 ± 1.53 in control mice) (Figure 59 I);
- immunopositive ML cells OD (32.19 ± 1.55 in He1 mice vs 18.57 ± 1.21 in control mice) (Figure 59 L).

# Sirt1
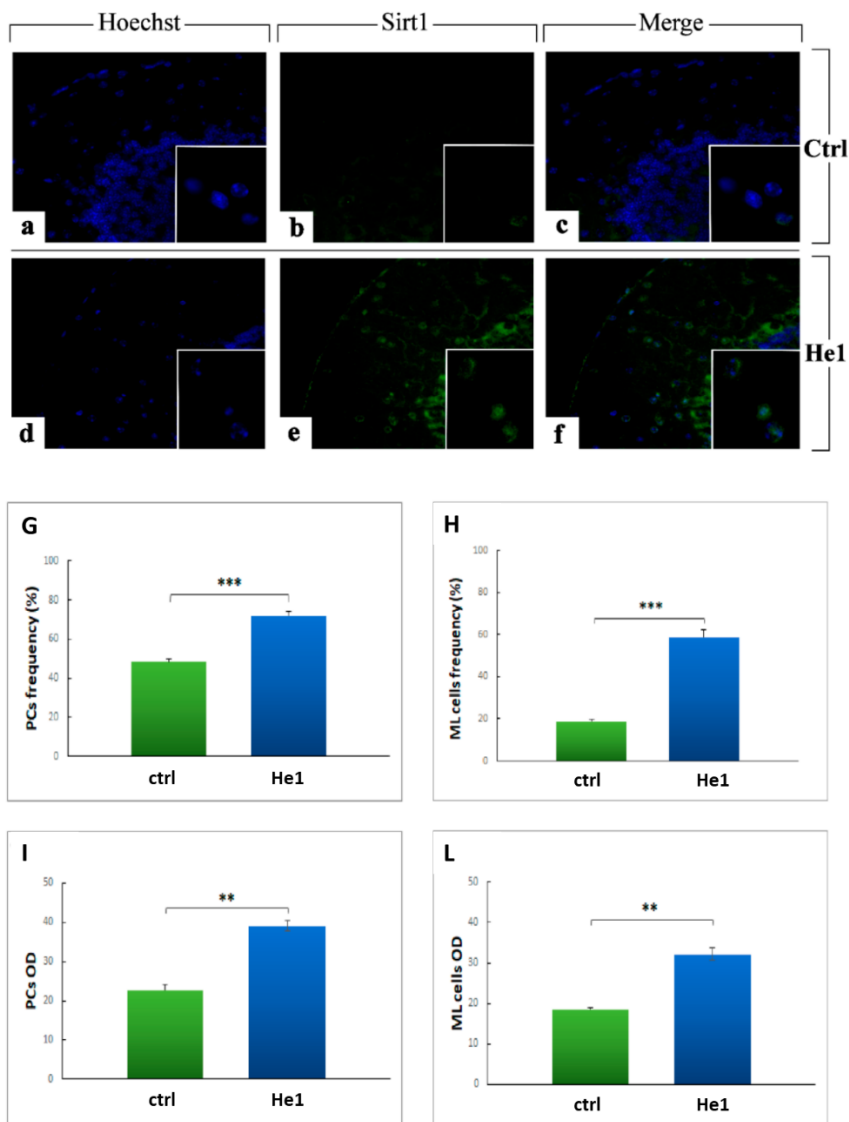


*Figure 59. Immunofluorescence for SIRT1 (green fluorescence) in control (a–c) and He1 mice (d–f). Nuclei were counterstained with Hoechst 33,258 (blue fluorescence). Objective magnification: 40x (a–f); 100x (inserts). Panels G-L show the histograms indicating quantitative analyses of frequency of SIRT1 expression in PC (G) and ML (H) cells and regarding the OD of PC (I) and ML (L) cells. Statistical results were performed by the Unpaired Student's t-test: significant values were reported for p < 0.01 (\*\*), and p < 0.001 (\*\*\*). From Roda et al., 2021.*

## 6.3.4 Effects on BBB functions during aging

Next, we performed immunohistochemical evaluations of the expression of Zonula Occludens-1 (ZO-1) and Occludin as specific markers of Blood-Brain Barrier (BBB) integrity since the BBB functionality impairment is related to the onset of dementia and aging-related neurodegenerative diseases.

ZO-1 is a multi-domain scaffold protein responsible for forming and maintaining tight junctions through the interaction with transmembrane adhesion molecules, signaling proteins, and cytoskeletal actin filaments (Monaco et al., 2021). In our samples, the distribution of ZO-1 appeared principally localized in the endothelium of cerebral microvessels, in the endothelial cell of the choroid plexus, and in the ependymal cells of the lateral ventricle (Figure 60). Notably, the ZO-1 immunopositivity appeared strongly evident in the He1 animals compared to control mice. Moreover, the capillary endothelium showed an irregular and interrupted gross morphology in the untreated animals compared to He1 mice. The quantitative analysis confirmed a significant increase of ZO-1 OD values in He1 treated mice compared to untreated animals in:

- the cortical capillaries (135.109 ± 2.74 vs. 112.901 ± 2.40, respectively; Figure 60 G);
- the hippocampal endothelium (114.990 ± 1.03 vs. 101.900 ± 1.97, respectively; Figure 60 H);
- the hypothalamic endothelium (128.593 ± 3.56 vs. 108.487 ± 4.90, respectively; Figure 60 I).

Concerning ZO-1 expression in ependymal cells (Figure 61), a more evident OD increase appeared in He1 mice compared to controls (OD values: 153.923 ± 2.21 vs. 129.826 ± 2.75, respectively; Figure 61 E). Regarding ZO-1 expression in the choroid plexus (Figure 61), a similar but slighter OD increase was measured in the endothelial cells comparing He1 mice with the untreated controls (OD values: 138.149 ± 3.46 vs. 122.134 ± 3.54, respectively; Figure 61 F).
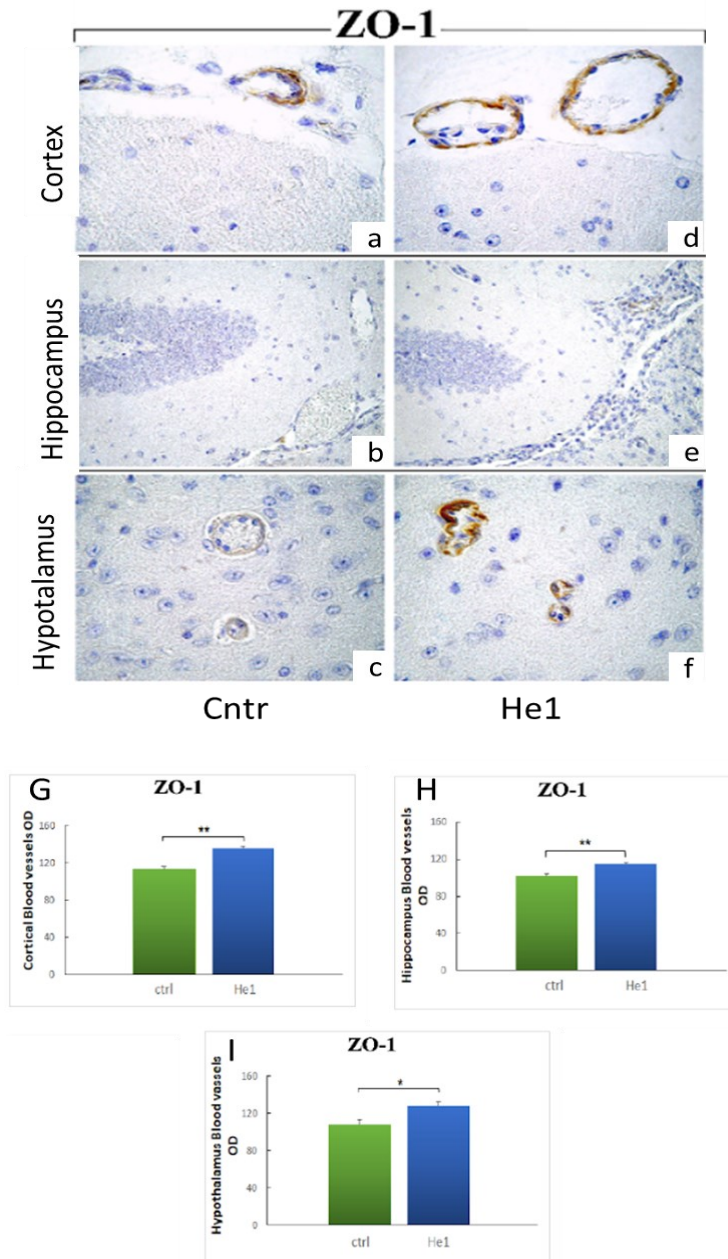
*Figure 60. ZO-1 DAB-immunostaining reaction in untreated (a–c) and He1-treated mice (d–f) considering cortical, hippocampal, and hypothalamic blood vessels. Light microscopy magnification: 40×. Panels G, H, I display histograms showing the quantitative analyses of ZO-1 OD for cortical (G), hippocampal (H), and hypothalamic (I) blood vessels. Statistical results were performed by the Unpaired Student's t-test: significant values were reported for $p < 0.05$ (*), and $p < 0.01$ (**).*

*Figure 61. ZO-1 DAB-immunostaining reaction in untreated (a,b) and He1-treated mice (c,d) considering ependymal and choroid plexus, respectively. Light microscopy magnification: 40×. Panels E and F display histograms showing the quantitative analyses of ZO-1 OD for ependymal cell (E) and choroid plexus (F). Statistical results were performed by the Unpaired Student's t-test: significant values were reported for p < 0.05 (\*), and p < 0.01 (\*\*).*

Following, we assessed the distribution of Occludin in the brain as a specific transmembrane protein required for tight junctions' detection (Figure 62 and 63).

Occludin immunoreactivity was markedly evident in He1 animals (Figure 62), where Occludin-positive blood vessels were detected. Also for this marker, the quantitative analysis showed a significant increase in the OD immunopositivity of He1 mice compared to untreated animals in:

- Cortical vessels endothelium (181.874 ± 1.76 vs. 84.521 ± 3.48, respectively; Figure 62 G);
- Hippocampal vessels endothelium (126.860 ± 3.05 vs. 75.431 ± 2.06, respectively; Figure 62 H);
- Hypothalamic vessels endothelium (186.634 ± 8.72 vs. 132.259 ± 3.57, respectively; Figure 62 I).
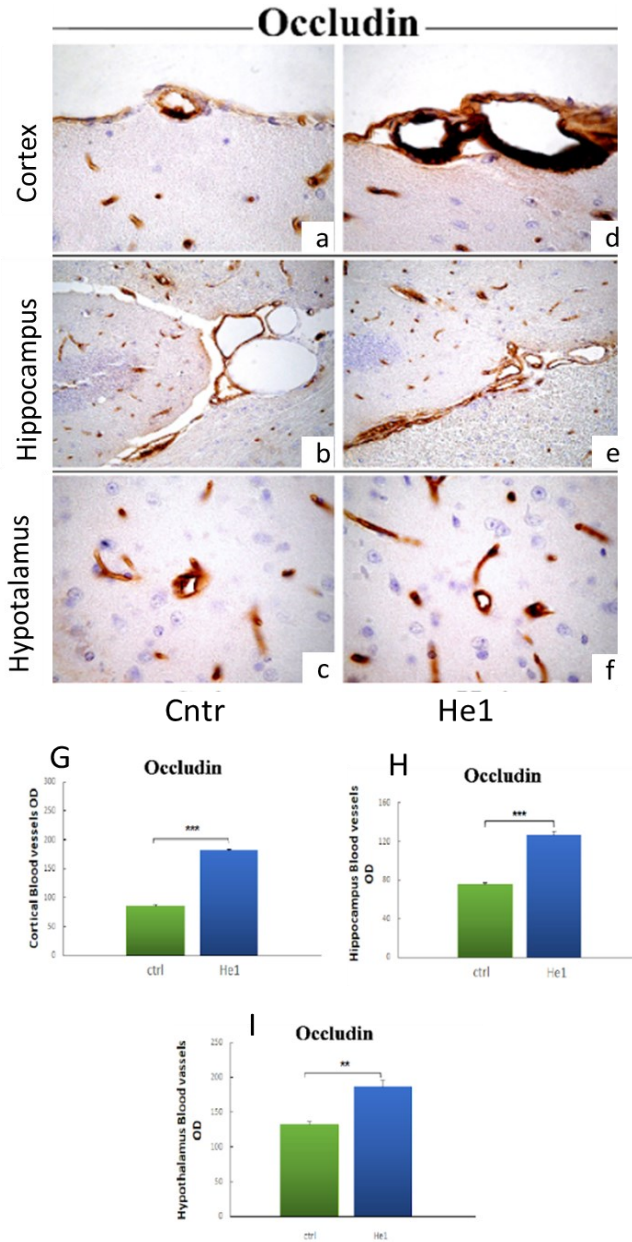
Figure 62. Occludin DAB-immunostaining reaction in untreated (a–c) and He1-treated mice (d–f) considering cortical, hippocampal, and hypothalamic blood vessels. Light microscopy magnification: 40×. Panels G, H, I display histograms showing the quantitative analyses of occludin for cortical (G), hippocampal (H), and hypothalamic (I) blood vessels, respectively. Statistical results were performed by the Unpaired Student's t-test: significant values were reported for $p < 0.05$ (*), and $p < 0.01$ (**).

Next, we investigated the expression of occludin in ependymal cells and choroid plexus (Figure 63).

The ependymal cells covering the lateral ventricle appeared regularly stained in He1 treated animals compared to controls, but the quantitative analysis did not show significant differences (93.450 ± 4.60 vs. 75.281 ± 9.68; Figure 63 E).

The choroid plexus-immunostaining highlighted a strong Occludin-positivity in He1 mice compared to untreated animals too. Indeed, immunopositivity of choroid plexus cells highlighted a significant increase in OD in He1 mice compared to untreated animals (141.607 ± 2.38 vs. 122.712 ± 6.18; respectively; Figure 63 F).
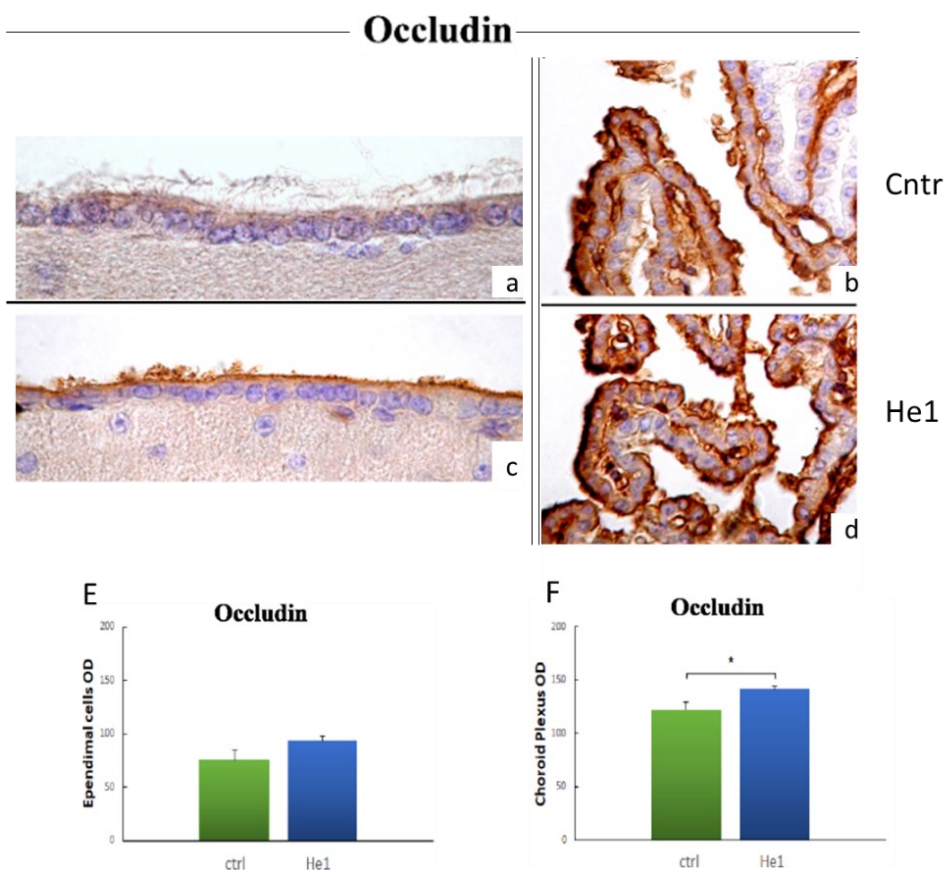


Figure 63. Occludin DAB-immunostaining reaction in untreated (a,b) and He1-treated mice (c,d) considering ependymal and choroid plexus, respectively. Light microscopy magnification: 40×. Panels E and F display histograms showing the quantitative analyses of occludin OD for ependymal cells (E) and choroid plexus (F). Statistical results were performed by the Unpaired Student's t-test: significant values were reported for p < 0.05 (*), and p < 0.01 (**).

To integrate the study of the BBB integrity during aging, we investigated the expression of Glut1 protein, a specific type of glucose transporter widely expressed in both luminal and abluminal membranes of endothelial cells. Glut1 exclusively mediates glucose transfer across the BBB. Since a high amount of glucose is essential for brain and neurons metabolism, this protein plays a crucial role in preserving normal neurological functions (Patching, 2017).

In our samples, the distribution of Glut1 appeared mainly localized in the endothelium of the cerebral capillaries, in the choroid plexus, and in the ependymal cells of the lateral ventricle (Figure 64 and 65). Endothelial cells showed very intense Glut1 immunopositivity in He1 treated animals compared to untreated mice. Indeed, the quantitative analysis demonstrated a significant increase in He1 treated mice compared to untreated animals in the OD values of:

- the cortical capillaries (178.574 ± 3.59 vs. 152.496 ± 7.85, respectively; Figure 64 G);
- the hippocampal endothelium (162.678 ± 8.86 vs. 87.133 ± 5.66, respectively; Figure 64 H);
- the hypothalamic endothelium (160.894 ± 6.88 vs. 138.475 ± 5.14, respectively; Figure 64 I).

Concerning the ependymal cells, we detected a non-significant increase of OD values appeared in He1 mice compared to control ones (105.214 ± 0.91 vs. 76.052 ± 4.41, respectively; Figure 65 E). Instead, regarding the choroid plexus, a significant OD increase was measured in the endothelial cells comparing He1 treated mice and untreated animals (184.060 ± 8.08 vs. 137.437 ± 2.45, respectively; Figure 65 F),
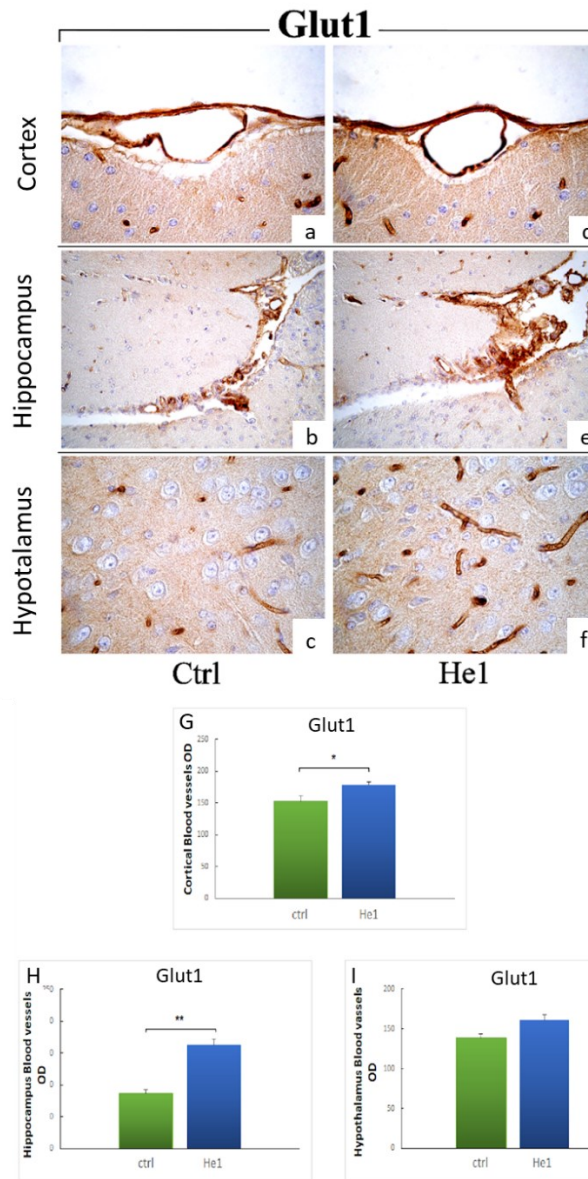
*Figure 64. Glut-1 DAB-immunostaining reaction in untreated (a–c) and He1-treated mice (d–f) considering cortical, hippocampal, and hypothalamic blood vessels. Light microscopy magnification: 40×. Panels G, H, I display histograms showing the quantitative analyses of Glut-1 for cortical (G), hippocampal (H), and hypothalamic (I) blood vessels, respectively. Statistical results were performed by the Unpaired Student's t-test: significant values were reported for $p < 0.05$ (*), and $p < 0.01$ (**).*
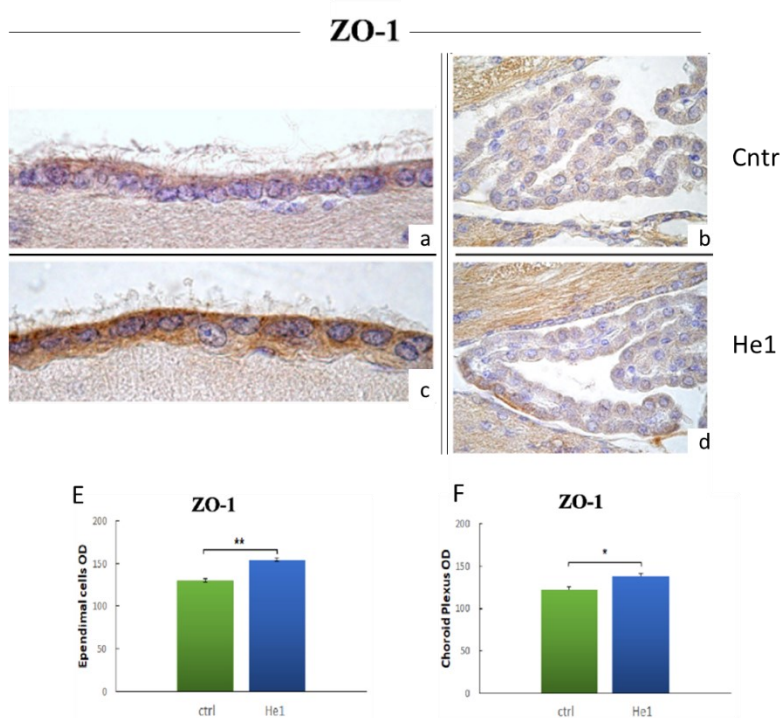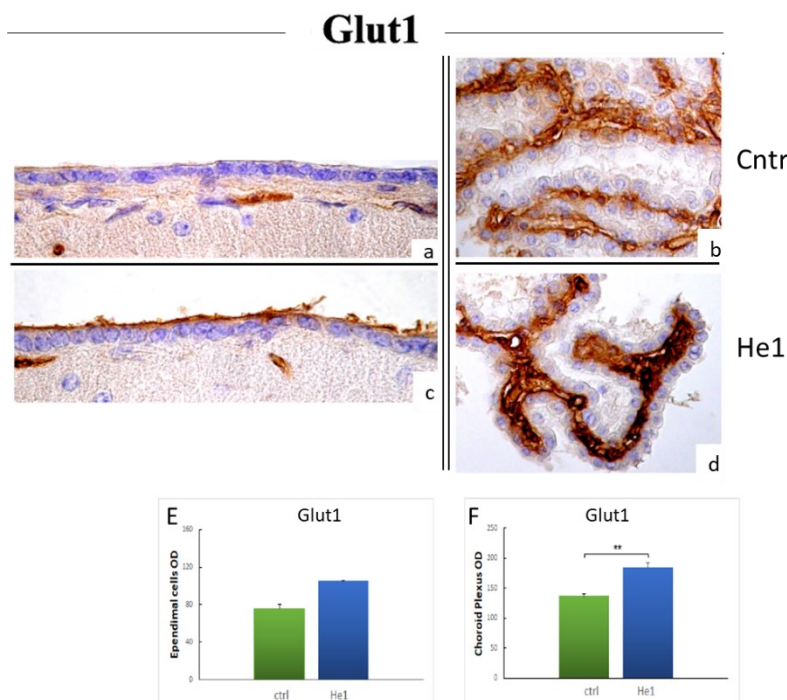
*Figure 65. Glut1 DAB-immunostaining reaction in untreated (a,b) and He1-treated mice (c,d) ependymal and choroid plexus cells, respectively. Light microscopy magnification: 40×. Panels E and F display histograms showing the quantitative analyses of Glut1-OD for both ependymal cells (E) and choroid plexus (F). Statistical results were performed by the Unpaired Student's t-test: significant values were reported for p < 0.01 (\*\*).*

## 6.3.5 Enhancement of hippocampal and cerebellar proliferation and neurogenesis

To further investigate the molecular mechanism of He1 effect, we performed immunohistochemistry on the hippocampus and cerebellum of He1 and untreated control mice at T5, investigating the expression of proliferating cell nuclear antigen (PCNA) and doublecortin (DCX) as specific markers of cell proliferation and neurogenesis, respectively.

### 6.3.5.1 PCNA evaluation

PCNA is a nuclear protein that plays an essential role in nucleic acid turnover as a component of the replication and repair (Boehm et al., 2016).
PCNA immunolabelling showed a higher cell density percentage expression in the hippocampal dentate gyrus (DG) granule cells and in the CA3 pyramidal neurons of He1 mice compared to control mice (22.89% ± 6.09 vs. 10.80% ± 3.09, respectively; Figure 66). Similarly, in the cerebellar cortex, the immunopositive cells (possibly both neuronal or glial cells) were predominantly localized in the width of the outer molecular layer, and PCNA-positive cells were in higher number in He1 mice than controls (25.60% ± 6.66 vs. 8.19% ± 4.43, respectively; Figure 66).

### 6.3.5.2 DCX evaluation

DCX is a cytoplasm marker for newborn neurons and migrating neuroblasts during neurogenesis (Ayanlaja et al., 2017). Regarding cytoplasmic DCX expression, He1 treated mice showed more immunopositive cells than control animals in the hippocampal DG granule cells (cell frequency percentage: 8.45% ± 3.02 vs. 0.22% ± 0.45, respectively, Figure 67 A and B). In the cerebellar cortex, DCX positive cells were less expressed and mainly localized in the molecular layer, and the cell frequency percentage was slightly and no significant higher in the He1 group than control animals (4.68 ± 3.06 vs. 0.26% ± 0.79, respectively) (Figure 67).
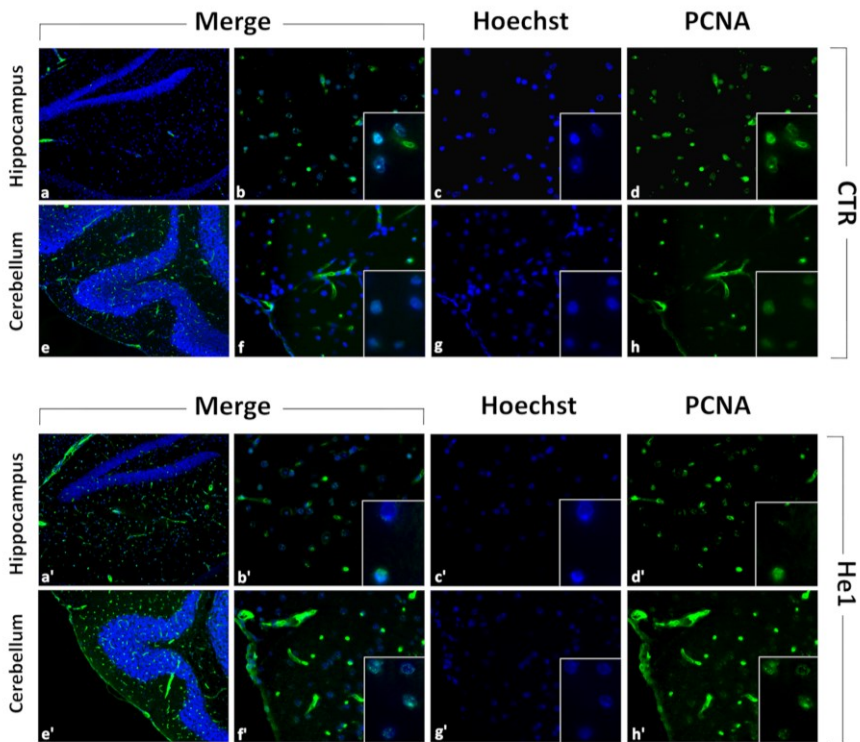
**(B)**
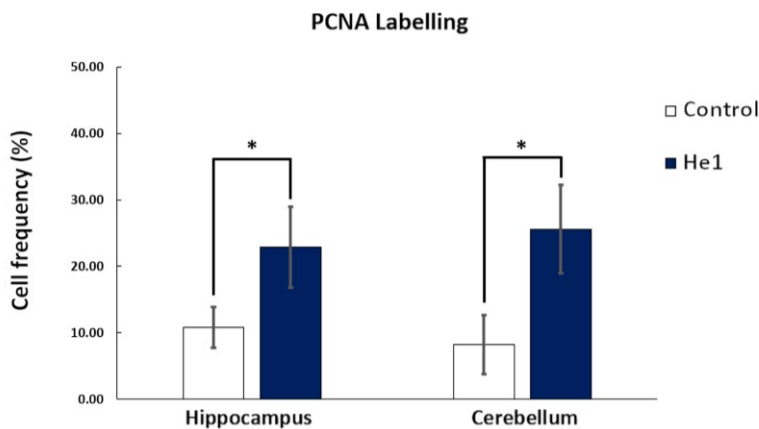


*Figure 66: PCNA labeling in control (CNTR) and He1 mice in the hippocampus (a, b, c, d, and a', b', c', d', respectively) and cerebellum (e, f, g, h, and e', f', g', h', respectively). Objective magnification: 20 x (a, e and a', e'); 40 x (b–d, f–h and b'–d', f'–h'); 100 x (insert in b–d, f–h, b'–d', f'–h'). B: Cell frequency percentage of PCNA labeling of hippocampal and cerebellar cells in control (white) and He1 (blue) mice. Statistical results were performed by the Unpaired Student's t-test: significant values were reported for p < 0.05 (\*). From Ratto et al., 2019.*
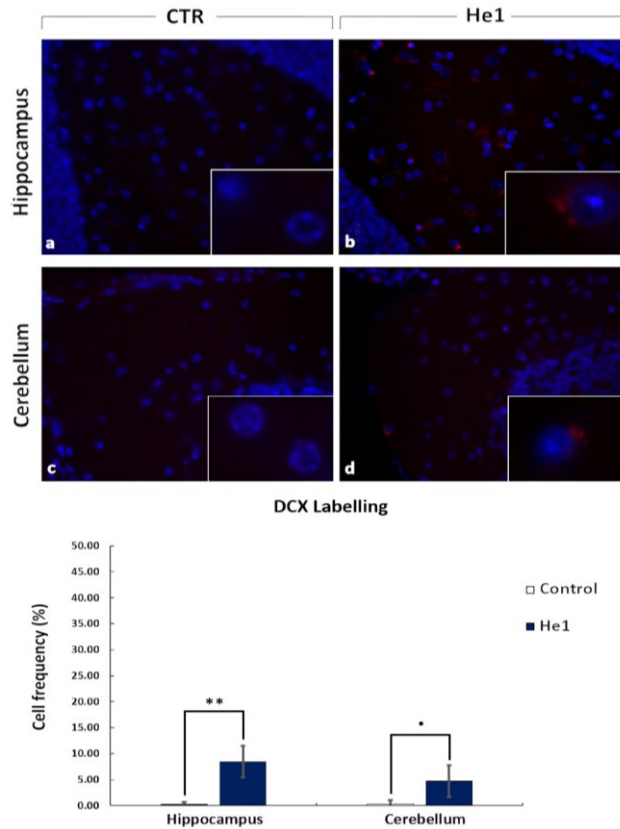
*Figure 67: DCX labeling in control (CNTR) and He1 mice in the hippocampus (a and b, respectively) and cerebellum (c and d, respectively). Objective magnification: 40 x (a–d), 100 x (insert). B: Cell frequency percentage of DCX labeling of hippocampal DG and cerebellar molecular layer in control and He1 mice. Statistical results were performed by the Unpaired Student's t-test: significant values were reported for p < 0.05 (*).*

## 6.3.5 Effects on gut microbiome composition

We also studied the effect of He1 during aging on the intestinal microbial communities using 16S ribosomal RNA (rRNA) gene sequencing.
When looking at overall microbiota composition, during senescence, the alpha-diversity (Faith phylogenetic metrics) was similar between control and He1 treated mice both at T4 and T5, so pre- and post-treatment (Figure 68 A). Remarkably, also the beta-diversity observed in non-metric multidimensional scaling (NMDS) analysis did not reveal different clusters in control and He1 groups at T4 and T5 (Data not shown). So, the two-

months oral supplementation with *H. erinaceus* did not significantly change the overall microbiome composition. However, compared to control mice, during aging, the He1 supplementation significantly increased the relative abundance of genera *Clostridia UCG-014, Lachnospiraceae_NK4A136*, and *Eubacterium xylanophilum*, whereas significantly reduced the relative abundance of *Odoribacter, Clostridia vadinBB60*, and *Muribaculaceae* (Figure 68 B).

A



B
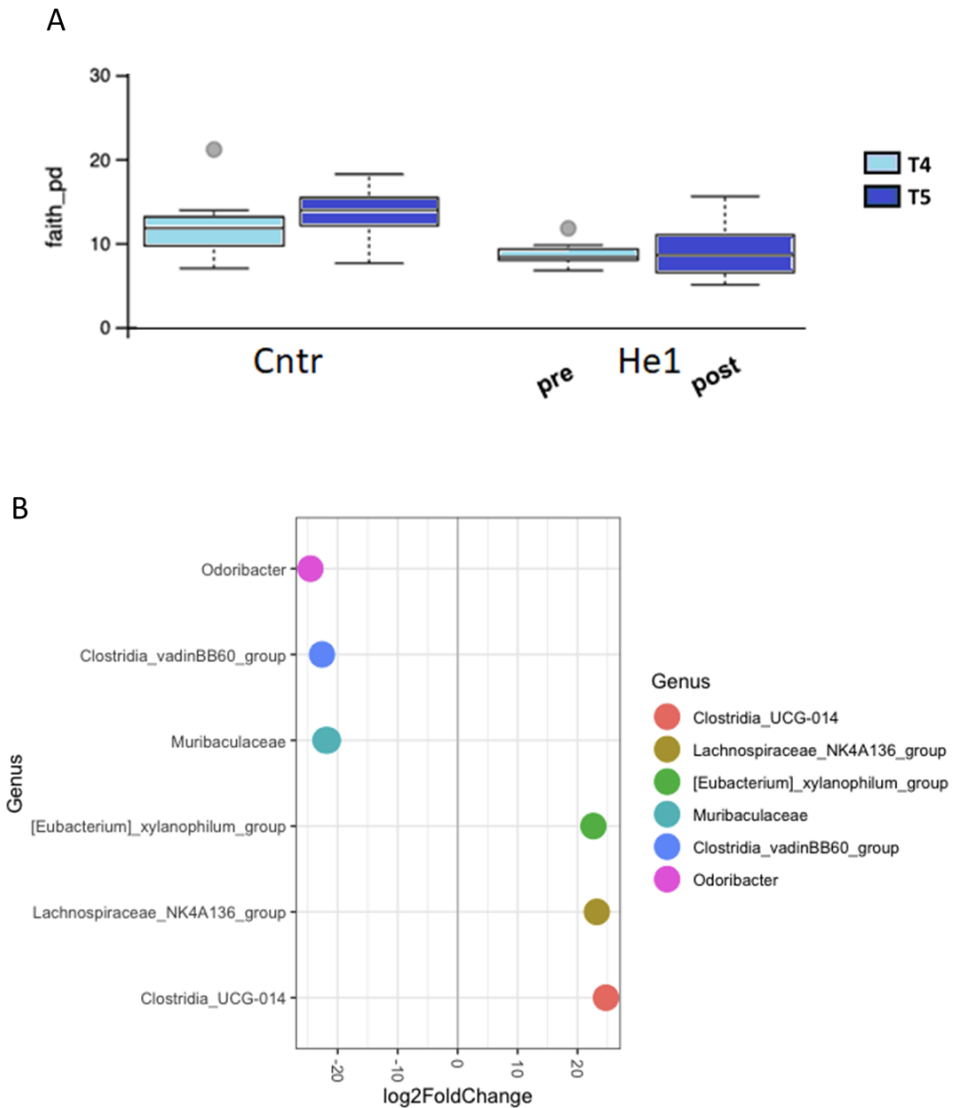


*Figure 68: He1 effects on gut microbiota composition. A: faith_pd alpha diversity in control mice and He1 treated animals at T4 and T5. B: Differential abundance at T5 in control mice vs. He1 treated animals.*

## 6.4 The effect of He2 in frailty prevention

In the second set of animals, we tested the preventive effect of He2 (an enriched-EGT primordium extract, in which there were no present nootropic metabolites) on frailty development in wild-type mice. In particular, we investigated the effect of eight-month (from 15 to 23 months) He2 oral supplementation in mice on (i) locomotor performances, (ii) cognitive functions, and (iii) oxidative stress pathway in CNS.

To achieve these aims, starting from 15 months, nine random mice (He2 group) were supplemented with 1 mg/die of He2, whereas the remaining six mice did not receive any supplement (control group). As previously discussed, we selected this dose for simulating the oral supplementation used in humans (about one g/day).

### 6.4.1 Effects on locomotor and cognitive performances

#### 6.4.1.1 Effects on locomotor performances

Firstly, we investigated the preventive effect of He2 on locomotor frailty onset in wild-type mice studying the locomotor capabilities. Figure 69 shows the proceeding of locomotors parameters during aging comparing control (red) and He2 (green) groups. As previously reported (Figure 37), in control mice, all recorded parameters worsened during aging with different timing (Figure 69). Notably, the oral supplementation with He2 for eight months significantly improved locomotor performances in mice regarding the resting time and total distance at 23 months (Figure 69 C and D). A similar non-significant trend was observed for the mean and maximum speeds.

Next, we calculated the locomotor FI for each parameter and, averaging the four locomotor FIs, we obtained the global Locomotor FI, which significantly increased during aging both in control and He2 treated mice in a straight way, as demonstrated by linear least-square regression analysis ($R^2$ = 0.9838 and $R^2$ = 0.9397, respectively). However, interestingly, the increase in the He2 group is statistically lower compared to control animals (Figure 69 E). Indeed, the linear least-square regression for locomotor FIs analysis changed the slope from 0.133 for control group to 0.087 for He2 mice (Figure 69 E).
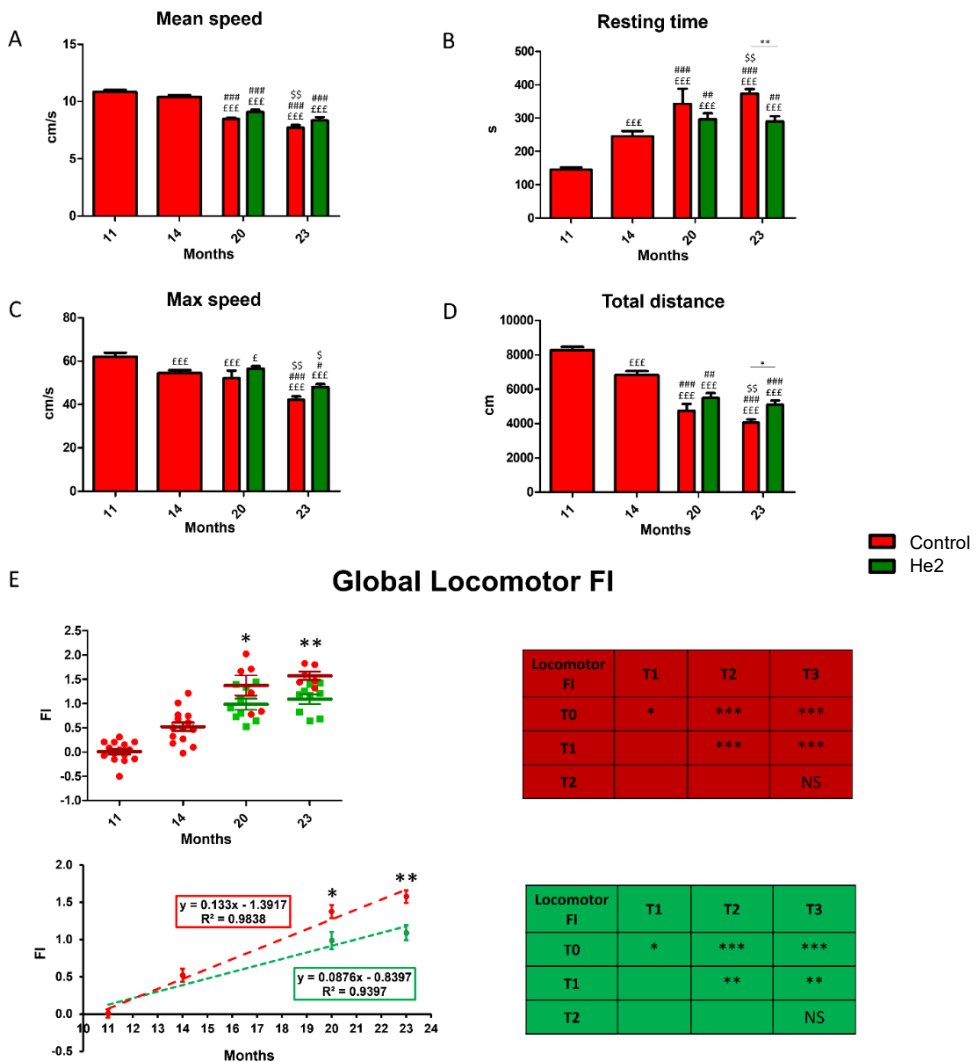
Figure 69: Locomotor performances decline during physiological aging is recovered through He2 oral supplementation. A: Mean speed (cm/s); B: resting time (s); C: max speed (cm/s); D: total distance (cm). E: Scatter plot of the global locomotor FIs (up left), the linear least-square regression of experimental points (down left), and table showing statistical results regarding aging effect in wild-type control (red, upright) and treated (green, down right) animals. For each panel, red bars or dots show data regarding control group, whereas green bars or dots show data belonging to He2 mice. For panel A, B, C, D, and tables of panel E: statistical results were performed by One-way ANOVA for repeated measures: £ vs 11 months (T0), # vs 14 months; $ vs 20 months. Statistical results regarding the comparison between C and P group (scatter plot and linear least-square regression of panel E) were performed by using Two-way ANOVA for repeated measures: *. For all described symbols: p < 0.05 (£, #, $, *); p < 0.01 (££, ##, $$, **);  p < 0.001 (£££, ###, $$$, ***).

## 6.4.1.2 Effects on  the "knowledge component" of Recognition memory

We also investigated the preventive effect of He2 in wild-type mice on the "knowledge component" of recognition memory decline during aging.

As previously reported (Figure 39), Figure 70 shows the decline of "knowledge"  during physiological aging. All the parameters recorded during the Emergence task and NOR test worsened during aging, with different timing.

Notably, the oral supplementation with He2 during aging significantly prevented the cognitive decline in wild-type mice regarding all recorded parameters both at T2 and T3. Indeed, the He2 group showed similar values for all recorded parameters in adulthood and senescence phases, and significantly differed from the control mice at both experimental times (Figure 70).

Analogously with precedent evaluations, we obtained the global knowledge cognitive FI. The knowledge cognitive FI significantly increased during aging in control animals (red dots) in a straight way, as demonstrated by linear least-square regression analysis ($R^2$=0.9912), whereas He2 treated mice (green dots) did not show an increase of knowledge cognitive FI during aging, demonstrating the preventive effect of the oral supplementation with He2 on "knowledge" component of recognition memory decline (Figure 70 F).
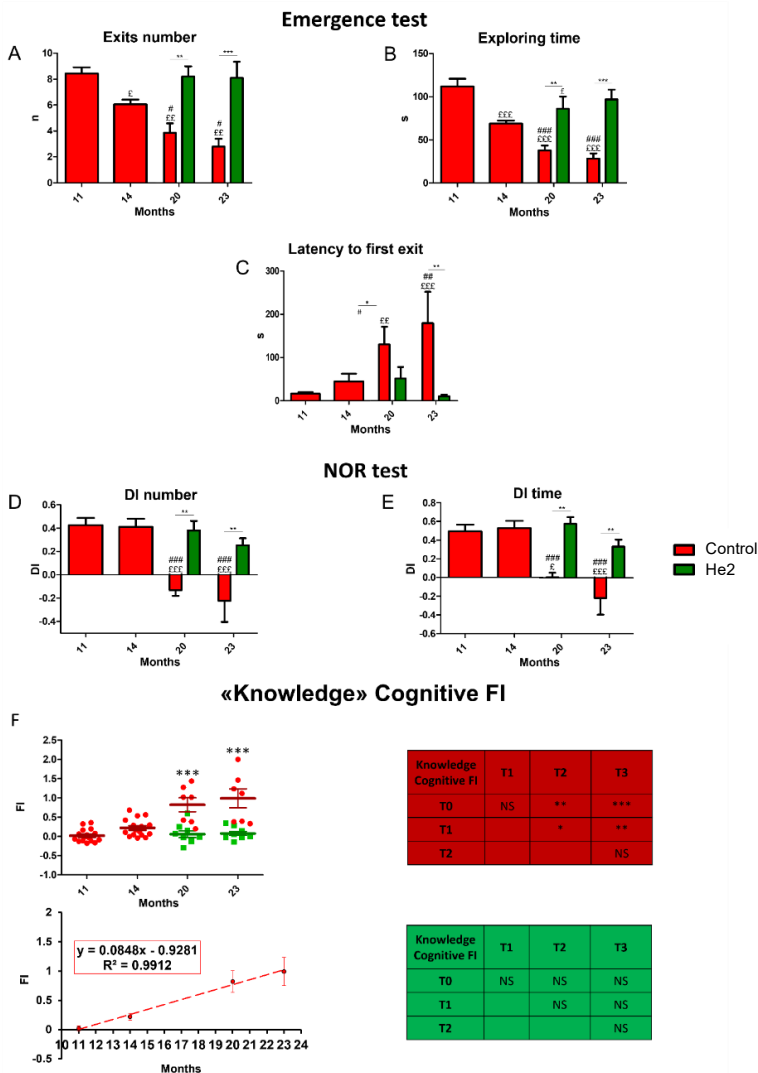
*Figure 70: Knowledge component of recognition memory decline during physiological aging in wild-type mice and its prevention with He2 oral supplementation. Panels A, B, and C refer to Emergence test: A: exit number; B: exploring time (s); C: first latency to exit (s). Panel D and E refer to NOR test: D: Number of approaches DI; E: time of approaches DI. F: Knowledge cognitive FIs (up left) and the linear least-square regression of experimental points of control mice (down left) and table showing statistical results regarding aging effect in wild-type control (up right) and He2 (down right) animals. For panels A, B, C, D, E, and tables in F: statistical results were performed by One-way ANOVA for repeated measures: £ vs. 11 months (T0), # vs. 14 months; $ vs. 20 months. Statistical results regarding the comparison between C and P groups (scatter plot and linear least-squares regression of panel F) were performed using Two-way Anova for repeated measures: *. For all described symbols: p < 0.05 (£, #, $, *); p < 0.01 (££, ##, $$, **);  p < 0.001 (£££, ###, $$$, ***).*

## 6.4.2 The effect on the "remember" component of Recognition memory

Next, we also investigated the preventive effect of 8-months He2 oral supplementation in wild-type mice on the "remember component" of recognition memory decline during physiological aging. Figure 71 shows the proceeding of "remember" cognitive parameters during aging in control and He2 groups.

As previously reported (Figure 40), the cognitive parameter evaluated during the Y maze task, such as the alternation triplets' percentage decreased appreciably at T2 (Figure 71 A) during physiological aging. Notably, the oral supplementation with He2 during aging significantly boosted this cognitive deterioration in wild-type mice: the He2 group showed higher alternation triplets' percentage in senescence compared to adulthood.

Also the cognitive parameters recorded during the OL test, such as the number and the time of approaches DIs, significantly worsened at T3 in control mice (Figure 71 B and C). Notably, the oral supplementation with He2 during aging significantly prevented this cognitive decline in wild-type mice, acting yet at T2. Indeed, the He2 group showed similar values for all recorded parameters in adulthood and senescence phases and significantly differed to control mice at both experimental times.

Notably, the remember cognitive FI significantly increased during aging in control animals in a straight way ($R^2 =0.9814$), whereas He2 mice showed that the remember cognitive FI after supplementation reached a value lower than in young animals, suggesting a boosting effect of this component despite the animal age (Figure 71 D).
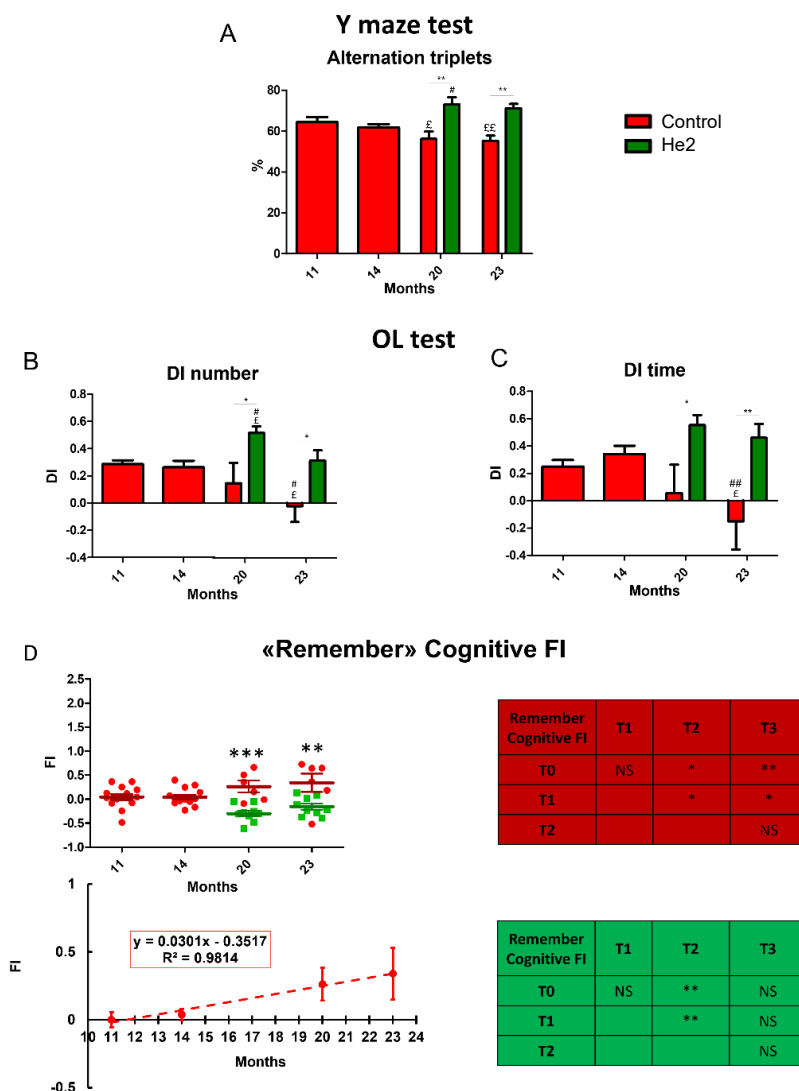
Figure 71: Remember component of recognition memory decrease during physiological aging in wild-type mice and its prevention with He2 supplementation. Panel A and B refer to OL test: A: Number of approaches DI exit number; B: time of approaches DI. Panel C refers to the Y maze task: Alternation triplets %. D: Remember cognitive FIs, with linear least-square regression of experimental points and table showing statistical results regarding aging effect in wild-type control animals. For panels A, B, C, and tables in E: statistical results were performed by One-way ANOVA for repeated measures: £ vs. 11 months (T0) and # vs. 14 months. Statistical results regarding the comparison between C and P groups (scatter plot and linear least-square regression of panel D) were performed using Two-way ANOVA for repeated measures: *. For all described symbols: p < 0.05 (£, #, $, *); p < 0.01 (££, ##, $$, **); p < 0.001 (£££, ###, $$$, ***).

## 6.4.2 The effect on oxidative stress in the cerebellum

As previously reported, oxidative stress is one of the most significant factors involved in neurodegeneration associated with aging. To evaluate specific markers of oxidative stress pathways, we investigated the expression of NOS2 and COX2. The immunohistochemical reactions highlighted the NOS2 and COX2 expression in all layers of the cerebellum, both in control and He2 mice.

Regarding NOS2 (Figure 72), the immunohistochemical reactions revealed an evident immunoreactivity in the large soma of Purkinje neurons, more marked in control mice (Figure 72 a-c and g) compared to He2 group (Figure 72 d-f and h). Further, several heavily NOS2-immunopositive mossy fibers were observed in the IGL, showing the same intensity pattern already reported for PCs (Figure 72, a-c and g vs. d-f and h). Likewise, the analysis of NOS2-immunoreactivity OD, evaluated both at PCs soma and mossy fibers level, demonstrated a significant decrease in He2 animals compared to control mice (PCs OD: 70.73 ± 3.91 vs. 157.86 ± 4.85 and mossy fibers OD: 89.79 ± 3.71 vs. 146.01 ± 4.03, respectively).

In particular, concerning COX2, an evident immunoreactivity was observed in the somas of Purkinje Cells (PCs). A clear immunoreactivity was also detected in IGL, localized in the large mossy fiber rosettes and in several Golgi cells (GCs). These observed immunoreactivities appeared significantly more intense in control mice (Figure 73, a-c and g) than He2 animals (Figure 73, d-f and h). In accordance, the subsequent quantitative analysis confirmed the significant decrease of COX2 immunoreactivity:

- PCs OD: 110.60 ± 2.51 in control mice vs. 77.66 ± 3.23 in He2 mice;
- mossy fibers rosettes OD: 34.94 ± 1.81 in control mice vs. 51.80 ± 2.35 in He2 mice
- GCs OD: 76.73 ± 4.91 in control mice vs. 117.37 ± 1.89 in He2 mice.
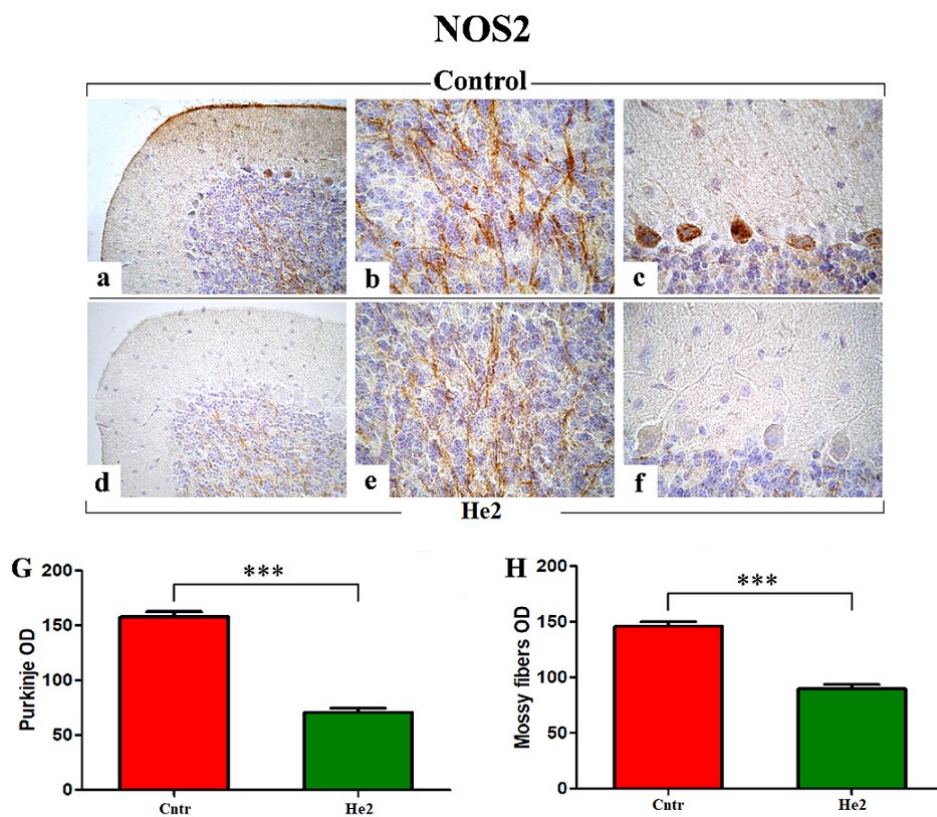
# NOS2



*Figure 72: Immunohistochemical labeling for NOS2 in control (a, b, and c) and He2 (d, e, and f) mice. Histograms showing the quantitative analysis of Optical Density (OD) in Purkinje cells (G) and mossy fibers (H). Statistical results were performed by the Unpaired Student's t-test: significant values were reported for p < 0.001 (***).*
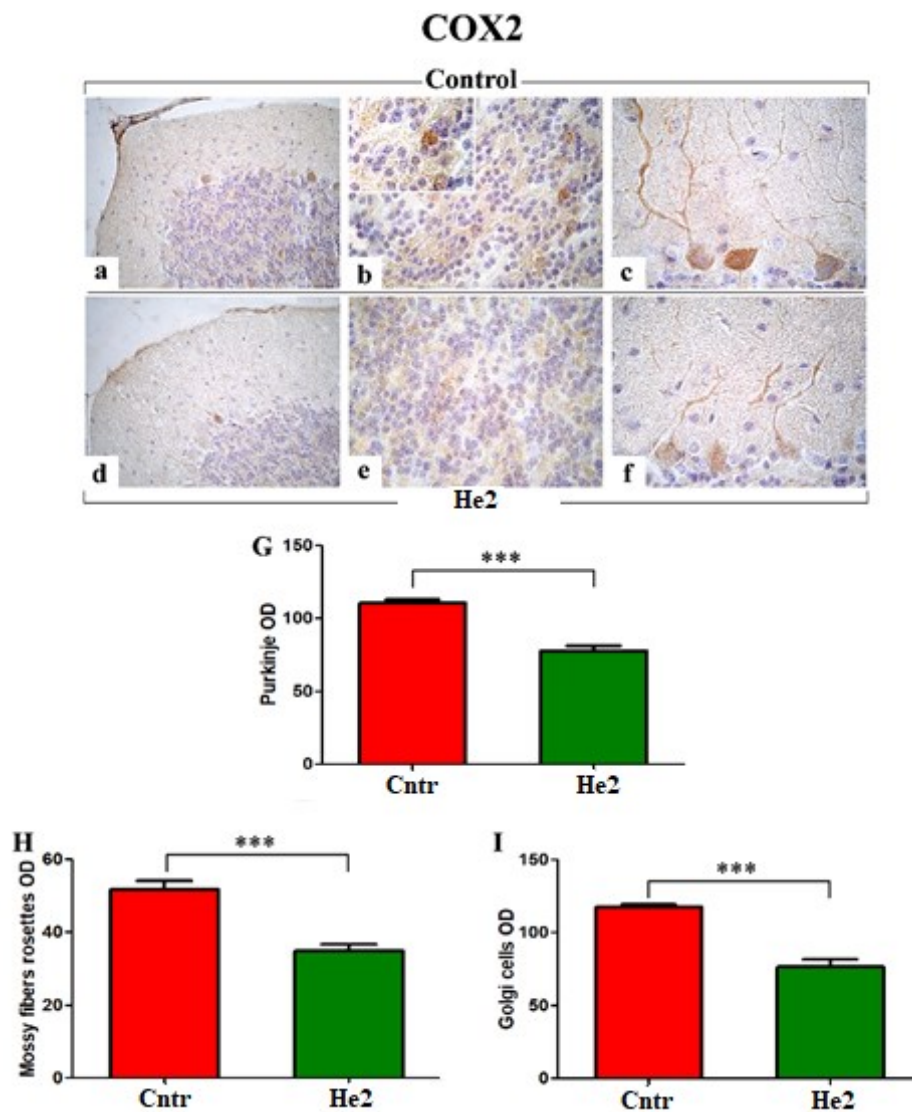
Figure 73: COX2 DAB-immunostaining in control (a, b, and c) and He2 (d, e, and f) mice. Panels G, H, and I show the histograms indicating the quantitative analysis of Optical Density (OD) in Purkinje cells (G), mossy fibers rosettes (H), and Golgi cells (I). Statistical results were performed by the Unpaired Student's t-test: significant values were reported for $p < 0.001$ (***).

## 6.4.3 The effect on the apoptosis in the cerebellum

p53 is a marker for programmed cell death induction for its capability to induce the arrest of cell growth and enhanced apoptosis.

The immunoreaction for p53 showed its expression in Purkinje cells and IGL, where immunoreactive mossy fibers were observed. Nonetheless, notably, the p53 immunopositivity pattern was opposite compared to those evidenced for COX2 and NOS2, with the heaviest immunoreactivity observed in He2 mice (Figure 74 d-f) compared to the control group (Figure 74 a-c). Accordingly, the following quantitative analysis demonstrated an increased p53-immunoreactivity OD, evaluated both at PCs as well as at mossy fibers levels, in He2 mice compared to control animals (PCs: 68.28 ± 2.97 vs. 59.89 ± 1.68 and mossy fibers: 78.50 ± 3.93 vs. 50.57 ± 2.46, respectively) (Figure 74, G and H).
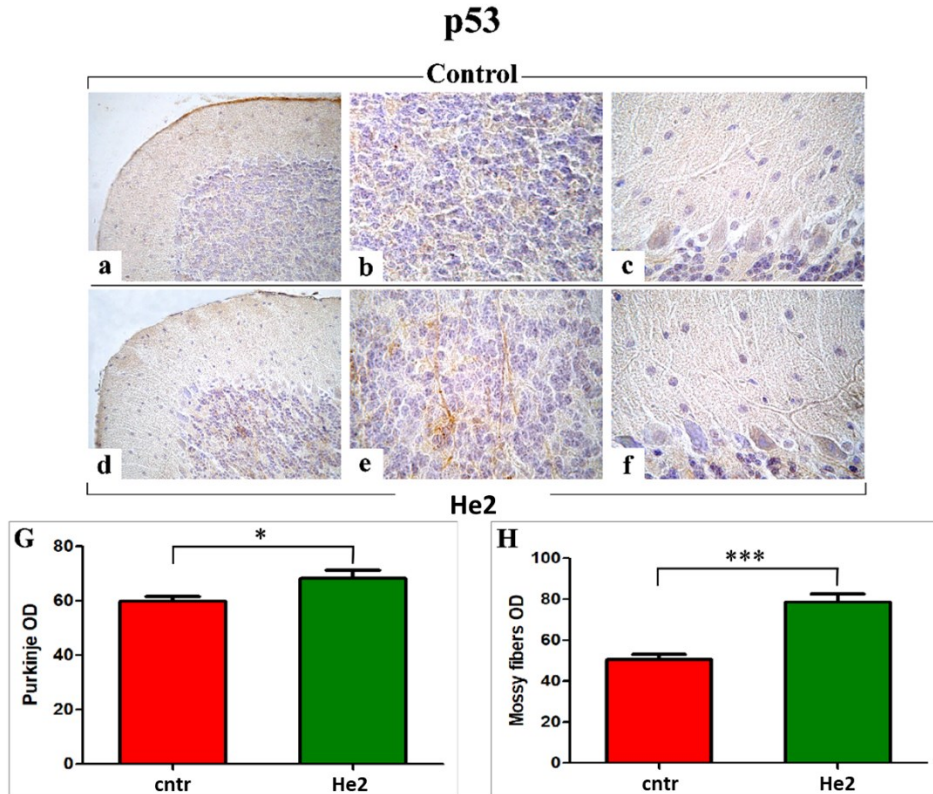


Figure 74: p53 DAB-immunostaining in control (a, b, and c) and He2 (d, e, and f) mice. The histograms showing the quantitative analysis of Optical Density (OD) in Purkinje cells (G) and mossy fibers (H). Statistical results were performed by the Unpaired Student's t-test: significant values were reported for p<0.05 (*) and p < 0.001 (***).

## 6.5 A clinical trial: The effect of H. erinaceus oral supplementation on mood and sleep disorders in overweight and obese patients

This clinical study investigated the effect of the dietary supplement based on *H. erinaceus*, the "*Micotherapy Hericium*" (provided by A.V.D. Reform s.r.l.) on mood and sleep disorders in overweight and obese patients underwent low-calorie diet. The study design foresaw three experimental times: the recruitment time (T0), two months of "*Micotherapy Hericium*" oral supplementation (T1), and after two months from "*Micotherapy Hericium*" suspension (T2).

So, at T0, 77 patients with sleep and/or mood disorders and with a body mass index (BMI) ≥ 25 Kg/m$^2$ were enrolled from IRCCS Foundation Policlinico Hospital (Milan, Italy). For four months (from T0 to T2), all the volunteers underwent a low-calorie diet of 1400 kcal for women and 1700 kcal for men, with the following macronutrient composition: CHO 52%, lipids 30%, and protein 18%. Thirty-seven patients received only the low-calorie diet, whereas forty participants received both the low-calorie diet for four months and two months of *H. erinaceus* oral supplementation (from T0 to T1). For more details, see the *Materials and Method section*.

BMI decreases in a no-significant way similarly in the two experimental groups control and *H. erinaceus* groups, suggesting that the BMI reduction depends only on the low-calorie diet (Figure 75).



| BMI [kg/m$^2$] | Control | H. erinaceus |
|---|---|---|
| T0 | 33.36 ± 0.83 | 33.12 ± 0.84 |
| T1 | 32.08 ± 0.88 | 32.01 ± 0.82 |
| T2 | 31.76 ± 1.41 | 31.63 ± 0.72 |
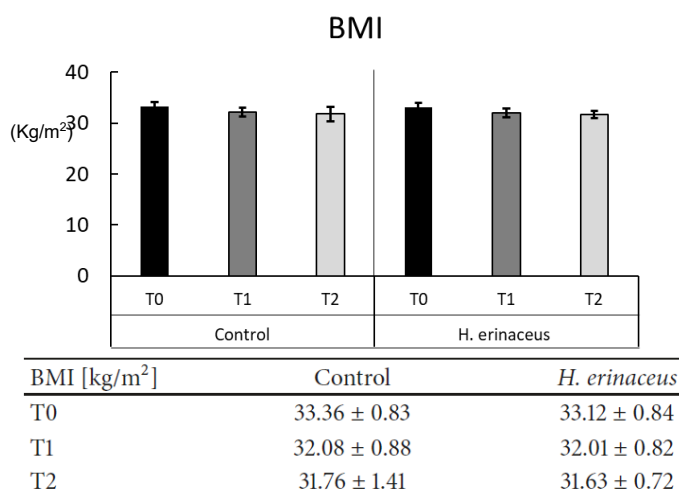
*Figure 75: BMI of control and H. erinaceus groups at T0, T1, and T2. Statistical differences, tested by two-way ANOVA, were not present.*

## 6.5.1 Effects on mood disorders in overweight and obese patients

### 6.5.1.1 Mood disorders evaluated by Zung's Depression and Anxiety Scales and Binge Eating Scale.

At the recruitment time (T0), all volunteers were tested for quantitative evaluation of the psychological symptoms according to Zung's depression scale, Zung's anxiety scale, and the BES. Each subject was positive for at least one of the mood disorders (anxiety, depression, or binge-eating; Table 9). Only 0-5% of patients showed high depression and anxiety levels, whereas a high binge eating score was recorded in 21.6% of patients. Moderate depression, anxiety, and BES were present in 32–39.3% of subjects. The remaining patients were distributed in the low or very low depression, low anxiety, and low BES score (Table 13).

|  | % Very low | % Low | % Moderate | % High |
|---|---|---|---|---|
| **ZDS** | 12.5 | 50.5 | 32 | 5 |
| **ZAS** | - | 60.7 | 39.3 | 0 |
| **BES** | - | 44.6 | 33.8 | 21.6 |

*Table 13: Quantitative evaluation at T0 (recruitment time) of psychological symptoms. Patients' percentage in different scale score of Zung Depression Scale (ZDS), Zung Anxiety Scale (ZAS), and Binge Eating Scale (BES).*

The mean score values for the Zung depression scale, Zung anxiety scale, and BES at different experimental time points in control (Figure 76 A) and *H. erinaceus* (Figure 76 B) groups demonstrated (i) no differences between control and *H. erinaceus* groups for depression, (ii) a significant improvement in anxiety disorder of about 12.6%, and (iii) a significant decrease in the BES score both in the control patients and after *H. erinaceus* supplementation (percentage of decrease: 31.5% vs. 32.7% at T1 and 55.5% vs. 38.2% at T2 in control and *H. erinaceus* groups, respectively). The decrease of BES score is similar in control and *H. erinaceus* groups, suggesting that *H. erinaceus* oral supplementation had no additional effect than a low-calorie diet on eating disorders.

Next, we selected only patients positive for mood disorders at the recruitment time (n=14 for depression and n=15 for anxiety in the control group, n= 16 for depression and n=15 for anxiety in the *H. erinaceus* group). Firstly, we investigated in the control group the effect of low-calorie diet alone, and any statistically significant difference in mean value score for mood disorders was recorded (Figure 76 C). Next, we studied the effects of *H. erinaceus* oral supplementation only in patients positive at T0, and regarding depression, 40% of patients belonging to the *H.*

*erinaceus* group fell in moderate symptoms and 7.5% in a high degree in Zung depression scale (mean score value 48.8 ± 1.03). After two months of *H. erinaceus* oral supplementation (at T1), the mean score value decreased to 43.5 ± 1.54, indicating a low degree of depression symptomatology. The value remained similar after two months of *H. erinaceus* wash-out (T2, mean score value 43.2 ± 2.38) (Figure 76 D). Regarding anxiety at T0, among selected patients for anxiety symptomatology, 42.5% fell in moderate and 2.5% in high degree in Zung anxiety scale (mean score value 47.7 ± 1.66). After two months of *H. erinaceus* treatment (T1), the mean score decreased to 39 ± 1.68, indicating a low degree of anxiety symptomatology. The value remained constant after two months of *H. erinaceus* wash-out (T2, mean score value 38.3 ± 1.68) (Figure 76 D).
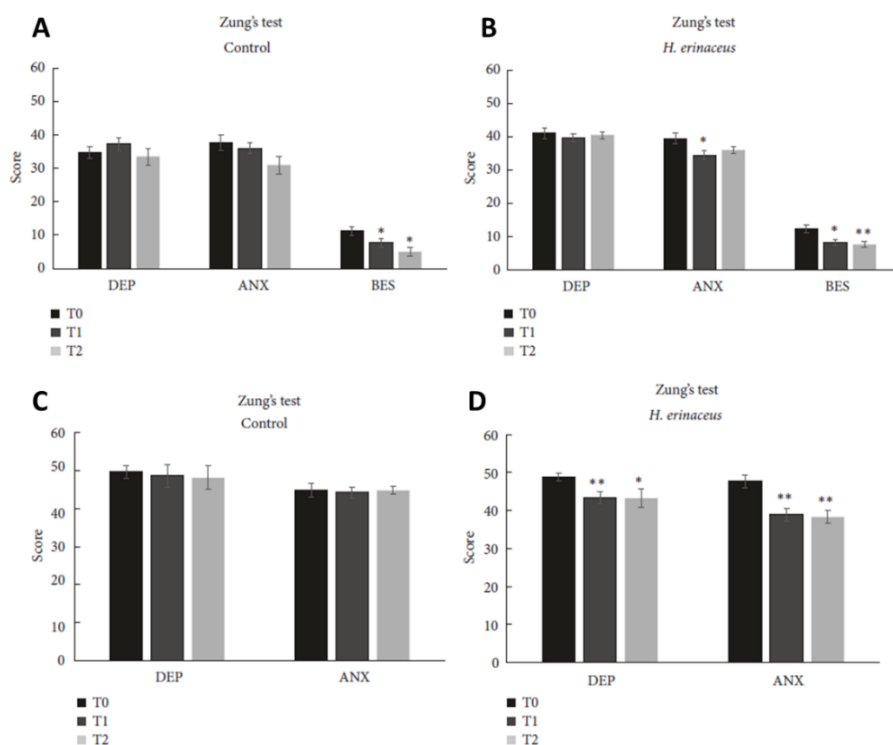


*Figure 76: Mean scores ± SEM of Zung depression (DEP), Zung anxiety (ANX), and binge eating scale (BES) tested by self-evaluation in control (A) and H. erinaceus (B) at T0, T1, and T2. C: Patients of control group selected for symptomatology D: Patients selected for symptomatology before (T0), after (T1), and in H. erinaceus wash-out condition (T2). p<0.05 (*) and p<0.01 (**) were obtained by the comparison versus T0 of the corresponding experimental group (according to two-way ANOVA). From Vigna et al., 2019.*

## 6.5.1.2 Mood disorders evaluated by SCL-90 test

For *H. erinaceus* treated patients, we investigated the effect of the supplementation on depression, anxiety, and sleep disorders also using the SCL-90 (Figure 77). Both depression, anxiety, and sleep disorders tested with SCL-90 significantly decreased after 2-months of *H. erinaceus* oral supplementation (Figure 77 A). Depression symptoms significantly decreased by 34.9% and 36% at T1 and T2, respectively. Anxiety symptoms significantly decreased by 49.6% at T1, and it was maintained by 41.9% at T2. Sleep disorders reduced by 34.4% at T1 and decreased by 39.1% at T2. Notably, there was no wash-out effect after 2-months of the *H. erinaceus* supplementation suspension because the improvements in the different mood and sleep disorders were retained.

Furthermore, as performed for Zung tests, we studied the effect of *H. erinaceus* supplementation only in patients positive at T0 for depression (n=19), anxiety (n=18), and sleep disorders (n=27, Figure 77 B) in the SCL-90 test. We obtained an even clear picture of the *H. erinaceus* effect on mood disorders by selecting patients for symptomatology. After two months of *H. erinaceus* oral supplementation, depressed patients on the mean fell close to 1 score value, that is, the limit value to recognize depression symptomatology. The effect was still evident after two months of *H. erinaceus* wash-out (T2). For anxiety disorder, the *H. erinaceus* treatment effect was more evident, and patients fell under the limit value for anxiety disorder. Furthermore, after *H. erinaceus* oral supplementation, patients with sleep disorders moved from a very high-value score (>2) to close to 1 score value, and the effect persisted at T2. The score of sleep disorder was significantly reduced by 44.25% at T1 and 38.13% at T2.
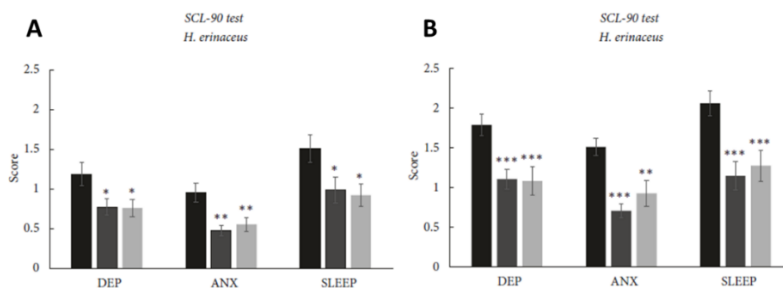


*Figure 77: A: Mean scores ± SEM obtained in SCL-90 test in H. erinaceus group at T0, T1, and T2 regarding depression (DEP), anxiety (ANX), and sleep disorders (SLEEP) symptoms. B: Patients selected for symptomatology. The p<0.05 (*) and p<0.01 (**) were obtained by the comparison versus T0 (according to one-way ANOVA, Tukey post hoc test). From Vigna et al., 2019.*

## 6.5.1.3 Mood disorders evaluated by Combined Analysis

We also investigated the effects of two-months *H. erinaceus* oral supplementation during low-calorie diet in overweight and obese patients with mood disorders by the combined analysis of Zung's and SCL-90 tests for depression (n = 22) and anxiety (n = 20) (Figure 78). Data obtained by Zung's and SCL-90 tests were normalized to the value of T0 (obtained before *H. erinaceus* oral supplementation). Two months of *H. erinaceus* treatment significantly reduced depression by 27.2% at T1 and by 29.4% at T2 and reduced in a significant way anxiety by 38.8% at T1 and by 33.2% at T2. Notably, all subjects moved from the "moderate state" to the "low state" for anxiety and depression after two months of *H. erinaceus* oral supplementation, and the effect remained after two months of wash-out.
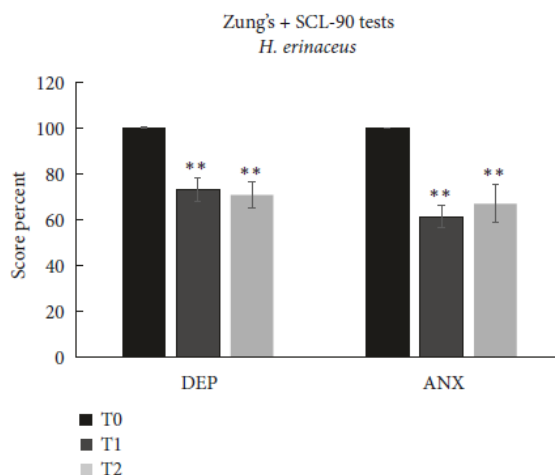


*Figure 78: Patients selected for symptomatology positive at T0. Depression (DEP) and anxiety (ANX) at T0, T1, and T2. p<0.01 (\*\*) indicates the comparison between T1 and T2 versus T0 (according to one-way ANOVA, Tukey post hoc test). From Vigna et al., 2019.*

## 6.5.2 Pro-BDNF and BDNF Serum Level

Given BDNF implication both in obesity and mood disorders, we investigated the hypothesis that *H. erinaceus* increases the circulating BDNF levels, thus, allowing its use as a potential clinical biomarker.

We selected patients with both anxiety, depression, and sleep disorders at T0 (n = 10) and measured serum pro-BDNF and BDNF levels at T0, T1, and T2. After two months of *H. erinaceus* supplementation, at T1, the serum pro-BDNF level significantly increased, whereas any change in serum BDNF level was detected. Interesting, at T2, there was a significant decrease in serum BDNF level without change in pro-BDNF levels (Figure 79 A). The increase in the pro-BDNF/BDNF ratio after two months of *H. erinaceus* oral supplementation (T1) reflected the increase in pro-BDNF at T1, whereas the increase after washout (T2) reflected the decrease in BDNF at T2 (Figure 79 B).
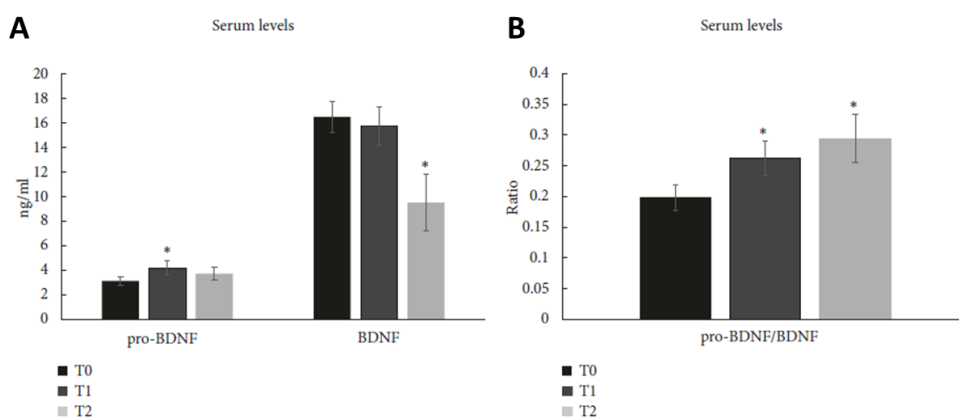


*Figure 79: A: pro-BDNF and BDNF serum levels reported as mean ± SEM in H. erinaceus group at T0, T1, and T2. B: serum pro-BDNF/BDNF ratio. p<0.05 (*) indicates significant differences between different times versus T0 tested by paired Student's t-test. From Vigna et al., 2019.*

# 7. Discussion

The aims of this Ph.D. project were to (i) develop a non-invasive methodology for monitoring the locomotor and cognitive decline in wild-type mice during physiological aging, (ii) quantify the content of nootropic and bioactive molecules in different samples of *H. erinaceus* to obtain standardized extracts, (iii) investigate the effects in frailty reversion of two-months oral supplementation with *H. erinaceus* standardized extracts in mice during aging, (iv) study the capabilities of *H. erinaceus* standardized extracts in prevention of aging and frailty onset in mice, (v) identify the molecular mechanism by which *H. erinaceus* exerts its effects, and (vi) finally, investigate the effects of two-months oral supplementation with an *H. erinaceus* supplement in overweight and obese humans with mood and sleep disorders.

To date, only few papers have been published about the effect of *H. erinaceus* supplementation in rodents and humans in the absence of diseases, so this thesis could be innovative and of great interest.

Furthermore, it should be noted that in this work, we used a translational approach with the purpose to transfer all the results obtained in preclinical model to humans: "from bench to bedside". For this reason, we monitored in mice locomotor parameters (mean and maximum speed, resting time, and the total distance covered in open arena test) that compared well to phenotypic frailty parameters evaluated in humans (gait speed and the level of physical activity) (Fried et al., 2001), and we investigated cognitive parameters similar to those studied in humans cognitive evaluations. Indeed, to measure cognitive impairment during aging in humans, often researchers use mainly the Stenberg Item Recognition Paradigm (SIRP) (Nosofsky et al., 2011). During this task, several items, called the "positive set", are shown and should be memorized during this test. The positive set can be composed of numbers, words, or images. After a delay, a single item is presented, and the subject should decide if the object was present among the "positive set". To achieve a translational approach during physiological aging, we selected in mice spontaneous behavioral tests resembling those described for humans, the emergence and the NOR tasks, that allows to assess anti-neophobia behavior and study the novelty recognition memory for a new environment and for new objects, respectively. Moreover, to measure cognitive impairment during aging in humans, clinicians and researchers also use the Four mountains test and Image-location memory tasks. Four mountains test is usually used to

evaluate the hippocampal memory in patients with MCI, dementia, and early Alzheimer's Disease. In this test, patients see an image and, after a delay time, must choose an image from 4 alternatives: one (the positive response) shows the same place from a different viewpoint, whereas (the wrong response) the remaining three images are landscapes whose topography differs from the correct one (Chan et al., 2016). In the Image-location memory test, patients must memorize the position of a variable number of images and then have to remember the image positions both from the same point of view and with different angulations (Shrager et al., 2007). To achieve a translational approach during physiological aging, we selected in mice spontaneous behavioral tests resembling those described for humans, Y maze and OL tests.

Additionally, we supplemented mice with a dose (1 mg/die) that mimics the dose used in humans supplementation (1 g/die), both in the study of the reversion and the prevention of frailty.

Aging is a physiological process characterized by various symptoms, such as phenotypic frailty and cognitive decline, that in a chronic condition can become disabling (Mitinsky et al., 2001; Xue, 2011). Thanks to the discovery of new molecular mechanisms underlying senescence, the study of aging has found great success in the scientific community.

Firstly, we tuned a non-invasive methodology for obtaining frailty index (FI) for both locomotor and cognitive performances to monitor mice functions during physiological aging. Concordantly with literature data (Singhal et al., 2020), we demonstrated a decrease in locomotor and cognitive activities during aging.

Remarkably, we investigated in particular both the knowledge and remember component of recognition memory, showing that from 11 to 23 months in mice, the remember component displayed a minimal decline compared with the knowledge component. These results could be explained fundamentally in three ways: (i) most probably this kind of memory is not seriously affected by aging, or (ii) the tests used for investigating it are not efficacious, or (iii) it has already deteriorated before 11 months. This evidence confirmed the dual-process model hypothesis of recognition memory, where "knowledge" and "remember" components are differently affected by aging and are placed in two different brain areas, i.e., hippocampus and parahippocampal cortex.

Notably, we found that both locomotor and cognitive performances worsened linearly during aging in mice, but the locomotor decline is steeper than the cognitive one, suggesting that when mice start to develop phenotypic frailty, they became at risk of developing cognitive decline as

well. So, our results demonstrated that locomotor frailty anticipates the cognitive decline in recognition memory, suggesting that cognitive decline could be intercepted by monitoring locomotor performances.

Next, we investigated the effect of physiological aging on gut microbiota composition. It is known that the gut microbiome is highly sensitive to environmental stimuli, and its composition changes during the lifespan of the host: it can adapt composition and functionality in relation to the different host conditions. For this reason, longitudinal studies, like this work, are necessary to understand the microbiota changes occurring over time (Santoro et al., 2017). To isolate the only effect of aging as much as possible, we maintained mice for all experimental time in the same conditions, i.e., water, food, temperature, and humidity never changed.

Firstly, we demonstrated that aging significantly affected the overall gut microbiome composition. In particular, we found different trends in the alpha-diversity changes during aging: Shannon index increased, whereas Faith index decreased. Since Faith diversity considers the phylogenetic distance while Shannon index did not, these results suggested that the ASV number increased during aging, whereas the ASV diversity did not. So, in adulthood, mice had bacteria that carried out different functions, whereas in the aged mice, despite displaying a higher number of different species, they belong to very similar taxa, suggesting that they are similar from a functional point of view.

Next, we estimated the interindividual variation through the beta-diversity, demonstrating the formation of five consequential clusters in each time. The effect of time between the different groups longitudinally increases, creating a huge gap between the adult and senescent mice microbiota, and, therefore, confirming that aging significantly affected the overall microbiota composition.

Regarding the taxonomy, the most abundant phyla were *Bacteroidetes* and *Firmicutes,* whose relative abundance did not change significantly throughout the life span. A critical evidence was the disappearance of the V*errucomicrobia* and the high decrease of *Deferribacterota* in the senescence. Confirming these results at the Phylum taxonomic level, the *Akkermansiaceae* (Phylum *Verrucomicrobia*; genus *Akkermansia*) disappeared in the senescence. On the contrary, at the same time, the *Muribaculaceae* and *Rikenellaceae* families appeared. The most represented genera were *Parabacteroides* and *Lachnospiraceae_NK4A136_group,* whose relative abundances did not significantly change during aging. The genera with the most significant variations, besides the genus *Akkermansia*, were *Clostridia_vandinBB60* and *Alistipes,* which significantly increased during aging.

Some of these modifications need to be understood more in depth. Notably, we found that *Akkermansia* disappeared during aging in mice

between 20 and 21.5 months. *Akkermansia* is a genus with a critical role in metabolic and gastrointestinal diseases. *Akkermansia* stimulates the communication between gut microbiota bacteria and maintains the integrity of the gut barrier, regulating the host immune response and reducing local inflammation. Furthermore, *Akkermansia* influences the fats and sugars metabolism (Macchione et al., 2019). Notably, all these factors are also involved in the pathogenesis of neurodegenerative diseases. Indeed, a change in *Akkermansia* relative abundance is associated with metabolic diseases (i.e. diabetes, inflammatory bowel disease, and obesity) (Derrien et al., 2017; Naito et al., 2018; Macchione et al., 2019) and also with neurodegenerative diseases (i.e., Alzheimer and Parkinson diseases) (Gerhardt and Mohajeri, 2018; Heintz-Buschart et al., 2018; Nishiwaki et al., 2020). Recently, Ou et al. (2020) and Higarza et al. (2021) demonstrated that *Akkermansia* improves cognitive performances in two different preclinical models. In particular, Ou et al. (2020) found that the *Akkermansia* gavage, in addition to regulating the inflammation and sugars metabolism, significantly reduces the Aβ 40–42 levels in the cerebral cortex and improves the spatial and recognition memory of APP/PS1 mice, a model of AD (Ou et al., 2020). Higarza et al. (2021) demonstrated that *Akkermansia* gavage restored cognitive impairment related to nonalcoholic steatohepatitis in rats (Higarza et al., 2021).

In our experiment, simultaneously with the disappearance of *Akkermansia*, *Muribaculaceae* (previously known as S24-7) appeared. *Muribaculaceae* family is one of the major utilisers of mucus-derived monosaccharides in the gut, contributing to SCFAs production (Sibai et al., 2020), in particular, propionate (Smith et al., 2019; Pereira et al., 2020). The SCFAs have a pivotal role in the host's homeostasis and physiology, and SCFAs concentrations are predictive of the host's lifespan (Smith et al., 2019). Indeed, *Muribaculaceae* bacterial family is found as a dominant bacteria taxa in the gut of *Spalax leucodon,* an exceptional animal model for its longevity, and its presence could explain the healthy and long life span of this model (Pereira et al., 2020). Previous works demonstrated a lower abundance of the *Muribaculaceae* family in aged mice compared to young animals, and anti-aging interventions partially reversed the gut microbiota composition of elderly mice, also increasing the relative abundance of the *Muribaculacea* (Han et al., 2020; Shenghua et al., 2020). On the contrary, during physiological aging, we found an increase in *Muribaculacea* relative abundance paralleled by the disappearing of *Akkermansia*. In this regard, we hypothize a possible compensatory/adaptive and homeostatic mechanism at the base of this result.

Furthermore, we demonstrated that *Lachnospiraceae NK4A136,* a SCFAs producer group, relative abundance remained stable during aging.

Recently, Kim et al. (2021) showed an increase of *Lachnospiraceae NK4A136* during aging comparing mice of 2.5 and 20 months (Kim et al., 2021). In this study, we found a similar *Lachnospiraceae NK4A136* relative abundance of aged 20-months-old mice, but we investigated the gut microbiome composition in a different time window, from 11 months onwards. Confirming this hypothesis, Laubitz et al., 2021 demonstrated that 40 weeks-old mice displayed a higher relative abundance of *Lachnospiraceae NK4A136* than seven-week-old mice.

Furthermore, we found a significant increase in *Clostridia vadinBB60* between 11 and 17 months. This genus is slightly discussed in the literature. However, recently, Juckel and colleagues (2021), in patients with schizophrenia, suggested that an increase in the *Clostridia vadinBB60* group could be responsible for the neuroplasticity reduction in the central nervous system (CNS). So, we speculate that the *Clostridia vadinBB60* relative abundance increase could determine and contribute to a reduction of CNS neuroplasticity also in aged mice.

Next, we demonstrated a significant increase in *Rikenellaceae* family during the aging process. Notably, in our samples, *Alistipes* genus represented all *Rikenellaceae* family. There are contrasting data in the literature regarding this genus (Parker et al., 2020); some works reported its potential in gastrointestinal and cardiovascular diseases prevention, whereas other evidence demonstrated its pro-inflammatory activity and its relationship with depression (Naseribafrouei et al., 2014) and its pathogenic role in cancer (Yang et al., 2017). To date, 13 species of *Alistipes* were isolated (Parker et al., 2020), and probably some of these exert beneficial properties, whereas other species have pro-inflammatory behavior and lead to disease onset. We speculated that there was an increase in *Alistipes* species with a pro-inflammatory profile in our samples.

Whether the gut microbiota modifications are cause or effect of aging remains a challenge to explore. However, it is certain that gut dysbiosis can activate different signaling pathways in enteric cells, leading to the overproduction of pro-inflammatory substances, which cause a leaky gut and spreading of inflammation form local, to systemic, to the brain causing neuroinflammation. Additionally, intestinal dysbiosis interferes with the physiological production of SCFAs, neurotransmitters, and intestinal hormones, all of which are critical for the brain function.

The standardization of dietary supplements and medicinal mushrooms and herbs is a very pressing and actual problem (Wasser, 2014; Dwyer and Coates, 2018).

During this Ph.D. project, we performed chemical analyses for quantifying the presence of specific bioactive molecules in two *H. erinaceus* samples

available in the Italian Culture Collection of Pavia University (MicUNIPV): ethanol sporophore and mycelium extracts of *H. erinaceus* strain (He1) and ethanol primordium extract of *H. erinaceus* strain 2 (He2). The nootropic and bioactive molecules present in *H. erinaceus* are known to cross the blood-brain barrier (BBB) and exert a neuroactive effect on the CNS (Lai et al., 2013). Using HPLC-UV-ESI/MS technique and comparing with standards, we quantified the amount of selected nootropic and bioactive metabolites in He1 and He2 extracts. First, we found an amount of 150 µg/g of Erinacine A in He1 lyophilized mycelium. This content is similar to that found by Krzyczkowski et al. (2010), using the most favorable combination of nutrients. Regarding Hericenone C and D, we quantified in the He1 sporophore an amount of respectively 500 µg/g and about 20 µg/g, like that found by Lee et al. (2016), in different strains of *H. erinaceus*. Furthermore, we quantified the amount of L+-ergothioneine (EGT), and we found that the EGT content in He1 lyophilized mycelium was 580 µg/g and in He1 lyophilized sporophore was 340 µg/g. Regarding He2 lyophilized primordium, we found an EGT content of 1.30 mg/g and no nootropic molecules. The EGT concentration in He1 mycelium was higher compared to literature data (149 µg/g and 400 µg/g) (Cohen et al., 2014; Chen et al., 2012, respectively), whereas the EGT concentration in He1 sporophore was lower compared to literature data (629.96 µg/g, 960 µg/g, and 1120 µg/g) (Cohen et al., 2014; Lee et al., 2009; Kalaras et al., 2017, respectively). The EGT content of He2 primordium was notably higher than that found in the He1 mycelium and sporophore extracts (for primordium, to my knowledge, no literature data are available). The relevant EGT amount measured in our samples confirmed recent data, demonstrating that fungi are undoubtedly the leading natural dietary source of EGT (Beelman et al., 2021).

Notably, we observed a content of nootropic and bioactive metabolites similar or higher than literature data suggesting the correctness of our cultivation parameters (such as temperature, ventilation, and nutrients).

These bioactive metabolites are known for their beneficial effects on animals' and humans' health. EGT is a molecule with outstanding antioxidant and cytoprotective properties in several animal and human tissues, including CNS (Cheah and Halliwell, 2012; Halliwell et al., 2018). Several works demonstrated the neuroprotective properties of EGT in different models of dementia and Alzheimer's diseases (Song et al., 2010; Halliwell et al., 2018; Cheah et al., 2019; Kameda et al., 2020). Furthermore, in a recent paper, Kameda et al., 2020 identified as marker of frailty the blood EGT reduction.

Erinacine A and Hericenones C and D are molecules with nootropic effects, known for their capability to cross the BBB and for their effects on CNS: (i) stimulating the synthesis of growth factors, such as NGF (Kawagishi et al., 1993; Kawagishi et al., 1991; Ma et al., 2013); (ii) promoting hippocampal neurogenesis (Tzeng et al., 2018; Ryu et al., 2018); and (iii) ameliorating the Alzheimer's disease and dementia-like pathologies in humans and animal models (Zhang et al., 2016; Tzeng et al., 2018; Cordaro et al., 2021).

Previous studies conducted in our laboratory demonstrated a beneficial effect of a commercial supplement based on *H. erinaceus* on adult wild type mice. In particular, *H. erinaceus* oral supplementation significantly improved locomotor (Rossi et al., 2018) and cognitive performances in NOR and emergence behavioral tests, enhancing the novelty-seeking behavior and the knowledge component of recognition memory. In hippocampal brain slices, in the mossy fibers and CA3 neuron synapse an increase in the frequency of spontaneous and an increase in the amplitude of evoked excitatory synaptic currents were recorded (Brandalise et al., 2017). However, in adult wild-type mice, two months of *H. erinaceus* treatment did not improve cognitive performances in Y maze and OL tests, demonstrating that a supplement based on *H. erinaceus* mycelium and sporophore extract did not act on the remember component of recognition memory. Notably, these results confirmed once again the dual-component hypothesis of recognition memory, where "knowledge" and "remember" components are placed in and supported by two different brain areas (Rossi et al., 2018).

The results reported in my Ph.D. thesis confirmed the selective effect of the extracts obtaneid by He1 mycelium and sporophore (containing erinacine A, hericenones C and D, and EGT) on locomotor activity, on the novelty-seeking behavior, and on the knowledge component of recognition memory, not only in adulthood but also during aging. Accordingly, there was no effect on the remember component of recognition memory both in adulthood and during aging (data not shown). In particular, we accessed these results by He1 oral supplementation (with a dose mimicking the amount used in human supplementation) in frail wild-type mice from 21.5 to 23.5 months. Hence, we demonstrated that two months of oral supplementation with He1 significantly reverted the locomotor and cognitive frailty during aging and increased the exploration of novel stimuli. In particular, whereas treated He1 mice at 21.5 months

were significantly frailer than control animals, the He1 supplementation brought mice back to comparable levels at 23.5 months.

Literature data demonstrated that the cerebellar cortex (in particular, lobules VI–VIII) is notably involved in the aging-induced locomotor and cognitive decline (Bernard et al., 2014).
Hence, we investigated the cerebellar cytoarchitecture of VI–VIII lobules in aged control and He1 treated mice (of 23.5 months), demonstrating a significant alteration in cerebellar cytoarchitecture in control aged mice where we described (i) shrinkage of about half of the Purkinje neurons, (ii) a significant decrease in the cerebellar volume, (iii) a reduction in the molecular layer (ML) thickness, and (iv) a critical fibrotic response. Notably, the He1 treated mice displayed less Purkinje neurons shrunken and fibrotic tissue and greater cerebellar volume and ML width than control mice.

Next, to better investigate the molecular mechanism by which *H. erinaceus* exerts its effects on locomotor and cognitive performances, we performed immunohistochemistry on CNS (in particular on cerebellum) to evaluate the expression of different markers involved in different pathways, like inflammation, oxidative stress, neuron metabolism, BBB functions, and neurogenesis.

Firstly, we investigated the inflammatory levels in the cerebellum since, during normal aging, neuroinflammation occurs in CNS (Sparkman and Johnson, 2008), and the chronic inflammation state (inflammaging) is one of the major causes of age-related decline and disease (Khansari et al., 2009).
As expected, we demonstrated in the cerebellum a significant expression of the pro-inflammatory IL-6 in aged mice. In parallel, we demonstrated an increase of GFAP immunopositive cells and fibers in aged animals, suggesting the astrocytes' reactive/activated state (Liddelow et al., 2017; Palmer et al., 2019). Probably the reactive gliosis is a consequence of the pro-inflammatory environment, and reactive gliosis exacerbates the inflammation, creating a vicious circle that sustains the neuroinflammaging, fibrosis, and gliosis. Notably, the He1 treatment significantly reduced both IL-6 expression, hence inflammation, and gliosis.
Next, we investigated the expression of HIF1α and VEGF. Aerobic organisms has to deal with the deficient oxygen availability or hypoxia in different physiological and pathological states, and in order to counteract

this deficiency they develop adaptive systems. In mammals, the first response to hypoxia is the increase in HIFs expression (Majmundar et al., 2010). Recent evidence suggested that HIF-1α overexpression is also involved in cancer onset and progression (Rashid et al., 2021). Furthemore, hypoxia also regulated the VEGF expression. VEGF, through very complex signaling, is fundamental in (i) vasculogenesis, the generation of new blood vessels *ex novo*, (ii) angiogenesis, the generation of new vessels from pre-existing vessels, and (iii) the homeostasis of vascular endothelium (Apte et al., 2019). It was recently demonstrated that VEGF signaling also acts as a nootropic factor (Deyama et al., 2019), improving neuronal survival during aging. HIF1 α and VEGF are two critical cellular metabolic sensors and play a crucial role in regulating cellular metabolism and inflammatory pathways (Yu et al., 2018).

We demonstrated in cerebellum a significant reduction of the expression of HIF1α in aged mice treated with He1 compared to aged control animals, suggesting that the He1 treatment improved brain tissue.  Moreover, we demonstrated a significant increase of VEGF expression in the cerebellum of the He1 group compared to control mice, indicating that the He1 supplementation had a nootropic activity, enhanced the angiogenesis during aging, and maintained the correct homeostasis in endothelial cells.

Next, we investigated the oxidative stress markers because free radicals excess is one of the leading causes of inflammaging (Forrester et al., 2018) and because a body of literature undeniably suggested that oxidative damage is crucially involved in aging-associated cognitive and locomotor impairment (Khansari et al., 2019). Indeed, free radicals accumulate in cells during aging and can trigger phenomena that lead to the onset of neurodegenerative diseases. Experimental investigations demonstrated that longer-lived animals display reduced oxidative damage and/or increased resistance to oxidative stress, acquired through dietary restriction or genetic manipulations (Liu and Xu, 2011; Vatner et al., 2020). In line with these results, our present findings proved the protective role of *H. erinaceus* supplementation in cognitive and locomotor aging-related decline, triggering a partial oxidative stress recovery in aged mice. In particular, for evaluating oxidative stress, we investigated the expression of several markers, such as SOD1, NOS2, and COX2.

Regarding the SOD1 expression, we demonstrated a significant reduction of positive cells in the molecular layer (ML) of the cerebellum in He1 treated mice compared to control mice. High levels of SOD1 expression could suggest cells attempting to buffer the oxidative stress, higher in control mice. Furthermore, the He1 supplementation decreased the

expression of NOS2 in mice cerebellum. A decrease in NOS2, the inducible form of NOS, could suggest that the He1 supplementation triggered an antioxidant response, reducing oxidative stress. Once again, the expression of COX2 was decreased in the He1 treated animals compared to controls, confirming the hypothesis of lower oxidative stress in He1 treated mice cerebellar cortex. Notably, Kushairi and colleagues (2019) demonstrated *in vitro* a significant neuroprotective and anti-inflammatory activity of *H. erinaceus* by increasing antioxidant enzyme activity and decreasing free radicals in neurons. This Ph.D. work confirmed these data and gave them even more value by demonstrating these effects *in vivo.*

Next, we investigated the expression of SIRT1, a NAD$^+$-dependent histone deacetylase protein that can delay cellular aging and extend lifespan by modulating several cellular pathways, including DNA repair, oxidative stress, and inflammation (Lee et al., 2019). Indeed, SIRT1 expression significantly decreases during aging, leading to neuronal degeneration and cognitive decline. Accordingly, there is a relationship between a high level of SIRT1 activation and the decrease in senescent cells (Chen et al., 2020), indicating that molecules that activate SIRT1 pathways display a senomorphic activity. In this Ph.D. thesis, we demonstrated that the He1 oral supplementation significantly increased the SIRT1 expression in the cerebellum of aged mice, suggesting a senomorphic activity of He1 extracts in mice brains. Accordingly, in 2020, Amara et al. published a paper showing the *in vitro* neuroprotective effect of *H. erinaceus* in induced neurotoxicity, also through SIRT1 expression modulation.

Next, we investigated the BBB functions in aged control and He1 treated animals. BBB is composed of basal lamina, astrocytic endfeet processes, pericytes, and endothelial cells that interact with each other to control the passage of different molecules from the blood circulation to the brain parenchyma. It is known that the BBB permeability increases during aging due to the impairment of tight junctions' structure and function (Costea et al., 2019; Propson et al., 2021). Indeed, the "leaky" BBB is a common feature in cognitive decline and neurodegenerative disease, allowing the pass of proinflammtory molecules from the blood circulation to the brain parenchyma.

Two useful markers which are essential for the formation and preservation of tight junctions and, consequently, for BBB integrity are ZO-1 and occludin (Gawdi and Emmady, 2021).

We found that He1 treatment significantly increased the ZO-1 and occludin expression in ependymal cells, choroid plexus, cortical, hippocampal, and hypothalamic blood vessels, suggesting that *H. erinaceus* oral supplementation is efficacious in preserving BBB structure and function during aging. These results well corroborate the decrease of neuroinflammation previously described.

In parallel, we also assessed the expression of Glut1 on the BBB of aged control and He1 treated mice. As known, glucose is the principal energy source of neurons and Glut1 is the carbohydrate transport uniporter responsible for the passage of glucose across the BBB (Gawdi and Emmady, 2021). In our samples, we found an increase in Glut1 expression in the choroid plexus and cortical and hippocampal blood vessels in He1 animals, suggesting once again that *H. erinaceus* preserves BBB function and improves neuronal metabolism.

Furthermore, a recent review highlighted the importance of Glut-1 and SIRT1 in preventing hyperglycemia, acting on the insulin signaling, linking diabetes mellitus to the Alzheimer's disease (Shieh et al., 2020).

We also demonstrated increased hippocampal and cerebellar cell proliferation and neurogenesis by using PCNA and DCX immunodetection, respectively. Ryu et al., 2018, similarly demonstrated in adult C57BL/6 mice that chronic administration of *H. erinaceus* extracts for one month significantly increases the expression of PCNA and Ki67 in hippocampal progenitor cells, suggesting an increase in their proliferation and in adult hippocampal neurogenesis. Regarding the cerebellum, in my knowledge, no data are reported about neurogenesis, but our data evidenced the presence of very few proliferating neuroblasts. Notably, during aging, in neuronal stem cells, the ability to proliferate and to produce neuronal decrease, and this process contribute to aging-related cognitive decline. Remarkably, our results suggest that oral supplementation with He1 increased the cell proliferation and the neurogenesis in hippocampus and cerebellum in frail elderly mice. Hippocampal neurogenesis is involved in higher cognitive function and, new neuronal cells, generated by adult neurogenesis, could contribute to neural plasticity throughout the whole lifespan.

Furthermore, these results corroborated the capability of *H. erinaceus* to perform BDNF/NGF-like effects, stimulating neurogenesis.

Medicinal mushrooms are considered very important for maintaining gut microbial balance, so they are also considered a potential source of prebiotics (Panda et al., 2021). Indeed, we also investigated the

effect of the He1 oral supplementation of gut microbiota composition in frail aged mice. Firstly, we demonstrated that this treatment did not change the overall gut microbiota composition, as demonstrated by similar alpha- and beta-diversities in control and He1 groups. Consistent with our results, several studies in the literature reported that probiotic or prebiotic oral supplementation in the elderly did not modify overall microbiome composition (Badal et al., 2020). However, He1 oral supplementation significantly changed the relative abundance of few but important genera, with a significant increase in the relative abundance of *Clostridia UCG-014, Lachnospiraceae_NK4A136,* and *Eubacterium xylanophilum*, and a significant reduction of *Odoribacter, Clostridia vadinBB60*, and *Muribaculaceae*.

As previously discussed, *Muribaculaceae* are SCFAs bacteria producers with healthy-promoting activities. Contrary to the expected, we found a reduction in its relative abundance after two months of He1 treatment, but concomitantly with locomotor and cognitive performances improvement, suggesting that probably other microbiome variations compensated *Muribaculaceae* decrease.

Generally, the *Clostridium* genus exercises many beneficial effects on gut function, producing SCFAs, exerting an anti-inflammatory activity, communicating with the immune system, and strengthening the gut barrier (Guo et al., 2020). However, few *Clostridium* species (for example, *Clostridium difficile*) exert adverse effects on host health, leading, for example, to pseudomembranous colitis and diarrhea.

The *Clostridia UCG-014* is a species very little discussed. The few published articles discussed *Clostridia UCG-014* as a pro-inflammatory bacteria (Wang et al., 2021; Liu et al., 2021) and described its relationship with fasting blood glucose (Zhao et al., 2021). Contrary to expectations, we found an increase in *Clostridia UCG-014* relative abundance after He1 supplementation.

Furthermore, we found a significant reduction in *Clostridia vadinBB60* relative abundance after He1 supplementation. As previously reported, this genus is marginally examined in the literature, but the few evidence supported that its increase is associated with neuroplasticity decrease. So, the *Clostridia vadinBB60* decrease could influence positively CNS neuroplasticity.

Notably, we also found an increase in *Lachnospiraceae NK4A136* in He1 treated mice*.* This bacterial group has the potential to be a probiotic with a possible role in bile acids metabolism and cholesterol homeostasis (Huang et al., 2019; Wu et al., 2020). Indeed, *Lachnospiraceae NK4A136*

group is a butyrate producer, and its relative abundance has been shown to be reduced in patients with dementia (Stadlbauer et al., 2020).

*Eubacterium xylanophilum* also has a role in SCFAs production: it can produce formic, acetic, and butyric acids from xylans (Van Gylswyk and van der Toorn, 1985; Mukherjee et al., 2020), and, notably, we demonstrated *Eubacterium xylanophilum* relative abundance increased in He1 samples.

Finally, we found a reduction in *Odoribacter* genus. A recent study conducted by Zhou and colleagues (2021) demonstrated that *Odoribacter* relative abundance is changed in people with Alzheimer's Disease compared to control (Zhou et al., 2021). Furthermore, Ren et al. (2020) demonstrated in patients affected by Parkinson's disease that individuals with cognitive impairment displayed a higher relative abundance of *Odoribacter* and a lower *Ruminococcus* concentration compared to healthy controls and patients without cognitive dysfunctions. This evidence suggested that *Odoribacter* is negatively correlated with cognitive performances.

Altogether, these results pave the way to a prebiotic role of *H. erinaceus*, modulating in a complex way microbiota intestinal homostasis, suggesting a psychobiotics effect.

The capabilities of *H. erinaceus* in reducing senescence and modulating microbiota composition give strength to the theories that are based on microbiome modulation therapies with age-delaying and longevity-promoting purposes (Boyajian et al., 2021; Sharma, 2022).

Furthermore, the finding that He1 positively modulated gut microbiota composition well corroborated the improvement of BBB functions and the decreased inflammation. Indeed, growing evidence supports the role of gut microbiota-derived molecules in the pathogenesis of neurodegenerative diseases. Microbiota's gut metabolites could reach brain tissue through the gut-brain axis and cross a "leaky" BBB, typically observed in elderly people. This event could consequently trigger the release of toxins and pathogen components that ultimately could affect CNS homeostasis (Costea et al., 2019).

Next, in another set of experiments, we investigated the preventive effect of *H. erinaceus* in frailty onset. In particular, we assessed this potential by treating mice with the He2 primordium extract for eight months, from adulthood (15 months) to senescence (23 months). Notably, primordium consists of the transition stage between mushroom mycelium and sporophore, and it is formed by dense mycelial cords that develop with negative geotropism.

Remarkably, the He2 primordium extract did not contain erinacine A and hericenones C and D but only a high EGT content, probably allowing us to study the isolate contribution of this metabolite in our model. In wild-type mice, eight months of He2 oral supplementation significantly improved novelty-seeking behavior, locomotor, and cognitive performances in all tasks carried, surprisingly, also enhancing the remember component of recognition memory. Furthermore, remarkably, the supplementation for eight months with He2 displayed more beneficial effects than the supplementation for two months with He1 both on locomotor and cognitive performances. Notably, regarding the cognitive evaluations, we demonstrated that He2 supplementation determined similar behavior in adulthood and senescence phases, as confirmed by the cognitive FIs during aging, which did not increase during the time in He2 mice. More precisely, He2 supplementation determined similar performances in the emergence and NOR tests in adult and senescent mice, whereas aged He2 treated mice displayed better performances than adult mice in the Y maze and OL tasks. These results again support that the recognition memory is a dual process supported by two different brain structures and that *H. erinaceus* bioactive metabolites act in a selective way on the two components.

So, comparing with the effects previously described of He1, we found that He2 primordium extract had a more significant improvement on the locomotor activity and on the knowledge component of recognition memory and was also effective on the "remember" component. This differences were related to the presence of a high concentration of EGT and to the longer duration of treatment, but we cannot exclude the presence in the primordium of other no detected nootropic metabolites.

For investigating the molecular mechanisms of EGT-enriched He2 extract, we performed immunohistochemistry on cerebellum brain slices of aged control and He2 treated aged mice (of 23 months). In particular, since EGT is the elective antioxidant, we investigated the expression of COX2 and NOS2 in the cerebellar cortex. Similar to He1 treatment, we found that He2 supplementation significantly reduced the COX2 and NOS2 expression, suggesting that EGT-enriched He2 extract had significant antioxidant activity *in vivo*.

These results related to oxidative stress pathways were further corroborated by data on p53, known to play a crucial role in modulating oxidative stress and aging (Rufini et al., 2013).

In response to many stressors, including oxidative stress, p53 is activated as a transcription regulator, leading to a rapid accumulation of itself in stressed cells. Indeed, many studies suggested that oxidative stress may

elicit a specific p53 transcriptional response to control cellular senescence and aging (Liu et al., 2013; Chen et al., 2017). Moreover, p53 is able to influence a variety of molecular pathways through posttranslational modifications, including protein phosphorylation, methylation, and ubiquitination.

However, it has to be taken into consideration that oxidative stress conditions do not always induce cell aging since evidences indicate that when the oxidative unbalance is mild, p53 can induce the expression of antioxidant genes to prevent cell death. By contrast, enhanced p53 levels could accelerate the generation of free radicals and induce cell death under severe cellular stress.

Moreover, *in vivo* investigations demonstrated that (i) p53-overexpressing transgenic mice did not display any signs of accelerated aging, (ii) transgenic mice with increased p53 activity displayed normal life span, and (iii) mice with an additional copy of p53 showed an enhanced expression of antioxidant activity and decreased levels of endogenous oxidative stresses, correlating with increased life span (Liu et al., 2011; Rufini et al., 2013).

These controversial data support the notion that the precise role of p53 in cell aging is complex and strictly linked to the environmental situation. In this context, p53 activation in response to low oxidative stress could protect cells against oxidative damage, thus supporting the role of p53 in the maintenance of tissue homeostasis.

In line with these results, we demonstrate an increase of p53 expression in He2 mice, in which a decrease of COX2 and NOS2 had contextually been demonstrated, led us to hypothesize that the p53 enhancement could prevent the accumulation of oxidative stress molecules at high levels, inhibiting senescence progression, thus achieving delayed aging in these mice.

In perspective, it could be interesting to demonstrate if He2 described effects are specifically addressed to senescent cells, which over time would cause damage to brain tissue.

Altogether, these results (both performed with He1 and He2 samples) clearly demonstrated that the *H. erinaceus* standardized extracts are effective in locomotor and cognitive frailty prevention and reversion in the preclinical model. Regarding the molecular mechanism by which *H. erinaceus* exerts its effect, we found that *H. erinaceus* extracts (i) improve gut microbiome composition and BBB function, (ii) enhance cell proliferation and neurogenesis, (iii) activate antioxidant and anti-inflammatory pathways, and (iv) have neuroprotective and senomorphic

effects, restoring the appropriate cytoarchitecture and cellular function in aged brain cells. The mechanism of action of *H. erinaceus* exploits the ability to stimulate the synthesis and the release of neurotrophic factors, i.e., BDNF or NGF. Indeed, previous works reported that in the peripheral nervous system, *H. erinaceus* stimulates the expression of the NGF, promoting the regeneration of peripheral nerve injury at least in the early stage of recovery (Wong et al., 2011). This event could also occur in the CNS, where *in vivo* administration of *H. erinaceus* showed an increase in the NGF mRNA expression (Mori et al., 2008).

Furthermore, during aging, neuronal stem cells exhibit reduced proliferation and neuron production, which is thought to contribute to age-related cognitive decline (Apple et al., 2017). Remarkable, our results suggest that the oral supplementation with *H. erinaceus* increased the cell proliferation and the neurogenesis in CNS of frail elderly mice. Notably, hippocampal neurogenesis is involved in higher cognitive function and, new DG granule cells, generated by adult neurogenesis, could contribute to neural plasticity throughout the whole lifespan. Surprisingly, we also found an increased cell proliferation and active neurogenesis in the cerebellum in elderly frail mice.

Among other *H. erinaceus* effects, we demonstrated an increase in novelty-seeking behavior, essential in mammalian species for the interaction with the environment. Notably, a reduction in novelty-seeking behavior is a risk factor for anxiety and depression onset, as well as a symptom of these mood disorders (Stedenfeld et al., 2011; Duclot et al., 2011).

The neurotrophic hypothesis of depression originates in the late nineties and the beginning of the new century. Firstly preclinical research and, immediately afterward, clinical research showed that subjects undergoing stressful events lost brain neuron tropism and neuronal plasticity. In parallel, other clinical researches have shown that the volume of some brain areas (i.e., hippocampus, prefrontal cortex, and nucleus accumbens) of subjects with severe depression is significantly reduced compared to healthy subjects (van Tol et al., 2010; Otte et al., 2016).

Analogously, the discovery that the treatment with antidepressant drugs in depressed animal models and patients significantly reverts the neuronal hypotropism and the reduction of brain volume has suggested that these drugs can restore at least in part the neuronal tropism and the affective, emotional, and cognitive sphere (Zanos et al., 2018). The evidence that antidepressant drugs can activate, also in non-specif ways, different genes involved in neuronal tropism has brought new knowledge on the

etiopathogenesis of depression. In particular, these studies highlighted that trophic factors, i.e., NGF, BDNF, and glial cell-derived neurotrophic factor (GDNF), play a crucial role in mediating the therapeutic effects of antidepressant drugs (Lang et al., 2013; Björkholm and Monteggia, 2016; Sharma et al., 2016; Peng et al., 2020). These results have stimulated numerous researches to develop trophic molecules capable of overstepping the human BBB and having a tropic effect in the CNS. As previously reported, several bioactive metabolites of *H. erinaceus* display nootropic effects, stimulating the synthesis and release of NGF and BDNF in the CNS and enhancing adult neurogenesis.

Furthermore, for some authors, mood disorders are considered inflammatory conditions mediated by pro-inflammatory cytokines, including interleukin-6 (Dowlati et al., 2010; Lang et al., 2016). Probably, these pro-inflammatory cytokines could interact with several pathophysiological domains relevant to depression, such as neurotransmission, neuronal tropism, and synaptic plasticity.

Give this framework, finally, in this Ph.D. thesis, we investigated the effects of two months of *H. erinaceus* oral supplementation on sleep and mood disorders in obese and overweight patients who underwent a low-calorie diet. Indeed, several works also demonstrated a relationship between obesity and mood disorders (Soczynska et al., 2011; Jantaratnotai et al., 2017; Milaneschi et al., 2019).

Firstly, we investigated the mood disorders in all recruited patients (control and *H. erinaceus* treated subjects) using Zung's depression and anxiety tests. Notably, patients who underwent the low-calorie diet and supplemented with *H. erinaceus* for two months significantly reduced depression and anxiety symptoms, in addition to binge eating disorders. The low-calorie diet alone did not mitigate the mood disorders but significantly reduced binge eating disorders, suggesting that the dietary regimen is sufficient to improve emotional eating. Then, we studied the effect of *H. erinaceus* in selected patients with mood disorders using the SCL-90 test, confirming and exacerbating the effect of *H. erinaceus* oral supplementation in reducing mood and sleep disorders. Notably, the effect of *H. erinaceus* oral supplementation lasted in the absence of treatment for at least two months, suggesting that *H. erinaceus* could exert an effect on neuronal plasticity, as expected by an NGF- or BDNF-like effect (Bothwell, 2014; Leal et al., 2017; Mondal and Fatima, 2019).

These results confirmed the antidepressive and antianxiety effects of *H. erinaceus* described in the literature and demonstrated both in preclinical models (Chiu et al., 2018; Chong et al., 2021) and in clinical trials (Nagano

et al., 2010). In particular, Chong and colleagues (2021) demonstrated that the antidepressant effect of *H. erinaceus* occurs by enhancing neurogenesis and reducing neuroinflammation through the BDNF-TrkB-CREB signaling pathway. Given these data and the implication of BDNF in both obesity and mood disorders, we investigated the serum proBDNF/BDNF ratio in patients. In particular, in CNS, pro-BDNF and BDNF exert two opposite roles: the pro-BDNF displays pro-apoptotic function and decreases the synaptic efficacy (Teng et al., 2005; Yang et al., 2009), whereas mature BDNF exerts neurotrophic effects, influencing dendritic spines morphology and function and the adult neurogenesis (Colucci-D'Amato et al., 2020). Notably, unexpectedly, we found a significant increase in serum pro-BDNF/BDNF ratio both after two months of *H. erinaceus* supplementation (for the increase in pro-BNDF levels) and after two months of washout ( for the significant reduction of serum BDNF levels). Hence, further investigations are necessary to study the regulation of cleavage of pro-BDNF into mature BDNF and the mechanism by which pro-BDNF and BDNF cross the BBB because it is unknown how and whether mature BDNF increase in CNS is mirrored in serum BDNF levels. Furthermore, we cannot exclude that the serum pro-BDNF/BDNF ratio is not a valuable biomarker for evaluating mood disorders' improvement. However, the mood disorders' improvement was undoubtedly associated with a change in pro-BDNF/BDNF ratio, suggesting that additional examinations are necessary for understanding the role of pro-BDNF and BDNF.

The main limitations of this Ph.D. project regarding the preclinical study were (i) the sample size and (ii) it was conducted only on male mice. Furthermore, other critical points are currently under study, such as (i) individuation of possible biological markers of frailty, evaluating, for example, inflammatory profile and inflamma-miRs expression, (ii) the development of models for evaluating and predicting the relationship between gut microbiome modifications and frailty, (iii) other immunohistochemistry analysis to investigate other mechanisms by which the *H. erinaceus* standardized extracts exert their beneficial effects (iv) ultrastructural studies with the transmission electron microscope (TEM), and (v) more specific quantification with Western Blot analysis. However, thanks to the translational approach, the possibility of transferring the acquired knowledge "from bench to bedside" on humans should be noted.

Regarding the clinical study, the main limitations were (i) the limited number of patients and (ii) the absence of the placebo group. Hence, it

will be necessary to confirm these results by randomized placebo-controlled trials.

In conclusion, *H. erinaceus* could be a potential candidate in (i) reverting and avoiding physical frailty, (ii) preventing and treating aging-related cognitive decline and neurodegenerative diseases, and (iii) reducing sleep disorders, anxiety, and depression. In particular, thanks to the interdisciplinary approach followed during this Ph.D. thesis, we understood the molecular mechanisms by which *H. erinaceus* acts its effects, modulating in a pleiotropic way the gut microbiome, BBB function, oxidative stress, inflammation, and adult neurogenesis.

So, oral intake of *H.erinaceus* is a safe and convenient supplement for physical frailty, dementia, and mood disorders prevention and/or partial reversion.

# 8. References

Adams MM, Donohue HS, Linville MC, Iversen EA, Newton IG, Brunso-Bechtold JK. Age-related synapse loss in hippocampal CA3 is not reversed by caloric restriction. Neuroscience. 2010; 171(2):373-82. doi: 10.1016/j.neuroscience.2010.09.022.

Allen AP, Hutch W, Borre YE, Kennedy PJ, Temko A, Boylan G, Murphy E, Cryan JF, Dinan TG, Clarke G. Bifidobacterium longum 1714 as a translational psychobiotic: modulation of stress, electrophysiology and neurocognition in healthy volunteers. Transl Psychiatry. 2016; 6(11):e939. doi: 10.1038/tp.2016.191.

Altar CA. Neurotrophins and depression. Trends Pharmacol Sci. 1999; 20(2):59-61. doi: 10.1016/s0165-6147(99)01309-7.

Amara I, Scuto M, Zappalà A, Ontario ML, Petralia A, Abid-Essefi S, Maiolino L, Signorile A, Trovato Salinaro A, Calabrese V. Hericium Erinaceus Prevents DEHP-Induced Mitochondrial Dysfunction and Apoptosis in PC12 Cells. Int J Mol Sci. 2020; 21(6):2138. doi: 10.3390/ijms21062138.

Ameen-Ali KE, Easton A, Eacott MJ. Moving beyond standard procedures to assess spontaneous recognition memory. Neurosci Biobehav Rev. 2015; 53:37-51. doi: 10.1016/j.neubiorev.2015.03.013.

Andersen JK. Oxidative stress in neurodegeneration: cause or consequence? Nat Med. 2004; 10 Suppl:S18-25. doi: 10.1038/nrn1434.

Anderson MJ, Willis TJ. Canonical Analysis of Principal Coordinates: A Useful Method of Constrained Ordination for Ecology. Ecology. 2003; 84:511-525. doi:10.1890/0012-9658(2003)084[0511:CAOPCA]2.0.CO;2.

Andreotti JP, Silva WN, Costa AC, Picoli CC, Bitencourt FCO, Coimbra-Campos LMC, Resende RR, Magno LAV, Romano-Silva MA, Mintz A, Birbrair A. Neural stem cell niche heterogeneity. Semin Cell Dev Biol. 2019; 95:42-53. doi: 10.1016/j.semcdb.2019.01.005.

Apte RS, Chen DS, Ferrara N. VEGF in Signaling and Disease: Beyond Discovery and Development. Cell. 2019; 176(6):1248-1264. doi: 10.1016/j.cell.2019.01.021.

Arai H, Satake S, Kozaki K. Cognitive Frailty in Geriatrics. Clin Geriatr Med. 2018; 34(4):667-675. doi: 10.1016/j.cger.2018.06.011.

Aubertin-Leheudre M, Woods AJ, Anton S, Cohen R, Pahor M. Frailty Clinical Phenotype: A Physical and Cognitive Point of View. Nestle Nutr Inst Workshop Ser. 2015; 83:55-63. doi: 10.1159/000382061.

Ayanlaja AA, Xiong Y, Gao Y, Ji G, Tang C, Abdikani Abdullah Z, Gao D. Distinct Features of Doublecortin as a Marker of Neuronal Migration and Its Implications in Cancer Cell Mobility. Front Mol Neurosci. 2017; 10:199. doi: 10.3389/fnmol.2017.00199.

Bäckhed F, Ley RE, Sonnenburg JL, Peterson DA, Gordon JI. Host-bacterial mutualism in the human intestine. Science. 2005; 307(5717):1915-20. doi: 10.1126/science.1104816.

Badal VD, Vaccariello ED, Murray ER, Yu KE, Knight R, Jeste DV, Nguyen TT. The Gut Microbiome, Aging, and Longevity: A Systematic Review. Nutrients. 2020; 12(12):3759. doi: 10.3390/nu12123759.

Bailly C, Gao JM. Erinacine A and related cyathane diterpenoids: Molecular diversity and mechanisms underlying their neuroprotection and anticancer activities. Pharmacol Res. 2020; 159:104953. doi: 10.1016/j.phrs.2020.104953.

Bana B, Cabreiro F. The Microbiome and Aging. Annu Rev Genet. 2019; 53:239-261. doi: 10.1146/annurev-genet-112618-043650.

Bandeen-Roche K, Xue QL, Ferrucci L, Walston J, Guralnik JM, Chaves P, Zeger SL, Fried LP. Phenotype of frailty: characterization in the women's health and aging studies. J Gerontol A Biol Sci Med Sci. 2006; 61(3):262-6. doi: 10.1093/gerona/61.3.262.

Barrio C, Arias-Sánchez S, Martín-Monzón I. The gut microbiota-brain axis, psychobiotics and its influence on brain and behaviour: A systematic review. Psychoneuroendocrinology. 2021; 137:105640. doi: 10.1016/j.psyneuen.2021.105640.

Bartsch T, Wulff P. The hippocampus in aging and disease: From plasticity to vulnerability. Neuroscience. 2015; 309:1-16. doi: 10.1016/j.neuroscience.2015.07.084.

Baylis D, Bartlett DB, Patel HP, Roberts HC. Understanding how we age: insights into inflammaging. Longev Healthspan. 2013; 2(1):8. doi: 10.1186/2046-2395-2-8.

Beelman RB, Phillips AT, Richie JP Jr, Ba DM, Duiker SW, Kalaras MD. Health consequences of improving the content of ergothioneine in the food supply. FEBS Lett. 2021. doi: 10.1002/1873-3468.14268.

Ben Haim L, Carrillo-de Sauvage MA, Ceyzériat K, Escartin C. Elusive roles for reactive astrocytes in neurodegenerative diseases. Front Cell Neurosci. 2015; 9:278. doi: 10.3389/fncel.2015.00278.

Bermúdez-Humarán LG, Salinas E, Ortiz GG, Ramirez-Jirano LJ, Morales JA, Bitzer-Quintero OK. From Probiotics to Psychobiotics: Live Beneficial Bacteria Which Act on the Brain-Gut Axis. Nutrients. 2019; 11(4):890. doi: 10.3390/nu11040890.

Bernard JA, Seidler RD. Moving forward: age effects on the cerebellum underlie cognitive and motor declines. Neurosci Biobehav Rev. 2014; 42:193-207. doi: 10.1016/j.neubiorev.2014.02.011. Apple DM, Solano-Fonseca R, Kokovay E. Neurogenesis in the aging brain. Biochem Pharmacol. 2017; 141:77-85. doi: 10.1016/j.bcp.2017.06.116.

Biagi E, Franceschi C, Rampelli S, Severgnini M, Ostan R, Turroni S, Consolandi C, Quercia S, Scurti M, Monti D, Capri M, Brigidi P, Candela M. Gut Microbiota and Extreme Longevity. Curr Biol. 2016; 26(11):1480-5. doi: 10.1016/j.cub.2016.04.016.

Bibbò S, Ianiro G, Giorgio V, Scaldaferri F, Masucci L, Gasbarrini A, Cammarota G. The role of diet on gut microbiota composition. Eur Rev Med Pharmacol Sci. 2016 Nov;20(22):4742-4749. PMID: 27906427.

Bird CM. The role of the hippocampus in recognition memory. Cortex. 2017; 93:155-165. doi: 10.1016/j.cortex.2017.05.016.

Björkholm C, Monteggia LM. BDNF - a key transducer of antidepressant effects. Neuropharmacology. 2016; 102:72-9. doi: 10.1016/j.neuropharm.2015.10.034.

Boehm EM, Gildenberg MS, Washington MT. The Many Roles of PCNA in Eukaryotic DNA Replication. Enzymes. 2016; 39:231-54. doi: 10.1016/bs.enz.2016.03.003.

Bokulich NA, Kaehler BD, Rideout JR, Dillon M, Bolyen E, Knight R, Huttley GA, Gregory Caporaso J. Optimizing taxonomic classification of marker-gene amplicon sequences with QIIME 2's q2-feature-classifier plugin. Microbiome. 2018; 6(1):90. doi: 10.1186/s40168-018-0470-z.

Bolyen E, Rideout JR, Dillon MR, Bokulich NA, Abnet CC, Al-Ghalith GA, Alexander H, Alm EJ, Arumugam M, Asnicar F, Bai Y, Bisanz JE, Bittinger K, Brejnrod A, Brislawn CJ, Brown CT, Callahan BJ, Caraballo-Rodríguez AM, Chase J, Cope EK, Da Silva R, Diener C, Dorrestein PC, Douglas GM, Durall DM, Duvallet C, Edwardson CF, Ernst M, Estaki M, Fouquier J, Gauglitz JM, Gibbons SM, Gibson DL, Gonzalez A, Gorlick K, Guo J, Hillmann B, Holmes S, Holste H, Huttenhower C, Huttley GA, Janssen S, Jarmusch AK, Jiang L, Kaehler BD, Kang KB, Keefe CR, Keim P, Kelley ST, Knights D, Koester I, Kosciolek T, Kreps J, Langille MGI, Lee J, Ley R, Liu YX, Loftfield E, Lozupone C, Maher M, Marotz C, Martin BD, McDonald D, McIver LJ, Melnik AV, Metcalf JL, Morgan SC, Morton JT, Naimey AT, Navas-Molina JA, Nothias LF, Orchanian SB, Pearson T, Peoples SL, Petras D, Preuss ML, Pruesse E, Rasmussen LB, Rivers A, Robeson MS 2nd, Rosenthal P, Segata N, Shaffer M, Shiffer A, Sinha R, Song SJ, Spear JR, Swafford AD, Thompson LR, Torres PJ, Trinh P, Tripathi A, Turnbaugh PJ, Ul-Hasan S, van der Hooft JJJ, Vargas F, Vázquez-Baeza Y, Vogtmann E, von Hippel M, Walters W, Wan Y, Wang M, Warren J, Weber KC, Williamson CHD, Willis AD, Xu ZZ, Zaneveld JR, Zhang Y, Zhu Q, Knight R, Caporaso JG. Reproducible, interactive, scalable and extensible microbiome data science using QIIME 2. Nat Biotechnol. 2019 Aug;37(8):852-857. doi: 10.1038/s41587-019-0209-9. Erratum in: Nat Biotechnol. 2019; 37(9):1091.

Borodina I, Kenny LC, McCarthy CM, Paramasivan K, Pretorius E, Roberts TJ, van der Hoek SA, Kell DB. The biology of ergothioneine, an antioxidant nutraceutical. Nutr Res Rev. 2020; 33(2):190-217. doi: 10.1017/S0954422419000301.

Bothwell M. NGF, BDNF, NT3, and NT4. Handb Exp Pharmacol. 2014; 220:3-15. doi: 10.1007/978-3-642-45106-5_1.

Boyajian JL, Ghebretatios M, Schaly S, Islam P, Prakash S. Microbiome and Human Aging: Probiotic and Prebiotic Potentials in Longevity, Skin Health and Cellular Senescence. Nutrients. 2021; 13(12):4550. doi: 10.3390/nu13124550.

Brady CA, Attardi LD. p53 at a glance. J Cell Sci. 2010; 123(Pt 15):2527-32. doi: 10.1242/jcs.064501.

Brandalise F, Cesaroni V, Gregori A, Repetti M, Romano C, Orrù G, Botta L, Girometta C, Guglielminetti ML, Savino E, Rossi P. Dietary Supplementation of Hericium erinaceus Increases Mossy Fiber-CA3 Hippocampal Neurotransmission and Recognition Memory in Wild-

Type Mice. Evid Based Complement Alternat Med. 2017; 2017:3864340. doi: 10.1155/2017/3864340.

Brodziak A, Brewczyński A, Bajor G. Clinical significance of knowledge about the structure, function, and impairments of working memory. Med Sci Monit. 2013; 19:327-38. doi: 10.12659/MSM.883900.

Brown MW, Aggleton JP. Recognition memory: what are the roles of the perirhinal cortex and hippocampus? Nat Rev Neurosci. 2001; 2(1):51-61. doi: 10.1038/35049064.

Burda JE, Sofroniew MV. Reactive gliosis and the multicellular response to CNS damage and disease. Neuron. 2014; 81(2):229-48. doi: 10.1016/j.neuron.2013.12.034.

Burke SN, Ryan L, Barnes CA. Characterizing cognitive aging of recognition memory and related processes in animal models and in humans. Front Aging Neurosci. 2012; 4:15. doi: 10.3389/fnagi.2012.00015.

Burokas A, Arboleya S, Moloney RD, Peterson VL, Murphy K, Clarke G, Stanton C, Dinan TG, Cryan JF. Targeting the Microbiota-Gut-Brain Axis: Prebiotics Have Anxiolytic and Antidepressant-like Effects and Reverse the Impact of Chronic Stress in Mice. Biol Psychiatry. 2017; 82(7):472-487. doi: 10.1016/j.biopsych.2016.12.031.

Callahan BJ, McMurdie PJ, Rosen MJ, Han AW, Johnson AJ, Holmes SP. DADA2: High-resolution sample inference from Illumina amplicon data. Nat Methods. 2016; 13(7):581-3. doi: 10.1038/nmeth.3869.

Cesari M, Calvani R, Marzetti E. Frailty in Older Persons. Clin Geriatr Med. 2017; 33(3):293-303. doi: 10.1016/j.cger.2017.02.002.

Chan D, Gallaher LM, Moodley K, Minati L, Burgess N, Hartley T. The 4 Mountains Test: A Short Test of Spatial Memory with High Sensitivity for the Diagnosis of Pre-dementia Alzheimer's Disease. J Vis Exp. 2016; (116):54454. doi: 10.3791/54454.

Chance Nicholson W, Pfeiffer K. Sleep Disorders and Mood, Anxiety, and Post-Traumatic Stress Disorders: Overview of Clinical Treatments in the Context of Sleep Disturbances. Nurs Clin North Am. 2021; 56(2):229-247. doi: 10.1016/j.cnur.2021.02.003.

Cheah IK, Feng L, Tang RMY, Lim KHC, Halliwell B. Ergothioneine levels in an elderly population decrease with age and incidence of cognitive decline; a risk factor for neurodegeneration? Biochem Biophys Res Commun. 2016; 478(1):162-167. doi: 10.1016/j.bbrc.2016.07.074.

Cheah IK, Halliwell B. Ergothioneine, recent developments. Redox Biol. 2021; 42:101868. doi: 10.1016/j.redox.2021.101868.

Cheah IK, Halliwell B. Ergothioneine; antioxidant potential, physiological function and role in disease. Biochim Biophys Acta. 2012; 1822(5):784-93. doi: 10.1016/j.bbadis.2011.09.017.

Cheah IK, Ng LT, Ng LF, Lam VY, Gruber J, Huang CYW, Goh FQ, Lim KHC, Halliwell B. Inhibition of amyloid-induced toxicity by ergothioneine in a transgenic Caenorhabditis elegans model. FEBS Lett. 2019; 593(16):2139-2150. doi: 10.1002/1873-3468.13497.

Chen C, Zhou M, Ge Y, Wang X. SIRT1 and aging related signaling pathways. Mech Ageing Dev. 2020; 187:111215. doi: 10.1016/j.mad.2020.111215.

Chen F, Liu Y, Wong NK, Xiao J, So KF. Oxidative Stress in Stem Cell Aging. Cell Transplant. 2017; 26(9):1483-1495. doi: 10.1177/0963689717735407.

Chen S, Hillman DE. Dying-back of Purkinje cell dendrites with synapse loss in aging rats. J Neurocytol. 1999; 28(3):187-96. doi: 10.1023/a:1007015721754.

Chen X, Guo C, Kong J. Oxidative stress in neurodegenerative diseases. Neural Regen Res. 2012; 7(5):376-85. doi: 10.3969/j.issn.1673-5374.2012.05.009.

Chen Y, Qin C, Huang J, Tang X, Liu C, Huang K, Xu J, Guo G, Tong A, Zhou L. The role of astrocytes in oxidative stress of central nervous system: A mixed blessing. Cell Prolif. 2020; 53(3):e12781. doi: 10.1111/cpr.12781.

Chen SY, Ho KJ, Hsieh YJ, Wang LT, Mau JL. Contents of lovastatin, γ-aminobutyric acid and ergothioneine in mushroom fruiting bodies and mycelia. LWT Food Sci. Technol. 2012, 47, 274–278. doi:10.1016/j.lwt.2012.01.019.

Chiu CH, Chyau CC, Chen CC, Lee LY, Chen WP, Liu JL, Lin WH, Mong MC. Erinacine A-Enriched Hericium erinaceus Mycelium Produces Antidepressant-Like Effects through Modulating BDNF/PI3K/Akt/GSK-3β Signaling in Mice. Int J Mol Sci. 2018; 19(2):341. doi: 10.3390/ijms19020341.

Choi WS, Kim YS, Park BS, Kim JE, Lee SE. Hypolipidaemic Effect of Hericium erinaceum Grown in Artemisia capillaris on Obese Rats. Mycobiology. 2013; 41(2):94-9. doi: 10.5941/MYCO.2013.41.2.94.

Chong PS, Poon CH, Roy J, Tsui KC, Lew SY, Phang MWL, Tan RJY, Cheng PG, Fung ML, Wong KH, Lim LW. Neurogenesis-dependent antidepressant-like activity of Hericium erinaceus in an animal model of depression. Chin Med. 2021; 16(1):132. doi: 10.1186/s13020-021-00546-8.

Chung HY, Cesari M, Anton S, Marzetti E, Giovannini S, Seo AY, Carter C, Yu BP, Leeuwenburgh C. Molecular inflammation: underpinnings of aging and age-related diseases. Ageing Res Rev. 2009; 8(1):18-30. doi: 10.1016/j.arr.2008.07.002.

Chung HY, Kim DH, Lee EK, Chung KW, Chung S, Lee B, Seo AY, Chung JH, Jung YS, Im E, Lee J, Kim ND, Choi YJ, Im DS, Yu BP. Redefining Chronic Inflammation in Aging and Age-Related Diseases: Proposal of the Senoinflammation Concept. Aging Dis. 2019; 10(2):367-382. doi: 10.14336/AD.2018.0324.

Chung HY, Sung B, Jung KJ, Zou Y, Yu BP. The molecular inflammatory process in aging. Antioxid Redox Signal. 2006; 8(3-4):572-81. doi: 10.1089/ars.2006.8.572.

Clemente JC, Ursell LK, Parfrey LW, Knight R. The impact of the gut microbiota on human health: an integrative view. Cell. 2012; 148(6):1258-70. doi: 10.1016/j.cell.2012.01.035.

Cloninger CR. A systematic method for clinical description and classification of personality variants. A proposal. Arch Gen Psychiatry. 1987; 44(6):573-88. doi: 10.1001/archpsyc.1987.01800180093014.

Cobley JN, Fiorello ML, Bailey DM. 13 reasons why the brain is susceptible to oxidative stress. Redox Biol. 2018; 15:490-503. doi: 10.1016/j.redox.2018.01.008.

Cohen JD, McClure SM, Yu AJ. Should I stay or should I go? How the human brain manages the trade-off between exploitation and exploration. Philos Trans R Soc Lond B Biol Sci. 2007; 362(1481):933-42. doi: 10.1098/rstb.2007.2098.

Cohen N, Cohen J, Asatiani MD, Varshney VK, Yu HT, Yang YC, Li YH, Mau JL, Wasser SP. Chemical composition and nutritional and medicinal value of fruit bodies and submerged cultured mycelia of culinary-medicinal higher Basidiomycetes mushrooms. Int J Med Mushrooms. 2014; 16(3):273-91. doi: 10.1615/intjmedmushr.v16.i3.80.

Colucci-D'Amato L, Speranza L, Volpicelli F. Neurotrophic Factor BDNF, Physiological Functions and Therapeutic Potential in Depression, Neurodegeneration and Brain Cancer. Int J Mol Sci. 2020; 21(20):7777. doi: 10.3390/ijms21207777.

Cordaro M, Salinaro AT, Siracusa R, D'Amico R, Impellizzeri D, Scuto M, Ontario ML, Cuzzocrea S, Di Paola R, Fusco R, Calabrese V. Key Mechanisms and Potential Implications of Hericium erinaceus in NLRP3 Inflammasome Activation by Reactive Oxygen Species during Alzheimer's Disease. Antioxidants (Basel). 2021; 10(11):1664. doi: 10.3390/antiox10111664.

Corvaglia V, Cilli D, Scopa C, Brandi R, Arisi I, Malerba F, La Regina F, Scardigli R, Cattaneo A. ProNGF Is a Cell-Type-Specific Mitogen for Adult Hippocampal and for Induced Neural Stem Cells. Stem Cells. 2019; 37(9):1223-1237. doi: 10.1002/stem.3037. Mondal AC, Fatima M. Direct and indirect evidences of BDNF and NGF as key modulators in depression: role of antidepressants treatment. Int J Neurosci. 2019; 129(3):283-296. doi: 10.1080/00207454.2018.1527328.

Costa VD, Tran VL, Turchi J, Averbeck BB. Dopamine modulates novelty seeking behavior during decision making. Behav Neurosci. 2014; 128(5):556-66. doi: 10.1037/a0037128.

Costea L, Mészáros Á, Bauer H, Bauer HC, Traweger A, Wilhelm I, Farkas AE, Krizbai IA. The Blood-Brain Barrier and Its Intercellular Junctions in Age-Related Brain Disorders. Int J Mol Sci. 2019; 20(21):5472. doi: 10.3390/ijms20215472.

Crocq MA. A history of anxiety: from Hippocrates to DSM. Dialogues Clin Neurosci. 2015;17(3):319-25. doi: 10.31887/DCNS.2015.17.3/macrocq.

Cryan JF, O'Riordan KJ, Cowan CSM, Sandhu KV, Bastiaanssen TFS, Boehme M, Codagnone MG, Cussotto S, Fulling C, Golubeva AV, Guzzetta KE, Jaggar M, Long-Smith CM, Lyte JM, Martin JA, Molinero-Perez A, Moloney G, Morelli E, Morillas E, O'Connor R, Cruz-Pereira JS, Peterson VL, Rea K, Ritz NL, Sherwin E, Spichak S, Teichman EM, van de Wouw M, Ventura-Silva AP, Wallace-Fitzsimons SE, Hyland N, Clarke G, Dinan TG. The Microbiota-Gut-Brain Axis. Physiol Rev. 2019; 99(4):1877-2013. doi: 10.1152/physrev.00018.2018.

da Costa JP, Vitorino R, Silva GM, Vogel C, Duarte AC, Rocha-Santos T. A synopsis on aging-Theories, mechanisms and future prospects. Ageing Res Rev. 2016; 29:90-112. doi: 10.1016/j.arr.2016.06.005.

Dalton A, Mermier C, Zuhl M. Exercise influence on the microbiome-gut-brain axis. Gut Microbes. 2019; 10(5):555-568. doi: 10.1080/19490976.2018.1562268.

De Groot DMG, Bierman EPB. Numerical changes in rat hippocampal synapses: an effect of "aging"? Acta Stereol. 1987; 6:53-58.

Deborah Glasofer. Generalized Anxiety Disorder: Symptoms and Diagnosis. Part of Generalized Anxiety Disorder Guide. Verywellmind. 2021. https://www.verywellmind.com/dsm-5-criteria-for-generalized-anxiety-disorder-1393147.

Dent E, Kowal P, Hoogendijk EO. Frailty measurement in research and clinical practice: A review. Eur J Intern Med. 2016; 31:3-10. doi: 10.1016/j.ejim.2016.03.007.

Derrien M, Belzer C, de Vos WM. Akkermansia muciniphila and its role in regulating host functions. Microb Pathog. 2017; 106:171-181. doi: 10.1016/j.micpath.2016.02.005.

Deshmukh S, Sridhar K, Gupta MK. Hericium erinaceus -A Rich Source of Diverse Bioactive Metabolites. Fungal Biotec. 2021; 1(2):10–38 doi:10.5943/FunBiotec/1/2/2.

Deyama S, Bang E, Kato T, Li XY, Duman RS. Neurotrophic and Antidepressant Actions of Brain-Derived Neurotrophic Factor Require Vascular Endothelial Growth Factor. Biol Psychiatry. 2019; 86(2):143-152. doi: 10.1016/j.biopsych.2018.12.014.

Dhahbi JM. Circulating small noncoding RNAs as biomarkers of aging. Ageing Res Rev. 2014; 17:86-98. doi: 10.1016/j.arr.2014.02.005. Epub 2014 Mar 4. PMID: 24607831.

Dickstein DL, Weaver CM, Luebke JI, Hof PR. Dendritic spine changes associated with normal aging. Neuroscience. 2013; 251:21-32. doi: 10.1016/j.neuroscience.2012.09.077.

Diling C, Chaoqun Z, Jian Y, Jian L, Jiyan S, Yizhen X, Guoxiao L. Immunomodulatory Activities of a Fungal Protein Extracted from Hericium erinaceus through Regulating the Gut Microbiota. Front Immunol. 2017; 8:666. doi: 10.3389/fimmu.2017.00666.

Dinan TG, Cryan JF. The Microbiome-Gut-Brain Axis in Health and Disease. Gastroenterol Clin North Am. 2017 Mar;46(1):77-89. doi: 10.1016/j.gtc.2016.09.007. Epub 2017 Jan 4. PMID: 28164854.

Doba N, Tokuda Y, Goldstein NE, Kushiro T, Hinohara S. A pilot trial to predict frailty syndrome: the Japanese Health Research Volunteer

Study. Exp Gerontol. 2012; 47(8):638-43. doi: 10.1016/j.exger.2012.05.016.

Dowlati Y, Herrmann N, Swardfager W, Liu H, Sham L, Reim EK, Lanctôt KL. A meta-analysis of cytokines in major depression. Biol Psychiatry. 2010; 67(5):446-57. doi: 10.1016/j.biopsych.2009.09.033.

Du F, Wang HX, Ng TB. [An amylase from fresh fruiting bodies of the monkey head mushroom Hericium erinaceum]. Prikl Biokhim Mikrobiol. 2013; 49(1):29-33. Russian. doi: 10.7868/s0555109913010042.

Duclot F, Hollis F, Darcy MJ, Kabbaj M. Individual differences in novelty-seeking behavior in rats as a model for psychosocial stress-related mood disorders. Physiol Behav. 2011; 104(2):296-305. doi: 10.1016/j.physbeh.2010.12.014.

Duman RS, Monteggia LM. A neurotrophic model for stress-related mood disorders. Biol Psychiatry. 2006; 59(12):1116-27. doi: 10.1016/j.biopsych.2006.02.013.

Dutta S, Sengupta P. Men and mice: Relating their ages. Life Sci. 2016; 152:244-8. doi: 10.1016/j.lfs.2015.10.025.

Dwyer JT, Coates PM. Why Americans Need Information on Dietary Supplements. J Nutr. 2018; 148(suppl_2):1401S-1405S. doi: 10.1093/jn/nxy081.

Ey J, Schömig E, Taubert D. Dietary sources and antioxidant effects of ergothioneine. J Agric Food Chem. 2007; 55(16):6466-74. doi: 10.1021/jf071328f.

Faraji J, Karimi M, Soltanpour N, Moharrerie A, Rouhzadeh Z, Lotfi H, Hosseini SA, Jafari SY, Roudaki S, Moeeini R, Metz GA. Oxytocin-mediated social enrichment promotes longer telomeres and novelty seeking. Elife. 2018; 7:e40262. doi: 10.7554/eLife.40262.

Fares J, Bou Diab Z, Nabha S, Fares Y. Neurogenesis in the adult hippocampus: history, regulation, and prospective roles. Int J Neurosci. 2019; 129(6):598-611. doi: 10.1080/00207454.2018.1545771.

Ferrucci L, Fabbri E. Inflammageing: chronic inflammation in ageing, cardiovascular disease, and frailty. Nat Rev Cardiol. 2018; 15(9):505-522. doi: 10.1038/s41569-018-0064-2.

Finkel T, Holbrook NJ. Oxidants, oxidative stress and the biology of ageing. Nature. 2000; 408(6809):239-47. doi: 10.1038/35041687.

Foltran RB, Diaz SL. BDNF isoforms: a round trip ticket between neurogenesis and serotonin? J Neurochem. 2016; 138(2):204-21. doi: 10.1111/jnc.13658.

Forrester SJ, Kikuchi DS, Hernandes MS, Xu Q, Griendling KK. Reactive Oxygen Species in Metabolic and Inflammatory Signaling. Circ Res. 2018; 122(6):877-902. doi: 10.1161/CIRCRESAHA.117.311401.

Forsythe P, Kunze WA, Bienenstock J. On communication between gut microbes and the brain. Curr Opin Gastroenterol. 2012; 28(6):557-62. doi: 10.1097/MOG.0b013e3283572ffa.

Foster JA, McVey Neufeld KA. Gut-brain axis: how the microbiome influences anxiety and depression. Trends Neurosci. 2013; 36(5):305-12. doi: 10.1016/j.tins.2013.01.005.

Franceschi C, Campisi J. Chronic inflammation (inflammaging) and its potential contribution to age-associated diseases. J Gerontol A Biol Sci Med Sci. 2014; 69 Suppl 1:S4-9. doi: 10.1093/gerona/glu057.

Franceschi C, Garagnani P, Parini P, Giuliani C, Santoro A. Inflammaging: a new immune-metabolic viewpoint for age-related diseases. Nat Rev Endocrinol. 2018; 14(10):576-590. doi: 10.1038/s41574-018-0059-4.

Fraundorf SH, Hourihan KL, Peters RA, Benjamin AS. Aging and recognition memory: A meta-analysis. Psychol Bull. 2019; 145(4):339-371. doi: 10.1037/bul0000185.

Fried LP, Tangen CM, Walston J, Newman AB, Hirsch C, Gottdiener J, Seeman T, Tracy R, Kop WJ, Burke G, McBurnie MA, Cardiovascular Health Study Collaborative Research Group. Frailty in older adults: evidence for a phenotype. J Gerontol A Biol Sci Med Sci. 2001; 56(3):M146-56. doi: 10.1093/gerona/56.3.m146.

Friedman M. Chemistry, Nutrition, and Health-Promoting Properties of Hericium erinaceus (Lion's Mane) Mushroom Fruiting Bodies and Mycelia and Their Bioactive Compounds. J Agric Food Chem. 2015; 63(32):7108-23. doi: 10.1021/acs.jafc.5b02914.

Frielingsdorf H, Simpson DR, Thal LJ, Pizzo DP. Nerve growth factor promotes survival of new neurons in the adult hippocampus. Neurobiol Dis. 2007 Apr;26(1):47-55. doi: 10.1016/j.nbd.2006.11.015.

Fujita K. p53 Isoforms in Cellular Senescence- and Ageing-Associated Biological and Physiological Functions. Int J Mol Sci. 2019; 20(23):6023. doi: 10.3390/ijms20236023.

Gardier AM, Guiard BP, Guilloux JP, Repérant C, Coudoré F, David DJ. Interest of using genetically manipulated mice as models of depression to evaluate antidepressant drugs activity: a review. Fundam Clin Pharmacol. 2009; 23(1):23-42. doi: 10.1111/j.1472-8206.2008.00640.x.

Gawdi R, Emmady PD. Physiology, Blood Brain Barrier. 2020 Dec 19. In: StatPearls [Internet]. Treasure Island (FL): StatPearls Publishing; 2021.

Gerbec B, Tavčar E, Gregori A, Kreft S, Berovic M. Solid State Cultivation of Hericium erinaceus Biomass and Erinacine: A Production. J Bioproces Biotech. 2015, 5, 1–5. doi: 10.4172/2155-9821.1000210

Gerhardt S, Mohajeri MH. Changes of Colonic Bacterial Composition in Parkinson's Disease and Other Neurodegenerative Diseases. Nutrients. 2018; 10(6):708. doi: 10.3390/nu10060708.

Giblin W, Lombard DB. Chapter 3 - Sirtuins, Healthspan, and Longevity in Mammals, Editor(s): Matt R. Kaeberlein, George M. Martin, Handbook of the Biology of Aging (Eighth Edition), Academic Press, 2016, Pages 83-132. doi:10.1016/B978-0-12-411596-5.00003-4.

Gocłowska MA, Ritter SM, Elliot AJ, Baas M. Novelty seeking is linked to openness and extraversion, and can lead to greater creative performance. J Pers. 2019; 87(2):252-266. doi: 10.1111/jopy.12387.

Gomaa EZ. Human gut microbiota/microbiome in health and diseases: a review. Antonie Van Leeuwenhoek. 2020; 113(12):2019-2040. doi: 10.1007/s10482-020-01474-7.

Gomaa EZ. Human gut microbiota/microbiome in health and diseases: a review. Antonie Van Leeuwenhoek. 2020; 113(12):2019-2040. doi: 10.1007/s10482-020-01474-7.

Goyal D, Ali SA, Singh RK. Emerging role of gut microbiota in modulation of neuroinflammation and neurodegeneration with emphasis on Alzheimer's disease. Prog Neuropsychopharmacol Biol Psychiatry. 2021; 106:110112. doi: 10.1016/j.pnpbp.2020.110112.

Graves LV, Moreno CC, Seewald M, Holden HM, Van Etten EJ, Uttarwar V, McDonald CR, Delano-Wood L, Bondi MW, Woods SP, Delis DC, Gilbert PE. Effects of Age and Gender on Recall and Recognition

Discriminability. Arch Clin Neuropsychol. 2017; 32(8):972-979. doi: 10.1093/arclin/acx024.

Gronier B, Savignac HM, Di Miceli M, Idriss SM, Tzortzis G, Anthony D, Burnet PWJ. Increased cortical neuronal responses to NMDA and improved attentional set-shifting performance in rats following prebiotic (B-GOS®) ingestion. Eur Neuropsychopharmacol. 2018; 28(1):211-224. doi: 10.1016/j.euroneuro.2017.11.001.

Guarner F, Malagelada JR. Gut flora in health and disease. Lancet. 2003; 361(9356):512-9. doi: 10.1016/S0140-6736(03)12489-0.

Guo P, Zhang K, Ma X, He P. *Clostridium* species as probiotics: potentials and challenges. J Anim Sci Biotechnol. 2020; 11:24. doi: 10.1186/s40104-019-0402-1.

Halliwell B, Cheah IK, Tang RMY. Ergothioneine - a diet-derived antioxidant with therapeutic potential. FEBS Lett. 2018; 592(20):3357-3366. doi: 10.1002/1873-3468.13123.

Han D, Li Z, Liu T, Yang N, Li Y, He J, Qian M, Kuang Z, Zhang W, Ni C, Guo X. Prebiotics Regulation of Intestinal Microbiota Attenuates Cognitive Dysfunction Induced by Surgery Stimulation in APP/PS1 Mice. Aging Dis. 2020; 11(5):1029-1045. doi: 10.14336/AD.2020.0106.

Haran JP, Bucci V, Dutta P, Ward D, McCormick B. The nursing home elder microbiome stability and associations with age, frailty, nutrition and physical location. J Med Microbiol. 2018; 67(1):40-51. doi: 10.1099/jmm.0.000640

Hare BD, Duman RS. Prefrontal cortex circuits in depression and anxiety: contribution of discrete neuronal populations and target regions. Mol Psychiatry. 2020; 25(11):2742-2758. doi: 10.1038/s41380-020-0685-9.

Hazekawa M, Kataoka A, Hayakawa K, Uchimasu T, Furuta R, Irie K, Yoshida M, Fujioka T, Egashira N, Oishi R, Mishima K, Uchida T, Iwasaky K, Fujiwara M. Neuroprotective effect of repeated treatment with Hericiumerinaceum in mice subjected to middle cerebral artery occlusion. J Health Sci. 2010; 56:296–303. doi: 10.1248/jhs.56.296

He X, Wang X, Fang J, Chang Y, Ning N, Guo H, Huang L, Huang X, Zhao Z. Structures, biological activities, and industrial applications of the polysaccharides from Hericium erinaceus (Lion's Mane) mushroom: A review. Int J Biol Macromol. 2017; 97:228-237. doi: 10.1016/j.ijbiomac.2017.01.040.

Heintz-Buschart A, Pandey U, Wicke T, Sixel-Döring F, Janzen A, Sittig-Wiegand E, Trenkwalder C, Oertel WH, Mollenhauer B, Wilmes P. The nasal and gut microbiome in Parkinson's disease and idiopathic rapid eye movement sleep behavior disorder. Mov Disord. 2018; 33(1):88-98. doi: 10.1002/mds.27105.

Heintz-Buschart A, Wilmes P. Human Gut Microbiome: Function Matters. Trends Microbiol. 2018; 26(7):563-574. doi: 10.1016/j.tim.2017.11.002.

Hernandez-Segura A, Nehme J, Demaria M. Hallmarks of Cellular Senescence. Trends Cell Biol. 2018; 28(6):436-453. doi: 10.1016/j.tcb.2018.02.001.

Higami Y, Shimokawa I. Apoptosis in the aging process. Cell Tissue Res. 2000; 301(1):125-32. doi: 10.1007/s004419900156.

Higarza SG, Arboleya S, Arias JL, Gueimonde M, Arias N. *Akkermansia muciniphila* and environmental enrichment reverse cognitive impairment associated with high-fat high-cholesterol consumption in rats. Gut Microbes. 2021; 13(1):1-20. doi: 10.1080/19490976.2021.1880240.

Hirano T. IL-6 in inflammation, autoimmunity and cancer. Int Immunol. 2021; 33(3):127-148. doi: 10.1093/intimm/dxaa078.

Huang S, Pang D, Li X, You L, Zhao Z, Cheung PC, Zhang M, Liu D. A sulfated polysaccharide from Gracilaria Lemaneiformis regulates cholesterol and bile acid metabolism in high-fat diet mice. Food Funct. 2019; 10(6):3224-3236. doi: 10.1039/c9fo00263d.

Hussain T, Murtaza G, Yang H, Kalhoro MS, Kalhoro DH. Exploiting Anti-Inflammation Effects of Flavonoids in Chronic Inflammatory Diseases. Curr Pharm Des. 2020; 26(22):2610-2619. doi: 10.2174/1381612826666200408101550.

Inanaga K. Recovery from Schizophrenia with Bioactive Substances in Hericium erinaceum. Int J Sch Cog Psychol. 2015. S1:1.

Inglés M, Gambini J, Mas-Bargues C, García-García FJ, Viña J, Borrás C. Brain-Derived Neurotrophic Factor as a Marker of Cognitive Frailty. J Gerontol A Biol Sci Med Sci. 2017; 72(3):450-451. doi: 10.1093/gerona/glw145.

Ishimoto T, Kato Y. Ergothioneine in the brain. FEBS Lett. 2022. doi: 10.1002/1873-3468.14271.

Jackson MA, Jeffery IB, Beaumont M, Bell JT, Clark AG, Ley RE, O'Toole PW, Spector TD, Steves CJ. Signatures of early frailty in the gut microbiota. Genome Med. 2016; 8(1):8. doi: 10.1186/s13073-016-0262-7. Erratum in: Genome Med. 2016;8(1):21. Jackson, Matt [corrected to Jackson, Matthew A].

Jandhyala SM, Talukdar R, Subramanyam C, Vuyyuru H, Sasikala M, Nageshwar Reddy D. Role of the normal gut microbiota. World J Gastroenterol. 2015; 21(29):8787-803. doi: 10.3748/wjg.v21.i29.8787.

Janeček Š, Svensson B, MacGregor EA. α-Amylase: an enzyme specificity found in various families of glycoside hydrolases. Cell Mol Life Sci. 2014; 71(7):1149-70. doi: 10.1007/s00018-013-1388-z.

Jang JH, Aruoma OI, Jen LS, Chung HY, Surh YJ. Ergothioneine rescues PC12 cells from beta-amyloid-induced apoptotic death. Free Radic Biol Med. 2004; 36(3):288-99. doi: 10.1016/j.freeradbiomed.2003.11.005.

Jantaratnotai N, Mosikanon K, Lee Y, McIntyre RS. The interface of depression and obesity. Obes Res Clin Pract. 2017; 11(1):1-10. doi: 10.1016/j.orcp.2016.07.003.

Jiang S, Wang S, Sun Y, Zhang Q. Medicinal properties of Hericium erinaceus and its potential to formulate novel mushroom-based pharmaceuticals. Appl Microbiol Biotechnol. 2014; 98(18):7661-70. doi: 10.1007/s00253-014-5955-5.

Juckel G, Manitz MP, Freund N, Gatermann S. Impact of Poly I:C induced maternal immune activation on offspring's gut microbiome diversity - Implications for schizophrenia. Prog Neuropsychopharmacol Biol Psychiatry. 2021; 110:110306. doi: 10.1016/j.pnpbp.2021.110306.

Kalaras MD, Richie JP, Calcagnotto A, Beelman RB. Mushrooms: A rich source of the antioxidants ergothioneine and glutathione. Food Chem. 2017; 233:429-433. doi: 10.1016/j.foodchem.2017.04.109.

Kameda M, Teruya T, Yanagida M, Kondoh H. Frailty markers comprise blood metabolites involved in antioxidation, cognition, and mobility. Proc Natl Acad Sci U S A. 2020; 117(17):9483-9489. doi: 10.1073/pnas.1920795117.

Kawagishi H, Ando M, Mizuno T. Hericenone A and B as cytotoxic principles from the mushroom Hericium erinaceum. Tetrahedron Lett. 1990; 31, 373– 376.

Kawagishi H, Ando M, Sakamoto H, Yoshida S, Ojima F, Ishiguro Y, Ukai N, Furukawa S. Erinacines A, B and C, strong stimulators of nerve growth factor (NGF)-synthesis, from the mycelia of Hericium erinaceum. Tetrahedron Lett. 1994, 35, 1569–1572.

Kawagishi H, Ando M, Sakamoto H, Yoshida S, Ojima F, Ishiguro Y, Ukai N, Furukawa S. Hericenones C, D and E, stimulators of nerve growth factor (NGF)-synthesis, from the mushroom Hericium erinaceum. Tetrahedron Lett. 1991, 32, 4561–4564.

Kawagishi H, Ando M, Shinba K, Sakamoto H, Yoshida S, Ojima F, Ishiguro Y, Nobuo U, Shoei F. Chromans, hericenones F, G and H from the mushroom Hericium erinaceum. Phytochemistry. 1992; 32(1):175-178.

Kawagishi H, Shimada A, Shirai R, Okamoto K, Ojima F, Sakamoto H, Ishiguro Y, Furukawa S. Erinacines A, B and C, strong stimulators of nerve growth factor (NGF)-synthesis, from the mycelia of Hericium erinaceum, Tetrahedron Letters. 1994; 35(10): 1569-1572. doi:10.1016/S0040-4039(00)76760-8.

Kawagishi H, Zhuang C. Compounds for dementia from *Hericium erinaceum*. Drugs of the Future. (2008); 33(2):149-155. doi: 10.1358/dof.2008.033.02.1173290

Kelaiditi E, Cesari M, Canevelli M, van Kan GA, Ousset PJ, Gillette-Guyonnet S, Ritz P, Duveau F, Soto ME, Provencher V, Nourhashemi F, Salvà A, Robert P, Andrieu S, Rolland Y, Touchon J, Fitten JL, Vellas B; IANA/IAGG. Cognitive frailty: rational and definition from an (I.A.N.A./I.A.G.G.) international consensus group. J Nutr Health Aging. 2013; 17(9):726-34. doi: 10.1007/s12603-013-0367-2.

Kempermann G, Song H, Gage FH. Neurogenesis in the Adult Hippocampus. Cold Spring Harb Perspect Biol. 2015; 7(9):a018812. doi: 10.1101/cshperspect.a018812.

Khan MA, Tania M, Liu R, Rahman MM. Hericium erinaceus: an edible mushroom with medicinal values. J Complement Integr Med. 2013; 10:/j/jcim.2013.10.issue-1/jcim-2013-0001/jcim-2013-0001.xml. doi: 10.1515/jcim-2013-0001. PMID: 23735479.

Khansari N, Shakiba Y, Mahmoudi M. Chronic inflammation and oxidative stress as a major cause of age-related diseases and cancer. Recent Pat Inflamm Allergy Drug Discov. 2009; 3(1):73-80. doi: 10.2174/187221309787158371.

Kim HJ, Moon CM, Kang JL, Park EM. Aging effects on the diurnal patterns of gut microbial composition in male and female mice. Korean J Physiol Pharmacol. 2021; 25(6):575-583. doi: 10.4196/kjpp.2021.25.6.575.

Kim S, Jazwinski SM. The Gut Microbiota and Healthy Aging: A Mini-Review. Gerontology. 2018; 64(6):513-520. doi: 10.1159/000490615.

Kirkwood TB. Understanding the odd science of aging. Cell. 2005; 120(4):437-47. doi: 10.1016/j.cell.2005.01.027.

Kirwan R, McCullough D, Butler T, Perez de Heredia F, Davies IG, Stewart C. Sarcopenia during COVID-19 lockdown restrictions: long- term health effects of short-term muscle loss. Geroscience. 2020; 42(6):1547-1578. doi: 10.1007/s11357-020-00272-3.

Kobayashi S, Tamura T, Koshishiba M, Yasumoto T, Shimizu S, Kintaka T, Nagai K. Total Synthesis, Structure Revision, and Neuroprotective Effect of Hericenones C-H and Their Derivatives. J Org Chem. 2021; 86(3):2602-2620. doi: 10.1021/acs.joc.0c02681.

Kogut MH, Lee A, Santin E. Microbiome and pathogen interaction with the immune system. Poult Sci. 2020; 99(4):1906-1913. doi: 10.1016/j.psj.2019.12.011.

Koh SS, Ooi SC, Lui NM, Qiong C, Ho LT, Cheah IK, Halliwell B, Herr DR, Ong WY. Effect of Ergothioneine on 7-Ketocholesterol-Induced Endothelial Injury. Neuromolecular Med. 2021; 23(1):184-198. doi: 10.1007/s12017-020-08620-4.

Konjevod M, Nikolac Perkovic M, Sáiz J, Svob Strac D, Barbas C, Rojo D. Metabolomics analysis of microbiota-gut-brain axis in neurodegenerative and psychiatric diseases. J Pharm Biomed Anal. 2021; 194:113681. doi: 10.1016/j.jpba.2020.113681.

Krzyczkowski W, Malinowska E, Herold F. Erinacine A biosynthesis in submerged cultivation of Hericium erinaceum: Quantification and improved cultivation. Eng Life Sci. 2010; 10:446–457. doi :10.1002/elsc.201000084

Kudryavtseva AV, Krasnov GS, Dmitriev AA, Alekseev BY, Kardymon OL, Sadritdinova AF, Fedorova MS, Pokrovsky AV, Melnikova NV, Kaprin AD, Moskalev AA, Snezhkina AV. Mitochondrial dysfunction and oxidative stress in aging and cancer. Oncotarget. 2016; 7(29):44879-44905. doi: 10.18632/oncotarget.9821.

Kuo HC, Lu CC, Shen CH, Tung SY, Hsieh MC, Lee KC, Lee LY, Chen CC, Teng CC, Huang WS, Chen TC, Lee KF. Hericium erinaceus mycelium and its isolated erinacine A protection from MPTP-induced neurotoxicity through the ER stress, triggering an apoptosis cascade. J Transl Med. 2016; 14:78. doi: 10.1186/s12967-016-0831-y. Retraction in: J Transl Med. 2021 Feb 15; 19(1):67.

Kushairi N, Phan CW, Sabaratnam V, David P, Naidu M. Lion's Mane Mushroom, Hericium erinaceus (Bull.: Fr.) Pers. Suppresses H2O2-Induced Oxidative Damage and LPS-Induced Inflammation in HT22 Hippocampal Neurons and BV2 Microglia. Antioxidants (Basel). 2019 Aug 1;8(8):261. doi: 10.3390/antiox8080261. PMID: 31374912; PMCID: PMC6720269.

La Rosa F, Clerici M, Ratto D, Occhinegro A, Licito A, Romeo M, Iorio CD, Rossi P. The Gut-Brain Axis in Alzheimer's Disease and Omega-3. A Critical Overview of Clinical Trials. Nutrients. 2018; 10(9):1267. doi: 10.3390/nu10091267.

Lai PL, Naidu M, Sabaratnam V, Wong KH, David RP, Kuppusamy UR, Abdullah N, Malek SN. Neurotrophic properties of the Lion's mane medicinal mushroom, Hericium erinaceus (Higher Basidiomycetes) from Malaysia. Int J Med Mushrooms. 2013; 15(6):539-54. doi: 10.1615/intjmedmushr.v15.i6.30.

Lang UE, Borgwardt S. Molecular mechanisms of depression: perspectives on new treatment strategies. Cell Physiol Biochem. 2013;31(6):761-77. doi: 10.1159/000350094. Epub 2013 May 31. PMID: 23735822.

Laubitz D, Typpo K, Midura-Kiela M, Brown C, Barberán A, Ghishan FK, Kiela PR. Dynamics of Gut Microbiota Recovery after Antibiotic Exposure in Young and Old Mice (A Pilot Study). Microorganisms. 2021; 9(3):647. doi: 10.3390/microorganisms9030647.

Lauretani F, Meschi T, Ticinesi A, Maggio M. "Brain-muscle loop" in the fragility of older persons: from pathophysiology to new organizing models. Aging Clin Exp Res. 2017; 29(6):1305-1311. doi: 10.1007/s40520-017-0729-4.

Leal G, Bramham CR, Duarte CB. BDNF and Hippocampal Synaptic Plasticity. Vitam Horm. 2017; 104:153-195. doi: 10.1016/bs.vh.2016.10.004.

Lee DG, Kang HW, Park CG, Ahn YS, Shin Y. Isolation and identification of phytochemicals and biological activities of Hericium ernaceus and

their contents in Hericium strains using HPLC/UV analysis. J Ethnopharmacol. 2016; 184:219-25. doi: 10.1016/j.jep.2016.02.038.

Lee KF, Chen JH, Teng CC, Shen CH, Hsieh MC, Lu CC, Lee KC, Lee LY, Chen WP, Chen CC, Huang WS, Kuo HC. Protective effects of Hericium erinaceus mycelium and its isolated erinacine A against ischemia-injury-induced neuronal cell death via the inhibition of iNOS/p38 MAPK and nitrotyrosine. Int J Mol Sci. 2014; 15(9):15073-89. doi: 10.3390/ijms150915073.

Lee SH, Lee JH, Lee HY, Min KJ. Sirtuin signaling in cellular senescence and aging. BMB Rep. 2019; 52(1):24-34. doi: 10.5483/BMBRep.2019.52.1.290.

Lee WY, Park EJ, Ahn JK, Ka KH. Ergothioneine contents in fruiting bodies and their enhancement in mycelial cultures by the addition of methionine. Mycobiology. 2009 Mar;37(1):43-7. doi: 10.4489/MYCO.2009.37.1.043.

Lehtinen MK, Bonni A. Modeling oxidative stress in the central nervous system. Curr Mol Med. 2006; 6(8):871-81. doi: 10.2174/156652406779010786.

Levy M, Blacher E, Elinav E. Microbiome, metabolites and host immunity. Curr Opin Microbiol. 2017; 35:8-15. doi: 10.1016/j.mib.2016.10.003.

Levy MJF, Boulle F, Steinbusch HW, van den Hove DLA, Kenis G, Lanfumey L. Neurotrophic factors and neuroplasticity pathways in the pathophysiology and treatment of depression. Psychopharmacology (Berl). 2018; 235(8):2195-2220. doi: 10.1007/s00213-018-4950-4.

Ley RE, Turnbaugh PJ, Klein S, Gordon JI. Microbial ecology: human gut microbes associated with obesity. Nature. 2006; 444(7122):1022-3. doi: 10.1038/4441022a.

Li G, Yu K, Li F, Xu K, Li J, He S, Cao S, Tan G. Anticancer potential of Hericium erinaceus extracts against human gastrointestinal cancers. J Ethnopharmacol. 2014; 153(2):521-30. doi: 10.1016/j.jep.2014.03.003.

Li IC, Lee LY, Chen YJ, Chou MY, Wang MF, Chen WP, Chen YP, Chen CC. Erinacine A-enriched Hericium erinaceus mycelia promotes longevity in Drosophila melanogaster and aged mice. PLoS One. 2019; 14(5):e0217226. doi: 10.1371/journal.pone.0217226.

Li IC, Lee LY, Tzeng TT, Chen WP, Chen YP, Shiao YJ, Chen CC. Neurohealth Properties of Hericium erinaceus Mycelia Enriched

with Erinacines. Behav Neurol. 2018; 2018:5802634. doi: 10.1155/2018/5802634. PMID: 29951133; PMCID: PMC5987239.

Li TJ, Lee TY, Lo Y, Lee LY, Li IC, Chen CC, Chang FC. Hericium erinaceus mycelium ameliorate anxiety induced by continuous sleep disturbance in vivo. BMC Complement Med Ther. 2021; 21(1):295. doi: 10.1186/s12906-021-03463-3.

Li W, Zhou W, Kim EJ, Shim SH, Kang HK, Kim YH. Isolation and identification of aromatic compounds in Lion's Mane Mushroom and their anticancer activities. Food Chem. 2015; 170:336-42. doi: 10.1016/j.foodchem.2014.08.078.

Li W, Zhou W, Song SB, Shim SH, Kim YH. Sterol fatty acid esters from the mushroom Hericium erinaceum and their PPAR transactivational effects. J Nat Prod. 2014; 77(12):2611-8. doi: 10.1021/np500234f.

Li Z, Lu G, Luo E, Wu B, Li Z, Guo J, Xia Z, Zheng C, Su Q, Zeng Y, Chan WY, Su X, Qiu X, Zheng X, Cai Q, Xu Y, Chen Y, Fan Y, Chen W, Yu Z, Chen X, Zheng C, Wang M, Poon WS, Luo X. Oral, Nasal, and Gut Microbiota in Parkinson's Disease. Neuroscience. 2022; 480:65-78. doi: 10.1016/j.neuroscience.2021.10.011.

Liang S, Wu X, Hu X, Wang T, Jin F. Recognizing Depression from the Microbiota‾Gut‾Brain Axis. Int J Mol Sci. 2018; 19(6):1592. doi: 10.3390/ijms19061592.

Liddelow SA, Guttenplan KA, Clarke LE, Bennett FC, Bohlen CJ, Schirmer L, Bennett ML, Münch AE, Chung WS, Peterson TC, Wilton DK, Frouin A, Napier BA, Panicker N, Kumar M, Buckwalter MS, Rowitch DH, Dawson VL, Dawson TM, Stevens B, Barres BA. Neurotoxic reactive astrocytes are induced by activated microglia. Nature. 2017; 541(7638):481-487. doi: 10.1038/nature21029.

Liguori I, Russo G, Curcio F, Bulli G, Aran L, Della-Morte D, Gargiulo G, Testa G, Cacciatore F, Bonaduce D, Abete P. Oxidative stress, aging, and diseases. Clin Interv Aging. 2018; 13:757-772. doi: 10.2147/CIA.S158513.

Lin MT, Beal MF. The oxidative damage theory of aging. Clinical Neuroscience Research. 2003. Volume 2, Issues 5–6, 2003, Pages 305-315. doi:10.1016/S1566-2772(03)00007-0.

Lino de Oliveira C, Bolzan JA, Surget A, Belzung C. Do antidepressants promote neurogenesis in adult hippocampus? A systematic review

and meta-analysis on naive rodents. Pharmacol Ther. 2020; 210:107515. doi: 10.1016/j.pharmthera.2020.107515.

Little AR, Benkovic SA, Miller DB, O'Callaghan JP. Chemically induced neuronal damage and gliosis: enhanced expression of the proinflammatory chemokine, monocyte chemoattractant protein (MCP)-1, without a corresponding increase in proinflammatory cytokines(1). Neuroscience. 2002;115(1):307-20. doi: 10.1016/s0306-4522(02)00359-7.

Liu D, Xu Y. p53, oxidative stress, and aging. Antioxid Redox Signal. 2011; 15(6):1669-78. doi: 10.1089/ars.2010.3644.

Liu J, DU C, Wang Y, Yu Z. Anti-fatigue activities of polysaccharides extracted from Hericium erinaceus. Exp Ther Med. 2015; 9(2):483-487. doi: 10.3892/etm.2014.2139.

Liu JH, Li L, Shang XD, Zhang JL, Tan Q. Anti-Helicobacter pylori activity of bioactive components isolated from Hericium erinaceus. J Ethnopharmacol. 2016; 183:54-58. doi: 10.1016/j.jep.2015.09.004.

Liu L, Liu C, Wang Y, Wang P, Li Y, Li B. Herbal Medicine for Anxiety, Depression and Insomnia. Curr Neuropharmacol. 2015; 13(4):481-93. doi: 10.2174/1570159x1304150831122734.

Liu PS, Chueh SH, Chen CC, Lee LY, Shiu LY. Lion's Mane Medicinal Mushroom, Hericium erinaceus (Agaricomycetes), Modulates Purinoceptor-Coupled Calcium Signaling and Murine Nociceptive Behavior. Int J Med Mushrooms. 2017; 19(6):499-507. doi: 10.1615/IntJMedMushrooms.v19.i6.20.

Liu S, Wang J, Zhu D, Fu Y, Lukowiak K, Lu YM. Generation of functional inhibitory neurons in the adult rat hippocampus. J Neurosci. 2003; 23(3):732-6. doi: 10.1523/JNEUROSCI.23-03-00732.2003.

Liu Y, Zhou M, Yang M, Jin C, Song Y, Chen J, Gao M, Ai Z, Su D. *Pulsatilla chinensis* Saponins Ameliorate Inflammation and DSS-Induced Ulcerative Colitis in Rats by Regulating the Composition and Diversity of Intestinal Flora. Front Cell Infect Microbiol. 2021; 11:728929. doi: 10.3389/fcimb.2021.728929.

Lloyd-Price J, Abu-Ali G, Huttenhower C. The healthy human microbiome. Genome Med. 2016; 8(1):51. doi: 10.1186/s13073-016-0307-y.

López-Otín C, Blasco MA, Partridge L, Serrano M, Kroemer G. The hallmarks of aging. Cell. 2013; 153(6):1194-217. doi: 10.1016/j.cell.2013.05.039.

Love MI, Huber W, Anders S. Moderated estimation of fold change and dispersion for RNA-seq data with DESeq2. Genome Biol. 2014; 15(12):550. doi: 10.1186/s13059-014-0550-8.

Lu QQ, Tian JM, Wei J, Gao JM. Bioactive metabolites from the mycelia of the basidiomycete Hericium erinaceum. Nat Prod Res. 2014; 28(16):1288-92. doi: 10.1080/14786419.2014.898145.

Lynch SV, Pedersen O. The Human Intestinal Microbiome in Health and Disease. N Engl J Med. 2016; 375(24):2369-2379. doi: 10.1056/NEJMra1600266.

Ma BJ, Ma JC, Ruan Y. Hericenone L, a new aromatic compound from the fruiting bodies of Hericium erinaceus. Chinese Journal of Natural Medicines. 2012; 10(5):363-365.

Ma BJ; Shen JW, Yu HY, Ruan Y, Wu TT, Zhao, X. Hericenones and erinacines: Stimulators of nerve growth factor (NGF) biosynthesis in Hericium erinaceus.; Hericenones and erinacines: stimulators of nerve growth factor (NGF) biosynthesis in Hericium erinaceus. Mycology. 2013; 1 (2), 92–98. Doi: 10.1080/21501201003735556.

Macchione IG, Lopetuso LR, Ianiro G, Napoli M, Gibiino G, Rizzatti G, Petito V, Gasbarrini A, Scaldaferri F. Akkermansia muciniphila: key player in metabolic and gastrointestinal disorders. Eur Rev Med Pharmacol Sci. 2019; 23(18):8075-8083. doi: 10.26355/eurrev_201909_19024.

Macfarlane S, Macfarlane GT. Regulation of short-chain fatty acid production. Proc Nutr Soc. 2003; 62(1):67-72. doi: 10.1079/PNS2002207.

Majmundar AJ, Wong WJ, Simon MC. Hypoxia-inducible factors and the response to hypoxic stress. Mol Cell. 2010; 40(2):294-309. doi: 10.1016/j.molcel.2010.09.022.

Malberg JE, Eisch AJ, Nestler EJ, Duman RS. Chronic antidepressant treatment increases neurogenesis in adult rat hippocampus. J Neurosci. 2000; 20(24):9104-10. doi: 10.1523/JNEUROSCI.20-24-09104.2000.

Mangiola F, Nicoletti A, Gasbarrini A, Ponziani FR. Gut microbiota and aging. Eur Rev Med Pharmacol Sci. 2018; 22(21):7404-7413. doi: 10.26355/eurrev_201811_16280.

Mariat D, Firmesse O, Levenez F, Guimarães V, Sokol H, Doré J, Corthier G, Furet JP. The Firmicutes/Bacteroidetes ratio of the human

microbiota changes with age. BMC Microbiol. 2009; 9:123. doi: 10.1186/1471-2180-9-123.

Markham JA, McKian KP, Stroup TS, Juraska JM. Sexually dimorphic aging of dendritic morphology in CA1 of hippocampus. Hippocampus. 2005; 15(1):97-103. doi: 10.1002/hipo.20034.

Martin CR, Osadchiy V, Kalani A, Mayer EA. The Brain-Gut-Microbiome Axis. Cell Mol Gastroenterol Hepatol. 2018; 6(2):133-148. doi: 10.1016/j.jcmgh.2018.04.003.

Matthews BR. Memory dysfunction. Continuum (Minneap Minn). 2015; 21(3 Behavioral Neurology and Neuropsychiatry):613-26. doi: 10.1212/01.CON.0000466656.59413.29.

Mattson MP, Maudsley S, Martin B. BDNF and 5-HT: a dynamic duo in age-related neuronal plasticity and neurodegenerative disorders. Trends Neurosci. 2004; 27(10):589-94. doi: 10.1016/j.tins.2004.08.001.

Mayer EA, Tillisch K, Gupta A. Gut/brain axis and the microbiota. J Clin Invest. 2015; 125(3):926-38. doi: 10.1172/JCI76304.

McCay CM, Maynard LA, Sperling G, Barnes LL. The Journal of Nutrition. Volume 18 July--December, 1939. Pages 1--13. Retarded growth, life span, ultimate body size and age changes in the albino rat after feeding diets restricted in calories. Nutr Rev. 1975; 33(8):241-3. doi: 10.1111/j.1753-4887.1975.tb05227.x.

McMurdie PJ, Holmes S. phyloseq: an R package for reproducible interactive analysis and graphics of microbiome census data. PLoS One. 2013; 8(4):e61217. doi: 10.1371/journal.pone.0061217.

Mercier F, Kitasako JT, Hatton GI. Anatomy of the brain neurogenic zones revisited: fractones and the fibroblast/macrophage network. J Comp Neurol. 2002; 451(2):170-88. doi: 10.1002/cne.10342.

Milaneschi Y, Simmons WK, van Rossum EFC, Penninx BW. Depression and obesity: evidence of shared biological mechanisms. Mol Psychiatry. 2019; 24(1):18-33. doi: 10.1038/s41380-018-0017-5.

Misiti F, Castagnola M, Zuppi C, Giardina B, Messana I. Role of ergothioneine on S-nitrosoglutathione catabolism. Biochem J. 2001; 356(Pt 3):799-804. doi: 10.1042/0264-6021:3560799.

Mitchell SJ, Martin-Montalvo A, Mercken EM, Palacios HH, Ward TM, Abulwerdi G, Minor RK, Vlasuk GP, Ellis JL, Sinclair DA, Dawson J, Allison DB, Zhang Y, Becker KG, Bernier M, de Cabo R. The SIRT1

activator SRT1720 extends lifespan and improves health of mice fed a standard diet. Cell Rep. 2014; 6(5):836-43. doi: 10.1016/j.celrep.2014.01.031.

Mitnitski AB, Mogilner AJ, Rockwood K. Accumulation of deficits as a proxy measure of aging. ScientificWorldJournal. 2001; 1:323-36. doi: 10.1100/tsw.2001.58.

Molendijk ML, Haffmans JP, Bus BA, Spinhoven P, Penninx BW, Prickaerts J, Oude Voshaar RC, Elzinga BM. Serum BDNF concentrations show strong seasonal variation and correlations with the amount of ambient sunlight. PLoS One. 2012; 7(11):e48046. doi: 10.1371/journal.pone.0048046.

Monaco A, Ovryn B, Axis J, Amsler K. The Epithelial Cell Leak Pathway. Int J Mol Sci. 2021; 22(14):7677. doi: 10.3390/ijms22147677.

Morgan XC, Segata N, Huttenhower C. Biodiversity and functional genomics in the human microbiome. Trends Genet. 2013; 29(1):51-8. doi: 10.1016/j.tig.2012.09.005.

Mori K, Inatomi S, Ouchi K, Azumi Y, Tuchida T. Improving effects of the mushroom Yamabushitake (Hericium erinaceus) on mild cognitive impairment: a double-blind placebo-controlled clinical trial. Phytother Res. 2009; 23(3):367-72. doi: 10.1002/ptr.2634.

Mori K, Kikuchi H, Obara Y, Iwashita M, Azumi Y, Kinugasa S, Inatomi S, Oshima Y, Nakahata N. Inhibitory effect of hericenone B from Hericium erinaceus on collagen-induced platelet aggregation. Phytomedicine. 2010; 17(14):1082-5. doi: 10.1016/j.phymed.2010.05.004.

Mori K, Obara Y, Hirota M, Azumi Y, Kinugasa S, Inatomi S, Nakahata N. Nerve growth factor-inducing activity of Hericium erinaceus in 1321N1 human astrocytoma cells. Biol Pharm Bull. 2008; 31(9):1727-32. doi: 10.1248/bpb.31.1727.

Morrison DJ, Preston T. Formation of short chain fatty acids by the gut microbiota and their impact on human metabolism. Gut Microbes. 2016; 7(3):189-200. doi: 10.1080/19490976.2015.1134082.

Mukherjee A, Lordan C, Ross RP, Cotter PD. Gut microbes from the phylogenetically diverse genus *Eubacterium* and their various contributions to gut health. Gut Microbes. 2020; 12(1):1802866. doi: 10.1080/19490976.2020.1802866.

Nagano M, Shimizu K, Kondo R, Hayashi C, Sato D, Kitagawa K, Ohnuki K. Reduction of depression and anxiety by 4 weeks Hericium

erinaceus intake. Biomed Res. 2010; 31(4):231-7. doi: 10.2220/biomedres.31.231.

Nagpal R, Mainali R, Ahmadi S, Wang S, Singh R, Kavanagh K, Kitzman DW, Kushugulova A, Marotta F, Yadav H. Gut microbiome and aging: Physiological and mechanistic insights. Nutr Healthy Aging. 2018; 4(4):267-285. doi: 10.3233/NHA-170030.

Naito Y, Uchiyama K, Takagi T. A next-generation beneficial microbe: *Akkermansia muciniphila*. J Clin Biochem Nutr. 2018; 63(1):33-35. doi: 10.3164/jcbn.18-57.

Nakamura T, Sugiura S, Kobayashi D, Yoshida K, Yabuuchi H, Aizawa S, Maeda T, Tamai I. Decreased proliferation and erythroid differentiation of K562 cells by siRNA-induced depression of OCTN1 (SLC22A4) transporter gene. Pharm Res. 2007; 24(9):1628-35. doi: 10.1007/s11095-007-9290-8.

Nechita D, Nechita F, Motorga R. A review of the influence the anxiety exerts on human life. Rom J Morphol Embryol. 2018; 59(4):1045-1051.

Newton IG, Forbes ME, Linville MC, Pang H, Tucker EW, Riddle DR, Brunso-Bechtold JK. Effects of aging and caloric restriction on dentate gyrus synapses and glutamate receptor subunits. Neurobiol Aging. 2008; 29(9):1308-18. doi: 10.1016/j.neurobiolaging.2007.03.009.

Nishiwaki H, Ito M, Ishida T, Hamaguchi T, Maeda T, Kashihara K, Tsuboi Y, Ueyama J, Shimamura T, Mori H, Kurokawa K, Katsuno M, Hirayama M, Ohno K. Meta-Analysis of Gut Dysbiosis in Parkinson's Disease. Mov Disord. 2020; 35(9):1626-1635. doi: 10.1002/mds.28119.

Noh HJ, Yang HH, Kim GS, Lee SE, Lee DY, Choi JH, Kim SY, Lee ES, Ji SH, Kang KS, Park HJ, Kim JR, Kim KH. Chemical constituents of Hericium erinaceum associated with the inhibitory activity against cellular senescence in human umbilical vascular endothelial cells. J Enzyme Inhib Med Chem. 2015; 30(6):934-40. doi: 10.3109/14756366.2014.995181.

Norden DM, Muccigrosso MM, Godbout JP. Microglial priming and enhanced reactivity to secondary insult in aging, and traumatic CNS injury, and neurodegenerative disease. Neuropharmacology. 2015; 96(Pt A):29-41. doi: 10.1016/j.neuropharm.2014.10.028.

Nosofsky RM, Little DR, Donkin C, Fific M. Short-term memory scanning viewed as exemplar-based categorization. Psychol Rev. 2011; 118(2):280-315. doi: 10.1037/a0022494.

Obara Y, Nakahata N. The Signaling Pathway of Neurotrophic Factor Biosynthesis. Drug News Perspect. 2002; 15(5):290-298. doi: 10.1358/dnp.2002.15.5.840042.

Oksanen J, Blanchet FG, Kindt R, Legendre P, Minchin P, O'Hara RB, Simpson G, Solymos P, Stevens MHH, Wagner H. Vegan: community ecology package. R package vegan, vers. 2.2-1. 2015.

Osadchiy V, Martin CR, Mayer EA. The Gut-Brain Axis and the Microbiome: Mechanisms and Clinical Implications. Clin Gastroenterol Hepatol. 2019; 17(2):322-332. doi: 10.1016/j.cgh.2018.10.002.

Otte C, Gold SM, Penninx BW, Pariante CM, Etkin A, Fava M, Mohr DC, Schatzberg AF. Major depressive disorder. Nat Rev Dis Primers. 2016; 2:16065. doi: 10.1038/nrdp.2016.65.

Ou Z, Deng L, Lu Z, Wu F, Liu W, Huang D, Peng Y. Protective effects of Akkermansia muciniphila on cognitive deficits and amyloid pathology in a mouse model of Alzheimer's disease. Nutr Diabetes. 2020; 10(1):12. doi: 10.1038/s41387-020-0115-8.

Palagini L, Cipollone G, Masci I, Novi M, Caruso D, Kalmbach DA, Drake CL. Stress-related sleep reactivity is associated with insomnia, psychopathology and suicidality in pregnant women: preliminary results. Sleep Med. 2019; 56:145-150. doi: 10.1016/j.sleep.2019.01.009.

Palliyaguru DL, Moats JM, Di Germanio C, Bernier M, de Cabo R. Frailty index as a biomarker of lifespan and healthspan: Focus on pharmacological interventions. Mech Ageing Dev. 2019; 180:42-48. doi: 10.1016/j.mad.2019.03.005.

Palmer AL, Ousman SS. Astrocytes and Aging. Front Aging Neurosci. 2018; 10:337. doi: 10.3389/fnagi.2018.00337.

Panda SK, Luyten W. Medicinal mushrooms: Clinical perspective and challenges. Drug Discov Today. 2021, 22:S1359-6446(21)00498-0. doi: 10.1016/j.drudis.2021.11.017.

Parks RJ, Fares E, Macdonald JK, Ernst MC, Sinal CJ, Rockwood K, Howlett SE. A procedure for creating a frailty index based on deficit accumulation in aging mice. J Gerontol A Biol Sci Med Sci. 2012; 67(3):217-27. doi: 10.1093/gerona/glr193.

Patching SG. Glucose Transporters at the Blood-Brain Barrier: Function, Regulation and Gateways for Drug Delivery. Mol Neurobiol. 2017; 54(2):1046-1077. doi: 10.1007/s12035-015-9672-6.

Paul R, Grieve SM, Chaudary B, Gordon N, Lawrence J, Cooper N, Clark CR, Kukla M, Mulligan R, Gordon E. Relative contributions of the cerebellar vermis and prefrontal lobe volumes on cognitive function across the adult lifespan. Neurobiol Aging. 2009; 30(3):457-65. doi: 10.1016/j.neurobiolaging.2007.07.017.

Pedersen BK. Physical activity and muscle-brain crosstalk. Nat Rev Endocrinol. 2019; 15(7):383-392. doi: 10.1038/s41574-019-0174-x.

Peng Z, Zhang C, Yan L, Zhang Y, Yang Z, Wang J, Song C. EPA is More Effective than DHA to Improve Depression-Like Behavior, Glia Cell Dysfunction and Hippcampal Apoptosis Signaling in a Chronic Stress-Induced Rat Model of Depression. Int J Mol Sci. 2020; 21(5):1769. doi: 10.3390/ijms21051769.

Pereira FC, Wasmund K, Cobankovic I, Jehmlich N, Herbold CW, Lee KS, Sziranyi B, Vesely C, Decker T, Stocker R, Warth B, von Bergen M, Wagner M, Berry D. Rational design of a microbial consortium of mucosal sugar utilizers reduces Clostridiodes difficile colonization. Nat Commun. 2020; 11(1):5104. doi: 10.1038/s41467-020-18928-1.

Perez-Muñoz ME, Arrieta MC, Ramer-Tait AE, Walter J. A critical assessment of the "sterile womb" and "in utero colonization" hypotheses: implications for research on the pioneer infant microbiome. Microbiome. 2017; 5(1):48. doi: 10.1186/s40168-017-0268-4.

Phan CW, David P, Naidu M, Wong KH, Sabaratnam V. Therapeutic potential of culinary-medicinal mushrooms for the management of neurodegenerative diseases: diversity, metabolite, and mechanism. Crit Rev Biotechnol. 2015; 35(3):355-68. doi: 10.3109/07388551.2014.887649.

Phan CW, Lee GS, Hong SL, Wong YT, Brklječa R, Urban S, Abd Malek SN, Sabaratnam V. Hericium erinaceus (Bull.: Fr) Pers. cultivated under tropical conditions: isolation of hericenones and demonstration of NGF-mediated neurite outgrowth in PC12 cells via MEK/ERK and PI3K-Akt signaling pathways. Food Funct. 2014; 5(12):3160-9. doi: 10.1039/c4fo00452c.

Piggott DA, Tuddenham S. The gut microbiome and frailty. Transl Res. 2020 Jul;221:23-43. doi: 10.1016/j.trsl.2020.03.012.

Propson NE, Roy ER, Litvinchuk A, Köhl J, Zheng H. Endothelial C3a receptor mediates vascular inflammation and blood-brain barrier permeability during aging. J Clin Invest. 2021; 131(1):e140966. doi: 10.1172/JCI140966.

Prunas A, Sarno I, Preti E, Madeddu F, Perugini M. Psychometric properties of the Italian version of the SCL-90-R: a study on a large community sample. Eur Psychiatry. 2012; 27(8):591-7. doi: 10.1016/j.eurpsy.2010.12.006.

Quast C, Pruesse E, Yilmaz P, Gerken J, Schweer T, Yarza P, Peplies J, Glöckner FO. The SILVA ribosomal RNA gene database project: improved data processing and web-based tools. Nucleic Acids Res. 2013; 41(Database issue):D590-6. doi: 10.1093/nar/gks1219.

Quigley EM. Gut bacteria in health and disease. Gastroenterol Hepatol (N Y). 2013; 9(9):560-9.

Quigley EM. Microbiota-Brain-Gut Axis and Neurodegenerative Diseases. Curr Neurol Neurosci Rep. 2017; 17(12):94. doi: 10.1007/s11910-017-0802-6.

Quinn SR, O'Neill LA. A trio of microRNAs that control Toll-like receptor signalling. Int Immunol. 2011; 23(7):421-5. doi: 10.1093/intimm/dxr034. Epub 2011 Jun 6. PMID: 21652514.

Radi E, Formichi P, Battisti C, Federico A. Apoptosis and oxidative stress in neurodegenerative diseases. J Alzheimers Dis. 2014; 42 Suppl 3:S125-52. doi: 10.3233/JAD-132738.

Rashid M, Zadeh LR, Baradaran B, Molavi O, Ghesmati Z, Sabzichi M, Ramezani F. Up-down regulation of HIF-1α in cancer progression. Gene. 2021; 798:145796. doi: 10.1016/j.gene.2021.145796.

Ratto D, Corana F, Mannucci B, Priori EC, Cobelli F, Roda E, Ferrari B, Occhinegro A, Di Iorio C, De Luca F, Cesaroni V, Girometta C, Bottone MG, Savino E, Kawagishi H, Rossi P. Hericium erinaceus Improves Recognition Memory and Induces Hippocampal and Cerebellar Neurogenesis in Frail Mice during Aging. Nutrients. 2019; 11(4):715. doi: 10.3390/nu11040715.

Rea IM, Gibson DS, McGilligan V, McNerlan SE, Alexander HD, Ross OA. Age and Age-Related Diseases: Role of Inflammation Triggers and Cytokines. Front Immunol. 2018; 9:586. doi: 10.3389/fimmu.2018.00586.

Ren T, Gao Y, Qiu Y, Jiang S, Zhang Q, Zhang J, Wang L, Zhang Y, Wang L, Nie K. Gut Microbiota Altered in Mild Cognitive Impairment

Compared With Normal Cognition in Sporadic Parkinson's Disease. Front Neurol. 2020; 11:137. doi: 10.3389/fneur.2020.00137.

Rhodes S, Greene NR, Naveh-Benjamin M. Age-related differences in recall and recognition: a meta-analysis. Psychon Bull Rev. 2019; 26(5):1529-1547. doi: 10.3758/s13423-019-01649-y.

Rietze R, Poulin P, Weiss S. Mitotically active cells that generate neurons and astrocytes are present in multiple regions of the adult mouse hippocampus. J Comp Neurol. 2000; 424(3):397-408.

Rinninella E, Raoul P, Cintoni M, Franceschi F, Miggiano GAD, Gasbarrini A, Mele MC. What is the Healthy Gut Microbiota Composition? A Changing Ecosystem across Age, Environment, Diet, and Diseases. Microorganisms. 2019; 7(1):14. doi: 10.3390/microorganisms7010014.

Robbins PD, Jurk D, Khosla S, Kirkland JL, LeBrasseur NK, Miller JD, Passos JF, Pignolo RJ, Tchkonia T, Niedernhofer LJ. Senolytic Drugs: Reducing Senescent Cell Viability to Extend Health Span. Annu Rev Pharmacol Toxicol. 2021; 61:779-803. doi: 10.1146/annurev-pharmtox-050120-105018.

Robertson DA, Savva GM, Kenny RA. Frailty and cognitive impairment-- a review of the evidence and causal mechanisms. Ageing Res Rev. 2013; 12(4):840-51. doi: 10.1016/j.arr.2013.06.004.

Rockwood K, Blodgett JM, Theou O, Sun MH, Feridooni HA, Mitnitski A, Rose RA, Godin J, Gregson E, Howlett SE. A Frailty Index Based On Deficit Accumulation Quantifies Mortality Risk in Humans and in Mice. Sci Rep. 2017 Feb 21;7:43068. doi: 10.1038/srep43068. PMID: 28220898; PMCID: PMC5318852.

Rockwood K, Mitnitski A. Frailty in relation to the accumulation of deficits. J Gerontol A Biol Sci Med Sci. 2007; 62(7):722-7. doi: 10.1093/gerona/62.7.722.

Roda E, Priori EC, Ratto D, De Luca F, Di Iorio C, Angelone P, Locatelli CA, Desiderio A, Goppa L, Savino E, Bottone MG, Rossi P. Neuroprotective Metabolites of Hericium erinaceus Promote Neuro-Healthy Aging. Int J Mol Sci. 2021; 22(12):6379. doi: 10.3390/ijms22126379.

Rodrigues DMF, Freitas AC, Rocha-Santos TAP, Vasconcelos MW, Roriz M, Rodríguez-Alcalá LM, Gomes AMP, Duarte AC. Chemical composition and nutritive value of *Pleurotus citrinopileatus var cornucopiae, P. eryngii, P. salmoneo stramineus, Pholiota nameko*

and *Hericium erinaceus*. J Food Sci Technol. 2015; 52:6927–6939. doi: 10.1007/s13197-015-1826-z

Rogers J, Zornetzer SF, Bloom FE, Mervis RE. Senescent microstructural changes in rat cerebellum. Brain Res. 1984; 292(1):23-32. doi: 10.1016/0006-8993(84)90886-2.

Rossi P, Cesaroni V, Brandalise F, Occhinegro A, Ratto D, Perrucci F, Lanaia V, Girometta C, Orrù G, Savino E. Dietary Supplementation of Lion's Mane Medicinal Mushroom, Hericium erinaceus (Agaricomycetes), and Spatial Memory in Wild-Type Mice. Int J Med Mushrooms. 2018; 20(5):485-494. doi: 10.1615/IntJMedMushrooms.2018026241.

Ruan Q, D'Onofrio G, Sancarlo D, Greco A, Lozupone M, Seripa D, Panza F, Yu Z. Emerging biomarkers and screening for cognitive frailty. Aging Clin Exp Res. 2017; 29(6):1075-1086. doi: 10.1007/s40520-017-0741-8.

Ruan Q, Yu Z, Chen M, Bao Z, Li J, He W. Cognitive frailty, a novel target for the prevention of elderly dependency. Ageing Res Rev. 2015 Mar;20:1-10. doi: 10.1016/j.arr.2014.12.004. Epub 2014 Dec 30. PMID: 25555677.

Rufini A, Tucci P, Celardo I, Melino G. Senescence and aging: the critical roles of p53. Oncogene. 2013; 32(43):5129-43. doi: 10.1038/onc.2012.640.

Ryu S, Kim HG, Kim JY, Kim SY, Cho KO. Hericium erinaceus Extract Reduces Anxiety and Depressive Behaviors by Promoting Hippocampal Neurogenesis in the Adult Mouse Brain. J Med Food. 2018; 21(2):174-180. doi: 10.1089/jmf.2017.4006.

Sadighi Akha AA. Aging and the immune system: An overview. J Immunol Methods. 2018; 463:21-26. doi: 10.1016/j.jim.2018.08.005.

Saitsu Y, Nishide A, Kikushima K, Shimizu K, Ohnuki K. Improvement of cognitive functions by oral intake of Hericium erinaceus. Biomed Res. 2019; 40(4):125-131. doi: 10.2220/biomedres.40.125.

Salazar N, Arboleya S, Valdés L, Stanton C, Ross P, Ruiz L, Gueimonde M, de Los Reyes-Gavilán CG. The human intestinal microbiome at extreme ages of life. Dietary intervention as a way to counteract alterations. Front Genet. 2014; 5:406. doi: 10.3389/fgene.2014.00406.

Salazar N, Valdés-Varela L, González S, Gueimonde M, de Los Reyes-Gavilán CG. Nutrition and the gut microbiome in the elderly. Gut Microbes. 2017; 8(2):82-97. doi: 10.1080/19490976.2016.1256525.

Salim S. Oxidative Stress and the Central Nervous System. J Pharmacol Exp Ther. 2017 ;360(1):201-205. doi: 10.1124/jpet.116.237503.

Salvucci E. The human-microbiome superorganism and its modulation to restore health. Int J Food Sci Nutr. 2019; 70(7):781-795. doi: 10.1080/09637486.2019.1580682.

Samuel P, Tsapekos M, de Pedro N, Liu AG, Casey Lippmeier J, Chen S. Ergothioneine Mitigates Telomere Shortening under Oxidative Stress Conditions. J Diet Suppl. 2020;1-14. doi: 10.1080/19390211.2020.1854919.

Sandhu KV, Sherwin E, Schellekens H, Stanton C, Dinan TG, Cryan JF. Feeding the microbiota-gut-brain axis: diet, microbiome, and neuropsychiatry. Transl Res. 2017; 179:223-244. doi: 10.1016/j.trsl.2016.10.002.

Santoro A, Ostan R, Candela M, Biagi E, Brigidi P, Capri M, Franceschi C. Gut microbiota changes in the extreme decades of human life: a focus on centenarians. Cell Mol Life Sci. 2018; 75(1):129-148. doi: 10.1007/s00018-017-2674-y.

Sarkar A, Lehto SM, Harty S, Dinan TG, Cryan JF, Burnet PWJ. Psychobiotics and the Manipulation of Bacteria-Gut-Brain Signals. Trends Neurosci. 2016; 39(11):763-781. doi: 10.1016/j.tins.2016.09.002.

Saurman V, Margolis KG, Luna RA. Autism Spectrum Disorder as a Brain-Gut-Microbiome Axis Disorder. Dig Dis Sci. 2020; 65(3):818-828. doi: 10.1007/s10620-020-06133-5.

Scott KA, Ida M, Peterson VL, Prenderville JA, Moloney GM, Izumo T, Murphy K, Murphy A, Ross RP, Stanton C, Dinan TG, Cryan JF. Revisiting Metchnikoff: Age-related alterations in microbiota-gut-brain axis in the mouse. Brain Behav Immun. 2017; 65:20-32. doi: 10.1016/j.bbi.2017.02.004.

Sharma AN, da Costa e Silva BF, Soares JC, Carvalho AF, Quevedo J. Role of trophic factors GDNF, IGF-1 and VEGF in major depressive disorder: A comprehensive review of human studies. J Affect Disord. 2016; 197:9-20. doi: 10.1016/j.jad.2016.02.067.

Sharma R. Emerging Interrelationship Between the Gut Microbiome and Cellular Senescence in the Context of Aging and Disease:

Perspectives and Therapeutic Opportunities. Probiotics Antimicrob Proteins. 2022: 1–16. doi: 10.1007/s12602-021-09903-3.

Shenghua P, Ziqin Z, Shuyu T, Huixia Z, Xianglu R, Jiao G. An integrated fecal microbiome and metabolome in the aged mice reveal anti-aging effects from the intestines and biochemical mechanism of FuFang zhenshu TiaoZhi(FTZ). Biomed Pharmacother. 2020; 121:109421. doi: 10.1016/j.biopha.2019.109421.

Shenker JI, Singh G. Sleep and Dementia. Mo Med. 2017; 114(4):311-315.

Shieh JC, Huang PT, Lin YF. Alzheimer's Disease and Diabetes: Insulin Signaling as the Bridge Linking Two Pathologies. Mol Neurobiol. 2020; 57(4):1966-1977. doi: 10.1007/s12035-019-01858-5.

Shimada A, Tsuzuki M, Keino H, Satoh M, Chiba Y, Saitoh Y, Hosokawa M. Apical vulnerability to dendritic retraction in prefrontal neurones of ageing SAMP10 mouse: a model of cerebral degeneration. Neuropathol Appl Neurobiol. 2006; 32(1):1-14. doi: 10.1111/j.1365-2990.2006.00632.x.

Shimbo M, Kawagishi H, Yokogoshi H. Erinacvine A increases catecholamine and nerve growth factor content in the central nervous system of rats. Nutrition Research. 2005; 25:617-623. doi:10.1016/J.NUTRES.2005.06.001

Shortt C, Hasselwander O, Meynier A, Nauta A, Fernández EN, Putz P, Rowland I, Swann J, Türk J, Vermeiren J, Antoine JM. Systematic review of the effects of the intestinal microbiota on selected nutrients and non-nutrients. Eur J Nutr. 2018; 57(1):25-49. doi: 10.1007/s00394-017-1546-4.

Shrager Y, Bayley PJ, Bontempi B, Hopkins RO, Squire LR. Spatial memory and the human hippocampus. Proc Natl Acad Sci U S A. 2007; 104(8):2961-6. doi: 10.1073/pnas.0611233104.

Sibai M, Altuntaş E, Yıldırım B, Öztürk G, Yıldırım S, Demircan T. Microbiome and Longevity: High Abundance of Longevity-Linked Muribaculaceae in the Gut of the Long-Living Rodent *Spalax leucodon*. OMICS. 2020; 24(10):592-601. doi: 10.1089/omi.2020.0116.

Sikora E, Bielak-Zmijewska A, Dudkowska M, Krzystyniak A, Mosieniak G, Wesierska M, Wlodarczyk J. Cellular Senescence in Brain Aging. Front Aging Neurosci. 2021; 13:646924. doi: 10.3389/fnagi.2021.646924.

Sikora E, Bielak-Żmijewska A, Mosieniak G. What is and what is not cell senescence. Postepy Biochem. 2018; 64(2):110-118. English. doi: 10.18388/pb.2018_120.

Silva YP, Bernardi A, Frozza RL. The Role of Short-Chain Fatty Acids From Gut Microbiota in Gut-Brain Communication. Front Endocrinol (Lausanne). 2020; 11:25. doi: 10.3389/fendo.2020.00025.

Simen AA, Bordner KA, Martin MP, Moy LA, Barry LC. Cognitive dysfunction with aging and the role of inflammation. Ther Adv Chronic Dis. 2011; 2(3):175-95. doi: 10.1177/2040622311399145.

Singhal G, Morgan J, Jawahar MC, Corrigan F, Jaehne EJ, Toben C, Breen J, Pederson SM, Manavis J, Hannan AJ, Baune BT. Effects of aging on the motor, cognitive and affective behaviors, neuroimmune responses and hippocampal gene expression. Behav Brain Res. 2020; 383:112501. doi: 10.1016/j.bbr.2020.112501.

Smith BJ, Miller RA, Ericsson AC, Harrison DC, Strong R, Schmidt TM. Changes in the gut microbiome and fermentation products concurrent with enhanced longevity in acarbose-treated mice. BMC Microbiol. 2019; 19(1):130. doi: 10.1186/s12866-019-1494-7.

Snyder JS, Choe JS, Clifford MA, Jeurling SI, Hurley P, Brown A, Kamhi JF, Cameron HA. Adult-born hippocampal neurons are more numerous, faster maturing, and more involved in behavior in rats than in mice. J Neurosci. 2009; 29(46):14484-95. doi: 10.1523/JNEUROSCI.1768-09.2009.

Soczynska JK, Kennedy SH, Woldeyohannes HO, Liauw SS, Alsuwaidan M, Yim CY, McIntyre RS. Mood disorders and obesity: understanding inflammation as a pathophysiological nexus. Neuromolecular Med. 2011; 13(2):93-116. doi: 10.1007/s12017-010-8140-8.

Song TY, Chen CL, Liao JW, Ou HC, Tsai MS. Ergothioneine protects against neuronal injury induced by cisplatin both in vitro and in vivo. Food Chem Toxicol. 2010; 48(12):3492-9. doi: 10.1016/j.fct.2010.09.030.

Song TY, Lin HC, Chen CL, Wu JH, Liao JW, Hu ML. Ergothioneine and melatonin attenuate oxidative stress and protect against learning and memory deficits in C57BL/6J mice treated with D-galactose. Free Radic Res. 2014; 48(9):1049-60. doi: 10.3109/10715762.2014.920954.

Sparkman NL, Johnson RW. Neuroinflammation associated with aging sensitizes the brain to the effects of infection or stress. Neuroimmunomodulation. 2008; 15(4-6):323-30. doi: 10.1159/000156474.

Squire LR, Dede AJ. Conscious and unconscious memory systems. Cold Spring Harb Perspect Biol. 2015; 7(3):a021667. doi: 10.1101/cshperspect.a021667.

Squire LR. Memory systems of the brain: a brief history and current perspective. Neurobiol Learn Mem. 2004; 82(3):171-7. doi: 10.1016/j.nlm.2004.06.005.

Stadlbauer V, Engertsberger L, Komarova I, Feldbacher N, Leber B, Pichler G, Fink N, Scarpatetti M, Schippinger W, Schmidt R, Horvath A. Dysbiosis, gut barrier dysfunction and inflammation in dementia: a pilot study. BMC Geriatr. 2020; 20(1):248. doi: 10.1186/s12877-020-01644-2.

Stampfli AR, Blankenfeldt W, Seebeck FP. Structural basis of ergothioneine biosynthesis. Curr Opin Struct Biol. 2020; 65:1-8. doi: 10.1016/j.sbi.2020.04.002.

Stanojlovic M, Pallais Yllescas JP Jr, Mavanji V, Kotz C. Chemogenetic activation of orexin/hypocretin neurons ameliorates aging-induced changes in behavior and energy expenditure. Am J Physiol Regul Integr Comp Physiol. 2019; 316(5):R571-R583. doi: 10.1152/ajpregu.00383.2018.

Stedenfeld KA, Clinton SM, Kerman IA, Akil H, Watson SJ, Sved AF. Novelty-seeking behavior predicts vulnerability in a rodent model of depression. Physiol Behav. 2011; 103(2):210-6. doi: 10.1016/j.physbeh.2011.02.001.

Sternberg SA, Wershof Schwartz A, Karunananthan S, Bergman H, Mark Clarfield A. The identification of frailty: a systematic literature review. J Am Geriatr Soc. 2011; 59(11):2129-38. doi: 10.1111/j.1532-5415.2011.03597.x.

Suganya K, Koo BS. Gut-Brain Axis: Role of Gut Microbiota on Neurological Disorders and How Probiotics/Prebiotics Beneficially Modulate Microbial and Immune Pathways to Improve Brain Functions. Int J Mol Sci. 2020 Oct 13;21(20):7551. doi: 10.3390/ijms21207551. PMID: 33066156; PMCID: PMC7589356.

Tabas I, Glass CK. Anti-Inflammatory Therapy in Chronic Disease: Challenges and Opportunities. Science. 2013; 339:166–72. doi:10.1126/science.1230720.

Taliaz D, Stall N, Dar DE, Zangen A. Knockdown of brain-derived neurotrophic factor in specific brain sites precipitates behaviors associated with depression and reduces neurogenesis. Mol Psychiatry. 2010; 15(1):80-92. doi: 10.1038/mp.2009.67.

Tamburini S, Shen N, Wu HC, Clemente JC. The microbiome in early life: implications for health outcomes. Nat Med. 2016 Jul 7;22(7):713-22. doi: 10.1038/nm.4142. PMID: 27387886.

Tang RMY, Cheah IK, Yew TSK, Halliwell B. Distribution and accumulation of dietary ergothioneine and its metabolites in mouse tissues. Sci Rep. 2018; 8(1):1601. doi: 10.1038/s41598-018-20021-z.

Teng HK, Teng KK, Lee R, Wright S, Tevar S, Almeida RD, Kermani P, Torkin R, Chen ZY, Lee FS, Kraemer RT, Nykjaer A, Hempstead BL. ProBDNF induces neuronal apoptosis via activation of a receptor complex of p75NTR and sortilin. J Neurosci. 2005; 25(22):5455-63. doi: 10.1523/JNEUROSCI.5123-04.2005.

Ticinesi A, Nouvenne A, Cerundolo N, Catania P, Prati B, Tana C, Meschi T. Gut Microbiota, Muscle Mass and Function in Aging: A Focus on Physical Frailty and Sarcopenia. Nutrients. 2019; 11(7):1633. doi: 10.3390/nu11071633.

Ticinesi A, Tana C, Nouvenne A, Prati B, Lauretani F, Meschi T. Gut microbiota, cognitive frailty and dementia in older individuals: a systematic review. Clin Interv Aging. 2018; 13:1497-1511. doi: 10.2147/CIA.S139163.

Toda T, Parylak SL, Linker SB, Gage FH. The role of adult hippocampal neurogenesis in brain health and disease. Mol Psychiatry. 2019 Jan;24(1):67-87. doi: 10.1038/s41380-018-0036-2.

Tovote P, Fadok JP, Lüthi A. Neuronal circuits for fear and anxiety. Nat Rev Neurosci. 2015; 16(6):317-31. doi: 10.1038/nrn3945.

Truschel Jessica. Depression Definition and DSM-5 Diagnostic Criteria. Psycom. 2020. https://www.psycom.net/depression-definition-dsm-5-diagnostic-criteria/

Tsai-Teng T, Chin-Chu C, Li-Ya L, Wan-Ping C, Chung-Kuang L, Chien-Chang S, Chi-Ying HF, Chien-Chih C, Shiao YJ. Erinacine A-enriched Hericium erinaceus mycelium ameliorates Alzheimer's

disease-related pathologies in APPswe/PS1dE9 transgenic mice. J Biomed Sci. 2016; 23(1):49. doi: 10.1186/s12929-016-0266-z.

Turnbaugh PJ, Ley RE, Hamady M, Fraser-Liggett CM, Knight R, Gordon JI. The human microbiome project. Nature. 2007; 449(7164):804-10. doi: 10.1038/nature06244.

Turner DA, Deupree DL. Functional elongation of CA1 hippocampal neurons with aging in Fischer 344 rats. Neurobiol Aging. 1991; 12(3):201-10. doi: 10.1016/0197-4580(91)90098-5.

Turriziani P, Serra L, Fadda L, Caltagirone C, Carlesimo GA. Recollection and familiarity in hippocampal amnesia. Hippocampus. 2008; 18(5):469-80. doi: 10.1002/hipo.20412.

Tzeng TT, Chen CC, Chen CC, Tsay HJ, Lee LY, Chen WP, Shen CC, Shiao YJ. The Cyanthin Diterpenoid and Sesterterpene Constituents of Hericium erinaceus Mycelium Ameliorate Alzheimer's Disease-Related Pathologies in APP/PS1 Transgenic Mice. Int J Mol Sci. 2018 Feb 17;19(2):598. doi: 10.3390/ijms19020598. PMID: 29463001; PMCID: PMC5855820.

Urbán N, Guillemot F. Neurogenesis in the embryonic and adult brain: same regulators, different roles. Front Cell Neurosci. 2014; 8:396. doi: 10.3389/fncel.2014.00396.

Ursell LK, Clemente JC, Rideout JR, Gevers D, Caporaso JG, Knight R. The interpersonal and intrapersonal diversity of human-associated microbiota in key body sites. J Allergy Clin Immunol. 2012 May;129(5):1204-8. doi: 10.1016/j.jaci.2012.03.010.

van der Lugt B, Rusli F, Lute C, Lamprakis A, Salazar E, Boekschoten MV, Hooiveld GJ, Müller M, Vervoort J, Kersten S, Belzer C, Kok DEG, Steegenga WT. Integrative analysis of gut microbiota composition, host colonic gene expression and intraluminal metabolites in aging C57BL/6J mice. Aging (Albany NY). 2018; 10(5):930-950. doi: 10.18632/aging.101439.

Van Gylswyk NO, van der Toorn JJTK. Eubacterium uniforme sp. nov. and Eubacterium xylanophilum sp. nov., Fiber-Digesting Bacteria from the Rumina of Sheep Fed Corn Stover. INTERNATIONAL JOURNAL OF SYSTEMATIC BACTERIOLOgy. 1985; 35(3): 323-6. doi.org/10.1099/00207713-35-3-323

van Tol MJ, van der Wee NJ, van den Heuvel OA, Nielen MM, Demenescu LR, Aleman A, Renken R, van Buchem MA, Zitman FG, Veltman DJ. Regional brain volume in depression and anxiety disorders.

Arch Gen Psychiatry. 2010; 67(10):1002-11. doi: 10.1001/archgenpsychiatry.2010.121.

van Tongeren SP, Slaets JP, Harmsen HJ, Welling GW. Fecal microbiota composition and frailty. Appl Environ Microbiol. 2005; 71(10):6438-42. doi: 10.1128/AEM.71.10.6438-6442.2005.

Vatner SF, Zhang J, Oydanich M, Berkman T, Naftalovich R, Vatner DE. Healthful aging mediated by inhibition of oxidative stress. Ageing Res Rev. 2020; 64:101194. doi: 10.1016/j.arr.2020.101194.

Vázquez E, Barranco A, Ramírez M, Gruart A, Delgado-García JM, Martínez-Lara E, Blanco S, Martín MJ, Castanys E, Buck R, Prieto P, Rueda R. Effects of a human milk oligosaccharide, 2'-fucosyllactose, on hippocampal long-term potentiation and learning capabilities in rodents. J Nutr Biochem. 2015; 26(5):455-65. doi: 10.1016/j.jnutbio.2014.11.016.

Vigna L, Morelli F, Agnelli GM, Napolitano F, Ratto D, Occhinegro A, Di Iorio C, Savino E, Girometta C, Brandalise F, Rossi P. Hericium erinaceus Improves Mood and Sleep Disorders in Patients Affected by Overweight or Obesity: Could Circulating Pro-BDNF and BDNF Be Potential Biomarkers? Evid Based Complement Alternat Med. 2019; 2019:7861297. doi: 10.1155/2019/7861297.

Vilar M, Mira H. Regulation of Neurogenesis by Neurotrophins during Adulthood: Expected and Unexpected Roles. Front Neurosci. 2016 Feb 9;10:26. doi: 10.3389/fnins.2016.00026. PMID: 26903794; PMCID: PMC4746328.

Visentin APV, Colombo R, Scotton E, Fracasso DS, da Rosa AR, Branco CS, Salvador M. Targeting Inflammatory-Mitochondrial Response in Major Depression: Current Evidence and Further Challenges. Oxid Med Cell Longev. 2020;2 020:2972968. doi: 10.1155/2020/2972968.

von Bernhardi R, Eugenín-von Bernhardi L, Eugenín J. Microglial cell dysregulation in brain aging and neurodegeneration. Front Aging Neurosci. 2015 Jul 20;7:124. doi: 10.3389/fnagi.2015.00124. PMID: 26257642; PMCID: PMC4507468.

von Bohlen Und Halbach O, von Bohlen Und Halbach V. BDNF effects on dendritic spine morphology and hippocampal function. Cell Tissue Res. 2018; 373(3):729-741. doi: 10.1007/s00441-017-2782-x.

Wang HX, Ng TB. A new laccase from dried fruiting bodies of the monkey head mushroom Hericium erinaceum. Biochem Biophys Res Commun. 2004; 322(1):17-21. doi: 10.1016/j.bbrc.2004.07.075.

Wang HX, Wang YP. Gut Microbiota-brain Axis. Chin Med J (Engl). 2016; 129(19):2373-80. doi: 10.4103/0366-6999.190667.

Wang M, Gao Y, Xu D, Konishi T, Gao Q. Hericium erinaceus (Yamabushitake): a unique resource for developing functional foods and medicines. Food Funct. 2014; 5(12):3055-64. doi: 10.1039/c4fo00511b.

Wang X, Wang W, Li L, Perry G, Lee HG, Zhu X. Oxidative stress and mitochondrial dysfunction in Alzheimer's disease. Biochim Biophys Acta. 2014; 1842(8):1240-7. doi: 10.1016/j.bbadis.2013.10.015.

Wang XY, Yin JY, Zhao MM, Liu SY, Nie SP, Xie MY. Gastroprotective activity of polysaccharide from Hericium erinaceus against ethanol-induced gastric mucosal lesion and pylorus ligation-induced gastric ulcer, and its antioxidant activities. Carbohydr Polym. 2018; 186:100-109. doi: 10.1016/j.carbpol.2018.01.004.

Wang Y, Nan X, Zhao Y, Jiang L, Wang H, Zhang F, Hua D, Liu J, Yao J, Yang L, Luo Q, Xiong B. Dietary Supplementation of Inulin Ameliorates Subclinical Mastitis via Regulation of Rumen Microbial Community and Metabolites in Dairy Cows. Microbiol Spectr. 2021; 9(2):e0010521. doi: 10.1128/Spectrum.00105-21.

Wasser SP. Medicinal Mushrooms in Human Clinical Studies. Part I. Anticancer, Oncoimmunological, and Immunomodulatory Activities: A Review. Int J Med Mushrooms. 2017; 19(4):279-317. doi: 10.1615/IntJMedMushrooms.v19.i4.10.

Wen J, Wang Y, Yuan M, Huang Z, Zou Q, Pu Y, Zhao B, Cai Z. Role of mismatch repair in aging. Int J Biol Sci. 2021; 17(14):3923-3935. doi: 10.7150/ijbs.64953.

Wingo T, Nesil T, Choi JS, Li MD. Novelty Seeking and Drug Addiction in Humans and Animals: From Behavior to Molecules. J Neuroimmune Pharmacol. 2016; 11(3): 456-70. doi: 10.1007/s11481-015-9636-7.

Wolf SA, Boddeke HW, Kettenmann H. Microglia in Physiology and Disease. Annu Rev Physiol. 2017; 79:619-643. doi: 10.1146/annurev-physiol-022516-034406.

Wong KH, Naidu M, David P, Abdulla MA, Abdullah N, Kuppusamy UR, Sabaratnam V. Peripheral Nerve Regeneration Following Crush Injury to Rat Peroneal Nerve by Aqueous Extract of Medicinal

Mushroom Hericium erinaceus (Bull.: Fr) Pers. (Aphyllophoromycetideae). Evid Based Complement Alternat Med. 2011; 2011:580752. doi: 10.1093/ecam/neq062. Epub 2011 Aug 11. Erratum in: Evid Based Complement Alternat Med. 2018 Dec 16;2018:9820769.

Wu L, Zinellu A, Milanesi L, Rubino S, Kelvin D, Carru C. Gut Microbiota Pattern of Centenarians. Centenarians an example of positive biology. Springer Nature Switzerland AG. 2019. doi:10.1007/978-3-030-20762-5_9.

Wu MR, Chou TS, Huang CY, Hsiao JK. A potential probiotic-Lachnospiraceae NK4A136 group: Evidence from the restoration of the dietary pattern from a high-fat diet. Research Square. 2020, preprint. doi:10.21203/rs.3.rs-48913/v1

Wu T, Xu B. Antidiabetic and antioxidant activities of eight medicinal mushroom species from China. Int J Med Mushrooms. 2015; 17(2):129-40. doi: 10.1615/intjmedmushrooms.v17.i2.40.

Wu X, George RL, Huang W, Wang H, Conway SJ, Leibach FH, Ganapathy V. Structural and functional characteristics and tissue distribution pattern of rat OCTN1, an organic cation transporter, cloned from placenta. Biochim Biophys Acta. 2000; 1466(1-2):315-27. doi: 10.1016/s0005-2736(00)00189-9.

www.gbif.org

Xie Z, Chen F, Li WA, Geng X, Li C, Meng X, Feng Y, Liu W, Yu F. A review of sleep disorders and melatonin. Neurol Res. 2017; 39(6):559-565. doi: 10.1080/01616412.2017.1315864.

Xue QL. The frailty syndrome: definition and natural history. Clin Geriatr Med. 2011; 27(1):1-15. doi: 10.1016/j.cger.2010.08.009.

Yang F, Je HS, Ji Y, Nagappan G, Hempstead B, Lu B. Pro-BDNF-induced synaptic depression and retraction at developing neuromuscular synapses. J Cell Biol. 2009; 185(4):727-41. doi: 10.1083/jcb.200811147.

Yang NC, Lin HC, Wu JH, Ou HC, Chai YC, Tseng CY, Liao JW, Song TY. Ergothioneine protects against neuronal injury induced by β-amyloid in mice. Food Chem Toxicol. 2012; 50(11):3902-11. doi: 10.1016/j.fct.2012.08.021.

Yang XD, Wang LK, Wu HY, Jiao L. Effects of prebiotic galacto-oligosaccharide on postoperative cognitive dysfunction and

neuroinflammation through targeting of the gut-brain axis. BMC Anesthesiol. 2018; 18(1):177. doi: 10.1186/s12871-018-0642-1.

Yang Y, Zhao C, Diao M, Zhong S, Sun M, Sun B, Ye H, Zhang T. The Prebiotic Activity of Simulated Gastric and Intestinal Digesta of Polysaccharides from the Hericium erinaceus. Molecules. 2018; 23(12):3158. doi: 10.3390/molecules23123158.

Yu Q, Dong L, Li Y, Liu G. SIRT1 and HIF1α signaling in metabolism and immune responses. Cancer Lett. 2018; 418:20-26. doi: 10.1016/j.canlet.2017.12.035.

Zanos P, Gould TD. Mechanisms of ketamine action as an antidepressant. Mol Psychiatry. 2018; 23(4):801-811. doi: 10.1038/mp.2017.255.

Zhang F, Wu C, Jia C, Gao K, Wang J, Zhao H, Wang W, Chen J. Artificial intelligence based discovery of the association between depression and chronic fatigue syndrome. J Affect Disord. 2019; 250:380-390. doi: 10.1016/j.jad.2019.03.011.

Zhang H, Petit GH, Gaughwin PM, Hansen C, Ranganathan S, Zuo X, Smith R, Roybon L, Brundin P, Mobley WC, Li JY. NGF rescues hippocampal cholinergic neuronal markers, restores neurogenesis, and improves the spatial working memory in a mouse model of Huntington's Disease. J Huntingtons Dis. 2013; 2(1):69-82. doi: 10.3233/JHD-120026.

Zhang J, An S, Hu W, Teng M, Wang X, Qu Y, Liu Y, Yuan Y, Wang D. The Neuroprotective Properties of Hericium erinaceus in Glutamate-Damaged Differentiated PC12 Cells and an Alzheimer's Disease Mouse Model. Int J Mol Sci. 2016; 17(11):1810. doi: 10.3390/ijms17111810.

Zhang P, Kishimoto Y, Grammatikakis I, Gottimukkala K, Cutler RG, Zhang S, Abdelmohsen K, Bohr VA, Misra Sen J, Gorospe M, Mattson MP. Senolytic therapy alleviates Aβ-associated oligodendrocyte progenitor cell senescence and cognitive deficits in an Alzheimer's disease model. Nat Neurosci. 2019; 22(5):719-728. doi: 10.1038/s41593-019-0372-9.

Zhang T, Yang Y, Liang Y, Jiao X, Zhao C. Beneficial Effect of Intestinal Fermentation of Natural Polysaccharides. Nutrients. 2018; 10(8):1055. doi: 10.3390/nu10081055.

Zhang Z, Lv G, Pan H, Pandey A, He W, Fan L. Antioxidant and hepatoprotective potential of endo-polysaccharides from Hericium

erinaceus grown on tofu whey. Int J Biol Macromol. 2012; 51(5):1140-6. doi: 10.1016/j.ijbiomac.2012.09.002.

Zhao JD, Li Y, Sun M, Yu CJ, Li JY, Wang SH, Yang D, Guo CL, Du X, Zhang WJ, Cheng RD, Diao XC, Fang ZH. Effect of berberine on hyperglycaemia and gut microbiota composition in type 2 diabetic Goto-Kakizaki rats. World J Gastroenterol. 2021; 27(8):708-724. doi: 10.3748/wjg.v27.i8.708.

Zhao M, Tuo H, Wang S, Zhao L. The Effects of Dietary Nutrition on Sleep and Sleep Disorders. Mediators Inflamm. 2020; 2020:3142874. doi: 10.1155/2020/3142874.

Zhou Y, Wang Y, Quan M, Zhao H, Jia J. Gut Microbiota Changes and Their Correlation with Cognitive and Neuropsychiatric Symptoms in Alzheimer's Disease. J Alzheimers Dis. 2021;81(2):583-595. doi: 10.3233/JAD-201497.

Ziv I, Melamed E. Editorial: apoptosis in the aging brain. Apoptosis. 2010; 15(11):1285-91. doi: 10.1007/s10495-010-0536-2.

Parker BJ, Wearsch PA, Veloo ACM, Rodriguez-Palacios A. The Genus Alistipes: Gut Bacteria With Emerging Implications to Inflammation, Cancer, and Mental Health. Front Immunol. 2020; 11:906. doi: 10.3389/fimmu.2020.00906.

Naseribafrouei A, Hestad K, Avershina E, Sekelja M, Linløkken A, Wilson R, Rudi K. Correlation between the human fecal microbiota and depression. Neurogastroenterol Motil. 2014; 26(8):1155-62. doi: 10.1111/nmo.12378.

Yang Y, Jobin C. Novel insights into microbiome in colitis and colorectal cancer. Curr Opin Gastroenterol. 2017; 33(6):422-427. doi: 10.1097/MOG.0000000000000399.

# 9. Appendix: A new study of inward and outward rectifying potassium currents in U251 glioblastoma cells

## *Introduction*

Glioblastoma (GBM, WHO grade IV astrocytoma) is the most common and malignant brain tumor (Barbieri et al., 2018) arising from glial cells. Compared to other central nervous system cancers, GBM is characterized by strong invasiveness and pro-angiogenic behavior that turn into a very poor prognosis with a mean survival rate of about 15 months (Stupp et al., 2009). The aggressive invasiveness and infiltrative behavior of glioma cells make complete surgical resection impossible (Maher et al., 2001) with, therefore, consequent rapid relapses. Additionally, GBM possesses a small subpopulation of cells called cancer stem cells (CSCs) which are incredibly resistant to radiotherapy and chemotherapy (Lathia et al., 2011). Furthermore, death evasion minimized the effect of all therapeutic strategies currently available, and the increased cell invasion is the prominent feature that prevents a successful treatment (Louis et al., 2007).

GBM cells migrate *via* the narrow space in the brain parenchyma (De Vleeschouwer et al., 2017) that is generally smaller than the soma of the cells (Liu et al., 2018). To make that possible, GBM cells undergo a cell shrinkage to reduce their volume by about 30%, followed by migration and invasion (Armento et al., 2017). The cell shrinkage is achieved by the release of cytoplasmatic water in order to reach the osmotic equilibrium in the cell. Several recent evidences suggest that some ion channels and transporters are involved in the modulation of the cell volume. Chloride ($Cl^-$) and Potassium ($K^+$) are the two main ionic gradients that have been previously reported to be altered in GBM cells. Indeed, $Cl^-$ and $K^+$ gradient have been shown to be essential for migration and invasion processes in GBM (Turner and Sontheimer, 2014). Due to the cytosolic calcium fluctuations during GBM cells migration, the family of $Ca^{2+}$-activated $K^+$ channels, such as KCa3.1 (intermediate conductance $K^+$ channel or IK) and Kca1.1 (large-conductance $K^+$ channel or BK), is overexpressed in the brain of GBM patients, and there is a direct relationship between the expression of these channels and the progression of GBM. Thanks to their calcium sensitivity, it has been shown that these channels are positively

activated by different neurotransmitters or bioactive molecules that lead to intracellular $Ca^{2+}$ increases, with a resulting efflux of $K^+$ and water. Consequently, the GBM cells reduce their volume, which enables them to migrate through the narrow space of the parenchyma tissue in the brain (Catacuzzeno and Franciolini, 2018).

Overexpression of BK channels has been reported in cells lines of GBM and in biopsies of GBM patients (Catacuzzeno et al., 2015) and, in addition, the channel structure seems to be altered with a consequent increase in the sensitivity of the intracellular calcium concentration ($[Ca^{2+}]_i$) (Ransom et al., 2002).

Typically, the BK channel is a tetrameric large-conductance $K^+$ channel, widely expressed in both neurons and glial cells (Lee and Cui, 2010). The BK channel is characterized by an outwardly rectifying current that shows both voltage and $[Ca^{2+}]_i$ dependence (Cui et al., 2009). Voltage and $[Ca^{2+}]_i$ dependence act in concert, since $[Ca^{2+}]_i$ has a strong impact on BK voltage dependence (Schreiber and Salkoff, 1997) and, notably, the $Ca^{2+}$ sensors and the voltage-sensing domain of BK channel interact with each other, determining BK channel open probability (Lorenzo-Ceballos et al., 2019). It has been demonstrated in GBM that $[Ca^{2+}]_i$ oscillation along with different values of the resting membrane potential (RMP) (depolarized versus hyperpolarized) are involved in cell migration, invasiveness, and proliferation (Ronde' et al., 2000, Catacuzzeno et al., 2011). Nevertheless, the intracellular mechanisms targeted by $[Ca^{2+}]_i$ changes are not fully understood (Catacuzzeno et al., 2011). Recently, cyclic variation of both voltage and calcium concentration in GBM cells has led to the hypothesis that the BK channel, considering its overexpression, can be one of the critical targets in triggering the glioblastoma migration and invasion process (Catacuzzeno et al., 2015).

The onset of GBM is the consequence of a defective process of neural stem cells differentiation or of the so-called "somatic evolution" process, in which a differentiated glial cell accumulates mutations (Batista et al., 2014).

Another channel involved in GBM is the inward rectifier $K^+$ channel. One of the significant functions of glial cells in the CNS is to preserve ionic homeostasis during neuronal activity *via* the potassium spatial buffering phenomenon that requires the activation of inwardly rectifying $K^+$ channels (Kir) activity (Olsen and Sontheimer, 2008). Notably, a reduced expression or functionality of Kir 4.1 channels was detected in human brain cancers, including in GBM (Thuringer et al., 2017).

Physiologically, Kir 4.1 channel is mostly expressed in the glial cells of the brain and, in particular, in mature astrocytes, where the high potassium permeability is mediated to a large extent by the Kir 4.1 channels. This condition leads to two functional consequences: (i) the negative RMP, which is closer to the potassium equilibrium potential, and (ii) the buffering of the extracellular potassium after neuronal activity (Butt and Kalsi, 2006, Chever et al., 2010). Since a fraction of the Kir 4.1 channels is physiologically constitutively open, it has been proved that Kir 4.1 channel plays a crucial role in the homeostatic regulation of the RMP of the cells, in particular during glia maturation (Olsen and Sontheimer, 2008).

In conclusion, in the last years, several evidences have revealed that many ion channels and pumps have an impaired expression in cancers and their mis-regulation is responsible for high proliferative rate as well as migration and invasiveness. Indeed, the term oncochannelopathies has been recently coined to define several cancers, including GBM.

## *Aim of the work*

A part of my Ph.D. activity was focused on the migration process in GBM, which is the most aggressive, undifferentiated, and common type of astrocytoma (Louis et al., 2007). GBM is resistant to the therapies currently available such as surgical resection followed by chemotherapy and radiotherapy, giving frequent relapses caused by its high invasion rate (Berger and Sanai, 2008). For this reason, a better knowledge of the cellular mechanisms regarding GBM migration and invasiveness is necessary in order to develop new therapeutic strategies for this disease. Therefore, we studied the invasiveness process in human U251 GBM cells, focusing on the characterization of potassium channels to identify the mechanisms underlying the GBM cell migration. Furthermore, considering GBM as oncochannelopathy, the purpose of this research was to better understand the real contribution of BK channels along with the Kir 4.1 on the GBM invasiveness, focusing on their biophysical properties and on their osmo-electric effect at the physiological $[Ca^{2+}]_i$ and RMP of GBM cells.

For this purpose, we applied the wound healing assay to induce U251 cell migration. The experimental plan consisted of two experimental time points: (i) basal condition (80% confluence cells) and (ii) 24 h after the wound healing assay (t1) (Figure 1). At t1, the cells within (intra) and outside (extra) the scratch were studied by using the perforated patch-clamp technique that allows $[Ca^{2+}]_i$ to follow physiological oscillations.

Since it is known that the $[Ca^{2+}]_i$ oscillation is involved in migration and invasiveness, the intracellular mechanisms targeted by $[Ca^{2+}]_i$ changes are not well understood (Catacuzzeno et al., 2011), we tested the effect of inducing calcium oscillation by menthol on potassium currents.

Menthol activates a Transient Receptor Potential cation channel subfamily M (melastatin) member 8 (TRPM8) that causes $Ca^{2+}$ influx, and consequently an increase in BK currents and migration in human GBM cells (Weaver et al., 2006; Wondergem and Bartley, 2009).

Furthermore, only few papers have described the possible role of BK channels in migration upon artificial $[Ca^{2+}]_i$ rise, but nobody have described the role of BK channels at the RMP and at the physiological $[Ca^{2+}]_i$ oscillation, also in relation to other channels that at the RMP are constitutively open, such as Kir 4.1. Indeed, in this project, we proposed a possible mechanism in which BK and Kir 4.1 channels interact together allowing GBM migration and invasiveness.

Summarizing, in the attempt to develop new therapeutic strategies for avoiding relapses on GBM patients, the purposes of this project on the GBM U251 cell line are: (i) to understand the contribution of BK channels along with the Kir 4.1 at the physiological conditions (i.e., spontaneous $[Ca^{2+}]_i$ oscillation and RMP), (ii) to investigate the involvement of Kir 4.1 and BK channels in migration and invasion.
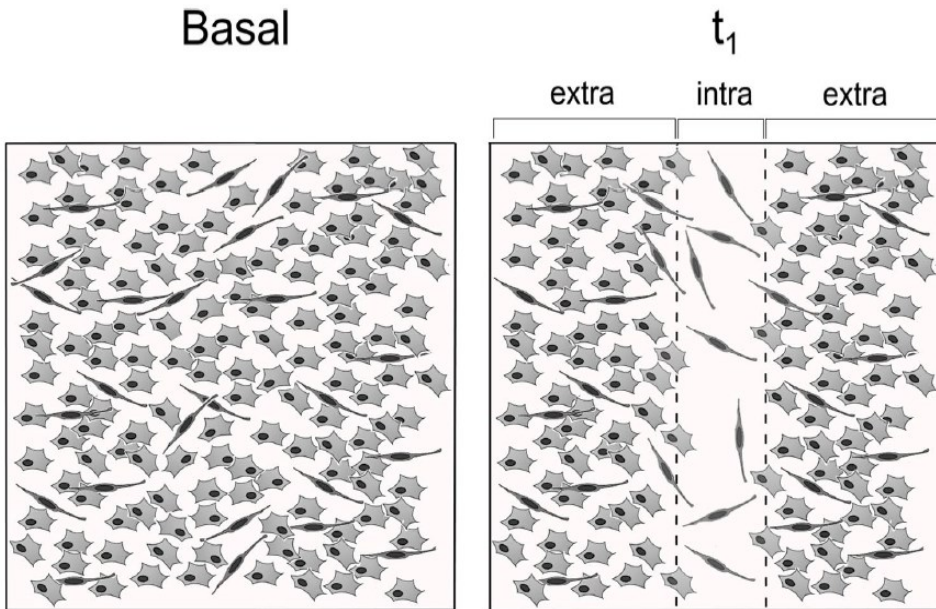


*Figure 1: Schematic illustration describing selected experimental conditions: basal, intra and extra scratch at t1 (24 h after wound healing assay). From Ratto et al., 2019.*

## *Results and discussion*

### *i.Migration process in flattened and polarized cells*

In all different tested experimental conditions, basal, t1 intra and t1 extra scratch, U251 cells displayed two different main morphologies: flattened or polarized.

Focusing on the invasive process, we performed immunocytochemistry to identify the expression of active-Cdc42, a migration marker that stained U251 cell cytoplasm. The immunoreactivity was enhanced in polarized cells compared to flattened ones. In particular, the mean fluorescence density per cell gradually increased in polarized cells from basal condition to extra to intra scratch cells at t1, whereas the mean fluorescence remained constant in flattened cells in different experimental conditions (Figure 2).

### *ii.Electrophysiological Recordings intra and extra scratch*

We performed perforated patch-clamp on polarized cells intra and extra the wounded area at t1. This technique allowed us to avoid rundown of currents and to maintain the $[Ca^{2+}]_i$ at physiological levels, and, therefore, to record currents in a constitutive condition.

Polarized cells analyzed intra (n=54) and extra (n=33) scratch at t1 displayed a depolarized RMP, respectively of − 31.7 ± 1.4 mV and − 34.7 ± 1.7 mV, as expected by an undifferentiated state of GBM cells.

Notably, about 85% of cells analyzed intra scratch (n=46 out of 54) showed both outward and inward constitutive rectifier currents. The remained 15%, instead, did not display any currents (Fig. 3 A). On the contrary, most of the cells analyzed outside the scratch did not display any currents (78%; n=26 out of 33) and only 21% showed both inward and outward rectifier currents (Fig. 3 B). Notably, inward and outward currents' amplitudes were directly related, as demonstrated by the straight-line interpolation ($R^2$ = 0.7654). Furthermore, intra scratch polarized cells showed larger outward and inward rectifier currents than extra scratch polarized cells (Fig. 3 C). It should be noted that the amplitude of inward rectifier currents was significantly lower in U251 cells compared to differentiated glial cells (Higashimori and Sontheimer, 2007) and, consequently, the RMP is more depolarized. These data indicate that at

RMP only a tiny number of inward rectifier channels were functionally active in GBM cells.
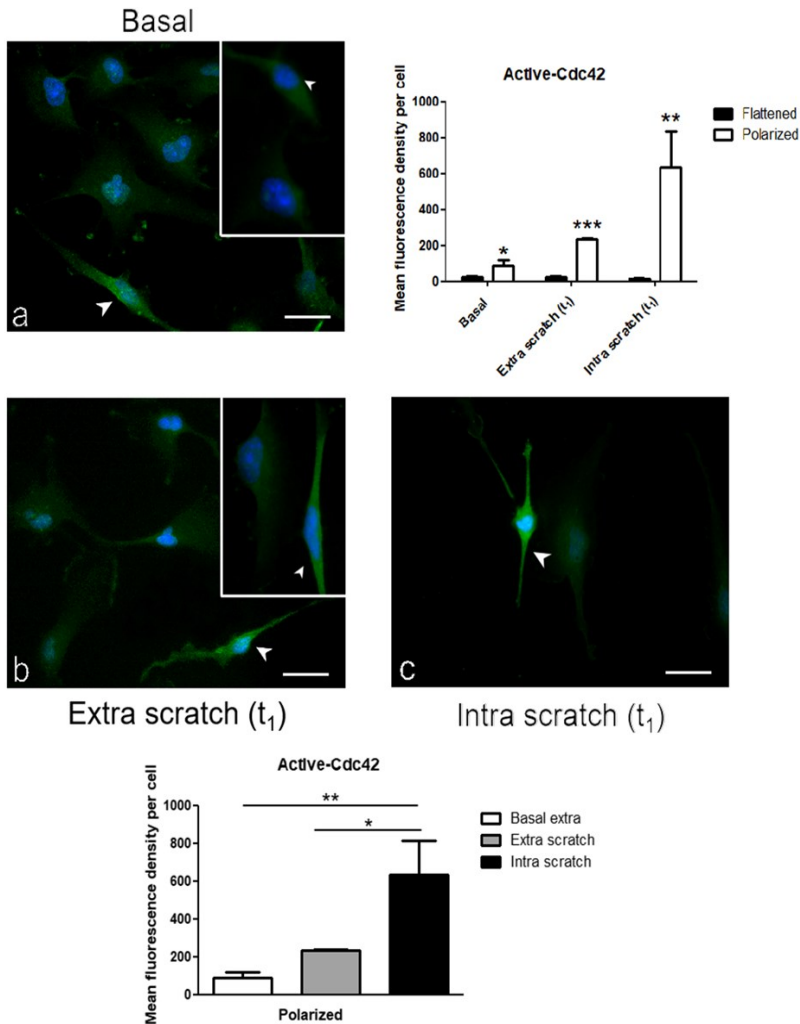


*Figure 2: Immunostaining for active Cdc-42 (green fluorescence) in different experimental conditions: basal (a), extra (t1; b), and intra (t1; c) scratch. Nuclei were counter-stained with Hoechst (blue fluorescence). Scale bar: 40 μm. The top right histogram shows the mean fluorescence density per cell in flattened (black) and polarized (white) cells in the three experimental conditions. The histogram below shows the mean fluorescence density per polarized cells in the three different experimental conditions. Statistical results were performed by analysis of variance (ANOVA) with Post hoc Bonferroni's test. P-values: * for $p < 0.05$; **for $p < 0.01$; *** for $p < 0.001$. From Ratto et al., 2019.*
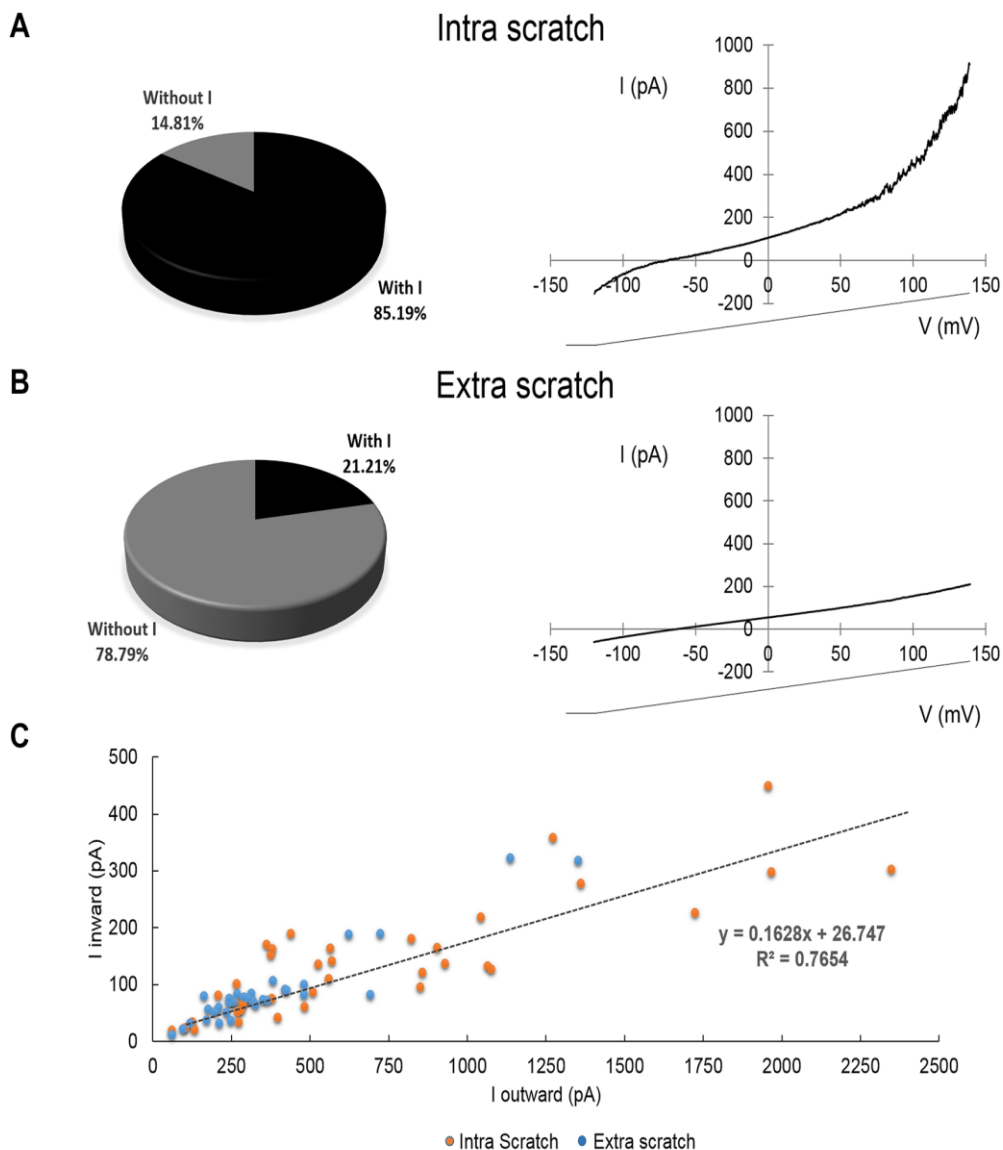
*Figure 3: Currents recorded intra and extra scratch in polarized cells. A, B) Pie charts displayed the percentage of polarized cells with or without inward and outward rectifier currents intra (A left) and extra (B left) scratch. Examples of averaged experimental traces recorded intra and extra scratch are reported, respectively, in the right of panel A and B. C) Liner relationship between inward (y axis) and outward (x axis) rectifier currents intra (orange) and extra (blue) scratch is showed in panel C. From Ratto et al., 2019.*

### iii.Biophysical and pharmacological characterization of inward and outward rectifier currents.

We first used a pharmacological approach to characterize the recorded currents, applying selective blockers by local bath perfusion.

Inward rectifier current was entirely blocked by the perfusion of Barium ($Ba^+$) 1 mM (Fig. 4 A), as demonstrated by eliciting hyperpolarized pulses (in steps of 10 mV) from a holding potential of -40 mV to -120 mV (n=17). Figure 4 panel B shows an example of experimental trace (empty dots) obtained by using digital subtraction (control – barium) of depolarizing ramp protocols (from -120 t0 -60 mV with a rate corresponding to 0.077 mV/ms) and fitted by the following equation (black line):

$$I(V) = \frac{G_{\max}(V - V_{\mathrm{rev}})}{1 + e^{(V-V_{1/2})/K}} \qquad \text{Equation 1}$$

where:

*Table 1: parameters that define the modified Boltzmann equation.*

| | |
|---|---|
| $G_{\max}$ | The maximum conductance (nS) |
| $V_{\mathrm{rev}}$ | The reversal potential (mV) |
| $V_{1/2}$ | The potential at which the current is half-activated (mV) |
| k | The voltage dependence of activation (1/mV) |

Thanks to this procedure, we found the values of $G_{\max}$, $V_{\mathrm{rev}}$, $V_{1/2}$, and k for the barium-sensitive currents of 17 polarized cells and we reconstructed the mean I-V plots (Fig. 4 C) by using the mean values reported in table 2.

*Table 2: Biophysical features of inward rectifier currents recorded n polarized cells intra scratch.*

| $G_{\max}$ (nS) | $V_{\mathrm{rev}}$ (mV) | $V_{1/2}$ (mV) | $K$ (mV$^{-1}$) |
|---|---|---|---|
| 3.5±0.7 | −69.2±1.1 | −104.7±7.1 | 34.4±4.5 |

Known that $G(V)=I(V)/(V-V_{\mathrm{rev}})$, we also obtained the normalized conductance (Fig. 4 D) by using the following formula:

$$\frac{G}{G_{\max}} = \frac{1}{1 + e^{\left(V - \frac{V_1}{2}\right)/K}} \qquad \text{Equation 2}$$

*Figure 4: Biophysical and pharmacological properties of constitutively inward rectifier current recorded in polarized cells intra scratch. A) Inward currents were blocked by Ba$^+$ 1 mM perfusion (n=17). The barium-sensitive currents have been obtained by digital subtraction: control- barium. B) An experimental trace (empty dots) obtained by using a voltage-ramp protocol. The experimental points have been fitted with Equation 1 (black line). For panel A and B the voltage-clamp protocol is shown in the bottom of the panel. C) Averaged I-V plot were obtained by using the averaged values reported in table 2. D) Normalized conductance of inward rectifier current has been reconstructed using Equation 2. From Ratto et al., 2019.*

All these results (the block by Barium and the biophysical properties, such as the weak voltage-dependent rectification) allowed us to characterize inward rectifier current as mediated by Kir 4.1 channels (Ruppersberg, 2000).

We used a similar approach to investigate the outward rectifier current. Outward rectifier current was completely blocked by the perfusion of Tetraethylammonium (TEA) 3 mM (n=28) or Iberiotoxin (Ibtx) 100 nM (n=3), specific blocker for BK channels. On the contrary, the current was insensitive to clotrimazole 10 µM, a specific blocker for IK channels (n=28) (Fig. 5 A).

Analogous to inward rectifier current, we performed a similar biophysical analysis by using the following equations:

$$I(V) = \frac{G_{max}\left(V - V_{rev}\right)}{1 + e^{-(V - V_{1/2})/K}}$$ *Equation 3*

$$\frac{G}{G_{max}} = \frac{1}{1 + e^{-\left(V - \frac{V_1}{2}\right)/K}}$$ *Equation 4*

In particular, experimental I-V traces (empty points), elicited by using a depolarizing voltage-clamp ramp protocol from + 50 to +140 mV, were fitted by using the equation 3 (Fig. 5 B). Thanks to the fitting, we obtained the values of $G_{max}$, $V_{rev}$, $V_{1/2}$, and $k$ for the TEA-sensitive currents of 28 polarized cells perfused by TEA intra scratch and we reconstructed the mean I-V plots (Fig. 5 C) by using the mean values reported in table 3.

*Table 3: Biophysical features of outward rectifier currents recorded in polarized cells intra scratch.*

| $G_{max}$ (nS) | $V_{rev}$ (mV) | $V_{1/2}$ (mV) | $K$ (mV$^{-1}$) |
|---|---|---|---|
| 5.0±0.6 | − 69.6±0.8 | 114.9±2.9 | 14.0±1.2 |

The mean normalized conductance (Fig 5 D) of the TEA-sensitive BK current was reconstructed by using equation 4.

Figure 5 F, finally, shows the activation time constant of BK current at different membrane potentials, that, notably, it was faster at + 140 mV compared to other lower potentials ($p < 0.05$, Fig. 5 F).

All these results indicated that the outward rectifier current was mediated by BK channels, whereas intermediate potassium currents were not detectable.
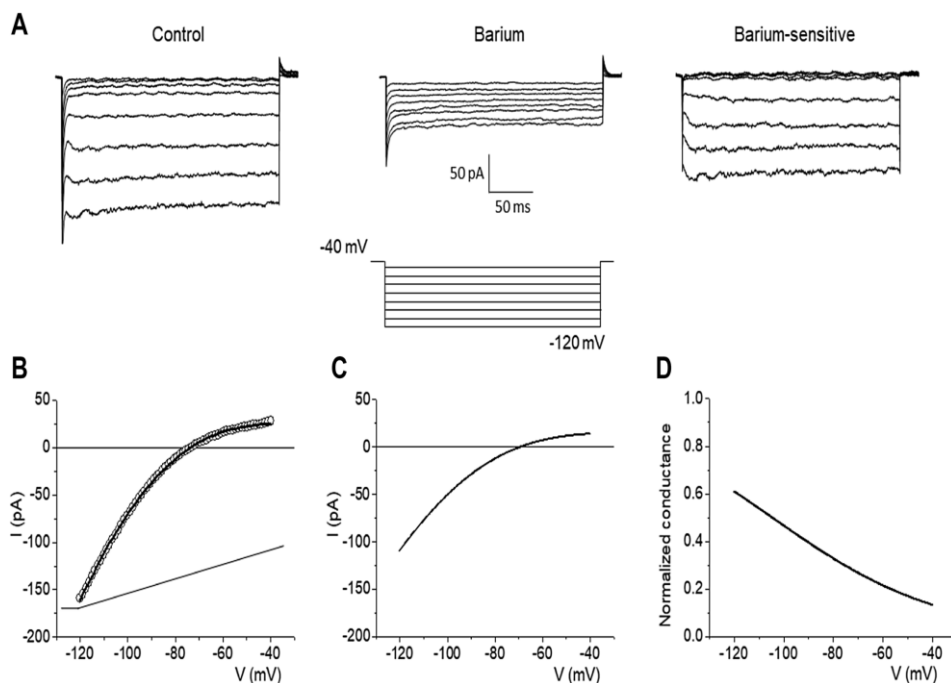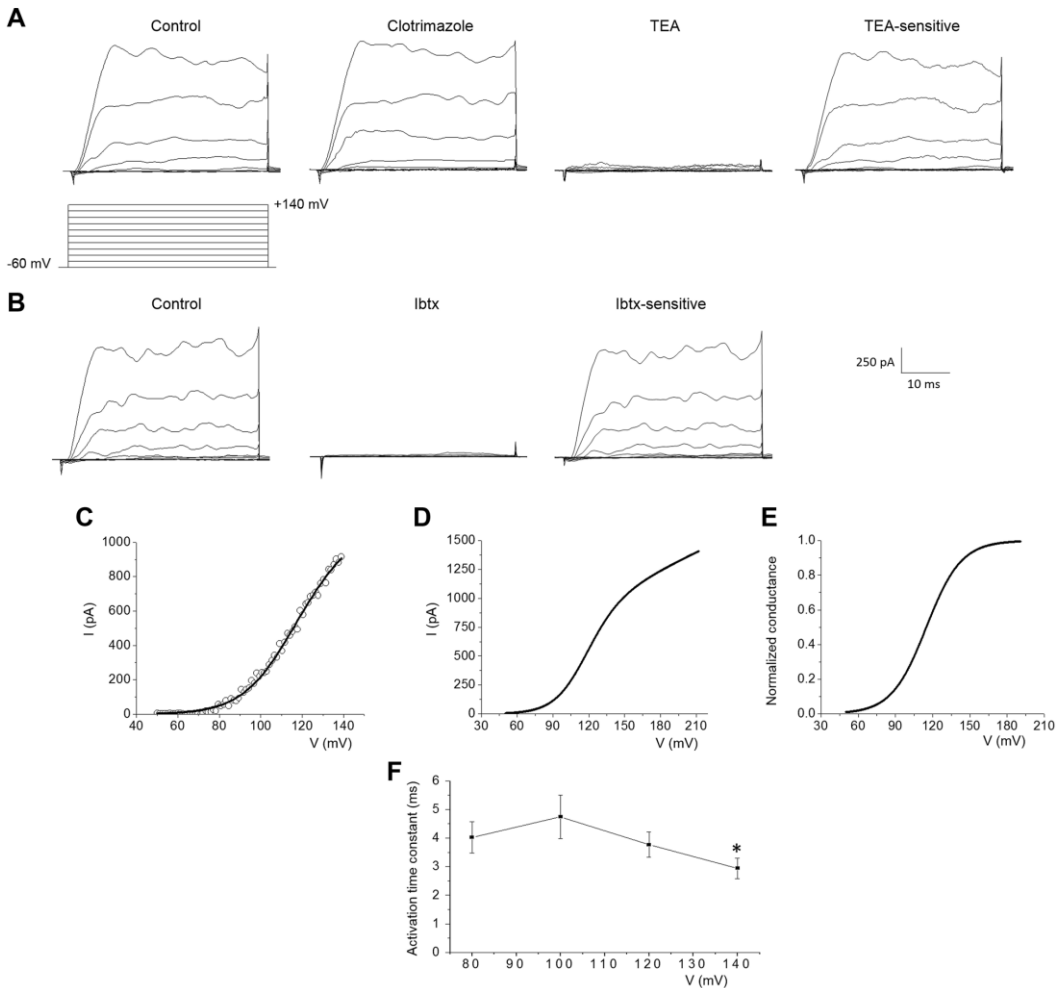
Figure 5: Biophysical and pharmacological properties of constitutively outward rectifier current recorded in polarized cells inside the scratch. A and B) Outward rectifier currents were blocked by TEA 3 mM (n=28) or Ibtx 100 nM (n=3) perfusion, but not by Clotrimazole 10 μM (n = 28). The blockers-sensitive currents have been obtained by digital subtraction: control - TEA or Ibtx. In the center left, it is reported the voltage-clamp protocol eliciting depolarized pulses (in steps of + 20 mV) from a holding potential of -60 mV to +140 mV. C) An example of experimental trace (empty plot) obtained using a voltage-ramp protocol (from +50 to +140 mV). The experimental points have been fitted with Equation 3 (black line). D) Averaged I-V plot was obtained by using the averaged values reported in table 3 inserted in the Equation 3. E) Normalized conductance of outward rectifier current has been reconstructed by using Equation 4. F) Activation time constant (ms) of outward rectifier current at different membrane potentials (mV). From Ratto et al., 2019.

## iv. Menthol Modulation of Kir4.1 and BK currents

We demonstrated that the wound healing induced migration that was matched with functional and related activation of Kir 4.1 and BK currents, therefore suggesting that a common mechanism triggered BK and Kir4.1 increase. One possible mechanism could be the increase of intracellular $Ca^{2+}$ concentration, which appears to be a conserved feature among migratory cells.

So, for investigating this calcium involvement hypothesis, we studied the effect of menthol, a TRPM8 agonist, which increases $[Ca^{2+}]_i$ (Wondergem and Bartley, 2009). The 100 µM menthol local perfusion increased both Kir 4.1 and BK currents in all polarized cells tested intra scratch, regardless of the presence (n=15) or not (n=5) of basal constitutive currents (Fig. 6 A and B, respectively). The currents amplitude reached the same value in cells with and without constitutive currents, indicating that TRPM8 activation and the consequent $[Ca^{2+}]_i$ increase could reach a similar effect despite the difference in constitutive currents. In particular, in cells with constitutively currents, menthol perfusion increased Kir4.1 by about 66% (from - 76.45 ± 19.47 pA to -226.60 ± 16.78 pA) and BK current by about 67% (from 409.15 ± 119.17 to 1244.23 ± 112.67), whereas in cells without constitutively currents menthol perfusion elicited aKir4.1 current of -203.16 ± 53.80 pA (mean amplitude at -120 mV) and an outward rectifier current of 1329.13 ± 266.76 pA (mean amplitude at +140 mV, Fig. 6 B).

After menthol bath perfusion, the liner relationship between inward and outward rectifier currents was maintained, indicating, again, a direct relationship between the Kir4.1 and BK currents amplitudes ($R^2$ = 0.7365, Fig. 6 C) and suggesting that $[Ca^{2+}]_i$ increase is a common cellular mechanism triggering Kir 4.1 and BK channels.
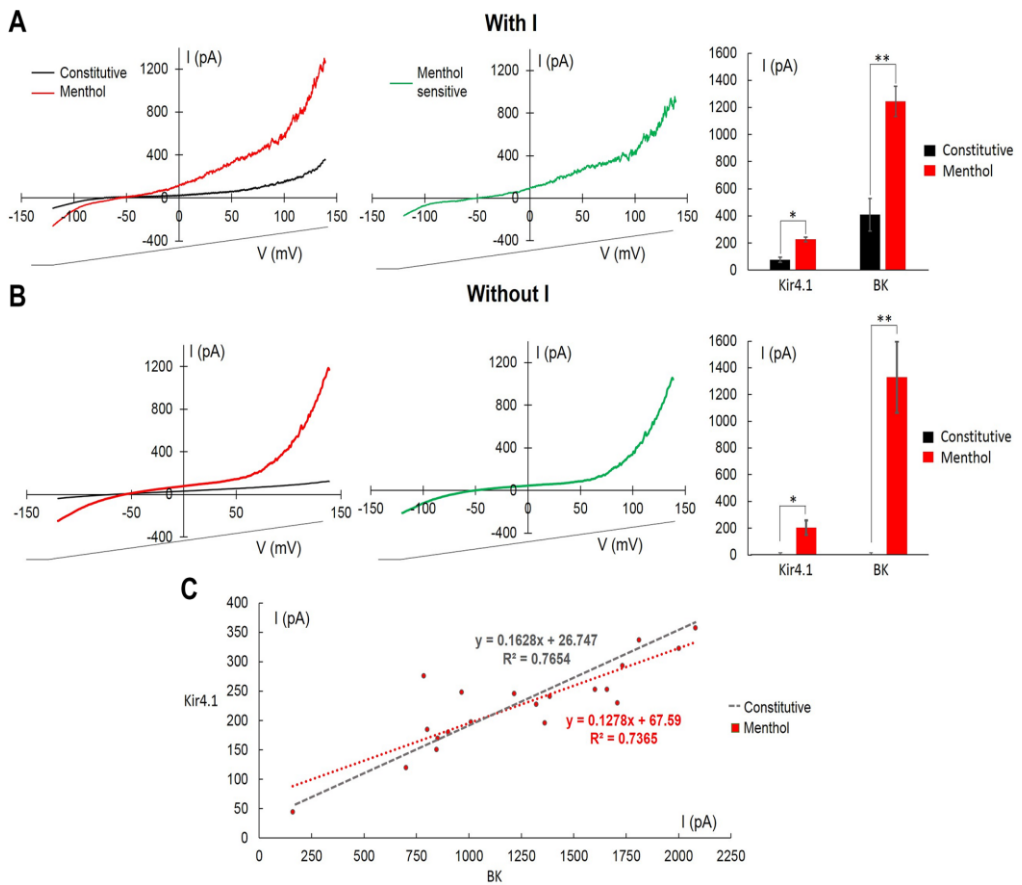
*Figure 6. Menthol perfusion increased inward and outward rectifier currents in polarized cells intra scratch. A, B) Left traces: averaged experimental traces elicited before (constitutive condition, black), and after menthol (100 µM; red) in polarized cells with (panel A) and without (panel B) constitutively active currents. In the center: experimental menthol-sensitive traces (green) obtained after digital subtraction: menthol – constitutive condition. On the right: histograms summarizing the absolute values of inward (Kir 4.1) and outward (BK) rectifier currents elicited at -120 mV and + 140 mV, respectively, before (constitutive, black) and after (red) menthol perfusion. Statistical results were performed by analysis of variance (ANOVA) with Post hoc Bonferroni's test. P-values: * for p < 0.05; ** for p < 0.01. C) Liner relationship between inward (Kir 4.1, y axis) and outward (BK, x axis) rectifier currents before (constitutive condition, grey) and after menthol perfusion (red) is showed in panel C. From Ratto et al., 2019.*

The menthol-evoked currents were blocked by the same blockers previously tested in constitutive conditions. Indeed, Kir 4.1 current was blocked by 81.5% using Ba+ 1 mM (Fig. 7 A) and BK current was blocked by 72% using TEA 3 mM (Fig. 7 B).

Whereas the calcium dependence of BK channels is well established in the literature (Wondergem and Bartley, 2009), the calcium dependence of Kir 4.1 channel has not yet reported.

So, to verify this result, we carried out experiments at different $[Ca^{2+}]_{out}$. Menthol 100 μM perfusion in the absence of $[Ca^{2+}]_{out}$ did not have any effect on BK and Kir 4.1 currents, whereas the addition of $[Ca^{2+}]_{out}$ 3 mM evoked both currents (Fig. 7 C). So, we speculated that a calcium-dependent mechanism could cause the recruitment to the cell surface of Kir 4.1 channels (from the nucleus or other store cell compartments) or their activation through an intracellular modulation involving, for example, phosphatases or kinases.
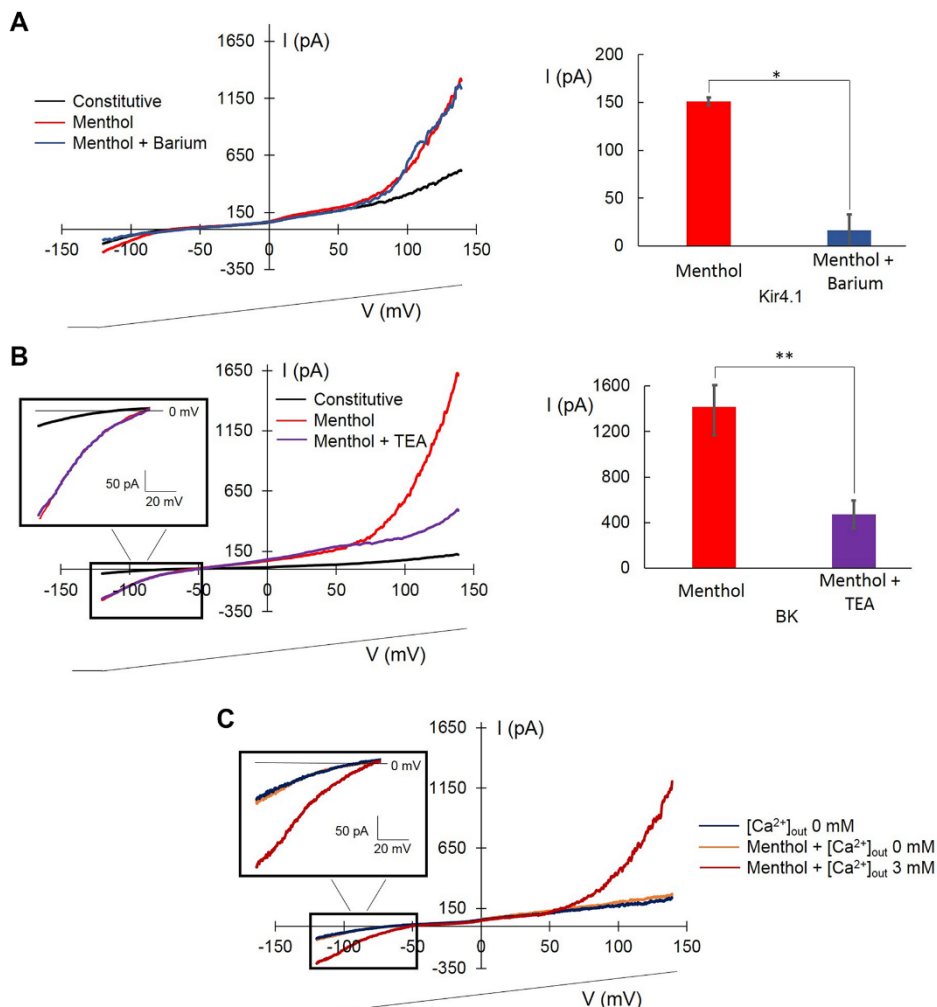
*Figure 7. Pharmacological properties of menthol induced inward and outward rectifier currents inside the scratch. The voltage-ramp protocol is shown at the bottom. A) On the left: averaged experimental traces elicited before (constitutive, black), after menthol (100 µM; red), and after barium (1mM; blue) perfusion. On the right: histogram summarizing the effect of menthol and barium perfusion at -120 mV on the absolute value of inward rectifier current. B) On the left: averaged experimental traces elicited before (constitutive, black), after menthol (100 µM; red), and TEA (3mM; violet) perfusion. On the right: histogram summarizing the effect of menthol and TEA perfusion at +140 mV on outward rectifier current. Statistical results were performed by Student's t-test. $p$ values: \* for $p < 0.05$; \*\* for $p < 0.01$. C) Averaged experimental traces showing constitutive currents obtained with $[Ca^{2+}]_{out}$ 0 mM (dark blue), $[Ca^{2+}]_{out}$ 0 mM plus 100 µM menthol (orange), and $[Ca^{2+}]_{out}$ 3 mM plus menthol (dark red). From Ratto et al., 2019.*

# v.The effect of activation and inhibition of BK and Kir 4.1 channels on migration rate

To study how ionic $K^+$ currents influence U251 cell migration, we tested whether the pharmacological inhibition of Kir 4.1 and BK channels, alone or alongside the activation of TRPM8 channels by menthol, changed the percentage of scratch closure 24 h after the wound healing assay. Ibtx 100 nM treatment for 24 h inhibited the U251 cell migration alone or alongside the treatment with menthol 100 µM, and when Ibtx was combined with $Ba^+$ 1 mM exposure, the migration was reduced even more. On the contrary, menthol 100 µM promoted migration, as demonstrated by the higher percentage of scratch wound closure (Fig. 8).

Therefore, the pharmacological block of BK and Kir 4.1 channels, alone or alongside the activation of TRPM8 channels by menthol, inhibited the migration of U251 cells in a two-dimensional migration assay, demonstrating a direct role of these channels in the invasion process. In particular, the difference between the inhibition induced by Ibtx alone or combined with $Ba^+$ revealed a direct role of both channels in U251 cell migration. So, the simultaneous block of Kir 4.1 along with the BK channels seems to be an effective strategy for blocking GBM cell invasiveness in the wound healing assays, with (menthol presence) or without external $[Ca^{2+}]_i$ perturbation. This suggests that the two classes of potassium channels are mutually involved in the shrinkage of the cell *via* the regulation of $K^+$ gradient.
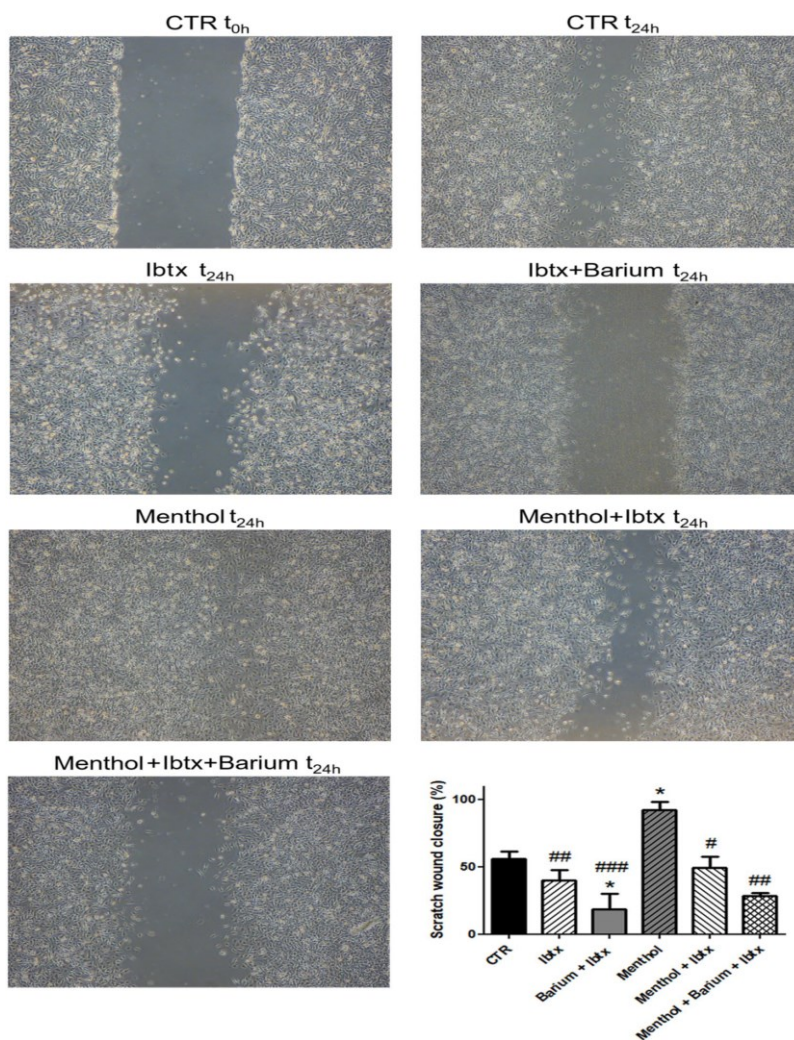
*Figure 8: Effect of the Kir4.1 and BK pharmacological inhibition on U251 cell migration 24 hr after the wound healing assay, alone or alongside the activation of TRPM8 by menthol. The different images display pictures at t0 or after 24 h of continuous exposure in the different experimental conditions indicated in the figure. The concentrations used were the same used in electrophysiological experiments: Ibtx 100 nM, barium 1 mM, and menthol 100 μM. The histogram shows the scratch wound closure (%) at t1 in different experimental conditions. * Statistical significance between control condition (CTR) and the other experimental conditions. # Statistical significance between menthol condition and the other pharmacological experimental conditions. Statistical results were performed by analysis of variance (ANOVA) with Post hoc Bonferroni's test. P-values: * for p < 0.05; **for p < 0.01; *** for p < 0.001. From Ratto et al., 2019.*

## vi.Kir 4.1 and BK channels function state at the RPM: a cooperative link for inducing migration?

During the physiological process, Kir 4.1 channel plays a role in the homeostatic regulation of the RMP of the cell, essential for the glia maturation that settled the RMP at around -80 mV (Olsen and Sontheimer, 2008). The Kir 4.1 peculiar current-voltage relation (Fig. 10 A) is due to weak voltage-dependence rectification at negative membrane potential and to the voltage-dependent pore block from the inner side of the channel, by magnesium and some other organic cations like polyamine at more positive membrane potential (Ruppersberg, 2000). At potentials more positive to the $K^+$ equilibrium (about –80 mV), this block limits the amount of $K^+$ that can go across the channel. In the GBM cells, it is demonstrated a downregulation or mislocation of Kir 4.1 channels (Olsen and Sontheimer, 2004) and it has been correlated to the dramatic shift in the RMP to more depolarized values, to about -40/-30 mV (see chapter ii: *Electrophysiological Recordings intra and extra scratch* in Results and Discussion session).

Due to Kir 4.1 internalization in the cytosol during GBM progression, very little attention has been paid in literature to the residual activity of the Kir 4.1 channels at the RMP. Nevertheless, our results suggest that despite the functional downregulation of the Kir 4.1 channels, there is still a significant fraction of this channel expressed in the membrane that, at the value of the RMP of the GBM cells, exerts a constitutive outward $K^+$ current (Fig. 10 B) that might play a role in cell volume changes.

The fact that the Kir 4.1 channel is internalized but not degraded (Olsen and Sontheimer, 2004) suggests that it can still perform a functional role as a readable pool that is potentially re-inserted into the membrane in a relatively short time, as suggested by a calcium-dependent upregulation of the functional Kir 4.1 current after menthol 100 μM local perfusion.

Lastly, we tentatively proposed how Kir 4.1 and BK channels might work in concert during the GBM cell invasion:

i)     Glia cells in physiological condition (Fig. 10 A): glia cells expressed a high amount of Kir 4.1 channels that is involved in the ionic homeostasis by buffering the ambient $K^+$ during high neuronal activity. Additionally, glial cells have strongly hyperpolarized RMP and the Kir 4.1 is involved in its maintenance (in fact, the reversing potential of Kir 4.1 in normal condition is around -75/-80 mV). BK channels, on the other hand, are also expressed but are in a closed state at this RMP and $[Ca^{2+}]_i$. Indeed, at

resting $[Ca^{2+}]_i$ (about 10-100 nM), BK channels open only at membrane potentials higher than +10 mV (Lee and Cui, 2010).

ii)      GBM morphological change (Fig. 10 B): the alteration in the Cl⁻ and $K^+$ equilibrium in the cells *prior* migration leads to a more depolarized RMP (about -40/-30 mV). Consequently, the reversal potential of Kir 4.1 is no longer aligned with the RMP, but instead, it sets the channel to a constitutively open state with a small but steady net outward flow of $K^+$. It is notable that in basal condition GBM cells use the efflux of water to change their shape, but the total surface of the cell is actually not reduced, probably due to the formation of lamellipodia, as suggested by the cell capacitance increase after menthol perfusion (data not shown). Probably, in this phase, BK channels are overexpressed in their splicing isoform (known as gBK) which increases the sensitivity to the calcium concentration (Ransom and Liu, 2002). Therefore, despite the RMP is still below the BK activating curve, some calcium fluctuations could depolarize the cell and could shift the BK activation curve to a more hyperpolarized potential allowing a transient opening of BK channels (Catacuzzeno et al., 2011; Fig 10 C). Under this conditions BK channels could contribute efficiently and cooperate with the Kir 4.1 channels in the total efflux of potassium and consequent shrinkage. It agrees with our result demonstrating that the block of Kir 4.1 and BK channels succeeds in reducing U251 cell migration.

iii)      GBM invasiveness in the healthy surrounding tissue: When a GBM cell invades the extracellular matrix in the brain, the process could require an additional reduction of the cytosolic volume. The increase in pressure that the extracellular matrix applies to the GBM cell induces a mechanic stress on the membrane, that could activate BK channels (Wawrzkiewicz-Jałowiecka et al., 2018). Moreover, this mechanic constrain might lead to a possible biochemical cascade with a consequent increase of $[Ca^{2+}]_i$ that, again, shifts the voltage activation curve of BK channel to a more hyperpolarized potential (Charles et al., 1999). Overall, an increased pressure on GBM cell membrane turns into a higher functional BK channels activation that significantly increases the outward flux of cytosolic water with consequent volume reduction and higher capability to migrate efficiently (Fig. 10 C). Once the cell has passed through the mechanic constrain, pressure release reduces the fraction of active BK channels and the activation balance between the two channels should come back to the situation described in point (ii) (Fig. 10 B).
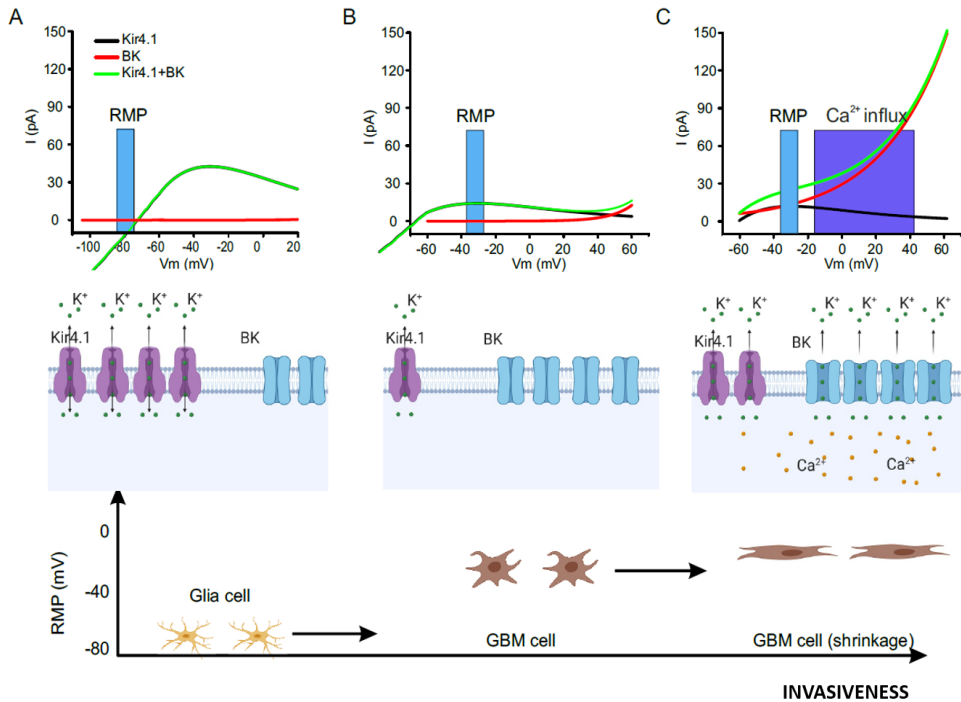
*Figure 10: A proposed action mechanism for BK and Kir 4.1 channels. A) In normal glial cells the RMP is set at hyperpolarized potentials (-70/-80 mV) so that Kir 4.1 channel exerts a homeostatic equilibrium of it and BK channels are in the close state. Top panel shows the kinetics of BK and Kir 4.1 channels in the range of the RMP (blu bar). Middle panel shows a representation of the expression and functional state of the two channels and the direction of the ionic potassium flow ($K^+$). On the Bottom, there is the graphical representation of glial cells in relationship with their RMP. B) When glia turns into GBM cells the RMP shift to a more depolarized potential (top and bottom) due to a downregulation of Kir 4.1 channel while BK channel is overexpressed (middle). C) The increasing pressure on the GBM cells membrane during migration in the brain parenchyma exerts a double effect, activating BK channel and raising the $[Ca^{2+}]i$, that results into the opening of the BK channels (top and middle) with a consequent cell shrinkage (bottom) allowing the migration of the GBM cells. From Brandalise et al., 2020.*

## *Conclusion and future prospects*

The results obtained give new insights on the physiological role and modulation of BK and Kir 4.1 channels in U251 GBM cells. These novel findings can support in developing new therapeutic strategies targeting ion channels for reducing the invasion behavior of GBM cells in adjacent healthy tissues.

Summarizing the main conclusions of this Ph.D. research activity are:

i. Polarized cells were in migration, as opposed to flattened cells.
ii. Migrated U251 polarized cells displayed functional outward rectifier current and a residual inward rectifier current.
iii. Pharmacological inhibition and biophysical proprieties identified the inward rectifier current as mediated by Kir 4.1 channels and outward rectifier current by BK channels, whereas IK currents were negligible.
iv. A $K^+$ leakage was present at the RMP (-40/-30 mV) of the GBM cell, due to Kir 4.1 constant activation in this cancer model. $K^+$ leakage was exacerbated after menthol perfusion, which elicited both BK and Kir 4.1 currents through a calcium-dependent mechanism. Indeed, after menthol perfusion, the shift on the left of the BK activation curve caused an increased leakage of potassium currents at the RMP.
v. The expression of Kir 4.1 and BK channels was paired both during migration and after menthol modulation. Therefore, we hypothesize that both migration and menthol modulation would share an increase of $[Ca^{2+}]_i$ modulating Kir 4.1 and BK channels.
vi. We demonstrated the direct involvement of both BK and Kir 4.1 channels in the migration process.
vii. We developed a theory for explaining the functional involvement of Kir 4.1 and BK channels during GBM migration, referring on normal RPM and $[Ca^{2+}]_i$.
viii. These novel findings can aid in designing new therapeutic strategies targeting ion channels (BK and Kir 4.1 channels) to stop the invasiveness of GBM cells in surrounding healthy tissues, and thus reducing the relapses number.

The following steps of this research will be focused on:

i. The investigation of the link between menthol perfusion and Kir 4.1 channels activation.

ii. The use of current clamp protocols to record the shift in the resting membrane potential.

iii. The study of the Kir 4.1 and BK channels co-expression with proteins involved in migration process.

iv. For obtaining an exhaustive dissection of the GBM cell invasiveness, the study of the involvement of other channels, such as $Cl^-$ channels and leak channels.

v. The use of time-lapse microscopy to observe how cells migrate, their morphology, and their direction of migration.

vi. The study of intracellular calcium oscillation during the migration process, for example, using calcium-imaging.

vii. The study of the currents expressed by the cell on the side of the scratch.

# *References*

Armento A, Ehlers J, Schötterl S, Naumann U. Molecular Mechanisms of Glioma Cell Motility. In: De Vleeschouwer S, editor. Glioblastoma [Internet]. Brisbane (AU): Codon Publications; 2017 Sep 27. Chapter 5.

Barbieri F, Würth R, Pattarozzi A, Verduci I, Mazzola C, Cattaneo MG, Tonelli M, Solari A, Bajetto A, Daga A, Vicentini LM, Mazzanti M, Florio T. Inhibition of Chloride Intracellular Channel 1 (CLIC1) as Biguanide Class-Effect to Impair Human Glioblastoma Stem Cell Viability. Front Pharmacol. 2018; 9:899. doi: 10.3389/fphar.2018.00899.

Batista CM, Mariano ED, Barbosa BJ, Morgalla M, Marie SK, Teixeira MJ, Lepski G. Adult neurogenesis and glial oncogenesis: when the process fails. Biomed Res Int. 2014; 2014:438639. doi: 10.1155/2014/438639.

Sanai N, Berger MS. Glioma extent of resection and its impact on patient outcome. Neurosurgery. 2008; 62(4): 753-64; discussion 264-6. doi: 10.1227/01.neu.0000318159.21731.cf.

Bordey A, Sontheimer H, Trouslard J. Muscarinic activation of BK channels induces membrane oscillations in glioma cells and leads to inhibition of cell migration. J Membr Biol. 2000; 176(1): 31-40. doi: 10.1007/s00232001073.

Butt AM, Kalsi A. Inwardly rectifying potassium channels (Kir) in central nervous system glia: a special role for Kir4.1 in glial functions. J Cell Mol Med. 2006; 10(1): 33-44. doi: 10.1111/j.1582-4934.2006.tb00289.x.

Catacuzzeno, L., Aiello, F., Fioretti, B., Sforna, L., Castigli, E., Ruggieri, P., Tata, A.M., Calogero, A. and Franciolini, F., 2011. Serum-activated K and Cl currents underlay U87-MG glioblastoma cell migration. Journal of cellular physiology, 226(7), pp.1926-1933.

Catacuzzeno L, Aiello F, Fioretti B, Sforna L, Castigli E, Ruggieri P, Tata AM, Calogero A, Franciolini F. Serum-activated K and Cl currents underlay U87-MG glioblastoma cell migration. J Cell Physiol. 2011; 226(7): 1926-33. doi: 10.1002/jcp.22523.

Catacuzzeno L, Franciolini F. Role of KCa3.1 Channels in Modulating Ca2+ Oscillations during Glioblastoma Cell

Migration and Invasion. Int J Mol Sci. 2018; 19(10): 2970. doi: 10.3390/ijms19102970.

Charles AC, Merrill JE, Dirksen ER, Sanderson MJ. Intercellular signaling in glial cells: calcium waves and oscillations in response to mechanical stimulation and glutamate. Neuron. 1991; 6(6): 983-92. doi: 10.1016/0896-6273(91)90238-u.

Chever O, Djukic B, McCarthy KD, Amzica F. Implication of Kir4.1 channel in excess potassium clearance: an in vivo study on anesthetized glial-conditional Kir4.1 knock-out mice. J Neurosci. 2010; 30(47): 15769-77. doi: 10.1523/JNEUROSCI.2078-10.2010.

Cui J, Yang H, Lee US. Molecular mechanisms of BK channel activation. Cell Mol Life Sci. 2009 Mar;66(5):852-75. doi: 10.1007/s00018-008-8609-x.

De Vleeschouwer S, Bergers G. Glioblastoma: To Target the Tumor Cell or the Microenvironment? In: De Vleeschouwer S, editor. Glioblastoma [Internet]. Brisbane (AU): Codon Publications; 2017 Sep 27. Chapter 16.

Higashimori H, Sontheimer H. Role of Kir4.1 channels in growth control of glia. Glia. 2007; 55(16): 1668-79. doi: 10.1002/glia.20574.

Kraft R, Krause P, Jung S, Basrai D, Liebmann L, Bolz J, Patt S. BK channel openers inhibit migration of human glioma cells. Pflugers Arch. 2003; 446(2): 248-55. doi: 10.1007/s00424-003-1012-4.

Lathia JD, Heddleston JM, Venere M, Rich JN. Deadly teamwork: neural cancer stem cells and the tumor microenvironment. Cell Stem Cell. 2011; 8(5): 482-5. doi: 10.1016/j.stem.2011.04.013.

Lee US, Cui J. BK channel activation: structural and functional insights. Trends Neurosci. 2010; 33(9): 415-23. doi: 10.1016/j.tins.2010.06.004.

Liu CA, Chang CY, Hsueh KW, Su HL, Chiou TW, Lin SZ, Harn HJ. Migration/Invasion of Malignant Gliomas and Implications for Therapeutic Treatment. Int J Mol Sci. 2018; 19(4): 1115. doi: 10.3390/ijms19041115.

Lorenzo-Ceballos Y, Carrasquel-Ursulaez W, Castillo K, Alvarez O, Latorre R. Calcium-driven regulation of voltage-sensing domains in BK channels. Elife. 2019; 8: e44934. doi: 10.7554/eLife.44934.

Louis DN, Ohgaki H, Wiestler OD, Cavenee WK, Burger PC, Jouvet A, Scheithauer BW, Kleihues P. The 2007 WHO classification of tumours of the central nervous system. Acta Neuropathol. 2007; 114(2): 97-109. doi: 10.1007/s00401-007-0243-4. Erratum in: Acta Neuropathol. 2007 Nov;114(5):547.

Maher EA, Furnari FB, Bachoo RM, Rowitch DH, Louis DN, Cavenee WK, DePinho RA. Malignant glioma: genetics and biology of a grave matter. Genes Dev. 2001; 15(11): 1311-33. doi: 10.1101/gad.891601.

Olsen ML, Sontheimer H. Mislocalization of Kir channels in malignant glia. Glia. 2004; 46(1): 63-73. doi: 10.1002/glia.10346.

Olsen ML, Sontheimer H. Functional implications for Kir4.1 channels in glial biology: from K+ buffering to cell differentiation. J Neurochem. 2008; 107(3):589-601. doi: 10.1111/j.1471-4159.2008.05615.x.

Ransom CB, Liu X, Sontheimer H. BK channels in human glioma cells have enhanced calcium sensitivity. Glia. 2002; 38(4): 281-91. doi: 10.1002/glia.10064.

Rondé P, Giannone G, Gerasymova I, Stoeckel H, Takeda K, Haiech J. Mechanism of calcium oscillations in migrating human astrocytoma cells. Biochim Biophys Acta. 2000; 1498(2-3): 273-80. doi: 10.1016/s0167-4889(00)00102-6.

Ruppersberg JP. Intracellular regulation of inward rectifier K+ channels. Pflugers Arch. 2000; 441(1): 1-11. doi: 10.1007/s004240000380.

Schreiber M, Salkoff L. A novel calcium-sensing domain in the BK channel. Biophys J. 1997; 73(3): 1355-63. doi: 10.1016/S0006-3495(97)78168-2.

Stupp R, Hegi ME, Mason WP, van den Bent MJ, Taphoorn MJ, Janzer RC, Ludwin SK, Allgeier A, Fisher B, Belanger K, Hau P, Brandes AA, Gijtenbeek J, Marosi C, Vecht CJ, Mokhtari K, Wesseling P, Villa S, Eisenhauer E, Gorlia T, Weller M, Lacombe D, Cairncross JG, Mirimanoff RO; European

Organisation for Research and Treatment of Cancer Brain Tumour and Radiation Oncology Groups; National Cancer Institute of Canada Clinical Trials Group. Effects of radiotherapy with concomitant and adjuvant temozolomide versus radiotherapy alone on survival in glioblastoma in a randomised phase III study: 5-year analysis of the EORTC-NCIC trial. Lancet Oncol. 2009; 10(5): 459-66. doi: 10.1016/S1470-2045(09)70025-7.

Thuringer D, Chanteloup G, Boucher J, Pernet N, Boudesco C, Jego G, Chatelier A, Bois P, Gobbo J, Cronier L, Solary E, Garrido C. Modulation of the inwardly rectifying potassium channel Kir4.1 by the pro-invasive miR-5096 in glioblastoma cells. Oncotarget. 2017; 8(23): 37681-37693. doi: 10.18632/oncotarget.16949.

Turner KL, Sontheimer H. Cl- and K+ channels and their role in primary brain tumour biology. Philos Trans R Soc Lond B Biol Sci. 2014; 369(1638): 20130095. doi: 10.1098/rstb.2013.0095.

Wawrzkiewicz-Jałowiecka A, Trybek P, Machura Ł, Dworakowska B, Grzywna ZJ. Mechanosensitivity of the BK Channels in Human Glioblastoma Cells: Kinetics and Dynamical Complexity. J Membr Biol. 2018; 251(5-6): 667-679. doi: 10.1007/s00232-018-0044-9.

Weaver AK, Bomben VC, Sontheimer H. Expression and function of calcium-activated potassium channels in human glioma cells. Glia. 2006; 54(3): 223-33. doi: 10.1002/glia.20364.

Wondergem R, Bartley JW. Menthol increases human glioblastoma intracellular Ca2+, BK channel activity and cell migration. J Biomed Sci. 2009; 16(1): 90. doi: 10.1186/1423-0127-16-90.

# 11. Acknowledgments

I would like to thank all the people who have contributed to achieving this goal.

Firstly, I want to thank my supervisors, Prof. Rossi and Bottone, for welcoming me into their laboratories and to have supported my research activity.

I would also like to thank Prof. Savino for her collaborations and for allowing us to use *H. erinaceus* present in MicUNIPV.

A special thanks to Prof. Elisa Roda for her constant support, both human and experimental.

I want to thank Quantia Consulting, particularly Anna Sandionigi, for the great support in microbiome analysis.

Thanks also to Prof. Kawagishi of the Shizuoka University in Japan, that provided the standard molecules of erinacine A, hericenone C and hericenone D, essentially for quantifying nootropic molecules in our *H. erinaceus* samples.

During these three years, I could meet some beautiful people with whom I spent moments of intense work and others of pure fun. So, many precious and special thanks to my colleagues for helping and supporting me and to all the people I met during the Ph.D. years.

Finally, but most importantly, I want to thank all my family, my parents, my brother, my aunt, my grandma, my husband, and my beloved son Davidone.

## 12.     List of original manuscripts

*Article*

# Hericium erinaceus Improves Recognition Memory and Induces Hippocampal and Cerebellar Neurogenesis in Frail Mice during Aging

Daniela Ratto [1], Federica Corana [2], Barbara Mannucci [2], Erica Cecilia Priori [1], Filippo Cobelli [1], Elisa Roda [1,3], Beatrice Ferrari [1], Alessandra Occhinegro [1], Carmine Di Iorio [1], Fabrizio De Luca [1], Valentina Cesaroni [4], Carolina Girometta [4], Maria Grazia Bottone [1], Elena Savino [4], Hirokazu Kawagishi [5] and Paola Rossi [1,*]

[1]  Department of Biology and Biotechnology "L. Spallanzani", University of Pavia, 27100 Pavia, Italy; daniela.ratto01@universitadipavia.it (D.R.); ericacecilia.priori01@universitadipavia.it (E.C.P.); filippo.cobelli01@universitadipavia.it (F.Cob.); elisa.roda@unipv.it (E.R.); beatrice.ferrari01@universitadipavia.it (B.F.); alessandra.occhinegro01@universitadipavia.it (A.O.); carmine.diiorio01@universitadipavia.it (C.D.I.); fabrizio.deluca01@universitadipavia.it (F.D.L.); mariagrazia.bottone@unipv.it (M.G.B.)
[2]  Centro Grandi Strumenti, University of Pavia, 27100 Pavia, Italy; federica.corana@unipv.it (F.Cor.); barbara.mannucci@unipv.it (B.M.)
[3]  Laboratory of Clinical & Experimental Toxicology, Pavia Poison Centre, National Toxicology Information Centre, Toxicology Unit, ICS Maugeri SpA, IRCCS Pavia, 27100 Pavia, Italy
[4]  Department of Earth and Environmental Sciences, University of Pavia, 27100 Pavia, Italy; valentina.cesaroni01@universitadipavia.it (V.C.); carolina.girometta01@universitadipavia.it (C.G.); elena.savino@unipv.it (E.S.)
[5]  Research Institute of Green Science and Technology, Shizuoka University; 422-8529 Shizuoka, Japan; kawagishi.hirokazu@shizuoka.ac.jp
*  Correspondence: paola.rossi@unipv.it; Tel: +0039-0382-896076

**Abstract:** Frailty is a geriatric syndrome associated with both locomotor and cognitive decline, implicated in both poor quality of life and negative health outcomes. One central question surrounding frailty is whether phenotypic frailty is associated with the cognitive impairment during aging. Using spontaneous behavioral tests and by studying the dynamic change during aging, we demonstrated that the two form of vulnerability, locomotor and recognition memory decline, develop in parallel and therefore, integration of the motoric and cognitive evaluations are imperative. We developed an integrated frailty index based on both phenotypic and recognition memory performances. *Hericium erinaceus* (*H. erinaceus*) is a medicinal mushroom that improves recognition memory in mice. By using HPLC-UV-ESI/MS analyses we obtained standardized amounts of erinacine A and hericenones C and D in *H. erinaceus* extracts, that were tested in our animal model of physiological aging. Two-month oral supplementation with *H. erinaceus* reversed the age-decline of recognition memory. Proliferating cell nuclear antigen (PCNA) and doublecortin (DCX) immunohistochemistry in the hippocampus and cerebellum in treated mice supported a positive effect of an *H. erinaceus* on neurogenesis in frail mice.

**Keywords:** aging; phenotypic frailty; cognitive decline; *Hericium erinaceus*; erinacines; hericenones; medicinal mushrooms supplementation; neurogenesis

## 1. Introduction

Recent reports on the European population suggest that by 2060, 30% of Europeans will be over the age of 65. Frailty is a geriatric syndrome associated with poor quality of life and negative health outcomes, such as acute illness, falls, hospitalization, disability, dependency, and mortality, adjusted for comorbidities [1,2,3], in the absence of recognized disabilities or organ-specific diseases. Health declines in frailty are accelerated and accompanied by the failure of homeostatic mechanisms [4,5].

Fried defined phenotypic frailty as an aging-associated phenotype expressing at least three of the following symptoms: weakness, weight loss, slow walking speed, fatigue, and a low level of physical activity [1]. Most older people gradually become frail and oscillations between non-frail, pre-frail, and frail are not uncommon [6]. Cognitive impairment is a decline of cognitive functions such as remembering, reasoning, and planning, ranging from mild forms of forgetfulness to severe dementia. Cognition-impaired frailty in human studies was associated with global cognition and perceptual speed, but not with episodic memory [7]. Quality of life in the elderly is particularly affected by impairments in the functioning of the memory system [8]. In order to evaluate the inclusion of cognitive performances in frailty clinical diagnosis [9], it is necessary to first determine whether phenotypic frailty is associated with cognitive impairment [10].

Several epidemiological studies have reported that higher levels of phenotypic frailty increases the risk of cognitive impairment and dementia [11,12,13], and that higher levels of cognitive impairment or dementia increase the risk of phenotypic frailty [14,15,16]. This suggests that frailty may be an early indicator for subsequent cognitive decline. Understanding the mechanisms by which phenotypic frailty is linked to cognitive impairment has implications for the management of those susceptible for both phenotypic frailty and cognitive impairment.

*Hericium erinaceus* (*H. erinaceus*) is found in Europe, Asia, North America, Oceania, and generally throughout the north temperate latitudes. In Italy, it is considered quite rare; it occurs along the Apennines mountain chain, near Sicily and Sardinia, while in the North only few sporadic sightings have been reported.

*H. erinaceus* is an edible mushroom widely used as herbal medicine, in all areas mentioned above and in a few East Asian countries. Since 1990, studies on *H. erinaceus* secondary metabolites reported several (about 70) structurally related terpenoids, such as erinacines, hericenones, hericerins, hericenes, hericenols, and erinacerins [17,18,19].

All of the above-mentioned molecules, except erinacines, share a geranyl side chain bonded to a resorcinol framework; that is, they are aromatic compounds containing the 6-alkyl-2,4-dihydroxybenzoic acid unit also known as β-resorcylate [20]. Erinacines are classified as cyathane-type diterpenoids, including 20 members of 24 different diterpenoids in *H. erinaceus* [18]. The standardization of dietary supplements from medicinal mushrooms is still in its early stages, because proper standards and protocols are lost and cannot guarantee product quality [21,22].

Existing data have suggested that there is a neuroprotective effect of dietary supplementation with *H. erinaceus* in mice subjected to middle cerebral artery occlusion [23]. Furthermore, *H. erinaceus* provided a partial recovery of intellectual function of patients with a mild cognitive impairment or against other forms of neurodegenerative diseases, including dementia and Alzheimer's [24,25,26]. It has been shown that erinacines A–I and hericenones C–H are responsible for the neuroprotective effects of stimulating Nerve Growth Factor (NGF) [27,28] and of brain derived neurotrophic factor (BDNF) synthesis in vitro [29,30]. A possible role of polysaccharides in neuroprotection has been suggested as well [25,27,31]. Additionally, the effects of *H. erinaceus* on recognition memory and on hippocampal mossy fiber-CA3 neurotransmission in wild-type middle-aged mice was recently published [32,33]. Among the neurogenic zones, hippocampus is the most interesting area in the adult brain, because it is involved in higher cognitive function, such as memory processes and certain affective behaviors. In particular adult and persistent hippocampal neurogenesis generates new excitatory neurons in the dentate gyrus and contributes in a significant way to plasticity across the life span [34].

In the current report, we have created a frailty index for locomotor and recognition memory performance and we examined the relationship between them in aging, wild-type mice. Furthermore,

we observed the effect of an *H. erinaceus* supplement (He1) containing a known amount of Erinacine A, Hericenone C, and Hericenone D on frailty. Moreover, we assessed the He1 effect on hippocampal and cerebellum neurogenesis in frailty animals, by investigating specific protein markers representative of cell proliferation activity and newborn neurons occurrence.

## 2. Materials and Methods

### 2.1. Animals

Fifteen wild-type male mice (strain C57BL-6J), starting at 11 months old, were maintained in single cages in the Animal Care Facility at University of Pavia on a 12-h light/dark cycle. Water and food were provided ad libitum. All experiments were carried out in accordance with the guidelines laid out by the institution's animal welfare committee, the Ethics Committee of Pavia University (Ministry of Health, License number 774/2016-PR).

In vivo experiments were performed at six different experimental times (Figure 1), between 11 and 23.5 months old.
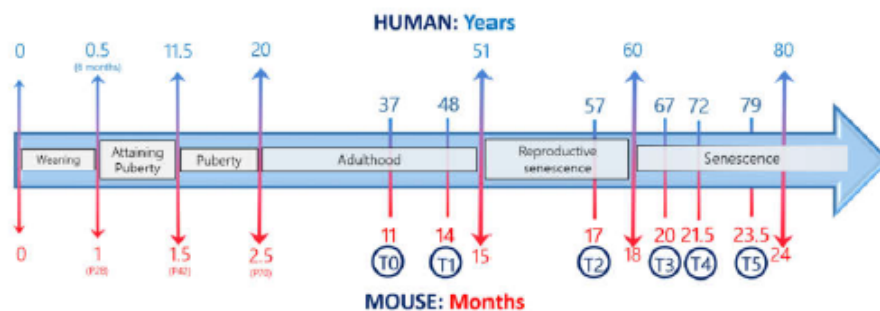


**Figure 1.** Comparative age between men and mice during their life span and the chosen experimental times (modified by Dutta and Sengupta, 2016).

Seven out of fifteen mice, starting from 21.5 months old, received for two months a drink made by a mixture of He1 mycelium and sporophore as ethanol extracts solubilized in water, in such a way that every mouse received 1 mg of supplement per day. This amount was chosen to mimic the oral supplementation in humans (about 1g/day). Daily consumption of water and supplements was monitored for each mouse.

At each experimental time, mice were weighed; no statistically significant change was recorded either during aging or between the He1 and control groups.

### 2.2. Apparatus and Procedures

We performed a spontaneous behavioral test to study locomotor activity and recognition memory in mice. For all experiments, researchers were blinded to the group assignment (control and He1). Mice activity was quantified by SMART video tracking system with a selected sampling time of 40 ms/point (2 Biological Instruments, Besozzo, Varese, Italy) and Sony CCD color video camera (PAL). All mice, at different times from T0 until T5, performed two spontaneous tests, Emergence and Novel Object Recognition (NOR) tasks. Emergence and NOR tasks are used to assess recognition memory for the environment and the object, respectively.

### 2.2.1. Emergence Test

We carried out emergence tests in accordance with procedures described by Brandalise et al., 2017 [32]. In the emergence test, we measured total distance and resting time covered in the familiar

compartment as locomotor parameters, while we measured the number of exits, latency of first exit, and the time of exploration outside as cognitive indicators (Table 1).

**Table 1.** selected parameters to measure locomotor and cognitive performances in each task. DI = discrimination index between novel/repositioned and familiar object. NOR = novel object recognition.

| Test | Locomotor Parameters | Cognitive Parameters |
|---|---|---|
| **Emergence** | Resting Time In (s) Total Distance In (cm) | Exit Number ($n$) Latency of First Exit (s) Time of Exploration (s) |
| **NOR** | (Open Arena) Resting Time (s) Total Distance (cm) Max Speed (cm/s) Mean Speed (cm/s) | Number of Approaches: DI Time of Approaches: DI |

### 2.2.2. Novel Object Recognition Task

We carried out novel object recognition tasks in accordance with procedures described by Brandalise et al., 2017 [32], consisting of three primary phases: open arena, familiarization, and test. To assess locomotor activity, mice were observed for 15 min while freely exploring the open-field arena in the absence of objects. Locomotor parameters of mean speed, maximum speed, resting time, and the total distance covered in the arena (Table 1) were all considered. During test phase, we measured the number of approaches and the time of approaches to the familiar and the novel objects as cognitive parameters (Table 1). To evaluate the discrimination between novel and familiar objects, we calculated the Mean Novelty Discrimination Index (DI) by using the following formula (1) [35],

$$DI = (n-f)/(n+f) \tag{1}$$

where $n$ is the average time or number of approaches to the novel object and f is the average time or number of approaches to the familiar one (Table 1). This index ranges from −1 to 1, where −1 means complete preference for the familiar object, 0 means no preference, and 1 means complete preference for the novel object.

### 2.3. The Frailty Index

A variant of Parks's methodology [36,37] was used to calculate the Frailty Index (FI). In Parks's procedure for creating the FI, a graded scale was calculated as follows: values that were 1 standard deviation (SD) above or below the mean reference value were given a frailty value of 0.25; values that differed by 2 SD were scored as 0.5; values that differed by 3 SD were given a value of 0.75, and values that were more than 4 SD above or below the mean received a frailty value of 1. Parameters that differed from T0 reference values by less than 1 SD received a score of 0.

Park's procedure, as described above, was changed in order to obtain more accurate values during aging. The mean value and the standard deviation (SD) for each of the parameters were calculated at T0. The values obtained in each mouse at different times, from T0 to T5, were compared to the mean value at T0, by using the following formula (2):

$$FI = ((Value\text{-}Mean\ Value\ at\ T0))/(SD\ at\ T0)^*0.25 \tag{2}$$

This procedure was applied for both Locomotor FI and Cognitive FI. Finally, to obtain LAC (Locomotor And Cognitive) FI we averaged the Locomotor and Cognitive FIs.

### 2.4. H. erinaceus

The He1 (strain 1 of *H. erinaceus*) was isolated from a basidioma collected in 2013 in Siena province (Region Tuscany, Italy) from a live specimen of *Quercus ilex* [38]. The basidioma was aseptically cut in small portions (about 1 mm³) that were placed into Petri dishes with 2% malt extract agar as a culture medium (MEA, Biokar Diagnostics). Chloramphenicol at 50 ppm was added in this first step. Incubation was performed at 24 °C in complete darkness. The strain was maintained in the Italian Culture Collection of Pavia University (MicUNIPV).

### 2.4.1. Extraction Procedures

Lyophilized mycelium and sporophores of He1 were extracted in 70% ethanol, per the procedure described by Gerbec et al. [39]. In details, one gram of dry substrate was blended with 10 mL of 70% ethanol and left in the thermostat overnight at 50°C. Before withdrawing, the material was stirred for one hour and was centrifuged at 4000 rpm for three minutes. The supernatant was stored at -20°C.

### 2.4.2. HPLC-UV-ESI/MS Method

HPLC-UV-ESI/MS analyses were carried out on a Thermo Scientific LCQ FLEET system, equipped with a PAD-UV detector working at 254 nm (Thermo Scientific®, San Jose, CA, USA). The chromatographic separation was performed using an Ascentis Express F5 HPLC column (150 × 3.0 mm, 2.7 μm particle size Sigma Aldrich, Milan, Italy) maintained at 40 °C, with a flow rate of 0.3 mL/min and an injection volume of 20 μL. The following gradient method was utilized with water containing 0.1% formic acid (solvent A) and acetonitrile (solvent B): 0–9 min (30–50% B), 9–27 min (50–60% B), 27–54 min (60–100% B), 54–69 min (100–30% B), and 69-75 min (30% B); all solvents are from Sigma Aldrich, Milan, Italy. The HPLC system was interfaced to the ion trap mass spectrometer with an Electro Spray Ionization (ESI) ion source. The compounds were analyzed under positive (ESI+) ion conditions. The ion spray and capillary voltage were set at 5kV and 10V, respectively, in positive ion mode. The capillary temperature was 400 °C. The acquisition was performed both in Full Scan mode (mass range 200–2000 Da) and MS/MS Dependent Scan mode. The data station utilized the Xcalibur MS Software Version 2.1 (Thermo Scientific®, San Jose, CA, USA).

Erinacine A and hericenones C and D were used as standards [40,41]. Stock solutions (1 mg/mL) of erinacine A and hericenones C and D were prepared in 70% ethanol. Standard solutions with the final concentration range of 1–25 μg/mL for erinacine A and 20–100 μg/mL for hericenones C and D were prepared. Linear least-square regression analysis for the calibration curves showed correlation coefficients of 0.9968, 0.9945, and 0.9951, respectively, for erinacine A, hericenones C, and hericenones D with respect to the peak area, demonstrating a good linear relationship in the different ranges tested. Each concentration was analyzed in triplicate.

### 2.5. Tissue Sampling: Hippocampal and Cerebellar Specimens Preparation

Mice were anesthetized by isoflurane inhalation (Aldrich, Milwaukee, WI, USA) before decapitation.

The brain and cerebellum were immediately excised as previously described [42], washed in 0.9% NaCl, and fixed by immersion for 48 h at room temperature in Carnoy's solution (6 absolute ethanol/3 chloroform/1 acetic acid). The tissues were then kept in absolute ethanol for one hour, followed by acetone for 50 min, and finally embedded in Paraplast X-TRA (Sigma Aldrich, Milan, Italy). Eight micron-thick sections, collected on silane-coated slides, of brain and cerebellar vermis were cut in the sagittal plane.

### 2.6. Immunohistochemistry: Fluorescence Microscopy Assessment and Quantification of Cell Proliferation and Neurogenesis

To avoid possible staining differences due to small changes in the procedure, the immunoreactions were carried out simultaneously on slides from controls and treated animals. Paraffin-embedded sections were deparaffinized in xylene, rehydrated through a series of graded alcohol treatments and rinsed in phosphate-buffered saline (PBS, Sigma).

PCNA (PC10), a 37 kDa molecular weight protein also known as cyclin, was employed as marker of cell proliferation. In particular, in cells fixed with organic solvents, the PCNA was demonstrated to be strongly associated in the nuclear regions where DNA synthesis is occurring [43]. DCX is considered a marker for neuronal precursors and migrating neuroblasts during neurogenesis recovery [44]. The presence and distribution of PCNA and DCX was assessed using commercial antibodies on murine specimens, focusing on the hippocampus and cerebellum. Brain and cerebellar sections of control and He1 mice were incubated overnight at room temperature with the primary

antibody: (i) mouse monoclonal antibody against PCNA (1:600, Abcam, Cambridge, MA, USA), and (ii) goat polyclonal antibody against DCX (1:100, Santa Cruz Biotechnology, Santa Cruz, CA, USA). After washing in phosphate buffer saline (PBS), sections were incubated for one hour with the secondary antibody: (i) Alexa Fluor 488-conjugated anti-mouse (1:100, Molecular Probes, Space, Milano, Italy) and (ii) Alexa Fluor 594-conjugated anti-goat (1:100, Molecular Probes, Space, Milano, Italy),in a dark, moist chamber. Then the nuclei were counterstained for 10 min with 0.1 μg/mL Hoechst 33258 (Sigma Aldrich, Milan, Italy). After PBS washing, coverslips were mounted in a drop of Mowiol (Calbiochem, San Diego, CA, USA).

Sections were observed by fluorescence microscopy with an Olympus BX51 equipped with a 100- W mercury lamp used under the following conditions: 330–385 nm excitation filter (excf), 400 nm dichroic mirror (dm), and 420 nm barrier filter (bf) for Hoechst 33258; 450–480 nm excf, 500 nm dm, and 515 nm bf for the fluorescence of Alexa 488; 540 nm excf, 580 nm dm, and 620 nm bf for Alexa 594. Images were recorded with an Olympus MagnaFire cam and processed with the Olympus Cell F software.

Immunofluorescence quantification was performed by calculating the percentage of PCNA or DCX immunocytochemically positive nuclei or cytoplasm of nervous cells (from the hippocampus and cerebellum) of a total number (about 300) for each animal and experimental condition, in a minimum of 10 randomly selected high-power microscopic fields.

### 2.7. Statistics

Data are reported as mean ± standard error of the mean (SEM). We performed Bartlett and Shapiro Wilk Tests to establish and confirm the normality of parameters. To verify statistically significant differences, we used a one-way Anova for repeated measures of the aging of mice and a two-way Anova for the effect of *H. erinaceus* supplementation. The statistical analysis for immunofluorescence was carried out using an Unpaired Student's t-test. The differences are considered statistically significant for $p < 0.05$ (*), $p < 0.01$ (**), $p < 0.001$ (***), and $p < 0.0001$ (****). Statistical analyses were performed with GraphPad Prism 7.0 software (GraphPad Software Inc., La Jolla, CA, USA).

## 3. Results

### 3.1. Locomotor and Recognition Memory during Physiological Aging

We first investigated locomotor performance and recognition memory during physiological aging in healthy mice ($n$ = 15) using different spontaneous behavioral tests. Novelty recognition memory for a new environment and for novel objects was tested by way of emergence and NOR tasks, respectively.

We carried out behavioral spontaneous tests in mice at 11 (T0), 14 (T1), 17 (T2), 20 (T3), 21.5 (T4), and 23.5 (T5) months old. For the reader to understand the practical application of these tests, a comparison of the different developmental stages between humans and mice during their life span, according to Dutta and Sengupta is outlined in Figure 1 [45]. To monitor the physiological aging in mice, we choose six experimental times: T0 and T1 corresponding to adulthood phase, T2 to reproductive senescence, and T3, T4, and T5 to senescence phase.

Figure 2A shows the locomotor parameters measured in the open arena during aging. Total distance and resting time decreased from T0 to T1, stabilizing at T3. Mean speed in the open arena changed at T2 and then worsened with the aging. Maximum speed worsened later, in senescence phases T4 and T5.

Figures 2B and 2C show the cognitive parameters measured in emergence and in NOR, respectively. In the emergence test latency to the first exit, the exit number and the exploring time worsened from T0 to T1 and then remained relatively stable, whereas the latency to the first exit worsening again in the senescence phase. In the NOR test, the time of approach and the number of approaches decreased in T2 and even more in senescence phase.
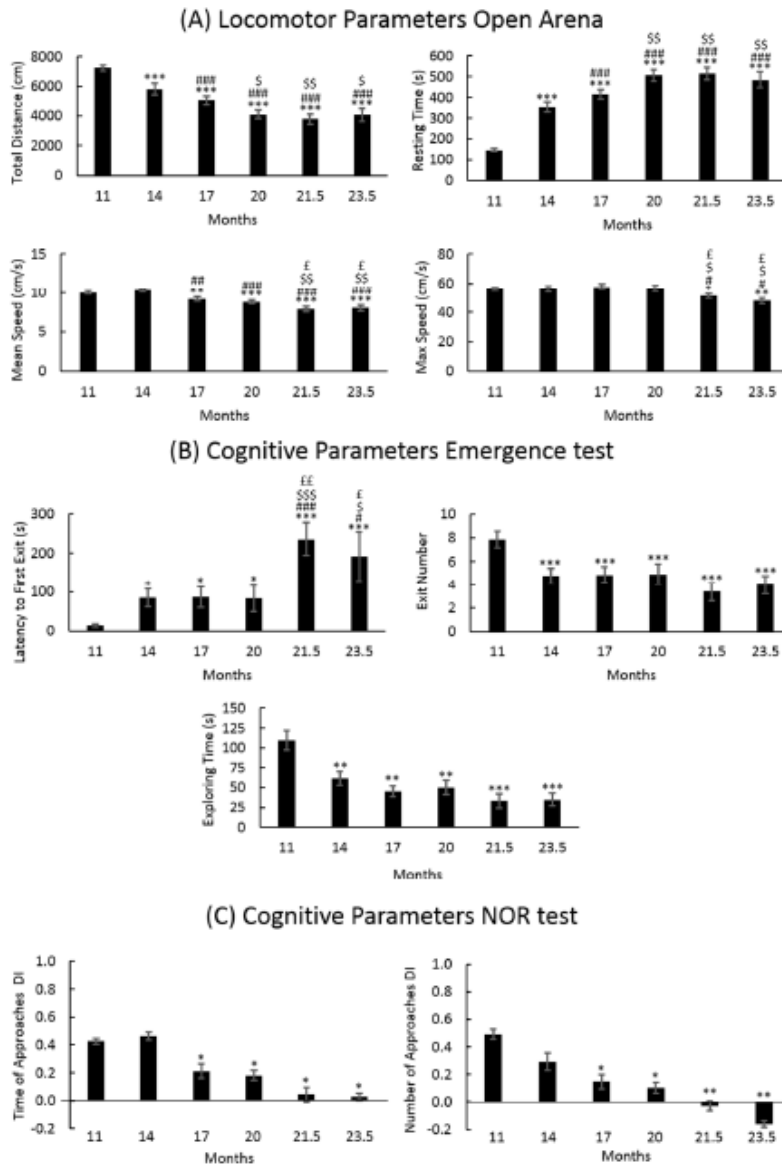
**Figure 2.** Locomotor and cognitive parameters during aging. (**A**) Locomotor parameters: total distance, resting time, mean speed, and max speed measured in open arena during aging. (**B**) cognitive parameters: latency to first exit, exit number, and exploring time measured in emergence, and (**C**) cognitive parameters: discrimination index (DI) of the time of approaches and of the number of approaches measured in NOR test. Statistical results were performed by Anova for repeated measures: * vs T0, # vs T1, $ vs T2, and £ vs T3. For all symbols reported $p < 0.05$ (*, #, $, £), $p < 0.01$ (**, ##, $$, ££), $p < 0.001$ (***, ###, $$$, £££).

### 3.1.1. Locomotor Frailty Index

We calculated the Locomotor Frailty Index (FI) for each of the parameters reported in Table 1, then averaged the values for each experimental time. Figure 3, Panel A shows the Locomotor FIs from T0 to T5 and the linear least-square regression analysis, with $R^2 = 0.8912$. Results from a one-way ANOVA are reported in Figure 3. These results suggest that during physiological aging, locomotor performances decline linearly from the adulthood to the senescence stage.

The slope obtained by the linear least-square regression analysis (slope value = 0.1044) indicated that for every three months passed, locomotor activity decreased by about 35.43%, yielding a significantly different Locomotor FI value from the previous one each time.
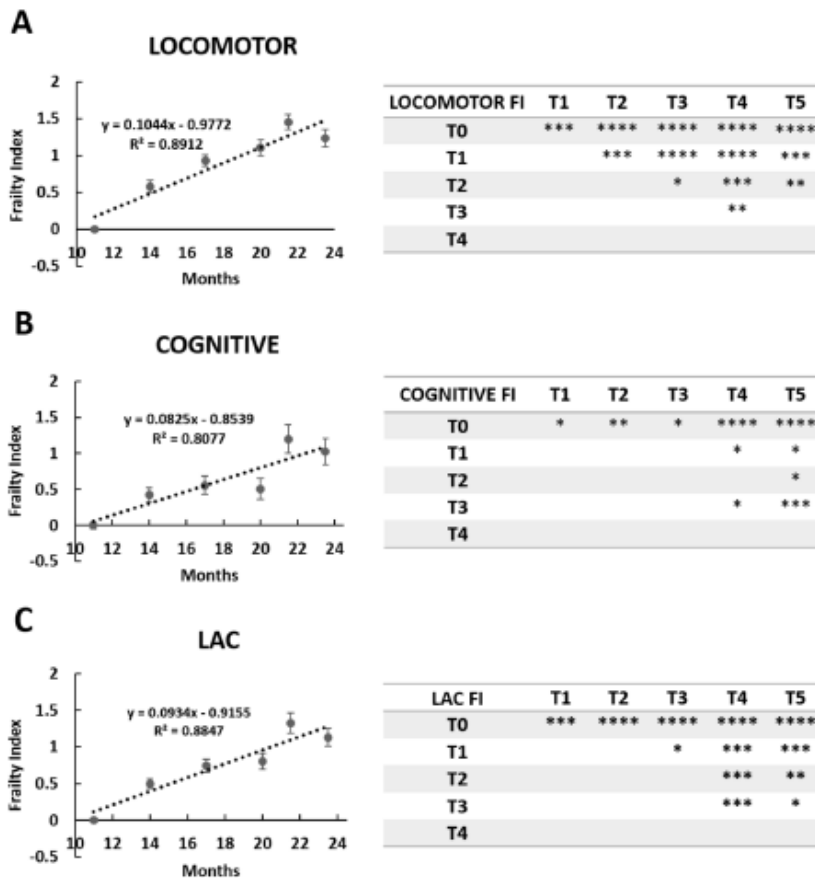


**A** LOCOMOTOR

| LOCOMOTOR FI | T1 | T2 | T3 | T4 | T5 |
|---|---|---|---|---|---|
| T0 | *** | **** | **** | **** | **** |
| T1 | | *** | **** | **** | *** |
| T2 | | | * | *** | ** |
| T3 | | | | ** | |
| T4 | | | | | |

**B** COGNITIVE

| COGNITIVE FI | T1 | T2 | T3 | T4 | T5 |
|---|---|---|---|---|---|
| T0 | * | ** | * | **** | **** |
| T1 | | | | * | * |
| T2 | | | | | * |
| T3 | | | | * | *** |
| T4 | | | | | |

**C** LAC

| LAC FI | T1 | T2 | T3 | T4 | T5 |
|---|---|---|---|---|---|
| T0 | *** | **** | **** | **** | **** |
| T1 | | | * | *** | *** |
| T2 | | | | *** | ** |
| T3 | | | | *** | * |
| T4 | | | | | |

**Figure 3.** Locomotor, cognitive, and LAC (locomotor and cognitive) decline during physiological aging in mice. Locomotor (panel (**A**)), cognitive (panel (**B**)), and LAC (panel (**C**)) Frailty Index during physiological aging in mice. Linear regressions of experimental points and statistical results were reported. $p < 0.05$ (*), $p < 0.01$ (**), $p < 0.001$ (***).

### 3.1.2. Cognitive Frailty Index

Novelty recognition memory was evaluated, resulting in a calculation of the Cognitive Frailty Index (FI) during aging (Figure 3B). Cognitive FI was calculated using a linear least-square regression analysis, with $R^2 = 0.8077$. Results from a one-way ANOVA are reported in Figure 3.

The slope obtained by the linear least-square regression analysis (slope value = 0.0825) indicated that for every 3 months passed, recognition memory declined by about 26.04%, yielding a significantly different Cognitive FI value the previous one each time.

### 3.1.3. Cognitive Frailty Index

In order to evaluate a global trend of both phenotypic and cognitive decline in physiological aging, we calculated the Locomotor and Cognitive FI (LAC frailty index) by averaging all frailty indices obtained prior to evaluating the locomotor and cognitive performances during aging (Figure 3C). The LAC FI significantly increased from T0 to T5. Similarly, as previously described for Locomotor FI and Cognitive FI, the LAC FI values follow a linear trend ($R^2$ = 0.8847) (Figure 3C). The slope obtained by the linear least-square regression analysis (slope value = 0.0934) indicated that for every 3 months passed, the frailty of the mouse increased by about 30.7%.

### 3.2. Identification and Quantification of Erinacine A, Hericenone C, and Hericenone D

In order to identify and quantify the bioactive metabolites of interest, we analyzed the mycelium and sporophore extracts of He1 using HPLC-UV-ESI/MS. Erinacine A and hericenones C and D were identified by comparing both retention times and ESI/MS spectra with the authentic standards.

Characteristic ions of Erinacine A in the ESI/MS spectrum (Figure 4) are sodium and potassium adducts of a single molecule as well as a dimer (Table 2). Hericenone C and D spectra (Figure 5) present just [M+H]+ and [M+Na]+ ions (Table 2).
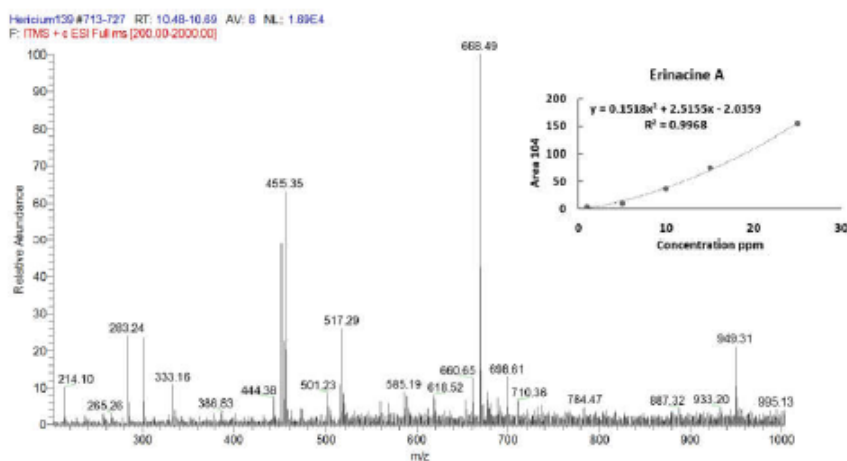


**Figure 4.** ESI/MS spectrum of Erinacine A. Panel (top, right) reports calibration curves and linear regression curve for Erinacine A.
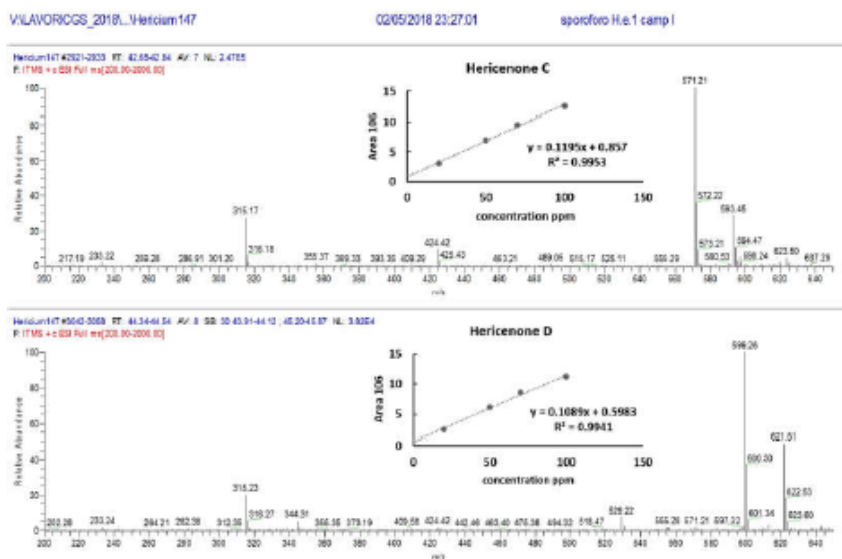
**Figure 5.** ESI/MS spectra of Hericenone C and D. Panels (top, right) report calibration curves for Hericenone C and D.

**Table 2.** shows the Erinacine A, Hericenones C and D molecular formula, molecular weight, chemical structure, characteristic structure, and content in 1 g of dried He1 mycelium and sporophore.

| | Molecular Formula | Molecular Weight (g/moL) | Chemical Structure | Characteristic Ions (m/z) | Content (µg/g) |
|---|---|---|---|---|---|
| **Erinacine A** | $C_{25}H_{36}O_6$ | 432.56 |  | 455 [M+Na]⁺<br>452 [2M+K+H]²⁺<br>668 [3M+K+H]²⁺<br>949<br>[2M+HCOOH+K]⁺ | 150 in mycelium |
| **Hericenone C** | $C_{35}H_{54}O_6$ | 570.81 | <br>R = Palmitoyl | 571 [M+H]⁺<br>593 [M+Na]⁺ | 500 in basidioma |
| **Hericenone D** | $C_{37}H_{58}O_6$ | 598.87 | <br>R = Stearoyl | 599 [M+H]⁺<br>621 [M+Na]⁺ | <20 in basidioma |

Erinacine A was detected using HPLC/ESI-MS. By comparing the retention time and molecular ion or mass spectra, we confirmed the peak identification. We quantified it by comparing the peak areas with those of the standard (Figure 6). The calibration curve was constructed by injecting

248

standard mixture solutions at five concentrations (1, 5, 10, 15, and 25 µg/mL). The linear least-square regression analysis for the calibration curve showed a correlation coefficient of r = 0.9968. The level of Erinacine A present in mycelium of He1 calculated by the calibration curve was 150 µg/g (Table 2).
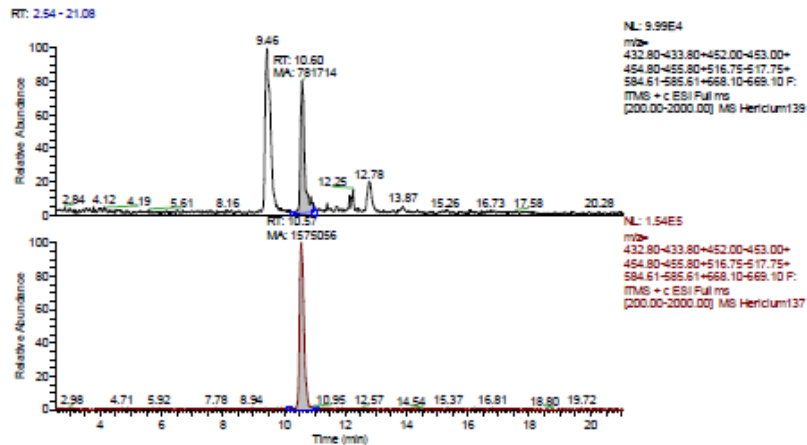


**Figure 6.** MS (Mass Spectrum) traces of He1 mycelium and Erinacine A (Rt 10,57) standard. Peak area of Erinacine A is pointed out.

The hericenones C and D chromatographic conditions produced a good resolution of adjacent peaks. UV detection provided sufficient sensitivity for each analyte, allowing proper quantification of both compounds by comparing the peak areas in the UV trace with those of the standards (Figure 7). Calibration curves were constructed by injecting the standard mixture solutions at four concentrations (20, 50, 75, 100 µg/mL.). Linear least-square regression analysis for the calibration curves showed correlation coefficients of r = 0.9945 and r = 0.9951, respectively, for hericenones C and D. The levels of hericenones C and D present in He1 basidioma, calculated by calibration curves, were 500 µg/g and less than 20 µg/g, respectively (Table 2).
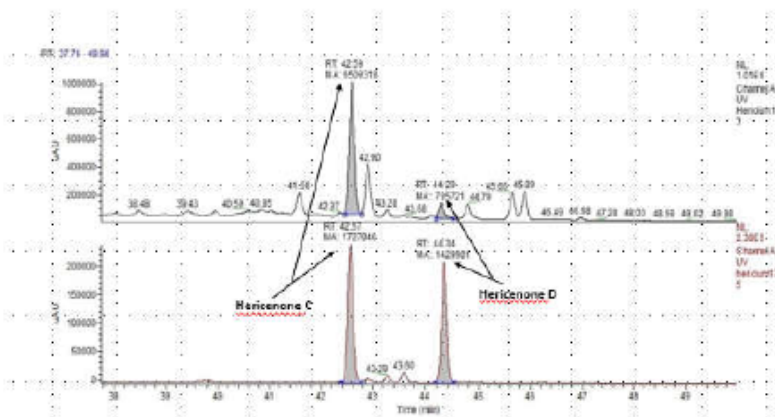


**Figure 7.** UV (Ultra Violet) traces of He1 sporophore (top) and Hericenone C (Rt 42.57) and D (Rt 44.34) standards (bottom). Peak areas corresponding to Hericenone C and D are pointed out.

### 3.3. He1 Supplementation Improved Recognition Memory Performances during Aging

We investigated cognitive and locomotor performances after oral *H. erinaceus* supplementation on frail mice. Seven mice with a T4 LAC FI score measured of more than 1.30 received a mixture of components made by He1 mycelium and basidioma for two months until T5.

Figure 8 shows the frailty index before (T4) and after He1 supplementation (T5). He1 supplementation improved recognition memory in mice during aging, characterized by a Cognitive FI decrease from 1.71 ± 0.21 to 0.72 ± 0.22. Locomotor performances before and after He supplementation were not significant different. Considering together locomotor and memory performances by means of the LAC index, He1 regressed aged-related frailty, but this change in LAC index was completely driven by the improve in memory function.
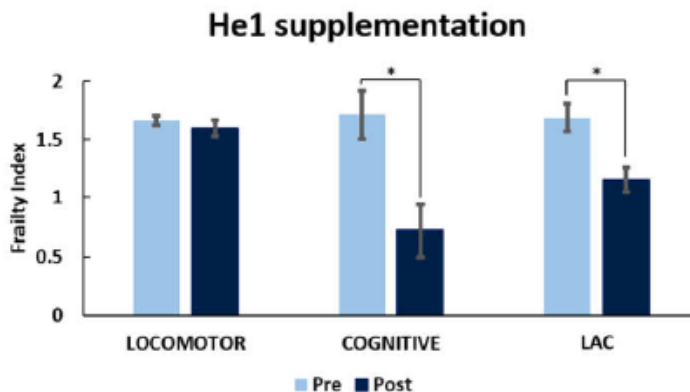


**Figure 8.** *H. erinaceus* improved recognition memory during mice aging. Value measured pre-supplementation (pre) and post-supplementation (post) on locomotor, recognition memory, and LAC (Locomotor And Cognitive) FI. $p < 0.05$ (*).

### 3.4. He1 Supplementation Improved Hippocampal and Cerebellum Proliferation and Neurogenesis

To examine the molecular mechanism involved in the He1 effect on aging mice, we performed immunocytochemical studies on different cerebral tissues, i.e. the hippocampus and cerebellum, testing both the proliferating the cell nuclear antigen (PCNA) and doublecortin (DCX) as specific markers of active proliferation and neurogenesis, respectively. We performed immunocytochemistry on He1 frail mice and on untreated (control) animals at T5.

Preliminary data seem to demonstrate that cell proliferating activity achieved the highest expression in both brain areas in He1 mice compared to control animals. Specifically, the PCNA nuclear immunolabelling appeared more marked in the hippocampal dentate gyrus (DG) granule cells and in the CA3 pyramidal neurons, while the immunopositive cells (possibly granular or glial cells) predominantly localized in the width of the outer molecular layer in the cerebellar cortex (Figure 9A). Notably, clusters of PCNA-positive cells, possibly newborn granule cells, were observed suggesting the occurrence of a recovered proliferation wave (Figure 9A). Accordingly, quantitative analysis demonstrated that the PCNA labelling frequency detected in He1 treated mice (22.89% ± 6.09) reached significantly higher values compared to those measured in controls (10.80% ± 3.09, p < 0.05) in the hippocampus. Similarly, the PCNA labelling frequency detected in He1 mice (25.60% ± 6.66) reached significantly higher values compared to those measured in controls (8.19% ± 4.43, p < 0.05), in the cerebellum (Figure 9B).

In He1 mice, hippocampus showed a more marked DCX labelling compared to control animals. In particular, DCX immunolabelling appeared more intense in the dentate gyrus (DG) granule cells

in the hippocampus (Figure 10A, panel a and b). In the cerebellar cortex the immunopositivity was less expressed, nonetheless mainly localized in cells present in the molecular layer (Figure 10A, panel c and d). Quantitative analysis showed that the DCX labelling frequency in He1 mice achieved significantly higher values compared to those measured in control animals in hippocampus (8.45% $\pm$ 3.02 vs 0.22% $\pm$ 0.45, respectively, with $p < 0.05$). In the cerebellum the DCX labelling frequency displayed a trend of increase in He1 mice but did not reached the threshold for the statistically significant difference compared to controls (4.68 $\pm$ 3.06 vs 0.26% $\pm$ 0.79, respectively, with $p = 0.073$) (Figure 10B). It should be noted that the DCX labelling frequency in control animals is only about 0.2% in both hippocampus and cerebellum. As the PCNA labelling identifies DNA repair as well as duplication, and DCX positivity links to the presence of newborn neurons, the increased expression of this cytochemical marker may be the manifestation of different biological responses involving the recovery of cell proliferation and neurogenesis, potentially highlighting the occurrence of an upswing phase owed to the neurobiological effects exerted by the oral supplementation with He1.
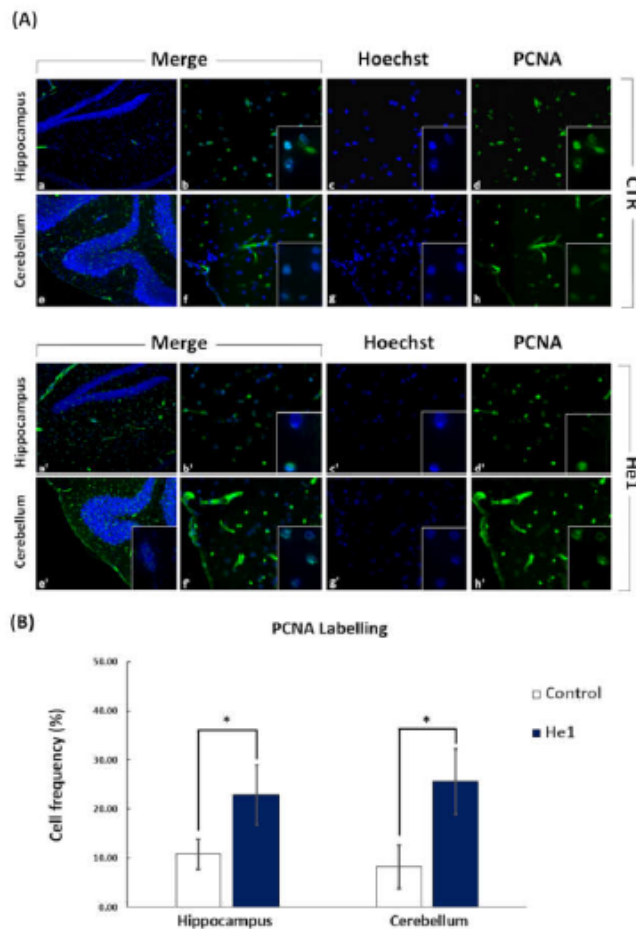


**Figure 9.** Panel (A) shows cell proliferating activity immunocytochemically detected by PCNA (Proliferating Cell Nuclear Antigen) labelling, observed at T5 after 2 months oral supplementation with He1 in both hippocampus and cerebellum, (a'–d' and e'–h', respectively), compared to control

untreated mice (CTR) (a–h). Cell proliferation was significantly enhanced in He1 mice, with the labelling appearing more intense in the hippocampal DG granule cells and in CA3 pyramidal neurons (a′–d′) and in cerebellar molecular layer (e′–h′), compared to controls (a-d and e-h, respectively), predominantly localized in the DG granule cells and in CA3 pyramidal neurons, as also in the width of the cerebellar. Objective magnification: 20 x (a, e and a′, e′); 40 x (b-d, f-h and b′-d′, f′-h′); 100 x (insert in b-d, f-h, b′-d′, f′-h′). Panel (**B**) shows changes in the percentage of PCNA labelling index of hippocampal and cerebellar cells in He1 mice. $p < 0.05$ (*).
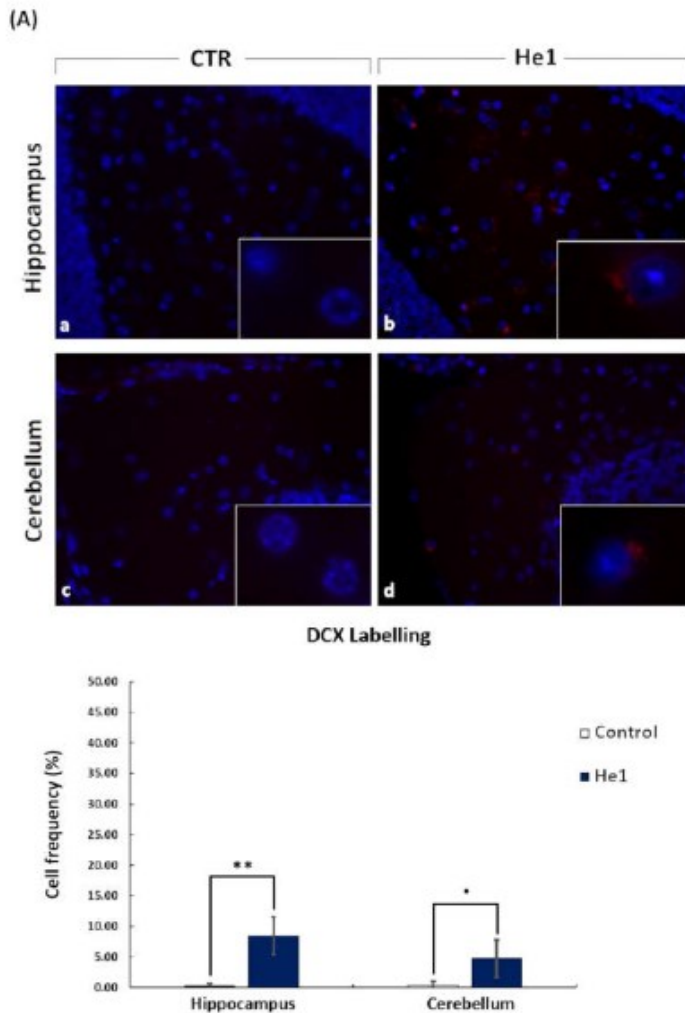


**Figure 10.** Panel (**A**) shows doublecortin (DCX) immunocytochemistry, observed at T5 after 2 months oral supplementation with He1 in hippocampus and cerebellum (b and d), compared to control mice (a and c). Objective magnification: 40 x (a-d); 100 x (inserts). Panel (**B**) shows the cell frequency percentage of DCX labelling in the hippocampal dentate gyrus and cerebellar molecular layer in control and He1 mice. $p < 0.01$ (**), $p = 0.07$ (*).

## 4. Discussion

The aim of this study was to develop an index to monitor locomotor and cognitive frailty in aging mice in vivo and to study the effect of *H. erinaceus* extracts containing a known amount of erinacines A and hericenones C and D. The mechanism of action of He1 was evaluated by immunocytochemistry.

We developed a frailty index score (LAC FI) based both on locomotor and cognitive decline during aging. To achieve a translational approach, we chose to monitor locomotor indicators that compare well to phenotypic frailty indicators in humans, such as gait speed and the level of physical activity [1]. We therefore measured the mean and maximum speed, resting time, and the total distance covered in an open arena test.

In concordance with Fried's phenotype model [1] and with Parks observations on activity level [36], the current paper demonstrates that the locomotor performances of mice progressively worsened during aging. The locomotor FI increased significantly during aging, with a linear progression from 11 to 23.5 months. We have developed a simplified, non-invasive method to monitor the development of frailty during mice aging, using a FI measured according to Whitehead [37].

Researchers use often the Stenberg Item Recognition Paradigm (SIRP) to measure cognitive impairment during aging in humans [46,47], during which a small group of items, called the positive set, is presented for the subject to memorize. After a delay, a single item is presented that may (familiar) or may not have (novel) been shown before and the subject is asked to answer "yes" or "no" to indicate their recognition of the item. The NOR and the emergence test in mice assess the same ability to recognize a familiar and a novel object [48] or a new environment. We measured exit numbers, the latency of the first exit and the time of exploration in the emergence test and the number and time of approaches in the NOR test [32] as cognitive parameters. We preferred to use different parameters, as suggested by Ennaceur et al., because it has been recognized that this methodology supports the validity and interpretation of the data of a behavioral experiment [49].

Locomotor and Cognitive Frailty Index scores were interpolated by a straight line. The slope of the linear regression indicates that locomotor performances decreases at a steeper rate than cognitive performances during the mouse's life span. Therefore, the data, therefore, indicate that locomotor frailty is associated with lower performance in recognition memory. These data suggest that when mice meet frailty criteria, they should be seen as mice at risk of cognitive decline.

Standardization, efficacy, and the mechanism of action of medicinal mushroom products is a pressing problem [21]. Thanks to the comparison with standard measures, we have identified and quantified erinacines A in the mycelium, and hericenones C and D in the sporophore of He1 using the HPLC-UV-ESI/MS technique. It is worth noting that the content of 0.15 mg/g of erinacine A present in mycelium in this *Hericium* strain is comparable to that reported by Krzyczkowski et al. under the use of the most favorable combination of nutrients [50]. By monitoring the temperature and ventilation during the processing, Chen et al. subsequently obtained the highest content of erinacine A, suggesting a carbon-to-nitrogen ratio of 6 and a pH value of 4 may be important parameters in promoting the biosynthesis of erinacine A [51].

Basidioma of *H. erinaceus* contains a considerable quantity of bioactive molecules such as hericenones. The quantity of hericenones C and D in our sample of *H. erinaceus* was 0.5 mg/g and 0.02 mg/g, respectively, similar to that reported by Lee et al. in some wild-type and local varieties of *H. erinaceus* strains [52].

To be able to best generalize our results to humans, we decided to use an amount of the mycelium and basidioma extracts to mimic the supplementation used in humans. It should be noted that in vitro and in vivo effects of erinacine A and hericenones on NGF synthesis [53], on reducing amyloid burden [51], on reducing amyloid plaques, and on recovering from impairments in Morris water maze tasks [54] were obtained by using a daily millimolar concentration starting from 1-until 30 mg/Kg body weight [55]. In our experimental condition, we used 100-fold lower concentration.

Using the same experimental condition, we previously described the effect of *H. erinaceus* on improving recognition memory and the increase in spontaneous and evoked excitatory synaptic

current in mossy fiber-CA3 synapses [32,33]. Similarly, Rossi et al. showed that two months of *H. erinaceus* treatment increased locomotor performances in mice [33]. The current paper confirms that He1 supplementation may increase recognition memory performance in mice during aging and may also revert the cognitive decline in frail mice.

Hippocampal neurogenesis is pivotally involved in higher cognitive function and, new excitatory dentate gyrus (DG) granule cells, generated by adult hippocampal neurogenesis, contributes significantly to neural plasticity throughout the entire life duration. Our data showed in hippocampus the recovery of cell proliferation in DG granule cells and CA3 pyramidal neurons and the presence of progenitor cells in DG granule cells. These data are in accordance with a recent in vivo study by Ryu et al. [56], supporting the notion that *H. erinaceus* extract administration promotes hippocampal neurogenesis in the adult mouse brain.

There is, currently, a dearth of literature available on the cerebellum area. An in vitro investigation showed the ability of *H. erinaceus* to promote the normal development of cerebellar cells, demonstrating a regulatory effect on the myelin genesis process [57]. Recently, Trovato and colleagues [58] demonstrated in vivo the neuroprotective action of *H. erinaceus* through the up-regulation of lipoxin A4 and modulation of stress responsive vitagene proteins. Our data supports the occurrence of a cell proliferation upswing in the cerebellum, as evidenced by the presence of several PCNA-immunopositive cells, possibly granular cells. Traditionally, the adult cerebellum is commonly considered as a "non-neurogenic" area. Nonetheless, our present results concerning cerebellar cortex demonstrated the presence of DCX-immunopositive cells localized in the molecular layer of He1-treated mice, suggesting the occurrence of newborn immature nervous cells.

In accordance with our preliminary results, recent investigations hypothesized the existence of stem cell populations within the cortex of the adult cerebellum that express stem cell markers and that can give rise to neuronal progeny when expanded in vitro and subsequently transplanted back into the murine cerebellum [59]. Therefore, further in-depth experiments, testing additional molecular markers, need to be carried out to confirm these data, initially identifying the PCNA-immunopositive proliferating cell type and then corroborating the occurrence of a "non-canonical" cerebellar neurogenic process in adult mice.

## 5. Conclusions

In conclusion, we suggest that during aging, the two form of vulnerability in locomotor and cognitive performances develop in parallel and therefore, we need to integrate motoric and cognitive evaluations. As suggested by Lauretani et al., an investigation of the "brain-muscle loop" in a simultaneous assessment of all aspects that may progressively lead to loss of independence is imperative [60]. Furthermore, *H. erinaceus* is a seemingly good candidate to regress recognition memory decline during aging, possibly through an increase in neurogenesis in the hippocampus and cerebellum. These findings rise the possibility that *H. erinaceus* extracts could be a new therapeutic strategy for preventing or treating neurodegenerative diseases such as dementia and Alzheimer's, as suggested by other authors [24,25,26]. Future studies should investigate the mechanisms involved in this at a cellular level.

**Author Contributions:** D.R., A.O., C.D.I. carried out the behavior experimental tasks and the experimental analysis. F.C., B.M., V.C., C.G. carried out HPLC-UV-ESI/MS. E.C.P., F.C., B.F., F.D.L. carried out the immunoistological experiments and analysis. D.R., E.R., P.R. wrote the manuscript. M.G.B., H.K., E.S. critically analyzed and reviewed the manuscript.

**Conflicts of Interest:** The authors declare no conflict of interest.

## References

1. Fried, L.P.; Tangen, C.M.; Walston, J.; Newman, A.B.; Hirsch, C.; Gottdiener, J.; Seeman, T.; Tracy, R.; Kop, W.J.; Burke, G.; et al. Frailty in older adults: Evidence for a phenotype. *J. Gerontol. A Biol. Sci. Med. Sci.* **2001**, *56*, 46–56.
2. Bandeen-Roche, K.; Xue, Q.L.; Ferrucci, L.; Walston, J.; Guralnik, J.M.; Chaves, P.; Zeger, S.L.; Fried, L.P. Phenotype of Frailty: Characterization in the women's health and aging studies. *J. Gerontol. A Biol. Sci. Med. Sci.* **2001**, *61*, 262–266, doi:10.1093/gerona/61.3.262.
3. Hogan, D.B.; Mackinght, C.; Bergman, H. Models, definitions, and criteria of Frailty. *Aging Clin. Exp. Res.* **2003**, *15*, 1–29.
4. Ferrucci, L.; Cavazzini, C.; Corsi, A.; Bartali, B.; Russo, C.R.; Lauretani, F.; Ferrucci, L.; Cavazzini, C.; Corsi, A.M.; Bartali, B.; et al. Biomarkers of frailty in older persons. *J. Endocrinol. Invest.* **2002**, *25*, 10–15.
5. Taffet, G.E. Physiology of aging. In *Geriatric Medicine*; Springer: New York, NY, USA, 2003; pp. 27–35.
6. Espinoza, S.E.; Jung, I.; Hazuda, H. Frailty transitions in the San Antonio Longitudinal Study of Aging. *J. Am. Geriatr. Soc.* **2012**, *60*, 652–660, doi:10.1111/j.1532-5415.2011.03882.x.
7. Boyle, P.A.; Buchman, A.S.; Wilson, R.S.; Leurgans, S.E.; Bennett, D.A. Physical frailty is associated with incident mild cognitive impairment in community-based older persons. *J. Am. Geriatr. Soc.* **2010**, *58*, 248–255, doi:10.1111/j.1532-5415.2009.02671.x.
8. Brodziak, A.; Brewczyński, A.; Bajor, G. Clinical significance of knowledge about the structure, function, and impairments of working memory. *Med. Sci. Monit.* **2013**, *19*, 327–338, doi:10.12659/MSM.883900.
9. Sternberg, S.A.; Wershof-Schwartz, A.; Karunananthan, S.; Bergman, H.; Mark-Clarfield, A. The identification of frailty: A systematic literature review. *J. Am. Geriatr. Soc.* **2011**, *59*, 2129–2138, doi:10.1111/j.1532-5415.2011.03597.x.
10. Robertson, D.A.; Savva, G.M.; Kenny, R.A. Frailty and cognitive impairment-a review of the evidence and causal mechanisms. *Ageing Res. Rev.* **2013**, *12*, 840–851, doi:10.1016/j.arr.2013.06.004.
11. Auyeung, T.W.; Lee, J.S.W.; Kwok, T.; Woo, J. Physical frailty Predicts future cog-nitive decline a four-year Prospective study in 2737 cognitively normal olderadults. *J. Nutr. Health Aging* **2011**, *15*, 690–694.
12. Mitnitski, A.; Fallah, N.; Rockwood, K. A multistate model of cognitive dynamics in relation to frailty in older adults. *Ann. Epidemiol.* **2011**, *21*, 507–516, doi:10.1016/j.annepidem.2011.01.006.
13. Samper-Ternent, R.; Al-Snih, S.; Raji, M.A.; Markides, K.S.; Ottenbacher, K.J. Relationship between frailty and cognitive decline in older Mexican Americans. *J. Am. Geriatr. Soc.* **2008**, *56*, 1845–1852, doi:10.1111/j.1532-5415.2008.01947.x.
14. Aranda, M.P.; Ray, L.A.; Snih, S.A.; Ottenbacher, K.J.; Markides, K.S. The pro-tective effect of neighborhood composition on increasing frailty among older Mexican Americans: A barrio advantage? *J. Aging Health* **2011**, *23*, 1189–1217, doi:10.1177/0898264311421961.
15. Doba, N.; Tokuda, Y.; Goldstein, N.E.; Kushiro, T.; Hinohara, S. A pilot trial to predict frailty syndrome: The Japanese Health Research Volunteer Study. *Exp. Gerontol.* **2012**, *47*, 638–643, doi:10.1016/j.exger.2012.05.016.
16. Raji, M.A.; Al Snih, S.; Ostir, G.V.; Markides, K.S.; Ottenbacher, K.J. Cognitive status and future risk of frailty in older Mexican Americans. *J. Gerontol. Biol Sci Med Sci* **2010**, *65*, 1228–1234, doi:10.1093/gerona/glq121.
17. Kawagishi, H.; Ando, M.; Mizuno, T. Hericenone A and B as cytotoxic principles from the mushroom Hericium erinaceum. *Tetrahedron Lett.* **1990**, *31*, 373–376, doi:10.1016/S0040-4039(00)94558-1.
18. Friedman, M. Chemistry, Nutrition, and Health-Promoting Properties of Hericium erinaceus (Lion's Mane) Mushroom Fruiting Bodies and Mycelia and Their Bioactive Compounds. *J. Agric. Food Chem.* **2015**, *63*, 7108–7123, doi:10.1021/acs.jafc.5b02914.
19. He, X.; Wang, X.; Fang, J.; Chang, Y.; Ning, N.; Guo, H.; Huang, L.; Huang, X.; Zhao, Z. Structures, biological activities, and industrial applications of the polysaccharides from Hericium erinaceus (Lion's Mane) mushroom: A review. *Int. J. Biol. Macromol.* **2017**, *97*, 228–237, doi:10.1016/j.ijbiomac.2017.01.040.
20. Cookson, R.; Barrett, T.N.; Barrett, A.G. β-Keto-dioxinones and β,δ-diketo-dioxinones in biomimetic resorcylate total synthesis. *Acc. Chem. Res.* **2015**, *48*, 628–642, doi:10.1021/ar5004169.
21. Wasser, S.P. Medicinal mushroom science: Current perspectives, advances, evidences, and challenges. *Biomed. J.* **2014**, *37*, 345–356, doi:10.4103/2319-4170.138318.

22. Wasser, S.P. Medicinal Mushrooms in Human Clinical Studies. Part I. Anticancer, Oncoimmunological, and Immunomodulatory Activities: A Review. *Int. J. Med. Mushrooms* **2017**, *19*, 279–317, doi:10.1615/IntJMedMushrooms.v19.i4.10.

23. Hazekawa, M.; Kataoka, A.; Hayakawa, K.; Uchimasu, T.; Furuta, R.; Irie, K.; Yoshida, M.; Fujioka, T.; Egashira, N.; Oishi, R.; et al. Neuroprotective effect of repeated treatment with Hericium erinaceum in mice subjected to middle cerebral artery occlusion. *J. Health Sci.* **2010**, *56*, 296–303, doi:10.1248/jhs.56.296.

24. Mori, K.; Inatomi, S.; Ouchi, K.; Azumi, Y.; Tuchida, T. Improving effects of the mushroom Yamabushitake (Hericium erinaceus) on mild cognitive impairment: A double-blind placebo-controlled clinical trial. *Phytother. Res.* **2009**, *23*, 367–372, doi:10.1002/ptr.2634.

25. Kawagishi, H.; Zhuang, C. Compounds for dementia from Hericium erinaceum. *Drug Future* **2008**, *33*, 149–155, doi:10.1358/dof.2008.033.02.1173290.

26. Tsai-Teng, T.; Chin-Chu, C.; Li-Ya, L.; Wan-Ping, C.; Chung-Kuang, L.; Chien-Chang, S.; Chi-Ying, H.F.; Chien-Chih, C., Shiao, Y.J. Erinacine A-enriched Hericium erinaceus mycelium ameliorates Alzheimer's disease-related pathologies in APPswe/PS1dE9 transgenic mice. *J. Biomed. Sci.* **2016**, *23*, 49, doi:10.1186/s12929-016-0266-z.

27. Mori, K.; Obara, Y.; Hirota, M.; Azumi, Y.; Kinugasa, S.; Inatomi, S.; Nakahata, N. Nerve growth factor-inducing activity of Hericium erinaceus in 1321N1 human astrocytoma cells. *Biol. Pharm. Bull.* **2008**, *31*, 1727–1732, doi:10.1248/bpb.31.1727.

28. Kawagishi, H.; Shimada, A.; Hosokawa, S.; Mori, H.; Sakamoto, H.; Ishiguro, Y.; Sakemi, S.; Bordner, J.; Kojima, N.; Furukawa, S. Erinacines E, F, and G, stimulators of nerve growth factor (NGF)-synthesis, from the mycelia of Hericium erinaceum. *Tetrahedron Lett.* **1996**, *37*, 7399–7402, doi:10.1016/0040-4039(96)01687-5.

29. Chiu, C.H.; Chyau, C.C.; Chen, C.C.; Lee, L.Y.; Chen, W.P.; Liu, J.L.; Lin, W.H.; Mong, M.C. Erinacine A-Enriched Hericium erinaceus Mycelium Produces Antidepressant-Like Effects through Modulating BDNF/PI3K/Akt/GSK-3β Signaling in Mice. *Int. J. Mol. Sci.* **2018**, *19*, pii: e341, doi:10.3390/ijms19020341.

30. Rupcic, Z.; Rascher, M.; Kanaki, S.; Köster, R.W.; Stadler, M.; Wittstein, K. Two New Cyathane Diterpenoids from Mycelial Cultures of the Medicinal Mushroom Hericium erinaceus and the Rare Species, Hericium flagellum. *Int. J. Mol. Sci.* **2018**, *19*, pii: E740, doi:10.3390/ijms19030740.

31. Wong, K.H.; Naidu, M.; David, P.; Abdulla, M.A.; Abdullah, N.; Kuppusamy, U.R.; Sabaratnam, V. Peripheral Nerve Regeneration Following Crush Injury to Rat Peroneal Nerve by Aqueous Extract of Medicinal Mushroom Hericium erinaceus (Bull.: Fr) Pers. (Aphyllophoromycetideae). *Evid. Based Complement. Alternat. Med.* **2011**, 580752, doi:10.1093/ecam/neq062.

32. Brandalise, F.; Cesaroni, V.; Gregori, A.; Repetti, M.; Romano, C.; Orrù, G.; Botta, L.; Girometta, C.; Guglielminetti, M.L.; Savino, E.; et al. Dietary Supplementation of Hericium erinaceus Increases Mossy Fiber-CA3 Hippocampal Neurotransmission and Recognition Memory in Wild-Type Mice. *Evid. Based Complement. Alternat. Med.* **2017**, 3864340, doi:10.1155/2017/3864340.

33. Rossi, P.; Cesaroni, V.; Brandalise, F.; Occhinegro, A.; Ratto, D.; Perrucci, F.; Lanaia, V.; Girometta, C.; Orrù, G.; Savino, E. Dietary Supplementation of Lion's Mane Medicinal Mushroom, Hericium erinaceus (Agaricomycetes), and Spatial Memory in Wild-Type Mice. *Int. J. Med. Mushrooms* **2018**, *20*, 485–494, doi:10.1615/IntJMedMushrooms.2018026241.

34. Kempermann, G.; Song, H.; Gage, F.H. Neurogenesis in the adult hippocampus. *Cold Spring Harb. Perspect. Biol.* **2015**, *7*, doi:10.1101/cshperspect.a018812.

35. Silvers, J.M.; Harrod, S.B.; Mactutus, C.F.; Booze, R.M. Automation of the novel object recognition task for use in adolescent rats. *J. Neurosci. Methods* **2007**, *166*, 99–103, doi:10.1016/j.jneumeth.2007.06.032.

36. Parks, R.J.; Fares, E.; Macdonald, J.K.; Ernst, M.C.; Sinal, C.J.; Rockwood, K.; Howlett, S.E. A Procedure for Creating a Frailty Index Based on Deficit Accumulation in Aging Mice. *J. Gerontol. Biol. Sci. Med. Sci.* **2012**, *67*, 217–227, doi:10.1093/gerona/glr193.

37. Whitehead, J.C.; Hildebrand, B.A.; Sun, M.; Rockwood, M.R.; Rose, R.A.; Rockwood, K.; Howlett, S.E. A clinical frailty index in aging mice: Comparisons with frailty index data in humans. *J. Gerontol. Biol. Sci. Med. Sci.* **2014**, *69*, 621–632, doi:10.1093/gerona/glt136.

38. Cesaroni, V.; Brusoni, M.; Cusaro, C.M.; Girometta, C.; Perini, C.; Picco, A.M.; Rossi, P.; Salerni, E.; Savino, E. Phylogenetic comparison between Italian and worldwide Hericium species. *IJMM* **2019**, submitted.

39. Gerbec, B.; Tavčar, E.; Gregori, A.; Kreft, S.; Berovic, M. Solid State Cultivation of Hericium erinaceus Biomass and Erinacine A Production. *J. Bioproces. Biotech.* **2015**, *5*, 1–5, doi:10.4172/2155-9821.1000210.

40. Kawagishi, H.; Ando, M.; Sakamoto, H.; Yoshida, S.; Ojima, F.; Ishiguro, Y.; Ukai, N.; Furukawa, S. Hericenones C, D and E, stimulators of nerve growth factor (NGF)-synthesis, from the mushroom Hericium erinaceum. *Tetrahedron Lett.* **1991**, *32*, 4561–4564, doi:10.1016/0040-4039(91)80039-9.

41. Kawagishi, H.; Ando, M.; Sakamoto, H.; Yoshida, S.; Ojima, F.; Ishiguro, Y.; Ukai, N.; Furukawa, S. Erinacines A, B and C, strong stimulators of nerve growth factor (NGF)-synthesis, from the mycelia of Hericium erinaceum. *Tetrahedron Lett.* **1994**, *35*, 1569–1572, doi:10.1016/S0040-4039(00)76760-8.

42. D'Angelo, E.; Rossi, P.; DeFilippi, G.; Magistretti, J.; Taglietti, V. The relationship between synaptogenesis and expression of voltage-dependent currents in cerebellar granule cells in situ. *J. Physiol. Paris* **1994**; *88*, 197–207.

43. Shi, J.; Zhong, X.; Song, Y.; Wu, Z.; Gao, P.; Zhao, J.; Sun, J.; Wang, J.; Liu, J.; Wang, Z. Long non-coding RNA RUNX1-IT1 plays a tumour-suppressive role in colorectal cancer by inhibiting cell proliferation and migration. *Cell Biochem. Funct.* **2019**, *37*, 11–20, doi:10.1002/cbf.3368.

44. Ayanlaja, A.A.; Xiong, Y.; Gao, Y.; Ji, G.; Tang, C.; Abdikani Abdullah, Z.; Gao, D. Distinct Features of Doublecortin as a Marker of Neuronal Migration and Its Implications in Cancer Cell Mobility. *Front. Mol. Neurosci.* **2017**, *10*, 199, doi:10.3389/fnmol.2017.00199.

45. Dutta, S.; Sengupta, P. Men and mice: Relating their ages. *Life Sci.* **2016**, *152*, 244–248, doi:10.1016/j.lfs.2015.10.025.

46. Sternberg Task. Dual Mechanisms of Cognitive Control, Washington University in St. Louis. Available online: http://pages.wustl.edu/dualmechanisms/sternberg-task#sbergdesc (accessed on 26 March 2019).

47. Nosofsky, R.M.; Little, D.R.; Donkin, C.; Fific, M. Short-term memory scanning viewed as exemplar-based categorization. *Psychol. Rev.* **2011**, *118*, 280–315, doi:10.1037/a0022494.

48. Brodziak, A.; Kołat, E.; Różyk-Myrta, A. In Search of Memory Tests Equivalent for Experiments on Animals and Humans. *Med. Sci. Monit.* **2014**, *20*, 2733–2739, doi:10.12659/MSM.891056.

49. Ennaceur, A.L.; Michalikova, S.; Bradford, A.; Ahmed, S. Detailed analysis of the behavior of Lister and Wistar rats in anxiety, object recognition and object location tasks. *Behav. Brain. Res.* **2005**, *159*, 247–266.

50. Krzyczkowski, W.; Malinowska, E.; Herold, F. Erinacine A biosynthesis in submerged cultivation of Hericium erinaceum: Quantification and improved cultivation. *Eng. Life Sci.* **2010**, *10*, 446–457.

51. Chen, C.C.; Tzeng, T.T.; Chen, C.C.; Ni, C.L.; Lee, L.Y.; Chen, W.P.; Shiao, Y.J.; Shen, C.C. Erinacine S, a rare sesterterpene from the mycelia of Hericium erinaceus. *J. Nat. Prod.* **2016**, *79*, 438–441, doi:10.1016/j.bbr.2004.11.006.

52. Lee, D.G.; Kang, H.W.; Park, C.G.; Ahn, Y.S.; Shin, Y. Isolation and identification of phytochemicals and biological activities of Hericium ernaceus and their contents in Hericium strains using HPLC/UV analysis. *J. Ethnopharmacol.* **2016**, *184*, 219–225, doi:10.1016/j.jep.2016.02.038.

53. Kawagishi, H.; Mori, H.; Uno, A.; Kimura, A.; Chiba, S. A sialic acid-binding lectin from the mushroom Hericium erinaceum. *FEBS Lett.* **1994**, *340*, 56–58.

54. Tzeng, T.T.; Chen, C.C.; Chen, C.C.; Tsay, H.J.; Lee, L.Y.; Chen, W.P.; Shen, C.C.; Shiao, Y.J. The cyanthin diterpenoid and sesterterpene constituents of Hericium erinaceus mycelium ameliorate Alzheimer's disease-related pathologies in APP/PS1 transgenic mice. *Int. J. Mol. Sci.* **2018**, *19*, 598, doi:10.3390/ijms19020598.

55. Li, I.C.; Lee, L.Y.; Tzeng, T.T.; Chen, W.P.; Chen, Y.P.; Shiao, Y.J.; Chen, C.C. Neurohealth Properties of Hericium erinaceus Mycelia Enriched with Erinacines. *Behav. Neurol.* **2018**, 1–10, doi:10.1155/2018/5802634.

56. Ryu, S.; Kim, H.G.; Kim, J.Y.; Kim, S.Y.; Cho, K.O. Hericium erinaceus Extract Reduces Anxiety and Depressive Behaviors by Promoting Hippocampal Neurogenesis in the Adult Mouse Brain. *J. Med. Food.* **2018**, *21*, 174–180, doi:10.1089/jmf.2017.4006.

57. Kolotushkina, E.V.; Moldavan, M.G.; Voronin, K.Y.; Skibo, G.G. The influence of Hericium erinaceus extract on myelination process in vitro. *Fiziol. Zhurnal* **2003**, *49*, 38–45.

58. Trovato, R.; Siracusa, R.; Di Paola, M.; Scuto, M.L.; Ontario, O.; Bua, P.; Di Mauro, M.A.; Toscano, C.C.T.; Petralia, L.; Maiolino, A.; et al. Redox modulation of cellular stress response and lipoxin A4 expression by Hericium Erinaceus in rat brain: Relevance to Alzheimer's disease pathogenesis. *Immun. Ageing* **2016**, *13*, 23, doi:10.1186/s12979-016-0078.

59. Ahlfeld, J.; Filser, S.; Schmidt, F.; Wefers, A.K.; Merk, D.J.; Glaß, R.; Herms, J.; Schüller, U. Neurogenesis from Sox2 expressing cells in the adult cerebellar cortex. *Sci. Rep.* **2017**, *7*, 6137, doi:10.1038/s41598-017-06150-x.

60.  Lauretani, F.; Meschi, T.; Ticinesi, A.; Maggio, M. "Brain-muscle loop" in the fragility of older persons: From pathophysiology to new organizing models. *Aging Clin. Exp. Res.* **2017**, *6*, 1305–1311, doi:10.1007/s40520-017-0729-4.

*Article*

# Neuroprotective Metabolites of *Hericium erinaceus* Promote Neuro-Healthy Aging

Elisa Roda [1,†], Erica Cecilia Priori [2,†], Daniela Ratto [2], Fabrizio De Luca [2], Carmine Di Iorio [2], Paola Angelone [2], Carlo Alessandro Locatelli [1], Anthea Desiderio [3], Lorenzo Goppa [3], Elena Savino [3], Maria Grazia Bottone [2,‡] and Paola Rossi [2,*,‡]

1. Laboratory of Clinical & Experimental Toxicology, Pavia Poison Centre, National Toxicology Information Centre, Toxicology Unit, Istituti Clinici Scientifici Maugeri IRCCS, 27100 Pavia, Italy; elisa.roda@icsmaugeri.it (E.R.); carlo.locatelli@icsmaugeri.it (C.A.L.)
2. Department of Biology and Biotechnology "L. Spallanzani", University of Pavia, 27100 Pavia, Italy; ericacecilia.priori01@universitadipavia.it (E.C.P.); daniela.ratto01@universitadipavia.it (D.R.); fabrizio.deluca01@universitadipavia.it (F.D.L.); carmine.diiorio01@universitadipavia.it (C.D.I.); paola.angelone01@universitadipavia.it (P.A.); mariagrazia.bottone@unipv.it (M.G.B.)
3. Department of Earth and Environmental Science, University of Pavia, 27100 Pavia, Italy; anthea.desiderio01@universitadipavia.it (A.D.); lorenzo.goppa01@universitadipavia.it (L.G.); elena.savino@unipv.it (E.S.)
* Correspondence: paola.rossi@unipv.it; Tel.: +39-038-298-6076 or +39-038-259-2414
† These co-first authors contributed equally to this work.
‡ These co-last authors contributed equally to this work.

**Abstract:** Frailty is a geriatric syndrome associated with both locomotor and cognitive decline, typically linked to chronic systemic inflammation, i.e., *inflammaging*. In the current study, we investigated the effect of a two-month oral supplementation with standardized extracts of *H. erinaceus*, containing a known amount of Erinacine A, Hericenone C, Hericenone D, and L-ergothioneine, on locomotor frailty and cerebellum of aged mice. Locomotor performances were monitored comparing healthy aging and frail mice. Cerebellar volume and cytoarchitecture, together with inflammatory and oxidative stress pathways, were assessed focusing on senescent frail animals. *H. erinaceus* partially recovered the aged-related decline of locomotor performances. Histopathological analyses paralleled by immunocytochemical evaluation of specific molecules strengthened the neuroprotective role of *H. erinaceus* able to ameliorate cerebellar alterations, i.e., milder volume reduction, slighter molecular layer thickness decrease and minor percentage of shrunken Purkinje neurons, also diminishing inflammation and oxidative stress in frail mice while increasing a key longevity regulator and a neuroprotective molecule. Thus, our present findings demonstrated the efficacy of a non-pharmacological approach, based on the dietary supplementation using *H. erinaceus* extract, which represent a promising adjuvant therapy to be associated with conventional geriatric treatments.

**Keywords:** healthy aging; frailty; cerebellum; *inflammaging*; oxidative stress; ergothioneine; *Hericium erinaceus*; neuroprotection

## 1. Introduction

Aging is a universal process characterized by a gradual decline in physical and cognitive functions. As age increases, a variety of changes occur, including brain atrophy, oxidative stress, and reduced antioxidant mechanisms, contributing to impairment of cognitive and locomotor performances [1].

The term frailty was proposed to describe a multisystemic impairment scenario, which negatively affects the health of an elderly individual, contributing to aggravate a clinical condition that is often already compromised. Recently, the World Health Organization (WHO) recognized frailty as an increasingly widespread syndrome that should be prevented, reversed, or at least mitigated to improve the quality of life in the elderly [2].

Frailty is a complex geriatric syndrome characterized by age-associated declines in physiologic reserve and functions through multiorgan systems, leading to enhanced vulnerability for adverse health outcomes [3,4]. Compelling evidence linked frailty to both immunosenescence and chronic systemic inflammation, the so-called *inflammaging* [5–7]. This latter mechanism is a typical biomarker of accelerated aging, being also a risk factor for cardiovascular diseases, cancer, dementia, cognitive decline, and physical disabilities [7,8]. In addition, *inflammaging* increases susceptibility to stress-related molecules [6,7].

Several works demonstrated that locomotor frailty predicts cognitive impairment and dementia during aging [9–12], and, in particular, the locomotor decline seems to be a risk factor of future cognitive deterioration [13,14]. In this scenario, the prevention, detection and the reversion of physical frailty is imperative, aimed at avoiding neurodegenerative diseases pathogenesis and cognitive impairment outcomes.

An imbalance in the REDOX system is critical not only in aging but even more in frail subjects. The accumulation of reactive oxygen and nitrogen species (RONS) during aging induces cellular damages and contributes to the onset of age-associated tissue impairment. Based on this evidence, the oxidative stress theory of aging was formulated and, over the years, the role of oxidative stress in the worsening of age-related diseases has been consolidated [15]. A redox imbalance is particularly critical in frail subjects during aging. Furthermore, oxidative stress induces the secretion of proinflammatory molecules and chemokines that promote protein degradation and contribute to cellular degeneration [16].

The brain is very sensitive to oxidative stress-induced damage, and the overproduction of free radicals during aging is suggested to be responsible for age-associated brain structural corrosion and functional decline [1]. Experimental and clinical evidence supported that age-related brain atrophy could worsen locomotor and cognitive performances [1]. Specifically, aged-derived increase of oxidative stress leads to cellular damages in the cerebellum, e.g., gray matter volume reduction and atrophy [17].

Furthermore, the morphological signs observed in cerebellum have been correlated with slow walking speed and reduction in both physical and social behaviors suggesting that frailty could promote neuronal degeneration in elderly patients [12,18]. Notably, cerebellar Purkinje neurons are vulnerable to aging, displaying considerable alterations in both morphology and function, e.g., cell number reduction and decrease in synapse density [19].

*Hericium erinaceus* is an edible and medicinal mushroom and it seems to stand out as an exceptional health-promoting species. Available generally in North temperate latitudes (including Italy), *H. erinaceus* can be identified by its long spines, for its appearance on hardwoods and its tendency to grow with a single tuft of dangling spines. Given its shape, it is also known as Lion's mane and Monkey Head Mushroom [20,21]. *H. erinaceus* is able to regulate cytokines and mitogen-activated protein kinases expressions, and transcription factors at the molecular level: *H. erinaceus* performs medicinal activities at tissue, organ, and organism levels. Indeed, *H. erinaceus* synthesizes at least 70 different bioactive metabolites, such as β-glucans, erinacines, hericenones, alkaloids, sterols, and volatile aroma compounds [21]. Thanks to these biological compounds, *H. erinaceus* exerts many health-promoting properties [21], such as antibiotic [22,23], anticancer [24,25], antioxidant [26,27], antifatigue [28], antisenescence [14,29], neuroprotective [30–32], antidepressive, and antianxiety [33,34] activities.

Furthermore, both in *H. erinaceus* fruiting body and mycelium ergothioneine is found [35]. L-ergothioneine is a water-soluble thiol that can only be absorbed from the diet because animals and plants cannot synthesize this compound, produced solely by bacteria and mushrooms. L-ergothioneine displays antioxidant and cytoprotective capabilities [36,37]. An increasing number of scientific articles demonstrated the potential of L-ergothioneine as therapy for several diseases, such as preeclampsia [38,39], neurodegenerative [40–43], cardiovascular [44,45], and endothelial-muscular [46–48] pathologies.

Based on this knowledge, *H. erinaceus* appears an excellent candidate to prepare novel mushroom-based pharmaceuticals/medicines and functional foods [20]. Neverthe-

260

less, the standardization of medicinal mushrooms-derived dietary supplements is still in development, since proper standards and protocols have yet to be identified [49].

Our previous findings demonstrated the neuroprotective action and nootropic effect of *H. erinaceus* in adult wild-type mice. Specifically, dietary supplementation with *H. erinaceus* was effective at (i) increasing hippocampal neurotransmission, locomotor performances and recognition memory in wild-type mice [50,51], and (ii) improving recognition memory in frail mice during aging, also inducing hippocampal and cerebellar neurogenesis [14].

In the current study, we investigated the effect of a two-month oral supplementation with standardized extracts of *H. erinaceus* (He1), containing a known amount of Erinacine A, Hericenone C, Hericenone D, and L-ergothioneine, on locomotor frailty and cerebellum of aged mice. We decided to supplement only frail mice, then compare them to healthy aged animals to explore the potential occurrence of a recovery process, in which *H. erinaceus*-supplemented frail mice could have reverted, at least in part, to healthy aging.

Specifically, we monitored the locomotor performances comparing animals belonging to the two experimental groups (healthy aged vs. frail mice), and, further, we evaluated the cerebellar volume and cytoarchitecture, together with inflammatory and oxidative stress pathways, jointly with a neuroprotective molecule and a key longevity regulator, focusing on senescent frail animals.

## 2. Results

### 2.1. Array of Metabolites in Hericium erinaceus Extract

Italian *Hericium erinaceus* (He1) was collected in Siena province (Tuscany, Italy) and identified on the macro- and micro-morphological characteristics of the species. Culturing and extraction procedures are meticulously reported in Materials and Methods section (see Section 4.3).

Using HPLC-UV-ESI/MS, and by comparison with standard solutions, the presence and amount of different metabolites, i.e., Erinacine A, Hericenone C, Hericenone D was identified and quantified [14,52]. Specifically, He1 extract contained 150 µg/g Erinacine A, 500 µg/g Hericenone C, and about 20 µg/g Hericenone D.

In addition, the amount of ergothioneine (ET) in mycelium and sporophore extracts of He1 was measured. The ET calibration curve was constructed with concentrations ranging from 10 to 350 µg/mL (see Section 4). Linear least-square regression analysis for the calibration curve showed correlation coefficient of 0.9925 with respect to the peak area (Figure 1, Panel A, top right insert), demonstrating a good linear relationship in the different ranges tested.

In particular, ET was identified by comparing retention time and ESI/MS-MS spectrum with the authentic standard. Typical ions of ET in the ESI/MS spectrum (Figure 1, Panel A) are hydrogen, sodium and potassium adducts (Table 1). ESI-MS/MS spectrum of ET (Figure 1, Panel B) obtained by fragmentation of ion $m/z$ 230 shows two fragment ions $m/z$ 186 and $m/z$ 127 (Table 1). To obtain better sensitivity, ET was then quantified by multiple-reaction-monitoring (MRM) transition $m/z$ 230 > 127.

Figure 1 panel C displays the traces regarding the standard molecule of ET at 70 ppm. On the top, the figure shows the UV trace and, on the bottom, it represents the mass spectrum (MS) trace (MS/MS Selected Reaction Monitoring $m/z$ 230 > $m/z$ 186 traces).

Figure 1 panel D displays the mass spectrometry (MS) chromatographic traces of He1 lyophilized mycelium. Notably, both ESI-MS/MS spectrum of the standard molecule of ET at 70 ppm (retention time at 3.16 min; Figure 1, Panel C) and the He1 mycelium spectrum showed the peak of ET (retention time at 3.09; Figure 1, Panel D). By comparison with the calibration curve, we measured the content of ET in He1 lyophilized mycelium. It should be noted that the ET content of 580 µg/g is slightly more compared to data reported in literature (0.4 mg/g reported by Chen et al. [53]).
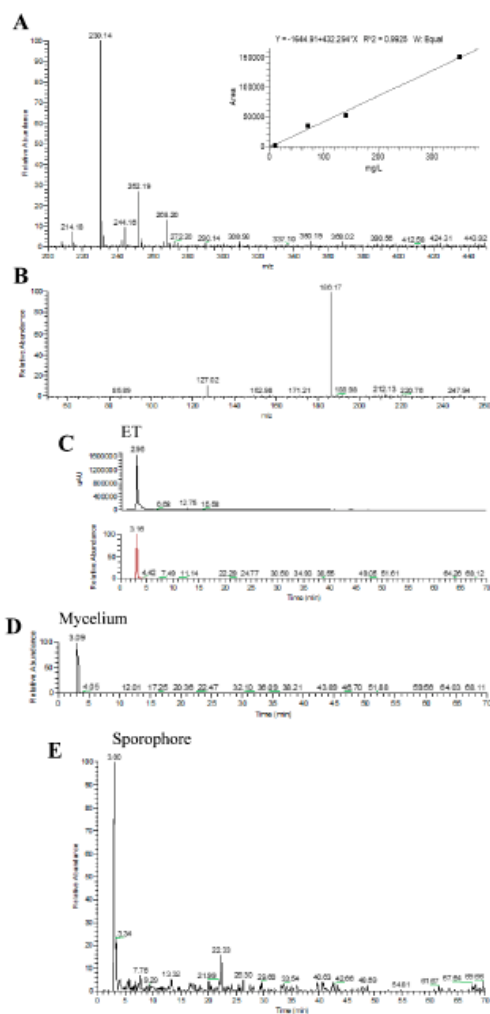
**Figure 1.** HPLC-UV-ESI/MS was used for quantifying the Ergothioneine (ET) amount in He1 extracts. (**A**) ESI/MS spectrum of ET. Panel (top, right) reports calibration curve and linear regression curve for ET. (**B**) ESI-MS/MS spectrum of ET obtained by fragmentation of ion $m/z$ 230 shows two fragment ions $m/z$ 186 and $m/z$ 127. (**C**) Standard molecule of L-(+)-ET at 70 ppm: UV trace (top) and mass spectrum (MS)/MS Selected Reaction Monitoring $m/z$ 230 > $m/z$ 186 trace (bottom). (**D**) MS/MS Selected Reaction Monitoring $m/z$ 230 > $m/z$ 186 trace of He1 mycelium. (**E**) MS/MS Selected Reaction Monitoring $m/z$ 230 > $m/z$ 186 trace of He1 WT sporophore.

262

**Table 1.** Ergothioneine molecular formula, molecular weight, chemical structure, characteristic and fragment ions, and mycelium and sporophore amounts are summarized.

| Molecular Formula | Molecular Weight (g/moL) | Chemical Structure | ESI/MS Characteristic Ions (*m/z*) | ESI-MS/MS Fragment Ions (*m/z*) | Content (mg/g) |
|---|---|---|---|---|---|
| C9H15N3O2S | 229.3 | | 230 [M+H]+ <br> 252 [M+Na]+ <br> 268 [M+K]+ | 186 [M+H-CO$_2$]+ <br> 127 [M+H-CO$_2$-(CH3)3N]+ | 0.58 (mycelium) <br> 0.34 (sporophore) |

Figure 1 panel E shows the mass spectrometry (MS) chromatographic traces of the He1 sporophore. The content of ET (retention time at 3.00) in the He1 WT sporophore was 0.34 mg/g (d.w.), measured by comparison with ET calibration curve. This value is slightly smaller compared to data reported in literature, i.e., 0.96 mg/g [54] and 1.12 mg/g [55].
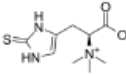
### 2.2. H. erinaceus Reverted the Locomotor Decline during Senescence in Wild-Type Mice

During senescence, the mean speed and resting time were recognized as the most sensitive locomotor parameters, decreasing with aging, while the maximum speed (cm/s) did not change with frailty [14].

Therefore, locomotor performances were measured by the mean speed (cm/s) and the resting time (s) in untreated (n = 8) versus He1 treated mice (n = 7) at 21.5 (T1) and 23.5 (T2) months of age. Locomotor frailty index (FI) was obtained by averaging the mean speed and the resting time FIs and its measurement at T1 was the selection criteria for dividing the mice in two groups: non-frail and frail mice (see Section 4).

In untreated mice, the mean speed decreased significantly during aging of 11.4% in the open arena test (Figure 2, Panel A), and a similar nonsignificant trend was observed in the emergence test (Figure 2, Panel B). Before *H. erinaceus* treatment, at T1, frail mice displayed a significant decrease of the mean speed compared to untreated mice by 20% in the open arena and by 16.9% in the emergence test. After *H. erinaceus* treatment this decline remained unchanged in the open arena test and significantly improved in the emergence test (Figure 2, Panels A and B). Overall, the averaged mean speed (from open arena and emergence test) significantly decreased during senescence in untreated mice from T1 to T2, whereas significantly increased after He1 treatment in frail mice (Figure 2, Panel C). Notably, whereas the untreated and pre-He1 treated mice showed significant differences at T1 in both open arena and emergence test, the treatment brought mice back to comparable levels at T2.

In untreated mice, in the open arena test, the resting time significantly increased by 9.4%, and a nonstatistically significant difference was observed in the emergence test. Before He1 treatment, at T1, frail mice displayed a significant increase of resting time compared to untreated mice by 18.16% in the open arena and by 21.74% in the emergence test. Interestingly, at T2 He1 treatment reverted the increase in resting time recorded in untreated mice between T1 and T2, caused by the ageing process. In particular, the resting time in He1 treated mice at T2 slightly decreased in the open arena (Figure 3, Panel A), and decreased 12.44% in the emergence test, reaching the statistical significance (Figure 3, Panel B). The averaged resting time (from open arena and emergence test) significantly increased during senescence in untreated mice, whereas it significantly decreased, by about 9%, in He1 treated mice (Figure 3, Panel C). Notably, whereas the untreated and He1 treated mice showed significant differences at T1, the treatment brought mice back to comparable levels at T2.

Finally, we investigated the effects of physiological aging and *H. erinaceus* supplementation by tuning an overall locomotor FI.

263

**A**

**Open Arena**

**B**

**Emergence**

**C**

**Averaged mean speed**

T1
T2
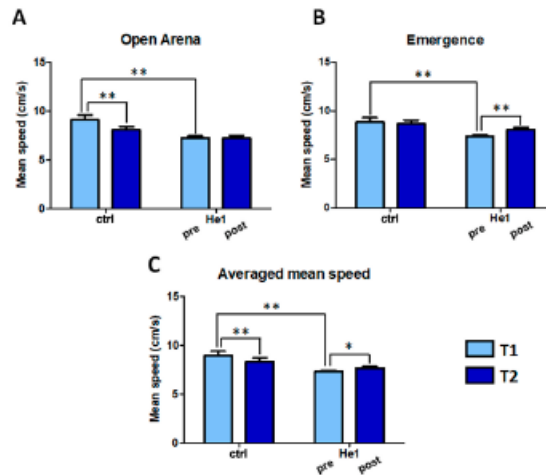
**Figure 2.** *H. erinaceus* treatment reverted the mean speed decline during senescence. Mean speed (cm/s) estimated during open arena test (Panel **A**) and emergence task (Panel **B**). Panel **C**: Averaged mean speed, calculated between mean speed obtained in open arena and emergence tests in untreated and He1 treated mice before (T1) and after (T2) treatment. Two-way ANOVA was performed for statistical analysis: * $p < 0.05$; ** $p < 0.01$.

**A**

**Open Arena**

**B**

**Emergence**

**C**

**Averaged resting time**

T1
T2

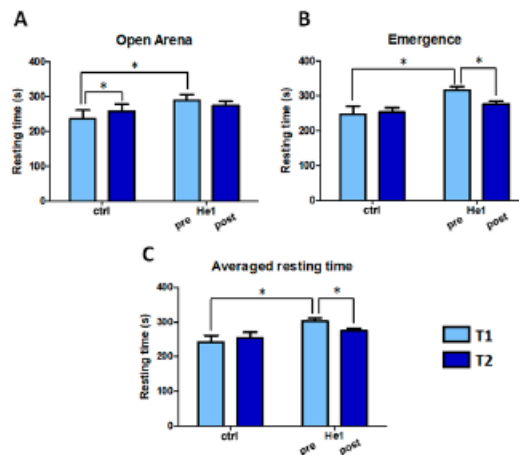**Figure 3.** *H. erinaceus* treatment reverted the resting time increase during aging: mean resting time (s) estimated during open arena (Panel **A**) and emergence tasks (Panel **B**). Panel **C**: Averaged resting time obtained by both tasks, in untreated (ctrl) and He1 treated mice (He1) before (T1) and after (T2) treatment. Two-way ANOVA was performed for statistical analysis: * $p < 0.05$.

264

At T1, the overall locomotor FI of the frail mice (pre-He1 treated animals) was 51% higher than that measured in untreated mice ($2.36 \pm 0.07$ vs. $1.63 \pm 0.21$, Figure 4). Interestingly, the *H. erinaceus* treatment significantly decreased by about 10% of the overall locomotor frailty index ($2.36 \pm 0.07$ at T1 vs. $2.12 \pm 0.09$ at T2), whereas it significantly increased between T1 and T2 in untreated mice ($1.63 \pm 0.21$ at T1 vs. $1.79 \pm 0.17$ at T2). Notably, whereas the pre-He1 treated mice were significantly frailer compared to untreated animals at T1, the treatment brought mice back to comparable levels, with no significant differences in the locomotor frailty index at T2 between the two experimental groups (Figure 4).
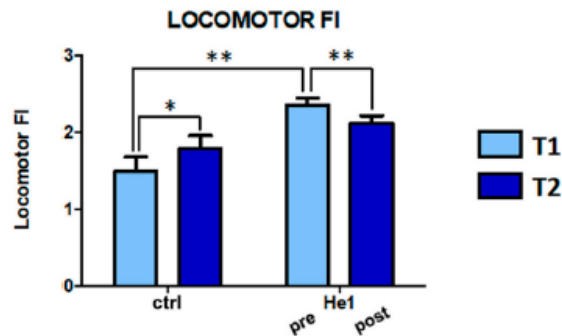


**Figure 4.** Locomotor frailty index in untreated and He1 treated mice at T1 and T2. Two-way ANOVA was performed for statistical analysis: * $p > 0.05$; ** $p < 0.01$.

*2.3. H. erinaceus Effect on Cerebellar Cytoarchitecture, Neuroinflammation and Oxidative Stress Pathway*

Histochemical and immunohistochemical reactions were conducted on sagittal sections of the cerebellar vermis from both untreated (Ctrl) and *Hericium*-treated mice (He1) at T2 (23,5-month-old mice). The evaluations were performed on the posterior region, specifically on the neocerebellar lobules VI–VIII, known to be particularly impacted by age and correlated with general cognitive and motor function [56–59].

2.3.1. H&E and Nissl Staining

We evaluated the cerebellar volume together with morphological characteristics of cerebellar cortex, exploiting potential cytoarchitecture alterations, comparing senescent untreated animals with He1-supplemented aged mice, using Haematoxylin and Eosin (H&E) and Nissl staining.

Similarly, H&E and Nissl results (Figure 5) demonstrated a well-preserved physiological cerebellar cytoarchitecture in both groups, displaying the typical three-layered cortical organization, i.e., molecular, Purkinje, and granular layers (ML, PCs, and IGL, respectively, from the outer to inner one). The ML was formed of few small cells together with numerous fibers. The large pyriform PCs appeared regularly arranged in a single row along the outer margin of the IGL with vesicular nuclei. The IGL showed tightly packed small rounded cells with deeply stained nuclei. Neither malformation or supernumerary extroversions, nor PCs loss (total number of PCs) were detected (Figure 5, Panel A).

265

## H&E and Nissl staining
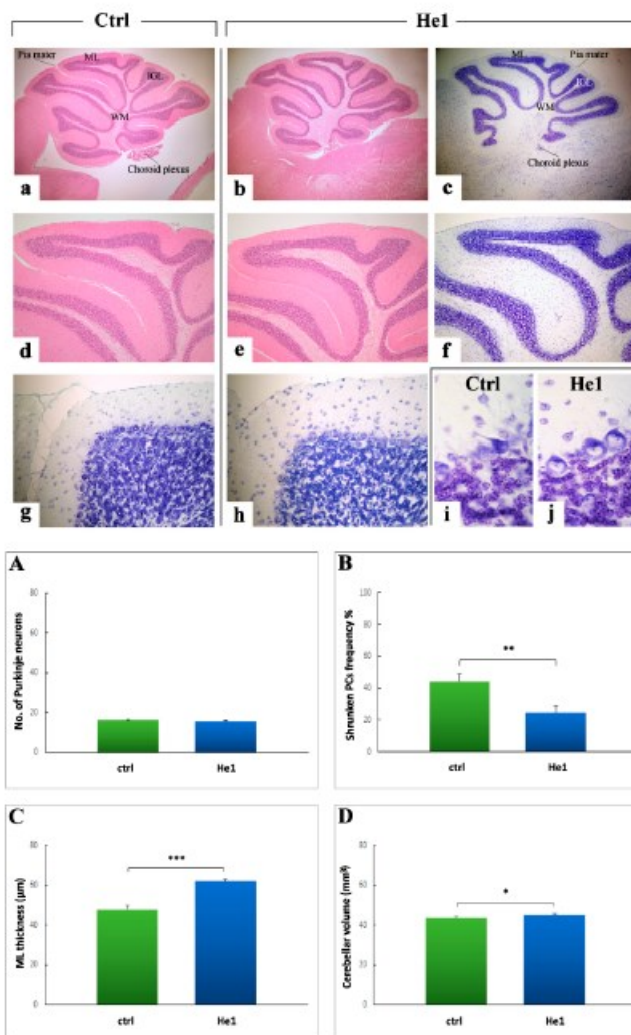


**Figure 5.** Representative H&E and Nissl-stained cerebellar specimens, in untreated (**a,d,g,i**) and He1-treated mice (**b,c,e,f,h,j**). Light microscopy magnification: 20× (**a–c**); 40× (**d–h**); 100× (**i,j**). Panels (**A–D**) Histograms showing the quantitative measurement of the whole number of PCs, the percentage of shrunken PCs, the ML width and the entire cerebellar volume, respectively. $p$ values calculated by unpaired Student's $t$-test: * $p < 0.05$; ** $p < 0.01$; *** $p < 0.001$.

Nonetheless, comparing animals from the two experimental groups, age-related changes were determined in untreated mice only, in which (i) the volume of the entire cerebellum was significantly reduced ($43.73 \pm 0.44$ mm$^3$), (ii) about 44% of the total PCs appeared evidently shrunken, and, parallelly, (iii) a significant reduction of the ML thickness ($47.81 \pm 2.23$ µM) was measured. Notably, He1 supplementation seemed to play a significant protective effect since He1 animals exhibited a bigger cerebellar size ($45.35 \pm 0.39$ mm$^3$), only 24% of the total PCs was characterized by an altered morphology and the ML was greater in width ($62.02 \pm 0.98$ µM) (Figure 5, Panel C, respectively).

2.3.2. Picrosirius Red Staining: Fibrillar Collagen Networks Evaluation

Picrosirius Red (PSR) staining was employed as the most sensitive tool to appraise collagen networks in paraffin-embedded tissue sections. In both experimental groups, i.e., untreated and He1 mice, collagen fibers were evidently localized in the meninges (Figure 6). Notably, some clusters of histochemically positive cells were observed in the upper external part of the molecular layer (ML) in untreated animals only (Figure 6, insert in c), while both He1 and untreated mice displayed PSR positive basal laminae of the cerebellar capillaries.

Notably, in the ML (Figure 6, Panel A) as well as at pial surface level (Figure 6, Panel B), the quantitative analysis evidenced a significant decrease of collagen fibers optical density (OD) in He1 mice compared to untreated animals ($74.22 \pm 2.15$ vs. $84.71 \pm 1.82$, $p < 0.001$ in GCs and $74.39 \pm 2.89$ vs. $85.91 \pm 1.79$, $p < 0.01$, in meninges, respectively). These data obtained using bright field microscopy were further confirmed by confocal microscopy observation.

2.3.3. Inflammatory Pathway (IL6, GFAP) and HIF1α Assessment

Based on literature evidence supporting the role played by immune system in influencing brain plasticity phenomena and occurrence of age-dependent enhanced neuroinflammation, we first performed an immunohistochemical evaluation of the presence/distribution of the pro-inflammatory cytokine Interleukin-6 (IL6), as specific markers of inflammatory pathway.
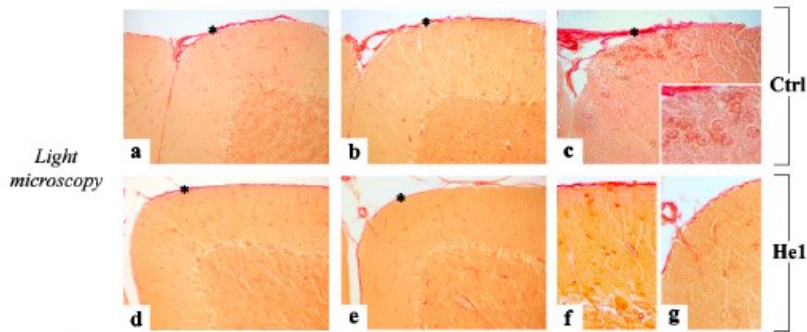
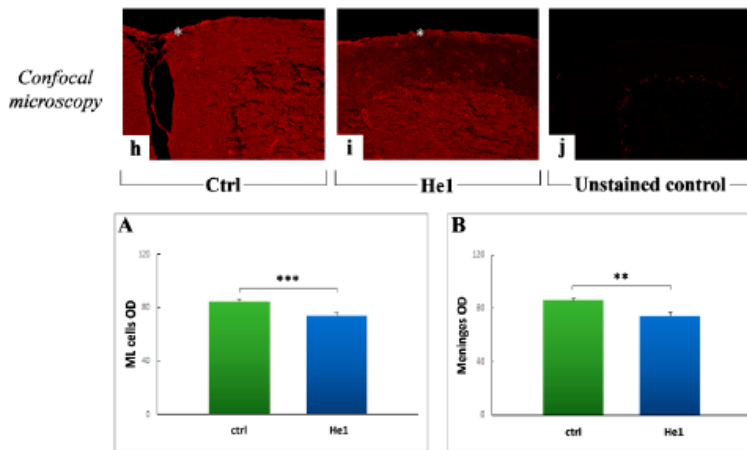**Picrosirius Red**



Figure 6. Cont.

267

**Figure 6.** Representative PSR-stained cerebellar specimens, in untreated (a–c,h,j) and He1-treated mice (d–g,i) investigated by both light and confocal microscopy. Magnification: 40× (a–e,h–j); 100× (insert in c,f,g). Panels (**A**, **B**) Histograms showing the quantitative analysis of histochemically positive ML cells and meningeal fibers OD, respectively. $p$ values calculated by unpaired Student's $t$-test: (**) < 0.01, and (***) < 0.001. Asterisks in a–e,h–i: meningeal fibers.

The IL6 immunopositivity was mainly observed in numerous cells localized closed to the Purkinje neurons soma, both in untreated mice and He1 animals (Figure 7a,c). Notably, the presence of numerous thin IL6-positive fibers, which ran parallel in the thickness of molecular layer (ML) reaching the pial surface, was only detected in untreated animals (Figure 7b). These fibers, appearing more markedly stained in the upper part of this layer, showed a regular feature. The observed IL6 immunopositive cells and fibers could be reasonably considered as the main constituents of the Bergmann glia (BG), with astrocytic cell bodies around the Purkinje cells and the polarized processes, i.e., radial fibers, extending over the full depth of the ML (Figure 7i). The quantitative analysis of IL6 immunopositive BG cells frequency ($50.92 \pm 3.23$ vs. $69.24 \pm 2.60$, $p < 0.05$) and OD ($100.02 \pm 0.31$ vs. $105.56 \pm 0.72$, $p < 0.001$) (Figure 7, Panels A and B, respectively) revealed a significant decreased in He1 mice compared to untreated animals.

As a second step, based on the notion that a reactive gliosis could be a direct consequence of IL6 overexpression [60,61], we assessed the presence/distribution of Glial fibrillary acidic protein (GFAP), as a specific molecular marker of the Bergmann glia (Figure 8). The GFAP immunoreactivity was markedly evident in untreated animals (Figure 8a–d), in which manifest GFAP-positive glial fibers were detected. These fibers appeared sometimes thickened and twisted, with an irregular course in the thickness of ML, being frequently more marked in some area of this layer. Several GFAP-positive fibers often displayed a thickened and intensely stained end-feet in the pial surface of the ML. Moreover, a significant number of GFAP-immunopositive IGL astrocytes were observed. Differently, an almost complete absence of immunonopositive fibers was detected in the ML of He1 mice, in which rare IGL immunoreactive astrocytes were also observed (Figure 8e–h).
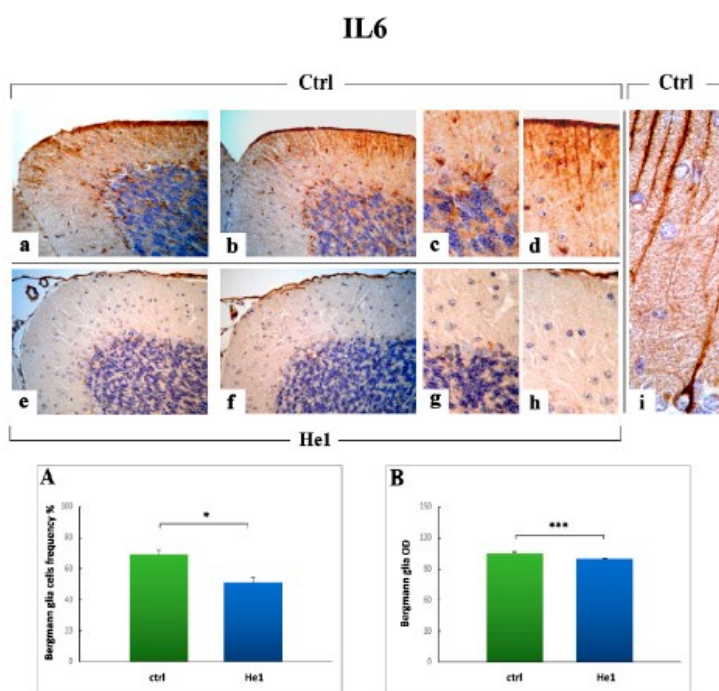
# IL6



**Figure 7.** IL6 DAB-immunostaining reaction in untreated (a–d,i) and He1-treated mice (e–h). Light microscopy magnification: 40× (a,b,e,f); 100× (c,d,g,h). Panels (A,B) Histograms showing immunopositive BG cells frequency and OD, respectively. $p$ values calculated by unpaired Student's $t$-test: * $p < 0.05$, *** $p < 0.001$.

The quantitative analyses confirmed a significant decrease in both GFAP immunopositive fibers and astrocytes density (Figure 8, Panels A and C) and OD (Figure 8, Panels B and D), respectively, in He1 mice compared to untreated animals, according to the previous resulted obtained after IL6 staining. Specifically, the following measurements were achieved comparing untreated to He1 mice: GFAP-immunopositive BG cells density ($87.61 \pm 22.75$ vs. $539.95 \pm 46.57$, $p < 0.001$); GFAP immunopositive BG area/ML area ($6.53 \pm 1.53$ vs. $34.49 \pm 5.68$, $p < 0.001$); GFAP immunoreactive IGL astrocytes density ($1033.42 \pm 110.54$ vs. $1557.39 \pm 80.76$, $p < 0.01$); GFAP immunoreactive astrocytes OD ($112.14 \pm 1.90$ vs. $122.28 \pm 0.68$, $p < 0.001$).

To integrate the study of the inflammatory pathway, based on the notion that hypoxia-inducible factors (HIFs) play as essential regulators of inflammation [62,63], we investigated the expression of HIF1α, which is regulated at protein level in an oxygen-sensitive manner, and is known as a critical transcription factor with an essential role in aging-related pathology [64]. Moreover, since angiogenic cytokines may upregulate vascular endothelial factor (VEGF), whose expression is also directly induced by HIF1α, we additionally examined VEGF, as a peculiar molecule known for its wide-ranging functions, known for its role in angiogenesis and vasculogenesis, to promote vascular development, permeability, and en-

269

dothelial outspreading, but also investigated based on its role as a neurogenic, neurotrophic and neuroprotective factor in the nervous system [65].

## GFAP



**Figure 8.** GFAP DAB-immunostaining reaction in untreated (a–d) and He1-treated mice (e–h). Light microscopy magnification: 40× (a,b,e,f); 100× (c,d,g,h). Panels (A–D) Histograms showing quantitative analyses of BG immunopositive cell density, ratio between GFAP-immunopositive area in the ML and whole ML area, IGL immunopositive astrocytes density and OD, respectively. $p$ values calculated by unpaired Student's $t$-test: ** $p < 0.01$, *** $p < 0.001$.

The HIF1α immunopositivity was clearly detected in blood vessels, i.e., vascular endothelial cells, localized in the whole width of the cerebellar cortex, both in untreated animals and He1 mice (Figure 9). In fact, the presence of widespread HIF1α-positive vessels, mainly localized in the thickness of ML and characterized by the presence of several convoluted ramifications, was detected (Figure 9). These vessels, markedly stained, appeared particularly numerous and extended in untreated animals compared to He1 mice. The subsequent quantitative analysis supported a significant decrease of both blood vessels area and OD in He1 mice compared to untreated ones (Figure 9, Panels A and B;

270

$1.65 \pm 0.15$ vs. $5.60 \pm 0.59$, $p < 0.001$ and $161.66 \pm 3.16$ vs. $178.21 \pm 3.57$, $p < 0.01$, for area and OD, respectively).
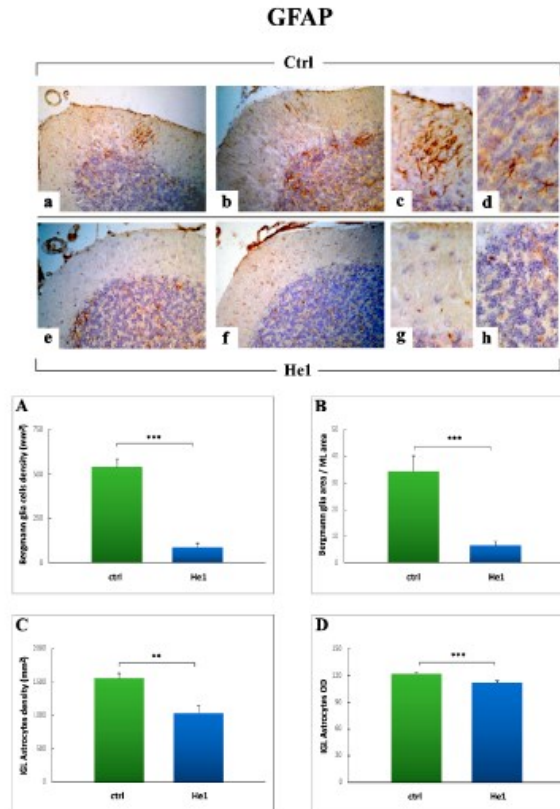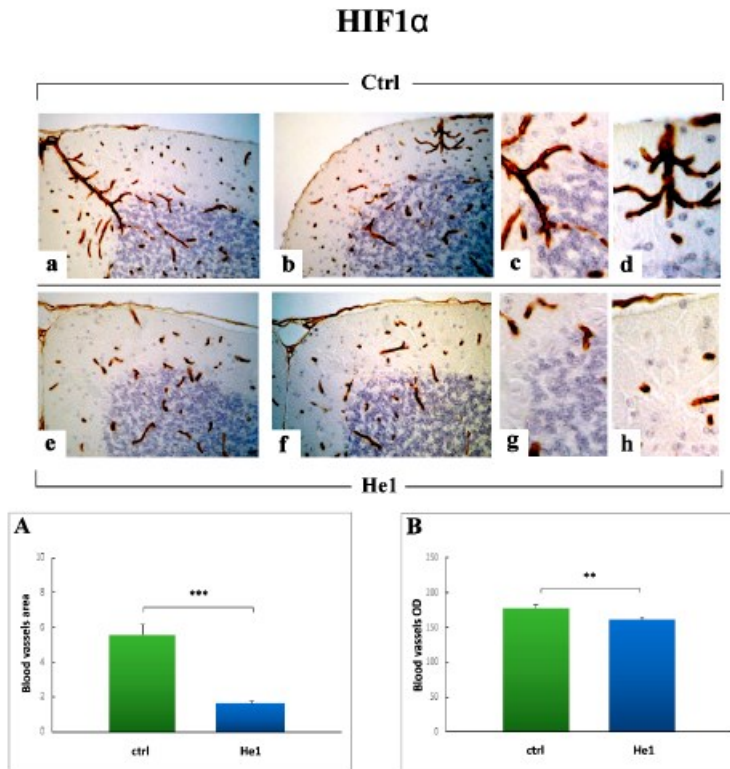
# HIF1α



**Figure 9.** HIF1α DAB-immunostaining reaction in untreated (a–d) and He1-treated mice (e–h). Light microscopy magnification: 40× (a,b,e,f); 100× (c,d,g,h). Panels (**A,B**) Histograms showing HIF1α-immunopositive blood vessels area and OD, respectively. $p$ values calculated by unpaired Student's $t$-test ** $p < 0.05$, *** $p < 0.001$.

Concerning VEGF (Figure 10), the immunopositivity appeared evidently localized in the sizeable soma of Purkinje neurons, evidently more marked in He1 mice (Figure 10d,f) compared to untreated animals (Figure 10a,c). Showing a similar trend (i) a striking immunoreactivity was also detected in the large mossy fiber rosettes located in the IGL (Figure 10b,e). Notably, the meningeal formation at the pial surface was also significantly immunomarked (Figure 10d). Any immunopositivity was observed in cerebellar cortex blood vessels neither in He1 mice nor in untreated animals (Figure 10a–f).
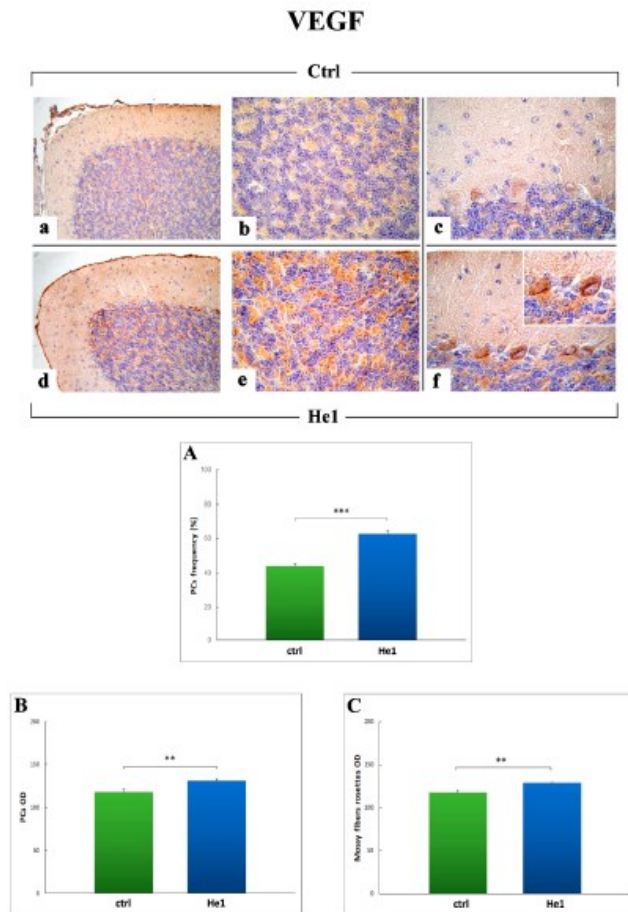
# VEGF



**Figure 10.** VEGF DAB-immunostaining reaction in untreated (a–c) and He1-treated mice (d–f). Light microscopy magnification: 40× (a–f); 100× (*insert* in f). Panels (**A–C**) Histograms showing the quantitative measurement of VEGF-immunoreactive cell frequency and OD for both Purkinje neurons and mossy fibers rosettes. $p$ values calculated by unpaired Student's $t$-test: ** $p < 0.01$, *** $p < 0.001$.

VEGF-immunoreactivity, quantitatively measured in terms of immunopositive PCs cell frequency, significantly increased in He1 treated mice compared to untreated animals ($62.80 \pm 1.76$ vs. $44.10 \pm 1.22$, $p < 0.001$, respectively) (Figure 10, Panel A). As well, the assessment of VEGF-immunoreactivity OD, evaluated both at PCs soma and mossy fiber rosettes levels, significantly increased in He1 mice compared to untreated ones

272

$(130.94 \pm 1.82$ vs. $117.93 \pm 0.77$, $p < 0.01$ and $128.74 \pm 0.96$ vs. $117.62 \pm 1.82$, $p < 0.01$, respectively) (Figure 10, Panels B and C).

### 2.3.4. Oxidative Stress Pathway: SOD1, NOS2 and COX2 Immunohistochemical Assessment

Literature evidence highlighted oxidative damage involvement in aging and age-associated cognitive impairment as a consequence of an increased reactive oxygen species (ROS) production and/or a decrease in antioxidant scavengers [66]. We assessed by immunohistochemistry the presence/distribution of Superoxide Dismutase 1 (SOD1), Nitric oxide synthase 2 (NOS2) and Cyclooxygenase 2 (COX2), as typical markers of the oxidative stress pathway.

The localization and expression of SOD1 revealed a widespread distribution both in untreated animals (Figure 11a–d) and He1 mice (Figure 11e–h); specifically, numerous SOD1-immunopositive cells were detected in the width of the ML (Figure 11d,h). Interestingly, some SOD1-immunopositive small cells lying just beneath the PC layer, possibly Lugaro cells, were identifiable in untreated mice only (Figure 11c). Notably, the quantitative analysis of SOD1 immunopositive cells frequency ($54.44 \pm 1.86$ vs. $63.52 \pm 1.26$, $p < 0.05$) and OD ($122.99 \pm 0.68$ vs. $123.15 \pm 0.43$) (Figure 11, Panels A and B, respectively), performed considering the ML layer, revealed a significant decrease in He1 mice compared to untreated animals.
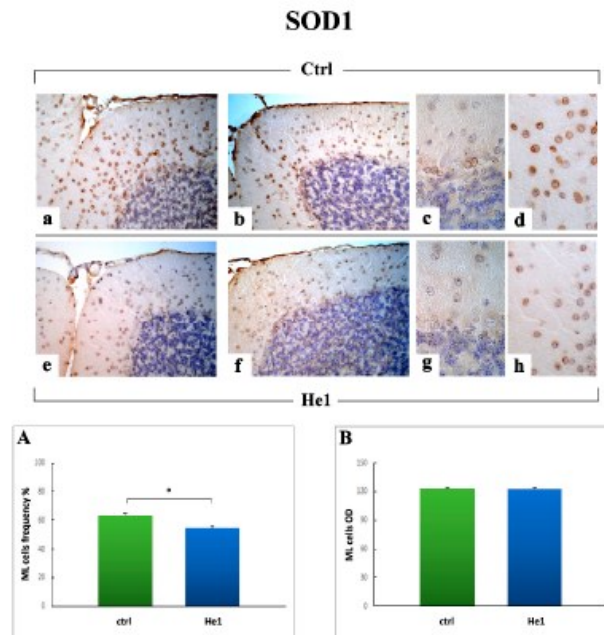


**Figure 11.** SOD1-Immunohistochemical labeling in untreated (a–d) and He1-treated mice (e–h). Light microscopy magnification: 40× (a,b,e,f); 100× (c,d,g,h). Panels (A,B) Histograms illustrating the quantitative measurement of SOD1 immunopositive cell frequency and OD, respectively. *p* values calculated by unpaired Student's *t*-test: * $p < 0.05$.

Concerning NOS2, a marked immunopositivity appeared evidently localized in the large soma of Purkinje neurons, both in untreated (Figure 12a–c) and He1 mice (Figure 12e–g). A clear immunopositivity was also detected in IGL, localized in the large mossy fiber rosettes (Figure 12d,h). Similarly to the observed SOD1 trend, NOS2-immunoreactivity, quantitatively measured in terms of cell frequency, i.e., immunopositive Purkinje neurons soma, significantly decrease in He1 treated animals compared to untreated animals ($22.01 \pm 1.07$ vs. $31.31 \pm 0.99$, $p < 0.01$). (Figure 12, Panel A). Likewise, the analysis of NOS2-immunoreactivity OD, evaluated both at mossy fiber rosettes and Purkinje cell soma levels, significantly decrease in He1 mice compared to untreated ones ($59.81 \pm 0.91$ vs. $76.52 \pm 0.28$, $p < 0.001$ and $57.66 \pm 0.59$ vs. $64.98 \pm 0.62$, $p < 0.01$, respectively) (Figure 12, Panels B and C).
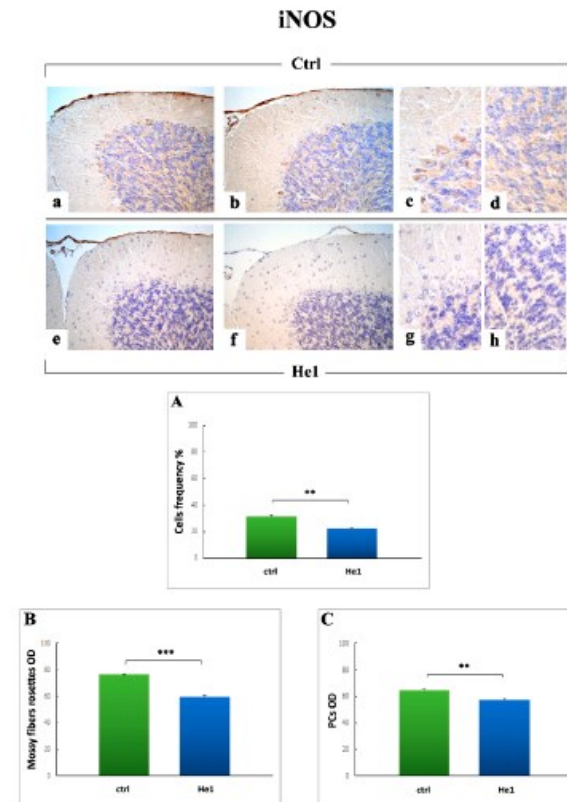


**Figure 12.** Immunohistochemical labeling for NOS2 in untreated animals (a–d) and He1 mice (e–h). Objective magnification: $40\times$ (a,b,e,f); $100\times$ (c,d,g,h). Panels (A–C) Histograms presenting the quantitative measurement of NOS2 immunopositive cell frequency, and OD evaluation for both mossy fibers rosettes as well as Purkinje neurons. $p$ values calculated by unpaired Student's $t$-test: ** $p < 0.01$, *** $p < 0.001$.

Regarding COX2, a clear immunoreactivity was observed in the somas and main dendrites of Purkinje neurons, appearing more marked in untreated animals (Figure 13a,b) compared to He1 mice (Figure 13c,d). Notably, some heavily immunopositive Golgi cells were also observed in the IGL of untreated mice only. In accordance to the qualitative data, the successive quantitative analysis confirmed a significant decrease of COX2 immunoreactivity, evaluated in terms of both cell frequency and OD, in He1 mice compared to untreated animals ($62.32 \pm 1.67$ vs. $79.67 \pm 1.71$, $p < 0.01$ and $108.65 \pm 0.30$ vs. $121.93 \pm 0.49$, $p < 0.001$, respectively. Figure 13, Panels A and B).
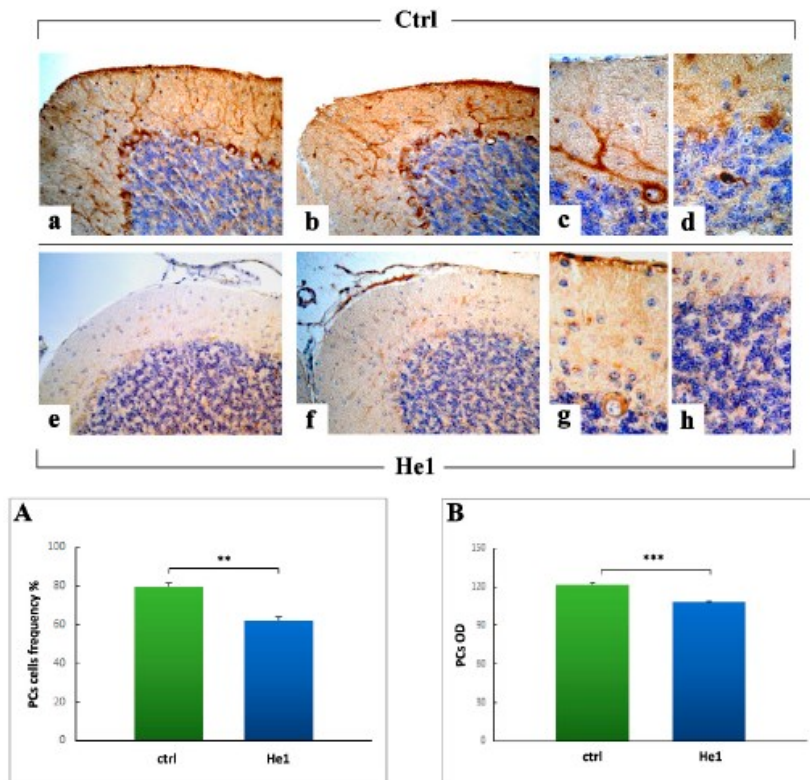


**Figure 13.** COX2 DAB-immunostaining reaction in untreated (a,b) and He1 mice (c,d). Light microscopy magnification: $40\times$ (a,c); $100\times$ (b,d). Panels (**A,B**) Histograms showing the quantitative determination of COX2 immunopositive cell frequency and OD. $p$ values calculated by unpaired Student's $t$-test: ** $p < 0.01$, *** $p < 0.001$.

### 2.3.5. Key Longevity Regulator: SIRT1

To further enhance the study of aging process and mechanisms, we finally investigated SIRT1, possessing a pivotal role impinging on ageing and lifespan, crucially affecting several activities in CNS neurons.

The evaluation of SIRT1 localization and expression showed a prevalent distribution in the ML and PCs layers, with a stronger immunolabeling in He1 mice compared to controls (Figure 14a–f); specifically, numerous SIRT1-immunopositive cells were detected in the ML thickness and the presence of several immunoreactive Purkinje cells soma was also observed (Figure 14b,c,e,f). Notably, the quantitative measurement of SIRT1 immunopositive ML cells frequency ($59.00 \pm 3.81$ vs. $19.00 \pm 1.08$, $p < 0.001$) and OD ($321.19 \pm 15.48$ vs. $185.69 \pm 3.21$, $p < 0.01$) demonstrated a significant increase in He1 treated mice compared to controls (Figure 14, Panels B and D). Concerning immunopositive PCs soma, the quantitative analyses established a significant increase of SIRT1 immunoreactivity, evaluated in terms of both cell frequency and OD, in He1 animals compared to untreated mice ($72.32 \pm 2.46$ vs. $48.00 \pm 1.44$, $p < 0.001$ and $390.14 \pm 13.34$ vs. $226.00 \pm 15.31$, $p < 0.01$, respectively. Figure 14, Panels A and C).
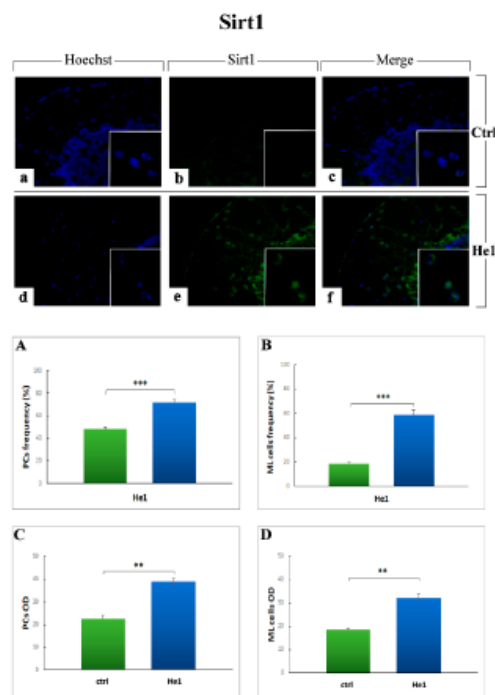
## Sirt1



**Figure 14.** Immunofluorescence reaction for SIRT1 (green fluorescence) in untreated (a–c) and He1 mice (d–f). Nuclei were counterstained with Hoechst 33,258 (blue fluorescence). Objective magnification: $40\times$ (a–f); $100\times$ (*inserts*). Panels (A–D) Histograms showing quantitative analyses of SIRT1 immunopositive ML cell frequency and OD and immunoreactive PCs soma frequency and OD, respectively. *p* values calculated by unpaired Student's *t*-test: ** $p < 0.01$, *** $p < 0.001$.

## 3. Discussion

Literature evidence strongly supports that cerebellum, other than the cerebral cortex, is crucially implicated in age-related cognitive and motor declines. Moreover, several works in humans, non-human primates and rodents underscore the importance of investigating cerebellar subregions, as aging differentially impacts the cerebellar areas associated with cognitive and motor function [67]. Numerous findings further implicate the cerebellum in motor declines in older adults, also supporting the idea that cerebellar-prefrontal circuits may be especially important for motor and cognitive performance in older age. Thus, a clear pattern emerged, confirming that cerebellum is related to performance across a variety of motor and cognitive task domains in older individuals.

In previous works, we tuned a phenotypic and cognitive frailty index and we monitored frailty during physiological aging. Interestingly, locomotor decline preceded and was faster compared to cognitive decline. In particular, we focused on the effects of *H. erinaceus* extract on the partial recovery of recognition memory of novelty during physiological aging. In the present study, we focused on locomotor performance recovery in frail mice and we described, by means of different spontaneous tasks and by measuring different locomotor parameters, that *H. erinaceus* partially recovered frailty decline of locomotor performances. Notably, taken together, our data are in agreement with a double protective effect on both locomotor and cognitive decline of *H. erinaceus* during physiological aging in mice.

Cerebellum volumetric decrease may be a key factor contributing to the age-related declines seen in both motor and cognitive performances [58,59,68,69].

Thus, based on literature data, taking into consideration that (i) cerebellar subregions are distinctly related to performance in elderly, and (ii) the posterior vermis region of the cerebellum is particularly affected by ageing [59,70], we focused our study on neocerebellar lobules VI–VIII.

H&E and Nissl findings clearly evidenced an age-related alteration in untreated mice during physiological ageing, in which both the cerebellar volume and ML width were significantly reduced and about half of the PCs appeared shrunken. Notably, He1 animals exhibited a significantly greater cerebellar size and ML thickness, fewer altered PCs, paralleled by a significant reduction of fibrotic response, thus supporting a considerable protective role of He1 supplementation on aging in frail mice. Concerning PCs and ML, our data is in accordance with previous experimental evidence demonstrating that during normal aging, deafferentation of PCs leads to their progressive defoliation and, thus, to a thinner ML in rodent cerebellum [71,72].

Moreover, in line with our findings, age-dependent changes in cerebellar size have also been described in clinical and experimental research, suggesting a decrease in cerebellum size with aging [67,72–75].

Concerning the inflammatory pathway, our findings revealed a significant decrease of IL6 immunopositive cells and fibers (both in terms of frequency and OD) in He1 mice compared to untreated animals. Notably, this outcome was accompanied by a parallel significant reduction of both GFAP immunopositive fibers and astrocytes (density as well as OD) in He1 mice only. These data matched and appeared strictly linked, in that the observed IL6 immunopositive cells and fibers could be reasonably considered as the main constituents of the BG glia, with astrocytic cell bodies around the PCs and the radial fibers running the width of the ML, which also appeared immunoreactive for GFAP. In this view, we may hypothesize that the observed reactive gliosis could be a direct consequence of IL6 overexpression, known to arise with aging [60,61,76] or even that an opposite mechanism may occur.

Interestingly, recent data demonstrated that cerebellar reactive gliosis disrupts the spatial distribution of excitatory amino acids transporter 1 or glutamate aspartate transporter, resulting in an increase in extracellular glutamate concentrations and cytotoxicity. In addition, activated astrocytes and microglia have been demonstrated to release various

proinflammatory molecules, including IL6 and tumor necrosis factor (TNF), implicated in neurodegeneration and negatively affecting Purkinje neuron function and survival [77].

Moreover, it has to be taken into consideration that glial reactivity increases with age and that hypertrophic, reactive astrocytes predominate in old brains, indicating the occurrence of a chronic neuroinflammation phenomena, the so-called "inflammaging" [78]. Moreover, complex changes in the immune system during aging were reported and referred to as immunosenescence, commonly accompanied by low-grade chronic inflammation thought to crucially contribute to neuroinflammation [79]. This latter aging hallmark is reported to have a dichotomous impact on glial activation, as these cells release pro- and anti-inflammatory cytokines and chemokines, antioxidants, free radicals, and neurotrophic factors, depending on the age and stimuli, even though the precise underlying mechanisms are still unknown. Furthermore, experimental studies in lab rodents revealed that astrocytes undergo age-dependent gene expression changes which contribute to synapse loss and neuroinflammation in a region-specific manner, thus revealing a selective vulnerability of some brain areas, e.g., cerebellum and hippocampus, to the aging process [80,81]. Recently, the involvement of neuroinflammation and gliosis in the pathogenesis of age-related and neurodegenerative diseases, e.g., Alzheimer, has been emphasized by compelling evidence from basic and clinical research studies [82,83].

In recent years, another assumption has gained particular attention hypothesizing the existence of a "molecular inflammatory theory of aging", based on which the activation of redox-sensitive transcriptional factors by age-related oxidative stress causes the upregulation of proinflammatory gene expression. As a consequence, several proinflammatory molecules would be produced, leading to systemic and organ inflammation processes. During aging, this inflammatory cascade is particularly amplified, and has been linked with the role played by ROS, able to modulate various signals causing accelerated cellular senescence.

Accordingly, many reports documented the complex relationship between oxidative stress and inflammation, showing inflammation-mediated oxidative damage and remarking that oxidative stress may act as a critical mechanism linking inflammation, excessive extracellular matrix deposition and apoptosis. Nonetheless, whether the inflammatory or the oxidative stress response occurs firstly, still remains a highly debated question.

With regard to oxidative stress pathway, our findings demonstrated a marked reduction of both iNOS and COX2 immunopositivity in He1 mice only, paralleled by a concurrent slighter, but even significant, decrease of SOD1 immunoreactivity.

A bulk of literature undoubtedly proved that oxidative damage is involved in aging and age-associated cognitive impairment. In fact, during aging, neurons tend to gather impaired/aggregated proteins and damaged mitochondria, as a consequence of oxidative stress. The increased production of reactive oxygen species (ROS) together with the reduction in antioxidant scavengers represent the key players in this unbalanced process. Thus, a failure in the normal antioxidant defense mechanisms arises, which renders the aged brain more vulnerable to the consequences of oxidative stress [82,83]. Several experimental investigations demonstrated that longer-lived animals show reduced oxidative damage and/or increased resistance to oxidative stress, gained through dietary restriction or genetic manipulations in mice which increased lifespan [84]. In line with these latter, our present results supported the protective role of the oral supplementation with *H. erinaceus*, able to diminish expression levels of iNOS, COX2, and also SOD1, thus possibly increase lifespan or even ameliorate the quality of life together with locomotor performances.

Our data are in line with previous literature evidence demonstrating that natural extract-enriched diet reduced age-associated increases in COX-2 and iNOS expressions [85].

Our findings on inflammatory and oxidative stress pathways were further integrated by the data on HIF1α, known to play a crucial role in aging-related pathology, including vascular diseases [64]. Emerging evidence has identified HIF1α as a critical transcription factor with an essential role in regulating cellular senescence associated with aging, which is in turn associated with alterations in HIF1α production and function [64,86]. Certainly,

it has to be underlined that published data on HIF1α often appear contradictory, since its upregulation resulted either protective or detrimental, depending on the measurement conditions. For example, increased HIF1α levels typically determined in age-related and neurodegenerative pathologies, e.g., Alzheimer's and Parkinson's diseases, have been indicated as a clear sign of advanced disease progression. Differently, other literature evidence implied the attenuated activity of HIF1 in senescent tissues as a key factor in the decreased ability to respond to hypoxic stress [87].

Our results evidenced a specific HIF1α immunoreactivity in vascular endothelial cells, in the width of the entire cerebellar cortex. Notably, we measured a significant decrease of both blood vessels area and OD in He1 mice compared to untreated animals. These data could be related to the role of HIF1α as a regulator of angiogenesis and inflammation in aging disorders, by promoting pro-inflammatory cytokine expression and, consequently, inflammatory cells recruitment, often associated with increased VEGF levels. In particular, based on the notion that HIF1α increases with age, perhaps due to enhanced hypoxia and oxidative stress, also acting as a master regulator in vascular aging [64,87], our results supported a positive protective action of *H. erinaceus*, able to maintain HIF1α levels stable over time, or even to decrease them. These protein levels could be linked to the reduction of both inflammation and oxidative stress, above reported in He1 mice only, as well as to a decrease of hypoxic conditions due to medicinal mushroom action, capable of mitigating age-associated alterations.

Concerning VEGF, its role in neural protection has recently gained much interest. In fact, other than vasculo-angiogenic properties, recent findings pointed out VEGF's role as a neurogenic, neurotrophic and neuroprotective factor in the nervous system, particularly implicated as a key player in the cerebellum [65]. Specifically, in the cerebellum, VEGF is extensively expressed in neurons, glia and endothelial cells with higher levels in Purkinje neurons. Notably, in adult CNS, VEGF is able to arouse neuronal recovery from injuries, e.g., strokes or epilepsy seizures, while, on the contrary, VEGF low level or depletion can negatively influence Purkinje neurons survival, facilitating neuronal injury outcome [65,88]. Interestingly, the role of VEGF in the age-related neurodegenerative diseases, e.g., Alzheimer's disease (AD) dementia, is still debated and controversial since diverse literature evidence exists for both up- and downregulation of VEGF in the brain. Nonetheless, growing evidence supports a neuroprotective role played by VEGF family protein expression associates in cognitive aging and AD pathology [89].

Our present results revealed a significant increase of VEGF expression levels, mainly localized in Purkinje cells soma and mossy fibers rosettes, in He1 treated mice only, evaluated in terms of both cell frequency and OD, while a complete lack of immunoreactivity was evidenced at blood vessels level. These data corroborate the neuroprotective action of *H. erinaceus* standardized extracts, whose intake led to a restoration/enhancement of VEGF expression levels, supporting the role of VEGF as an important nootropic factor capable of improving neurotrophic support to cerebellar neurons, thus ensuring or at least bettering their survival in aged-related conditions.

Finally, our data established that the oral supplementation with *H. erinaceus* was able to increase SIRT1 expression levels, possibly improving animal lifespan, also ameliorating both quality of life as well as locomotor performances.

SIRT1 is known to be strongly implicated in the aging process of diverse organisms, including mammals, based on its ability to integrate multiple signaling and transcriptional pathways, in which SIRT1 participates to regulate cellular senescence, metabolic disorders, autophagy, DNA damage and mitochondrial dysfunction, all of which are hallmarks of aging [90–92]. SIRT1 role as longevity regulator is well-known, since it acts as a key molecule in neuronal plasticity, cognitive functions, as well as protection against ageing-associated neuronal degeneration and cognitive decline [92]. In accordance with previous studies demonstrating that SIRT1 is associated with lifespan extension and other antiaging effects, specifically broadening mice life expectancy when overexpressed in the brain [92,93], our results led us to reasonably hypothesize that He1 supplementation was able to activate

an antioxidant mechanism by increasing the expression of SIRT1, which in turn decreases ROS levels, inhibiting apoptosis and promoting cell survival and neuroprotection. Notably, we may suppose that *H. erinaceus* oral supplementation could activate a stabilization mechanism in the regulation of the protein homeostasis of SIRT1 promoting healthy ageing.

In summary, our present findings clearly supported a neuroprotective action of *H. erinaceus* supplementation, able to ameliorate the cerebellar condition in aged frail mice compared to untreated animals (Figure 15). Specifically, our data mainly evidenced a bettering of the gross anatomy and cytoarchitectural situation, with a clear reduction of inflammation, gliosis, and oxidative stress, accompanied by (i) increase of neuroprotection and (ii) enhancement of a master key longevity regulator, paralleled by improvement of locomotor performances (Figure 15). Therefore, it is reasonable to believe that the bioactive metabolite array contained in the *H. erinaceus* significantly impacted on cellular mechanisms and molecular pathways typically linked to age-related neurodegeneration and locomotor impairments. Moreover, cerebellum, other than prefrontal cortex, appeared as a good predictor of locomotor performance declines during aging, suggesting that forthcoming investigations, focusing on this area and its relationship with age-related disorders pathogenesis, would be especially enlightening.



**Figure 15.** Schematic illustration summarizing main findings and the take-home message of the manuscript.

The present findings are consistent with the well-established role of *H. erinaceus* as the "choice" medicinal mushroom capable of (i) promoting positive brain and nerve health-related activities by inducing the nerve growth factor from its bioactive ingredient [94]; (ii) impacting on inflammation typically linked to age-related neurodegenerative disease, i.e., ischemic stroke, Parkinson's and Alzheimer disease, mainly acting in specific brain areas, i.e., cerebellum and cortex [32,94,95]; (iii) minimizing the oxidative stress-related consequences characteristics of brain aging and neurodegenerative disorders [83]; (iv) reducing anxiety and depressive behaviors by promoting hippocampal neurogenesis in the adult mouse [96].

Finally, it has to be highlighted that our current data are in line, and even strengthened, our previous findings demonstrating that dietary supplementation with *H. erinaceus* was effective at (i) increasing hippocampal neurotransmission, locomotor performances and recognition memory in wild-type mice [50,51], and (ii) improving recognition memory in frail mice during aging, also inducing hippocampal and cerebellar neurogenesis [14].

For completeness, it has however to be mentioned that in the present study we evaluated the effects of a particular *H. erinaceus* strain extract, characterized by the presence of different metabolites (i.e., Erinacine A, Hericenone C, Hericenone D, and ergothioneine), precisely quantified using HPLC-UV-ESI/MS by comparison with specific standard solutions. During our next investigations, it would be advantageous either to perform a further in-depth chemical analysis employing additional standards to identify other unknown metabolites contained in the currently employed He1 extract or to assess the potential nootropic action of other metabolite-enriched *H. erinaceus* strains. Moreover, our results could be replicated and thus further confirmed on a larger set of animals which could be randomized into different experimental groups, also widening the exploited age-related markers.

As a final point, it has to be underscored that we presently employed both open field and emergence tests for measuring the extent of locomotor frailty in order to reach a translational approach with human test, since the gait speed is one of the accepted clinical parameters used in Fried's phenotype model for frailty in older adults. This simplified, noninvasive method allows us to monitor the development of frailty during mice aging both as phenotypic and cognitive frailty. Nonetheless, further investigations would also include additional locomotor and performance tests, including for example grip strength, rotarod test or voluntary wheel running, paralleled by cognitive tests, assessing recognition memory, e.g., novel object recognition and object location tasks [51], that are used to monitor cognitive frailty development during ageing. These future data would further strengthen the current results also in accordance with literature evidence, underlining that frailty index score needs to be tuned by a number of different locomotor parameters since it has been recognized that several task parameters need to be recorded to validate and give interpretation of behavioral experiment data.

## 4. Materials and Methods

### 4.1. Animals and Treatments

Fifteen C57BL-6J wild-type male mice were purchased from Charles River Italia (Calco, Italy). The pathogen-free mice were acclimatized at least 2 weeks before conducting the experiments. Mice were maintained in the Animal Care Facility of University of Pavia at $21 \pm 2\,°C$, with humidity at $50 \pm 10\%$, and on a 12 h light/dark cycle. Water and food were provided ad libitum. The experimental procedures were carried out in accordance with the guidelines laid out by the institution's animal welfare committee, the Ethics Committee of Pavia University (Ministry of Health, License number 774/2016-PR). Behavioral tests experiments were performed at three different animal ages: 11 (T0, recruitment time, including in adulthood), 21.5 (T1, senescence) and 23.5 (T2, senescence) months old. The seven frailest mice (He1 treated group), as assessed by locomotor frailty index, were supplemented for two months (starting from T1) with a drink made with a blend of *H. erinaceus* sphorophore and mycelium ethanol extracts solubilized in water (Figure 16), with the purpose to administer 1 mg supplement/mouse per day [14]. This amount was selected to mimic the oral supplementation in humans (about 1 g/day).
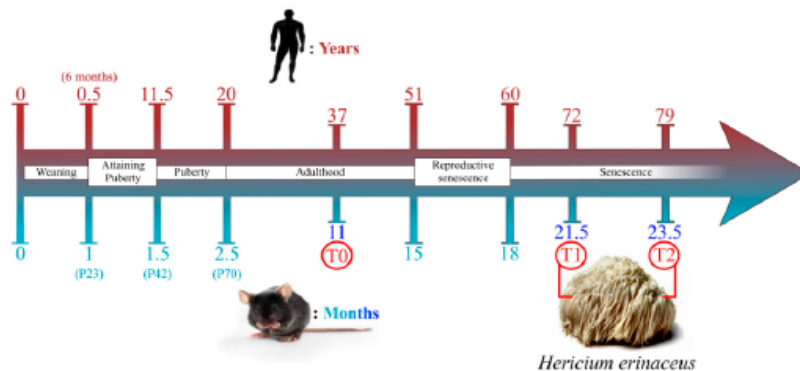


**Figure 16.** Schematic drawing summarizing experimental time course, chosen timepoints and comparison between men and mice age during their life span (modified from [14]).

### 4.2. Behavioral Tests and Locomotor Frailty Index

In vivo experiments were performed for investigating locomotor abilities of mice. For all experiments, researchers were blinded to the group assignment (untreated and He1 treated mice). Mice performances were measured by SMART video tracking system (2 Biological Instruments, Besozzo, Varese, Italy) and Sony CCD color video camera (PAL). All mice, at different experimental times, performed two spontaneous behavioral tests: open arena and emergence tasks. In the open arena test, mice were left free to explore an empty arena of 63 × 42 cm. During the emergence test, mice were placed in a familiar cage with a hole through which they can emerge in a larger arena without walls [51]. Both tests lasted 8 min; mean speed (cm/s), resting time (s), and max speed (cm/s) were evaluated. For each parameter the corresponding locomotor frailty index (FI) was calculated by using the following formula [14]:

$$FI = (Value - Mean\ Value\ at\ T0)/(SD\ at\ T0) \times 0.25$$

Averaging the different locomotor FIs for the two selected parameters (mean speed and resting time), we obtained an overall Locomotor FI, which described the overall locomotor decline during senescence.

### 4.3. H. erinaceus

The He1 (strain 1 of *H. erinaceus*) was isolated from a wildtype sporophore collected in 2013 in Siena province (Tuscany, Italy) from a *Quercus ilex* [97]. The sporophore was aseptically cut and placed in 2% malt extract agar as a culture medium (MEA, Biokar Diagnostics) [14]. The isolated strain was further maintained in the Fungal Research Culture Collection of Pavia University (MicUNIPV).

#### 4.3.1. Extraction Procedures

Based on the lack of formerly published standardized extraction protocol for the ergothioneine (ET), we adopted the method described by Cesaroni et al. [97,98] as a starting point, and then rearranged it with the extraction procedure already reported in Corana et al. [52] and Ratto et al. [14] for erinacines and hericenones, metabolites present in *H. erinaceus*. In detail, 1 g of lyophilized mycelium or sporophore of He1 was blended with 10 mL of ethanol 70%, and left in the thermostat overnight at 50 C. Before withdrawing, the material was stirred for one hour and was centrifuged at 4000 rpm for three minutes. The supernatant was stored at 20 °C. The detailed procedures were previously described by Ratto et al., Lee et al., and Gerbec et al. [14,52,99,100].

#### 4.3.2. HPLC-UV-ESI/MS Method

HPLC-UV-ESI/MS analyses were carried out as previously reported [14].

In order to identify and measure the amount of ET, we analyzed the mycelium and sporophore extracts of He1 using HPLC-UV-ESI/MS, by comparing to ET standard. L-(+)-Ergothioneine (ET; E7521-5MG, Sigma Aldrich, Milan, Italy) was used as standard. The ET calibration curve was constructed by injecting standard mixture solutions at five concentrations (10, 70, 150, 350 µg/mL). Each concentration was analyzed in triplicate.

### 4.4. Tissue Sampling, Histology, Immunohistochemical and Immunofluorescence Evaluations

For each treatment, cerebellar tissues were processed for the following morphological and histochemical evaluations.

#### 4.4.1. Cerebellar Specimens Preparation

At the age of 23.5 months (T2), mice were anesthetized by isoflurane inhalation (Aldrich, Milwaukee, WI, USA) before decapitation. Cerebella were immediately excised as previously described [101], washed in 0.9% NaCl, and fixed by immersion for 48 h at room temperature in Carnoy's solution (6 absolute ethanol/3 chloroform/1 acetic acid).

Tissues were then kept in absolute ethanol for one hour, followed by acetone, and finally embedded in Paraplast X-TRA (Sigma Aldrich, Milan, Italy). Eight micron-thick sections, collected on silane-coated slides, of cerebellar vermis were cut in the sagittal plane.

#### 4.4.2. Post-Embedding Cerebellar Volume Estimation

The Cavalieri method was employed, following procedures previously described [75,102]. Briefly, sections were traced on the Nissl-stained sections at $4\times$ magnification to estimate the surface area. No discrimination among separate layers was made due to sections thickness. Then, the following formula was used to estimate the volume of the whole cerebellum:

$$Volume = P * T * A(p)$$

P was the sum of the points counted in all sections, T was the thickness of sections (8 µm), and A(p) was the area associated with each point; $[100\ µm/40]^2$ (where $4\times$ was the magnification and 100 µm was the distance between each point).

#### 4.4.3. H&E and Nissl Staining

Subsequently, to overall evaluate structural changes and neuronal cytoarchitecture by light microscopy, H&E and Nissl staining were performed as previously described [103–105]. The slides were then observed and scored with a bright-field Zeiss Axioscop Plus 612 microscope. Specifically, 5 slides (about 20 randomized sections) per animal were analyzed; 5 microscopic fields were examined in each section for each mouse per time/condition, with the operator blinded to the experimental condition. The images were recorded with an Olympus Camedia C-5050 digital camera and stored on a PC running Olympus software.

#### 4.4.4. Picrosirius Red (PSR) Staining

Serial tissue sections were stained for 1 h with a PicroSirius red (PSR) solution (0.1% of Sirius red in saturated aqueous picric acid), followed by a wash in 5% acidified water [106,107], for collagen staining. Lastly, the sections were dehydrated in ethanol, cleared in xylene, and finally mounted in Eukitt (Kindler, Freiburg, Germany).

#### 4.4.5. Immunohistochemistry: Light and Fluorescence Microscopy Assessment

Immunohistochemical reactions were carried out simultaneously on slides from different experimental groups to avoid possible staining differences due to small changes in the procedures. Immunohistochemical and immunofluorescence procedures were performed using commercial antibodies on murine cerebellar specimens, to investigate expression and distribution of specific markers representative of inflammation, reactive gliosis, oxidative stress and age-related mechanisms: (i) Interleukin-6 (IL6), (ii) Glial fibrillary acidic protein (GFAP), (iii) hypoxia-inducible factor (HIF1α), (iv) Cu–Zn superoxide dismutase-1 (SOD1), (v) nitric oxide synthase 2 (NOS2), and (vi) cyclo-oxygenase-2 (COX2), (vii) Sirtuin 1 (SIRT1), and (viii) vascular endothelial growth factor (VEGF).

Cerebellar sections of untreated and He1 mice were incubated overnight at room temperature in a dark moist chamber with selected monoclonal and polyclonal primary antibodies (Table 2) diluted in PBS. In detail, GFAP immunostaining was employed to mark specifically Bergmann glia [108,109]; IL6 has been investigated as valuable inflammation marker [61,110]; SOD1, NOS2 and COX2 were examined being specific molecules essentially involved in oxidative stress pathway [15,111–115]; SIRT1 was assessed for its pivotal role that impinges on cellular senescence and lifespan [90,92,116]; VEGF was considered possessing broad-ranging functions, both in vascular system and CNS [65].

Concerning immunohistochemical reactions detected using brightfield microscopy, proper biotinylated secondary antibodies (Table 2) and an avidin biotinylated horseradish peroxidase complex (Vector Laboratories, Burlingame, CA, USA) were used to reveal the sites of antigen/antibody interaction. The 3,3'-diaminobenzidine tetrahydrochloride peroxidase substrate (Sigma, St. Louis, MO, USA) was used as the chromogen. The nuclear counterstaining was achieved by employing Carazzi's Haematoxylin. Then, the sections

were dehydrated in ethanol, cleared in xylene, and finally mounted in Eukitt (Kindler, Freiburg, Germany). As negative untreated, some sections were incubated with PBS in the absence of the primary antibodies: no immunoreactivity was observed in this condition.

**Table 2.** Primary/secondary antibodies employed for immunocytochemical/immunofluorescence experimental procedures.

| | Antigen | Immunogen | Manufacturer, Species, Mono-Polyclonal, Catalogue or Lot No., RRID | Diluted Used |
|---|---|---|---|---|
| **Primary antibodies** | Anti-Interleukin-6 (M-19) | Purified antibody raised against a peptide mapping at the C-terminus of murine IL6 | Santa Cruz Biotechnology (Santa Cruz, CA, USA), Goat polyclonal IgG, Cat# sc-1265, RRID: AB_2127470 | 1:100 |
| | Anti-Glial fibrillary acidic protein (C-19) | Purified antibody raised against a peptide mapping at the C-terminus of GFAP of human origin | Santa Cruz Biotechnology (Santa Cruz, CA, USA), Goat polyclonal IgG, Cat# sc-6170, RRID: AB_641021 | 1:100 |
| | Anti-Hypoxia-inducible factors-1α (H1α 67) | Purified antibody raised against amino acids 432–528 of HIF-1α of human origin | Santa Cruz Biotechnology (Santa Cruz, CA, USA), Mouse monoclonal IgG, Cat# sc-53546, RRID: AB_629639 | 1:100 |
| | Anti-Superoxide Dismutase-1 (FL-154) | Purified antibody raised against amino acids 1–154 representing full-length human SOD-1 | Santa Cruz Biotechnology (Santa Cruz, CA, USA), Rabbit polyclonal IgG, Cat# sc-11407, RRID: AB_2193779 | 1:100 |
| | Anti-Nitric Oxide Synthases-2 (M19) | Purified antibody raised against a peptide mapping at the C-terminus of murine NOS-2 | Santa Cruz Biotechnology (Santa Cruz, CA, USA), Rabbit polyclonal IgG, Cat# sc-650, RRID: AB_631831 | 1:100 |
| | Anti-Cyclooxygenase-2 (M-19) | Purified antibody raised against a peptide mapping at the C-terminus of murine COX-2 | Santa Cruz Biotechnology (Santa Cruz, CA, USA), Goat polyclonal IgG, Cat# sc-1747, RRID: AB_2084976 | 1:100 |
| | Anti-Sirtuin1 | Purified antibody raised against amino acids 722–737 of murine SIRT1 with a C-terminal added lysine | Abcam (Cambridge, MA, USA), Rabbit polyclonal IgG, Cat# ab12193, RRID: AB_298923 | 1:100 |
| | Anti-VEGF | Purified antibody raised against a peptide corresponding to aa 1–140 of VEGF of human origin. | Santa Cruz Biotechnology (Santa Cruz, CA, USA), Rabbit polyclonal IgG, Cat# sc-507, RRID: AB_2212666 | 1:100 |
| **Secondary antibodies** | Biotinylated goat anti-rabbit IgG | Gamma immunoglobulins | Vector Laboratories (Burlingame, CA, USA), Goat, lot# PK-6101, RRID: AB_2336820 | 1:200 |
| | Biotinylated rabbit anti-goat IgG | Gamma immunoglobulins | Vector Laboratories (Burlingame, CA, USA), Rabbit, Cat# PK-6105, RRID: AB_2336824 | 1:200 |
| | Goat anti-Rabbit IgG (H+L) Cross-Adsorbed Secondary Antibody, Alexa Fluor 488 | Gamma Immunoglobulins (Heavy and Light chains) | Thermo Fisher scientific, Invitrogen (Waltham, MA USA), Cat# A-11008, RRID: AB_143165 | 1:100 |

Regarding immunofluorescence reactions, after washing in phosphate buffer saline (PBS), sections were incubated for one hour with the secondary antibody Alexa Fluor 488-conjugated anti-rabbit (1:100, Thermo Fisher scientific, Invitrogen, Waltham, MA, USA) in a dark moist chamber. Then the nuclei were counterstained for 10 min with 0.1 µg/mL Hoechst 33,258 (Sigma Aldrich, Milan, Italy). After PBS washing, coverslips were mounted in a drop of Mowiol (Calbiochem, San Diego, CA, USA).

### 4.4.6. Histochemical, Immunohistochemical and Immunofluorescence Evaluations

Regarding brightfield microscopy, the sections were observed with an Olympus BX51 optical microscope (model BX51TF). The images were acquired with an Olympus CAMEDIA C4040ZOOM camera.

For each selected marker, 5 slides (about 20 sections) per animal were analyzed. Cerebellar specimens with different immunolabeling extent were considered in both experimental groups. The figures show the most representative changes for each immunohistochemical reaction.

Histochemical and immunohistochemical labeling extent was evaluated on acquired digitized section images under exposure time avoiding any pixel saturation effect. The labeling intensity was measured utilizing densitometric analysis (Image-J 1.48i; NIH, Bethesda, MA, USA). Firstly, the color of images was inverted to obtain a positive signal lighter on a dark background (instead of the immunoperoxidase staining results), thus correlating the intensifying of immunopositivity with the optical density values increasing calculated by the software (expressed as mean of light intensity). The mask shape was adjusted depending on the spatial distribution, signal localization, different layer and cell types/fibers of the cerebellar specimens under measurement (using the polygon selection tool, to ensure the punctual evaluation of the positivity area only); the labeling was measured as the mean intensity value over the area. The immunocytochemical intensity, indicated as optical density (OD), was evaluated in 3 randomized images/section (making at least 10 measurements/image) per 5 slides/animal from each experimental group, with the operator blinded to the experimental condition. Results were recorded on Microsoft Office Excel Software spreadsheets and the analysis was achieved using the ImageJ software.

The following further measurements were performed: (i) ML thickness (by using a $40\times$ objective on H&E-stained slides) in µm; (ii) GFAP-immunopositive Bergmann glia area in $\mu m^2$/whole ML area in $\mu m^2$, (iii) GFAP-immunopositive cells density count (number of immunopositive cells/area in $mm^2$) and (iv) HIF1$\alpha$-immunopositive blood vessels area in $\mu m^2$/whole area in $\mu m^2$.

Concerning fluorescence microscopy, sections were observed with an Olympus BX51 optical microscope equipped with a 100-W mercury lamp used under the following conditions: 330–385 nm excitation filter (excf), 400 nm dichroic mirror (dm), and 420 nm barrier filter (bf) for Hoechst 33,258; 450–480 nm excf, 500 nm dm and 515 nm bf for the fluorescence of Alexa 488. Images were recorded with an Olympus MagnaFire camera and results were processed with the Olympus Cell F software.

Immunofluorescence quantification was performed by calculating frequency (percentage ratio) and optical density (OD) of SIRT1 immunopositive cells on a total number (about 300 cells) for each animal per experimental condition, in a minimum of 10 randomly selected high-power microscopic fields, with the operator blinded to the experimental condition.

### 4.5. Statistical Analysis

Data were reported as mean ± standard error of the mean (SEM). We performed Bartlett and Shapiro Wilk Tests to establish and confirm the normality of parameters. To verify statistically significant differences, we used a two-way Anova followed by Bonferroni's *post-hoc* test for the *H. erinaceus* supplementation effect in vivo. The statistical analysis for histochemical and immunohistochemical evaluations was carried out using an unpaired Student's *t*-test. The differences were considered statistically significant for

$p < 0.05$ (*), $p < 0.01$ (**), and $p < 0.001$ (***). Statistical analyses were performed with GraphPad Prism 7.0 software (GraphPad Software Inc., La Jolla, CA, USA).

## 5. Conclusions

In conclusion, our results provide experimental evidence that *H. erinaceus* may supply neuroprotective metabolites to be used as valuable, effective candidates for treating and preventing age-related neurodegenerative diseases. Altogether, our results support the potential feasibility of non-pharmacological approaches, including dietary supplementations using medicinal mushrooms extracts, as promising adjuvant therapies to be associated with conventional geriatric treatments.

**Author Contributions:** Conceptualization, P.R., E.S.; methodology, L.G., E.C.P., C.D.I., A.D.; software, D.R., F.D.L., P.A.; formal analysis, E.C.P., E.R., D.R., F.D.L., L.G.; investigation, C.D.I.; data curation, D.R., C.D.I.; writing—original draft preparation, E.C.P.; E.R.; D.R.; writing—review and editing, E.R. and P.R.; supervision, M.G.B., C.A.L., P.R. All authors have read and agreed to the published version of the manuscript.

**Institutional Review Board Statement:** The study was conducted according to the guidelines laid out by the institution's animal welfare committee, the Ethics Committee of Pavia University (Ministry of Health, License number 774/2016-PR).

**Informed Consent Statement:** Not applicable.

**Data Availability Statement:** Not applicable.

**Conflicts of Interest:** The authors declare no conflict of interest.

## References

1. Hamezah, H.S.; Durani, L.W.; Ibrahim, N.F.; Yanagisawa, D.; Kato, T.; Shiino, A.; Tanaka, S.; Damanhuri, H.A.; Ngah, W.Z.W.; Tooyama, I. Volumetric changes in the aging rat brain and its impact on cognitive and locomotor functions. *Exp. Gerontol.* **2017**, *99*, 69–79. [CrossRef]
2. Cesari, M.; Prince, M.; Thiyagarajan, J.A.; De Carvalho, I.A.; Bernabei, R.; Chan, P.; Gutierrez-Robledo, L.M.; Michel, J.-P.; Morley, J.E.; Ong, P.; et al. Frailty: An Emerging Public Health Priority. *J. Am. Med. Dir. Assoc.* **2016**, *17*, 188–192. [CrossRef]
3. Leng, S.; Chen, X.; Mao, G. Frailty syndrome: An overview. *Clin. Interv. Aging* **2014**, *9*, 433–441. [CrossRef]
4. Pansarasa, O.; Pistono, C.; Davin, A.; Bordoni, M.; Mimmi, M.C.; Guaita, A.; Cereda, C. Altered immune system in frailty: Genetics and diet may influence inflammation. *Ageing Res. Rev.* **2019**, *54*, 100935. [CrossRef] [PubMed]
5. Franceschi, C.; Capri, M.; Monti, D.; Giunta, S.; Olivieri, F.; Sevini, F.; Panourgia, M.P.; Invidia, L.; Celani, L.; Scurti, M.; et al. Inflammaging and anti-inflammaging: A systemic perspective on aging and longevity emerged from studies in humans. *Mech. Ageing Dev.* **2007**, *128*, 92–105. [CrossRef] [PubMed]
6. Hubbard, R.E.; O'Mahony, M.S.; Savva, G.; Calver, B.L.; Woodhouse, K.W. Inflammation and frailty measures in older people. *J. Cell. Mol. Med.* **2009**, *13*, 3103–3109. [CrossRef]
7. Ferrucci, L.; Fabbri, E. Inflammageing: Chronic inflammation in ageing, cardiovascular disease, and frailty. *Nat. Rev. Cardiol.* **2018**, *15*, 505–522. [CrossRef]
8. Hodes, R.J.; Sierra, F.; Austad, S.N.; Epel, E.; Neigh, G.N.; Erlandson, K.M.; Schafer, M.J.; LeBrasseur, N.; Wiley, C.; Campisi, J.; et al. Disease drivers of aging. *Ann. N. Y. Acad. Sci.* **2016**, *1386*, 45–68. [CrossRef]
9. Aranda, M.P.; Ray, L.A.; Al Snih, S.; Ottenbacher, K.J.; Markides, K.S. The Protective Effect of Neighborhood Composition on Increasing Frailty among Older Mexican Americans. *J. Aging Health* **2011**, *23*, 1189–1217. [CrossRef]
10. Doba, N.; Tokuda, Y.; Goldstein, N.E.; Kushiro, T.; Hinohara, S. A pilot trial to predict frailty syndrome: The Japanese Health Research Volunteer Study. *Exp. Gerontol.* **2012**, *47*, 638–643. [CrossRef] [PubMed]
11. Raji, M.A.; Al Snih, S.; Ostir, G.V.; Markides, K.S.; Ottenbacher, K.J. Cognitive Status and Future Risk of Frailty in Older Mexican Americans. *J. Gerontol. Ser. A Boil. Sci. Med. Sci.* **2010**, *65*, 1228–1234. [CrossRef]
12. Chen, W.-T.; Chou, K.-H.; Liu, L.-K.; Lee, P.-L.; Lee, W.-J.; Chen, L.-K.; Wang, P.-N.; Lin, C.-P. Reduced cerebellar gray matter is a neural signature of physical frailty. *Hum. Brain Mapp.* **2015**, *36*, 3666–3676. [CrossRef]

13. Samper-Ternent, R.; Al Snih, S.; Raji, M.A.; Markides, K.S.; Ottenbacher, K.J. Relationship between Frailty and Cognitive Decline in Older Mexican Americans. *J. Am. Geriatr. Soc.* 2008, 56, 1845–1852. [CrossRef] [PubMed]
14. Ratto, D.; Corana, F.; Mannucci, B.; Priori, E.C.; Cobelli, F.; Roda, E.; Ferrari, B.; Occhinegro, A.; Di Iorio, C.; De Luca, F.; et al. Hericium erinaceus Improves Recognition Memory and Induces Hippocampal and Cerebellar Neurogenesis in Frail Mice during Aging. *Nutrients* 2019, 11, 715. [CrossRef] [PubMed]
15. Liguori, I.; Russo, G.; Curcio, F.; Bulli, G.; Aran, L.; DELLA Morte, D.; Gargiulo, G.; Testa, G.; Cacciatore, F.; Bonaduce, D.; et al. Oxidative stress, aging, and diseases. *Clin. Interv. Aging* 2018, 13, 757–772. [CrossRef]
16. Uchmanowicz, I. Oxidative Stress, Frailty and Cardiovascular Diseases: Current Evidence. *Adv. Exp. Med. Biol.* 2020, 1216, 65–77. [CrossRef] [PubMed]
17. Cui, L.; Hofer, T.; Rani, A.; Leeuwenburgh, C.; Foster, T.C. Comparison of lifelong and late life exercise on oxidative stress in the cerebellum. *Neurobiol. Aging* 2009, 30, 903–909. [CrossRef]
18. Nadkarni, N.K.; Nunley, K.A.; Aizenstein, H.; Harris, T.B.; Yaffe, K.; Satterfield, S.; Newman, A.B.; Rosano, C.; Health ABC Study. Association Between Cerebellar Gray Matter Volumes, Gait Speed, and Information-Processing Ability in Older Adults Enrolled in the Health ABC Study. *J. Gerontol. Ser. A Boil. Sci. Med. Sci.* 2014, 69, 996–1003. [CrossRef]
19. Zhang, C.; Zhu, Q.; Hua, T. Aging of cerebellar Purkinje cells. *Cell Tissue Res.* 2010, 341, 341–347. [CrossRef]
20. Jiang, S.; Wang, S.; Sun, Y.; Zhang, Q. Medicinal properties of Hericium erinaceus and its potential to formulate novel mushroom-based pharmaceuticals. *Appl. Microbiol. Biotechnol.* 2014, 98, 7661–7670. [CrossRef]
21. Friedman, M. Chemistry, Nutrition, and Health-Promoting Properties of Hericium erinaceus (Lion's Mane) Mushroom Fruiting Bodies and Mycelia and Their Bioactive Compounds. *J. Agric. Food Chem.* 2015, 63, 7108–7123. [CrossRef]
22. Liu, J.-H.; Li, L.; Shang, X.-D.; Zhang, J.-L.; Tan, Q. Anti- Helicobacter pylori activity of bioactive components isolated from Hericium erinaceus. *J. Ethnopharmacol.* 2016, 183, 54–58. [CrossRef] [PubMed]
23. Kim, S.P.; Moon, E.; Nam, S.H.; Friedman, M. Hericium erinaceus Mushroom Extracts Protect Infected Mice against Salmonella Typhimurium-Induced Liver Damage and Mortality by Stimulation of Innate Immune Cells. *J. Agric. Food Chem.* 2012, 60, 5590–5596. [CrossRef]
24. Li, G.; Yu, K.; Li, F.; Xu, K.; Li, J.; He, S.; Cao, S.; Tan, G. Anticancer potential of Hericium erinaceus extracts against human gastrointestinal cancers. *J. Ethnopharmacol.* 2014, 153, 521–530. [CrossRef]
25. Li, W.; Zhou, W.; Kim, E.-J.; Shim, S.H.; Kang, H.K.; Kim, Y.H. Isolation and identification of aromatic compounds in Lion's Mane Mushroom and their anticancer activities. *Food Chem.* 2015, 170, 336–342. [CrossRef]
26. Wu, T.; Xu, B. Antidiabetic and antioxidant activities of eight medicinal mushroom species from China. *Int. J. Med. Mushrooms* 2015, 17, 129–140. [CrossRef] [PubMed]
27. Wang, X.-Y.; Yin, J.-Y.; Zhao, M.-M.; Liu, S.-Y.; Nie, S.-P.; Xie, M.-Y. Gastroprotective activity of polysaccharide from Hericium erinaceus against ethanol-induced gastric mucosal lesion and pylorus ligation-induced gastric ulcer, and its antioxidant activities. *Carbohydr. Polym.* 2018, 186, 100–109. [CrossRef] [PubMed]
28. Liu, J.; Du, C.; Wang, Y.; Yu, Z. Anti-fatigue activities of polysaccharides extracted from Hericium erinaceus. *Exp. Ther. Med.* 2015, 9, 483–487. [CrossRef]
29. Noh, H.J.; Yang, H.H.; Kim, G.S.; Lee, S.E.; Lee, D.Y.; Choi, J.H.; Kim, S.Y.; Lee, E.S.; Ji, S.H.; Kang, K.S.; et al. Chemical constituents of Hericium erinaceum associated with the inhibitory activity against cellular senescence in human umbilical vascular endothelial cells. *J. Enzym. Inhib. Med. Chem.* 2015, 30, 934–940. [CrossRef]
30. Mori, K.; Inatomi, S.; Ouchi, K.; Azumi, Y.; Tuchida, T. Improving effects of the mushroom Yamabushitake (Hericium erinaceus) on mild cognitive impairment: A double-blind placebo-controlled clinical trial. *Phytother. Res.* 2009, 23, 367–372. [CrossRef]
31. Tsai-Teng, T.; Chin-Chu, C.; Li-Ya, L.; Wan-Ping, C.; Chung-Kuang, L.; Chien-Chang, S.; Chi-Ying, H.F.; Chien-Chih, C.; Shiao, Y.-J. Erinacine A-enriched Hericium erinaceus mycelium ameliorates Alzheimer's disease-related pathologies in APPswe/PS1dE9 transgenic mice. *J. Biomed. Sci.* 2016, 23, 49. [CrossRef]
32. Zhang, J.; An, S.; Hu, W.; Teng, M.; Wang, X.; Qu, Y.; Liu, Y.; Yuan, Y.; Wang, D. The Neuroprotective Properties of Hericium erinaceus in Glutamate-Damaged Differentiated PC12 Cells and an Alzheimer's Disease Mouse Model. *Int. J. Mol. Sci.* 2016, 17, 1810. [CrossRef] [PubMed]
33. Nagano, M.; Shimizu, K.; Kondo, R.; Hayashi, C.; Sato, D.; Kitagawa, K.; Ohnuki, K. Reduction of depression and anxiety by 4 weeks Hericium erinaceus intake. *Biomed. Res.* 2010, 31, 231–237. [CrossRef]
34. Vigna, L.; Morelli, F.; Agnelli, G.M.; Napolitano, F.; Ratto, D.; Occhinegro, A.; Di Iorio, C.; Savino, E.; Girometta, C.; Brandalise, F.; et al. Hericium erinaceus Improves Mood and Sleep Disorders in Patients Affected by Overweight or Obesity: Could Circulating Pro-BDNF and BDNF Be Potential Biomarkers? *Evid.-Based Complement. Altern. Med.* 2019, 2019, 7861297. [CrossRef]
35. Cohen, N.; Cohen, J.; Asatiani, M.D.; Varshney, V.K.; Yu, H.-T.; Yang, Y.-C.; Li, Y.-H.; Mau, J.-L.; Wasser, S.P. Chemical Composition and Nutritional and Medicinal Value of Fruit Bodies and Submerged Cultured Mycelia of Culinary-Medicinal Higher Basidiomycetes Mushrooms. *Int. J. Med. Mushrooms* 2014, 16, 273–291. [CrossRef] [PubMed]
36. Halliwell, B.; Cheah, I.K.; Tang, R.M.Y. Ergothioneine—A diet-derived antioxidant with therapeutic potential. *FEBS Lett.* 2018, 592, 3357–3366. [CrossRef]
37. Tang, R.M.Y.; Cheah, I.K.-M.; Yew, T.S.K.; Halliwell, B. Distribution and accumulation of dietary ergothioneine and its metabolites in mouse tissues. *Sci. Rep.* 2018, 8, 1601. [CrossRef] [PubMed]

38. Kerley, R.N.; McCarthy, C.; Kell, D.B.; Kenny, L.C. The potential therapeutic effects of ergothioneine in pre-eclampsia. *Free. Radic. Biol. Med.* **2018**, *117*, 145–157. [CrossRef] [PubMed]

39. Williamson, R.D.; McCarthy, F.P.; Manna, S.; Groarke, E.; Kell, D.B.; Kenny, L.C.; McCarthy, C.M. L-(+)-Ergothioneine Significantly Improves the Clinical Characteristics of Preeclampsia in the Reduced Uterine Perfusion Pressure Rat Model. *Hypertension* **2020**, *75*, 561–568. [CrossRef]

40. Song, T.-Y.; Lin, H.-C.; Chen, C.-L.; Wu, J.-H.; Liao, J.-W.; Hu, M.-L. Ergothioneine and melatonin attenuate oxidative stress and protect against learning and memory deficits in C57BL/6J mice treated with D-galactose. *Free. Radic. Res.* **2014**, *48*, 1049–1060. [CrossRef]

41. Song, T.-Y.; Chen, C.-L.; Liao, J.-W.; Ou, H.-C.; Tsai, M. Ergothioneine protects against neuronal injury induced by cisplatin both in vitro and in vivo. *Food Chem. Toxicol.* **2010**, *48*, 3492–3499. [CrossRef]

42. Moncaster, J.; Walsh, D.T.; Gentleman, S.M.; Jen, L.-S.; Aruoma, O.I. Ergothioneine treatment protects neurons against N-methyl-D-aspartate excitotoxicity in an in vivo rat retinal model. *Neurosci. Lett.* **2002**, *328*, 55–59. [CrossRef]

43. Yang, N.-C.; Lin, H.-C.; Wu, J.-H.; Ou, H.-C.; Chai, Y.-C.; Tseng, C.-Y.; Liao, J.-W.; Song, T.-Y. Ergothioneine protects against neuronal injury induced by β-amyloid in mice. *Food Chem. Toxicol.* **2012**, *50*, 3902–3911. [CrossRef]

44. Smith, E.; Ottosson, F.; Hellstrand, S.; Ericson, U.; Orho-Melander, M.; Fernandez, C.; Melander, O. Ergothioneine is associated with reduced mortality and decreased risk of cardiovascular disease. *Heart* **2019**, *106*, 691–697. [CrossRef] [PubMed]

45. Servillo, L.; D'Onofrio, N.; Balestrieri, M.L. Ergothioneine Antioxidant Function: From Chemistry to Cardiovascular Therapeutic Potential. *J. Cardiovasc. Pharmacol.* **2017**, *69*, 183–191. [CrossRef]

46. Gökçe, G.; Arun, M.Z.; Ertuna, E. Ergothioneine prevents endothelial dysfunction induced by mercury chloride. *Exp. Ther. Med.* **2018**, *15*, 4697–4702. [CrossRef]

47. Koh, S.S.; Ooi, S.C.-Y.; Lui, N.M.-Y.; Qiong, C.; Ho, L.T.-Y.; Cheah, I.K.-M.; Halliwell, B.; Herr, D.R.; Ong, W.-Y. Effect of Ergothioneine on 7-Ketocholesterol-Induced Endothelial Injury. *Neuromol. Med.* **2021**, *23*, 184–198. [CrossRef] [PubMed]

48. D'Onofrio, N.; Servillo, L.; Giovane, A.; Casale, R.; Vitiello, M.; Marfella, R.; Paolisso, G.; Balestrieri, M.L. Ergothioneine oxidation in the protection against high-glucose induced endothelial senescence: Involvement of SIRT1 and SIRT6. *Free. Radic. Biol. Med.* **2016**, *96*, 211–222. [CrossRef] [PubMed]

49. Wasser, S. Medicinal mushroom science: Current perspectives, advances, evidences, and challenges. *Biomed. J.* **2014**, *37*, 345–356. [CrossRef] [PubMed]

50. Rossi, P.; Cesaroni, V.; Brandalise, F.; Occhinegro, A.; Ratto, D.; Perrucci, F.; Lanaia, V.; Girometta, C.; Orru, G.; Savino, E. Dietary Supplementation of Lion's Mane Medicinal Mushroom, *Hericium erinaceus* (Agaricomycetes), and Spatial Memory in Wild-Type Mice. *Int. J. Med. Mushrooms* **2018**, *20*, 485–494. [CrossRef]

51. Brandalise, F.; Cesaroni, V.; Gregori, A.; Repetti, M.; Romano, C.; Orrù, G.; Botta, L.; Girometta, C.; Guglielminetti, M.L.; Savino, E.; et al. Dietary Supplementation ofHericium erinaceusIncreases Mossy Fiber-CA3 Hippocampal Neurotransmission and Recognition Memory in Wild-Type Mice. *Evid.-Based Complement. Altern. Med.* **2017**, *2017*, 3864340. [CrossRef] [PubMed]

52. Corana, F.; Cesaroni, V.; Mannucci, B.; Baiguera, R.M.; Picco, A.M.; Savino, E.; Ratto, D.; Perini, C.; Kawagishi, H.; Girometta, C.E.; et al. Array of Metabolites in Italian Hericium erinaceus Mycelium, Primordium, and Sporophore. *Molecules* **2019**, *24*, 3511. [CrossRef]

53. Chen, S.-Y.; Ho, K.-J.; Hsieh, Y.-J.; Wang, L.-T.; Mau, J.-L. Contents of lovastatin, γ-aminobutyric acid and ergothioneine in mushroom fruiting bodies and mycelia. *LWT Food Sci. Technol.* **2012**, *47*, 274–278. [CrossRef]

54. Lee, W.Y.; Park, E.-J.; Ahn, J.K.; Ka, K.-H. Ergothioneine Contents in Fruiting Bodies and Their Enhancement in Mycelial Cultures by the Addition of Methionine. *Mycobiology* **2009**, *37*, 43–47. [CrossRef]

55. Kalaras, M.D.; Richie, J.P.; Calcagnotto, A.; Beelman, R.B. Mushrooms: A rich source of the antioxidants ergothioneine and glutathione. *Food Chem.* **2017**, *233*, 429–433. [CrossRef] [PubMed]

56. Raz, N.; Torres, I.J.; Spencer, W.D.; White, K.; Acker, J.D. Age-Related Regional Differences in Cerebellar Vermis Observed In Vivo. *Arch. Neurol.* **1992**, *49*, 412–416. [CrossRef]

57. Raz, N.; Dupuis, J.H.; Briggs, S.D.; McGavran, C.; Acker, J.D. Differential Effects of Age and Sex on the Cerebellar Hemi-spheres and the Vermis: A Prospective MR Study. *AJNR Am. J. Neuroradiol.* **1998**, *19*, 65–71. [PubMed]

58. Miller, T.D.; Ferguson, K.J.; Reid, L.M.; Wardlaw, J.M.; Starr, J.M.; Seckl, J.R.; Deary, I.J.; MacLullich, A.M.J. Cerebellar Vermis Size and Cognitive Ability in Community-Dwelling Elderly Men. *Cerebellum* **2012**, *12*, 68–73. [CrossRef]

59. Paul, R.; Grieve, S.M.; Chaudary, B.; Gordon, N.; Lawrence, J.; Cooper, N.; Clark, C.R.; Kukla, M.; Mulligan, R.; Gordon, E. Relative contributions of the cerebellar vermis and prefrontal lobe volumes on cognitive function across the adult lifespan. *Neurobiol. Aging* **2009**, *30*, 457–465. [CrossRef]

60. Chiang, C.-S.; Stalder, A.; Samimi, A.; Campbell, I.L. Reactive Gliosis as a Consequence of Interleukin-6 Expression in the Brain: Studies in Transgenic Mice. *Dev. Neurosci.* **1994**, *16*, 212–221. [CrossRef]

61. Rothaug, M.; Becker-Pauly, C.; Rose-John, S. The role of interleukin-6 signaling in nervous tissue. *Biochim. Biophys. Acta (BBA) Bioenerg.* **2016**, *1863*, 1218–1227. [CrossRef]

62. Imtiyaz, H.Z.; Simon, M.C. Hypoxia-Inducible Factors as Essential Regulators of Inflammation. *Curr. Top. Microbiol. Immunol.* **2010**, *345*, 105–120. [CrossRef]

63. Yeo, E.-J. Hypoxia and aging. *Exp. Mol. Med.* **2019**, *51*, 1–15. [CrossRef]

64. Alique, M.; Sánchez-López, E.; Bodega, G.; Giannarelli, C.; Carracedo, J.; Ramírez, R. Hypoxia-Inducible Factor-1α: The Master Regulator of Endothelial Cell Senescence in Vascular Aging. *Cells* 2020, 9, 195. [CrossRef]
65. Gehmeyr, J.; Maghnouj, A.; Tjaden, J.; Vorgerd, M.; Hahn, S.; Matschke, V.; Theis, V.; Theiss, C. Disabling VEGF-Response of Purkinje Cells by Downregulation of *KDR* via miRNA-204-5p. *Int. J. Mol. Sci.* 2021, 22, 2173. [CrossRef]
66. Castelli, V.; Benedetti, E.; Antonosante, A.; Catanesi, M.; Pitari, G.; Ippoliti, R.; Cimini, A.; D'Angelo, M. Neuronal Cells Rearrangement During Aging and Neurodegenerative Disease: Metabolism, Oxidative Stress and Organelles Dynamic. *Front. Mol. Neurosci.* 2019, 12, 132. [CrossRef] [PubMed]
67. Bernard, J.A.; Seidler, R. Moving forward: Age effects on the cerebellum underlie cognitive and motor declines. *Neurosci. Biobehav. Rev.* 2014, 42, 193–207. [CrossRef] [PubMed]
68. MacLullich, A.M.; Edmond, C.L.; Ferguson, K.J.; Wardlaw, J.M.; Starr, J.M.; Seckl, J.R.; Deary, I.J. Size of the neocerebellar vermis is associated with cognition in healthy elderly men. *Brain Cogn.* 2004, 56, 344–348. [CrossRef] [PubMed]
69. Hulst, T.; van der Geest, J.N.; Thürling, M.; Goericke, S.; Frens, M.A.; Timmann, D.; Donchin, O. Ageing shows a pattern of cerebellar degeneration analogous, but not equal, to that in patients suffering from cerebellar degenerative disease. *NeuroImage* 2015, 116, 196–206. [CrossRef] [PubMed]
70. Dimitrova, A.; Gerwig, M.; Brol, B.; Gizewski, E.R.; Forsting, M.; Beck, A.; Aurich, V.; Kolb, F.P.; Timmann, D. Correlation of cerebellar volume with eyeblink conditioning in healthy subjects and in patients with cerebellar cortical degeneration. *Brain Res.* 2008, 1198, 73–84. [CrossRef]
71. Rogers, J.; Zornetzer, S.F.; Bloom, F.E.; Mervis, R.E. Senescent microstructural changes in rat cerebellum. *Brain Res.* 1984, 292, 23–32. [CrossRef]
72. Yu, T.; Korgaonkar, M.S.; Grieve, S.M. Gray Matter Atrophy in the Cerebellum—Evidence of Increased Vulnerability of the Crus and Vermis with Advancing Age. *Cerebellum* 2016, 16, 388–397. [CrossRef] [PubMed]
73. Raz, N. Aging of the Brain and Its Impact on Cognitive Performance: Integration of Structural and Functional Findings. In *The Handbook of Aging and Cognition*; Craik, F.I.M., Salthouse, T.A., Eds.; Lawrence Erlbaum Associates: Mahwah, NJ, USA, 2000; pp. 1–90.
74. Murshed, K.A.; Ziylan, T.; Seker, M.; Cicekcibasi, A.E.; Acikgozoglu, S. Morphometric Assessment of Brain Stem and Cere-bellar Vermis with Midsagittal MRI: The Gender Differences and Effects of Age. *Neuroanatomy* 2003, 2, 35–38.
75. Taman, F.D.; Kervancioglu, P.; Kervancioglu, A.S.; Turhan, B. The importance of volume and area fractions of cerebellar volume and vermian subregion areas: A stereological study on MR images. *Childs Nerv. Syst.* 2019, 36, 165–171. [CrossRef] [PubMed]
76. Aniszewska, A.; Chłodzińska, N.; Bartkowska, K.; Winnicka, M.; Turlejski, K.; Djavadian, R. The expression of interleukin-6 and its receptor in various brain regions and their roles in exploratory behavior and stress responses. *J. Neuroimmunol.* 2015, 284, 1–9. [CrossRef] [PubMed]
77. Belozor, O.S.; Yakovleva, D.A.; Potapenko, I.V.; Shuvaev, A.N.; Smolnikova, M.V.; Vasilev, A.; Pozhilenkova, E.A. Extracellular S100β Disrupts Bergman Glia Morphology and Synaptic Transmission in Cerebellar Purkinje Cells. *Brain Sci.* 2019, 9, 80. [CrossRef] [PubMed]
78. Verkhratsky, A.; Zorec, R.; Rodríguez-Arellano, J.J.; Parpura, V. Neuroglia in Ageing. *Adv. Exp. Med. Biol.* 2019, 1175, 181–197. [CrossRef]
79. Di Benedetto, S.; Müller, L. Aging, Immunity, and Neuroinflammation: The Modulatory Potential of Nutrition. *Nutr. Immun.* 2019, 301–322. [CrossRef]
80. Cragnolini, A.B.; Montenegro, G.; Friedman, W.J.; Mascó, D.H. Brain-region specific responses of astrocytes to an in vitro injury and neurotrophins. *Mol. Cell. Neurosci.* 2018, 88, 240–248. [CrossRef]
81. Matias, I.; Morgado, J.; Gomes, F.C.A. Astrocyte Heterogeneity: Impact to Brain Aging and Disease. *Front. Aging Neurosci.* 2019, 11, 59. [CrossRef]
82. Trovato, A.; Siracusa, R.; Di Paola, R.; Scuto, M.; Fronte, V.; Koverech, G.; Luca, M.; Serra, A.; Toscano, M.; Petralia, A.; et al. Redox modulation of cellular stress response and lipoxin A4 expression by Coriolus versicolor in rat brain: Relevance to Alzheimer's disease pathogenesis. *Neurotoxicology* 2016, 53, 350–358. [CrossRef] [PubMed]
83. Trovato, A.; Siracusa, R.; Di Paola, R.; Scuto, M.; Ontario, M.L.; Bua, O.; Di Mauro, P.; Toscano, M.A.; Petralia, C.C.T.; Maiolino, L.; et al. Redox modulation of cellular stress response and lipoxin A4 expression by Hericium Erinaceus in rat brain: Relevance to Alzheimer's disease pathogenesis. *Immun. Ageing* 2016, 13, 23. [CrossRef] [PubMed]
84. Zhang, W.; Huang, Q.; Zeng, Z.; Wu, J.; Zhang, Y.; Chen, Z. Sirt1 Inhibits Oxidative Stress in Vascular Endothelial Cells. *Oxidative Med. Cell. Longev.* 2017, 2017, 7543973. [CrossRef]
85. Choi, Y.J.; Kim, H.S.; Lee, J.; Chung, J.; Lee, J.S.; Choi, J.S.; Yoon, T.R.; Kim, H.K.; Chung, H.Y. Down-regulation of oxidative stress and COX-2 and iNOS expressions by dimethyl lithospermate in aged rat kidney. *Arch. Pharmacal Res.* 2014, 37, 1032–1038. [CrossRef] [PubMed]
86. Frenkel-Denkberg, G.; Gershon, D.; Levy, A.P. The function of hypoxia-inducible factor 1 (HIF-1) is impaired in senescent mice. *FEBS Lett.* 1999, 462, 341–344. [CrossRef]
87. Leiser, S.F.; Kaeberlein, M. The hypoxia-inducible factor HIF-1 functions as both a positive and negative modulator of aging. *Biol. Chem.* 2010, 391, 1131–1137. [CrossRef] [PubMed]
88. Cvetanovic, M.; Patel, J.M.; Marti, H.; Kini, A.R.; Opal, P. Vascular endothelial growth factor ameliorates the ataxic phenotype in a mouse model of spinocerebellar ataxia type 1. *Nat. Med.* 2011, 17, 1445–1447. [CrossRef]

89. Mahoney, E.R.; Dumitrescu, L.; Moore, A.M.; Cambronero, F.E.; De Jager, P.L.; Koran, M.E.I.; Petyuk, V.A.; Robinson, R.A.S.; Goyal, S.; Schneider, J.A.; et al. Brain expression of the vascular endothelial growth factor gene family in cognitive aging and alzheimer's disease. *Mol. Psychiatry* **2021**, *26*, 888–896. [CrossRef]

90. Lee, S.-H.; Lee, J.-H.; Lee, H.-Y.; Min, A.K.-J. Sirtuin signaling in cellular senescence and aging. *BMB Rep.* **2019**, *52*, 24–34. [CrossRef]

91. Xu, C.; Wang, L.; Fozouni, P.; Evjen, G.; Chandra, V.; Jiang, J.; Lu, C.; Nicastri, M.; Bretz, C.; Winkler, J.D.; et al. SIRT1 is downregulated by autophagy in senescence and ageing. *Nat. Cell Biol.* **2020**, *22*, 1170–1179. [CrossRef]

92. Chen, C.; Zhou, M.; Ge, Y.; Wang, X. SIRT1 and aging related signaling pathways. *Mech. Ageing Dev.* **2020**, *187*, 111215. [CrossRef]

93. Satoh, A.; Brace, C.S.; Rensing, N.; Cliften, P.; Wozniak, D.F.; Herzog, E.; Yamada, K.A.; Imai, S.-I. Sirt1 Extends Life Span and Delays Aging in Mice through the Regulation of Nk2 Homeobox 1 in the DMH and LH. *Cell Metab.* **2013**, *18*, 416–430. [CrossRef]

94. Li, I.-C.; Lee, L.-Y.; Tzeng, T.-T.; Chen, W.-P.; Chen, Y.-P.; Shiao, Y.-J.; Chen, C.-C. Neurohealth Properties of *Hericium erinaceus* Mycelia Enriched with Erinacines. *Behav. Neurol.* **2018**, *2018*, 5802634. [CrossRef] [PubMed]

95. Li, I.-C.; Chang, H.-H.; Lin, C.-H.; Chen, W.-P.; Lu, T.-H.; Lee, L.-Y.; Chen, Y-W.; Chen, Y-P.; Chen, C.-C.; Lin, D.P.-C. Prevention of Early Alzheimer's Disease by Erinacine A-Enriched Hericium erinaceus Mycelia Pilot Double-Blind Placebo-Controlled Study. *Front. Aging Neurosci.* **2020**, *12*, 155. [CrossRef]

96. Ryu, S.; Kim, H.G.; Kim, J.Y.; Kim, S.Y.; Cho, K.-O. Hericium erinaceus Extract Reduces Anxiety and Depressive Behaviors by Promoting Hippocampal Neurogenesis in the Adult Mouse Brain. *J. Med. Food* **2018**, *21*, 174–180. [CrossRef] [PubMed]

97. Cesaroni, V.; Brusoni, M.; Cusaro, C.M.; Girometta, C.; Perini, C.; Picco, A.M.; Rossi, P.; Salerni, E.; Savino, E. Phylogenetic Comparison between Italian and Worldwide Hericium Species (Agaricomycetes). *Int. J. Med. Mushrooms* **2019**, *21*, 943–954. [CrossRef] [PubMed]

98. Bao, H.N.D.; Ushio, H.; Ohshima, T. Antioxidative Activity and Antidiscoloration Efficacy of Ergothioneine in Mushroom (Flammulina velutipes) Extract Added to Beef and Fish Meats. *J. Agric. Food Chem.* **2008**, *56*, 10032–10040. [CrossRef] [PubMed]

99. Lee, D.G.; Kang, H.-W.; Park, C.-G.; Ahn, Y.-S.; Shin, Y. Isolation and identification of phytochemicals and biological activities of Hericium ernaceus and their contents in Hericium strains using HPLC/UV analysis. *J. Ethnopharmacol.* **2016**, *184*, 219–225. [CrossRef]

100. Gregori, B.G.A.; Gerbec, E.T.B. Solid State Cultivation of Hericium erinaceus Biomass and Erinacine: A Production. *J. Bioprocess. Biotech.* **2015**, *5*, 1–5. [CrossRef]

101. D'Angelo, E.U.; Rossi, P.; Taglietti, V. Voltage-dependent Kinetics of N-Methyl-d-aspartate Synaptic Currents in Rat Cerebellar Granule Cells. *Eur. J. Neurosci.* **1994**, *6*, 640–645. [CrossRef]

102. Gyengesi, E.; Rangel, A.; Ullah, F.; Liang, H.; Niedermayer, G.; Asgarov, R.; Venigalla, M.; Gunawardena, D.; Karl, T.; Münch, G. Chronic Microglial Activation in the GFAP-IL6 Mouse Contributes to Age-Dependent Cerebellar Volume Loss and Impairment in Motor Function. *Front. Neurosci.* **2019**, *13*, 303. [CrossRef] [PubMed]

103. Avwioro, G. Histochemical Uses of Haematoxylin-A Review. *JPCS* **2011**, *1*, 24–34.

104. Kádár, A.; Wittmann, G.; Liposits, Z.; Fekete, C. Improved method for combination of immunocytochemistry and Nissl staining. *J. Neurosci. Methods* **2009**, *184*, 115–118. [CrossRef] [PubMed]

105. Roda, E.; Barni, S.; Milzani, A.; Dalle-Donne, I.; Colombo, G.; Coccini, T. Single Silver Nanoparticle Instillation Induced Early and Persisting Moderate Cortical Damage in Rat Kidneys. *Int. J. Mol. Sci.* **2017**, *18*, 2115. [CrossRef]

106. Junqueira, L.C.U.; Bignolas, G.; Brentani, R.R. Picrosirius staining plus polarization microscopy, a specific method for collagen detection in tissue sections. *J. Mol. Histol.* **1979**, *11*, 447–455. [CrossRef]

107. Lattouf, R.; Younes, R.; Lutomski, D.; Naaman, N.; Godeau, G.; Senni, K.; Changotade, S. Picrosirius Red Staining. *J. Histochem. Cytochem.* **2014**, *62*, 751–758. [CrossRef] [PubMed]

108. O'Callaghan, J.P. Neurotypic and gliotypic proteins as biochemical markers of neurotoxicity. *Neurotoxicol. Teratol.* **1988**, *10*, 445–452. [CrossRef]

109. Tykhomyrov, A.A.; Pavlova, A.S.; Nedzvetsky, V.S. Glial Fibrillary Acidic Protein (GFAP): On the 45th Anniversary of Its Discovery. *Neurophysiology* **2016**, *48*, 54–71. [CrossRef]

110. Tanaka, T.; Narazaki, M.; Kishimoto, T. IL-6 in Inflammation, Immunity, and Disease. *Cold Spring Harb. Perspect. Biol.* **2014**, *6*, a016295. [CrossRef] [PubMed]

111. Di Stefano, A.; Coccini, T.; Roda, E.; Signorini, C.; Balbi, B.; Brunetti, G.; Ceriana, P. Blood MCP-1 levels are increased in chronic obstructive pulmonary disease patients with prevalent emphysema. *Int. J. Chronic Obstr. Pulm. Dis.* **2018**, *13*, 1691–1700. [CrossRef]

112. Hua, X.; Chi, W.; Su, L.; Li, J.; Zhang, Z.; Yuan, X. ROS-induced Oxidative Injury involved in Pathogenesis of Fungal Keratitis via p38 MAPK Activation. *Sci. Rep.* **2017**, *7*, 10421. [CrossRef] [PubMed]

113. Kobylarek, D.; Iwanowski, P.; Lewandowska, Z.; Limphaibool, N.; Szafranek, S.; Labrzycka, A.; Kozubski, W. Advances in the Potential Biomarkers of Epilepsy. *Front. Neurol.* **2019**, *10*, 685. [CrossRef] [PubMed]

114. Abramson, S.B. Nitric oxide in inflammation and pain associated with osteoarthritis. *Arthritis Res. Ther.* **2008**, *10*, S2. [CrossRef] [PubMed]

115. Kasapoglu, M.; Özben, T. Alterations of antioxidant enzymes and oxidative stress markers in aging. *Exp. Gerontol.* **2001**, *36*, 209–220. [CrossRef]
116. Rodgers, J.T.; Lerin, C.; Gerhart-Hines, Z.; Puigserver, P. Metabolic adaptations through the PGC-1α and SIRT1 pathways. *FEBS Lett.* **2007**, *582*, 46–53. [CrossRef]

*molecules*

MDPI

*Article*

# Array of Metabolites in Italian *Hericium erinaceus* Mycelium, Primordium, and Sporophore

Federica Corana [1], Valentina Cesaroni [2], Barbara Mannucci [1], Rebecca Michela Baiguera [2], Anna Maria Picco [2], Elena Savino [2], Daniela Ratto [3], Claudia Perini [4], Hirokazu Kawagishi [5], Carolina Elena Girometta [2,*] and Paola Rossi [3]

[1] Centro Grandi Strumenti, University of Pavia, 27100 Pavia, Italy; federica.corana@unipv.it (F.C.); barbara.mannucci@unipv.it (B.M.)
[2] Department of Earth and Environmental Sciences, University of Pavia, 27100 Pavia, Italy; valentina.cesaroni01@universitadipavia.it (V.C.); rebeccamichela.baiguera01@universitadipavia.it (R.M.B.); annamaria.picco@unipv.it (A.M.P.); elena.savino@unipv.it (E.S.)
[3] Department of Biology and Biotechnology "L. Spallanzani", University of Pavia, 27100 Pavia, Italy; daniela.ratto@gmail.com (D.R.); paola.rossi@unipv.it (P.R.)
[4] Department of Life Sciences, University of Siena, 53100 Siena, Italy; claudia.perini@unisi.it
[5] Research Institute of Green Science and Technology, Shizuoka University, Shizuoka 422-8529, Japan; kawagishi.hirokazu@shizuoka.ac.jp
* Correspondence: carolinaelena.girometta@unipv.it; Tel.: +39-0382-984869

check for updates

**Abstract:** *Hericium erinaceus* is a medicinal mushroom that contains many molecules promising a plethora of therapeutic properties. In this study, the strain H.e.2 (MicUNIPV, University of Pavia, Italy) was isolated from a sporophore collected in Tuscany (Italy). Mycelium, primordium, and wild type and cultivated sporophores were analyzed by HPLC-UV-ESI/MS. Erinacine A in the mycelium and hericenones C and D in the sporophores were quantified by comparison with their standard molecules. For the first time, *H. erinaceus* primordium was also investigated for the presence of these molecules. Comparing with the literature data, hericenes, molecules structurally similar to hericenones, were present in all our samples. The highest contents of hericenones C and D were detected in cultivated sporophores, compared to the wild type. The comparison of these data with those of another Italian *H. erinaceus* strain (H.e.1 MicUNIPV) was discussed. The results led us to select *H. erinaceus* strains more suitable for mycelium production or sporophore cultivation to obtain extracts with a higher content of bioactive compounds. This work provides a further step towards standardizing the procedures in the development of dietary supplements made from mushrooms.

**Keywords:** medicinal mushroom; *Hericium erinaceus*; bioactive compounds; mycelium; sporophore; primordium; erinacines; hericenones; hericenes

## 1. Introduction

*Hericium erinaceus* (Bull.) Pers. is a fungus belonging to Basidiomycota, Agaricomycetes, Russulales, and Hericiaceae [1]. Among all mushrooms, *H. erinaceus*, an edible and medicinal mushroom in traditional Chinese medicine, has been widely reported to have healthy effects on: the central nervous system [2,3]; different cancerous cell lines, such as HepG2 (hepatoma), MCF7 (breast cancer), HL-60 (human acute promyelocytic leukemia), and SGC-7901 (human gastric cancer cells) [4–6]; depression [7]; diabetes [8]; lipedema [9]. It also exhibited a reversion of frailty cognitive decline during aging [10]. Up to now, about 70 different secondary metabolites have been isolated from either sporophore or mycelium, or both. The investigation of chemical constituents promising for their

properties is constantly being updated in the search for the discovery of a new drug source [11]. Both the high-weight metabolites (e.g., polysaccharides) and low-weight metabolites (e.g., polyketides, phenols, and terpenoids) include bioactive molecules, although each substance category provides in turn an extremely various bouquet of molecules, where only a fraction shows evidence for bioactivity [12–15]. Hericenones are low-weight aromatic compounds first isolated by Kawagishi et al. (1990) [14] from the sporophore of *H. erinaceus*. Up to now, eight different compounds have been recognized as hericenones (A–H) [11,16]. Hericenones C, D, and E have stimulating activity on the synthesis of nerve growth factor (NGF) [17]. Hericenone F has been reported to be responsible for an anti-inflammatory effect by reducing nitrogen monoxide (NO) release [18]. Analyses of dried sporophores have detected different volatile compounds, some of them represented by hexadecanoic acid, linoleic acid, phenylacetaldehyde, and benzaldehyde. The erinacines in *H. erinaceus* are a group of cyathane-type diterpenoids, including 20 members of 24 diterpenoids described by Tang et al. [19]. To date, 15 erinacines (A, B, C, D, E, F, G, H, I, P, Q, J, K, R, S) isolated from *H. erinaceus* mycelium have been identified and eight out of 15 show neuroprotective properties, such as enhancing NGF release (erinacines A–I), reducing amyloid-β deposition, increasing insulin-degrading enzyme (IDE) expression (erinacines A and S), and managing neuropathic pain (erinacine E), while the others have different pharmacological activities [12,20–26].

At present, *H. erinaceus* is widely used as a dietary supplement. Nevertheless, the lack of standardization strongly affects the quality and effective bioactivity of the final product. As above described, only a few molecules have been reported to stimulate NGF release, namely erinacines A–I from mycelium (the most studied being erinacine A) and hericenones C–D from sporophore. To obtain this specific target on neuroprotection, the standardization process of dietary supplements therefore relies on the selective detection and quantification of such molecules. A major problem at this concern is the availability of pure analytical standards, due to the difficulty in the isolation and achievement of suitable amounts.

The aim of this study is to analyze and compare different stages of *H. erinaceus* (mycelium, primordium, and sporophore) sampled in Tuscany (Italy), in order to detect the presence and to quantify the concentration of the target bioactive metabolites erinacine A and hericenones C and D. The results could be useful for suggesting optimization strategies for future dietary supplements.

## 2. Results

### 2.1. H. erinaceus Samples for Chemical Analyses

The *H. erinaceus* wild type (WT) sporophore analyzed in the present study was collected on a living holm oak (*Quercus ilex* L.) in the hilly area around Siena (Italy) in 2018. The sporophore was identified based on the macro- and micromorphological characteristics of the species [27]. The main features are reported in Table 1.

**Table 1.** Characteristics of *Hericium erinaceus* wild type sporophore.

|  | *H. erinaceus* |
|---|---|
| fresh weight (g) | 620 |
| dried weight (g) | 153 |
| diameter (cm) | about 20 |
| remarks on the sporophore | the collected specimen was mature, without any alteration by atmospheric or animal agents |

The strain obtained from the WT was confirmed to belong to *H. erinaceus* [28] and is maintained in the Fungal Research Culture Collection of Pavia University (MicUNIPV) as H.e.2.

The cultivation of *H. erinaceus* at the Botanical Garden of the University of Pavia (Italy) led to the collection of 44 sporophores, total weight 1344.2 g. The diameter of the collected samples was 6–15 cm.

The primordium can be considered the transition stage before sporophore. It is formed by dense mycelial cords developing with negative geotropism (Figure 1). Primordia were harvested after 60 days, at the maximum of their development, and the fresh material was analyzed.



**Figure 1.** Different stages of growth of the primordium. 30 (**A**), 45 (**B**), 60 (**C**) days of growth and fresh collected material (**D**).

### 2.2. Chemical Analyses

We processed 1 g of lyophilized mycelium, dried WT and cultivated sporophores, and fresh primordium for chemical analyses.

In order to identify and analyze the bioactive metabolites present in our samples, we compared them with the standard molecules of erinacine A and hericenones C and D by HPLC-UV-ESI/MS. The molecular formula, chemical structures, and molecular weight of these molecules are reported in Table 2 [29].

**Table 2.** Molecular formula, chemical structures, and molecular weights of erinacine A and hericenones C and D.
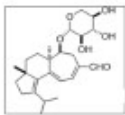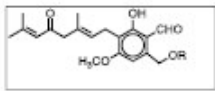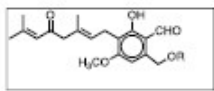
| | Erinacine A | Hericenone C | Hericenone D |
|---|---|---|---|
| molecular formula | $C_{25}H_{36}O_6$ | $C_{35}H_{54}O_6$ | $C_{37}H_{58}O_6$ |
| molecular weight (MW) (g/mol) | 432 | 570 | 598 |
| chemical structure | | R = palmitoyl | R = stearoyl |

Figure 2 shows the mass spectrum (MS) chromatographic traces of H.e.2 mycelium and the standard molecule of erinacine A. The standard erinacine A was detected using HPLC-UV-ESI/MS at the retention time (RT) of 10.44 min. By comparing the RT and molecular ion or mass spectra, the presence of this molecule in the H.e.2 mycelium was detected too. Besides, the chromatographic trace of H.e.2 mycelium also showed a peak at RT 12.58 min that belongs to a molecule not yet identified with a MW of 430 Da.

**Figure 2.** Mass spectrum (MS) traces of mycelium (top) and erinacine A molecule standard (bottom).

Figure 3 shows the UV chromatographic traces of H.e.2 mycelium and the standard molecules of hericenones C and D. In mycelium, hericenones C and D were not present. Moreover, the peaks at RT 46.46 min, 47.41 min, 47.63 min, and 48.83 min were supposed to be, respectively, hericene D, hericene A, hericene B, and hericene C, based on the data reported by Arnone et al. (1994) and Kobayashi et al. (2018) [30,31]. The molecular formula, chemical structures, and molecular weights of the hericenes are reported in Table 3 [29].



**Figure 3.** UV traces of mycelium (top) and the standard molecules of hericenones C and D (bottom).

**Table 3.** Molecular formula, chemical structures, and molecular weights of hericenes.

| | Hericene A | Hericene B | Hericene C | Hericene D |
|---|---|---|---|---|
| molecular formula | $C_{35}H_{56}O_5$ | $C_{37}H_{58}O_5$ | $C_{37}H_{60}O_5$ | $C_{37}H_{56}O_5$ |
| molecular weight (MW) (g/mol) | 556 | 582 | 584 | 580 |
| chemical structure | | |  | |
| | R = palmitoyl | R = oleoyl | R = stearoyl | R = lineoyl |

Our hypothesis was also confirmed by ion fragments in MS/MS spectra. Figure 4 reports the MS/MS-ESI spectra of hericenes: from top to bottom, hericenes D, A, B, and C are shown. The ion *m/z* 301 was present in all the spectra and derives from the loss of the side chain R. Spectra of hericenes D and B also show ions derived from fragmentation close to double bonds of R.
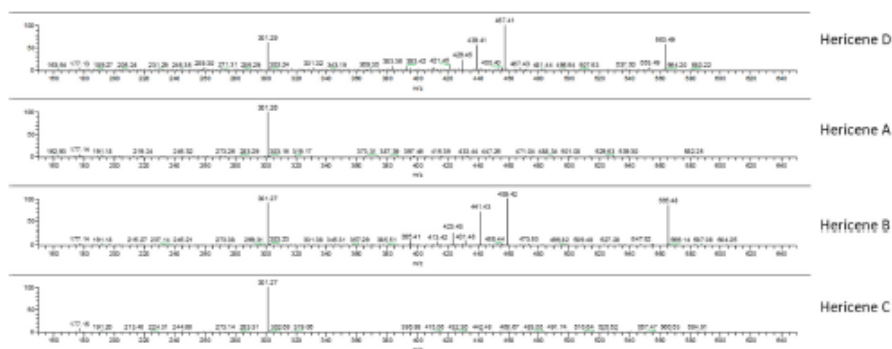


**Figure 4.** MS/MS-ESI spectra of hericenes D, A, B, and C (from top to bottom).

WT and cultivated sporophores were analyzed. The data were compared with the standard molecules hericenones C and D.

Figure 5 shows the UV chromatographic traces of the WT sporophore collected in Italy, the cultivated and the two standard molecules of hericenones: C detected at RT of 43.98 min and D detected at RT of 45.83 min. Hericenone C was detected in the WT at RT of 43.92 min and at RT of 43.94 in the cultivated sporophore. Hericenone D was detected at RT of 45.74 min in both samples. There were also other peaks close to these hericenones that could be attributed to hericenone E (RT of 42.72 min), hericenone I (RT of 44.18 min), and hericenone H (RT of 47.37 min) on the basis both of previous publications [16] and the similarity of their fragmentation pattern to that of hericenones C and D standard. In the same chromatogram (Figure 5), there were peaks that could be attributed to hericenes: from lower to higher RT hericene D (RT 46.28 min), hericene A (RT 47.37 or 47.38 min), hericene B (RT 47.52 or 47.53 min), and hericene C (RT 48.83 min).
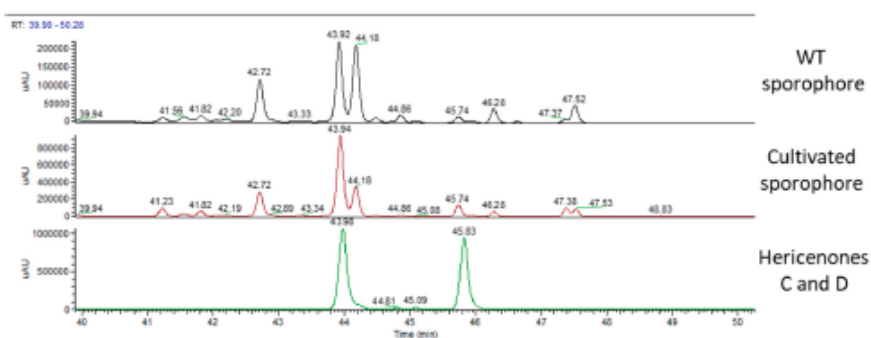


**Figure 5.** UV traces of wild type sporophore (top), cultivated sporophore (middle), and hericenones C (RT 43.98 min) and D (RT 45.83 min) standards (bottom).

Figure 6 displays MS chromatographic traces of the two sporophores and the standard molecule of erinacine A. The erinacine A molecule was not present in both sporophores. Besides, the

chromatographic traces also showed other peaks at RT of 11.29 and 12.52 min for the WT sporophores and at 11.44 and 12.50 min for the cultivated sporophores that belong to molecules not yet identified.
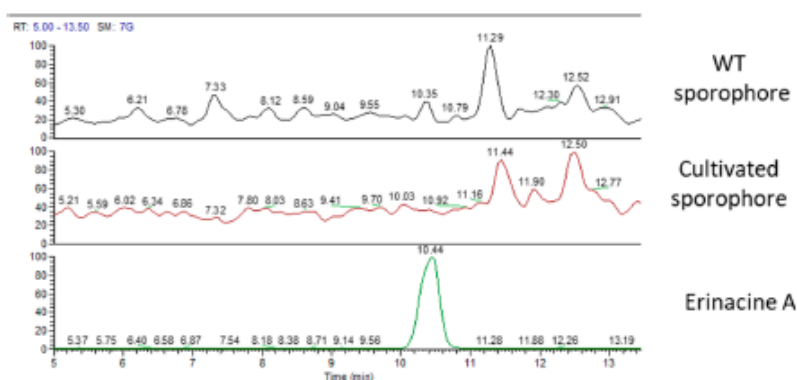


**Figure 6.** MS traces of wild type sporophore (top), cultivated sporophore (middle), and erinacine A standard molecules (bottom).

Chemical analyses of primordium showed neither erinacines (Figure 7) nor hericenones (Figure 8). MS trace of primordium (Figure 7) also showed a peak at RT of 11.37 min that has not yet been determined. Instead, the UV trace of primordium showed peaks at the same RT described for hericenes D, A, B, and C (Figure 8), as mentioned for the mycelium, and the WT and cultivated sporophores.



**Figure 7.** MS (mass spectrum) traces of primordium (top) and erinacine A molecule standard (bottom).

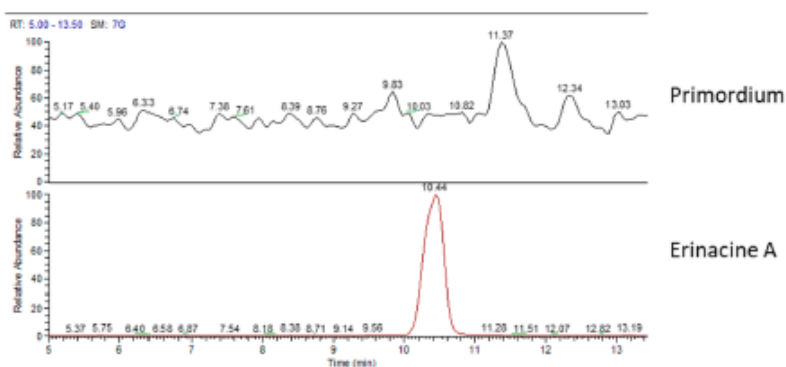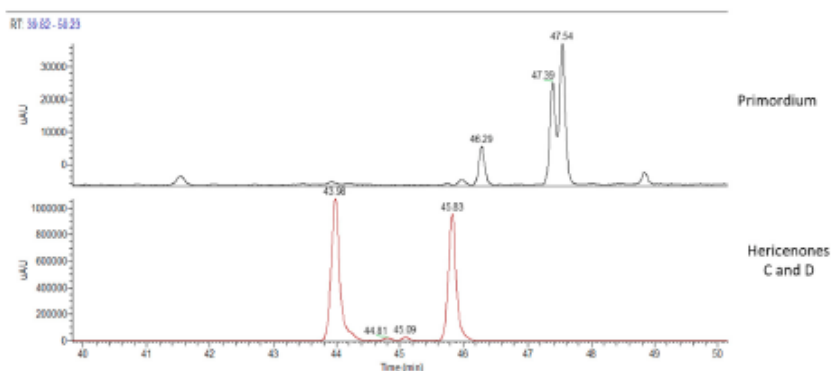**Figure 8.** UV traces of primordium (top) and hericenones C and D standards (bottom).

Table 4 summarizes the array of metabolites present in different stages of *H. erinaceus*.

**Table 4.** Presence of different molecules (erinacine A, hericenones C and D, and hericenes) in the lyophilized mycelium, fresh primordium, and dried sporophores.

|  | erinacine A | hericenone C | hericenone D | hericenes |
|---|---|---|---|---|
| mycelium | ✓ | - | - | ✓ |
| primordium | - | - | - | ✓ |
| WT sporophore | - | ✓ | ✓ | ✓ |
| cultivated sporophore | - | ✓ | ✓ | ✓ |

The content of erinacine A in H.e.2 mycelium and of hericenone C and D in sporophores were measured by the calibration curves [10] (Table 5).

**Table 5.** Content of erinacine A and hericenones C and D in H.e.2 lyophilized mycelium, fresh primordium and dried sporophores.

|  | Erinacine A (µg/g) | Hericenone C (µg/g) | Hericenone D (µg/g) |
|---|---|---|---|
| mycelium | 105 | - | - |
| primordium | - | - | - |
| WT sporophore | - | 760 | 100 |
| cultivated sporophore | - | 1560 | 188 |

Figure 9 summarizes the UV chromatographic traces of different samples where it is possible to identify peaks that are attributed to hericenes. From lower to higher RT, hericene D (RT at 46.47 or 42.29 or 46.28), hericene A (RT at 47.41 or 47.39 or 47.37 or 47.38), hericene B (RT at 47.63 or 47.54 or 47.52 or 47.53), and hericene C (RT at 48.83 or 48.84) were identified. As previously reported, hericenes were present in all the samples in different amounts.
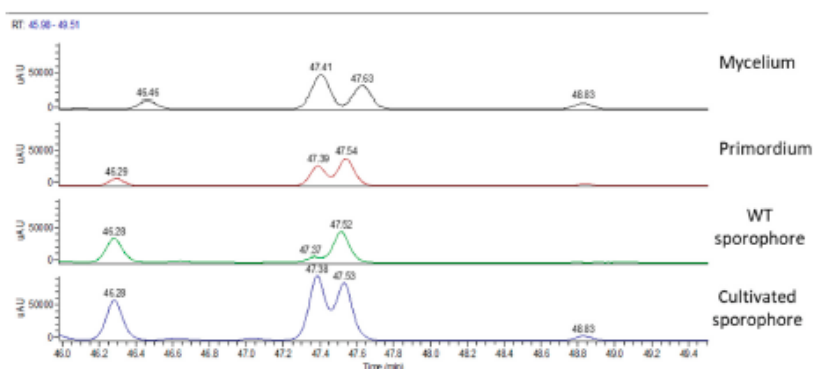
**Figure 9.** UV chromatographic traces of hericenes in (from top to bottom) mycelium, primordium, and wild type and cultivated sporophores.

Table 6 reports peak area values of hericenes A, B, C, and D in different samples.

**Table 6.** Content of hericenes in mycelium, primordium, and wild type (WT) and cultivated sporophores.

| | Total Area $10^3$ | Hericene A Area $10^3$ | Hericene B Area $10^3$ | Hericene C Area $10^3$ | Hericene D Area $10^3$ |
|---|---|---|---|---|---|
| mycelium | 684 | 327 | 232 | 51 | 74 |
| primordium | 557 | 201 | 262 | 21 | 73 |
| WT sporophore | 627 | 70 | 305 | / | 252 |
| cultivated sporophore | 1685 | 645 | 588 | 42 | 410 |

## 3. Discussion

At present, medicinal mushrooms such as *H. erinaceus* are exploited as dietary foods or supplements, producing beneficial effects by daily use in a balanced and varied diet. There are different products available on the market, increasing in number year by year. Despite this, there are still unresolved issues, including standardization and safety for the production of fungal supplement. Standardization is still in its early stage because of the lack of protocols and international guidelines [32].

This study is placed within an interdisciplinary research project to draw up the steps for the production of high quality dietary supplements to improve cognitive functions. The project has been following all the stages of the supply chain: strains selection, production, extraction, chemical analysis, and finally a pre-clinical test on animal models. More specifically, this study is the first step planned to analyze the array of some metabolites present in different growth stages of the *H. erinaceus* collected in Italy.

Thanks to the comparison with standard molecules, we were able to identify and quantify erinacine A in mycelium, hericenones C and D, and in wild type (WT) and cultivated sporophores.

In MicUNIPV, the Fungal Research Culture Collection at the University of Pavia (Italy), two strains of *H. erinaceus* collected in Italy are present to date: H.e.1 and H.e.2 [10,28]. The content of erinacine A in H.e.2 (105 µg/g) is slightly less compared to H.e.1 mycelium (150 µg/g) [10]. These amounts of erinacine A are comparable to that reported by Krzyczkowski et al. (2010) in improved submerged cultivation [33].

The same comparison between the WT sporophores showed that H.e.2 contains more hericenones C and D (760 µg/g and 100 µg/g, respectively) compared to H.e.1 (500 µg/g and <20 µg/g, respectively) [10]. These values are comparable with those of some strains reported by Lee et al. (2016) [18].

Therefore, given these data, the H.e.2 strain must be used for sporophore cultivation, whereas the H.e.1 for mycelium production.

By comparing the WT and cultivated sporophores of H.e.2, hericenones C and D in the cultivated sporophores are about two folds higher (1560 µg/g vs. 760 µg/g and 188 µg/g vs. 100 µg/g, respectively). Generally, wild sporophores exhibit biological variability, depending on the different growth environment and on seasonality. Conversely, the cultivated conditions are more stable. In particular, for the mycelial colonization, for the appearance of primordia, and the development of sporophores, the medium components (nitrogen, carbon, and mineral sources) and environmental factors (pH, temperature, and relative humidity) are fundamental in order to optimize the growth and to influence the bioactive metabolites production.

The primordium is an intermediate stage of the fungus between the mycelium and the sporophore development, characterized by the formation of spider-like aerial spines that grow above the culture medium. Generally, there are still few studies concerning primordium and none for *H. erinaceus* [34,35]. In our primordium, only hericenes were present, without any hericenone and erinacine. Hericenes are also found in mycelium and sporophores, both WT and cultivated, in agreement to what was reported by Arnone et al. (1994) [30] and Kobayashi et al. (2018) [31]. Preliminarily, in order to obtain a relative measure among the different samples, we compared the peak areas of the single hericenes detected, which were supposed to be A, B, C, and D, by HPLC-UV-ESI/MS. In particular, it is notable that in H.e.2 mycelium and primordium, hericenes A and B are more present compared to hericenes C and D. In cultivated sporophores, all hericenes are present, with a wider peak area if compared to the other samples. In WT sporophores, hericene C is absent and hericene A is at a lower level, whereas hericenes B and D peak areas have considerable values. Hericene B is present in fairly constant quantities in all samples, whereas hericene C is present in smaller quantities.

It should be noted that the cultivated sporophore has higher content than all the hericenes compared to the WT one. Similarly, the contents of hericenones C and D are higher in the cultivated sporophores than in the WT.

We could hypothesize a chemical correlation between hericenes and hericenones. Hericene A has a side chain with palmitoyl acid similar to hericenone C. Hericene C is similar to hericenone D with a side chain with stearic acid. Hericene D is similar to hericenone H and contains a side chain with a linoleoyl acid. Thus, in these paired molecules the side chain is maintained but hericenones differ from hericenes for their oxidation state. We can speculate that hericenone C derives from the oxidation of hericene A and hericenone D from the oxidation of hericene C. Other hericenones, such as I and E, could derive from the oxidation of hericenes B and D, respectively.

Up to now, ethanolic extracts obtained from H.e.1 mycelium and sporophores, with the standardized amounts of erinacine A and hericenones C and D, have been used to evaluate the effects of oral supplementation on cognitive decline in a mice model, during physiological aging [10]. Because of the different amounts of the neuroactive metabolites present in the different strains, now it is possible to prepare the best extract blend for in vivo tests. The present study contributes as it re-addresses the selection of raw material.

Further investigation will be carried out by setting different cultivation conditions to maximize the yield of bioactive metabolites.

## 4. Materials and Methods

### 4.1. Study Area and Sampling

Samplings were conducted in the hilly area around Siena (Tuscany, Italy), where both Mediterranean and temperate environments are present. The plant communities are dominated by holm oak (*Quercus ilex*), strawberry tree (*Arbutus unedo*), heather (*Erica arborea*), Mediterranean buckthorn (*Rhamnus alaternus*), juniper (*Juniperus communis*), and other deciduous species such as the

downy oak (*Q. pubescens*). *Q. ilex* is an important feature in the landscape, being usually prevalent and resistant to anthropic stress.

The wild type (WT) sporophore was collected from an old living specimen of *Q. ilex* and kept at 4 °C until experimental use.

### 4.2. H. erinaceus Samples for Chemical Analyses

The *H. erinaceus* samples processed for chemical analyses were: the WT sporophore (the sample was dried and maintained in a freezer at −20 °C for at least one month in order to avoid any further degradation); the strain isolated from it; the sporophores cultivated at the Botanical Garden of the University of Pavia (Italy) using the above mentioned isolated strain; the primordium that was the first aerial part consisting of mycelial cords.

### 4.3. H. erinaceus Strain Isolation

The isolation of mycelium in a pure culture from the WT was performed in accordance with the usual procedures [36–38]. Small pieces (up to 10 mm$^3$) were aseptically cut off from the center of the WT and inoculated into Petri dishes containing 2% malt extract agar (MEA, Biokar Diagnostics). Chloramphenicol at 50 ppm was added in this first step. Incubation was performed at 24 °C in complete darkness. The isolated strain is maintained in the Fungal Research Culture Collection of Pavia University (MicUNIPV).

### 4.4. H. erinaceus Sporophores Cultivation

The cultivation of *H. erinaceus* sporophores was performed in the mushroom greenhouse of the Botanical Garden at the University of Pavia (Italy). As the substrate, a mix of 70% oak sawdust, 20% rice bran, and 10% wheat straw, combined with 1% sucrose and 1% calcium carbonate, was used [36,39–41]. The substrate was mixed and hydrated, and then 300 g were placed in polypropylene bags with filters to allow gas exchange. Each bag was sterilized twice at 120 °C for 60 min.

In parallel, the spawn with *H. erinaceus* was prepared: the mycelium grew in sterilized polypropylene bags containing 300 g of hydrated barley. They were taken at 24 °C with 90% relative humidity (RH) in the dark for two weeks, until complete colonization.

We aseptically put and mixed 5% of spawn into each substrate bag. The cultivation room was kept at 24 °C and bathed to maintain high relative humidity (95%–100%).

Soon after the substrate was completely colonized by the mycelium, the bags were moved to a room where it was possible to carry out the light-dark cycle, maintaining the temperature at 18 °C–24 °C, the RH of 90%–95%, and good aeration condition to induce primordia formation.

In correspondence to the appearance of primordia, holes were made in the bags to allow the development of sporophores [36,39–41]. Once collected, the sporophores were weighed, measured, dried, and maintained frozen.

### 4.5. Extraction Procedures

The procedure of alcoholic extraction described by Lee et al. (2016) and Gerbec et al. (2015) [18,42] was followed with slight modification: 1 g of lyophilized mycelium/dried WT/cultivated sporophores/fresh primordium was blended with 10 mL of ethanol 70% and left in the thermostat at 50 °C for 24 h. At the end, the material was transferred for centrifugation (4000 rpm for 3 min) and the supernatant was stored at −20 °C for HPLC analysis.

### 4.6. HPLC-UV-ESI/MS Method

HPLC-UV-ESI/MS analyses were carried out on a LCQ FLEET system (Thermo Fisher Scientific, San Jose, CA, USA), equipped with a PAD-UV detector working at 254 nm. The chromatographic separation was performed using an F5 HPLC column 150 × 3.0 mm, 2.7 µm particle size

(Ascentis®Express, Merck KGaA, Darmstadt, Germany) maintained at 40 °C, with a flow rate of 0.3 mL/min and an injection volume of 20 μL. The mobile phase consisted of water containing 0.1% formic acid (solvent A) and acetonitrile (solvent B) (Table 7). The following gradient method was utilized: 0–9 min (30%–50% B), 9–27 min (50%–60% B), 27–54 min (60%–100% B), 54–69 min (100%–30% B), and 69–75 min (30% B).

**Table 7.** The mobile phase and the gradient method.

| Time | Solvent A | Solvent B |
|------|-----------|-----------|
| 0 | 70 | 30 |
| 9 | 50 | 50 |
| 27 | 40 | 60 |
| 54 | 00 | 100 |
| 69 | 70 | 30 |
| 75 | 70 | 30 |

An Electro Spray Ionization (ESI) interface was used as an ion source, under positive ion conditions (ESI+). The Ion Spray voltage and Capillary voltage were set at 5 kV and 10 V in positive ion mode. The capillary temperature was 400 °C. Acquisition was performed both in Full Scan mode (mass range 200–2000 Da) and Dependent Scan mode. The data station utilized the Xcalibur MS Software Version 2.1.

Stock solutions of erinacine A and hericenones C and D (1 mg/mL) were prepared in 70% ethanol. Standard solutions with the final concentration range of 1–25 μg/mL for erinacine A and 20–100 μg/mL for hericenones C and D were obtained by the proper dilution of stock solutions.

Calibration curves were constructed by injecting the standard mixture solutions at five concentrations (1, 5, 10, 15, 25 μg/mL) for erinacine A and at four concentrations (20, 50, 75, 100 μg/mL) for hericenone C and D. Linear least-square regression analysis for the calibration curves showed correlation coefficients of 0.9968, 09945, and 0.9951, respectively, for erinacine A, hericenones C, and hericenones D with respect to the peak area, demonstrating a good linear relationship in the different ranges tested. Each concentration was analyzed in triplicate [10].

## 5. Conclusions

In this study, an array of metabolites at different growth stages of the fungus *H. erinaceus* collected in Italy was analyzed. In particular, for the first time we described the array of metabolites present in primordium stage, i.e., the hericenes. These molecules are also present from the formation of the mycelium to the appearance of the primordium and up to the sporophore development. Experiments in the future will focus on testing the functional role of these molecules in vitro and in vivo.

In conclusion, in our opinion this methodological approach is a necessary step for developing dietary supplements with a higher and standardized content of bioactive metabolites.

## References

1. Mycobank. Available online: www.mycobank.org (accessed on 24 September 2019).
2. Rossi, P.; Cesaroni, V.; Brandalise, F.; Occhinegro, A.; Ratto, D.; Perrucci, F.; Lanaia, V.; Girometta, C.; Orrù, G.; Savino, E. Dietary Supplementation of Lion's Mane Medicinal Mushroom, *Hericium erinaceus* (Agaricomycetes), and Spatial Memory in Wild-Type Mice. *Int. J. Med. Mushrooms* **2018**, *20*, 485–494. [CrossRef] [PubMed]
3. Brandalise, F.; Cesaroni, V.; Gregori, A.; Repetti, M.; Romano, C.; Orrù, G.; Botta, L.; Girometta, C.; Guglielminetti, M.L.; Savino, E. Dietary Supplementation of *Hericium erinaceus* Increases Mossy Fiber-CA3 Hippocampal Neurotransmission and Recognition Memory in Wild-Type Mice. Evid. Based Complement. *Alternat. Med.* **2017**, 3864340. [CrossRef]
4. Li, Y.; Zhang, G.; Ng, T.B.; Wang, H. A novel lectin with antiproliferative and HIV-1 reverse transcriptase inhibitory activities from dried fruiting bodies of the monkey head mushroom *Hericium erinaceum*. *BioMed Res. Int.* **2010**, *2010*, 716515. [CrossRef] [PubMed]
5. Li, W.; Zhou, W.; Kim, E.J.; Shim, S.H.; Kang, H.K.; Kim, Y.H. Isolation and identification of aromatic compounds in Lion's Mane Mushroom and their anticancer activities. *Food Chem.* **2015**, *170*, 336–342. [CrossRef] [PubMed]
6. Zan, X.; Cui, F.; Li, Y.; Yang, Y.; Wu, D.; Sun, W.; Ping, L. *Hericium erinaceus* polysaccharide-protein HEG-5 inhibits SGC-7901 cell growth via cell cycle arrest and apoptosis. *Int. J. Biol. Macromol.* **2015**, *76*, 242–253. [CrossRef] [PubMed]
7. Vigna, L.; Morelli, F.; Agnelli, G.M.; Napolitano, F.; Ratto, D.; Occhinegro, A.; Di Iorio, C.; Savino, E.; Girometta, C.; Brandalise, F.; et al. *Hericium erinaceus* Improves Mood and Sleep Disorders in Patients Affected by Overweight or Obesity: Could Circulating Pro-BDNF and BDNF Be Potential Biomarkers? *Evid Based Complement Alternat Med.* **2019**, *2019*, 1–12. [CrossRef] [PubMed]
8. De Silva, D.D.; Rapior, S.; Hyde, K.D.; Bahkali, A.H. Medicinal mushrooms in prevention and control of diabetes mellitus—A review. *Fungal Divers.* **2012**, *56*, 1–29. [CrossRef]
9. Yang, B.K.; Park, J.B.; Song, C.H. Hypolipidemic Effect of an Exo-biopolymer Produced from a Submerged Mycelial Culture of *Hericium erinaceus*. *Biosci. Biotech. Bioch.* **2003**, *67*, 1292–1298. [CrossRef] [PubMed]
10. Ratto, D.; Corana, F.; Mannucci, B.; Priori, E.C.; Cobelli, F.; Roda, E.; Ferrari, B.; Occhinegro, A.; Di Iorio, C.; De Luca, F.; et al. *Hericium erinaceus* improves recognition memory and induces hippocampal and cerebellar neurogenesis in frail mice during aging. *Nutrients* **2019**, *11*, 715. [CrossRef]
11. Friedman, M. Chemistry, nutrition, and health-promoting properties of *Hericium erinaceus* (Lion's Mane) mushroom fruiting bodies and mycelia and their bioactive compounds. *J. Agric. Food Chem.* **2015**, *63*, 7108–7123. [CrossRef]
12. Kawagishi, H.; Shimada, A.; Shirai, R.; Okamoto, K.; Ojima, F.; Sakamoto, H.; Ishiguro, Y.; Furukawa, S. Erinacines A, B and C strong stimulators of nerve growth factor (NGF)-synthesis from the mycelia of *Hericium erinaceum*. *Tetrahedron Lett.* **1994**, *35*, 1569–1572. [CrossRef]
13. Ma, B.J.; Yu, H.Y.; Shen, J.W.; Ruan, Y.; Zhao, X.; Zhou, H.; Wu, T.T. Cytotoxic aromatic compunds from *Hericium erinaceum*. *J. Antibiotics* **2010**, *63*, 713–715. [CrossRef] [PubMed]
14. Kawagishi, H.; Ando, M.; Mizuno, T. Hericenone A and B as cytotoxic principles from the mushroom *Hericium erinaceum*. *Tetrahedron Lett.* **1990**, *31*, 373–376. [CrossRef]
15. Keong, C.Y.; Rashid, B.A.A.; Ing, Y.S.; Ismail, Z. Quantification and identification of polysaccharide contents in *Hericium erinaceus*. *Nutr. Food Sci.* **2007**, *37*, 260–271. [CrossRef]
16. Ma, B.J.; Shen, J.W.; Yu, H.Y.; Ruan, Y.; Wu, T.T.; Zhao, X. Hericenones and erinacines: Stimulators of nerve growth factor (NGF) biosynthesis in *Hericium erinaceus*. *Mycology* **2010**, *1*, 2–92. [CrossRef]
17. Kawagishi, H.; Ando, M.; Sakamoto, H.; Yoshida, S.; Ojima, F.; Ishiguro, Y.; Ukai, N.; Furukawa, S.C. Hericenones C, D and E, stimulators of nerve growth factor (NGF)-synthesis, from the mushroom *Hericium erinaceum*. *Tetrahedron Lett.* **1991**, *32*, 4561–4564. [CrossRef]
18. Lee, D.G.; Kang, H.W.; Park, C.G.; A, Y.S.; Shin, Y. Isolation and identification of pyotochemicals and biological activities of *Hericium erinaceus* and their contents in *Hericium* strains using HPLC/UV analysis. *J. Ethnopharmacol.* **2016**, *184*, 219–225. [CrossRef] [PubMed]
19. Tang, H.Y.; Yin, X.; Zhang, C.C.; Jia, Q.; Gao, J.M. Structure diversity, synthesis, and biological activity of cyathane diterpenoids in higher fungi. *Curr. Med. Chem.* **2015**, *22*, 2375–2391. [CrossRef]

20. Kawagishi, H.; Shimada, A.; Hosokawa, S.; Mori, H.; Sakamoto, H.; Ishiguro, Y.; Sakemi, S.; Bordner, J.; Kojima, N.; Furukawa, S. Erinacines E, F, and G, stimulators of nerve growth factor (NGF) synthesis from the mycelia of *Hericium erinaceum*. *Tetrahedron Lett.* **1996**, *37*, 7399–7402. [CrossRef]

21. Kawagishi, H.; Simada, A.; Shizuki, K.; Mori, H.; Sakamoto, H.; Furukawa, S. Erinacine D, a stimulator of NGF-synthesis from the mycelia of *Hericium erinaceum*. *Heterocycl Commun.* **1996**, *2*, 51–54. [CrossRef]

22. Lee, E.W.; Shizuki, K.; Hosokawa, S.; Suzuki, M.; Suganuma, H.; Inakuma, T.; Kawagishi, H. Two novel diterpenoids, erinacines H and I from the mycelia of *Hericium erinaceum*. *Biosci. Biotech. Biochem.* **2000**, *64*, 2402–2405. [CrossRef] [PubMed]

23. Kenmoku, H.; Sassa, T.; Kato, N. Isolation of erinacine P, a new parental metabolite of cyathane-xylosides from Hericium erinaceus and its biomimetic conversion into erinacines A and B. *Tetrahedron Lett.* **2000**, *41*, 4389–4393. [CrossRef]

24. Kenmoku, H.; Shimai, T.; Toyomasu, T.; Kato, N.; Sassa, T. Erinacine Q, a new erinacine from Hericium erinaceus, and its biosynthetic route to erinacine C in the basidiomycete. *Biosci. Biotech. Biochem.* **2002**, *66*, 571–575. [CrossRef] [PubMed]

25. Kawagishi, H.; Masui, A.; Tokuyamab, S.; Nakamurac, T. Erinacines J and K from the mycelia of *Hericium erinaceum*. *Tetrahedron Lett.* **2006**, *62*, 8463–8466. [CrossRef]

26. Ma, B.J.; Zhou, Y.; Li, L.Z.; Li, H.M.; Gao, Z.M.; Ruan, Y. A new cyathanexyloside from the mycelia of *Hericium erinaceum*. *Z Naturforsch* **2008**, *63b*, 1241–1242. [CrossRef]

27. Bernicchia, A.; Gorjon, S.P. *Hericium erinaceus*. In *Corticiaceae s.l. Fungi europaei*; Candusso: Alassio, Italy, 2010; Volume 12, pp. 318–319. ISBN 978-88-901057-9-8.

28. Cesaroni, V.; Brusoni, M.; Cusaro, C.M.; Girometta, C.; Perini, C.; Picco, A.M.; Rossi, P.; Salerni, E.; Savino, E. Phylogenetic Comparison between Italian and Worldwide *Hericium* Species (Agaricomycetes). *Int. J. Med. Mushrooms* **2019**, accepted.

29. PubChem. Available online: http://pubchem.ncbi.nlm.nih.gov/ (accessed on 26 September 2019).

30. Arnone, A.; Cardillo, R.; Nasini, G.; De Pava, O.V. Secondary mold metabolites: Part 46. Hericenes A-C and erinapyrone C, new metabolites produced by the fungus *Hericium erinaceus*. *J. Nat. Prod.* **1994**, *57*, 602–606. [CrossRef]

31. Kobayashi, S.; Hamada, Y.; Yasumoto, T.; Hashino, Y.; Masuyama, A.; Nagai, K. Total syntheses and endoplasmic reticulum stress suppressive activities of hericenes A-C and their derivatives. *Tetrahedron Lett.* **2018**, *59*, 1733–1736. [CrossRef]

32. Wasser, S.P. Medicinal Mushroom Science: Current Perspectives, Advances, Evidences, and Challenges. *Biomed. J.* **2014**, *37*, 345–356. [CrossRef]

33. Krzyczkowski, W.; Malinowska, E.; Herold, F. Erinacine A biosynthesis in submerged cultivation of *Hericium erinaceum*: Quantification and improved cultivation. *Eng. Life Sci.* **2010**, *10*, 446–457. [CrossRef]

34. Zhang, G.; Sun, Z.; Ren, A.; Shi, L.; Shi, D.; Li, X.; Zhao, M. The mitogen-activated protein kinase GlSlt2 regulates fungal growth, fruiting body development, cell wall integrity, oxidative stress and ganoderic acid biosynthesis in *Ganoderma lucidum*. *Fungal Genet. Biol.* **2017**, *104*, 6–15. [CrossRef] [PubMed]

35. Xie, C.; Gong, W.; Zhu, Z.; Yan, L.; Hu, Z.; Peng, Y. Comparative transcriptomics of *Pleurotus eryngii* reveals blue-light regulation of carbohydrate-active enzymes (CAZymes) expression at primordium differentiated into fruiting body stage. *Genomics* **2018**, *110*, 201–209. [CrossRef] [PubMed]

36. Stamets, P. The lion's mane mushroom. In *Growing Gourmet and Medicinal Mushrooms*, 3rd ed.; Ten Speed Press: Berkeley, Toronto, 2000; pp. 387–394. ISBN 13 978-1-58008-175-7.

37. Stalpers, J.A. Identification of wood-inhabiting Aphyllophorales in pure culture. *Stud. Mycol.* **1978**, *16*, 114.

38. Sturini, M.; Girometta, C.; Maraschi, F.; Savino, E.; Profumo, A. A preliminary investigation on Metal Bioaccumulation by *Perenniporia fraxinea*. *Bull. Environ. Contam. Toxicol.* **2017**, *98*, 508–512. [CrossRef] [PubMed]

39. Ko, H.G.; Park, H.G.; Park, S.H.; Choi, C.W.; Kim, S.H.; Park, W.M. Comparative study of mycelial growth and basidiomata formation in seven different species of the edible mushroom genus *Hericium*. *Bioresource Technol.* **2005**, *96*, 1439–1444. [CrossRef] [PubMed]

40. Hassan, F.R.H. Cultivation of the Monkey Head Mushroom (*Hericium erinaceus*) in Egypt. *J. App. Sci. Res.* **2007**, *3*, 1229–1233.

41. Savino, E.; Girometta, C.; Baiguera, R.M.; Cesaroni, V.; Guglielminetti, M.L.; Rodolfi, M.; Rossi, P.; Picco, A.M. Different approaches for *Hericium erinaceus* spawn in the perspective of gluten free products. *ISMS* **2016**, *19*, 106.
42. Gerbec, B.; Tavčar, E.; Gregori, A.; Kreft, S.; Berovic, M. Solid State Cultivation of *Hericium erinaceus* Biomass and Erinacine: A Production. *J. Bioproces. Biotech.* **2015**, *5*, 1–5. [CrossRef]

**Sample Availability:** Samples of the compounds are available from one of the authors (H. K.) under an MTA.

**ORIGINAL RESEARCH**

# Squaring the Circle: A New Study of Inward and Outward-Rectifying Potassium Currents in U251 GBM Cells

Daniela Ratto[1] · Beatrice Ferrari[1] · Elisa Roda[1,2] · Federico Brandalise[3] · Stella Siciliani[1] · Fabrizio De Luca[1] · Erica Cecilia Priori[1] · Carmine Di Iorio[1] · Filippo Cobelli[1] · Paola Veneroni[1] · Maria Grazia Bottone[1] · Paola Rossi[1]

## Abstract

In the present study, the functional role of the inwardly rectifying $K^+$ channel, Kir4.1, and large-conductance $Ca^{2+}$-activated $K^+$ (BK) channel during cell migration in U251 cell line was investigated. We focused on polarised cells which are positive for the active-Cdc42 migration marker. The perforated patch technique was used to avoid intracellular dialysis and to maintain physiological changes in intracellular calcium. Wound healing was employed to assay migration after 24 h. Polarised cells recorded displayed different hallmarks of undifferentiated glial cells: depolarised resting membrane potential and high membrane resistance. Cells recorded outside wounded area did not display either constitutive inward or outward rectification. After migration, U251 cells were characterised by a constitutively smaller Kir4.1 and larger BK currents with a linearly related amplitude. Menthol modulation increased both currents in a linearly dependent manner, indicating a common mechanism triggered by activation of transient receptor potential melastatin 8 (TRPM8), a $Ca^{2+}$-permeable non-selective cation channel. We hypothesised that both migration and menthol modulation would share an increase of intracellular calcium triggering the increase in Kir4.1 and BK channels. Immunocytochemistry demonstrated the cytoplasmic expression of both Kir4.1 and BK channels and a mislocation in the nucleus under basal conditions. Before and after migration, polarised cells increased the expression of Kir4.1 and BK channels both in the cytoplasm and nucleus. TEM ultrastructural analysis displayed a different nuclear distribution of Kir4.1 and BK channels. In the present study, the physiological role of Kir4.1 and BK currents at membrane potential, their involvement in migration, and the functional role of nuclear channels were discussed.

**Keywords** Glioblastoma · Inward rectifier · Outward rectifier · TRPM8 · Perforated patch clamp · U251

## Introduction

Most primary brain tumours in adult humans arise from glial cells. These neoplasms carry a very poor prognosis largely due to the diffuse invasiveness into normal brain that prevents successful surgical treatment (Ransom 2000; Holland 2001; Maher et al. 2001). The incidence of this type of brain tumour is increasing more and more, but no effective therapeutic strategies are available until now, mainly because the mechanisms underlying invasiveness in glioblastoma (GBM) remain largely unknown.

One of the main functions of glial cells in the brain is to maintain ionic homeostasis during neuronal activity via the potassium spatial buffering process that involves a specific subset of $K^+$ channels known as inwardly rectifying $K^+$ (or Kir) channels (Butt and Kalsi 2006; Olsen and Sontheimer 2008; Chever et al. 2010; Nwaobi et al. 2016; Thuringer et al. 2017). In particular, the barium-sensitive Kir4.1 encoded by the gene KCNJ10 is a prominent feature and key regulator of mature astrocytes. A reduced expression of Kir4.1 channels was detected in human brain tumours including astrocytomas and oligodendrogliomas (Olsen and Sontheimer 2004; Warth et al.

Daniela Ratto and Beatrice Ferrari are co-first authors.

✉ Paola Rossi
paola.rossi@unipv.it

1 Department of Biology and Biotechnology "L. Spallanzani", University of Pavia, 27100 Pavia, Italy

2 Toxicology Unit, Laboratory of Clinical & Experimental Toxicology, Pavia Poison Centre, National Toxicology Information Centre, ICS Maugeri SpA, IRCCS Pavia, 27100 Pavia, Italy

3 Department of Fundamental Neurosciences (NEUFO), University of Geneva, 1211 Geneva, Switzerland

🍪 Springer

2005; Higashimori and Sontheimer 2007; Zurolo et al. 2012; Thuringer et al. 2017).

GBM cell migration has been shown to heavily depend on ion channel activity (Catacuzzeno et al. 2011). Ion channels may contribute to the invasive behaviour by influencing salt and water movements between intracellular and extracellular compartments during shape and volume changes (Soroceanu et al. 1999). The large-conductance $Ca^{2+}$-activated $K^+$ (BK) channels and the volume-regulated Cl (IClVol) channels, both largely expressed in GBM cells, have been shown to underlay migration and enhance tumour progression in several experimental tumour models (Ransom and Sontheimer 2001; McFerrin and Sontheimer 2006). The intracellular $Ca^{2+}$ concentration $[Ca^{2+}]_i$ is involved in invasiveness, but the intracellular mechanisms targeted by $[Ca^{2+}]_i$ changes are not well understood (Catacuzzeno et al. 2011). Menthol is a TRPM8 agonist that stimulates influx of $Ca^{2+}$, BK channels membrane currents, and migration in human glioma DBTRG cells (Wondergem et al. 2008; Wondergem and Bartley 2009). Furthermore, the expression levels of TRPM8 are positively correlated with the migration and invasion of human glioblastoma U251 cells (Zeng et al. 2019).Thus, a thorough understanding of the functional role of Kir4.1 and BK channels involvement in cell migration alone or alongside the activation of TRPM8 could help develop new therapeutic strategies, targeting channels in the treatment of GBM. In the present study, the expression and the functional role of ion channel during cell migration was examined in vitro using the U251 cell line and a non-invasive perforated patch clamp technique.

## Materials and Methods

### Cell Culture, Migration Assay, and Immunocytochemistry

Human U251 MG cell line (Sigma-Aldrich, Rome, Italy) was cultured in 25 cm² flasks in Eagle's minimal essential medium (EMEM) supplemented with 1% glutamine, 1% non-essential amino acids, 1% sodium pyruvate, 10% foetal bovine serum, 1% penicillin/streptomycin, and maintained at 37 °C in a humidified atmosphere (95% air/5% $CO_2$). All cell culture reagents were purchased from Celbio s.p.a. and Euroclone s.p.a. (Pero, Milan, Italy).

For the cell migration assay, U251 cells were seeded on glass coverslips (22 mm × 22 mm) located in cell culture dishes (35 mm × 10 mm) until 90% of confluence for immunocytochemistry measures at basal. A disposable pipette tip (1-mL volume) was used to scratch wounds on the midline of the coverslip (width 800 μm). At 24 h after the wound healing assay (t1), the width was reduced to about the fifty percent. The effect of the pharmacological inhibition of the Kir4.1 and BK channels alone or after menthol-dependent activation of TRPM8 in wound healing assay in the presence of channels blockers after 24 h of continuous exposure to the respective single and combined treatments was investigated. We used the following concentrations: Ibtx 100 nM; Barium 1 mM; Menthol 100 μM. Each treatment condition was then examined by evaluating the percentage of scratch wound closure compared to the basal control condition.

For immunocytochemistry, a protocol previously described was used (Rangone et al. 2018; Ferrari et al. 2019). Primary and secondary antibodies employed for immunofluorescence reactions are summarised in Table 1.

**Table 1** Primary and secondary antibodies employed for immunofluorescence microscopy

| Primary antibody | Dilution (in PBS) | Secondary antibody | Dilution (in PBS) |
|---|---|---|---|
| Actin | | | |
| Alexa 594-Phalloidin (Molecular Probes, Invitrogen) | 1:500 | | |
| Active-Cdc42 | | | |
| Monoclonal mouse anti-active Cdc42 (BIOMOL GmbH, Hamburg, Germany) | 1:100 | Alexa 488-conjugated anti-mouse antibody (Molecular Probes, Invitrogen) | 1:200 |
| PCNA | | | |
| Monoclonal mouse (PC10) anti-PCNA (Abcam, Italy) | 1:200 | Alexa 488-conjugated anti-mouse antibody (Molecular Probes, Invitrogen) | 1:200 |
| BK channel | | | |
| Polyclonal rabbit anti-$KCa_{1.1}$ (KCNMA1) (Alomone Labs, Jerusalem, Israel) | 1:200 | Alexa 594-conjugated anti-rabbit antibody (Molecular Probes, Invitrogen) | 1:200 |
| KIR4.1 channel | | | |
| Polyclonal rabbit anti-$Kir_{4.1}$ (KCNJ10) (Alomone Labs, Jerusalem, Israel) | 1:100 | Alexa 594-conjugated anti-rabbit antibody (Molecular Probes, Invitrogen) | 1:200 |

307

Images were recorded using an Olympus BX51 microscope equipped with Olympus MagniFire camera system and processed with Olympus Cell F software, to analyse mean fluorescence density per cell (mean of immunofluorescence intensity normalised on the cell surface). Three independent experiments were performed for each antibody tested (number of cells tested in each experimental condition: $n = 10$ flattened cells, $n = 10$ polarised cells).

## TEM Ultrastructural Analysis

Cells were grown as above described. U251 cells were harvested using mild trypsinisation (0.25% trypsin in PBS containing 0.05% EDTA) and collected by centrifugation (800 rpm for 5 min). The samples were immediately fixed with 2% formaldehyde in PBS (2 h at room temperature), centrifuged (2000 rpm for 10 min) and washed with PBS. The cell pellets were pre-embedded in 2% agar and dehydrated with increasing concentrations of ethanol (30, 50, 70, 90 and 100%). Finally, the pellets were embedded in LR-white resin (Sigma-Aldrich, Italy) and polymerised at 60 °C for 24 h.

Ultrathin sections were obtained using ultramicrotome Rechter and then placed on nickel grids. Antibodies incubation and staining procedure were previously reported (Masiello and Biggiogera, 2017). Briefly, primary antibodies, i.e. anti-BK and anti-Kir4.1 channels (Table 1), were diluted in PBS containing 0.1% BSA and 0.05% Tween 20; secondary antibodies (Jackson ImmunoResearch) coupled with 6 nm-colloidal gold were diluted 1:20 in PBS.

Lastly, sections were observed under a Zeiss EM 900 transmission electron microscope operating at 80 kV, computerised through Epson Perfection 4990 Photo scanner at a resolution of 800 dpi, and then processed using the Epson Scan software.

## Electrophysiological Recording and Analysis Of Inward Rectifier (IR) and Outward Rectifier (OR) Currents

Whole-cell perforated patch clamp was performed as previously described ($n = 87$) (Horn and Marty 1988; D'Angelo et al. 1990; Bordey et al. 2000; Rossi et al. 2006), by using Axopatch-200B (Axon Instruments) patch clamp amplifier at the output cut-off frequency of 5 kHz.

The extracellular solution contained the following: 140 mM NaCl, 5 mM KCl, 10 mM HEPES, 10 mM glucose, 3 mM CaCl$_2$ and 1.2 mM MgSO$_4$, pH 7.4. The intrapipette solution contained 100 μg/mL Nystatin (Sigma/Fluka, Milan, Italy) and 140 mM KCl, 4 mM NaCl, 5 mM EGTA, 5 mM HEPES and 0.5 mM CaCl$_2$, pH 7.3. Series resistance ($R_s = 16 \pm 1.3$ MΩ), input resistance ($R_m$) and membrane capacitance ($C_m$, Table 2) were measured as previously described (Rossi et al. 1996).

Whole-cell perforated patch clamp stability was assessed over time every 5 min by monitoring $R_s$. The junction potential between the pipette and cytoplasm was 8.8 mV (Horn and Marty 1988) and the $I$–$V$ relationship was shifted to the left by this value.

The depolarising ramp from $-120$ to $+140$ mV was elicited at a rate corresponding to 0.077 mV/ms (sampling rate: 500 Hz). Other protocols are reported in the Figures. Mean amplitude was measured at $-120$ mV for Kir4.1 and $+140$ mV for BK.

To analyse inward rectifier (IR) and outward rectifier (OR) currents, a modified Boltzmann's equation was used (Hille and Schwarz 1978; Rossi et al. 1998, 2006; Ransom et al. 2002; Brandalise et al. 2016) as follows:

$$\text{for Kir4.1} \quad I(V) = \frac{G_{max}(V - V_{rev})}{1 + e^{(V - V_{1/2})/K}} \tag{1a}$$

$$\text{for BK} \quad I(V) = \frac{G_{max}(V - V_{rev})}{1 + e^{-(V - V_{1/2})/K}} \tag{1b}$$

$G_{max}$ is the maximal conductance, $V_{rev}$ is the reversal potential, $V_{1/2}$ is the potential at which the current is half-activated and $k$ is the voltage dependence of activation ($V^{-1}$). Once $V_{rev}$ and $G_{max}$ were known, and because

$$G(V) = \frac{I(V)}{V - V_{rev}}$$

it follows that

$$\text{for Kir4.1} \quad \frac{G}{G_{max}} = \frac{1}{1 + e^{\left(V - \frac{V1}{2}\right)/K}} \tag{2a}$$

$$\text{for BK} \quad \frac{G}{G_{max}} = \frac{1}{1 + e^{-\left(V - \frac{V1}{2}\right)/K}} \tag{2b}$$

Activation time constant of Kir4.1 and BK were obtained by fitting traces with a single exponential function. The electrophysiological data were analysed using Clampfit 10.6 (Axon Instruments, Molecular Devices LLC, Sunnyvale,

Table 2 $V_{rev}$, $R_m$ and $C_m$ in polarised cells recorded, within the wounded area, with constitutive currents and cells after menthol perfusion

|  | $V_m$ (mV) | $R_m$ (GΩ) | $C_m$ (pF) |
|---|---|---|---|
| Constitutive ($n = 46$) | $-30.9 \pm 1.5$ | $0.72 \pm 0.07$ | $29.9 \pm 3.2$ |
| Menthol ($n = 15$) | $-36.1 \pm 5.4$ | $0.76 \pm 0.22$ | $43.8 \pm 5.3$** |

**$p < 0.01$

**Fig. 1** Actin immunostaining. The upper schematic drawing describes selected experimental conditions. Micrographs show actin-immunopositive cytoskeleton (red fluorescence), revealing different cell morphologies at basal condition and at t1 (a, c and b, d, respectively); nuclear counterstaining with Hoechst 33,258 (blue fluorescence). White arrowhead indicate polarised cells. Scale bars: 200 μm (a, b), 20 μm (c, d)
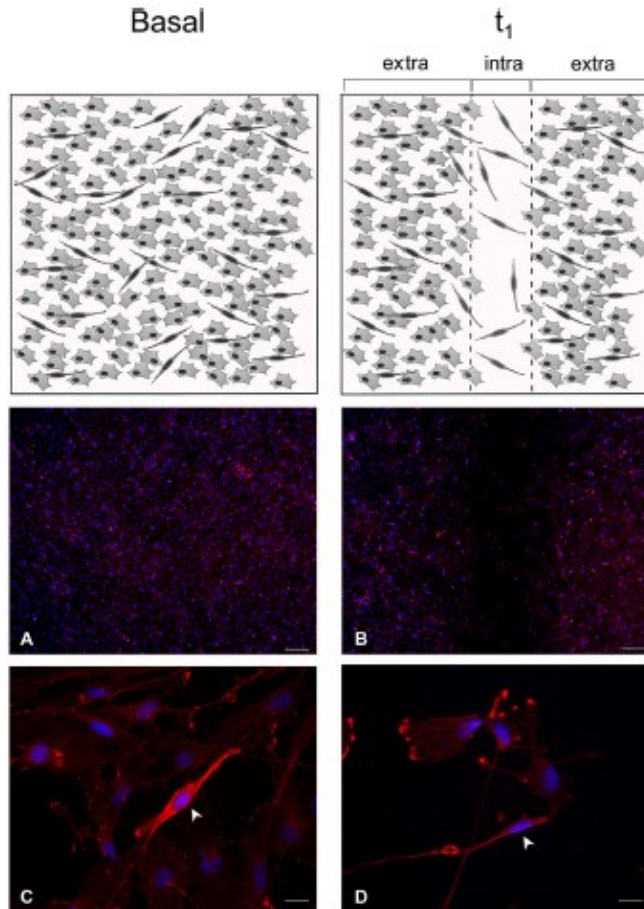
CA, USA) and Origin 6.0 (Origin Labs, Northampton, MA, USA).

Drugs were locally perfused for about 15 min using a multi-barrel pipette positioned at 50 μm from the recorded cell.

## Statistical Analysis

All data are reported as mean values ± standard error of the mean (SEM). We performed Bartlett's and Shapiro–Wilk's tests to establish and confirm the normality of parameters. Statistical significance was determined using one-way analysis of variance (ANOVA) with Post hoc Bonferroni's test and Student's $t$ test with Prism 5 (GraphPad Software, San Diego, CA, USA). $p$ values < 0.05 were considered statistically significant.
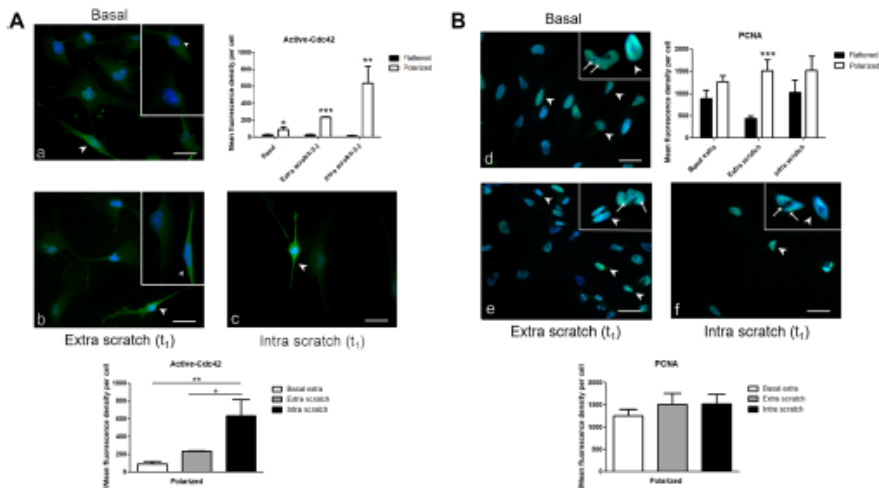
**Fig. 2** Active-Cdc42 and PCNA immunolabelling. Micrographs show active-Cdc42 (**A**) and PCNA immunostaining (**B**), both identified by green fluorescence, in flattened and polarised cells, evaluated at basal condition (a, d) and at t1, both outside (extra scratch, b, e) and within (intra scratch, c, f) wounded area. Histograms show the mean fluorescence density per cell. Nuclei were counterstained with Hoechst 33,258 (blue fluorescence). White arrowhead indicates polarised cell; thin white arrow indicates nuclear foci with spot-like labelling in flattened cells. Scale bar: 40 μm. $p$ values: *$p<0.05$; **$p<0.01$; ***$p<0.001$

## Results

The experimental plan consisted of two experimental time points: (i) a basal condition and (ii) 24 h after wound healing assay (t1). The t1 cells within (IN) and outside (OUT) the wounded area were studied.

### Flattened and Polarised Cells: Migration and Proliferation

At basal condition and t1, the actin-immunopositive cells showed two different features: a morphology characterised by polarised cytoplasmic protrusion, and a flattened one, namely polarised and flattened cells, respectively (Fig. 1).

The migration marker active-Cdc42 stained U251 cell cytoplasm. In particular, immunoreactivity was enhanced in polarised cells compared with flattened ones (Fig. 2a). Notably, in polarised cells, the mean fluorescence density per cell progressively increased from basal to OUT to IN (Fig. 2Ac), whereas in flattened cells, the fluorescence was lower remaining constant (Fig. 2Aa–c).

Anti-PCNA antibody [PC10] is specific for PCNA p36 protein, which is expressed at high levels in proliferating cells. In the nucleus, this marker forms nuclear foci that represent sites of ongoing DNA replication. These foci vary in morphology and number during the S phase (Leonhardt et al. 2000; Dellaire et al. 2006; Schönenberger et al. 2015).

We employed the proliferation marker PCNA which stained the U251 cells nuclei. No statistically significant differences were measured between flattened and polarised cells under different experimental conditions except for OUT (Fig. 2Bd–f). In detail, in polarised cells PCNA immunolabelling was homogeneously distributed in the nucleus, while in flattened cells the fluorescence appeared spot-like, indicating that these cells were actively cycling cells (Schönenberger et al. 2015).

### Electrophysiological Recordings IN and OUT the Wounded Area

Polarised cells recorded IN ($n=54$) and OUT ($n=33$) the wounded area at $t_1$ had a depolarised membrane potential ($-31.7\pm1.4$ mV and $-34.7\pm1.7$ mV, respectively).

The majority of recorded cells IN the wounded area (85.19%, $n=46/54$) showed both constitutive OR and IR currents (Fig. 3a), whereas the other cells did not display any currents. The majority of recorded cells OUT the wounded area (78.79%, $n=26/33$) did not display OR and IR currents (Fig. 3b) and the remaining cells displayed smaller IR
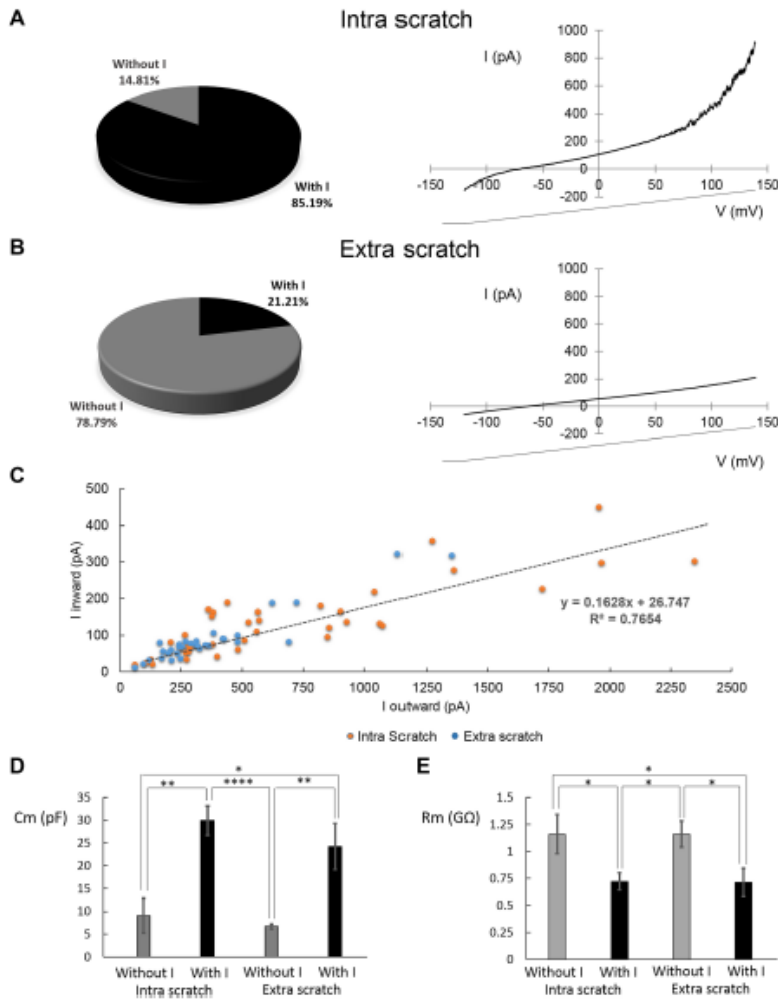
**Fig. 3** Currents recorded within and outside wounded area. **a**, **b** left panels, cells percentage with or without IR and OR within (intra scratch, $n = 54$, **a**) and outside (extra scratch, $n = 33$, **b**) wounded area. **a**, **b** Right panels, averaged traces. **c** Relationship between IR and OR currents within (orange points) and outside (blue points) wounded area. **d** Membrane capacitance measured in polarised cells recorded within ($n = 54$) and outside ($n = 33$) wounded area with or without constitutively currents. $p$ values: *$p < 0.05$; **$p < 0.01$; ***$p < 0.001$; ****$p < 0.0001$

311

**Fig. 4** Identification of constitutively Kir4.1 within wounded area. **a** IR was rapidly blocked by local perfusion of 1 mM Ba$^{2+}$ ($n=17$, sampling rate: 6.67 kHz). The barium-sensitive currents have been obtained by digital subtraction: control-barium. **b** The experimen-
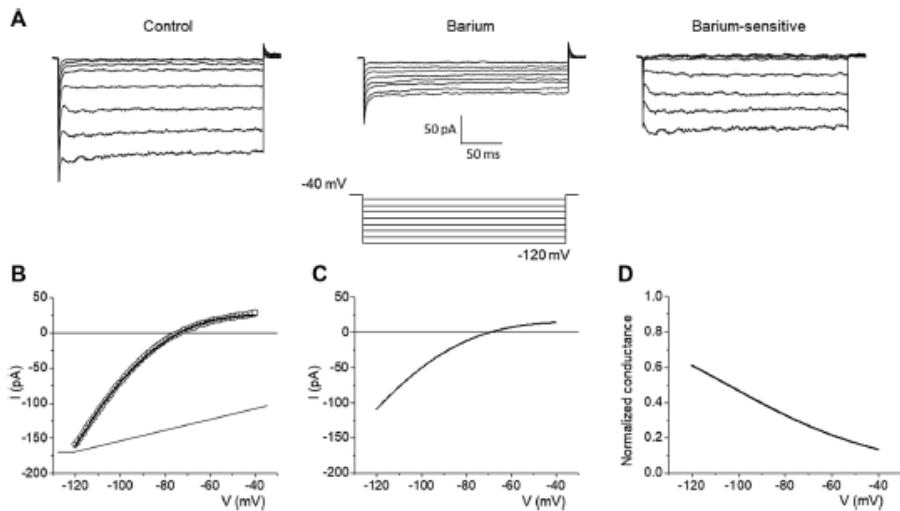
tal trace obtained using a voltage-ramp protocol have been fitted with Eq. 1a. **c** I–V plots obtained by the averaged values reported in Table 3. **d** Normalised conductance reconstructed using Eq. 2a

**Table 3** Biophysical properties of Kir4.1 and BK

|  | $G_{max}$ (nS) | $V_{rev}$ (mV) | $V_{1/2}$ (mV) | $K$ (mV$^{-1}$) |
|---|---|---|---|---|
| Kir4.1 |  |  |  |  |
| Barium-sensitive ($n=17$) | $3.5\pm0.7$ | $-69.2\pm1.1$ | $-104.7\pm7.1$ | $34.4\pm4.5$ |
| Menthol-sensitive ($n=5$) | $5.5\pm0.9^*$ | $-60.5\pm5.1$ | $-104.6\pm5.2$ | $28.7\pm7.3$ |
| BK |  |  |  |  |
| TEA-sensitive ($n=28$) | $5.0\pm0.6$ | $-69.6\pm0.8$ | $114.9\pm2.9$ | $14.0\pm1.2$ |

$^*p<0.05$

and OR currents ($n=7$, mean amplitude $-28.4\pm5.1$ pA and $441.9\pm81.8$ pA, respectively).

The amplitudes of OR and IR currents were interpolated with a straight line, indicating a direct correlation ($R^2=0.7654$, Fig. 3c). $C_m$ and $R_m$ values were associated with the presence or absence of the constitutive currents both IN and OUT the wounded area (Fig. 3d, e).

### Biophysical and Pharmacological Identification of Kir4.1 and BK Channels

IR was blocked by 1 mM Ba$^{2+}$ ($n=17$, Fig. 4a). The averaged I–V plots and the normalised conductance curve of the barium-sensitive IR was reconstructed by Eqs. 1a and 2a and Boltzmann's parameters are reported in Table 3

(Fig. 4b–d). IR had a weak voltage-dependent rectification and the activation time constant was about 4.8 ms. All the results identified the Kir4.1 channel (Olsen and Sontheimer 2004; Thuringer et al. 2017).

OR was insensitive to 10 µM clotrimazole but was blocked by 3 mM TEA ($n=28$, Fig. 5a) and 100 nM Iberiotoxin (Ibtx; $n=3$, Fig. 5b). The averaged I–V plots and the normalised conductance curve of the TEA-sensitive BK were reconstructed by Eqs. 1b and 2b and Boltzmann's parameters are reported in Table 3 (Fig. 5c–e). The activation time constant was faster at $+140$ mV ($p<0.05$, Fig. 5f). All the results identified the BK channel, whereas intermediate potassium currents were negligible.
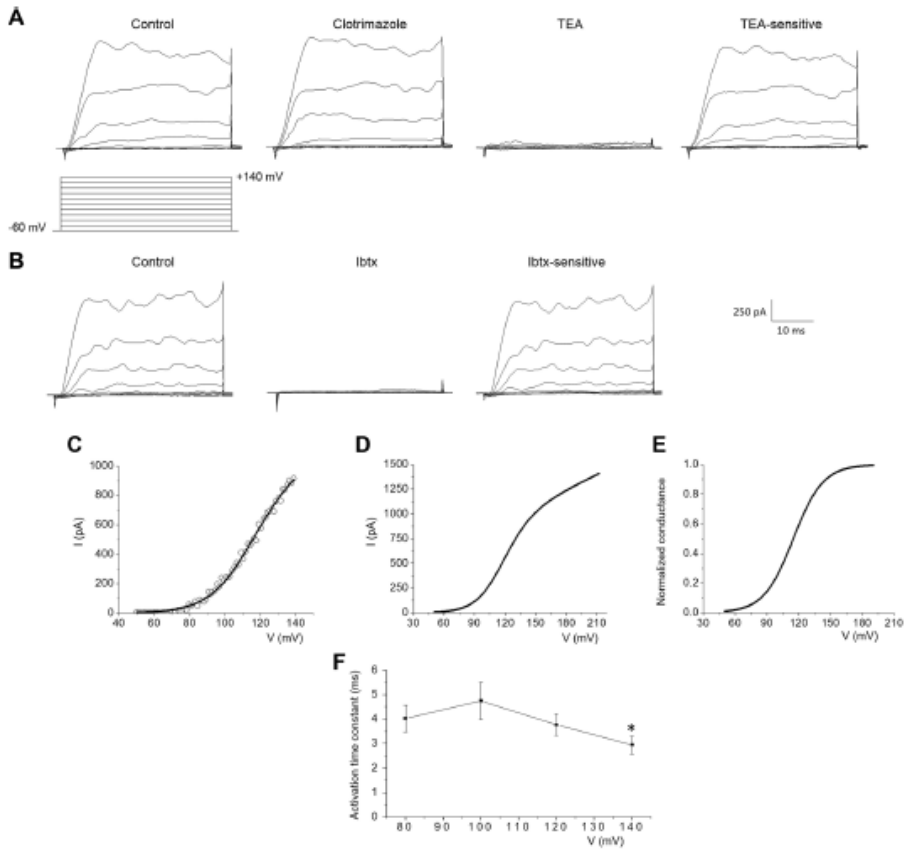
**Fig. 5** Identification of constitutively BK within wounded area. **a** OR rectifier currents were insensitive to local perfusion with 10 µM clotrimazole (n=28), but was blocked in about 2 min by local perfusion with 3 mM TEA (n=5, sampling rate: 20 kHz)). The TEA-sensitive currents have been obtained by digital subtraction: control-TEA. **b** OR rectifier currents were blocked in about 2 min by local perfusion with 100 nM Iberiotoxin (Ibtx) (n=3). The Ibtx-sensitive currents have been obtained by digital subtraction: control-Ibtx. **c** The experimental trace obtained using a voltage-ramp protocol have been fitted with Eq. 1b. **d** I–V plots obtained by the averaged values reported in Table 3. **e** Normalised conductance reconstructed by using Eq. 2b. **f** Voltage dependence of the activation time constant. p values: *p<0.05: activation time constant at+140 mV compared with 80, 100 and 120 mV

## Menthol Modulation of Kir4.1 and BK

We investigated the effect of menthol, a TRPM8 agonist, which increases $[Ca^{2+}]_i$, activation of BK channels, and the migration rate in human glioma cells (Wondergem et al. 2008; Wondergem and Bartley 2009).

100 µM menthol was perfused at t1 for about 15 min. In all cells tested IN the wounded area, after 9 min menthol increased both Kir4.1 and BK currents. After menthol perfusion, a difference between the amplitude of both Kir4.1 and BK in cells with (n=15) or without (n=5) constitutive currents was not observed (Fig. 6a, b).

Due to the unexpected result, menthol-sensitive Kir4.1 was further investigated using the same procedure previously described and the Kir4.1 normalised conductance was reconstructed (Table 3). $G_{max}$ was the statistically
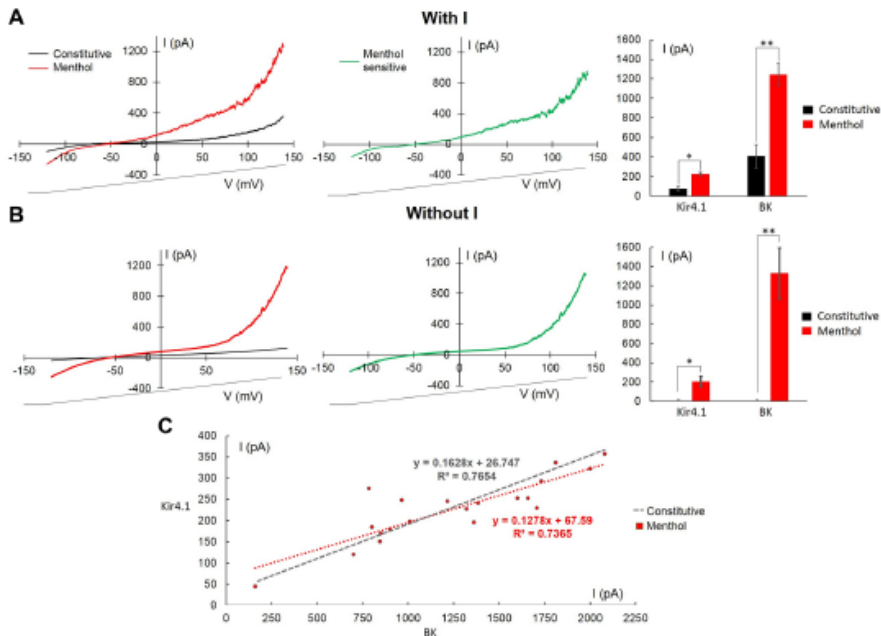
**Fig. 6** Menthol increased KIR4.1 and BK currents within wounded area. **a, b** Left: averaged traces elicited before (black), and 9 min after the beginning of local menthol perfusion (100 μM; red) in cells with ($n = 15$, **a**) and without ($n = 5$, **b**) KIR4.1 and BK. In the centre: experimental traces obtained after digital subtraction (menthol–constitutive, green). Right: summary results evaluated at $-120$ mV for KIR4.1 and at $+140$ mV for BK currents. **c** Relationship between KIR4.1 and BK after menthol perfusion (red). The straight line obtained for constitutive currents is shown for comparison (grey). $p$ values: *$p < 0.05$; **$p < 0.01$

significant different single parameter when comparing menthol-sensitive and constitutive Kir4.1 ($p < 0.05$).

After menthol activation, data points were interpolated with a straight line, indicating a direct correlation between the Kir4.1 and BK amplitudes ($R^2 = 0.7365$, Fig. 6c).

Menthol-induced Kir4.1 was blocked by barium (81.5% decrease, $n = 4$, Fig. 7a) and BK was blocked by TEA (72.1% decrease, $n = 7$, Fig. 7b).

The calcium dependence of BK channels is well demonstrated (Ransom et al. 2002; Wondergem and Bartley 2009), whereas the calcium dependence of KIR4.1 channels has not yet established. We carried out experiments at different $[Ca^{2+}]_{out}$ to address if the Kir4.1 effect by menthol activation, through TRPM8 receptor, was due to the increase in $[Ca^{2+}]_{in}$.

Figure 7c shows that the menthol perfusion in the absence of $[Ca^{2+}]_{out}$ did not have any effect on BK and Kir4.1, whereas 3 mM $[Ca^{2+}]_{out}$ elicited both currents ($n = 3$; Fig. 7c).

To address whether and how ionic channels influence U251 cell migration, we tested if the pharmacological inhibition of Kir and BK channels, alone or alongside the activation of TRPM8 channels by menthol, changed the percentage of scratch closure in wound healing assay. The effects were evaluated 24 h after the different experimental conditions illustrated in Fig. 8. A progressive inhibition of the migration was measured in cells exposed to Ibtx (100 nm) only and Ibtx combined with Barium (1 mM) alone or alongside the activation of TRPM8 channels by menthol (100 μm), whereas the treatment with menthol promoted migration.

Figure 9 shows the $I$–$V$ relationship closed to the $V_m$ for constitutive and menthol-sensitive currents. In the menthol-sensitive condition, the shift on the left in the BK activation potential caused an increased leakage of potassium currents at

$V_m$. The $V_m$ and $C_m$ values in cells with constitutive currents and after menthol perfusion are shown in Table 2; notably, after menthol perfusion, $C_m$ values increased.

### BK and Kir4.1 Immunostaining

In polarised cells, BK immunopositivity was present in both the cytoplasm and nucleus (Fig. 10a). The mean immunofluorescence density per cell was higher in the nucleus of cells
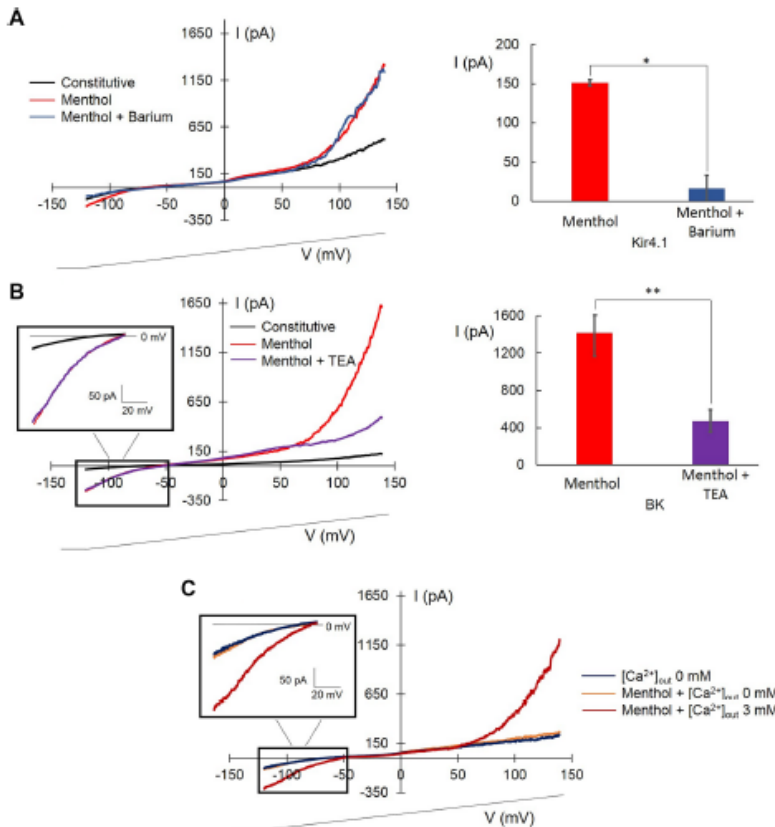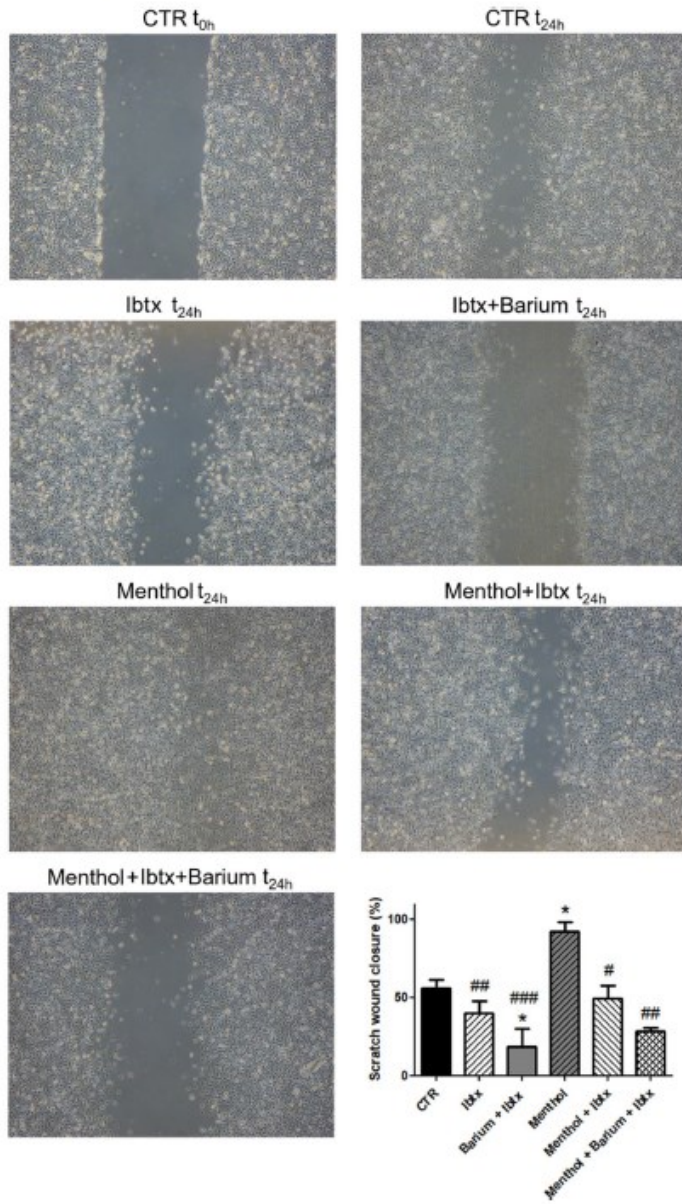
Fig. 8 Effect of the Kir4.1 and BK pharmacological inhibition on cell ▶ migration. Wound healing assay alone or alongside the activation of TRPM8 channels by menthol. Pictures after 24 h of continuous exposure in the different experimental conditions indicated in the figure. Concentrations used: Ibtx 100 nM; barium 1 mM; menthol 100 μM. The bar chart represents the analysis of scratch wound closure (%) at t1. *Statistical significance between control condition (CTR) and the other experimental conditions; #statistical significance between menthol condition and the other pharmacological experimental conditions. $p$ values: *$p<0.05$; **$p<0.01$



Fig. 7 Modulation of KIR4.1 and BK menthol-induced currents within wounded area. a, b Left: averaged experimental traces showing constitutive currents (black), 100 μM menthol (red), and menthol plus 1 mM barium (a, blue) or menthol plus 3 mM TEA (b, violet). Right: diagram showing the effect of barium at −120 mV ($n=4$, a) and TEA at +140 mV ($n=7$, b). In diagram are reported absolute values for KIR4.1. c Averaged experimental traces showing constitutive currents obtained with $[Ca^{2+}]_{out}$ 0 mM (dark blue), $[Ca^{2+}]_{out}$ 0 mM plus 100 μM menthol (orange), and $[Ca^{2+}]_{out}$ 3 mM plus menthol (dark red). The voltage-ramp protocol is shown at the bottom. $p$ values: *$p<0.05$; **$p<0.01$
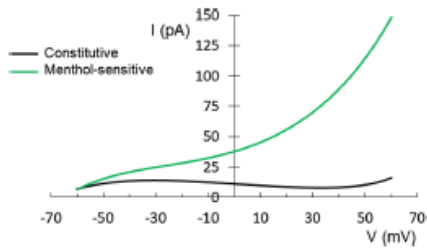
315

CTR $t_{0h}$

CTR $t_{24h}$

Ibtx $t_{24h}$

Ibtx+Barium $t_{24h}$

Menthol $t_{24h}$

Menthol+Ibtx $t_{24h}$

Menthol+Ibtx+Barium $t_{24h}$

**Fig. 9** IV relationship at physiological membrane potential before ($n = 46$) and after menthol application ($n = 15$)

OUT and IN the wounded area compared with basal condition (Fig. 10c). In the cytoplasm, a similar non-significant trend was observed.

Concerning Kir4.1, the immunopositivity was detected both in the cytoplasm and nucleus (Fig. 10b). The mean fluorescence density was higher both in the cytoplasm and nucleus of cells OUT the wounded area compared with basal condition (Fig. 10d). Therefore, scratch wounding triggered the increased expression of BK and Kir4.1 in the nucleus and cytoplasm. Notably, BK and Kir4.1 immunoreactions showed higher mean nuclear fluorescence density compared with that measured for the cytoplasm.

## Ultrastructural Analysis of BK and Kir4.1 Localisation

The EDTA-regressive technique revealed the ultrastructural localisation of BK and Kir4.1 channels. In the nucleus, the BK labelling was mainly detected near the heterochromatin rather than euchromatin. In particular, several marked spots were observed on RNA fibrils. The labelling of BK channel was also present in the cytoplasm and near the cell membrane. BK-positive membrane protrusions were also observed (Fig. 11Ab).

Ultrastructural analysis of Kir4.1 channels displayed a more heterogeneous localisation inside the nucleoplasm compared with BK. The Kir4.1 labelling was also detected near the cytoplasmic membrane and membrane vesicle (Fig. 11Bc,d).

## Discussion

In this study, the physiological roles of Kir4.1 and BK on the migration of U251 cells using perforated patch clamp recordings, immunostaining and TEM were investigated. Perforated patch technique was preferred to avoid rundown

of macroscopic currents, such as Kir4.1 currents, and to leave $[Ca^{2+}]_i$ free to change physiologically. To the best of our knowledge, this the first time the U251 cell line was studied under these physiological conditions.

Polarised cells resulted positive for active-Cdc42, a migration marker, and the immunopositivity progressively increased from basal to OUT to IN, whereas flattened cells were negative for active-Cdc42 immunostaining. Furthermore, in flattened cells we observed a spotted-like PCNA immunolabelling, whereas in polarised ones we observed a homogeneous staining, corroborating the "go-or-grow" phenotypic switch of GBM cells, a phenomenon described for brain tumours, where migration and proliferation are mutually exclusive behaviours (Hatzikirou et al. 2012). According to this hypothesis polarised cells exit the cell cycle and migrate, while flattened ones are actively cycling cells. Therefore, our focus was on polarised cells using the wound healing assay as a model of migration, and recording cells IN and OUT the wounded area.

Depolarised $V_m$ and high $R_m$ values in cells recorded IN and OUT the wounded area confirmed the undifferentiated state of these cells, indicating a low functional state of IR channels (Turner and Sontheimer 2014). In fact, the majority of U251 polarised cells recorded OUT the wounded area did not display either constitutive IR, confirming previous data (Olsen and Sontheimer 2008; Bordey et al. 2000; Bordey and Sontheimer 1998), or OR. Conversely, the majority of U251 migrated cells showed constitutively small IR and larger OR. Based on the pharmacological profile, biophysical features and immunocytochemistry, these currents were characterised as Kir4.1 and BK (Rosa et al. 2017). The data indicate the migration induced a functional activation of Kir4.1 and BK currents with amplitudes linearly related. A common mechanism triggering BK and Kir4.1 could be the increase in $[Ca^{2+}]_i$ that appears to be a conserved feature among migratory cells.

We tested our calcium hypothesis, by perfusing menthol, a TRPM8 agonist. Menthol perfusion IN the wounded area increased Kir4.1 and BK. The amplitude reached the same value in cells with and without constitutive currents, indicating TRPM8 activation and the consequent $[Ca^{2+}]_i$ elevation (Catacuzzeno et al. 2015), could reach a similar effect despite the difference in constitutive currents. The pharmacological block of BK and Kir41 channels, alone or alongside the activation of TRPM8 channels by menthol, inhibited the migration of U251 cells in wound healing assay demonstrating a direct role of these channels. In particular, the comparison between the inhibition induced by Ibtx alone and the inhibition caused by Ibtx combined with Barium demonstrated a direct role of both channels in migration process.
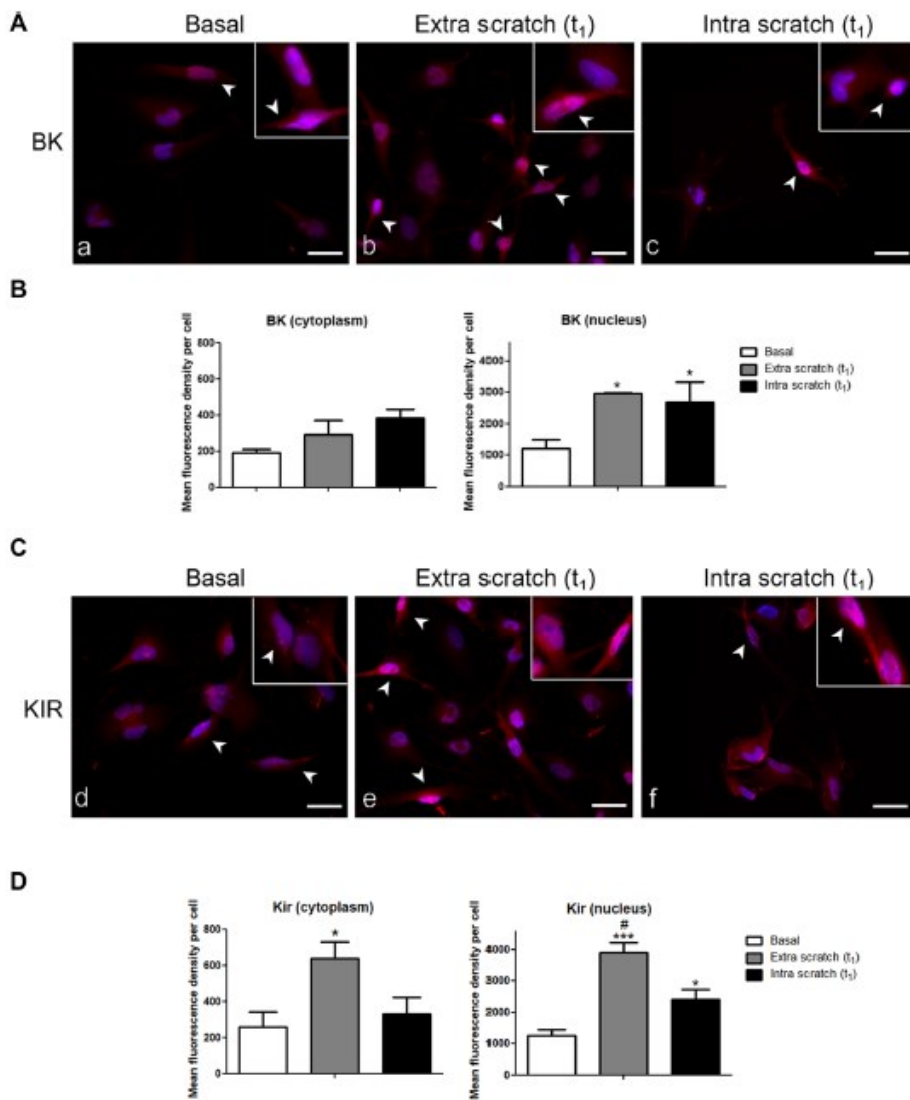
**Fig. 10** BK and KIR 4.1 Immunofluorescence staining. Micrographs showing the immunocytochemical detection of BK (**A**, red fluorescence) and Kir4.1 (**B**, red fluorescence) in the nucleus and cytoplasm of polarised cells at basal condition (a, d) and at t1, both outside (b, e) and within (c, f) the wounded area. Nuclei were counterstained with Hoechst 33,258 (blue fluorescence). Inserts: details of BK and Kir4.1 nuclear immunoreactivity. White arrowhead indicate polarised cells. Scale bar: 40 μm. Histograms show the mean fluorescent density per cell of BK (**C**) and Kir4.1 (**D**) in nucleus and cytoplasm. *statistical significance between cells at basal condition and at t1; #statistical significance between cells at t1 within and outside wounded area. $p$ values: *$p < 0.05$; **$p < 0.01$; ***$p < 0.001$

**Fig. 11** TEM ultrastructural analysis (EDTA-regressive staining technique): BK and KIR 4.1 channels localization. Transmission electron microscopy images obtained by EDTA-regressive staining technique. **A** Micrographs showing (a) nuclear BK labelling mainly detected closed to the heterochromatinic space, compared to euchromatin, and (b) cytoplasmic BK i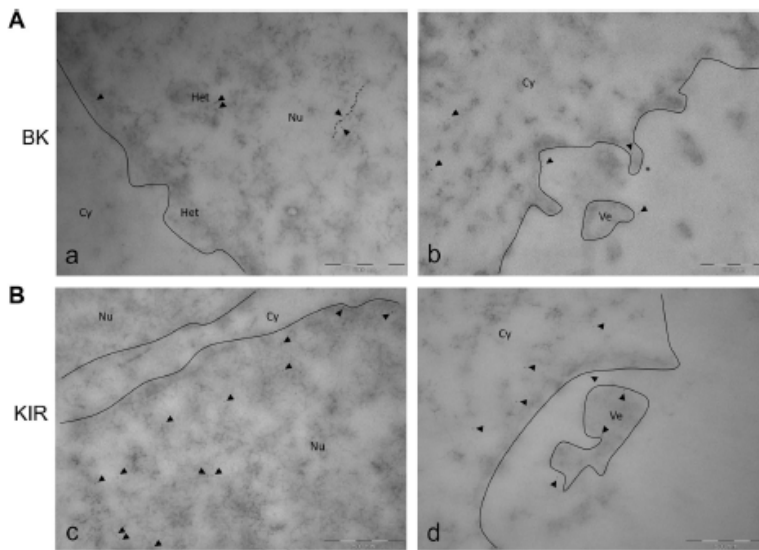mmunopositivity present nearby the cytoplasmic membrane, membrane protrusions (asterisk), also detectable in cell vesicles. **B** Micrographs showing (c) KIR 4.1 immunolabelling heterogeneously localised inside the nucleoplasm, and (d) cytoplasmic KIR 4.1 staining mostly present nearby the membrane and membrane vesicle. Continuous line: nuclear membrane. Black spots: Immunogold labelling for BK- and KIR 4.1; gold particles dimension: 6 nm (black arrowhead). Dashed line: RNA fibrils. *Cy* cytoplasm, *Nu* nucleus, *Het* heterochromatin, *Ve* vesicle. Bars: 500 nm

The calcium dependence of BK channels is well established and described by an increase in frequency and probability of channels to open (Ransom et al. 2002; Wondergem and Bartley 2009). However, data regarding the calcium dependence of KIR4.1 channels have not been published to date. It is feasible that a calcium-dependent mechanism caused the recruitment from the nucleus to the cell surface of Kir4.1, as suggested by nuclear compared to cytoplasm expression in immunocytochemistry, by the length of time required for the menthol effect in electrophysiological experiments (about 9 min), and by the electrophysiological experiments with different $[Ca^{2+}]_{out}$.

Due to the weak rectification of Kir4.1, a small $K^+$ leaky current (approximately 15 pA) was present at Vm, whereas after TRPM8 activation, the shift of the BK threshold at a more negative potential, probably caused by the increase of $[Ca^{2+}]_i$ (Barrett et al. 1982), elicited a greater increase of the leaky $K^+$ current.

Surprisingly, the amplitude of Kir4.1 and BK in migrated cells and after menthol perfusion displayed a linear relationship, indicating the increase in $[Ca^{2+}]i$ is a common molecular mechanism.

It should be noted that the expression of Kir4.1 channels was significantly reduced in U251 cells in all tested experimental conditions compared to the expression observed in normal astrocytes in physiological condition (Higashimori and Sontheimer 2007), in which Kir4.1 channels determine a more negative resting membrane potential. Therefore, only a small number of Kir4.1 channels were functionally active IN the wounded area, also after TRPM8 menthol activation.

The immunolabelling of BK and Kir4.1 channels was evident both in the cytoplasm and nucleus of GBM cells. The immunofluorescence density in the cytoplasm and nucleus was lower in the basal condition, however, was increased OUT and IN the wounded area. These data indicated that the scratch wounding was necessary and sufficient for triggering the expression of BK and Kir4.1 in the nucleus and cytoplasm. Furthermore, the immunofluorescence density IN and OUT the wounded area

was comparable, indicating channels expression both in migrated and non-migrated cells. Therefore, cells OUT the wounded area expressed Kir4.1 and BK; however, both channels were not in a functional state. In particular, Kir4.1 immunolabelling in the cytoplasm was present near the membrane and in membrane vesicles, whereas BK channels were also present in several protrusions.

TEM ultrastructural analysis revealed a heterogeneous labelling of Kir4.1 inside the nucleoplasm as previously described in D54MG (Olsen and Sontheimer 2004). Regarding BK immunostaining in the nucleosome (Li et al. 2014), the labelling was mainly detected close to the heterochromatin compared with euchromatin, suggesting a possible involvement of BK channels in chromatin remodelling.

In addition, data regarding the higher membrane capacitance value recorded in cells without currents (9 pF), with currents (29.9 pF) and after menthol modulation (43.8 pF) were intriguing. Thus, concerning migrated cells, we formulated the hypothesis that either gap junctions or larger lamellipodia, plasmatic actin-rich protrusions that contribute to cell migration and invasion (Abe et al. 2019), became electronically accessible to the patch clamp.

## Conclusion

The present study provides new insights on the physiological role and modulation of BK and Kir4.1 in U251 cells. Migrated cells displayed functional BK and a residual Kir4.1. $K^+$ leakage was present at the membrane potential of the cell and was exacerbated after application of menthol which modulated BK and Kir4.1, through a calcium-dependent mechanism. In two experimental conditions, i.e. during migration and after menthol modulation, the expression of Kir4.1 and BK channels was paired. We demonstrated the direct involvement of both BK and Kir4.1 channels in the migration, as evidences by the different wound closures percentages at t24h in the presence or the absence of channels activators or inhibitors.

The presence of nuclear Kir4.1 and BK channels was shown, further confirmed by ultrastructural analyses using TEM.

The functional role of nuclear Kir4.1 and BK channels and the menthol modulation of Kir4.1 are currently under investigation. These novel findings can aid in designing new therapeutic strategies targeting ion channels to stop the invasiveness of GBM cells in surrounding healthy tissues.

**Author's Contributions** Study concepts and design: Paola Rossi, Maria Grazia Bottone, Elisa Roda; Data acquisition, analysis and interpretation: Daniela Ratto, Beatrice Ferrari, Stella Siciliani; Quality control of data: Paola Veneroni, Filippo Cobelli, Erica Cecilia Priori; Statistical analysis: Fabrizio De Luca, Carmine Di Iorio; Manuscript preparation: Paola Rossi, Elisa Roda, Daniela Ratto, Beatrice Ferrari; Manuscript editing: Paola Rossi, Federico Brandalise, Daniela Ratto; Manuscript review: Elisa Roda, Maria Grazia Bottone.

## Compliance with Ethical Standards

## References

Abe T, La TM, Miyagaki Y, Oya E, Wei FY, Sumida K, Fujise K, Takeda T, Tomizawa K, Takei K, Yamada H (2019) Phosphorylation of cortactin by cyclin-dependent kinase 5 modulates actin bundling by the dynamin 1-cortactin ring-like complex and formation of filopodia and lamellipodia in NG108-15 glioma-derived cells. Int J Oncol 54:550–558. https://doi.org/10.3892/ijo.2018.4663

Barrett JN, Magleby KL, Pallotta BS (1982) Properties of single calcium-activated potassium channels in cultured rat muscle. J Physiol 331:211–230. https://doi.org/10.1113/jphysiol.1982.sp014370

Bordey A, Sontheimer H (1998) Electrophysiological properties of human astrocytic tumor cells in situ: enigma of spiking astrocytes. J. Neurophysiol 79:2782–2793. https://doi.org/10.1152/jn.1998.79.5.2782

Bordey A, Sontheimer H, Trouslard J (2000) Muscarinic activation of BK channels induces membrane oscillations in glioma cells and leads to inhibition of cell migration. J Membr Biol 176:31–40. https://doi.org/10.1007/s002320001073

Brandalise F, Lujan R, Leone R, Lodola F, Cesaroni V, Romano C, Gerber U, Rossi P (2016) Distinct expression patterns of inwardly rectifying potassium currents in developing cerebellar granule cells of the hemispheres and the vermis. EurJ Neurosci 43:1460–1473. https://doi.org/10.1111/ejn.13219

Butt AM, Kalsi A (2006) Inwardly rectifying potassium channels (Kir) in central nervous system glia: a special role for Kir4.1 in glial functions. J Cell Mol Med 10:33–44. https://doi.org/10.1111/j.1582-4934.2006.tb00289.x

Catacuzzeno L, Aiello F, Fioretti B, Sforna L, Castigli E, Ruggieri P, Tata AM, Calogero A, Franciolini F (2011) Serum-activated K and Cl currents underlay U87-MG glioblastoma cell migration. J Cell Physiol 226:1926–1933. https://doi.org/10.1002/jcp.22523

Catacuzzeno L, Caramia M, Sforna L, Belia S, Guglielmi L, D'Adamo MC, Pessia M, Franciolini F (2015) Reconciling the discrepancies on the involvement of large-conductance Ca(2+)-activated K channels in glioblastoma cell migration. Front Cell Neurosci 9:152. https://doi.org/10.3389/fncel.2015.00152

Chever O, Djukic B, McCarthy KD, Amzica F (2010) Implication of Kir4.1 channel in excess potassium clearance: an in vivo study on anesthetized glial-conditional Kir4.1 knock-out mice.

J Neurosci 30:15769–15777. https://doi.org/10.1523/JNEUROSCI.2078-10.2010

D'Angelo E, Rossi P, Garthwaite J (1990) Dual-component NMDA receptor currents at a single central synapse. Nature 346:467–470. https://doi.org/10.1038/346467a0

Dellaire G, Ching RW, Dehghani H, Ren Y, Bazett-Jones DP (2006) The number of PML nuclear bodies increases in early S phase by a fission mechanism. J Cell Sci 119:1026–1033. https://doi.org/10.1242/jcs.02816

Ferrari B, Urselli F, Gilodi M, Camuso S, Priori EC, Rangone B, Ravera M, Veneroni P, Zanellato I, Roda E, Osella D, Bottone MG (2019) New platinum-based prodrug Pt(IV)Ac-POA: antitumour effects in rat C6 glioblastoma cells. Neurotoxicol Res. https://doi.org/10.1007/s12640-019-00076-0

Hatzikirou H, Basanta D, Simon M, Schaller K, Deutsch A (2012) 'Go or Grow': the key to the emergence of invasion in tumour progression? Math Med Biol 29:49–65. https://doi.org/10.1093/imammb/dqq011

Higashimori H, Sontheimer H (2007) Role of Kir4.1 channels in growth control of glia. Glia 55:1668–1679. https://doi.org/10.1002/glia.20574

Hille B, Schwarz W (1978) Potassium channels as multi-ion single-file pores. J Gen Physiol 72:409–442. https://doi.org/10.1085/jgp.72.4.409

Holland EC (2001) Progenitor cells and glioma formation. Curr Opin Neurol 14:683–638. https://doi.org/10.1097/00019052-200112000-00002

Horn R, Marty A (1988) Muscarinic activation of ionic currents measured by a new whole-cell recording method. J Gen Physiol 92:145–159. https://doi.org/10.1085/jgp.92.2.145

Leonhardt H, Rahn HP, Weinzierl P, Sporbert A, Cremer T, Zink D, Cardoso MC (2000) Dynamics of DNA replication factories in living cells. J Cell Biol 149:271–280. https://doi.org/10.1083/jcb.149.2.271

Li B, Jie W, Huang L, Wei P, Li S, Luo Z, Friedman AK, Meredith AL, Han MH, Zhu XH, Gao TM (2014) Nuclear BK channels regulate gene expression via the control of nuclear calcium signaling. Nat Neurosci 17:1055–1063. https://doi.org/10.1038/nn.3744

Maher EA, Furnari FB, Bachoo RM, Rowitch DH, Louis DN, Cavenee WK, DePinho RA (2001) Malignant glioma: genetics and biology of a grave matter. Genes Dev 15:1311–1313. https://doi.org/10.1101/gad.891601

Masiello I, Biggiogera M (2017) Ultrastructural localization of 5-methylcytosine on DNA and RNA. Cell Mol Life Sci 74:3057–3064. https://doi.org/10.1007/s00018-017-2521-1

McFerrin MB, Sontheimer H (2006) A role for ion channels in glioma cell invasion. Neuron Glia Biol 2:39–49. https://doi.org/10.1017/S1744925X06000044

Nwaobi SE, Cuddapah VA, Patterson KC, Randolph AC, Olsen ML (2016) The role of glial-specific Kir4.1 in normal and pathological states of the CNS. Acta Neuropathol 132:1–21. https://doi.org/10.1007/s00401-016-1553-1

Olsen ML, Sontheimer H (2004) Mislocalization of Kir channels in malignant glia. Glia 46:63–73. https://doi.org/10.1002/glia.10346

Olsen ML, Sontheimer H (2008) Functional implications for Kir4.1 channels in glial biology: from K+ buffering to cell differentiation. J Neurochem 107:589–601. https://doi.org/10.1111/j.1471-4159.2008.05615.x

Rangone B, Ferrari B, Astesana V, Masiello I, Veneroni P, Zanellato I, Osella D, Bottone MG (2018) A new platinum-based prodrug candidate: Its anticancer effects in B50 neuroblastoma rat cells. Life Sci 210:166–176. https://doi.org/10.1016/j.lfs.2018.08.048

Ransom BR (2000) Glial modulation of neural excitability mediated by extracellular pH: a hypothesis revisited. Prog Brain Res 125:217–228. https://doi.org/10.1016/S0079-6123(00)25012-7

Ransom CB, Sontheimer H (2001) BK channels in human glioma cells. J Neurophysiol 85:790–803. https://doi.org/10.1152/jn.2001.85.2.790

Ransom CB, Liu X, Sontheimer H (2002) BK channels in human glioma cells have enhanced calcium sensitivity. Glia 38:281–291. https://doi.org/10.1002/glia.10064

Rosa P, Sforna L, Carlomagno S, Mangino G, Miscusi M, Pessia M, Franciolini F, Calogero A, Catacuzzeno L (2017) Over-expression of large-conductance calcium-activated potassium channels in human glioblastoma stem-like cells and their role in cell migration. J Cell Physiol 232:2478–2488. https://doi.org/10.1002/jcp.25592

Rossi P, D'Angelo E, Taglietti V (1996) Differential long-lasting potentiation of the NMDA and non-NMDA synaptic currents induced by metabotropic and NMDA receptor coactivation in cerebellar granule cells. Eur J Neurosci 8:1182–1189. https://doi.org/10.1111/j.1460-9568.1996.tb01286.x

Rossi P, De Filippi G, Armano S, Taglietti V, D'Angelo E (1998) The weaver mutation causes a loss of Inward Rectifier current regulation in premigratory granule cells of the mouse cerebellum. J Neurosci 18:3537–3547. https://doi.org/10.1523/JNEUROSCI.18-10-03537.1998

Rossi P, Mapelli L, Roggeri L, Gall D, de Kerchove DA, Schiffmann SN, Taglietti V, D'Angelo E (2006) Inhibition of constitutive inward rectifier currents in cerebellar granule cells by pharmacological and synaptic activation of GABA receptors. Eur J Neurosci 24:419–432. https://doi.org/10.1111/j.1460-9568.2006.04914.x

Schönenberger F, Deutzmann A, Ferrando-May E, Merhof D (2015) Discrimination of cell cycle phases in PCNA-immunolabeled cells. BMC Bioinform 16:180. https://doi.org/10.1186/s12859-015-0618-9

Soroceanu L, Manning TJ Jr, Sontheimer H (1999) Modulation of glioma cell migration and invasionusing Cl− and K+ ion channel blockers. J Neurosci 19:5942–5954. https://doi.org/10.1523/JNEUROSCI.19-14-05942.1999

Thuringer D, Chanteloup G, Boucher J, Pernet N, Boudesco C, Jego G, Chatelier A, Bois P, Gobbo J, Cronier L, Solary E, Garrido C (2017) Modulation of the inwardly rectifying potassium channel Kir4.1 by the pro-invasive miR-5096 in glioblastoma cells. Oncotarget 8:37681–37693. https://doi.org/10.18632/oncotarget.16949

Turner KL, Sontheimer H (2014) Cl and K channels and their role in primary brain tumour biology. Phil Trans R Soc 369:20130095. https://doi.org/10.1098/rstb.2013.0095

Warth A, Mittelbronn M, Wolburg H (2005) Redistribution of the water channel protein aquaporin-4 and the K+ channel protein Kir4.1 differs in low- and high-grade human brain tumors. Acta Neuropathol 109:418–426. https://doi.org/10.1007/s00401-005-0984-x

Wondergem R, Bartley JW (2009) Menthol increases human glioblastoma intracellular $Ca^{2+}$, BK channel activity and cell migration. J Biomed Sci 16:90. https://doi.org/10.1186/1423-0127-16-90

Zeng J, Wu Y, Zhuang S, Qin L, Hua S, Mungur R, Pan J, Zhu Y, Zhan R (2019) Identification of the role of TRPM8 in glioblastoma and its effect on proliferation, apoptosis and invasion of the U251 human glioblastoma cell line. Oncol Rep 42:1517–1526. https://doi.org/10.3892/or.2019.7260

Zurolo E, de Groot M, Iyer A, Anink J, van Vliet EA, Heimans JJ, Reijneveld JC, Gorter JA, Aronica E (2012) Regulation of Kir4.1 expression in astrocytes and astrocytic tumors: a role for interleukin-1 beta. J Neuroinflammation 9:280. https://doi.org/10.1186/1742-2094-9-280

# Deeper and Deeper on the Role of BK and Kir4.1 Channels in Glioblastoma Invasiveness: A Novel Summative Mechanism?

Federico Brandalise[1]*, Daniela Ratto[2], Roberta Leone[1], Federico Olivero[2], Elisa Roda[2,3], Carlo Alessandro Locatelli[3], Maria Grazia Bottone[2] and Paola Rossi[2]

[1] Department of Fundamental Neurosciences (NEUFO), University of Geneva, Geneva, Switzerland, [2] Department of Biology and Biotechnology "L. Spallanzani," University of Pavia, Pavia, Italy, [3] Pavia Poison Centre, National Toxicology Information Centre, Laboratory of Clinical & Experimental Toxicology, Toxicology Unit, Istituti Clinici Scientifici Maugeri IRCCS, Pavia, Italy

In the last decades, increasing evidence has revealed that a large number of channel protein and ion pumps exhibit impaired expression in cancers. This dysregulation is responsible for high proliferative rates as well as migration and invasiveness, reflected in the recently coined term oncochannelopathies. In glioblastoma (GBM), the most invasive and aggressive primary brain tumor, GBM cells modify their ionic equilibrium in order to change their volume as a necessary step prior to migration. This mechanism involves increased expression of BK channels and downregulation of the normally widespread Kir4.1 channels, as noted in GBM biopsies from patients. Despite a large body of work implicating BK channels in migration in response to an artificial intracellular calcium rise, little is known about how this channel acts in GBM cells at resting membrane potential (RMP), as compared to other channels that are constitutively open, such as Kir4.1. In this review we propose that a residual fraction of functionally active Kir4.1 channels mediates a small, but continuous, efflux of potassium at the more depolarized RMP of GBM cells. In addition, coinciding with transient membrane deformation and the intracellular rise in calcium concentration, brief activity of BK channels can induce massive and rapid cytosolic water loss that reduces cell volume (cell shrinkage), a necessary step for migration within the brain parenchyma.

**Keywords: glioblastoma, Kir4.1, BK channel, cancer, channelopathy**

## INTRODUCTION

Glioblastoma (GBM, WHO grade IV astrocytoma) is the most common and malignant brain tumor (Brat et al., 2007; Furnari et al., 2007; Barbieri et al., 2018). In comparison to the majority of solid tumors, it is characterized by strong invasive and pro-angiogenic behavior associated with a poor prognosis with a median survival rate of about 15 months (Stupp et al., 2009). Because of the diffuse and aggressive invasiveness of GBM, it is generally not possible to achieve complete surgical resection, resulting in rapid relapse (Holland, 2001; Maher et al., 2001). Furthermore,

322

GBMs contain a small subpopulation of so-called cancer stem cells (CSCs), which are extremely resistant to radio and chemotherapy (Vescovi et al., 2006; Lathia et al., 2011). Death evasion minimizes the effect of all therapeutic strategies currently available, but enhanced invasiveness is the major feature that prevents successful treatment (Louis et al., 2007).

## GLIOBLASTOMA AS A CHANNELOPATHY: THE ROLE OF CHLORIDE AND POTASSIUM IONIC EQUILIBRIUM IN GBM CELL INVASIVENESS

Glioblastoma cells migrate through narrow spaces in the brain parenchyma (De Vleeschouwer and Bergers, 2017) that are usually smaller than the soma of the cell (around 8 μm in diameter, Liu et al., 2018). To make that possible, GBM cells undergo a reduction in their volume of about 30% facilitating migration and invasion (Demuth and Berens, 2004; Armento et al., 2017). Such shrinkage is achieved by modifying the osmotic equilibrium in the cell allowing a net release of cytoplasmic water. Increasing evidence suggests that specific ion channels and transporters are involved in modulating the cell volume. The two main ionic gradients reported to be altered in glioma cells are for chloride (Cl⁻) and potassium (K⁺) ions (Turner et al., 2014).

In contrast to other neurons in the brain, glioma cells have a higher cytosolic Cl⁻ concentration (Habela et al., 2009). The chloride gradient is maintained and modulated by persistent activity of the Na⁺/K⁺/Cl⁻ cotransporter 1 (NKCC1), hence its expression has been linked with GBM invasiveness and severity grade (Garzon-Muvdi et al., 2012). The overexpression of the NKCC1 cotransporter leads to abnormal accumulation of Cl⁻ in the glioma cell cytosol (Haas and Sontheimer, 2010; Ben-Ari, 2017) so that upon opening of Cl⁻ channels (Barbieri et al., 2018), the altered electrochemical gradient results in an outward flow of this ion with concomitant osmotic loss of water from the intracellular milieu (through the aquaporin channels). The net result is a loss of cellular volume (Luo et al., 2020).

Along with Cl⁻ gradient, the altered K⁺ flux is also essential for invasion. In fact, due to the cytosolic calcium fluctuations during GBM cells migration, members of the family of Ca²⁺-activated K⁺ channels such as KCa3.1 (intermediate conductance K⁺ channel) and the BK channel (large conductance K⁺ channel), are overexpressed in 32% of glioma patients, and there is a linear correlation between the expression of these channels and the progression of the pathology. Due to their calcium sensitivity, it has been shown that such channels respond positively to bradykinin activation that increases intracellular Ca²⁺, with a resulting efflux of K⁺ and water (Reetz and Reiser, 1996; Catacuzzeno and Franciolini, 2018). As a consequence, the glioma cells reduce their total volume, which enables them to migrate through narrow spaces within the brain.

While the importance of the intermediate conductance K⁺ channel in GBM progression has been recently summarized in several works (Catacuzzeno et al., 2012; D'Alessandro et al., 2018;

Liu et al., 2019), the aim of this review is to underline the contributions of BK channels and Kir4.1 channels on GBM invasiveness, focusing on their biophysical properties and their osmo-electric effect at the RMP in GBM cells.

## THE BK CHANNEL: FROM STRUCTURE TO PHYSIOLOGY IN GLIOBLASTOMA CHANNELOPATHY

The BK channel is a tetrameric, large conductance K⁺ channel, widely expressed in both neurons and glia across development and adulthood (for an extensive review see Lee and Cui, 2010). The BK channel is characterized by an outwardly rectifying current that shows both voltage and calcium-concentration sensitivity (Nardi and Olesen, 2008; Cui et al., 2009).

Overexpression of this channel has been reported in biopsies of glioblastoma patients (Liu et al., 2002; Catacuzzeno et al., 2015) and intriguingly the channel structure also seems to be altered, since Ransom et al. (2002) reported that GBM cells expressed a splicing variant of the channel on the *hSlo* (the gene linked to the encoding part of the alpha subunit) with a consequent increase in the sensitivity to intracellular calcium concentration.

Intracellular calcium dynamics are involved in the regulation of a wide number of processes in the brain that span from synaptic plasticity (Brandalise and Gerber, 2014; Brandalise et al., 2016a; Keck et al., 2017) to remodeling of cytoskeleton (Lebart and Benyamin, 2006; Correll et al., 2008). In GBM it has been demonstrated that calcium fluctuations from the intracellular stores (reticulum) along with different states of the RMP (depolarized versus hyperpolarized) are linked to GBM cell migration as well as to the proliferative state of the cell (Rondé et al., 2000; Ishiuchi et al., 2002; Catacuzzeno et al., 2011). Cyclic variation of both voltage and calcium concentration in GBM cells has led to the hypothesis that BK channels, in light of their overexpression, can be one of the key targets in triggering glioblastoma migration and the invasion process (Catacuzzeno et al., 2015).

## TRYING TO EXPLAIN THE BK ROLE AT THE GBM RMP

The implication of BK channels in GBM cell migration and invasion has been reported by various groups (Klumpp et al., 2018; Rosa et al., 2018). Blockade of BK channels with iberiotoxin (IbTx) or tetraethylammonium (TEA) in two- dimensional migration assays inhibits GBM cell motility (Soroceanu et al., 1999; Basrai et al., 2002; Weaver et al., 2006). Furthermore, the increase of intracellular calcium induced by extracellular menthol application significantly increases BK current and the migration of GBM cells and this effect was reversed by BK channel blockers (Wondergem and Bartley, 2009; Ratto et al., 2019).

However, despite the known functional upregulation of BK channels in GBM, their dependence on membrane potential deserves further examination. At resting cytoplasmic free calcium concentration (10–100 nM), BK channels open only at membrane

potentials above +10 mV (Lee and Cui, 2010), significantly more depolarized than the RMP of around −40 mV measured in GBM cells (Catacuzzeno et al., 2015). In other words, BK channels at RPM are in the closed state. Additionally, in the two-dimensional migration assay, there is a general consensus that blockade of BK channels does not significantly reduce migration of GBM cells. Nevertheless, the reduction of GBM cell invasion due to BK pharmacological blockade is effective only when the intracellular calcium concentration is raised (for example, by menthol or acetylcholine bath application) (Bordey et al., 2000; Kraft et al., 2003; Wondergem and Bartley, 2009). Therefore, although activating BK channels undoubtedly boosts GBM cell migration due to K$^+$ efflux, the blockade of the same conductance under resting conditions does not prevent GBM invasiveness.

## Kir4.1 IN GLOBLASTOMA: PRIMUM MOVENS OF RMP DEPOLARIZATION IN GBM CELLS?

Kir4.1, one of the inwardly rectifying potassium channels (coded by the KCNJ10 gene) is largely expressed in the glia cells of the brain (Nichols and Lopatin, 1997). In mature astrocytes, the high potassium permeability is mediated to a large extent by the Kir4.1 channel with two functional consequences: first, the negative RMP that is closer to the potassium equilibrium potential, and, second, the buffering of extracellular potassium after neuronal activity (Butt and Kalsi, 2006; Chever et al., 2010). Because a fraction of the channels is constitutively open, it has been proven that Kir4.1 plays a role in the homeostatic regulation of the RMP : for example, this is a crucial mechanism in cerebellar granule cell development during migration (Rossi et al., 1998; Brandalise et al., 2016b) as well as for glia maturation that settles the RMP at around −80 mV (Olsen and Sontheimer, 2008). Their peculiar current/voltage relation (**Figure 1A**) is due to weak, voltage-dependent rectification and to voltage-dependent pore block, from the internal side of the channel, by magnesium and other organic cations such as polyamine (Ruppersberg, 2000). At potentials more positive to the K$^+$ equilibrium, this block limits the amount of K$^+$ that flows through the channel. Kir4.1 is also involved in the regulation of other pathways in astrocytes such as the BDNF expression (Ohno et al., 2018).

In GBM, a downregulation of Kir4.1 during the early stage of the tumor progression has been reported (Olsen and Sontheimer, 2004; Ratto et al., 2019), which is correlated to the dramatic shift in RMP of GBM cells to more depolarized values around −40/−30 mV (Olsen and Sontheimer, 2004). Due to their internalization during GBM progression, very little attention has been paid to the residual activity of the Kir4.1 channels at RMP. However, recent investigations have provided evidence that justifies a reconsideration of the impact of this channel on the later progression of GBM:

- Despite the internalization and consequent functional downregulation of Kir4.1, there is still a significant fraction of this channel expressed in the membrane which, at the RMP of GBM cells, mediates a constitutive outward

K$^+$ current (**Figure 1B**) that might play a role in the redistribution of cell volume and the consequent change in cell morphology.
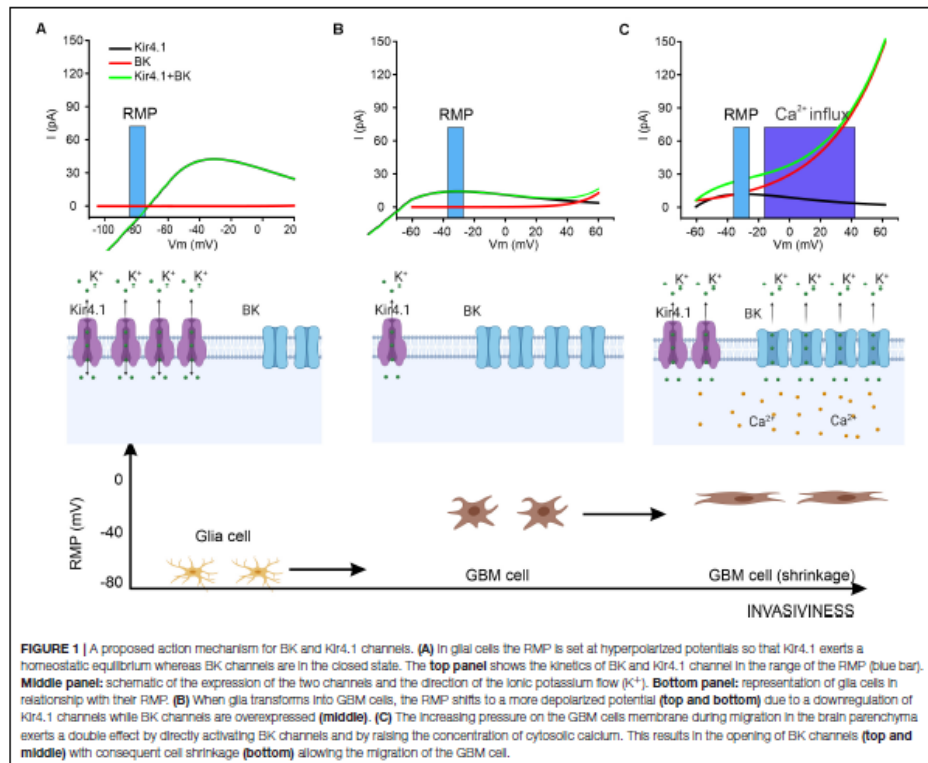- The fact that the channels are internalized but not degraded suggests that they still have a functional role as a readily available pool that is potentially re-inserted into the membrane in a relatively short time. Indeed, despite the fact that the mechanism is not yet understood, in Ratto et al., 2019, a calcium-dependent upregulation of Kir4.1-mediated current has been described within 9 min of menthol bath-application.
- The simultaneous block of Kir4.1 along with the BK channel seems to be an effective strategy for blocking GBM cell invasiveness in two-dimensional migration assays without additional perturbation (raising) of the cytosolic calcium concentration (Ratto et al., 2019). This suggests that the two classes of potassium channels are mutually involved in the shrinkage of the cell via regulation of the K$^+$ gradient.

## Kir4.1 AND BK CHANNELS: A SUMMATIVE LINK?

In the previous sections, we have summarized the literature on the role of BK and Kir4.1 channels in GBM invasiveness. We have linked the physiology of these two channels relating to the microenvironment of GBM cells (with particular interest in the K$^+$ electrical and osmotic gradient) raising some discrepancies between the channel biophysical properties and the electrochemical equilibrium range of GBM cells.

Now we tentatively propose how these two channels might work in concert during GBM cell invasion:

(1) Glia cells under physiological conditions: glia cells express a fairly high level of Kir4.1 that is known to be involved in ionic homeostasis by buffering ambient K$^+$ during neuronal activity. Moreover, glia cells have a strongly hyperpolarized RMP maintained mainly by Kir4.1 (the reversing potential of Kir4.1 in normal conditions is around −75/−80 mV). BK channels, on the other hand, are also expressed but are not activate at in the RMP (**Figure 1A**).

(2) Morphological changes in GBM cells: the severe alterations in Cl$^-$ and K$^+$ equilibrium in the cells prior to migration leads to a more depolarized RMP (−40 to −30 mV). Consequently, the reversal potential of Kir4.1 is no longer aligned with the RMP, and this sets the channel for a constitutively net outflow of K$^+$ ions (see **Figure 1B**). It is worth noting that in basal conditions, GBM cells seem to change their shape due to the efflux of water, but the total surface area of the cell is actually not reduced, probably due to the formation of lamellipodia. In this phase, BK channels are overexpressed in their spliced isoforms, which increases their sensitivity to the calcium concentration. Therefore, despite the fact that the RMP is still below the BK threshold, transient cytosolic

**FIGURE 1 |** A proposed action mechanism for BK and Kir4.1 channels. **(A)** In glial cells the RMP is set at hyperpolarized potentials so that Kir4.1 exerts a homeostatic equilibrium whereas BK channels are in the closed state. The **top panel** shows the kinetics of BK and Kir4.1 channel in the range of the RMP (blue bar). **Middle panel:** schematic of the expression of the two channels and the direction of the ionic potassium flow ($K^+$). **Bottom panel:** representation of glia cells in relationship with their RMP. **(B)** When glia transforms into GBM cells, the RMP shifts to a more depolarized potential **(top and bottom)** due to a downregulation of Kir4.1 channels while BK channels are overexpressed **(middle)**. **(C)** The increasing pressure on the GBM cells membrane during migration in the brain parenchyma exerts a double effect by directly activating BK channels and by raising the concentration of cytosolic calcium. This results in the opening of BK channels **(top and middle)** with consequent cell shrinkage **(bottom)** allowing the migration of the GBM cell.

calcium rise (Catacuzzeno et al., 2011; Li et al., 2020) could depolarize the cell and shift the activation curve to a more hyperpolarized potential allowing a transient opening of BK channels (**Figure 1C**). Under these conditions, BK channels can contribute efficiently and summate with Kir4.1 channels in controlling total efflux of potassium and consequent shrinkage. This scenario agrees with recent experimental evidence whereby blocking Kir4.1 and BK channels reduces GBM cell migration.

(3) Glioblastoma invasiveness in the brain parenchyma: When a GBM cell invades the extracellular matrix in the brain, the process requires a reduction of cytosolic volume. The increase in pressure that the extracellular matrix exerts on the GBM cell induces mechanical stress on the membrane, which has been suggested to activate BK channels (Zhao et al., 2010; Wawrzkiewicz-Jałowiecka et al., 2018). Moreover, this mechanical constraint might lead to a possible biochemical cascade with a consequent increase of intracellular calcium concentration that shifts the voltage

activation curve of the channel to a more hyperpolarized potential (Charles et al., 1991). Overall, increased pressure on the GBM cell membrane results in greater functional BK channel activation that significantly increases the efflux of cytosolic water with consequent additional reduction in volume and capability to migrate efficiently (**Figure 1C**). Following the mechanical compression, the relief of pressure reduces the fraction of active BK channels and the balance of activation between the two channels returns to the state described in point 2 (**Figure 1B**).

## CONCLUSION

This review has not only the purpose of summarizing the most recent evidence on the role of BK and Kir4.1 channels in GBM cell-migration, but underlines the need for examining the roles of these channels in the context of the different functional states of GBM cells. The emerging perspective that considers GBM

325

as a channelopathy is a promising field (Litan and Langhans, 2015; Prevarskaya et al., 2018). However, many questions must be yet addressed for a more comprehensive understanding. The intracellular calcium concentration and its spontaneous oscillations seem to be the main actor behind the scenes as it modulates a large fraction of the ion channels implicated in GBM invasion. Furthermore, recent work has proposed that BK channels are modulated by mechanical stress on the membrane indicating that the dynamics of GBM cell membrane changes must be investigated. Finally, $K^+$ equilibrium is a result of the interactions between a large variety of channels and pumps; in this review we focused on BK and Kir4.1 on account of their high conductance and their roles at RMP, respectively. However, for deeper insight into GBM cell invasiveness, future investigations should take into account other channels as well, such as intermediate conductance calcium-activated potassium channels and leak channels. In conclusion, a large number of potassium channels play a key role in GBM progression. However, despite that potassium channels offer a surface-accessible therapeutic target, the fact that they are largely expressed in other cell types such as neurons, glia and cardiomyocytes imposes a strong monitoring of the acceptable toxicity threshold induced by potentials specific blockers as a side effect.

## REFERENCES

Armento, A., Ehlers, J., Schötterl, S., and Naumann, U. (2017). *Molecular Mechanisms of Glioma Cell Motility*. Brisbane: Exon Publications, 73–93.

Barbieri, F., Würth, R., Pattarozzi, A., Verduci, I., Mazzola, C., Cattaneo, M. G., et al. (2018). Inhibition of chloride intracellular channel 1 (CLIC1) as biguanide class-effect to impair human glioblastoma stem cell viability. *Front. Pharmacol.* 9:899. doi: 10.3389/fphar.2018.00899

Basrai, D., Kraft, R., Bollensdorff, C., Liebmann, L., Benndorf, K., and Patt, S. (2002). BK channel blockers inhibit potassium-induced proliferation of human astrocytoma cells. *Neuroreport* 13, 403–407. doi: 10.1097/00001756-200203250-00008

Ben-Ari, Y. (2017). NKCC1 chloride importer antagonists attenuate many neurological and psychiatric disorders. *Trends Neurosci.* 40, 536–554. doi: 10.1016/j.tins.2017.07.001

Bordey, A., Sontheimer, H., and Trouslard, J. (2000). Muscarinic activation of BK channels induces membrane oscillations in glioma cells and leads to inhibition of cell migration. *J. Membr. Biol.* 176, 31–40. doi: 10.1007/s00232001073

Brandalise, F., Carta, S., Helmchen, F., Lisman, J., and Gerber, U. (2016a). Dendritic NMDA spikes are necessary for timing-dependent associative LTP in CA3 pyramidal cells. *Nat. Commun.* 7, 1–9.

Brandalise, F., and Gerber, U. (2014). Mossy fiber-evoked subthreshold responses induce timing-dependent plasticity at hippocampal CA3 recurrent synapses. *Proc. Natl. Acad. Sci. U.S.A.* 111, 4303–4308. doi: 10.1073/pnas.1317667111

Brandalise, F., Lujan, R., Leone, R., Lodola, F., Cesaroni, V., Romano, C., et al. (2016b). Distinct expression patterns of inwardly rectifying potassium currents in developing cerebellar granule cells of the hemispheres and the vermis. *Eur. J. Neurosci.* 43, 1460–1473. doi: 10.1111/ejn.13219

Brat, D. J., Scheithauer, B. W., Fuller, G. N., and Tihan, T. (2007). Newly codified glial neoplasms of the 2007 WHO classification of tumours of the central nervous system: angiocentric glioma, pilomyxoid astrocytoma and pituicytoma. *Brain Pathol.* 17, 319–324. doi: 10.1111/j.1750-3639.2007.00082.x

Butt, A. M., and Kalsi, A. (2006). Inwardly rectifying potassium channels (Kir) in central nervous system glia: a special role for Kir4.1 in glial functions. *J. Cell. Mol. Med.* 10, 33–44. doi: 10.1111/j.1582-4934.2006.tb00289.x

Catacuzzeno, L., Aiello, F., Fioretti, B., Sforna, L., Castigli, E., Ruggieri, P., et al. (2011). Serum-activated K and Cl currents underlay U87-MG glioblastoma cell migration. *J. Cell. Physiol.* 226, 1926–1933. doi: 10.1002/jcp.22523

Catacuzzeno, L., Caramia, M., Sforna, L., Belia, S., Guglielmi, L., D'Adamo, M. C., et al. (2015). Reconciling the discrepancies on the involvement of large-conductance Ca2+-activated K channels in glioblastoma cell migration. *Front. Cell. Neurosci.* 9:152. doi: 10.3389/fncel.2015.00152

Catacuzzeno, L., Fioretti, B., and Franciolini, F. (2012). Expression and role of the intermediate-conductance calcium-activated potassium channel KCa3. 1 in glioblastoma. *J. Signal Transduct.* 2012:421564.

Catacuzzeno, L., and Franciolini, F. (2018). Role of KCa3. 1 channels in modulating ca2+ oscillations during glioblastoma cell migration and invasion. *Int. J. Mol. Sci.* 19:2970. doi: 10.3390/ijms19102970

Charles, A. C., Merrill, J. E., Dirksen, E. R., and Sandersont, M. J. (1991). Intercellular signaling in glial cells: calcium waves and oscillations in response to mechanical stimulation and glutamate. *Neuron* 6, 983–992. doi: 10.1016/0896-6273(91)90238-u

Chever, O., Djukic, B., McCarthy, K. D., and Amzica, F. (2010). Implication of Kir4. 1 channel in excess potassium clearance: an in vivo study on anesthetized glial-conditional Kir4. 1 knock-out mice. *J. Neurosci.* 30, 15769–15777. doi: 10.1523/jneurosci.2078-10.2010

Correll, R. N., Pang, C., Niedowicz, D. M., Finlin, B. S., and Andres, D. A. (2008). The RGK family of GTP-binding proteins: regulators of voltage-dependent calcium channels and cytoskeleton remodeling. *Cell. Signal.* 20, 292–300. doi: 10.1016/j.cellsig.2007.10.028

Cui, J., Yang, H., and Lee, U. S. (2009). Molecular mechanisms of BK channel activation. *Cell. Mol. Life Sci.* 66, 852–875. doi: 10.1007/s00018-008-8609-x

D'Alessandro, G., Limatola, C., and Catalano, M. (2018). Functional roles of the Ca2+-activated K+ channel, KCa3. 1, in brain tumors. *Curr. Neuropharmacol.* 16, 636–643. doi: 10.2174/0929867324666170713103621

De Vleeschouwer, S., and Bergers, G. (2017). *Glioblastoma: To Target the Tumor Cell or the Microenvironment?*. Brisbane: Exon Publications, 315–340.

Demuth, T., and Berens, M. E. (2004). Molecular mechanisms of glioma cell migration and invasion. *J. Neurooncol.* 70, 217–228. doi: 10.1007/s11060-004-2751-6

Furnari, F. B., Fenton, T., Bachoo, R. M., Mukasa, A., Stommel, J. M., Stegh, A., et al. (2007). Malignant astrocytic glioma: genetics, biology, and paths to treatment. *Genes Dev.* 21, 2683–2710. doi: 10.1101/gad.1596707

Garzon-Muvdi, T., Schiapparelli, P., ap Rhys, C., Guerrero-Cazares, H., Smith, C., Kim, D. H., et al. (2012). Regulation of brain tumor dispersal by NKCC1

326

through a novel role in focal adhesion regulation. *PLoS Biol.* 10:e1001320. doi: 10.1371/journal.pbio.1001320

Haas, B. R., and Sontheimer, H. (2010). Inhibition of the sodium-potassium-chloride cotransporter isoform-1 reduces glioma invasion. *Cancer Res.* 70, 5597–5606. doi: 10.1158/0008-5472.can-09-4666

Habela, C. W., Ernest, N. J., Swindall, A. F., and Sontheimer, H. (2009). Chloride accumulation drives volume dynamics underlying cell proliferation and migration. *J. Neurophysiol.* 101, 750–757. doi: 10.1152/jn.90840.2008

Holland, E. C. (2001). Progenitor cells and glioma formation. *Curr. Opin. Neurol* 14, 683–688. doi: 10.1097/00019052-200112000-00002

Ishiuchi, S., Tsuzuki, K., Yoshida, Y., Yamada, N., Hagimura, N., Okado, H., et al. (2002). Blockage of Ca 2+-permeable AMPA receptors suppresses migration and induces apoptosis in human glioblastoma cells. *Nat. Med.* 8, 971–978. doi: 10.1038/nm746

Keck, T., Toyoizumi, T., Chen, L., Doiron, B., Feldman, D. E., Fox, K., et al. (2017). Integrating Hebbian and homeostatic plasticity: the current state of the field and future research directions. *Philos. Trans. R. Soc. B Biol. Sci.* 372:20160158. doi: 10.1098/rstb.2016.0158

Klumpp, L., Sezgin, E. C., Skardelly, M., Eckert, F., and Huber, S. M. (2018). KCa3. 1 channels and glioblastoma: in vitro studies. *Curr. Neuropharmacol.* 16, 627–635. doi: 10.2174/1570159x15666170808115821

Kraft, R., Krause, P., Jung, S., Basrai, D., Liebmann, L., Bolz, J., et al. (2003). BK channel openers inhibit migration of human glioma cells. *Pflügers Arch.* 446, 248–255. doi: 10.1007/s00424-003-1012-4

Lathia, J. D., Heddleston, J. M., Venere, M., and Rich, J. N. (2011). Deadly teamwork: neural cancer stem cells and the tumor microenvironment. *Cell Stem Cell* 8, 482–485. doi: 10.1016/j.stem.2011.04.013

Lebart, M. C., and Benyamin, Y. (2006). Calpain involvement in the remodeling of cytoskeletal anchorage complexes. *FEBS J.* 273, 3415–3426. doi: 10.1111/j.1742-4658.2006.05350.x

Lee, U. S., and Cui, J. (2010). BK channel activation: structural and functional insights. *Trends Neurosci.* 33, 415–423. doi: 10.1016/j.tins.2010.06.004

Li, X., Spelat, R., Bartolini, A., Cesselli, D., Ius, T., Skrap, M., et al. (2020). Mechanisms of malignancy in glioblastoma cells are linked to mitochondrial Ca2+ uniporter upregulation and higher intracellular Ca2+ levels. *J. Cell Sci.* 133:jcs237503. doi: 10.1242/jcs.237503

Litan, A., and Langhans, S. A. (2015). Cancer as a channelopathy: ion channels and pumps in tumor development and progression. *Front. Cell. Neurosci.* 9:86. doi: 10.3389/fncel.2015.00086

Liu, X., Chang, Y., Reinhart, P. H. and Sontheimer, H., (2002). Cloning and characterization of glioma BK, a novel BK channel isoform highly expressed in human glioma cells. *J. Neurosci.* 22, 1840–1849. doi: 10.1523/JNEUROSCI.22-05-01840.2002

Liu, C. A., Chang, C. Y., Hsueh, K. W., Su, H. L., Chiou, T. W., Lin, S. Z., et al. (2018). Migration/invasion of malignant gliomas and implications for therapeutic treatment. *Int. J. Mol. Sci.* 19:1115. doi: 10.3390/ijms19041115

Liu, J., Qu, C., Han, C., Chen, M. M., An, L. J., and Zou, W. (2019). Potassium channels and their role in glioma: a mini review. *Mol. Membr. Biol.* 35, 76–85. doi: 10.1080/09687688.2020.1729428

Louis, D. N., Ohgaki, H., Wiestler, O. D., Cavenee, W. K., Burger, P. C., Jouvet, A., et al. (2007). The 2007 WHO classification of tumours of the central nervous system. *Acta Neuropathol.* 114, 97–109. doi: 10.1007/978-94-007-1399-4_10

Luo, L., Guan, X., Begum, G., Ding, D., Gayden, J., Hasan, N., et al. (2020). Blockade of cell volume regulatory protein NKCC1 increases TMZ-induced glioma apoptosis and reduces astrogliosis. *Mol. Cancer Ther.* 19:910.

Maher, E. A., Furnari, F. B., Bachoo, R. M., Rowitch, D. H., Louis, D. N., Cavenee, W. K., et al. (2001). Malignant glioma: genetics and biology of a grave matter. *Genes Dev.* 15, 1311–1333. doi: 10.1101/gad.891601

Nardi, A., and Olesen, S. P. (2008). BK channel modulators: a comprehensive overview. *Curr. Med. Chem.* 15, 1126–1146. doi: 10.2174/092986708784221412

Nichols, C. G., and Lopatin, A. N. (1997). Inward rectifier potassium channels. *Annu. Rev. Physiol.* 59, 171–191.

Ohno, Y., Kinboshi, M., and Shimizu, S. (2018). Inwardly rectifying potassium channel Kir4. 1 as a novel modulator of BDNF expression in astrocytes. *Int. J. Mol. Sci.* 19:3313. doi: 10.3390/ijms19113313

Olsen, M. L., and Sontheimer, H. (2004). Mislocalization of Kir channels in malignant glia. *Glia* 46, 63–73. doi: 10.1002/glia.10346

Olsen, M. L., and Sontheimer, H. (2008). Functional implications for Kir4. 1 channels in glial biology: from K+ buffering to cell differentiation. *J. Neurochem.* 107, 589–601. doi: 10.1111/j.1471-4159.2008.05615.x

Prevarskaya, N., Skryma, R., and Shuba, Y. (2018). Ion channels in cancer: are cancer hallmarks oncochannelopathies? *Physiol. Rev.* 98, 559–621. doi: 10.1152/physrev.00044.2016

Ransom, C. B., Liu, X., and Sontheimer, H. (2002). BK channels in human glioma cells have enhanced calcium sensitivity. *Glia* 38, 281–291. doi: 10.1002/glia.10064

Ratto, D., Ferrari, B., Roda, E., Brandalise, F., Siciliani, S., De Luca, F., et al. (2019). Squaring the circle: a new study of inward and outward-rectifying potassium currents in U251 GBM cells. *Cell. Mol. Neurobiol.* 40, 813–828. doi: 10.1007/s10571-019-00776-3

Reetz, G., and Reiser, G. (1996). [Ca2+] i oscillations induced by bradykinin in rat glioma cells associated with Ca2+ store-dependent Ca2+ influx are controlled by cell volume and by membrane potential. *Cell Calcium* 19, 143–156. doi: 10.1016/s0143-4160(96)90083-4

Rondé, P., Giannone, G., Gerasymova, I., Stoeckel, H., Takeda, K., and Haiech, J. (2000). Mechanism of calcium oscillations in migrating human astrocytoma cells. *Biochim. Biophys. Acta Mol. Cell Res.* 1498, 273–280. doi: 10.1016/s0167-4889(00)00102-6

Rosa, P., Catacuzzeno, L., Sforna, L., Mangino, G., Carlomagno, S., Mincione, G., et al. (2018). BK channels blockage inhibits hypoxia-induced migration and chemoresistance to cisplatin in human glioblastoma cells. *J. Cell. Physiol.* 233, 6866–6877. doi: 10.1002/jcp.26448

Rossi, P., De Filippi, G., Armano, S., Taglietti, V., and D'Angelo, E. (1998). The weaver mutation causes a loss of inward rectifier current regulation in premigratory granule cells of the mouse cerebellum. *J. Neurosci.* 18, 3537–3547. doi: 10.1523/jneurosci.18-10-03537.1998

Ruppersberg, J. P. (2000). Intracellular regulation of inward rectifier K+ channels. *Pflügers Arch.* 441, 1–11. doi: 10.1007/s004240000380

Soroceanu, L., Manning, T. J., and Sontheimer, H. (1999). Modulation of glioma cell migration and invasion using Cl− and K+ ion channel blockers. *J. Neurosci.* 19, 5942–5954. doi: 10.1523/jneurosci.19-14-05942.1999

Stupp, R., Hegi, M. E., Mason, W. P., Van Den Bent, M. J., Taphoorn, M. J., Janzer, R. C., et al. (2009). Effects of radiotherapy with concomitant and adjuvant temozolomide versus radiotherapy alone on survival in glioblastoma in a randomised phase III study: 5-year analysis of the EORTC-NCIC trial. *Lancet Oncol.* 10, 459–466. doi: 10.1016/s1470-2045(09)70025-7

Turner, K. L., Honasoge, A., Robert, S. M., McFerrin, M. M., and Sontheimer, H. (2014). A proinvasive role for the Ca2+-activated K+ channel KCa3. 1 in malignant glioma. *Glia* 62, 971–981. doi: 10.1002/glia.22655

Vescovi, A. L., Galli, R., and Reynolds, B. A. (2006). Brain tumour stem cells. *Nat. Rev. Cancer* 6, 425–436. doi: 10.1038/nrc1889

Wawrzkiewicz-Jałowiecka, A., Trybek, P., Machura, Ł., Dworakowska, B., and Grzywna, Z. J. (2018). Mechanosensitivity of the bk channels in human glioblastoma cells: kinetics and dynamical complexity. *J. Membr. Biol.* 251, 667–679. doi: 10.1007/s00232-018-0044-9

Weaver, A. K., Bomben, V. C., and Sontheimer, H. (2006). Expression and function of calcium-activated potassium channels in human glioma cells. *Glia* 54, 223–233. doi: 10.1002/glia.20364

Wondergem, R., and Bartley, J. W. (2009). Menthol increases human glioblastoma intracellular Ca2+, BK channel activity and cell migration. *J. Biomed. Sci.* 16:90. doi: 10.1186/1423-0127-16-90

Zhao, H. C., Agula, H., Zhang, W., Wang, F., Sokabe, M., and Li, L. M. (2010). Membrane stretch and cytoplasmic Ca2+ independently modulate stretch-activated BK channel activity. *J. Biomech.* 43, 3015–3019. doi: 10.1016/j.jbiomech.2010.06.018

327

*Article*

# Novel Medicinal Mushroom Blend as a Promising Supplement in Integrative Oncology: A Multi-Tiered Study using 4T1 Triple-Negative Mouse Breast Cancer Model

Elisa Roda [1,2,†], Fabrizio De Luca [1,†], Carmine Di Iorio [1], Daniela Ratto [1], Stella Siciliani [1], Beatrice Ferrari [1], Filippo Cobelli [1], Giuseppina Borsci [1], Erica Cecilia Priori [1], Silvia Chinosi [3], Andrea Ronchi [4], Renato Franco [4], Raffaele Di Francia [5], Massimiliano Berretta [6], Carlo Alessandro Locatelli [2], Andrej Gregori [7], Elena Savino [8], Maria Grazia Bottone [1] and Paola Rossi [1,*]

[1] Department of Biology and Biotechnology "L. Spallanzani", University of Pavia, 27100 Pavia, Italy; elisa.roda@unipv.it (E.R.); fabrizio.deluca01@universitadipavia.it (F.D.L.); carmine.diiorio01@universitadipavia.it (C.D.I.); daniela.ratto01@universitadipavia.it (D.R.); stella.siciliani01@universitadipavia.it (S.S.); beatrice.ferrari01@universitadipavia.it (B.F.); filippo.cobelli01@universitadipavia.it (F.C.); giuseppina.borsci01@universitadipavia.it (G.B.); ericacecilia.priori01@universitadipavia.it (E.C.P.); mariagrazia.bottone@unipv.it (M.G.B.)

[2] Laboratory of Clinical & Experimental Toxicology, Pavia Poison Centre, National Toxicology, Information Centre, Toxicology Unit, ICS Maugeri SpA, IRCCS Pavia, 27100 Pavia, Italy; carlo.locatelli@icsmaugeri.it

[3] Clinica Veterinaria Curti Maria Grazia, 26841 Casalpusterlengo (LO), Italy; silvia.chinosi@yahoo.it

[4] Department of Mental and Physical Health and Preventive Medicine, Pathology Unit, Università della Campania "Luigi Vanvitelli", 80138 Napoli, Italy; andrea.ronchi@unicampania.it (A.R.); renato.franco@unicampania.it (R.F.)

[5] Gruppo Oncologico Ricercatori Italiani, GORI onlus, 33170 Pordenone, Italy; rdifrancia@iapharmagen.org

[6] Department of Medical Oncology, Istituto Nazionale Tumori, Centro di Riferimento Oncologico (CRO), 33081 Aviano (PN), Italy; berrettama@gmail.com

[7] Biotechnical Faculty, University of Ljubljana, Jamnikarjeva ulica 101, Ljubljana, Slovenia; andrej.gregori@zanaravo.com

[8] Department of Earth and Environmental Science, University of Pavia, 27100 Pavia, Italy; elena.savino@unipv.it

[*] Correspondence: paola.rossi@unipv.it; Tel.: +39-0382896076

[†] These authors contributed equally to this work.

check for updates

**Abstract:** Although medicinal mushroom extracts have been proposed as promising anti-cancer agents, their precise impacts on metastatic breast cancer are still to be clarified. For this purpose, the present study exploited the effect of a novel medicinal mushroom blend, namely Micotherapy U-care, in a 4T1 triple-negative mouse breast cancer model. Mice were orally administered with Micotherapy U-care, consisting of a mixture of *Agaricus blazei*, *Ophiocordyceps sinensis*, *Ganoderma lucidum*, *Grifola frondosa*, and *Lentinula edodes*. The syngeneic tumor-bearing mice were generated by injecting 4T1 cells in both supplemented and non-supplemented mice. After sacrifice 35 days later, specific endpoints and pathological outcomes of the murine pulmonary tissue were evaluated. (i) Histopathological and ultrastructural analysis and (ii) immunohistochemical assessment of TGF-ß1, IL-6 and NOS2, COX2, SOD1 as markers of inflammation and oxidative stress were performed. The QoL was comparatively evaluated. Micotherapy U-care supplementation, starting before 4T1 injection and lasting until the end of the experiment, dramatically reduced the pulmonary metastases density, also triggering a decrease of fibrotic response, and reducing IL-6, NOS, and COX2 expression. SOD1 and TGF-ß1 results were also discussed. These findings support the valuable potential of Micotherapy U-care as adjuvant therapy in the critical management of triple-negative breast cancer.

## 1. Introduction

Breast cancer (BC) is the most frequent cancer among women [1], impacting 2.1 million women each year, also causing the greatest number of cancer-related deaths. In 2018, it is estimated that 627,000 women died from BC; that is approximately 15% of all cancer deaths among women. While BC rates are higher among women in more developed regions, rates are increasing in nearly every region globally [2].

A great deal of progress has been made in the early detection and treatment of BC; thus, the survival has steadily increased in recent years [3], reaching the five-year relative survival rate at about 89% of the cases. However, not all patients benefited from those progresses, since the lack of effective treatments against metastasis is still the major hindrance to survival and quality of life of patients suffering from BC [4]. Approximately 10%–20% of all BCs are triple-negative breast cancer (TNBC), testing negative for estrogen and progesterone receptors and excess human epidermal growth factor receptor 2 (HER2) protein. This tumor phenotype is associated with either high proliferation or metastasis phenomena [5]. TNBC is the most difficult BC subgroup to treat due to its unresponsiveness to current clinical targeted therapies (e.g., hormonal therapy protocols or chemotherapeutics targeting HER2 protein receptors), high rate of recurrence, and poor prognosis. Presently, people suffering from TNBC receive taxane chemotherapies, such as paclitaxel, as their standard care. Nonetheless, the lack of a targeted therapy and the TNBC heterogeneity highlighted the urgent medical need to identify therapeutic targets and develop novel effective medicines capable to overcome drug resistance in this aggressive BC. A great deal of effort is currently devoted to find out whether certain treatments can interfere with cellular and molecular processes fueling TNBC growth, trying to create new medical therapies able to hinder the typical TNBC metastatic pattern (i.e., frequent occurrence of distant metastases, mainly localized in lung, central nervous system, and bones) often associated with poor prognosis [6,7].

One of the most promising sources for potential drug discovery in cancer therapy is compounds of fungal origin, i.e., medicinal mushrooms, which display anti-cancer, onco-immunological, and immuno-modulating activities, also improving quality of life during chemotherapy [8,9]. Medicinal mushrooms have been employed for hundreds of years, mainly in China and Asia, for the treatment of a wide range of diseases. Over the past 60 years, experimental and epidemiological studies focusing on fungi increased exponentially, and in recent years, the use of some medicinal mushrooms has been approved as adjuvant treatment in cancer therapy in Japan and China. Extensive clinical studies demonstrated their safe use as single agents or combined with conventional antiblastic-chemotherapy [10].

"Micotherapy U-care" is a novel medicinal mushroom blend supplement provided by A. V. D Reform s.r.l. (Noceto, Parma, Italy) consisting of a mixture of mycelium and sporophores extracts of five species, including *Agaricus blazei, Ophiocordyceps sinensis, Ganoderma lucidum, Grifola frondosa,* and *Lentinula edodes.* Anti-cancer, onco-immunological, and immuno-modulating properties of these five medicinal mushrooms have been previously described in vitro [11,12] and in preclinical [13] and clinical study [8].

The anti-cancer activities of mushrooms have been linked primarily to the modulation of the innate and cell-mediated immune response by branched polysaccharides (beta-glucans) or polysaccharides-protein complexes. Moreover, mushrooms contain bioactive high and low molecular weight molecules (triterpenes, steroids, polyphenols, alkaloids, etc.) in all the different mushroom stages, from mycelium to primordium, until the developed sporophore. Some of these bioactive compounds shared activity against aberrantly activated signaling pathways in cancer cells, modulating cell proliferation, cell survival, cell invasion, and angiogenesis [9].

*Agaricus blazei* Murrill was discovered about 50 years ago in Brazil, where it is known as the sun mushroom [14,15]. Anti-tumor and immuno-stimulant properties of *A. blazei* were broadly described [16]. In vitro study on estrogen-positive human BC cell line, MCF-7, demonstrated the anti-proliferative and anti-metastatic effect of an isoflavone-conjugated glycoprotein, extracted from *A. blazei* [17]. *A. blazei* revealed anti-oxidant activity in aging rats [18]. A phase I clinical study by Ohno analyzed the safety issues in BC patients in remission [19]. The quality of life (QoL) in gynecological cancer patients undergoing chemotherapy improved with *A.blazei* extract consumption. Specifically, the treatment increased the activity of the natural killer cells and reduced the adverse effects caused by conventional chemotherapy [20].

*Ophiocordyceps sinensis* (Berk.), native to high-altitude regions of Himalayas, consists of a fungus that parasitizes the larvae of the ghost moth (*Lepidoptera*), producing a fruiting body used as a Chinese herbal remedy. Several in vivo investigations showed the efficacy of *O. sinensis* in reducing BC metastasis [21]. This anti-cancer effect was also studied in 4T1 tumor-bearing mice growing metastatic breast tumors, describing effects on a panel of cytokines [13]. *O. sinensis* has also been shown to possess immunomodulatory [22] and anti-oxidant [23] properties.

*Ganoderma lucidum* (Ling Zhi, Reishi) is one of the most popular Asian fungi. Triterpenes, ganoderic acid, and their derivatives demonstrated a direct cytotoxic activity on a variety of cancer cells, including BC [24]. An extract containing β-glucans and triterpenes suppressed proliferation and metastatic potential of BC cells through the inhibition of Akt kinase and transcription factors AP-1 and NF-Kb [25,26]. A pilot study conducted on 48 BC patients undergoing endocrine therapy, described an improvement in cancer-related fatigue and QoL, along with less anxiety and depression and without adverse effects [27]. Many bioactive components of *G. lucidum* have shown potent anti-inflammatory effects [9]. Furthermore, it was also demonstrated that *G. lucidum* extracts decreased IL-8, IL-6, MMP-2, iNOS, IL-1, TNF-α, and MMP-9 secretion in human TNBC cells [28].

*Grifola frondosa* (Maitake, "dancing mushroom" in Japanese) is a culinary mushroom. In vitro studies using MCF7 cells described cellular mechanisms involved in apoptosis induction and neoplastic cell proliferation arrest [29,30]. Other *G. frondosa*–induced cellular mechanisms, such as a low P27 gene expression, have prognostic implications in early stages of mouse mammary pre-neoplasia [31], while a reduced activity of ITGA2 is highly associated with disease progression and clinical outcomes in BC [32,33]. The reduction of oxidative stress, particularly in terms of increased mitochondrial superoxide dismutase 2 (SOD2), was described in vitro [30]. Phase I/II clinical trials in BC patients demonstrated that oral administration of a *G. frondosa* extract is associated with both immunologically stimulatory and inhibitory measurable effects in peripheral blood [34].

*Lentinula edodes* (Shiitake) is an edible mushroom native to East Asia, where it has long been considered a delicacy as well as a medicinal mushroom. In vitro studies using human BC cell lineages exposed to *L. edodes* revealed cell growth inhibition paralleled by apoptosis induction [35]. Interestingly, in vivo investigations, assessing the lung-protective effects of a polysaccharide fraction extracted from *L. edodes* demonstrated a decreased inflammatory pathway activation paralleled by an improved antioxidant status [36]. Moreover, the efficacy of *L. edodes* mycelia extract was tested in BC patients undergoing post-operative adjuvant hormone therapy, demonstrating an improvement of immune function and QoL scores after a long-term oral administration [37]. Similarly, the concomitant use of mycelial *L. edodes* extract and oral immunomodulatory (REC75 therapy) can maintain host QoL and immune function [38]. An epidemiological study evaluating host QoL and immune function in BC patients co-administered with a combination of adjuvant chemotherapy and *L. edodes* mycelia extract supported the application of this extract as a useful oral adjuvant to anthracycline-based chemotherapies [39].

In the present investigation, we exploited the effect of an oral supplementation with "Micotherapy U-care" (M. U-care), a novel medicinal mushroom blend, consisting of a mixture of extracts from the above reported five varieties, in a 4T1 triple-negative mouse BC model. We addressed specific endpoints and pathological outcomes of the murine pulmonary tissue, the lung being one of the distant organs frequently involved in typical metastasis pattern of primary TNBC [7]. We evaluated different

markers of general lung toxicity, inflammation, fibrosis, and oxidative stress, both in parenchyma and metastases. In particular, morphological and molecular investigations included (i) pulmonary histopathological and ultrastructural evaluation and (ii) immunohistochemical assessment of pivotal markers of inflammation (i.e., TGF-β1 and IL-6) and oxidative stress (i.e., NOS2, COX2 and SOD1), respectively. Comparative data assessment was analyzed in terms of the biological responses to the Micotherapy U-care blend supplementation, starting before 4T1 injection and lasting until the end of the experiment, concerning either persistence or tendency to resolution of such effects. The QoL was evaluated in a comparative approach.

## 2. Results

A detailed flow diagram of the experimental design is shown in Figure 1A, together with a schematic drawing (Figure 1B) highlighting the main outcomes of the study.
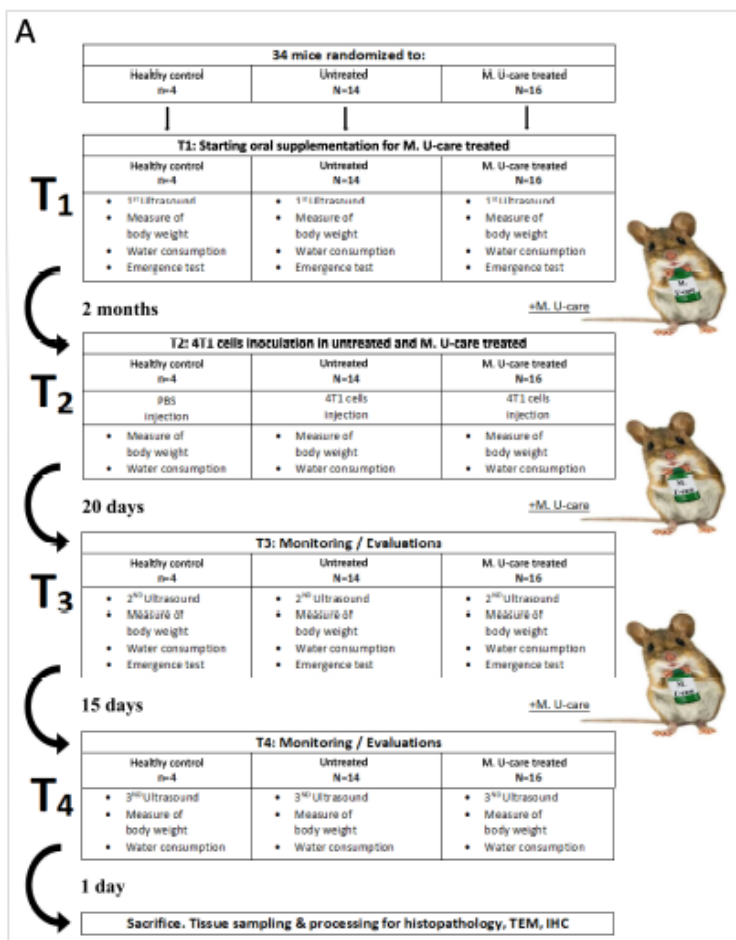


**Figure 1.** *Cont.*
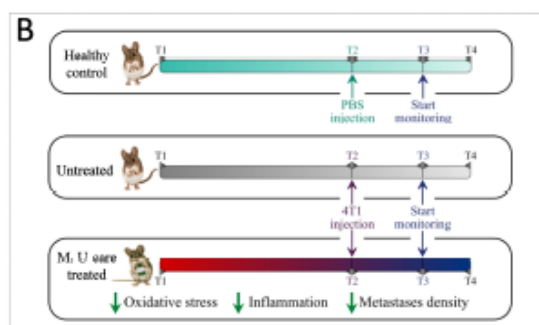
**Figure 1.** Experimental flow chart (**A**) and schematic drawing highlighting the main outcomes (**B**).

## 2.1. Quality of Life

First, it has to be underlined that no animals died throughout the whole experimental time course, from T0 to T4; thus, we had a survival rate of 100% in all the three experimental groups.

We monitored the quality of mice life, before and after 4T1 cells (or PBS) injections. We monitored the quality of mice life in the three experimental groups by creating a composite indicator of physical well-being formed by the body weight (Figure 2A), water (Figure 2B) and food consumption, and locomotor activity (Figure 2C).

Locomotor activity records measured in both M. U-care–treated and untreated mice were normalized to healthy controls data, at each corresponding experimental time (i.e., T1 and T3).

Furthermore, we measured the primary tumor volume. At T4, the primary tumor mass measured in M. U-Care–treated mice was significantly smaller compared to untreated animals (Figure 2D). As the core component of this multidimensional QoL assessment, we evaluated three items based on the locomotor activity determined in behavioral spontaneous test, such as average speed, total distance, and resting time. We checked the selected parameters throughout the entire experimental time (Figure 2E,F).

Notably, the scoring index showed that both at T3 and T4, M. U-care–treated mice reached a higher QoL score index compared to Untreated animals, and that the quality of life decreased in both experimental groups during time (Figure 2E). Nonetheless, the T4 score value measured in M. U-care–treated mice was comparable to the T3 score value determined in untreated animals.

At T4, all mice decreased about 4% of their body weight, this diminution probably being due to the deterioration of their general condition 35 days after the tumour injection. Noticeably, throughout the entire experimental time, the M. U-care–treated mice have the significantly highest water consumption compared to both untreated animals and healthy controls.

## 2.2. Histopathology (H&E Staining) and Ultrastructural Analysis (TEM)

We evaluated (i) the differential injury extent in lung parenchyma and (ii) morphological characteristics of metastases, comparing healthy controls, untreated, and M. U-care–treated mice by Haematoxylin and Eosin (H&E) and transmission electron microscopy (TEM).

H&E results demonstrated that the physiological pulmonary structure is clearly well preserved in healthy control mice (Figure 3a), while morphological alterations were manifest in the lung parenchyma of the tumor-induced mice, both M. U-care–treated vs. untreated mice, with the latter showing the more striking injury. Specifically, wall-thickened collapsed alveoli and desquamation, hemorrhagic foci, and parenchymal fibrosis were observed in non-supplemented mice.
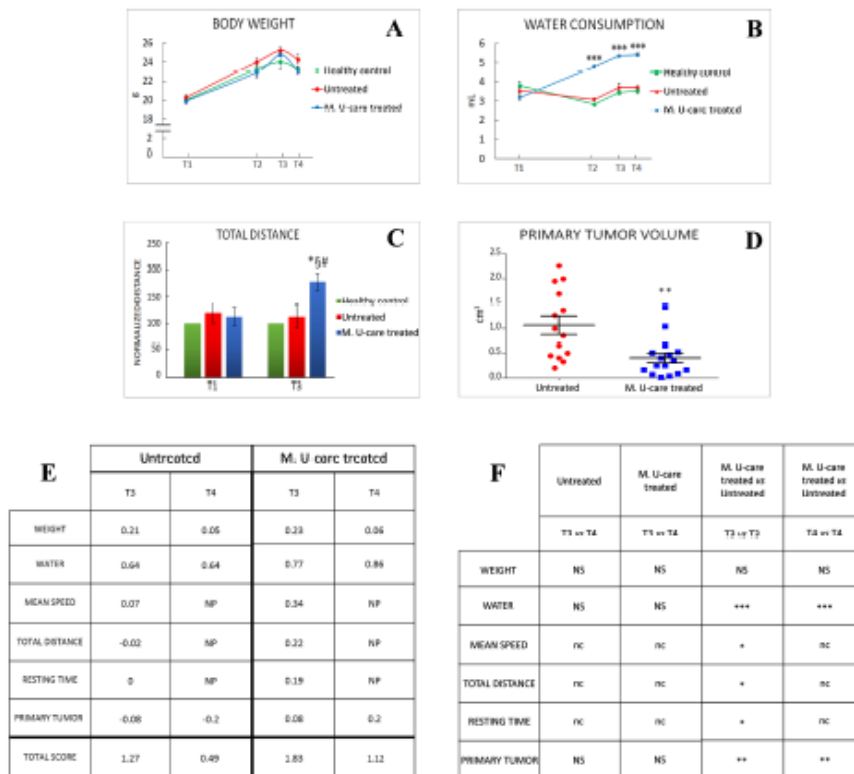
**E**

| | Untreated | | M. U care treated | |
|---|---|---|---|---|
| | T3 | T4 | T3 | T4 |
| WEIGHT | 0.21 | 0.06 | 0.23 | 0.06 |
| WATER | 0.64 | 0.64 | 0.77 | 0.86 |
| MEAN SPEED | 0.07 | NP | 0.34 | NP |
| TOTAL DISTANCE | -0.02 | NP | 0.22 | NP |
| RESTING TIME | 0 | NP | 0.19 | NP |
| PRIMARY TUMOR | -0.08 | -0.2 | 0.08 | 0.2 |
| TOTAL SCORE | 1.27 | 0.49 | 1.83 | 1.12 |

**F**

| | Untreated | M. U-care treated | M. U-care treated vs Untreated | M. U-care treated vs Untreated |
|---|---|---|---|---|
| | T3 vs T4 | T3 vs T4 | T3 vs T3 | T4 vs T4 |
| WEIGHT | NS | NS | NS | NS |
| WATER | NS | NS | *** | *** |
| MEAN SPEED | nc | nc | * | nc |
| TOTAL DISTANCE | nc | nc | * | nc |
| RESTING TIME | nc | nc | * | nc |
| PRIMARY TUMOR | NS | NS | ** | ** |

**Figure 2.** Quality of life and primary tumours features. (**A, B**) Weight gain and water consumption, respectively; water consumption: $p < 0.001$ (***) (two-way-ANOVA and Bonferroni's post-hoc test) was obtained comparing Micotherapy U-care (M. U-Care) treated to all other data reported. (**C**) Normalized value on healthy mice of total distance travelled during the 8 min of emergence test; $p < 0.05$ (*) (two-way-ANOVA and Bonferroni's post-hoc test) was obtained comparing M. U-Care treated to all other data reported. *: M. U-Care treated mice at T3 vs Untreated animals at T3. §: M. U-Care treated mice at T3 vs Untreated animals at T1. #: M. U-Care treated mice at T3 vs M. U-Care treated mice at T1. (**D**) Primary tumour mass volume: dot plot chart showing the entire mice population (each dot represents an individual mouse); $p < 0.01$ (**) (unpaired Student's t-test) was obtained comparing Untreated and M. U-Care treated groups. (**E**) Global quality life scoring index; NP: not performed. (**F**) Statistical analysis regarding global quality life scoring index: $p < 0.01$ (**) and $p < 0.001$ (***) (two-way-ANOVA and Bonferroni's post-hoc test) were obtained comparing M. U-Care and Untreated mice concerning the following parameters: weight, water consumption, and primary tumour; NS: not significant. $p < 0.05$ (*) (unpaired Student's t-test) was obtained comparing M. U-Care treated and Untreated groups concerning the following parameters: mean speed, total distance, and resting time; nc: not comparable.
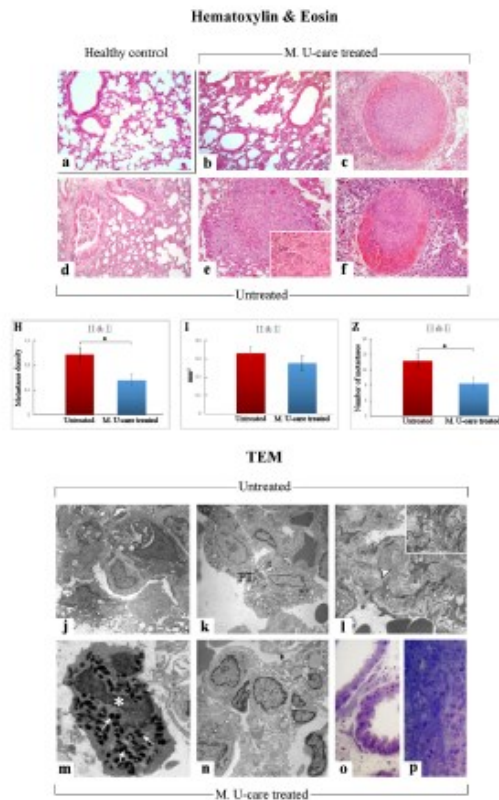
**Figure 3.** Representative lung parenchyma and metastasis specimens, investigated by both light (H&E) and llectron microscopy—TEM (a–f and j–p, respectively), from healthy control (a), Mic U-care–treated (b, c and m–p), and untreated (d–f and j–l) mice. The physiological pulmonary structure is clearly preserved in healthy controls (a). Selected structural alterations evidenced in pulmonary parenchyma as well as metastases feature of both M. U-care–treated and untreated mice are presented. PII: type II pneumocytes; arrowhead: collagen fibril bundles; asterisk: activated granulocyte; thin arrows: cytoplasmic crystalloid-containing eosinophil granules. Light (methylene blue staining on semithin sections) (o, p) and electron microscopy details of untreated (j–l) and M. U-care–treated (m–p) murine lung tissue. Light microscopy magnification: 40× (a–f); 60× (insert in e). Electron Microscopy original magnification: 5000× (j–l, n); 12,000× (m); 20,000× (insert in l), 60× (o, p). Histograms showing the quantitative analysis of density (**H**), area (**I**), and number (**Z**) of metastases. $p$ value calculated by unpaired Student's t-test: (*) < 0.05.

In M. U-care–treated mice the metastatic density as well as the number of metastatic nodules were significantly reduced compared to untreated animals ($0.56 \pm 0.09$ vs. $0.97 \pm 0.11$ and $8.5 \pm 1.66$ vs. $14.29 \pm 1.65$, for density and nodules number, respectively). A slight decrease of the single metastatic area was also determined in M. U-care–treated mice ($0.28 \pm 0.04$) compared to jntreated animals ($0.33 \pm 0.04$) (Figure 3H,I,Z and Table 1).

**Table 1.** Semiquantitative scoring of lung lesions in healthy control, untreated, and M. U-care–treated mice.

|  | Healthy Control | Untreated | M. U-care Treated | *p* Value |
|---|---|---|---|---|
| Alveolar structure alteration | – | +++ | ++ | * |
| Haemorrhagic foci | – | ++ | ++ | ns |
| Bronchiolar desquamation | – | ++ | + | * |
| Number of pulmonary metastases | – | ++ | + | * |

Degree scale: from absent/undetectable (–) to maximal (++++). *p* values calculated by Kruskal-Wallis followed by Dunn's post hoc test. (*) <0.05; ns = not statistically significant.

The qualitative observations revealed that the neoformations were widely distributed in the width of the lung, often localized in the outer layers. The metastatic tissues displayed heterogeneous cellularity, with prevalent nodular organization typically characterized by defined, tight clusters of round cells, but often exhibiting several other cell morphologies (e.g., fusiform, cubic, cylindrical shape) and dimensions, with the cytoplasmic part varying greatly. Fewer metastases showed columnar organization with homogeneous cellularity, displaying typical cell ropes with parallel orientation (Figure 3b–f and Table 1).

TEM examination revealed severe modification of the physiological pulmonary structure, characterized by wall-thickened collapsed alveoli and the presence of type II pneumocytes characterized by piles of vacuolated and surfactant-engulfed lamellar bodies (Figure 3 j,k,n–p). An inflammatory condition of the pulmonary tissue (i.e., enhanced presence of activated macrophages, lymphocytes and other inflammatory cells) was also detected together with parenchymal fibrosis, i.e., collagen fibril bundles deposition and accumulation (Figure 3l). These alterations appeared more pronounced in Untreated animals compared to M. U-care treated mice. Notably, the widespread presence of several activated eosinophilic granulocytes, exhibiting the characteristic presence of several cytoplasmic crystalloid-containing eosinophil granules, was evidently increased in M. U-care–treated mice (Figure 3m).

*2.3. Picrosirius Red Staining: Fibrillar Collagen Networks Evaluation*

Picrosirius Red staining is one the most sensitive methods to evaluate collagen fibers in paraffin sections [40]. Collagen fibers were predominantly localized in the metastases' marginal zone, notably encircling their outline. Moreover, several specimens displayed collagen fibrils bundles radiating from the bronchiolar wall to the lung parenchyma, also inside the tumors masses (Figure 4b,d,e).

The successive quantitative analysis evidenced an extremely significant enhancement of the histochemically positive bronchiolar wall area in untreated mice ($2.48 \pm 0.18$ mm$^2$), compared to both M. U-care–treated animals and healthy controls ($0.51 \pm 0.03$ and $0.48 \pm 0.01$ mm$^2$, respectively; Figure 4I). Similarly, concerning the bronchiolar wall OD, an extremely significant increase of the collagen fibers optical density was detected in intreated mice ($178.03 \pm 4.51$) compared to both M. U-care–treated animals and healthy controls ($134.48 \pm 4.09$ and $125.1 \pm 2.46$, respectively; Figure 4 Panel H).

Notably, concerning both bronchiolar wall area and OD, the comparison between M. U-care–treated mice and healthy controls showed the absence of any statistically significant difference, revealing a similar trend in these animal groups (Figure 4H,I).
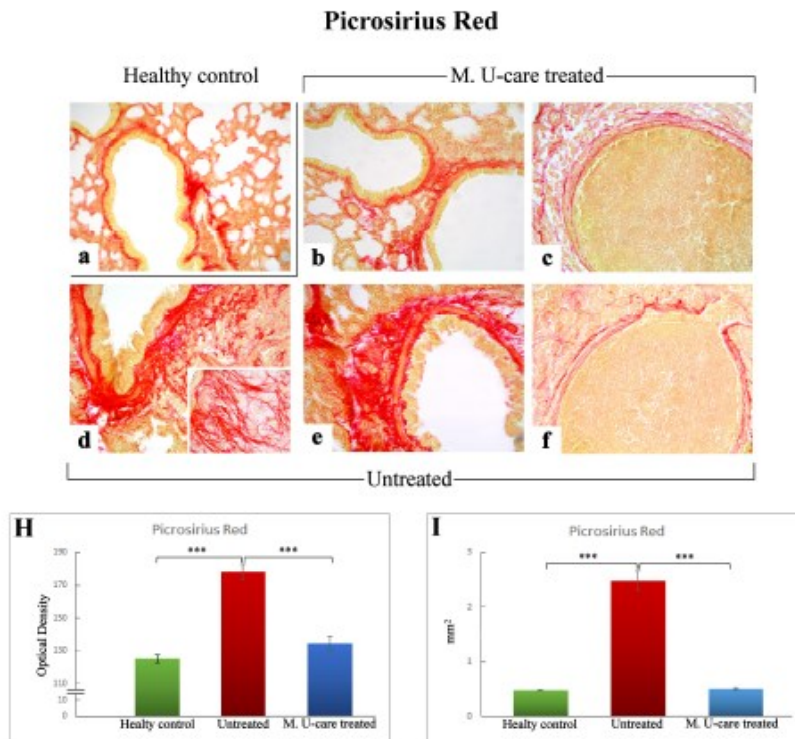
## Picrosirius Red



**Figure 4.** Representative Picrosirius Red stained pulmonary specimens (a–f) in healthy control (a), M. U-care–treated mice (b,c), and untreated (d–f) mice. A widespread occurrence of collagen fibrils bundles radiating from bronchiolar wall to the lung parenchyma, also inside the tumours masses, are observable (b,d,e). Collagen fibers encircling the metastases outline are also shown (c, f). Light microscopy magnification: 40× (a–f); 60× (insert in d). Histograms showing the quantitative analysis of collagen fibers OD (H) and bronchiolar wall area (I). $p$ value calculated using one-way ANOVA followed by Bonferroni's post-hoc test: (***) < 0.001.

### 2.4. Inflammatory Pathway: IL-6 and TGF-β1 Immunohistochemical Assessment

Based on literature evidences suggesting the key role played by pro- and anti-inflammatory cytokines balance in promoting BCs development, in the present investigation we performed an immunohistochemical evaluation of the presence/distribution of Interleukin-6 (IL-6) and Transforming Growth Factor-beta1 (TGF-β1), as specific markers of inflammatory pathway.

The cellular localization and distribution of IL-6 and TGF-β1, both involved in tissue injury and repair pathways, revealed an extensive spreading in alveolar pneumocytes (both type I and II), in metastatic cells as well as in bronchiolar epithelial cells (Figures 5b–g and 6b–g), particularly evident in collapsed alveolar area, evidencing the cellular inflammatory response.
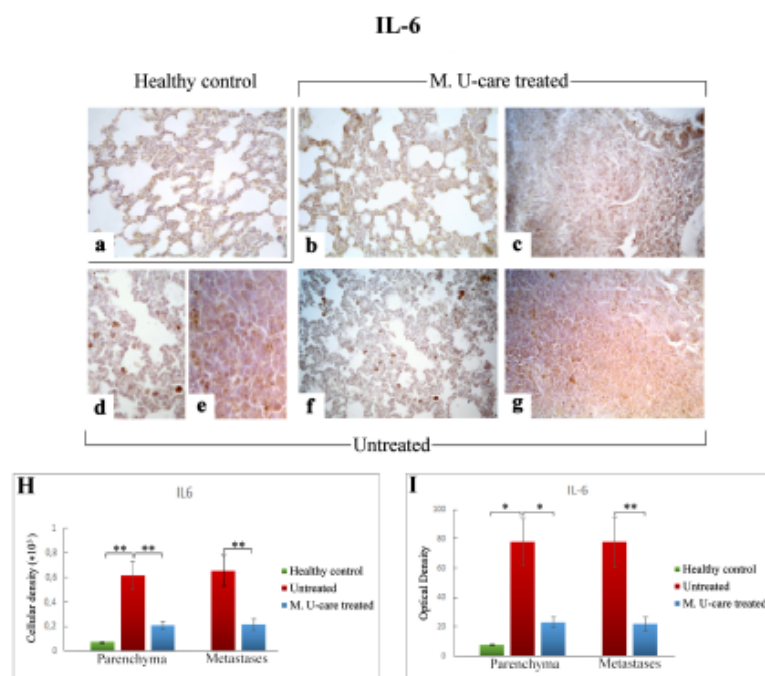
## IL-6



**Figure 5.** Immunohistochemical labelling for IL-6 in healthy control (**a**), Mic U-care–treated (**b, c**), and untreated (**d–g**) mice. While a weaker immunoreactivity is shown in M. U-care–treated mice, the heaviest IL-6-immunopositivity is observable in untreated mice in alveolar pneumocytes, in metastatic cells as well as in bronchiolar epithelial cells (**b–g**), evidenced by the presence of several immunopositive endothelial cells (**d,f**). IL-6 antigen appeared particularly overexpressed in metastatic tissue (**e,g**). Light microscopy magnification: 40× (**a–c,f,g**); 60× (**d,e**). Histograms showing the quantitative analysis of immunopositive cell density (**H**) and OD (**I**). $p$ values calculated by one-way ANOVA followed by Bonferroni's post-hoc test and unpaired Student's t-test for parenchyma and metastases, respectively: (*) < 0.05; (**) < 0.01.

Regarding lung parenchyma, the heaviest IL-6-immunopositivity was observed in untreated mice at alveolar and stromal levels, with several immunopositive endothelial cells in bronchiolar areas; IL-6 antigen resulted also overexpressed in metastatic tissue (Figure 5e,g). It should be noted that a dramatic increase of IL-6-immunoreactive cellular density (Figure 5 Panel H) and OD (Figure 5 Panel I) were measured in untreated mice (619.55 ± 115.97 and 77.78 ± 16.34, 655.02 ± 125.60 and 77.73 ± 17.04, for parenchyma and metastases, respectively), compared to M. U-care–treated animals (206.33 ± 31.03 and 23.02 ± 3.43, 215.46 ± 47.26, and 21.89 ± 4.94, for parenchyma and metastases, respectively). Notably, any statistically significant difference was determined in lung parenchyma when evaluating cellular density and OD comparing M. U-care–treated mice and healthy controls (206.33 ± 31.03 and 23.02 ± 3.43 vs. 72.23 ± 0.89 and 7.77± 0.14, respectively; Figure 5 Panel H and I).
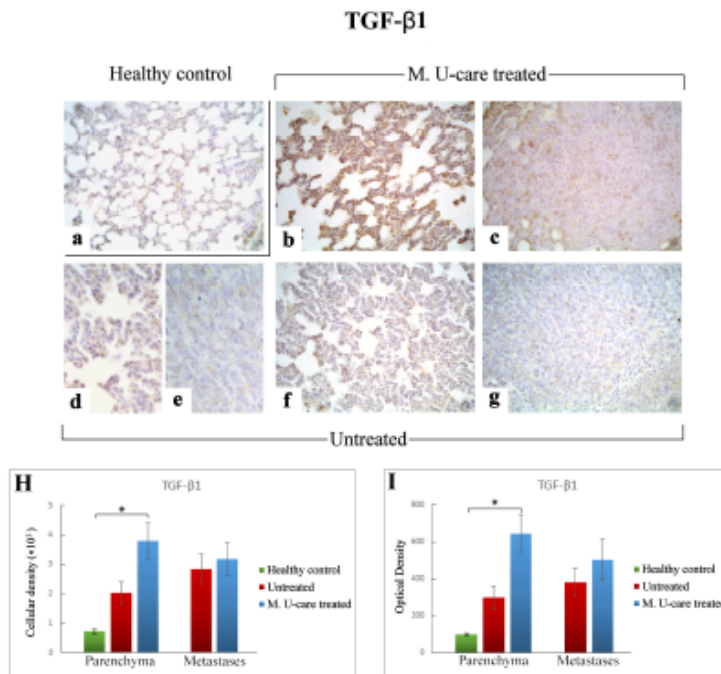
## TGF-β1



**Figure 6.** Immunostaining pattern of TGF-β1 expression in healthy control (**a**), M. U-care–treated (**b,c**), and untreated (**d–g**) mice. The heaviest immunoreactivity is observable in M. U-care–treated mice, mainly localized in alveolar pneumocytes, bronchiolar epithelial cells as well as in metastatic tissue (**b,c**). A slight immunopositivity is evident in untreated animals, both at parenchymal and metastatic level (**d–g**). Light microscopy magnification: 40× (**a–c,f,g**); 60× (**d,e**). Histograms illustrating the quantitative measurement of immunopositive cell density (**H**) and optical density (**I**). *p* values calculated by one-way ANOVA followed by Bonferroni's post-hoc test and unpaired Student's t-test for parenchyma and metastases, respectively: (*) < 0.05.

Differently, the quantitative analysis documented a significant increase of TGF-β1-immunoreactive cell density (Figure 6 Panel H) and OD (Figure 6 Panel I) in lung parenchyma of M. U-care–treated mice compared to healthy controls (3797.22 ± 598.20 and 645.61 ± 104.41 vs. 714.06 ± 69.04 and 98.31 ± 6.63, respectively). A slight increase of both TGF-β1-immunoreactive cell density and OD was observed in lung parenchyma of M. U-care–treated mice compared to untreated animals, even though no statistically significant difference was measured (3797.22 ± 598.20 and 645.61 ± 104.41 vs. 2014.33 ± 380.74 and 297.99 ± 60.25, respectively). Likewise, in metastases, a similar trend was observed for both cellular density and OD comparing M. U-care–treated mice and untreated animals (3173.90 ± 567.24 and 504.59 ± 110.11 vs. 2836.22 ± 498.32 and 382.49 ± 75.21; Figure 6H,I).

### 2.5. Oxidative Stress Pathway: SOD1, NOS2, and COX2 Immunohistochemical Assessment

In the present study, we assessed the presence/distribution of superoxide dismutase 1 (SOD1), nitric oxide synthase 2 (NOS2), and cyclooxygenase 2 (COX2), as specific markers essentially involved in oxidative stress pathway. The localization and distribution of SOD1, NOS2, and COX2, revealed a

widespread broadening in bronchiolar and alveolar cells, as well as in the metastatic masses, evidencing the pulmonary reaction to the cancer injury (Figures 7–9).
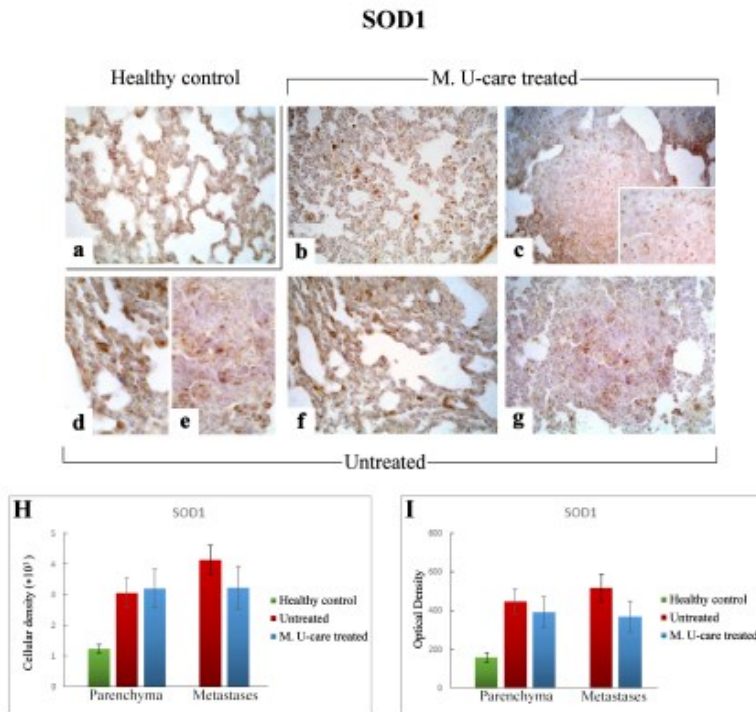


**Figure 7.** Immunostaining pattern of SOD1 expression in healthy control (a), M. U-care–treated (b,c), and untreated (d–g) mice. A slightly more marked SOD1-immunoreactivity is observable in untreated animals (d–g), mainly detectable in alveolar pneumocytes, bronchiolar epithelial cells (d,f) and in metastatic tissue, also (e,g). M. U-care–treated mice display a weaker immunolabelling (b,c). Light microscopy magnification: 40× (a–c,f,g); 60× (d,e, insert in c). Histograms showing the quantitative analysis of immunoreactive cell density (**H**) and optical density (**I**), both in the parenchyma and metastatic tissue. *p* values calculated by one-way ANOVA followed by Bonferroni's post-hoc test and unpaired Student's t-test for parenchyma and metastases, respectively.

Specifically, the localization of SOD1 showed a widespread distribution in alveolar pneumocytes, in metastatic tissue and some bronchiolar epithelial cells (Figure 7b–g). Noticeably, numerous SOD1-immunopositive activated macrophages were detected particularly evident in collapsed areas, appearing heavily labeled.

SOD1-immunoreactivity evaluated in pulmonary parenchyma in terms of cellular density and OD appeared enhanced in Untreated and M. U-care–treated mice ($3068.49 \pm 490.54$ and $448.33 \pm 65.14$ vs. $3203.68 \pm 627.56$ and $392.94 \pm 81.70$, respectively), compared to healthy controls ($1234.90 \pm 133.77$ and $160.74 \pm 21.78$), even if these differences were not statistically significant (Figure 7H,I). Concerning the metastatic tissue, similar cellular density and OD values were detected comparing M. U-care treated and Untreated mice ($3238.79 \pm 702.67$ and $368.82 \pm 81.03$ vs. $4143.29 \pm 483.66$ and $517.84 \pm 28.21$, respectively; Figure 7H,I).
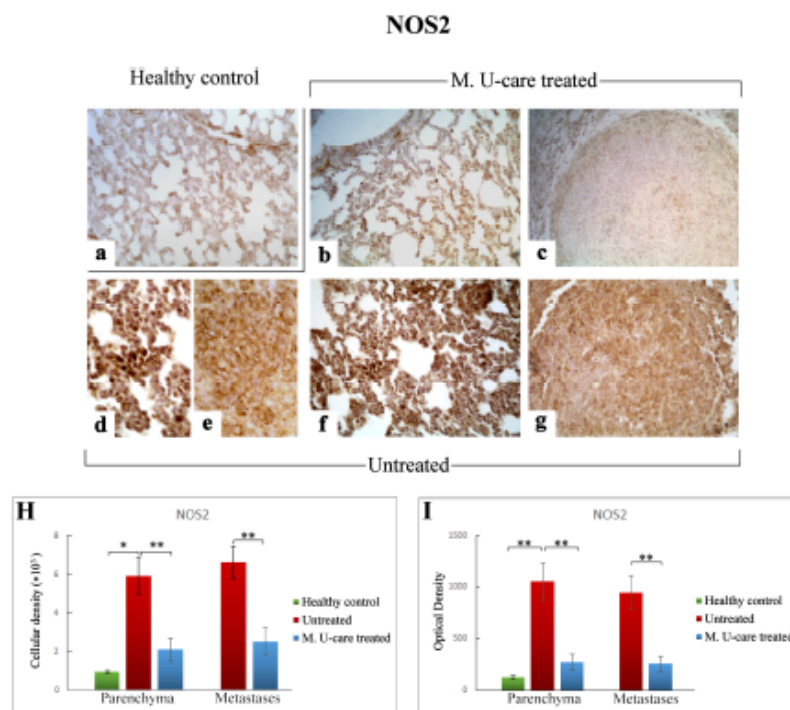
**Figure 8.** Representative micrographs showing NOS2 expression, detected by immunohistochemistry, in healthy control (a), M. U-care–treated (b,c), and untreated (d–g) mice. An intensely marked NOS2-immunolabelling is clearly observable in untreated mice (d–g), with the strongest immunopositivity evident at bronchiolar and alveolar level (d,f) as well as in metastases (e,g). A weaker immunoreactivity is perceivable in M. U-care treated animals (b, c). Light microscopy magnification: 40× (a–c,f,g); 60× (d,e). Histograms illustrating of the quantitative analysis of immunopositive cell density (H) and optical density (I). $p$ values calculated by one-way ANOVA followed by Bonferroni's post-hoc test and unpaired Student's t-test for parenchyma and metastases, respectively: (*) $< 0.05$; (**) $< 0.01$.

Similarly to the observed IL-6 trend, NOS2-immunoreactivity in lung parenchyma, evaluated in terms of both cellular density and OD, significantly enhanced in Untreated mice ($5915.47 \pm 971.84$ and $1051.52 \pm 184.63$) compared to both M. U-care–treated and healthy controls ($2112.37 \pm 589.46$ and $271.27 \pm 76.89$ vs. $935.80 \pm 72.42$ and $124.06 \pm 19.29$, respectively). Any significant difference was determined when comparing M. U-care–treated mice to healthy controls (Figure 8H,I). The strongest NOS2-immunopositivity was detected at the bronchiolar, alveolar, and metastatic levels in untreated mice, associated with the presence of several immunopositive inflammatory cells (Figure 8d–g). In metastases, a dramatic increase of NOS2-immunoreactive cell density and OD was measured in untreated animals compared to M. U-care–treated mice ($6606.67 \pm 855.87$ and $945.89 \pm 160.91$ vs. $2474.37 \pm 708.35$ and $255.57 \pm 72.03$, respectively; Figure 8H,I).
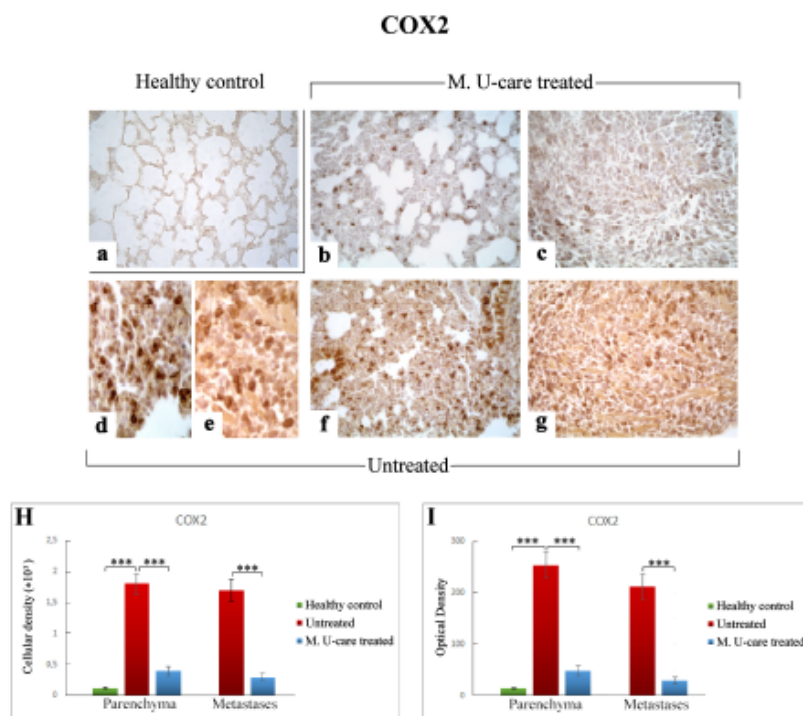
## COX2



**Figure 9.** COX2-immunostaining reaction in healthy control (**a**), M. U-care–treated (**b**,**c**), and untreated (**d**–**g**) mice. An extremely marked immunoreactivity is clearly observable in Untreated mice, mainly localized in alveolar pneumocytes and in some bronchiolar epithelial cells (**d**,**f**) as well as in metastatic tissue (**e**,**g**). M. U-care–treated animals display a weaker immunoreactivity (**b**,**c**). Light microscopy magnification: 40× (**a**–**c**,**f**,**g**); 60× (**d**,**e**). Histograms showing the quantitative measurement of immunopositive cell density (**H**) and optical density (**I**), both in the parenchyma and in metastatic tissue. $p$ values calculated by one-way ANOVA followed by Bonferroni's post-hoc test and unpaired Student's t-test for parenchyma and metastases, respectively: (***) < 0.001.

Accordingly to the above reported data regarding both IL-6 and NOS2, COX2 immunostaining in lung parenchyma evaluated in terms of both cellular density and OD was significantly increased in intreated compared to M. U-care–treated mice ($1806.66 \pm 159.56$ and $253.54 \pm 25.38$ vs. $394.39 \pm 74.68$ and $48.48 \pm 9.53$, respectively). No significant difference was measured when comparing M. U-care–treated mice to healthy controls ($394.39 \pm 74.68$ and $48.48 \pm 9.53$ vs. $120.52 \pm 8.16$ and $13.90 \pm 1.27$, respectively) (Figure 9H,I). In detail, most marked COX2-immunopositivity was mainly localized at alveolar and bronchiolar level, as well as in metastatic areas, often accompanied by the presence of immunoreactive inflammatory cells (Figure 9d–g).

Concerning the metastases, an extremely significant increase of both COX2-immunoreactive cell density and OD was determined in untreated mice compared to M. U-care–treated animals ($1700.29 \pm 178.33$ and $212.04 \pm 24.60$ vs. $292.15 \pm 56.24$ and $29.68 \pm 5.49$, respectively; Figure 9 Panel H and I).

## 3. Discussion

After traditional and novel therapies are widely employed [41], complementary and integrative medicine (CIM) was recently adopted as an innovative approach in oncological care, often associated with positive impacts in cancer patients in terms of better response to treatment, adverse side effects reduction, and quality of life (QoL) improvement [9].

One of the most promising integrative approaches in cancer therapy is mycotherapy, which appears to have several benefits, in terms of improvement of the patients' overall response rate to conventional oncological treatment, immunity function enhancement, and adverse side effects reduction.

Thus, aiming to explore the potential contribution of mycotherapy in the critical management of cancer patients, in the present investigation, we exploited the effect of a novel medicinal mushroom blend, namely Micotherapy U-care, in a 4T1 triple-negative mouse BC model. Specifically, we studied the murine pulmonary tissue with the goal to deeply comprehend Micotherapy U-care's impact on typical metastatic pattern of primary TNBC, evaluating the potential effects of its employment as a preventive treatment and as long-lasting supplementation.

Concerning QoL and the composite indicator of physical well-being assessment, it has to be noticed that, throughout the entire experimental duration, the M. U-care–treated mice had the higher water consumption compared to both untreated animals and healthy controls. In accordance to an increasing body of literature, we may hypothesise a role for fibroblast growth factor 21 (FGF21), known to stimulates water-drinking behaviour in mice [42], whose expression is regulated by nutritional status; in fact, changes in the FGF21 level are important for adaption to changes of the nutritional balance such as oversupply of macronutrients or changes of amino acid composition [43,44]. In the present investigation, M. U-care–treated mice only received the oral supplementation with the novel medicinal mushroom blend, whose intake may induce an increase of FGF21 levels, which may have a pivotal role in the thirst response.

H&E staining, recognizing various tissue types and the morphologic changes that form the basis of contemporary cancer diagnosis [45], together with TEM analysis, were used to reveal possible pulmonary morphological and ultrastructural alterations. These changes are dramatically manifest in the lung parenchyma of the tumor-induced mice, with the Untreated animals showing more striking injury regarding wall-thickened collapsed alveoli, hemorrhagic foci and parenchymal fibrosis compared to M. U-care–treated mice demonstrating a milder damage. Notably, concerning the metastatic density, we showed a statistically significant reduction (about 50%) in M. U-care–treated mice compared to untreated animals. Neoformations were often localized in the outer pulmonary area, and displayed heterogeneous cellularity, with prevalent nodular organization typically characterized by defined, tight clusters of round cells, nonetheless paralleled by a sporadic columnar organization with homogeneous cellularity, i.e., cell ropes with parallel orientations [46,47].

Furthermore, an enhanced presence of type II pneumocytes, characterized by piles of vacuolated and surfactant-engulfed lamellar bodies, was also observed in untreated mice. Notably, the widespread presence of several activated eosinophilic granulocytes, exhibiting the characteristic presence of numerous cytoplasmic crystalloid-containing eosinophil granules was evidently increased in M. U-care–treated mice only, thus suggesting that the medicinal mushroom blend may act on diverse cytokines balance, improving immune surveillance [9].

Collagen detection in histological samples represents an important procedure to estimate tissue localization and quantitative expression of connective fibers. In pathological conditions such as fibrosis, which results from an imbalance between collagen deposition and reabsorption due to chronic inflammatory processes, tissue collagen quantification represents an important tool in the clinical diagnosis as well as for outcome prediction and therapy individualization, as in the case of lungs [40]. In this view, Picrosirius Red staining revealed collagen fibrils bundles radiating from bronchiolar wall to the lung parenchyma, also inside the tumor masses; peculiarly, collagen fibers encircled the metastases outline. An extremely significant enhancement of the histochemically positive bronchiolar wall area and OD was measured in untreated mice (about five-fold greater), compared to M. U-care–treated

animals. Notably, the comparison between M. U-care–treated mice and healthy controls revealed the absence of any statistically significant difference.

Inflammation is a critical component of tumor progression, invasiveness and metastatic process [48–50], specifically in the case of TNBC characterized by high aggressiveness [51].

IL-6 plays a pivotal role in linking chronic inflammation to cancer initiation, growth and metastasis [52–55]. In the present investigation, a significant decrease of IL-6-immunoreactive cell density was measured in lung parenchyma and metastases of M. U-care–treated mice (about 3–4 fold lower) compared to untreated animals. Interestingly, no statistical difference was determined when comparing M. U-care–treated mice and healthy controls.

We may hypothesize that the lower expression of IL-6 determined in M. U-care–treated mice would be related to a decrease in cancer cell proliferation, in which IL-6 could act on Bcl-2 expression, altering the proliferation/apoptosis balance toward neoplastic cell apoptosis. This hypothesis seems to be strongly corroborated by previous in vitro findings, using BC cell models exposed to *G. frondosa* and *G. lucidum* [9,12,30,56].

Concerning TGF-β, this pleiotropic cytokine regulates numerous biological processes of various tissues in an autocrine and paracrine manner. The role of TGF-β in cancer is complicated, and its aberrant signaling activity is well known to play dual roles in cancer depending on tumor stage and cellular context [57–60]. Our data demonstrated a significant enhancement of both TGF-β1-immunoreactive cell density and OD (about 5–6 fold higher) in lung parenchyma of M. U-care–treated mice compared to healthy controls. Diversely, a similar TGFβ1 expression pattern was observed both in lung parenchyma as well as in metastatic tissue, comparing intreated and M. U-care treated–mice, revealing no statistically significant difference concerning cellular density or OD.

Growth factors, cytokines, and enzymes (e.g., TGF-β, IL-6, NOS2, and COX2) are known to stimulate the free radical species (reactive oxygen, ROS, and nitrogen, NOS, species) production, which promote tumor development and progression [61,62]. As a matter of fact, cancer cells express increased levels of anti-oxidant molecules to detoxify from ROS, but such an increase is not enough to counterbalance the intracellular ROS levels [63]. Indeed, a vicious circle takes place in which ROS activates inflammatory cells, stimulating the release of a variety of inflammatory cytokines, which subsequently mediates the tumor niche thus promoting cancer stem cell maintenance, replenishment and switch from epithelial to mesenchymal cell [64].

Literature data reported SOD1 overexpression in malignant BC cells, and the development of novel drug complexes targeting SOD activity can be considered as a promising strategy in the chemotherapy of malignant tumors [65]. In the present study, a similar SOD1 immunoreactivity was measured both in pulmonary parenchyma and metastases comparing M. U-care–treated and untreated animals, suggesting that Micotherapy U-care blend supplementation before tumor cells injection and throughout the following experimental time, seemed to not affect SOD1 expression pattern during tumor progression, until death.

Previous data suggested that co-expression of NOS2 and COX2 is a strong prognostic indicator in TNBC patients [66], also contributing to tumor aggressiveness and poor patient prognosis [67].

It has been widely documented that nitric oxide (NO) functional roles comprise a complex spectrum in the tumor context, touching on all hallmarks of cancer, and being also considered a tumor cell cytotoxic molecule, triggering apoptosis and necrosis [68]. NOS2 expression in cancer cells often predicts poor patient outcome [69].

COX2 is frequently expressed in many types of cancers exerting a pleiotropic and multifaceted role in genesis or promotion of carcinogenesis and cancer cell resistance to chemo- and radiotherapy [70].

In the present investigation, NOS2- and COX2-immunopositivity significantly enhanced in untreated mice, compared to both M. U-care–treated and healthy controls, in terms of cellular density and OD. The strongest immunoreactivity was localized at parenchymal and metastatic level, associated with the presence of several immunopositive inflammatory cells. Regarding the metastases, an

extremely significant increase of both NOS2- and COX2-immunoreactive cell density and OD was determined in untreated mice compared to M. U-care–treated animals.

Considering all the molecular markers immunohistochemically investigated, it was noticed that the comparative assessment of lung parenchyma and metastases revealed a matching trend of protein expression. This finding strongly suggests that the tumor microenvironment, consisting of surrounding lung parenchyma, mirrors the cellular processes occurring in metastatic tissue. In fact, our data highlighted that both considered tissue districts exhibited a similar alteration leaning, with the only exception of TGFβ1.

In particular, concerning this latter molecule, we may suppose that the significant enhancement detected in M. U-care–treated mice lung parenchyma only, might be due to the well-known TGFβ1 dichotomous effect [60,71]. Specifically, in the pulmonary normal and premalignant epithelial cancer cells, the increased activation of TGFβ signaling could promote cell-cycle arrest and apoptosis to sustain tissue homeostasis and to suppress aberrant cell growth, thereby playing a tumor-suppressive role. Relevantly, this hypothesis properly fits with the well-known anti-cancer and immuno-modulating activity broadly demonstrated for several medicinal mushroom supplementations.

Ultimately, our present data clearly demonstrated a significant reduced expression of specific oxidative stress markers in M. U-care–treated mice compared to untreated animals. In line with the above hypothesised role of FGF21 in thirst response, it has to be taken into account that this molecule is a potent hormone modulator able to reduce oxidative stress and in parallel increasing autophagy [72]. Concerning autophagy, a major process in maintaining intracellular homeostasis, degrading intracellular waste particularly in damaged tissues [73], it is a known target of FGF21 and a modulator of apoptosis and oxidative stress, but our analyses regarding cell death pathways are still ongoing. Nonetheless, we may hypothesise the activation of a cellular cascade in which an increase in FGF21 level enhances the autophagic occurrence, which may play an anti-metastatic role [73], thus triggering an impediment to tumour progression. This could be link with the dramatic reduced pulmonary metastasis density and nodules number that we detected in M. U-care–treated mice only, compared to untreated animals.

## 4. Materials and Methods

### 4.1. Blend Supplementation

The novel medicinal mushroom blend supplement Micotherapy U-care was provided by A.V.D. Reform s.r.l. (Noceto, Parma, Italy), consisting of a mixture of five fungal species (Table 2).

**Table 2.** Details on Micotherapy U-care supplement composition.

| Fungal Species | ID Code | Weight % Used in Blend | Part Used |
|---|---|---|---|
| Agaricus blazei | 7700 | 20% | Sporophores |
| Cordyceps sinensis | Cm2 | 20% | Sporophores and mycelia |
| Ganoderma lucidum | Gač | 20% | Sporophores |
| Grifola frondosa | Gf3 | 20% | Sporophores |
| Lentinula edodes | Le.ed.1 | 20% | Sporophores |

The identity of fungal strains used in Micotherapy U-care supplement production was confirmed by sequencing ITS regions. Fungal samples, grown in Petri dishes were homogenized using ultra turax homogenizer. Genomic DNA was extracted using DNeasy mini plant kit (Qiagen NV, Venlo, Netherlands) according to the manufacturer's protocol. ITS regions were amplified using two sets of primers: ITS F 5′-AGAAAGTCGTAACAAGGTTTCCGTAG-3′, ITS R 5′-TTTTCCTCCGCTCATTGATATGCTT-3′, ITS-g F 5′-TCCGTAGGTGAACCTGCGG-3′, and ITS-g R 5′-TCCTCCGCTTATTGATATGC-3′. Amplicons were checked using agarose gel electrophoresis

and purified using QIAquick PCR Purification Kit (Qiagen NV, the Netherlands). Purified PCR products were sequenced by Eurofins Genomics (Konstanz, Germany). Obtained sequences from both primer-pair products were joined into consensus sequence and aligned against known DNA sequences using NCBI Nucleotide Blast software.

All strains were maintained in the Mycomedica d.o.o. (Mycomedica Ltd., Podkoren 72, 4280, Kranjska Gora, Slovenia), except for *Agaricus blazei*, which was maintained in the Mycelia BVBA (Veldeken 27 9850, Deinze, Belgium).

Fruiting bodies and/or mycelia were cultivated on organic, plant-based substrate for two to four months at 23 °C in a 1000 ± 100 ppm $CO_2$ atmosphere. After harvesting, each kg of fresh material was extracted 3 h at 95 °C with 15 L of water with addition of 10% ethanol. After extraction, solids were filtered out and remaining liquid dried under vacuum (65 °C and 150 mbar) until moisture content lower than 7% was achieved. Dry extracts were milled using a Hosokawa Alpine UPZ160 mill into particles smaller than 200 μm and mixed according to specified proportions (Table 2).

All the raw materials and final products were routinely checked following GMP, in accordance to the hazard analysis and critical control points (HACCP) system, with guaranteed traceability.

In particular, QC of Micotherapy U-care mushroom blend were checked for each batch, as following: the polysaccharide content of Micotherapy U-care was determined using β-Glucan Assay Kit (Megazyme, LTD., Wicklow, Ireland) and expressed as total (α plus β) glucan content and 1,3-1,6 beta-glucans (Table 3).

**Table 3.** Nutrient composition of Micotherapy U-care (supplied by A. V. D. Reform s.r.l., Noceto, Parma, Italy).

| Components | Per Capsule (mg) |
|---|---|
| *Ganoderma lucidum* | 150 mg |
| *Grifola frondosa* | 150 mg |
| *Agaricus blazei* | 150 mg |
| *Cordyceps sinensis* | 150 mg |
| *Lentinula edodes* | 150 mg |
| Titled in polysaccharides (α plus β) | >30% |
| 1,3-1,6 Beta-glucans | >15% |

### 4.2. Cell Culture

The mice BC cell line, 4T1, was obtained from the American Type Culture Collection (ATCC, Manassas, Virginia, USA) and cultured in RPMI-1640 medium supplemented with 10% fetal bovine serum, 1% penicillin/streptomycin at 37 °C in a humidified atmosphere (95% air/5% $CO_2$). All cell culture reagents were from Euroclone S.p.A., Celbio S.p.A. (Pero, Milan, Italy).

### 4.3. Animals and Experimental Design

Thirty-four eight-week-old wild-type female mice (strain BALB/c) were purchased from Charles River Italia (Calco, Italy). The pathogen-free mice were acclimatized for at least three weeks before conducting the experiments. Mice were kept in cages with two mice at the Animal Care Facility of the University of Pavia at 21 ± 2 °C, with humidity at 50 ± 10%, and under a 12 h light/dark cycle throughout the experiments. Water and food (standard pellet) were provided ad libitum.

All experimental procedures were performed in compliance with the European Council Directive 2010/63/EU on the care and use of laboratory animals, also following the guidelines set by the institution's animal welfare committee, the Ethics Committee of Pavia University (Ministry of Health, License number 364/2018-PR, approval date:17 May 2018). Hence, all animals used in this research

have been treated humanely according to the institutional guidelines, with due consideration for the alleviation of distress and discomfort.

For experiments, researchers were blinded to the group assignment.

After the acclimatization, for a period of two months, 16 (M. U-care treated mice) out of 34 mice received a drink made of Micotherapy U-care provided by A.V.D. Reform s.r.l. (Noceto, Parma, Italy), consisting of a mixture of mycelium and sporophores extracts of five varieties, including *Agaricus blazei* (20%), *Cordyceps sinensis* (20%), *Ganoderma lucidum* (20%), *Grifola frondosa* (20%), and *Lentinula edodes* (20%).The mycotherapic blend was solubilized in water, in such a way that every mouse received 4 mg of supplement per day. This dose was chosen to mimic the oral supplementation in humans (about 1.5 g/day). The remaining mice, i.e., not-treated (untreated, $n = 14$) and healthy control mice ($n = 4$), were fed without any diet supplementation.

QoL in terms of body weight gain, water, food daily consumption, and locomotor activity were monitored daily.

The syngeneic tumor-bearing mice (untreated and M. U-care–treated) were generated by injecting $10^6$ of the 4T1 cells into the nape of the neck of the female BALB/c mice. The healthy control group was injected with a vehicle of phosphate-buffer saline (PBS). M. U-care–treated mice received Micotherapy U-care until sacrifice. Figure 1 shows the experimental design: T0: animals' randomization, T1: starting Micotherapy U-care oral supplementation for M. U-care–treated mice, only; T2 (about 2 months later): 4T1 cells inoculation in both untreated and M. U-care–treated mice; T3 (about 20 days later): starting monitoring and evaluations; T4 (about 15 days later): continuing monitoring and evaluations. At selected experimental times (from T1 to T4), stools, hair, and fluids were collected for further analyses. Tumor growth was monitored from T1 to T4 using ultrasound imaging. Mice locomotor activity was monitored at T1 and T3 by using a behavioral test. Primary tumor masses were visible to the naked eye as big nodules. The tumors were measured using a caliper, and the tumor volumes were calculated using the formula V = 1/2 (width$^2$ × length), as previously reported [74–76]. One day after T4, mice were euthanized.

Blood was withdrawn and centrifuged to obtain serum/plasma for future analysis, and lungs were collected.

Lung preparation for morphophysiological evaluations were performed through vascular perfusion of fixative [77]. After fixation, the lungs were carefully removed (see Section 4.4) and sectioned.

All tissue samples were processed for histopathology (hematoxylin and eosin (H&E) and Picrosirius Red staining), immunohistochemistry and ultrastructural evaluation by Transmission Electron Microscopy (TEM).

### 4.4. Emergence Test

All mice, at selected experimental times (T1 and T3), performed the emergence task, a spontaneous behavioral test, which is a variant of the open-field test that was designed to reduce anxiety by providing a safe enclosure within the open field. The emergence task was used to assess exploratory behavior and locomotor activities. Briefly, the free exploration test consists of housing mice in a compartment prior to giving the animal a free choice between a familiar compartment and a novel one. We carried out emergence tests following previously described protocols [78,79].

Mice activity was quantified by a SMART video tracking system with a selected sampling time of 40 ms/point (2 Biological Instruments, Besozzo, Varese, Italy) and a Sony CCD color video camera (PAL; Sony Europe B.V.- Italian headquarters, Milan, Italy) [79].

### 4.5. The Quality of Life Index

We assessed quality of life (QoL) using six items related to wellbeing and monitoring them during the time. For measuring QoL index, the average value and the standard deviation (SD) for each of the parameters were calculated at starting time (Ts) (T1 for average speed (cm/s), total distance (cm), resting time (s), and primary tumor volume; T2 for body weight (g) and water consumption (ml/die)).

The values obtained for each mouse at different times were compared to the average value at Ts using the following formula [79]:

$$QoL\ score = [(Value\text{-}Mean\ Value\ at\ Ts)/SD\ at\ Ts]^* \pm 0.25 \qquad (1)$$

Score values were added and resulted a QoL total score. A higher total score indicates a better quality of life.

### 4.6. Tissue Sampling, Histology, Immunohistochemistry, and Ultrastructural Morphology Evaluations

For each treatment, lung tissues were processed for the following morphological and histochemical evaluations.

#### 4.6.1. Lung Specimens Preparation

At necropsy, the top and the bottom regions of the right lungs of animals belonging to different experimental groups were dissected. Tissue samples were obtained according to a stratified random sampling scheme which is a suggested method for lung tissue in order to compensate for regional differences, which are known to exist in the lung [80] and to reduce the variability of the sampling means.

From each sample, 2–3 blocks were systematically derived, washed in NaCl 0.9% and post-fixed by immersion for 7 h in 4% paraformaldehyde in 0.1 M phosphate buffer (pH 7.4), dehydrated through a graded series of ethanol and finally embedded in Paraplast X-TRA. Eight-μm thick sections were cut in the transversal plane and collected on silane-coated slides.

#### 4.6.2. H&E: Histopathological Observations

Subsequently, to overall evaluate structural changes by light microscopy, H&E staining was performed [81]. The slides were then observed and scored with a bright-field Zeiss Axioscop Plus microscope (Carl Zeiss S.p.A., Milan, Italy). Specifically, five slides (about 20 sections) per animal were analyzed; five microscopic fields were examined in each section for each mouse per time/condition. The images were recorded with an Olympus Camedia C-5050 digital camera and stored on a PC running Olympus software (Olympus Italia, Segrate, MI, Italy).

#### 4.6.3. Picrosirius Red Staining

Serial tissue sections were stained for 1h with a Picrosirius Red solution (0.1% of Sirius Red in saturated aqueous picric acid), followed by a wash in 5% acidified water [82,83], for collagen bundle staining. Finally, the sections were dehydrated in ethanol, cleared in xylene, and mounted in Eukitt (Kindler, Freiburg, Germany).

#### 4.6.4. Immunohistochemistry: Inflammatory and Oxidative Stress Pathways Assessment

Immunocytochemical reactions were carried out simultaneously on slides of different experimental groups to avoid possible staining differences due to small changes in the procedures.

Immunohistochemistry was performed using commercial antibodies on mice lung specimens, to localize presence and distribution of different specific markers indicative of inflammation and oxidative stress: (i) Interleukin-6 (IL-6), (ii) Transforming Growth Factor-beta1 (TGF-$\beta$1), (iii) Cu–Zn superoxide dismutase-1 (SOD1), (iv) nitric oxide synthase 2 (NOS2), and (v) cyclo-oxygenase-2 (COX2).

Lung sections of healthy control, untreated, and M. U-care–treated mice were incubated overnight at room temperature in a dark moist chamber with selected monoclonal and polyclonal primary antibodies (Table 4) diluted in PBS. Proper biotinylated secondary antibodies (Table 4) and an avidin biotinylated horseradish peroxidase complex (Vector Laboratories, Burlingame, CA, USA) were used to reveal the sites of antigen/antibody interaction. The 3,3'-diaminobenzidine tetrahydrochloride peroxidase substrate (Sigma, St. Louis, MO, USA) was used as chromogen. The nuclear counterstaining was achieved by employing Carazzi's haematoxylin.

**Table 4.** Primary/secondary antibodies and respective dilution used for immunocytochemical experimental procedures.

| | Antigen | Immunogen | Manufacturer, Species, Mono-polyclonal, cat/lot. No., RRID | Diluted Used |
|---|---|---|---|---|
| **Primary antibodies** | Anti-Interleukin-6 (M-19) | Purified antibody raised against a peptide mapping at the C-terminus of IL-6 of mouse origin | Santa Cruz Biotechnology (Santa Cruz, CA, USA), Goat polyclonal IgG, Cat# sc-1265, RRID: AB_2127470 | 1:100 |
| | Anti-Transforming Growth Factor β1 (V) | Purified antibody raised against a peptide mapping at the C-terminus of TGF-β1 of human origin | Santa Cruz Biotechnology (Santa Cruz, CA, USA), Rabbit polyclonal IgG, Cat# sc-146, RRID: AB_632486 | 1:100 |
| | Anti-Superoxide Dismutase-1 (FL-154) | Purified antibody raised against amino acids 1–154 representing full length SOD1 of human origin | Santa Cruz Biotechnology (Santa Cruz, CA, USA), Rabbit polyclonal IgG, Cat# sc-11407, RRID: AB_2193779 | 1:100 |
| | Anti-Nitric Oxide Synthases-2 (M19) | Purified antibody raised against a peptide mapping at the C-terminus of NOS2 of mouse origin | Santa Cruz Biotechnology (Santa Cruz, CA, USA), Rabbit polyclonal IgG, Cat# sc-650, RRID: AB_631831 | 1:100 |
| | Anti-Cyclooxygenase-2(M-19) | Purified antibody raised against a peptide mapping at the C-terminus of COX2 of mouse origin | Santa Cruz Biotechnology (Santa Cruz, CA, USA), Goat polyclonal IgG, Cat# sc-1747, RRID: AB_2084976 | 1:100 |
| **Secondary antibodies** | Biotinylated goat anti-rabbit IgG | Gamma immunoglobulin | Vector Laboratories (Burlingame, CA, USA), Goat, lot# PK-6101, RRID: AB_2336820 | 1:200 |
| | Biotinylated rabbit anti-goat IgG | Gamma immunoglobulin | Vector Laboratories (Burlingame, CA, USA), Rabbit, Cat# PK-6105, RRID: AB_2336824 | 1:200 |

Then, the sections were dehydrated in ethanol, cleared in xylene, and finally mounted in Eukitt (Kindler, Freiburg, Germany). As negative controls, some sections were incubated with PBS in the absence of the primary antibodies: no immunoreactivity was observed in this condition.

### 4.6.5. Transmission Electron Microscopy (TEM): UA and LC Staining

Lung fragments (small blocks of about 1 mm$^3$) were fixed for 4 h by immersion in ice-cold 1.5% glutaraldehyde (Polysciences, Inc., Warrington, PA, USA) buffered with 0.07 M cacodylate buffer (pH 7.4), containing 7% sucrose, followed by post-fixation in OsO$_4$ (Sigma Chemical Co., St. Louis, MO, USA) in 0.1 M cacodylate buffer (pH 7.4) for 2 h at 4 °C, dehydrated in a graded series of ethanol and embedded in Epon 812. For light microscopy pre-examination, semithin sections (1 micrometer thick) were stained with 1% borated methylene blue. For electron microscopy, ultrathin sections (about 600 Å thick) were cut from the blocks, mounted on uncoated 200-mesh-copper grids, and doubly stained with saturated uranyl acetate in 50% acetone and Reynold's lead citrate solution. The specimens were examined with a Zeiss EM 300 electron microscope (Carl Zeiss S.p.A., Milan, Italy) operating at 80 kV.

### 4.6.6. Semiquantitative Lung Lesion Analysis

A scoring system was utilized to evaluate the pulmonary histopathology regarding the extent of tumor progression, parenchyma and metastasis morphology and various tissue damages using conventional brightfield microscopy according to a semiquantitative scale ranging from absent/undetectable (−) to maximum (++++). Specifically, 20 sections per $n = 3$ animals were analyzed, examining 5 microscopic fields in each section for each mouse per time/condition.

The localization and degree of lesions were recorded and graded as follows: (−) absent/undetectable lesions; (+) mild injury; (++) moderate damage; (+++) severe alteration; (++++) complete tissue devastation. Specifically, the following alterations were recorded: (i) alveolar structure alteration, (ii) bronchiolar epithelial cells desquamation, (iii) hemorrhagic foci incidence, (iv) number of pulmonary metastases. Peculiar primary tumor cancer features were recorded (Table 1). Concerning the metastases, we also considered (i) localization in the width of the lung and (ii) density and metastatic tissue organization (columnar vs. nodular).

### 4.6.7. Histochemical and Immunohistochemical Evaluations

For each selected marker, six slides (about 30 sections) per animal were analyzed. Pulmonary specimens with different immunolabelling extent were considered in all experimental groups. The figures show the most representative changes for each immunohistochemical reaction.

Histochemical and immunohistochemical labeling extent was evaluated on acquired digitized section images under exposure time avoiding any pixel saturation effect. The labeling intensity was measured utilizing densitometric analysis (Image-J 1.46p; NIH, Bethesda, MA, USA). The mask shape was adjusted depending on the spatial distribution of the lung specimens under measurement; the labeling was measured as the mean intensity value over the area.

The immunocytochemical intensity, indicated as optical density (OD), was evaluated in 30 cells/section per six slides/animal. Results were recorded on Microsoft Office Excel spreadsheets. OD was expressed as the product of OD value and immunopositive cell density ($*10^3$).

The following further measurements were performed: (i) Picrosirius Red–positive bronchiolar surface in mm$^2$/whole bronchiolar area in mm$^2$ and (ii) immunopositive cells density count (number of immunopositive cells/area in mm$^2$).

Concerning the metastases, both density (i.e., metastases number/surface area in mm$^2$) and area (mean area in mm$^2$/animal) were measured.

### 4.7. Statistics

Data were expressed as means ± standard error of the mean (SEM). The statistical analysis for Picrosirius Red staining was carried out using one-way ANOVA followed by Bonferroni's post-hoc

test. A Kruskal–Wallis non-parametric analysis of the semiquantitative histopathological data was performed, followed by Dunn's post-hoc test. Concerning immunohistochemistry of the lung parenchyma, the statistical differences among all experimental groups, i.e., healthy controls, M. U-care–treated, and untreated mice, were measured by one-way ANOVA followed by Bonferroni's post-hoc test. Differently, regarding the immunostainings of metastatic tissue, the statistical differences between M. U-care–treated and untreated mice were evaluated using an unpaired Student's t-test.

Two-way ANOVA and Bonferroni post-hoc tests were performed to compare the different groups regarding behavioral analysis. The differences were considered statistically significant for $p < 0.05$ (*), $p < 0.01$ (**), and $p < 0.001$ (***).

Statistical analyses were performed by using GraphPad Prism 7.0 (GraphPad Software Inc., La Jolla, CA, USA) and R software.

## 5. Conclusions

In conclusion, our data revealed that the medicinal mushrooms blend supplementation, starting before 4T1 cells injection and lasting until the end of the experiment, elicited a dramatic decrease of pulmonary metastases density. Additionally, Micotherapy U-care triggered a significant decline of both inflammatory and oxidative stress pathways as evidenced by the reduction of IL-6, NOS2, and COX2 expression pattern. We hypothesize that the measured metastases decrease can be ascribable either to direct Micotherapy U-care anti-cancer effect son lung cells or to secondary/indirect impacts of the medicinal mushroom blend on systemic inflammation and immunomodulation. We cannot exclude that both mechanisms may contribute to the observed striking effects. To properly address this dilemma, our still ongoing studies are investigating whether and how Micotherapy U-care may affect the apoptotic pathway. Preliminary data on p53 and Bcl2, whose critical role in human breast cancer is well known, seem to demonstrate an inverse expression trend of these two proteins, being the p53 overexpressed in Micotherapy U-care–treated mice. If confirmed and corroborated by further experiments, these data might support a possible role of p53 in down-regulating Bcl-2, possibly explaining the apoptosis induction by wild-type p53.

Taken together, these findings corroborate the use of Micotherapy U-care blend as a novel strategy to be used in the field of integrative oncology to improve the patient quality of life and reduce adverse side effects due to conventional cancer treatments. Thus, although further investigations are necessary to translate these experimental findings to clinical setting, turning them into new clinical therapeutic protocols, the present study remarkably supports the valuable potential of medicinal mushrooms extracts, being a natural source of novel drugs, as adjuvant therapy in the critical management of TNBC.

**Author Contributions:** Conceptualization, E.S., M.G.B., P.R, M.B., and R.D.F.; methodology, E.C.P., A.G., G.B., and F.C.; software, S.S. and B.F.; formal analysis, E.R., F.D.L., C.D.I., and D.R.; investigation, E.R., F.D.I., C.D.I., S.C., R.E., and A.R.; writing—original draft preparation, E.R., M.G.B., and P.R.; writing—review and editing, M.G.B, D.R., G.B.; supervision, E.R., C.A.L., and P.R. All authors have read and agreed to the published version of the manuscript.

**Conflicts of Interest:** The authors declare no conflict of interest.

## References

1. Bray, F.; Ferlay, J.; Soerjomataram, I.; Siegel, R.L.; Torre, L.A.; Jemal, A. Global cancer statistics 2018: GLOBOCAN estimates of incidence and mortality worldwide for 36 cancers in 185 countries. *Ca Cancer J. Clin.* **2018**, *68*, 394–424. [CrossRef] [PubMed]

2. WHO. Breast cancer. Available online: http://www.who.int/cancer/prevention/diagnosis-screening/breast-cancer/en/ (accessed on 15 November 2019).

3. Cardoso, F.; Harbeck, N.; Fallowfield, L.; Kyriakides, S.; Senkus, E.; ESMO Guidelines Working Group. Locally recurrent or metastatic breast cancer: ESMO Clinical Practice Guidelines for diagnosis, treatment and follow-up. *Ann. Oncol.* **2012**, *23* (Suppl. 7), vii11–vii19. [CrossRef] [PubMed]

4. Smith, R.A.; Duffy, S.W.; Tabár, L. Breast cancer screening: The evolving evidence. *Oncology* **2012**, *26*, 471–475. [PubMed]

5. Yadav, B.S.; Chanana, P.; Jhamb, S. Biomarkers in triple negative breast cancer: A review. *World J. Clin. Oncol.* **2015**, *6*, 252–263. [CrossRef] [PubMed]

6. Shao, F.; Sun, H.; Deng, C.X. Potential therapeutic targets of triple-negative breast cancer based on its intrinsic subtype. *Oncotarget* **2017**, *8*, 73329–73344. [CrossRef]

7. Yao, Y.; Chu, Y.; Xu, B.; Hu, Q.; Song, Q. Risk factors for distant metastasis of patients with primary triple-negative breast cancer. *Biosci. Rep.* **2019**, *39*, BSR20190288. [CrossRef]

8. Wasser, S.P. Medicinal Mushrooms in Human Clinical Studies. Part I. Anticancer, Oncoimmunological, and Immunomodulatory Activities: A Review. *Int. J. Med. Mushrooms* **2017**, *19*, 279–317. [CrossRef]

9. Rossi, P.; Difrancia, R.; Quagliariello, V.; Savino, E.; Tralongo, P.; Randazzo, C.L.; Berretta, M. B-glucans from *Grifola frondosa* and *Ganoderma lucidum* in breast cancer: An example of complementary and integrative medicine. *Oncotarget* **2018**, *9*, 24837–24856. [CrossRef]

10. Blagodatski, A.; Yatsunskaya, M.; Mikhailova, V.; Tiasto, V.; Kagansky, A.; Katanaev, V.L. Medicinal mushrooms as an attractive new source of natural compounds for future cancer therapy. *Oncotarget* **2018**, *9*, 29259–29274. [CrossRef]

11. Jiang, J.; Sliva, D. Novel medicinal mushroom blend suppresses growth and invasiveness of human breast cancer cells. *Int. J. Oncol.* **2010**, *37*, 1529–1536.

12. Alonso, E.N.; Ferronato, M.J.; Fermento, M.E.; Gandini, N.A.; Romero, A.L.; Guevara, J.A.; Facchinetti, M.M.; Curino, A.C. Antitumoural and antimetastatic activity of Maitake D-Fraction in triple-negative breast cancer cells. *Oncotarget* **2018**, *9*, 23396–23412. [CrossRef] [PubMed]

13. Cai, H.; Li, J.; Gu, B.; Xiao, Y.; Chen, R.; Liu, X.; Xie, X.; Cao, L. Extracts of *Cordyceps sinensis* inhibit breast cancer cell metastasis via down-regulation of metastasis-related cytokines expression. *J. Ethnopharmacol.* **2018**, *214*, 106–112. [CrossRef] [PubMed]

14. Mizuno, T.K. Kawariharatake, *Agaricus blazei* Murrill medicinal and dietary effects. *Food Rev. Int.* **1995**, *11*, 167–172. [CrossRef]

15. Firenzuoli, F.; Gori, L.; Lombardo, G. The Medicinal Mushroom *Agaricus blazei* Murrill: Review of Literature and Pharmaco-Toxicological Problems. *Evid. Based Complement. Altern. Med.* **2008**, *5*, 3–15. [CrossRef] [PubMed]

16. Da Silva de Souza, A.C.; Correa, V.G.; Goncalves, G.d.A.; Soares, A.A.; Bracht, A.; Peralta, R.M. *Agaricus blazei* Bioactive Compounds and their Effects on Human Health: Benefits and Controversies. *Curr. Pharm. Des.* **2017**, *23*, 2807–2834. [CrossRef] [PubMed]

17. Kim, Y.S.; Kim, B.H.; Kim, G.S.; Jang, J.S.; Kim, S.Y.; Choi, B.D.; Kim, J.O.; Ha, Y.L. Anti-carcinogenic actions of glycoprotein conjugated with isoflavones from submerged-liquid culture of *Agaricus blazei* mycelia through reciprocal expression of Bcl-2 and Bax proteins. *J. Biomed. Res.* **2014**, *15*, 200–206. [CrossRef]

18. De Sá-Nakanishi, A.B.; Soares, A.A.; de Oliveira, A.L.; Comar, J.F.; Peralta, R.M.; Bracht, A. Effects of treating old rats with an aqueous *Agaricus blazei* extract on oxidative and functional parameters of the brain tissue and brain mitochondria. *Oxid. Med. Cell Longev.* **2014**, *2014*, 563179. [CrossRef]

19. Ohno, S.; Sumiyoshi, Y.; Hashine, K.; Shirato, A.; Kyo, S.; Inoue, M. Phase I Clinical Study of the Dietary Supplement, *Agaricus blazei* Murill, in Cancer Patients in Remission. *Evid. Based Complement. Altern. Med.* **2011**, *2011*, 192381. [CrossRef]

20. Ahn, W.S.; Kim, D.J.; Chae, G.T.; Lee, J.M.; Bae, S.M.; Sin, J.I.; Kim, Y.W.; Namkoong, S.E.; Lee, I.P. Natural killer cell activity and quality of life were improved by consumption of a mushroom extract, *Agaricus blazei* Murill Kyowa, in gynecological cancer patients undergoing chemotherapy. *Int. J. Gynecol. Cancer* **2004**, *14*, 589–594. [CrossRef]

21. Jordan, J.L.; Nowak, A.; Lee, T.D.G. Activation of innate immunity to reduce lung metastases in breast cancer. *Cancer Immunol. Immunother.* **2010**, *59*, 789–797. [CrossRef]

22. Wang, J.; Nie, S.; Cui, S.W.; Wang, Z.; Phillips, A.O.; Phillips, G.O.; Li, Y.; Xie, M. Structural characterization and immunostimulatory activity of a glucan from natural *Cordyceps sinensis*. *Food Hydrocol.* **2017**, *67*, 139–147. [CrossRef]

23. Li, S.P.; Li, P.; Dong, T.T.; Tsim, K.W. Anti-oxidation activity of different types of natural *Cordyceps sinensis* and cultured *Cordyceps mycelia*. *Phytomedicine* **2001**, *8*, 207–212. [CrossRef] [PubMed]

24. Wu, T.S.; Shi, L.S.; Kuo, S.C. Cytotoxicity of *Ganoderma lucidum* triterpenes. *J. Nat. Prod.* **2001**, *64*, 1121–1122. [CrossRef] [PubMed]

25. Jiang, J.; Slivova, V.; Harvey, K.; Valachovicova, T.; Sliva, D. *Ganoderma lucidum* suppresses growth of breast cancer cells through the inhibition of Akt/NF-kappaB signaling. *Nutr. Cancer* **2004**, *49*, 209–216. [CrossRef] [PubMed]

26. Sliva, D.; Sedlak, M.; Slivova, V.; Valachovicova, T.; Lloyd, F.P.; Ho, N.W.Y. Biologic activity of spores and dried powder from *Ganoderma lucidum* for the inhibition of highly invasive human breast and prostate cancer cells. *J. Altern. Complement. Med.* **2003**, *9*, 491–497. [CrossRef] [PubMed]

27. Zhao, H.; Zhang, Q.; Zhao, L.; Huang, X.; Wang, J.; Kang, X. Spore Powder of *Ganoderma lucidum* Improves Cancer-Related Fatigue in Breast Cancer Patients Undergoing Endocrine Therapy: A Pilot Clinical Trial. *Evid. Based Complement. Altern. Med.* **2012**, *2012*, 809614. [CrossRef]

28. Jin, X.; Ruiz Beguerie, J.; Sze, D.M.Y.; Chan, G.C.F. *Ganoderma lucidum* (Reishi mushroom) for cancer treatment. *Cochrane Database Syst. Rev.* **2016**, *4*, CD007731. [CrossRef]

29. Soares, R.; Meireles, M.; Rocha, A.; Pirraco, A.; Obiol, D.; Alonso, E.N.; Joos, G.; Balogh, G. Maitake (D fraction) mushroom extract induces apoptosis in breast cancer cells by BAK-1 gene activation. *J. Med. Food* **2011**, *14*, 563–572. [CrossRef]

30. Alonso, E.N.; Orozco, M.; Nieto, A.E.; Balogh, G.A. Genes Related to Suppression of Malignant Phenotype Induced by Maitake D-Fraction in Breast Cancer Cells. *J. Med. Food* **2013**, *16*, 602–617. [CrossRef]

31. Said, T.K.; Moraes, R.C.; Singh, U.; Kittrell, F.S.; Medina, D. Cyclin-dependent kinase (cdk) inhibitors/cdk4/cdk2 complexes in early stages of mouse mammary preneoplasia. *Cell Growth Differ.* **2001**, *12*, 285–295.

32. Van 't Veer, L.J.; Dai, H.; van de Vijver, M.J.; He, Y.D.; Hart, A.A.M.; Mao, M.; Peterse, H.L.; van der Kooy, K.; Marton, M.J.; Witteveen, A.T.; et al. Gene expression profiling predicts clinical outcome of breast cancer. *Nature* **2002**, *415*, 530–536. [CrossRef] [PubMed]

33. Doughtery, E.R.; Jianping, H.; Bittner, M.L. Validation of Computational Methods in Genomics. *Curr. Genom.* **2007**, *8*, 1–19.

34. Deng, G.; Lin, H.; Seidman, A.; Fornier, M.; D'Andrea, G.; Wesa, K.; Yeung, S.; Cunningham-Rundles, S.; Vickers, A.J.; Cassileth, B. A phase I/II trial of a polysaccharide extract from *Grifola frondosa* (Maitake mushroom) in breast cancer patients: Immunological effects. *J. Cancer Res. Clin. Oncol.* **2009**, *135*, 1215–1221. [CrossRef] [PubMed]

35. Fang, N.; Li, Q.; Yu, S.; Zhang, J.; He, L.; Ronis, M.J.J.; Badger, T.M. Inhibition of growth and induction of apoptosis in human cancer cell lines by an ethyl acetate fraction from shiitake mushrooms. *J. Altern. Complement. Med.* **2006**, *12*, 125–132. [CrossRef]

36. Ren, Z.; Li, J.; Song, X.; Zhang, J.; Wang, W.; Wang, X.; Gao, Z.; Jing, H.; Li, S.; Jia, L. The regulation of inflammation and oxidative status against lung injury of residue polysaccharides by *Lentinula edodes*. *Int. J. Biol. Macromol.* **2018**, *106*, 185–192. [CrossRef]

37. Suzuki, N.; Takimoto, Y.; Suzuki, R.; Arai, T.; Uebaba, K.; Nakai, M.; Strong, J.M.; Tokuda, H. Efficacy of oral administration of *Lentinula eodedes* mycelia extract for breast cancer patients undergoing postoperative hormone therapy. *Asian Pac. J. Cancer Prev.* **2013**, *14*, 3469–3472. [CrossRef]

38. Nagashima, Y.; Maeda, N.; Yamamoto, S.; Yoshino, S.; Oka, M. Evaluation of host quality of life and immune function in breast cancer patients treated with combination of adjuvant chemotherapy and oral administration of *Lentinula edodes* mycelia extract. *Onco Targets Ther.* **2013**, *6*, 853–859. [CrossRef]

39. Nagashima, Y.; Yoshino, S.; Yamamoto, S.; Maeda, N.; Azumi, T.; Komoike, Y.; Okuno, K.; Iwasa, T.; Tsurutani, J.; Nakagawa, K.; et al. *Lentinula edodes* mycelia extract plus adjuvant chmotherapy for breast cancer patients: Results of a randomized study on host quality of life and immune function improvement. *Mol. Clin. Oncol.* **2017**, *7*, 359–366. [CrossRef]

40. Segnani, C.; Ippolito, C.; Antonioli, L.; Pellegrini, C.; Blandizzi, C.; Dolfi, A.; Bernardini, N. Histochemical Detection of Collagen Fibers by Sirius Red/Fast Green Is More Sensitive than van Gieson or Sirius Red Alone in Normal and Inflamed Rat Colon. *PLoS ONE* **2015**, *10*, e0144630. [CrossRef]

41. Pienta, K.J.; McGregor, N.; Axelrod, R.; Axelrod, D.E. Ecological therapy for cancer: Defining tumours using an ecosystem paradigm suggests new opportunities for novel cancer treatments. *Transl. Oncol.* **2008**, *1*, 158–164. [CrossRef]

42. Song, P.; Zechner, C.; Hernandez, G.; Cánovas, J.; Xie, Y.; Sondhi, V.; Wagner, M.; Stadlbauer, V.; Horvath, A.; Leber, B.; et al. The Hormone FGF21 Stimulates Water Drinking in Response to Ketogenic Diet and Alcohol. *Cell Metab.* **2018**, *27*, 1338–1347. [CrossRef] [PubMed]

43. Kim, K.H.; Lee, M.S. FGF21 as a stress hormone: The roles of FGF21 in stress adaptation and the treatment of metabolic diseases. *Diabetes Metab. J.* **2014**, *38*, 245–251. [CrossRef] [PubMed]

44. Martinez-Garza, U.; Torres-Oteros, D.; Yarritu-Gallego, A.; Marrero, P.F.; Haro, D.; Relat, J. Fibroblast Growth Factor 21 and the Adaptive Response to Nutritional Challenges. *Int. J. Mol. Sci.* **2019**, *20*, E4692. [CrossRef] [PubMed]

45. Fischer, A.H.; Jacobson, K.A.; Rose, J.; Zeller, R. Hematoxylin and eosin staining of tissue and cell sections. *CSH Protoc.* **2008**, *2008*, pdb-prot4986. [CrossRef]

46. Kenny, P.A.; Lee, G.Y.; Myers, C.A.; Neve, R.M.; Semeiks, J.R.; Spellman, P.T.; Lorenz, K.; Lee, E.H.; Barcellos-Hoff, M.H.; Petersen, O.W.; et al. The morphologies of breast cancer cell lines in three-dimensional assays correlate with their profiles of gene expression. *Mol. Oncol.* **2007**, *1*, 84–96. [CrossRef]

47. Krakhmal, N.V.; Zavyalova, M.V.; Denisov, E.V.; Vtorushin, S.V.; Perelmuter, V.M. Cancer Invasion: Patterns and Mechanisms. *Acta Nat.* **2015**, *7*, 17–28. [CrossRef]

48. Hanahan, D.; Weinberg, R.A. Hallmarks of cancer: The next generation. *Cell* **2011**, *144*, 646–674. [CrossRef]

49. Liou, G.Y.; Storz, P. Reactive oxygen species in cancer. *Free Radic. Res.* **2010**, *44*, 479–496. [CrossRef]

50. Fisher, D.T.; Appenheimer, M.M.; Evans, S.S. The two faces of IL-6 in the tumour microenvironment. *Semin. Immunol.* **2014**, *26*, 38–47. [CrossRef]

51. Liubomirski, Y.; Lerrer, S.; Meshel, T.; Rubinstein-Achiasaf, L.; Morein, D.; Wiemann, S.; Körner, C.; Ben-Baruch, A. Tumour-Stroma-Inflammation Networks Promote Pro-metastatic Chemokines and Aggressiveness Characteristics in Triple-Negative Breast Cancer. *Front. Immunol.* **2019**, *10*, 757. [CrossRef]

52. Garcia-Tuñón, I.; Ricote, M.; Ruiz, A.; Fraile, B.; Paniagua, R.; Royuela, M. IL-6, its receptors and its relationship with bcl-2 and bax proteins in infiltrating and in situ human breast carcinoma. *Histopathology* **2005**, *47*, 82–89. [CrossRef] [PubMed]

53. Coussens, L.M.; Zitvogel, L.; Palucka, A.K. Neutralizing tumour-promoting chronic inflammation: A magic bullet? *Science* **2013**, *339*, 286–291. [CrossRef] [PubMed]

54. Mantovani, A.; Allavena, P.; Sica, A.; Balkwill, F. Cancer-related inflammation. *Nature* **2008**, *454*, 436–444. [CrossRef]

55. Grivennikov, S.I.; Greten, F.R.; Karin, M. Immunity, inflammation, and cancer. *Cell* **2010**, *140*, 883–899. [CrossRef] [PubMed]

56. Barbieri, A.; Quagliariello, V.; Del Vecchio, V.; Falco, M.; Luciano, A.; Amruthraj, N.J.; Nasti, G.; Ottaiano, A.; Berretta, M.; Iaffaioli, R.V.; et al. Anticancer and Anti-Inflammatory Properties of *Ganoderma lucidum* Extract Effects on Melanoma and Triple-Negative Breast Cancer Treatment. *Nutrients* **2017**, *9*, E210. [CrossRef]

57. Joshi, A.; Cao, D. TGF-beta signaling, tumour microenvironment and tumour progression: The butterfly effect. *Front. Biosci.* **2010**, *15*, 180–194. [CrossRef]

58. Papageorgis, P.; Stylianopoulos, T. Role of TGFβ in regulation of the tumour microenvironment and drug delivery (review). *Int. J. Oncol.* **2015**, *46*, 933–943. [CrossRef]

59. Moore-Smith, L.D.; Isayeva, T.; Lee, J.H.; Frost, A.; Ponnazhagan, S. Silencing of TGF-β1 in tumour cells impacts MMP-9 in tumour microenvironment. *Sci. Rep.* **2017**, *7*, 8678. [CrossRef]

60. Massagué, J.; Gomis, R.R. The logic of TGFbeta signaling. *FEBS Lett.* **2006**, *580*, 2811–2820. [CrossRef]

61. Prasad, S.; Gupta, S.C.; Tyagi, A.K. Reactive oxygen species (ROS) and cancer: Role of antioxidative nutraceuticals. *Cancer Lett.* **2017**, *387*, 95–105. [CrossRef]

62. Kumari, S.; Badana, A.K.; Malla, R. Reactive Oxygen Species: A Key Constituent in Cancer Survival. *Biomark Insights* **2018**, *13*, 1177271918755391. [CrossRef] [PubMed]

63. Galadari, S.; Rahman, A.; Pallichankandy, S.; Thayyullathil, F. Reactive oxygen species and cancer paradox: To promote or to suppress? *Free Radic. Biol. Med.* **2017**, *104*, 144–164. [CrossRef] [PubMed]

64. Gu, H.; Huang, T.; Shen, Y.; Liu, Y.; Zhou, F.; Jin, Y.; Sattar, H.; Wei, Y. Reactive Oxygen Species-Mediated Tumour Microenvironment Transformation: The Mechanism of Radioresistant Gastric Cancer. *Oxid. Med. Cell Longev.* **2018**, *2018*, 5801209. [CrossRef] [PubMed]

65. Kepinska, M.; Kizek, R.; Milnerowicz, H. Metallothionein and Superoxide Dismutase-Antioxidative Protein Status in Fullerene-Doxorubicin Delivery to MCF-7 Human Breast Cancer Cells. *Int. J. Mol. Sci.* **2018**, *19*, E3253. [CrossRef]

66. Basudhar, D.; Bharadwaj, G.; Somasundaram, V.; Cheng, R.Y.S.; Ridnour, L.A.; Fujita, M.; Lockett, S.J.; Anderson, S.K.; McVicar, D.W.; Wink, D.A. Understanding the tumour micro-environment communication network from an NOS2/COX2 perspective. *Br. J. Pharm.* **2019**, *176*, 155–176. [CrossRef]

67. Esbona, K.; Yi, Y.; Saha, S.; Yu, M.; Van Doorn, R.R.; Conklin, M.W.; Graham, D.S.; Wisinski, K.B.; Ponik, S.M.; Eliceiri, K.W.; et al. The Presence of Cyclooxygenase 2, Tumour-Associated Macrophages, and Collagen Alignment as Prognostic Markers for Invasive Breast Carcinoma Patients. *Am. J. Pathol.* **2018**, *188*, 559–573. [CrossRef]

68. Brüne, B.; Courtial, N.; Dehne, N.; Syed, S.N.; Weigert, A. Macrophage NOS2 in Tumour Leukocytes. *Antioxid. Redox Signal.* **2017**, *26*, 1023–1043. [CrossRef]

69. Thomas, D.D.; Wink, D.A. NOS2 as an Emergent Player in Progression of Cancer. *Antioxid. Redox Signal.* **2017**, *26*, 963–965. [CrossRef]

70. Hashemi Goradel, N.; Najafi, M.; Salehi, E.; Farhood, B.; Mortezaee, K. Cyclooxygenase-2 in cancer: A review. *J. Cell Physiol.* **2019**, *234*, 5683–5699. [CrossRef]

71. Yeh, H.W.; Lee, S.S.; Chang, C.Y.; Lang, Y.D.; Jou, Y.S. A New Switch for TGFβ in Cancer. *Cancer Res.* **2019**, *79*, 3797–3805. [CrossRef]

72. Zhou, K.; Chen, H.; Lin, J.; Xu, H.; Wu, H.; Bao, G.; Li, J.; Deng, X.; Shui, X.; Gao, W.; et al. FGF21 augments autophagy in random-pattern skin flaps via AMPK signalling pathways and improves tissue survival. *Cell Death Dis.* **2019**, *10*, 872. [CrossRef] [PubMed]

73. Su, Z.; Yang, Z.; Xu, Y.; Chen, Y.; Yu, Q. Apoptosis, autophagy, necroptosis, and cancer metastasis. *Mol. Cancer* **2015**, *14*, 48. [CrossRef] [PubMed]

74. Kim, E.J.; Choi, M.R.; Park, H.; Kim, M.; Hong, J.E.; Lee, J.Y.; Chun, H.S.; Lee, K.W.; Yoon Park, J.H. Dietary fat increases solid tumor growth and metastasis of 4T1 murine mammary carcinoma cells and mortality in obesity-resistant BALB/c mice. *Breast Cancer Res.* **2011**, *13*, R78. [CrossRef] [PubMed]

75. Nigjeh, S.E.; Yeap, S.K.; Nordin, N.; Rahman, H.; Rosli, R. In Vivo Anti-Tumor Effects of Citral on 4T1 Breast Cancer Cells via Induction of Apoptosis and Downregulation of Aldehyde Dehydrogenase Activity. *Molecules* **2019**, *24*, E3241. [CrossRef] [PubMed]

76. Fu, Y.; Guo, F.; Chen, H.; Lin, Y.; Fu, X.; Zhang, H.; Ding, M. Core needle biopsy promotes lung metastasis of breast cancer: An experimental study. *Mol. Clin. Oncol.* **2019**, *10*, 253–260. [CrossRef] [PubMed]

77. Roda, E.; Bottone, M.G.; Biggiogera, M.; Milanesi, G.; Coccini, T. Pulmonary and hepatic effects after low dose exposure to nanosilver: Early and long-lasting histological and ultrastructural alterations in rat. *Toxicol. Rep.* **2019**, *6*, 1047–1060. [CrossRef]

78. Brandalise, F.; Cesaroni, V.; Gregori, A.; Repetti, M.; Romano, C.; Orrù, G.; Botta, L.; Girometta, C.; Guglielminetti, M.L.; Savino, E.; et al. Dietary Supplementation of *Hericium erinaceus* Increases Mossy Fiber-CA3 Hippocampal Neurotransmission and Recognition Memory in Wild-Type Mice. *Evid. Based Complement. Altern. Med.* **2017**, *2017*, 3864340. [CrossRef]

79. Ratto, D.; Corana, F.; Mannucci, B.; Priori, E.C.; Cobelli, F.; Roda, E.; Ferrari, B.; Occhinegro, A.; Di Iorio, C.; De Luca, F.; et al. *Hericium erinaceus* Improves Recognition Memory and Induces Hippocampal and Cerebellar Neurogenesis in Frail Mice during Aging. *Nutrients* **2019**, *11*, E715. [CrossRef]

80. Weibel, E.R. Morphometry of the human lung: The state of the art after two decades. *Bull. Eur. Physiopathol. Respir.* **1979**, *15*, 999–1013.

81. Avwioro, G. Histochemical Uses of Haematoxylin-A Review. *JPCS* **2011**, *1*, 24–34.

82. Junqueira, L.C.; Bignolas, G.; Brentani, R.R. Picrosirius staining plus polarization microscopy, a specific method for collagen detection in tissue sections. *Histochem. J.* **1979**, *11*, 447–455. [CrossRef] [PubMed]
83. Lattouf, R.; Younes, R.; Lutomski, D.; Naaman, N.; Godeau, G.; Senni, K.; Changotade, S. Picrosirius red staining: A useful tool to appraise collagen networks in normal and pathological tissues. *J. Histochem. Cytochem.* **2014**, *62*, 751–758. [CrossRef] [PubMed]

*molecules*

MDPI

*Article*

# From a Medicinal Mushroom Blend a Direct Anticancer Effect on Triple-Negative Breast Cancer: A Preclinical Study on Lung Metastases

Elisa Roda [1,2,*,†], Fabrizio De Luca [1,†], Carlo Alessandro Locatelli [2], Daniela Ratto [1], Carmine Di Iorio [1], Elena Savino [3], Maria Grazia Bottone [1] and Paola Rossi [1,*]

1   Department of Biology and Biotechnology "L. Spallanzani", University of Pavia, 27100 Pavia, Italy; fabrizio.deluca01@universitadipavia.it (F.D.L.); daniela.ratto01@universitadipavia.it (D.R.); carmine.diiorio01@universitadipavia.it (C.D.I.); mariagrazia.bottone@unipv.it (M.G.B.)
2   Laboratory of Clinical & Experimental Toxicology, Pavia Poison Centre, National Toxicology Information Centre, Toxicology Unit, Istituti Clinici Scientifici Maugeri IRCCS, 27100 Pavia, Italy; carlo.locatelli@icsmaugeri.it
3   Department of Earth and Environmental Science, University of Pavia, 27100 Pavia, Italy; elena.savino@unipv.it
*   Correspondence: elisa.roda@unipv.it (E.R.); paola.rossi@unipv.it (P.R.); Tel.: +39-0382-5924-14 (E.R.); +39-0382-8960-76 (P.R.)
†   These authors contributed equally to this work.

check for updates

**Abstract:** Bioactive metabolites isolated from medicinal mushrooms (MM) used as supportive treatment in conventional oncology have recently gained interest. Acting as anticancer agents, they interfere with tumor cells and microenvironment (TME), disturbing cancer development/progression. Nonetheless, their action mechanisms still need to be elucidated. Recently, using a 4T1 triple-negative mouse BC model, we demonstrated that supplementation with Micotherapy U-Care, a MM blend, produced a striking reduction of lung metastases density/number, paralleled by decreased inflammation and oxidative stress both in TME and metastases, together with QoL amelioration. We hypothesized that these effects could be due to either a direct anticancer effect and/or to a secondary/indirect impact of Micotherapy U-Care on systemic inflammation/immunomodulation. To address this question, we presently focused on apoptosis/proliferation, investigating specific molecules, i.e., PARP1, p53, BAX, Bcl2, and PCNA, whose critical role in BC is well recognized. We revealed that Micotherapy U-Care is effective to influence balance between cell death and proliferation, which appeared strictly interconnected and inversely related (p53/Bax vs. Bcl2/PARP1/PCNA expression trends). MM blend displayed a direct effect, with different efficacy extent on cancer cells and TME, forcing tumor cells to apoptosis. Yet again, this study supports the potential of MM extracts, as adjuvant supplement in the TNBC management.

**Keywords:** breast cancer; lung metastases; in vivo; apoptosis; complementary medicine; medicinal mushrooms

## 1. Introduction

Breast cancer (BC) is the most frequently diagnosed malignant neoplasm in women [1]. Due to the progress achieved both in early diagnosis and in novel therapeutic treatments, the death rate of BC is progressively decreasing, but BC still remains one of the leading causes of morbidity and mortality in females worldwide [2]. In particular, in Western countries BC metastases are the second cause of mortality among tumor patients [3,4].

Triple-negative breast cancer (TNBC) is characterized by the lack of expression of specific receptors, i.e., estrogens, progesterone, and epidermal growth factor 2, and represents about 15–20% of all BC diagnoses. Indeed, TNBC differs from other subgroups of BC for its increased growth and fast spreading, with reduced treatment possibilities (due to the absence of the three above reported receptors) and a worse outcome [5,6]. Actually, TNBC patients are extremely prone to metastasis and relapse [7] which mainly affect brain, liver, and, in particular, lungs [8]. Tumor progression to metastasis is a complex and many-sided process, affected by both intrinsic cellular mutational burden and several interactions between malignant and non-malignant cell types, and also constantly regulated by the various extrinsic microenvironmental niches [9].

The tumor microenvironment (TME), consisting of immune cells, fibroblasts, satellite cells, as well as blood and lymphatic vessels, plays a fundamental role in the tumor biology, i.e., the behavior of a bulk tumor, co-evolving in a delicate ecosystem with the tumor niche. This never-ending evolving process is governed by local and distant microenvironments, being also regulated by systemic inflammation. In fact, under cytokines, growth factors, and chemotactic stimuli induction, cancer cells recruit and transform stromal fibroblasts into malignant cells, which alter the extracellular matrix by secreting tumor-stimulating factors to facilitate tumor invasion and metastasis. Thus, based on the strict interaction between tumor cells and multicellular proinflammatory TME, cancer typical features also include the evasion of immune destruction, tumor promoting inflammation, and angiogenesis induction. Indeed, nowadays it is well-known that TME plays a crucial role in cancer progression, therapeutic response, and patient outcome [9–11]. Immunotherapy is a recent approach in cancer therapy, specifically addressed on TME [12]. Currently, the elite therapy for treating TNBC is the cytotoxic chemotherapy, characterized by several side effects [13,14]. A bulk of literature demonstrated that chemotherapy induces apoptosis and cancer is a pathology characterized by a dysregulation in cell cycle/death, in which the disruption of the apoptotic pathway leads to uncontrolled cell proliferation [15]. Anomalies in the apoptotic pathway are crucial for cancer genesis, evolution, and regression after treatment [16]. Indeed, the apoptosis rate is crucial in determining the fate between cancer progression and regression as well as in response to current available treatments, i.e., chemotherapy, radiotherapy, surgery, and hormonal therapies.

As a matter of fact, cells undergo apoptosis by changing the balance of proapoptotic and antiapoptotic genes [17]. The main actors involved in apoptosis pathway can be reduced to a few crucial proteins largely preserved through species [18]. In humans and mice, these key proteins belong to the Bcl-2 family [18], Poly (ADP-ribose) polymerase (PARP) [19], and p53 [20]. Bcl-2 family contains both inhibitors and promoters of apoptosis [18]. Acting as proapoptotic protein, Bax is an important tumor suppressor factor, and its reduced levels provide tumor cells with a selective survival advantage, contributing to their expansion [21]. Contrarily, acting as antiapoptotic protein, Bcl-2 plays an essential role as a cell survivor enhancer, and its increased expression level gives cancer cells with a selective survival gain [22]. Concerning PARPs, PARP1 is a nuclear protein which contributes in DNA single-strand break repair, and its dysregulation is involved in tumorigenesis phenomena to such a degree that PARP1 inhibitors have been authorized for the treatment of some types of BC, stimulating both apoptosis induction and synthetic lethality mechanism/DNA repair [23–27]. p53 protein is a nuclear protein known as tumor suppression factor, which plays a critical role deciding whether DNA would be repaired or the damaged cell will self-destruct, inducing programmed cell death [20,28]. Dysregulation of these mentioned proteins is a frequent feature of human malignant diseases and causal for therapy resistance. Tumor cells usually escape from apoptosis by downregulation of proapoptotic genes and/or hyperactivation of antiapoptotic genes. Therefore, apoptosis induction in cancer cells is considered an excellent approach for treating tumors [29].

It has also to be mentioned the PCNA pivotal role in cancer, owing to its function in cell proliferation. Since cancer is caused by and manifest through multiple mechanisms, many of which converging to deregulated proliferation at primary and metastatic sites, and PCNA is an indispensable

factor for cell cycle control, DNA replication, DNA nucleotide excision repair, and chromatin assembly, PCNA inhibition is considered to be another viable anticancer strategy [30,31].

In the last decades, considerable attention has been focused on developing/identifying new compounds for TNBC treatment with absent/minimal side adverse effects. Interestingly, in recent years the importance of naturally derived compounds has been highlighted as a source of anticancer and proapoptotic drugs [32]. One of the most promising sources for drug discovery in integrative oncology are medicinal mushrooms (MM), which have an established story of use in traditional oriental medicine and as nutritionally functional foods. MM display antitumor, proapoptotic, onco-immunological, and immunomodulatory effects in vitro and improve the quality of life in cancer patients during conventional anticancer treatments [33,34]. Indeed, in the last years, the use of several MM has been approved as adjuvant supplements in antitumor therapy in different countries.

Different MM produce hundreds of bioactive compounds which are able to influence, often in a synergistic way, numerous cancer-related pathways, also modulating cellular targets typically involved in cell proliferation, survival, and angiogenesis [33,35].

Several studies showed that the use of MM extracts or their compounds, alone or combined with conventional anticancer treatments, is safe and beneficial [33,35].

The present investigation is strictly linked to a previous study employing a 4T1 triple-negative mouse BC model to explore the effects of an oral supplementation with "Micotherapy U-care" (M. U-care), a medicinal mushroom blend, consisting of a mixture of 20% extracts of mycelia and sporophores of five MM, i.e., *Agaricus blazei*, *Ophiocordyceps sinensis*, *Ganoderma lucidum*, *Grifola frondosa*, and *Lentinula edodes* [36]. Each of these MM have been shown displays anticancer and immunomodulatory effects, both in vitro and in vivo, and in preclinical and clinical studies [34,37].

Using a syngeneic tumor-bearing mouse model of TNBC, we demonstrated that M. U-Care supplementation, starting before 4T1 cells injection and lasting throughout the whole experimental time (about 3 months), elicited (i) an increase in the quality of life, (ii) a dramatic decrease of lung metastases density and nodules number, and (iii) a substantial decrease of inflammatory and oxidative stress pathways, characterized by a similar protein expression trend in both lung TME and metastases [36]. Based on these results, we hypothesized that the supplement effects could have been ascribable either to a direct M. U-care anticancer effect on lung cells and/or to secondary/indirect impacts of the MM blend on systemic inflammation and immunomodulation. To punctually address this question, in the present study, we focused on the programmed cell death pathway, namely, apoptosis, by investigating specific molecules whose critical role in human BC is well known. With this aim, using immunohistochemistry, we evaluated the expression, localization and changes of the following proteins, i.e., PARP1, p53, Bax, and Bcl2, performing a comparative assessment on lung metastases and pulmonary parenchyma, namely, TME. For the sake of clarity, we focused on the pathological outcomes in the murine pulmonary tissue, as the lung is the one of the distant organs recurrently implicated in typical metastatic pattern of primary TNBC [7]. The apoptotic cell death was also examined by in situ detection of DNA fragmentation using the terminal deoxynucleotidyl-transferase (TUNEL) assay. In addition, based on the notion that proliferative activity of cancer cells is also a crucial prognostic marker in the tumor diagnosis, we investigated the role of Proliferating Cell Nuclear Antigen (PCNA), being a pivotal protein directly related to the degrees of tumor malignancy and diagnosis [38,39].

## 2. Results

Figure 1 emphasizes the key outcomes of the present investigation and also summarizes some major results of our previous study (for details see the work in [36]).
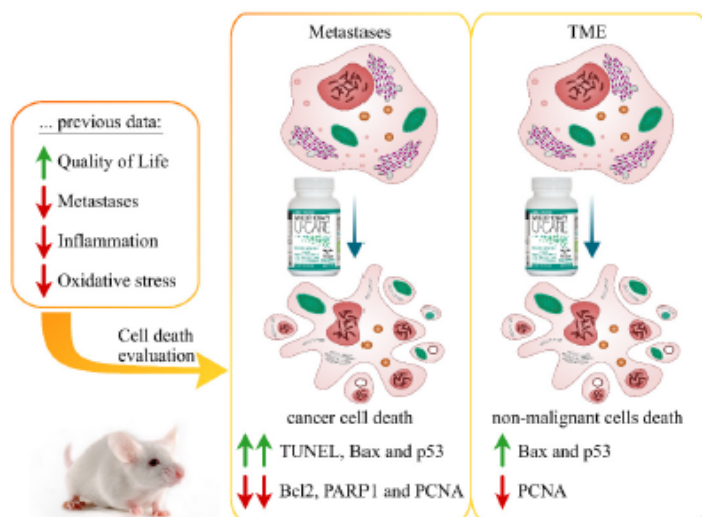
**Figure 1.** Graphic illustration underlining the main results.

## 2.1. Raw Materials, Extract Procedure, and Main Active Metabolites of Micotherapy U-Care Blend

The MM blend Micotherapy U-care was produced and supplied by A.V.D. Reform s.r.l. (Noceto, Parma, Italy) and it consists of a mixture of five fungal species, as reported in Table 1.

**Table 1.** Details on Micotherapy U-care supplement composition.

| Medicinal Mushroom | Fungal Part Used in Micotherapy U-Care | % Contained in Micotherapy U-Care | ID Code |
|---|---|---|---|
| *Agaricus blazei* | Fruiting body | 20% | 7700 |
| *Ophiocordyceps sinensin* | Fruiting body and mycelium | 20% | Cm2 |
| *Ganoderma lucidum* | Fruiting body | 20% | Gač |
| *Grifola frondosa* | Fruiting body | 20% | Gf3 |
| *Lentinula edodes* | Fruiting body | 20% | Le.ed.1 |

The specific MM species strains were established by genetic analyses, sequencing ITS regions and confirming the ID code. Each MM was ground, and total genomic DNA was extracted through the DNeasy mini plant kit (Qiagen NV, Venlo, Netherlands). The Internal Transcribed Spacer (ITS) regions of nuclear DNA were amplified by using PCR, applying two set of primers: ITS F 5′-AGAAAGTCGTAACAAGGTTTCCGTAG-3′, ITS R 5′-TTTTCCTCCGCTCATTGATATGCTT-3′, ITS-g F 5′-TCCGTAGGTGAACCTGCGG-3′, and ITS-g R 5′-TCCTCCGCTTATTGATATGC-3′. Next, the PCR products were purified, sequenced by Eurofins Genomics (Konstanz, Germany), and identified by using NCBI Nucleotide Blast software, version 2.9.0 (Table 1, ID code).

Next, the sporophores and/or mycelia were cultivated, harvested, and the fresh material was extracted for 3 h at 95 °C in distilled water with ethanol 10% (for 1 kg of raw material, 15 L of water-ethanol solution was used). After water-ethanol extraction, solid and liquid components were divided, and the fluid part was dehydrated until the humidity amount was smaller than 7%. Dry extracts were ground and blended to have the 20% of each selected mushroom in the MM blend Micotheraphy U-care (Table 1).

Finally, the polysaccharide content of Micotherapy U-care was determined by using a β-Glucan Assay Kit, and the polysaccharide content was more than 30%. Of this 30%, more than 15% of the polysaccharides were 1,3-1,6 β-glucans, the main active metabolites in Micotherapy U-care.

### 2.2. TUNEL Assay

TUNEL staining, as a typical marker of apoptotic events [40], revealed an extensive spreading in alveolar pneumocytes (both type I and II) and bronchiolar epithelial cells as well as in metastatic nodules (Figure 2).
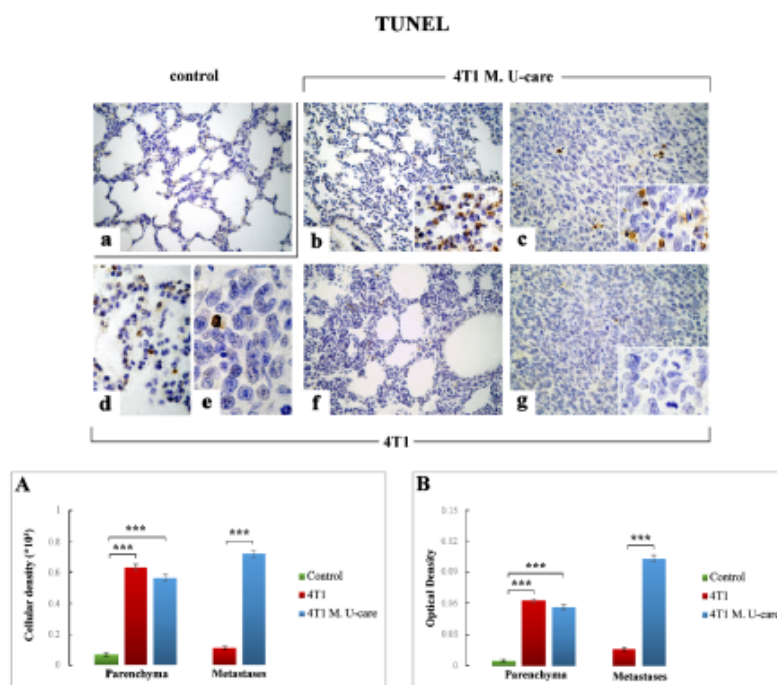


**Figure 2.** Terminal deoxynucleotidyl-transferase (TUNEL) immunostaining in healthy control (a), 4T1 M. U-care (b,c) and 4T1 (d–g) mice. Light microscopy magnification: 40× (a–c,f,g); 100× (d,e, insert in panels (b,c,g)). Panel (A) and (B): Histograms presenting immunopositive cell density and OD, respectively. *p* values calculated by unpaired Student's *t*-test: (***) < 0.001.

In particular, concerning the TME, TUNEL-immunoreactivity significantly increased in both 4T1 and 4T1 M. U-care mice (Figure 2b,d,f, respectively) compared to controls (Figure 2a).

The quantitative analysis showed an extremely significant increase of TUNEL-immunopositive cell density and OD comparing 4T1 animals to controls ($0.63 \pm 0.02$ vs. $0.07 \pm 0.01$ and $0.06 \pm 0.00$ vs. $0.01 \pm 0.00$, for cell density and OD, respectively) (Figure 2, Panels (A,B)). In a similar manner, an extremely significant immunoreactivity enhancement was detected when comparing 4T1 M. U-care mice to controls ($0.56 \pm 0.02$ vs. $0.07 \pm 0.01$ and $0.06 \pm 0.00$ vs. $0.01 \pm 0.00$, for cell density and OD, respectively). Diversely, a slight decrease of TUNEL-immunopositive cell density and OD was revealed in 4T1 M. U-care animals compared to 4T1 mice ($0.56 \pm 0.02$ vs. $0.63 \pm 0.02$ and $0.06 \pm 0.00$ vs. $0.06 \pm 0.00$, for cell density and OD, respectively) (Figure 2, Panels (A,B)).

Regarding metastases, an extremely significant increase of TUNEL-immunopositive cell density and OD was detected in 4T1 M. U-care mice compared to 4T1 animals (Figure 2c,e,g, respectively):

$0.72 \pm 0.02$ vs. $0.11 \pm 0.01$ and $0.10 \pm 0.00$ vs. $0.02 \pm 0.00$, for density and OD, respectively (Figure 2, Panels (A,B)). Notably, in 4T1 mice several mitoses were also observable (Figure 2, insert in Figure 2g).

### 2.3. PARP1, p53, Bax, Bcl2, and PCNA Immunohistochemical Assessment

The cellular expression, localization, and distribution of PARP1, p53, Bax, Bcl2, and PCNA, all involved in cell death and proliferation pathways, were explored.

The immunohistochemical evaluation of all these molecules revealed a widespread labeling in the metastatic nodules and/or in TME, at bronchiolar and alveolar level, evidencing a different efficacy of the MM blend, with the more marked effect on tumor cells.

### 2.3.1. PARP1

A very significant increase of PARP1-immunoreactive cell density was measured in the TME of 4T1 animals (Figure 3d,f) compared to controls (Figure 2a): $7.46 \pm 0.83$ vs. $1.85 \pm 0.14$, respectively (Figure 3, Panel (A)); similarly, a significant increase was detected when comparing 4T1 M. U-care mice (Figure 3b) to controls ($6.14 \pm 0.87$ vs. $1.85 \pm 0.14$, respectively). Notably, any difference was determined evaluating PARP1-immunopositive cell density in 4T1 animals and 4T1 M. U-care mice ($7.46 \pm 0.83$ vs. $6.14 \pm 0.87$, respectively) (Figure 3, Panel (A)).
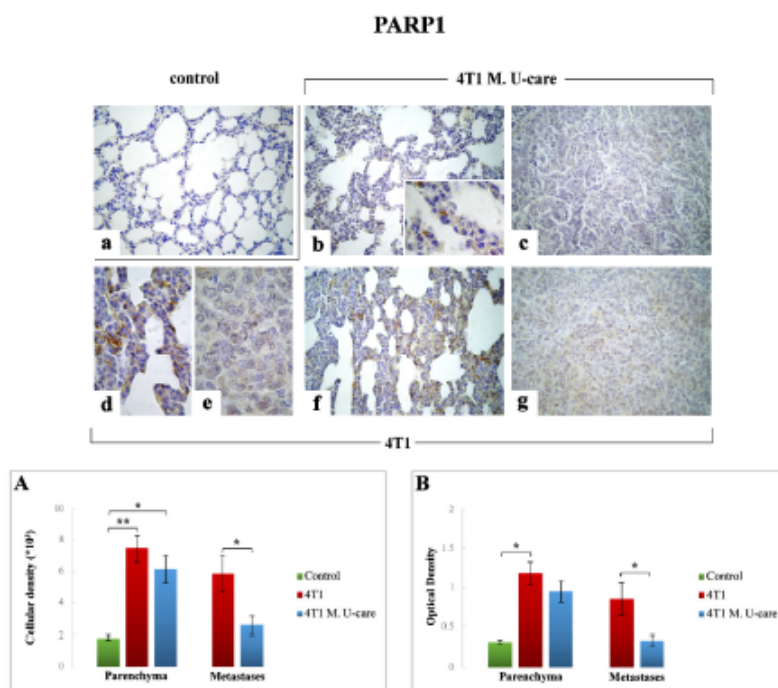
**PARP1**



**Figure 3.** Immunostaining reaction for PARP1 in healthy control (**a**), 4T1 M. U-care (**b,c**) and 4T1 (**d–g**) mice. Light microscopy magnification: 40× (**a–c,f,g**); 100× (**d,e**, insert in panel (**b**)). Panels (**A**) and (**B**): Histograms displaying immunopositive cell density and OD, respectively. *p* values calculated by Unpaired Student's *t*-test: (*) < 0.05 and (**) < 0.01.

Likewise, a significant increase of PARP1-immunoreactive OD was measured in 4T1 animals compared to controls ($1.19 \pm 0.14$ vs. $0.32 \pm 0.02$, respectively) (Figure 3, Panel (B)), while, differently, any difference was revealed evaluating PARP1-immunopositive OD in 4T1 animals compared to 4T1

M. U-care mice (1.19 ± 0.14 vs. 0.95 ± 0.14, respectively), or even between 4T1 M. U-care and controls (0.95 ± 0.14 vs. 0.32 ± 0.02, respectively) (Figure 3, Panel (B)).

Concerning the metastatic tissue, a significant increase of PARP1-immunopositive cell density and OD was determined in 4T1 mice compared to 4T1 M. U-care animals (5.85 ± 1.16 vs. 2.57 ± 0.57 and 0.85 ± 0.21 vs. 0.34 ± 0.07, for cell density and OD, respectively) (Figure 3, Panels (A,B)).

### 2.3.2. p53

Comparably to the above reported TUNEL immunostaining trend, p53 immunoreactivity was significantly increased in 4T1 M. U-care mice (Figure 4b,c) compared to both 4T1 animals (Figure 4d–g) and controls (Figure 4a). Specifically, a very significant increase of p53-immunopositive cell density and OD was determined in 4T1 M. U-care animals compared to 4T1 mice (6.42 ± 0.78 vs. 3.09 ± 0.65 and 1.11 ± 0.14 vs. 0.53 ± 0.12, for cell density and OD, respectively). A significant increase of p53-immunopositive cell density and OD was also observed when comparing 4T1 M. U-care animals to control (6.42 ± 0.78 vs. 2.93 ± 0.59 and 1.11 ± 0.14 vs. 0.49 ± 0.11, for cell density and OD, respectively). Differently, any significant difference was calculated when comparing 4T1 mice to controls (3.09 ± 0.65 vs. 2.93 ± 0.59 and 0.53 ± 0.12 vs. 0.49 ± 0.11, for cell density and OD, respectively) (Figure 4, Panel (A,B)).
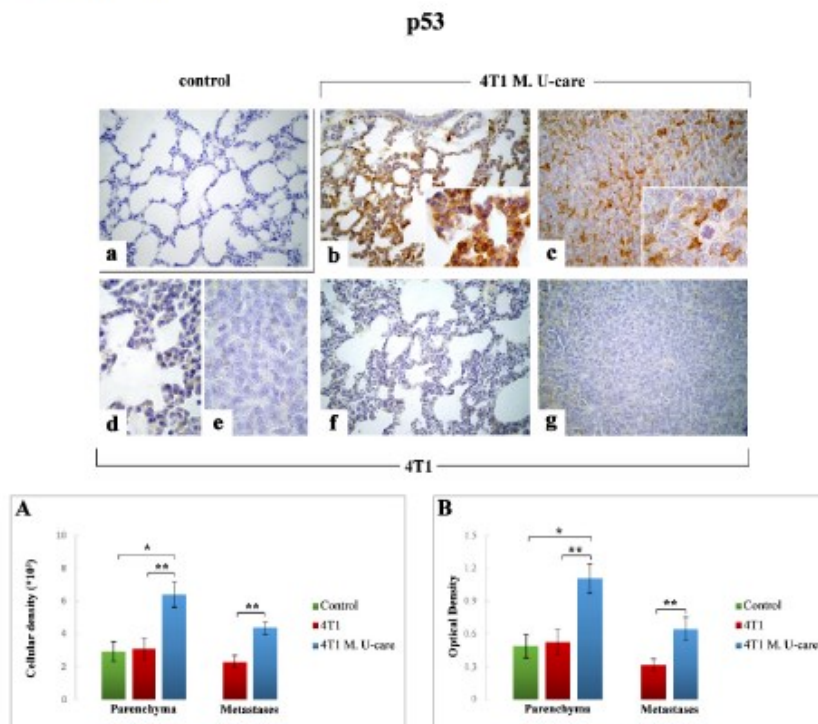


**Figure 4.** p53-immunostaining reaction in healthy control (a), 4T1 M. U-care (b,c) and 4T1 (d–g) mice. Light microscopy magnification: 40× (a–c,f,g); 100× (d,e, insert in panels (b,c)). Panels (A) and (B): Histograms showing immunopositive cell density and OD, respectively. $p$ values calculated by Unpaired Student's $t$-test: (*) < 0.05 and (**) < 0.01.

With regard to metastatic tissue, a very significant increase of both p53-immunoreactive cell density and OD was determined in 4T1 M. U-care mice compared to 4T1 animals (4.38 ± 0.63 vs. 2.29 ± 0.39 and 0.64 ± 0.10 vs. 0.32 ± 0.06, for density and OD, respectively) (Figure 4, Panels (A,B)).

### 2.3.3. Bax

Similarly to p53, a significant increase in Bax immunopositivity was observed in the TME of 4T1 M. U-care mice at alveolar and stromal level, with several immunopositive endothelial cells in bronchiolar areas (Figure 5b), compared to both 4T1 mice (Figure 5d,f) and controls (Figure 5a). In the same manner, Bax resulted overexpressed in metastatic nodules 4T1 M. U-care mice (Figure 5c), compared to 4T1 animals (Figure 5e,g). Notably, a significant increase of Bax-immunoreactive cell density was measured in 4T1 M. U-care animals compared to 4T1 mice (4.75 ± 0.48 vs. 3.13 ± 0.40, respectively). Likewise, a significant increase was observed in 4T1 M. U-care mice compared to control (4.75 ± 0.48 vs. 2.47 ± 0.28, respectively), while any difference was determined when comparing 4T1 animals and controls (3.13 ± 0.4 and 2.47 ± 0.28, respectively) (Figure 5, Panel (A)). Moreover, a significant increase of Bax-immunostaining OD was evidenced in 4T1 M. U-care mice, compared to both 4T1 and controls (0.76 ± 0.09 vs. 0.48 ± 0.07 and 0.76 ± 0.09 vs. 0.37 ± 0.04, respectively). Any significant difference was measured when comparing 4T1 mice to controls (0.48 ± 0.07 vs. 0.37 ± 0.04, respectively) (Figure 5, Panel (B)).

Concerning the metastases, an extremely significant increase of both Bax-immunopositive cell density and OD was determined in 4T1 M. U-care mice compared to 4T1 animals (4.47 ± 0.40 vs. 1.59 ± 0.31, and 0.58 ± 0.07 vs. 0.24 ± 0.06, respectively) (Figure 5, Panels (A,B)).
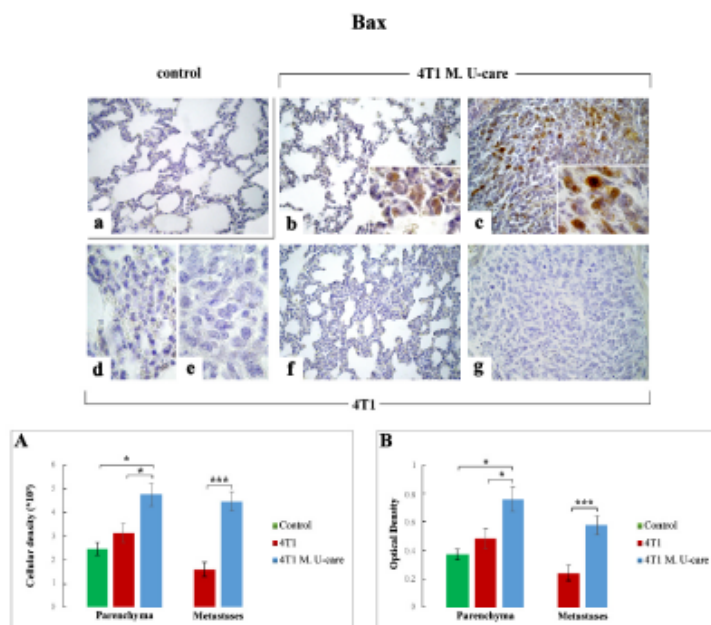


**Figure 5.** Immunohistochemical staining for Bax in healthy control (**a**), 4T1 M. U-care (**b,c**) and 4T1 (**d–g**) mice. Light microscopy magnification: 40× (**a–c,f,g**); 100× (**d,e**, insert in panels (**b,c**)). Panels (**A**) and (**B**): Histograms showing immunopositive cell density and OD, respectively. *p* values calculated by Unpaired Student's *t*-test: (*) < 0.05 and (***) < 0.001.

List of original manuscripts

### 2.3.4. Bcl2

Concerning the TME, Bcl2-immunoreactivity appeared slightly enhanced in both 4T1 and 4T1 M. U-care mice (Figure 6b,d,f, respectively) compared to controls (Figure 6a). Notably, a slight non-significant increase of Bcl2-immunoreactive cell density and OD was measured both in 4T1 and 4T1 M. U-care animals compared to controls (4.88 ± 0.69 vs. 4.89 ± 0.68 vs. 1.74 ± 0.15 and 0.86 ± 0.12 vs. 0.89 ± 0.13 vs. 0.32 ± 0.03, for density and OD, respectively). Any difference was evidenced evaluating Bcl2-immunopositive cell density and OD in 4T1 animals and 4T1 M. U-care mice (4.88 ± 0.69 vs. 4.89 ± 0.68 and 0.86 ± 0.12 vs. 0.89 ± 0.13, for density and OD, respectively) (Figure 6, Panels (A,B)).

Regarding the metastatic nodules (Figure 6c,e,g), contrarily to Bax, a very significant decrease of Bcl2-immunopositive cell density and OD was detected in 4T1 M. U-care mice compared to 4T1 (1.77 ± 0.32 vs. 3.29 ± 0.34 and 0.24 ± 0.04 vs. 0.52 ± 0.06, for density and OD, respectively) (Figure 6, Panels (A,B)).
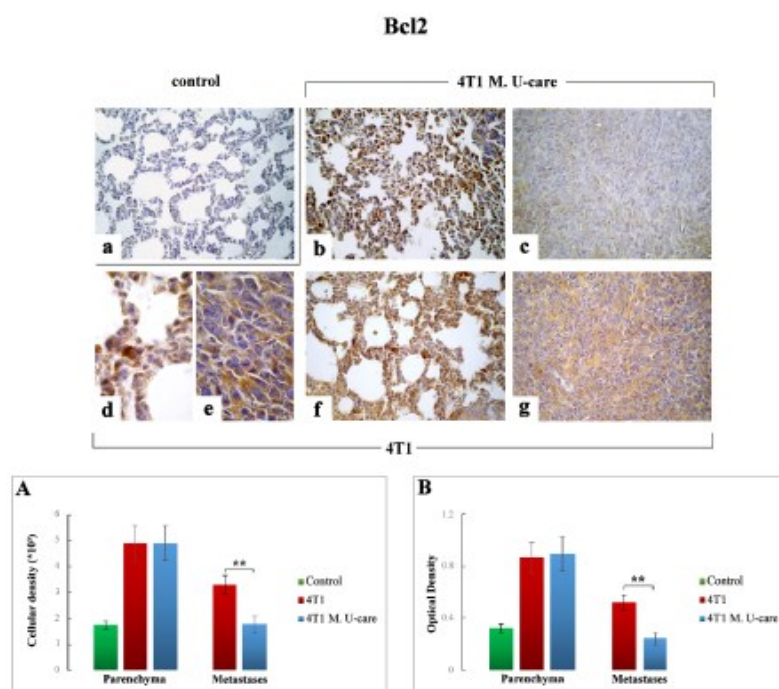


**Figure 6.** Bcl2-immunostaining reaction in healthy control (**a**), 4T1 M. U-care (**b,c**) and 4T1 (**d–g**) mice. Light microscopy magnification: 40× (**a–c,f,g**); 100× (**d,e**). Panels (**A**) and (**B**): Histograms showing immunopositive cell density and OD, respectively. *p* values calculated by Unpaired Student's *t*-test (**) < 0.01.

### 2.3.5. PCNA

PCNA-immunopositivity was extremely enhanced in TME of 4T1 mice (Figure 7d,f) compared to both 4T1 M. U-care (Figure 7b) and controls (Figure 7a). In particular, the quantitative analysis highlighted an extremely significant increase in PCNA-immunoreactive cell density and OD when comparing 4T1 animals to controls (0.40 ± 0.03 vs. 0.06 ± 0.01 and 0.93 ± 0.01 vs. 0.01 ± 0.00, for cell density and OD, respectively). In a similar manner, an extremely significant enhancement was detected when comparing 4T1 mice to 4T1 M. U-care animals (0.40 ± 0.03 vs. 0.17 ± 0.02 and 0.93 ± 0.01 vs.

0.02 ± 0.00, for cell density and OD, respectively). No significant differences were revealed in 4T1 M. U-care animals compared to control (0.17 ± 0.02 vs. 0.06 ± 0.01 and 0.02 ± 0.00 vs. 0.01 ± 0.00, for cell density and OD, respectively) (Figure 7, Panels (A,B)).

Concerning the metastatic tissue, an extremely significant decrease of PCNA-immunopositive cell density and OD was detected in 4T1 M. U-care mice (Figure 7c) compared to 4T1 animals (Figure 7e,g): 4.74 ± 0.28 vs. 9.57 ± 0.44 and 0.64 ± 0.04 vs. 1.77 ± 0.08, for density and OD, respectively (Figure 7, Panels (A,B)).
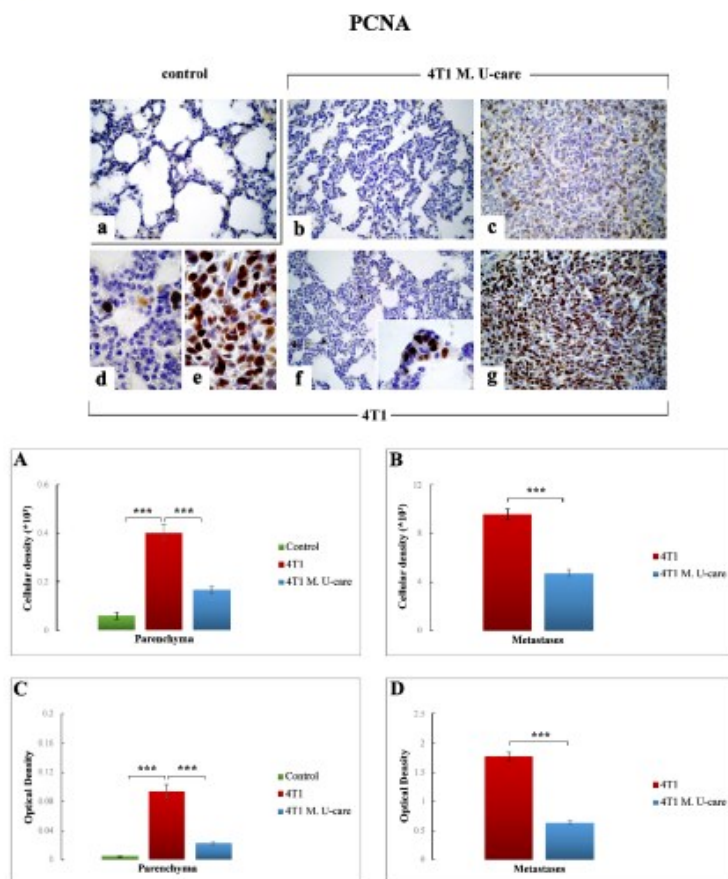


**Figure 7.** DAB-immunostaining reaction for PCNA in healthy control (**a**) 4T1 M. U-care (**b,c**), and 4T1 (**d–g**) mice. Light microscopy magnification: 40× (**a–c,f,g**); 100× (**d,e**, insert in panel (**f**)). Panels (**A**) and (**B**): Histograms showing immunopositive cell density. Panels (**C**) and (**D**): histograms exhibiting immunoreactive OD. $p$ values calculated by Unpaired Student's $t$-test: (***) < 0.001.

## 3. Discussion

Tumor development and progression are influenced by rearrangement of TME components, e.g., immune cells, fibroblasts, satellite cells, blood, and lymphatic vessels. Tumor cells are known to manipulate the function of cellular and non-cellular components through a complex signaling network to gain tumorigenesis, tumor maintenance, and drug resistance (MDR), taking advantage

of the non-malignant cells. Experimental and clinical data evidence that an in-depth analysis of the bidirectional communications and interactions between tumor cells and their surrounding dynamic TME is essential to identify the existing mechanisms of tumor expansion and invasion [41]. This complex network moreover involved apoptosis, also engaged to efficiently eliminate dysfunctional cells, plays an important role in both carcinogenesis and cancer treatment [42]. In particular, to guarantee its nourished growth, cancer is able to provide both endurance signals as well as mechanisms saving malignant cells from apoptosis. It is well known that an imbalance between cell proliferation and cell death typically characterizes cancer condition, in which several genetic aberrations may drive malignant cells to an uncontrolled progression and survival [43,44].

In our previous paper using the same preclinical model, i.e., 4T1 triple-negative mouse BC, we demonstrated that M. U-Care supplementation, starting 2 months before 4T1 injection and lasting throughout the whole experimental time (including tumor development and metastatization), produced a dramatic reduction of both lung metastases density and number. These effects were accompanied by a substantial decrease of inflammation and oxidative stress both in lung TME and metastases, together with a bettering of the QoL. [36]. Therefore, we hypothesized that the supplement effects could have been ascribable either to a direct anticancer effect and/or to the secondary/indirect impacts of the MM blend on systemic inflammation and immunomodulation. Therefore, aiming at addressing this crucial question, in the present investigation, we focused on the programmed cell death, investigating specific molecules, i.e., PARP1, p53, BAX, and Bcl2, pivotally involved in apoptotic pathway, whose critical role in human BC is well known. Further, in parallel we investigated PCNA expression pathway, based on the great interest on the pivotal role of PCNA in cancer cells proliferation, also taking into consideration that PCNA modifications may determine both tumor progression as well as the outcome of anticancer treatment.

Firstly, it has to be highlighted that performing a comparative assessment on cancer tissue, i.e., lung metastases, and surrounding TME by TUNEL assay, we revealed the existence of a different expression trend in 4T1 animals compared to 4T1 M. U-care mice. In detail, in these latter animals, an extremely intense immunopositivity was observed in the metastases, indicating an evident activation of the apoptotic pathway in cancer cells after the oral supplementation with the MM blend. Interestingly, this effect was definitely weaker in 4T1 animals, in which several mitoses were clearly observed in the tumor nodules, thus demonstrating the occurrence of an already active proliferation process. Concerning the TME, any statistical difference was measured comparing 4T1 M. U-care animals and 4T1 mice. These data corroborate the action of the MM blend, who display a powerful action able to drive metastatic cells to apoptosis, whereas was less effective with regards to the surrounding TME.

Concerning all evaluated apoptotic and proliferation markers, the comparative assessment of TME and metastases revealed diverse trends of protein expression, with the metastatic nodules being the most affected.

With regards to PARP1 levels, crucially implicated in tumorigenesis phenomena [24,26,27], the significant reduction observed in metastatic nodules of 4T1 M. U-care mice compared to 4T1 animals seemed to demonstrate a valuable action of the adjuvant micotherapic supplementation, suggesting a direct influence of the blend on tumor cells.

Our putative idea of a direct MM blend action able to determine an imbalance between proliferation and apoptosis, driving to a significant increase in apoptotic events, was further supported by p53 and Bax high expression levels measured in 4T1 M. U-care mice, showing the most striking effect in the metastatic nodules. By contrast, concerning both Bax and p53, an almost complete lack of effect was determined in 4T1 animals, in which the protein expression levels were similar to that observed in controls. Acting as proapoptotic protein, Bax should essentially play as a tumor suppressor factor. Consequently, reductions in its expression levels would provide tumor cells with a selective survival advantage, contributing to their expansion and invasion [21]. In particular, the reduced Bax expression levels can be traced back to an alteration of the p53 function which, by itself, is able to alter the levels of this proapoptotic protein [21]. Certainly, TP53 mutations are the most common genetic alterations in

breast cancer [28]. Notably, the increased immunopositivity for the wild type p53 isoform detected in 4T1 M. U-care mice could indicate a possible attempt to cell cycle arrest, in order to allow cellular repair processes and inhibit the proliferation of damaged cells.

Based on the notion that (i) several apoptotic stimuli induce cell death through a Bcl-2-regulated pathway and (ii) proteins belonging to Bcl2 family can play a dichotomous role, acting both as promoters as well as inhibitors of apoptotic events [21,45,46], we may suppose that the lower expression of Bcl-2 determined in metastatic tissue of 4T1 M. U-care mice could be related to a decrease in cancer cell proliferation, evidencing an alteration of the proliferation/apoptosis balance. This effect could also counteract the capacity of Bcl2 to trigger drug resistance at high expression [21,47]. Moreover, the overexpression of p53 in 4T1 M. U-Care mice may support a possible role of p53 in downregulating Bcl-2, feasibly explaining the apoptosis induction by wild type p53. Notably, it has to be underlined that, differently to all other evaluated markers, but similarly to TUNEL staining, we determined any difference in the Bcl-2 expression trend comparing metastases and TME in 4T1 M. U-care mice and 4T1 animals. Specifically, TME appeared to be unaffected by the mycotherapic oral supplementation, whereas the MM blend display a specific and selective effect restricted to the metastatic area.

In addition, concerning the proliferation marker PCNA, we evidenced a reduced expression in metastatic nodules in 4T1 M. U-care mice, thus highlighting an evident inhibitory effect of the MM blend on proliferation activity in tumor cells. Notably, a strong positive correlation between the expression of PCNA and COX2 in breast cancer has been recently highlighted [48], also in accordance with our previous findings [36].

Taken together the present data supported that the oral supplementation is effective to induce a peculiar swinging balance of cell death and proliferation, in which these two essential mechanisms appeared strictly interconnected and inversely related (see p53 and Bax vs. Bcl2 and PCNA expression trends). Notably, the MM blend bettered the cancer state with a direct effect, able to force tumor metastatic cells to an apoptotic fate.

In summary, all the present findings confirmed the protective role played by Micotherapy U-care blend in the lung metastases and surrounding TME. Our data further suggest that both an immunomodulatory anti-inflammatory systemic effect and a direct, selective anticancer effect act in a positive pleiotropic way. This double action mechanism, which (i) disturbs the TME signaling and (ii) targets the complex apoptotic pathway, could represent a promising approach for patient's treatment. In fact, in the search for novel therapeutic agents targeting tumor development and progression, MM-derived natural bioactive compounds, displaying multi-targeting potential, can overcome the disadvantages of monotherapy such as side effects and drug resistance. In particular, TNBC is the most aggressive malignant BC, difficult to treat due to its unresponsiveness to current clinical targeted treatments (e.g., hormonal therapy protocols or chemotherapeutics targeting HER2 protein receptors) and high rate of recurrence. In this scenario, the biological effects of combining M. U-care supplement with conventional therapies to target crucial cancer signaling pathways, i.e., proliferation and apoptosis, may interfere with cellular and molecular processes fueling TNBC growth, trying to create a new joint medical protocol able to hinder the typical TNBC metastatic pattern, i.e., frequent occurrence of distant metastases, mainly localized in lung, central nervous system, and bones, often associated with poor prognosis.

## 4. Materials and Methods

### 4.1. Cell Culture

The mice breast cancer cell line, 4T1, was acquired from American Type Culture Collection (ATCC) and maintained at 37 °C in a humidified atmosphere (95% air/5% $CO_2$) [36].

### 4.2. Animals and Experimental Plan

The detailed experimental design was previously describe in Roda et al. [36]. Briefly, 34 two-month-old wild type female BALB/c mice were obtained from Charles River Italia (Calco, Italy) and acclimatized for at least 3 weeks before the experiments.

All experiments were achieved in agreement with the European Council Directive 2010/63/EU and the Ethics Committee of Pavia University guidelines (Ministry of Health, License number 364/2018-PR). Therefore, all mice have been treated humanely, with due consideration for the reduction of pain and distress.

For execution of experiments and subsequent analyses, researchers were blinded to the designed group.

Sixteen (4T1 M. U-care mice) out of thirty-four mice were supplemented until sacrifice with a medicinal mushroom blend, namely, Micotherapy U-care (provided by A.V.D. Reform s.r.l., Noceto, Parma, Italy) consisting of a mixture of 20% extracts of sporophores and mycelia of five fungal species: *Agaricus blazei*, *Cordyceps sinensis*, *Ganoderma lucidum*, *Grifola frondosa*, and *Lentinula edodes* (see Table 1 and Results section). The mycotherapic blend was solubilized in water, selecting a dose of 4 mg supplement/mice per day to mimic the oral supplementation in humans (about 1.5 g/day). Otherwise, control ($n = 4$) and non-treated (4T1, $n = 14$) mice did not received any diet supplementation.

For the syngeneic tumor-bearing mice (4T1 and 4T1 M. U-care) generation see the work in [36].

The syngeneic tumor-bearing mice (4T1 and 4T1 M. U-care) were generated by injecting $1 \times 10^6$ of the 4T1 cells into the nape of the neck of the female Balb/C mice. Control animals were injected with phosphate-buffer saline (PBS). A survival rate of 100% was kept in all experimental groups, throughout the whole experimental time course.

Lung preparation was done by vascular perfusion of fixative [49]. Then, lungs were accurately removed, sectioned and then processed for immunohistochemistry.

### 4.3. Tissue Sampling and Immunohistochemistry

#### 4.3.1. Lung Specimens Preparation

The lung specimens preparation was previously described in detail [36]. Briefly, the top and the bottom regions of the right lungs of mice from each experimental group were dissected. Tissue samples were obtained according to a stratified random sampling scheme, fixed and processed as previously described [36]. Eight micrometer thick sections were cut in transversal plane and placed on silane-coated slides.

#### 4.3.2. TUNEL Staining

The reaction was performed using the terminal deoxynucleotidyl-transferase (TUNEL) assay (Oncogene Res. Prod., Boston, MA, USA). The lung sections were incubated for 5 min with 20 μg mL$^{-1}$ proteinase-K solution at room temperature, followed by treatment with 3% $H_2O_2$ to quench endogenous peroxidase activity. After incubation with the TUNEL solution (90 min with TdT/biotinylated dNTP and 30 min with HRP-conjugate streptavidin) in a humidified chamber at 37 °C, the reaction was developed using a 0.1% DAB solution. After nuclear counterstaining employing Carazzi's Hematoxylin, the sections were dehydrated in ethanol, cleared in xylene, and finally mounted in Eukitt (Kindler, Freiburg, Germany).

As a negative control, the TdT incubation was omitted; no staining was observed in these conditions.

#### 4.3.3. Immunohistochemistry: Apoptotic Pathway Assessment

Commercial antibodies were employed on murine lung specimens to investigate the expression of different specific apoptotic markers: (i) Poly (AD-ribose) polymerase 1(PARP1), (ii) p53, (iii) Bcl2 associated X-protein (Bax), (iv) B-cell lymphoma/leukemia protein (Bcl2), and (v) the proliferating cell

nuclear antigen (PCNA). Table 2 shows both primary and secondary antibodies as well as respective dilutions used for immunohistochemical experiments.

Immunohistochemical procedures have been conducted exactly as previously described [36].

**Table 2.** Primary/secondary antibodies and respective dilution used for immunohistochemical experimental procedures.

| | Antigen | Immunogen | Manufacturer, Species, Mono-Polyclonal, Cat/Lot. No., RRID | Dilution |
|---|---|---|---|---|
| Primary Antibodies | Anti-poly (ADP-ribose) polymerase (46D11) | Purified antibody raised against the residues surrounding Gly623 of human PARP-1 | Cell Signaling Technology (Danvers, MA, USA), Rabbit monoclonal IgG, Cat# 9532, RRID:AB_659884 | 1:100 |
| | Anti-p53 (Ab-5) | Purified antibody raised against the ~53 kDa wild type p53 protein of mouse origin | Sigma-Aldrich (St. Louis, MO, USA), Mouse monoclonal IgG2a, Cat# OP33-100UG, RRID:AB_564977 | 1:100 |
| | Anti-Bcl-2-associated X protein (P-19) | Purified antibody Raised against a peptide mapping at the amino terminus of Bax of mouse origin | Santa Cruz Biotechnology (Santa Cruz, CA, USA), Rabbit polyclonal IgG, Cat# sc-526, RRID:AB_2064668 | 1:100 |
| | Anti-B-Cell Leukemia/Lymphoma 2 protein (N-19) | Purified antibody raised against a peptide mapping at the N-terminus of Bcl-2 of human origin | Santa Cruz Biotechnology (Santa Cruz, CA, USA), Rabbit polyclonal IgG, Cat# sc-492, RRID:AB_2064290 | 1:100 |
| | Anti-Proliferating Cell Nuclear Antigen (Ab-1) | Purified antibody raised against the ~37 kDa PCNA protein of mouse origin | Sigma-Aldrich (St. Louis, MO, USA), Mouse monoclonal IgG2a, Cat# NA03-200UG, RRID:AB_213111 | 1:1000 |
| Secondary Antibodies | Biotinylated horse anti-mouse IgG | Gamma immunoglobulin | Vector Laboratories (Burlingame, CA, USA), Horse, Cat# PK-6102, RRID:AB_2336821 | 1:200 |
| | Biotinylated goat anti-rabbit IgG | Gamma immunoglobulin | Vector Laboratories (Burlingame, CA, USA), Goat, lot# PK-6101, RRID: AB_2336820 | 1:200 |

### 4.3.4. Immunohistochemical Evaluations

To prevent differences due to small procedural changes, immunohistochemical reactions were performed simultaneously on samples from different experimental groups. The expression of each selected marker was examined in six slides (about 30 sections) per mouse. The shown micrographs display the most representative pulmonary conditions and modifications for each immunohistochemical reaction.

Immunohistochemical labeling extent evaluation was previously described in detail [36].

The optical density (OD), intended as immunohistochemical intensity, was assessed in 30 cells/section per six slides/mouse. OD was related to the immunopositive cell density. In addition, immunopositive cells density count was evaluated, intended as number of immunopositive cells/area in mm$^2$.

*4.4. Statistics*

Data were expressed as mean ± standard error of the mean (SEM). Regarding the TME, the statistical differences among the three experimental groups were calculated by using one-way ANOVA followed by Bonferroni's post hoc test. Otherwise, for metastases, the statistical differences between 4T1 and 4T1 M. U-care mice were evaluated by using unpaired Student's *t*-test.

The differences were considered statistically significant for $p < 0.05$ (*), $p < 0.01$ (**), and $p < 0.001$ (***). Statistical analyses were performed by using GraphPad Prism 7.0 (GraphPad Software Inc., La Jolla, CA, USA).

## 5. Conclusions

Overall, these results support the use of oral supplementation with Micotherapy U-care blend as a new effective strategy to be used in the field of integrative oncology to decrease adverse side effects caused by conventional cancer therapies. All obtained results corroborated the Micotherapy U-care protective role in metastases and TME, in which an immunomodulatory anti-inflammatory systemic action together with a direct, selective anticancer mechanism exerted a positive pleiotropic effect. The Micotherapy U-care preventive and protective effect could affect the TME signaling and, at the same time, target the multifaceted apoptotic pathway. Once again, the present investigation highlights the importance of translational research in the development of clinically relevant therapeutic strategies. In particular, the growing use of translational research "from bench to bedside" in cancer medicine, could allow to overcome challenges which everlastingly hinder medicinal advancements, yielding significant advances in cancer therapeutics and also improvements in the ability to predict clinical course of patient's disease based on individual tumor characteristics. In this view, medicinal mushrooms extracts, being natural sources of novel drugs, could be used as effective adjuvant therapy in the critical management of TNBC.

## References

1. Jemal, A.; Bray, F.; Center, M.M.; Ferlay, J.; Ward, E.; Forman, D. Global cancer statistics. *CA Cancer J. Clin.* **2011**, *61*, 69–90. [CrossRef] [PubMed]
2. Cardoso, F.; Harbeck, N.; Fallowfield, L.; Kyriakides, S.; Senkus, E.; ESMO Guidelines Working Group. Locally recurrent or metastatic breast cancer: ESMO Clinical Practice Guidelines for diagnosis, treatment and follow-up. *Ann. Oncol.* **2012**, *23*, vii11–vii19. [CrossRef] [PubMed]
3. Zeeshan, R.; Mutahir, Z. Cancer metastasis: Tricks of the trade. *Bosn. J. Basic Med. Sci.* **2017**, *17*, 172–182. [CrossRef] [PubMed]
4. Schito, L.; Rey, S. Hypoxic pathobiology of breast cancer metastasis. *Biochim. Biophys. Acta Rev. Cancer* **2017**, *1868*, 239–245. [CrossRef]
5. Yadav, B.S.; Chanana, P.; Jhamb, S. Biomarkers in triple negative breast cancer: A review. *World J. Clin. Oncol.* **2015**, *6*, 252. [CrossRef]
6. Yeo, S.K.; Guan, J.L. Breast Cancer: Multiple Subtypes within a Tumor? *Trends Cancer* **2017**, *3*, 753–760. [CrossRef]

7. Yao, Y.; Chu, Y.; Xu, B.; Hu, Q.; Song, Q. Risk factors for distant metastasis of patients with primary triple-negative breast cancer. *Biosci. Rep.* **2019**, *39*. [CrossRef]
8. Iriondo, O.; Liu, Y.; Lee, G.; Elhodaky, M.; Jimenez, C.; Li, L.; Lang, J.; Wang, P.; Yu, M. TAK1 mediates microenvironment-triggered autocrine signals and promotes triple-negative breast cancer lung metastasis. *Nat. Commun.* **2018**, *9*, 1994. [CrossRef]
9. Chitty, J.L.; Filipe, E.C.; Lucas, M.C.; Herrmann, D.; Cox, T.R.; Timpson, P. Recent advances in understanding the complexities of metastasis. *F1000Research* **2018**, *7*, 1169. [CrossRef]
10. Katsuta, E.; Rashid, O.M.; Takabe, K. Clinical relevance of tumor microenvironment: Immune cells, vessels, and mouse models. *Hum. Cell* **2020**, *33*, 930–937. [CrossRef]
11. Buhrmann, C.; Shayan, P.; Banik, K.; Kunnumakkara, A.B.; Kubatka, P.; Koklesova, L.; Shakibaei, M. Targeting NF-κB Signaling by Calebin A, a Compound of Turmeric, in Multicellular Tumor Microenvironment: Potential Role of Apoptosis Induction in CRC Cells. *Biomedicines* **2020**, *8*, 236. [CrossRef] [PubMed]
12. Cacho-Diaz, B.; Garcia-Botello, D.R.; Wegman-Ostrosky, T.; Reyes-Soto, G.; Ortiz-Sánchez, E.; Herrera-Montalvo, L.A. Tumor microenvironment differences between primary tumor and brain metastases. *J. Transl. Med.* **2020**, *18*, 1. [CrossRef] [PubMed]
13. Nounou, M.I.; Elamrawy, F.; Ahmed, N.; Abdelraouf, K.; Goda, S.; Syed-Sha-Qhattal, H. Breast Cancer: Conventional Diagnosis and Treatment Modalities and Recent Patents and Technologies. *Breast Cancer* **2015**, *9*, 17–34. [CrossRef] [PubMed]
14. Zhao, Y.; Jing, Z.; Li, Y.; Mao, W. Berberine in combination with cisplatin suppresses breast cancer cell growth through induction of DNA breaks and caspase-3-dependent apoptosis. *Oncol. Rep.* **2016**, *36*, 567–572. [CrossRef] [PubMed]
15. Czabotar, P.E.; Lessene, G.; Strasser, A.; Adams, J.M. Control of apoptosis by the BCL-2 protein family: Implications for physiology and therapy. *Nat. Rev. Mol. Cell Biol.* **2014**, *15*, 49–63. [CrossRef]
16. Kadam, C.Y.; Abhang, S.A. Apoptosis Markers in Breast Cancer Therapy. *Adv. Clin. Chem.* **2016**, *74*, 143–193. [CrossRef]
17. Elmore, S. Apoptosis: A Review of Programmed Cell Death. *Toxicol. Pathol.* **2007**, *35*, 495–516. [CrossRef]
18. Parton, M.; Dowsett, M.; Smith, I. Studies of apoptosis in breast cancer. *BMJ* **2001**, *322*, 1528–1532. [CrossRef]
19. Hong, S.J.; Dawson, T.M.; Dawson, V.L. PARP and the Release of Apoptosis-Inducing Factor from Mitochondria; Madame Curie Bioscience Database. 2013. Available online: https://www.ncbi.nlm.nih.gov/books/NBK6179/ (accessed on 8 October 2020).
20. Aubrey, B.J.; Kelly, G.L.; Janic, A.; Herold, M.J.; Strasser, A. How does p53 induce apoptosis and how does this relate to p53-mediated tumour suppression? *Cell Death Differ.* **2018**, *25*, 104–113. [CrossRef]
21. Krajewski, S.; Thor, A.D.; Edgerton, S.M.; Moore, D.H.; Krajewska, M.; Reed, J.C. Analysis of Bax and Bcl-2 expression in p53-immunopositive breast cancers. *Clin. Cancer Res.* **1997**, *3*, 199–208.
22. Frenzel, A.; Grespi, F.; Chmelewskij, W.; Villunger, A. Bcl2 family proteins in carcinogenesis and the treatment of cancer. *Apoptosis* **2009**, *14*, 584–596. [CrossRef] [PubMed]
23. Slade, D. PARP and PARG inhibitors in cancer treatment. *Genes Dev.* **2020**, *34*, 360–394. [CrossRef] [PubMed]
24. Ossovskaya, V.; Koo, I.C.; Kaldjian, E.P.; Alvares, C.; Sherman, B.M. Upregulation of poly (ADP-Ribose) polymerase-1 (PARP1) in triple-negative breast cancer and other primary human tumor types. *Genes Cancer* **2010**, *1*, 812–821. [CrossRef] [PubMed]
25. Yu, S.W.; Andrabi, S.A.; Wang, H.; No, S.K.; Poirier, G.G.; Dawson, T.M.; Dawson, V.L. Apoptosis-inducing factor mediates poly(ADP-ribose) (PAR) polymer-induced cell death. *Proc. Nat. Acad. Sci. USA* **2006**, *103*, 18314–18319. [CrossRef]
26. Domagala, P.; Huzarski, T.; Lubinski, J.; Gugala, K.; Domagala, W. PARP-1 expression in breast cancer including BRCA1-associated, triple negative and basal-like tumors: Possible implications for PARP-1 inhibitor therapy. *Breast Cancer Res. Treat.* **2011**, *127*, 861–869. [CrossRef]
27. Schreiber, V.; Dantzer, F.; Amé, J.C.; De Murcia, G. Poly(ADP-ribose): Novel functions for an old molecule. *Nat. Rev. Mol. Cell Biol.* **2006**, *7*, 517–528. [CrossRef]
28. Bertheau, P.; Lehmann-Che, J.; Varna, M.; Dumay, A.; Poirot, B.; Porcher, R.; Turpin, E.; Plassa, L.F.; De Roquancourt, A.; Bourstyn, E.; et al. P53 in breast cancer subtypes and new insights into response to chemotherapy. *Breast* **2013**, *22*, S27–S29. [CrossRef]
29. Hanahan, D.; Weinberg, R.A. The hallmarks of cancer. *Cell* **2000**, *100*, 57–70. [CrossRef]

371

30. Wang, S.-C. PCNA: A silent housekeeper or a potential therapeutic target? *Trends Pharmacol. Sci.* **2014**, *35*, 178–186. [CrossRef]
31. Juríková, M.; Danihel, Ľ.; Polák, Š.; Varga, I. Ki67, PCNA, and MCM proteins: Markers of proliferation in the diagnosis of breast cancer. *Acta Histochem.* **2016**, *118*, 544–552. [CrossRef]
32. Varghese, E.; Samuel, S.M.; Sadiq, Z.; Kubatka, P.; Liskova, A.; Benacka, J.; Pazinka, P.; Kruzliak, P.; Büsselberg, D. Anti-Cancer Agents in Proliferation and Cell Death: The Calcium Connection. *Int. J. Mol. Sci.* **2019**, *20*, 3017. [CrossRef] [PubMed]
33. Rossi, P.; Difrancia, R.; Quagliariello, V.; Savino, E.; Tralongo, P.; Randazzo, C.L.; Berretta, M. B-glucans from Grifola frondosa and Ganoderma lucidum in breast cancer: An example of complementary and integrative medicine. *Oncotarget* **2018**, *9*, 24837–24856. [CrossRef] [PubMed]
34. Wasser, S.P. Medicinal mushrooms in human clinical studies. Part I. anticancer, oncoimmunological, and immunomodulatory activities: A review. *Int. J. Med. Mush.* **2017**, *19*, 279–317. [CrossRef]
35. Blagodatski, A.; Yatsunskaya, M.; Mikhailova, V.; Tiasto, V.; Kagansky, A.; Katanaev, V.L. Medicinal mushrooms as an attractive new source of natural compounds for future cancer therapy. *Oncotarget* **2018**, *9*, 29259–29274. [CrossRef] [PubMed]
36. Roda, E.; De Luca, F.; Di Iorio, C.; Ratto, D.; Siciliani, S.; Ferrari, B.; Cobelli, F.; Borsci, G.; Priori, E.C.; Chinosi, S.; et al. Novel medicinal mushroom blend as a promising supplement in integrative oncology: A multi-tiered study using 4t1 triple-negative mouse breast cancer model. *Int. J. Mol. Sci.* **2020**, *21*, 3479. [CrossRef]
37. Zmitrovich, I.V.; Belova, N.V.; Balandaykin, M.E.; Bondartseva, M.A.; Wasser, S.P. Cancer without Pharmacological Illusions and a Niche for Mycotherapy (Review). *Int. J. Med. Mush.* **2019**, *21*, 105–119. [CrossRef]
38. Bechtel, P.E.; Hickey, R.J.; Schnaper, L.; Sekowski, J.W.; Long, B.J.; Freund, R.; Liu, N.; Rodriguez-Valenzuela, C.; Malkas, L.H. A Unique Form of Proliferating Cell Nuclear Antigen Is Present in Malignant Breast Cells. *Cancer Res.* **1998**, *58*, 3264–3269.
39. Malkas, L.H.; Herbert, B.S.; Abdel-Aziz, W.; Dobrolecki, L.E.; Liu, Y.; Agarwal, B.; Hoelz, D.; Badve, S.; Schnaper, L.; Arnold, R.J.; et al. A cancer-associated PCNA expressed in breast cancer has implications as a potential biomarker. *Proc. Natl. Acad. Sci. USA* **2006**, *103*, 19472–19477. [CrossRef]
40. Coccini, T.; Manzo, L.; Roda, E. Safety Evaluation of Engineered Nanomaterials for Health Risk Assessment: An Experimental Tiered Testing Approach Using Pristine and Functionalized Carbon Nanotubes. *ISRN Toxicol.* **2013**, *2013*, 825427. [CrossRef]
41. Baghban, R.; Roshangar, L.; Jahanban-Esfahlan, R.; Seidi, K.; Ebrahimi-Kalan, A.; Jaymand, M.; Kolahian, S.; Javaheri, T.; Zare, P. Tumor microenvironment complexity and therapeutic implications at a glance. *Cell Commun. Signal.* **2020**, *18*, 59. [CrossRef]
42. Liu, Z.; Ding, Y.; Ye, N.; Wild, C.; Chen, H.; Zhou, J. Direct Activation of Bax Protein for Cancer Therapy. *Med. Res. Rev.* **2016**, *36*, 313–341. [CrossRef] [PubMed]
43. Wong, R.S. Apoptosis in cancer: From pathogenesis to treatment. *J. Exp. Clin. Cancer Res.* **2011**, *30*, 87. [CrossRef] [PubMed]
44. Yaacoub, K.; Pedeux, R.; Tarte, K.; Guillaudeux, T. Role of the tumor microenvironment in regulating apoptosis and cancer progression. *Cancer Lett.* **2016**, *378*, 150–159. [CrossRef] [PubMed]
45. Oltval, Z.N.; Milliman, C.L.; Korsmeyer, S.J. Bcl-2 heterodimerizes in vivo with a conserved homolog, Bax, that accelerates programed cell death. *Cell* **1993**, *74*, 609–619. [CrossRef]
46. Bodrug, S.E.; Aimé-Sempé, C.; Sato, T.; Krajewski, S.; Hanada, M.; Reed, J.C. Biochemical and functional comparisons of Mcl-1 and Bcl-2 proteins: Evidence for a novel mechanism of regulating Bcl-2 family protein function. *Cell Death Diff.* **1995**, *2*, 173–182.
47. Teixeira, C.; Reed, J.C.; Pratt, M.A. Estrogen promotes chemotherapeutic drug resistance by a mechanism involving Bcl-2 proto-oncogene expression in human breast cancer cells. *Cancer Res.* **1995**, *55*, 3902–3907.
48. Qiu, X.; Mei, J.; Yin, J.; Wang, H.; Wang, J.; Xie, M. Correlation analysis between expression of PCNA, Ki-67 and COX-2 and X-ray features in mammography in breast cancer. *Oncol. Lett.* **2017**, *14*, 2912–2918. [CrossRef]

49. Roda, E.; Bottone, M.; Biggiogera, M.; Milanesi, G.; Coccini, T. Pulmonary and hepatic effects after low dose exposure to nanosilver: Early and long-lasting histological and ultrastructural alterations in rat. *Toxicol. Rep.* **2019**, *6*, 1047–1060. [CrossRef]

**Sample Availability:** Samples of the compounds are available from the authors.

**Publisher's Note:** MDPI stays neutral with regard to jurisdictional claims in published maps and institutional affiliations.